National Library of Canada
Acquisitions and Bibliographic Services Branch
395 Wellington Street
Ottawa, Ontario
K1A 0N4

Bibliothèque nationale du Canada
Direction des acquisitions et des services bibliographiques
395, rue Wellington
Ottawa (Ontario)
K1A 0N4

Your file Votre référence

Our file Notre référence

NOTICE

The quality of this microform is heavily dependent upon the quality of the original thesis submitted for microfilming. Every effort has been made to ensure the highest quality of reproduction possible.

If pages are missing, contact the university which granted the degree.

Some pages may have indistinct print especially if the original pages were typed with a poor typewriter ribbon or if the university sent us an inferior photocopy.

Reproduction in full or in part of this microform is governed by the Canadian Copyright Act, R.S.C. 1970, c. C-30, and subsequent amendments.

AVIS

La qualité de cette microforme dépend grandement de la qualité de la thèse soumise au microfilmage. Nous avons tout fait pour assurer une qualité supérieure de reproduction.

S'il manque des pages, veuillez communiquer avec l'université qui a conféré le grade.

La qualité d'impression de certaines pages peut laisser à désirer, surtout si les pages originales ont été dactylographiées à l'aide d'un ruban usé ou si l'université nous a fait parvenir une photocopie de qualité inférieure.

La reproduction, même partielle, de cette microforme est soumise à la Loi canadienne sur le droit d'auteur, SRC 1970, c. C-30, et ses amendements subséquents.

Canada

UNIVERSITY OF ALBERTA

Flow and Erosion Around Bridge Piers

BY

Ferdous Ahm

A thesis submitted to the

Faculty of Graduate Studies and Research

in partial fulfillment of the requirements for the degree of

Doctor of Philosophy

in

Water Resources Engineering

DEPARTMENT OF CIVIL ENGINEERING

Edmonton, Alberta

Spring 1995

ISBN 0-612-01672-2

UNIVERSITY OF ALBERTA

RELEASE FORM

NAME OF AUTHOR: **Ferdous Ahmed**

TITLE OF THESIS: **Flow and Erosion Around Bridge Piers**

DEGREE: **Doctor of Philosophy**

YEAR THIS DEGREE GRANTED: **1995**

Ferdous Ahmed

Institute of Flood Control and Drainage Research
Bangladesh University of Engineering and Technology
Dhaka 1000, Bangladesh

Date: 14 Dec 1994

UNIVERSITY OF ALBERTA

FACULTY OF GRADUATE STUDIES AND RESEARCH

The undersigned certify that they have read, and recommend to the Faculty of Graduate Studies and Research for acceptance, a thesis entitled **Flow and Erosion Around Bridge Piers** submitted by **Ferdous Ahmed** in partial fulfillment of the requirements for the degree of **Doctor of Philosophy,**

in Water Resources Engineering.

.....
Dr. N. Rajaratnam (Supervisor)

.....
Dr. Peter M. Steffler (Co-supervisor)

.....
Dr. Faye E. Hicks

.....
Dr. John Shaw

.....
Dr. J. Don Scott

.....
Dr. Robert Ettema (External examiner)
University of Iowa, USA

Date: 13 Dec. 1994

To my parents

Abstract

The structure of flow and erosion around circular cylinders were investigated experimentally. Smooth and sand bed runs (with and without scour holes) were performed to study the effect of roughness and scour holes on the flow. Detailed measurements of velocity, pressure, bed shear stress and scour profiles were made.

The flow was profoundly influenced by the scour hole. A part of the flow went through the hole, relieving the accelerated flow around the cylinder and mitigating the skewing effect. The effect of the horseshoe vortex was indirect and through bringing more high velocity fluid to the cylinder sides. The downflow contributed to erosion only when the scour hole was well developed. In the downstream region, the deformed bed topography induced increased velocity, less fluctuation and reduced pressure drop. The roughness increased the downflow, bed shear stress amplification and the area of influence of the cylinder. It also mitigated the skewing effect.

The flow was analyzed in the light of three-dimensional turbulent boundary layer theories. Among various cross-flow models, Perry and Joubert's model gave the best result. All the near-wall similarity models gave almost identical results due to small cross-flow. The results were not very good.

Scouring was found to initiate in areas where the pressure gradient and the divergence of the bed shear vector were highest. Eight modes of sand movement were identified and their contribution in the erosion process was described. The performances of scour prediction methods were inadequate, with no improvement with time or theoretical basis noticed.

The shape of the scour hole remained similar with time and from experiment to experiment. In front of the cylinder, all linear scales were related to the scour depth but on the downstream side, different scales exhibited different trends and apparently depended on different parameters.

It was recommended that the dependence of various aspects of the flow (especially the horseshoe vortex system) and the erosion process explored here on different parameters be studied in greater detail.

Acknowledgments

I consider it a matter of great privilege and rare opportunity to work under the guidance of Professor N. Rajaratnam. His profound knowledge in fluid mechanics and keen interest in applying it to hydraulic problems have inspired me during the last few years. I am grateful to him for his support, encouragement and advice during all phases of this work.

Dr. P. M. Steffler read this thesis thoroughly and made many helpful comments and constructive criticisms. Dr. F. E. Hicks, Dr. J. Shaw and Dr. J. D. Scott acted as examiners and made numerous helpful suggestions. So did Dr. R. Ettema of the University of Iowa. All these improved the quality and clarity of this thesis. It is my pleasant duty to acknowledge all of these individuals and to thank them all. Any errors or omissions are, of course, mine.

In the laboratory, Seldon Lovell built all the experimental facilities. Martin Jasek helped me with the transducers. Shouhong Wu helped me in using the data acquisition programs. José Carlos de Araújo and other fellow students helped me in the laboratory from time to time. Olufemi Aderibigbe read part of the literature review on scouring and made helpful comments. I received a scholarship from the BUET-UofA Linkage Project during my studies at the UofA. It is my pleasure to record due appreciation for all of these.

I like to express my deepest gratitude to the people of Bangladesh for shouldering almost the entire cost of my education. I am also indebted to all the great minds whose philosophy, literature, music, and art I have enjoyed. The support and encouragement of my family members and friends are gratefully acknowledged. In particular, I like to thank my parents for all the nice things they have done for me and my wife for helping me cope with all the ups and downs that came with graduate studies.

Ferdous Ahmed

Table of Contents

4. Results, Analyses and Discussions

List of Tables

List of Figures

List of Symbols

Note: A list of frequently used symbols is given below. This does not include symbols that have been used only once or twice in this thesis, especially in connection to literature review. This omission will not cause any problem because such symbols have been defined at the appropriate places. For the sake of clarity, the notations used in the 3DTBL literature have been kept intact although sometimes it means using the same symbol for different quantities elsewhere. The dimensions are given in square brackets.

A	$\equiv \tan\beta$
$B, B_S, B_S^{'}$	constants in velocity profile equations
b	pier width perpendicular to the flow direction; equal to $2r$ in the case of circular cylinders [L]
b_w	wake width [L]
b'	$= b\cos\alpha + l\sin\alpha$
C	constant in the law of the wall
C_0	strength of horseshoe vortex as used in Qadar's equation [L^2/T]
c_f	local skin friction coefficient
C_p	pressure coefficient
C_{pb}	base pressure coefficient
C_D	drag coefficient
C_D^*	wake drag coefficient
D	sand diameter [L]
D_{50}	mean sand diameter [L]
D_s	scour depth measured below the water surface level [L]
D_{se}	value of D_s at equilibrium state [L]

d_s	scour depth measured below the ambient channel bed level [L]
d_{se}	value of d_s at equilibrium state [L]
e	$\equiv \tan \gamma_w$
F_b	bed factor used in regime theories ($=1.9\sqrt{D}$)
F_r	Preston tube calibration function for rough walls
F_s	Preston tube calibration function for smooth walls
$\mathbf{F}$	Froude number ($\equiv U_0 / \sqrt{g y_0}$)
$\mathbf{F}_c$	critical value of $\mathbf{F}$ corresponding to the initiation of sediment motion, *i.e.*, when $U_0 = U_{0c}$
$\mathbf{F}_p$	Pier Froude number ($= U_0 / \sqrt{gb}$)
$\mathbf{Fo}_v$	vortex Fourier number
f	silt factor used in regime theories ($=1.76\sqrt{D}$)
$f\langle\ \rangle$	function of
G	an universal function in Prandtl's model
$\mathbf{G}$	a sediment function ($\equiv (\rho_s - \rho) g D^3 / \rho \nu^2$)
g	acceleration due to gravity [L/T^2]; also an universal function in Prandtl's model
H	boundary layer shape parameter ($\equiv \delta_x^* / \theta_{xx}$) [L]
H_0	ambient value of H [L]
h	height of a cylinder [L]
h_0	static piezometric pressure head [L]
h_1, h_2, h_3	pressure heads sensed by different tubes of yaw or pitch probe [L] ; also metric coefficients used in the 3DTBL theories
h_{ref}	a known reference pressure head [L]

$\mathbf{i}, \mathbf{j}, \mathbf{k}$	unit vectors along (x, y, z) directions respectively
$K_1, \ldots, K_5$	coefficients of probe calibration
$K_{10}, \ldots, K_{50}$	coefficients of probe calibration
K_{ij}	curvature parameters
$K_{\alpha L}$	multiplying factor dependent on l / b and α
K_σ	ratio of $d_{se}(\sigma_g)$ to $d_{se}(\sigma_g = 1)$
k	scale of bed roughness [L]
k_s	Nikuradse's sand roughness [L]
k^+	$\equiv k u_* / \nu$
k_s^+	roughness Reynolds number ($\equiv k_s u_* / \nu$)
L	boundary layer development length [L]
L_p	center to center distance between piers [L]
l	length of pier in the longitudinal direction [L]
$\mathbf{N}$	$\equiv U_0 / \sqrt{(s_s - 1) g D}$; sediment number (also known as densimetric Froude number)
$\mathbf{N}_c$	critical value of $\mathbf{N}$ corresponding to the initiation of sediment motion, *i.e.*, when $U_0 = U_{0c}$
p	pressure [M/T^2/L]
P	piezometric pressure [M/T^2/L]
P_{00}	ambient piezometric pressure [M/T^2/L]
Q	volumetric water discharge rate [L^3/T]
$Q_{s,in}$	volumetric rate of sediment coming into scour hole [L^3/T]
$Q_{s,out}$	volumetric rate of sediment going out of scour hole [L^3/T]

q	discharge per unit width of the channel [$L^3/T/L$]; or magnitude of $\mathbf{q}$ [L/T]
q_d	"developed velocity" in Perry and Joubert's model [L/T]
q_e	value of q at the outer edge of the boundary layer [L/T]
q_{wake}	magnitude of $\mathbf{q}_{wake}$ [L/T]
q_{wall}	magnitude of $\mathbf{q}_{wall}$ [L/T]
q_*	shear velocity ($\equiv \sqrt{\tau_0 / \rho}$) [L/T]
$\mathbf{q}$	velocity vector in the 3DTBL theories [L/T]
$\mathbf{q}_e$	value of $\mathbf{q}$ at the edge of boundary layer [L/T]
$\mathbf{q}_{wake}$	wake component of $\mathbf{q}$ [L/T]
$\mathbf{q}_{wall}$	wall component of $\mathbf{q}$ [L/T]
q^+	$\equiv \hat{q} / \hat{q}_*$
$\hat{q}$	an equivalent velocity used in the 3DTBL theories [L/T]
$\hat{q}_*$	an equivalent shear velocity used in the 3DTBL theories [L/T]
$\mathbf{R}_p$	pier Reynolds number ($\equiv bU_0 / \nu$)
r	radius of a circular cylinder or pier [L]
r_0	radius of horseshoe vortex as used in Qadar's equation [L]
S	energy slope
S_{ij}	linear scales of scour hole with various subscripts (as defined in Section 4.6.2) [L]
$\mathbf{S}$	Strouhal number ($\equiv f b / U_\infty$)
$\mathbf{S}^*$	universal Strouhal number ($\equiv f b_w / V_w$)
S_s	specific gravity of sand
t	time since the scour starts [T]

t_{75}	time to reach 75% of d_{se} [T]
t_{90}	time to reach 90% of d_{se} [T]
t_{95}	time to reach 95% of d_{se} [T]
t_e	time to reach the equilibrium stage [T]
u,v,w	respectively longitudinal, vertical and transverse component of velocity vector $\mathbf{V}$; along (x,y,z) directions in the present experimental setup; along (ξ,η,ζ) directions in the 3DTBL theories [L/T]
u_e,v_e,w_e	values of (u,v,w) at the outer edge of the boundary layer along (ξ,η,ζ) directions in the 3DTBL theories [L/T]
u_x,u_y,u_z	respectively longitudinal, vertical and transverse component of velocity vector $\mathbf{q}$, along (u,v,w) directions in the 3DTBL theories [L/T]
u^+	$\equiv u/u_*$ or q/q_*
u_*	shear velocity ($\equiv \sqrt{\tau_0/\rho}$) [L/T]
u_{*0}	ambient shear velocity ($\equiv \sqrt{\tau_{00}/\rho}$) [L/T]
u_{*c}	critical shear velocity of sand ($\equiv \sqrt{\tau_c/\rho}$) [L/T]
u',v',w'	fluctuating components of (u,v,w) respectively [L/T]
U_0	depth-averaged velocity in a channel; section-averaged velocity in the present experiments [L/T]
U_{0c}	critical value of U_0 corresponding to initiation of general sediment transport [L/T]
U_{top}	velocity at the free surface [L/T]
U_y	ambient velocity at a distance y above channel bed [L/T]
U_∞	ambient velocity in the potential flow theory [L/T]
$\tilde{U}_{0c}$	critical value of U_0 that initiates scour near the pier as used by Kothyari *et al.* [L/T]

u_0	tangential velocity of the horseshoe vortex as used in Qadar's equation [L/T]
u_{top}	longitudinal velocity at the free surface [L/T]
u^+	$\equiv u / u_*$ or u / q_*
$\overline{u'^2}$, . . .	turbulent normal stresses [L^2/T^2]
$\overline{u'v'}$, . . .	turbulent shear stresses [L^2/T^2]
$\tilde{v}$	downflow in front of the cylinder [L/T]
$\tilde{v}_{max}$	maximum value of $\tilde{v}$ at any level [L/T]
V	magnitude of the velocity vector $\mathbf{V}$ [L/T]
V_{top}	magnitude of $\mathbf{V}_{top}$ [L/T]
V_w	$\equiv U_\infty(1 - C_{pb})^{1/2}$
$\mathbf{V}$	velocity vector
$\mathbf{V}_{top}$	velocity vector at the free surface
$\forall$	volume of scour hole [L^3]
X, Y, Z	$\equiv x / r, y / r, z / r$ in Appendix B
X_A , . . .	characteristic lengths of scour hole (as defined in Figure 4.6.1) [L]
x, y, z	directions of the Cartesian coordinate system in the 3DTBL theories; respectively longitudinal, vertical and transverse coordinate direction in the present experimental setup [L]
$\bar{x}, \bar{y}, \bar{z}$	dimensionless coordinates for scour hole (as defined in Section 4.6.2)
Y_B , . . .	characteristic lengths of scour hole (as defined in Figure 4.6.1) [L]
w^+	$\equiv w / w_*$
W	width of channel or flume [L]
y_0	depth of water in the channel [L]

y_p	location of the apex of Johnston's triangle [L]
y_r	regime depth [L]
y^+	$\equiv yu_* / \nu$ or yq_* / ν
y_p^+	$\equiv y_p q_* / \nu$
α	angle of attack of the flow with respect to pier axis; deflection of the main flow in the 3DTBL theories [degrees]
α_c	contraction ratio ($\equiv (L_p - b) / b$)
α_r	angle of repose of sand [degree]
β	an angle defined in Perry and Joubert's model [degree]
β_{expt}	experimental value of β [degree]
Δ	$\equiv (\rho_s - \rho) / \rho$
$\Delta\beta$	$\equiv \beta_{\text{expt}} - \beta$ [degree]
$\Delta\Gamma$	change in circulation [L^2/T]
Δp	difference between total and static pressure [$M/T^2/L$]
Δp_*	$\equiv \Delta p d^2 / 4\rho\nu^2$
Δ^*	Clauser's thickness parameter [L]
Δ_0^*	ambient value of Δ^* [L]
δ	boundary layer thickness [L]
δ^+	$\equiv \delta u_* / \nu$
δ^*	displacement thickness usually used with subscripts [L]
δ_x^*	displacement thickness in the x-direction [L]
$\delta_{x,0}^*$	ambient value of δ_x^* [L]
ε	energy thickness usually used with subscripts [L]

ϕ	angle of pitch [degree]
φ	velocity defect function
γ	angle of yaw in the 3DTBL theories [degree]
γ_w	angle of yaw at the wall [degree]
κ	von Karman's constant
Λ	mass flux across the flow depth per unit time per unit width [M/L/T]
Λ_0	ambient mass flux [M/L/T]
$\hat{\Lambda}$	mass flux ratio ($\equiv \Lambda / \Lambda_0$)
θ	angle of yaw [degree] ; also momentum thickness in the 3DTBL theories usually used with subscripts [L]
θ_{xx}	momentum thickness in the x-direction [L]
$\theta_{xx,0}$	ambient value of θ_{xx} [L]
θ_p	angle between pressure gradient vector and x-axis [degree]
θ_{top}	yaw angle of $\mathbf{V}_{top}$ [degree]
ρ	density of water [M/L^3]
ρ_s	density of sediment [M/L^3]
ν	kinematic viscosity of water [L^2/T]
Π	Coles' profile parameter
Π'	magnitude of $\bar{\Pi}'$
$\bar{\Pi}'$	profile parameter in Perry and Joubert's model
σ_g	geometric standard deviation ($\equiv \sqrt{D_{84.1} / D_{15.9}}$)
σ_u	standard deviation of u [L/T]
σ_V	standard deviation of V [L/T]

σ_ϕ	standard deviation of ϕ [degree]
σ_θ	standard deviation of θ [degree]
τ_0	shear stress on the channel bottom [M/T^2/L]
τ_{00}	ambient shear stress on the channel bottom [M/T^2/L]
τ_{0*}	$\equiv \tau_0 d^2 / 4\rho\nu^2$
τ_c	critical shear stress of sand [M/T^2/L]
τ_{0x}	component of τ_0 along x-direction [M/T^2/L]
τ_{0y}	component of τ_0 along y-direction [M/T^2/L]
$\tau_{0\xi}$	component of τ_0 along ξ-direction [M/T^2/L]
$\tau_{0\zeta}$	component of τ_0 along ζ-direction [M/T^2/L]
τ_{0c}	critical value of τ_0 corresponding to the initiation of sediment motion [M/T^2/L]
$\bar{\tau}_0$	bed shear stress vector [M/T^2/L]
τ_{HVS}	shear stress near the pier used by Kothyari *et al.* [M/T^2/L]
ξ, η, ζ	respectively longitudinal, vertical and transverse direction in the general curvilinear coordinate system of the 3DTBL theories [L]
ω	Coles' universal wake function
Ω	momentum flux across the flow depth per unit time per unit width [M/T^2]
Ω_0	ambient momentum flux [M/T^2]
$\hat{\Omega}$	momentum flux ratio ($\equiv \Omega / \Omega_0$)
ψ	stream function [L^2/T]
∇p	pressure gradient [M/T^2/L^2]

List of Abbreviations

2D	two-dimensional
2DTBL	two-dimensional turbulent boundary layer
3D	three-dimensional
3DTBL	three-dimensional turbulent boundary layer
AIAA	American Institute of Aeronautics and Astronautics
ASCE	American Society of Civil Engineers
ASME	American Society of Mechanical Engineers
BL	boundary layer
HVS	horseshoe vortex system
IAHR	International Association of Hydraulic Research
JSCE	Japanese Society of Civil Engineering
LDA	laser-doppler anemometry
LDV	laser-doppler velocimetry
LHS	left hand side (of an equation)
p.d.f.	probability distribution function
PFS	potential flow solution
POS	plane of symmetry
r.m.s.	root mean square
RHS	right hand side (of an equation)
TBL	turbulent boundary layer
TKE	turbulent kinetic energy

Chapter 1
Introduction

1.1 The Scour Problem

Scouring or the lowering of the river bed at a bridge site may be caused by several phenomena and is classified accordingly. *General scour* is the degradation of a river bed over a long reach as a response to a natural or man-made change. This kind of scour is generally treated as a part of the "aggradation and degradation" process of rivers. It results from the tendency of a river to attain a state of equilibrium. *Constriction scour* takes place when the active waterway is reduced for guiding the water through a narrower, more distinct section, thus making the bridge shorter and more economical. This type of scour is a result of the increase in velocity and bed shear stress. *Local scour* occurs as a result of the changed flow pattern around abutments and piers. General discussion about all types of scour may be found in standard texts on sediment transport (*e.g.*, Vanoni 1975, pp. 44-65; Raudkivi 1990, chapter 9).

It is also important to note that all types of scour can take place simultaneously at a particular location, but the magnitude of local scour is usually large compared to other types of scour and can be readily identified. The present work is concerned with local scour around bridge piers.

The scour of a river bed at a bridge pier may become deep enough to undermine the pier and eventually cause its collapse. Smith (1976) analyzed 143 incidents of bridge failures during the period from 1961 to 1975 from different countries, and found that 70 failed during floods of which 66 (46% of the total) could be attributed directly to scour.

More detailed information is available in the United States about bridges, their problems and countermeasures. A 1973 study of 383 bridge failures caused by floods showed that 25% involved pier damage and 72% involved abutment damage (Richardson *et al.* 1993). Brice and Bloggett (1978) indicated that the local scour at piers to be a problem of about equal incidence to that at abutments. In the USA, approximately 86% of the 577,000 bridges in the National Bridge Inventory are built over streams (Lagasse *et al.* 1991). A recent estimate shows $2.4 billion in annual flood loss due to bridge damage/failures (Rhodes and Trent 1993). Statistics from other countries are rare but are probably similar.

The main reason for the interest in the bridge scour problem seems to be the need to estimate the maximum scour that can occur during the lifetime of a bridge. Most of the studies, therefore, had the prediction of maximum scour depth as their primary objective. Small-scale experiments in the laboratory were the primary means of observing the scouring process and formulating prediction methods. Very few field data were available until recently. For the lack of anything better, these methods were applied in the field, but with little success. These scour formulas are listed among others by Melville (1973, 1975) and Dargahi (1982). The experimental investigations are summarized by Neill (1964a), Breusers *et al.* (1977) and Raudkivi (1991).

The understanding of the scouring process and the flow structure was impeded by the complexities of three-dimensional separated flows, sediment transport under complex flow conditions, and the interaction of the changing mobile bed with the flow and sediment transport. As a result, attempts at investigating the flow have been intermittent (*e.g.*, Bonasoundas 1973, Hjorth 1975, Melville 1975, Dargahi 1987). Nevertheless, it is generally acknowledged that a lack of knowledge about the flow has retarded the understanding of the scouring process and hence the accuracy in scour prediction.

It appears from previous works that while much effort has been given to experimental studies of local scour, analysis of the turbulent flow field associated with it has received only a small amount of attention. This is unfortunate because the flow is one of the basic and most important aspects of the whole problem. Once this aspect is reasonably understood, the chance of understanding other aspects increases enormously. With this motivation, the present study was undertaken to investigate the flow structure and to relate it to the scouring process.

1.2 Objectives of This Thesis

The principal objective of this study is to explore the flow structure around bridge piers in alluvial river beds. Secondary objectives are to elucidate the scouring process and to relate it to the flow structure.

The principal objective consists of the following components:

(a) A detailed literature survey on the scour problem and of other branches of fluid mechanics, in order to put the scour problem in broader perspective.

(b) Measurement of the detailed velocity, pressure and bed shear stress fields around a circular cylinder with and without the scour hole. Both smooth and rough (with and without a scour hole) beds were used.

(c) Analysis of the flow field in terms of the theories of three-dimensional turbulent boundary layers.
(d) Investigation of the similarities in velocity and bed shear distribution.
(e) Visualization of the flow pattern, especially the secondary flows and vortex systems.
(f) Study of the effect of bed roughness and scour hole on items (b-e).

The secondary objectives are as follow:

(g) Observation of the scouring process.
(h) Measurement of the geometric properties of scour hole with time.
(i) Application of similarity concepts to the scour hole development.
(j) Study of the effects of scouring process on the flow structure.
(k) Study of the effects of the flow structure on the erosion process and scour hole development.

1.3 Organization of This Thesis

Chapter 1 presents a general discussion on the scour problem and the objectives of this study.

Chapter 2 surveys the previous research on the local scour around bridge piers and other related branches of fluid mechanics that are helpful in understanding it. This chapter starts with the empirical scour prediction methods and the concepts behind them. It is followed by a literature review on the mechanism of local scour. Then the concepts of the three-dimensional boundary layers are reviewed. Next, the structure of the flow around a cylinder is discussed. The chapter concludes with a discussion on the different aspects of the scour problem and the available tools that can be used to study them.

Chapter 3 describes the equipment and the experimental procedures. A section on experimental errors and uncertainty estimate is included. Finally the experiments and the characteristics of the approach flows are given.

Chapter 4 presents the experimental results in detail. Analyses of and discussions on the results are also presented. A summary of the experimental results concludes this chapter.

Chapter 5 presents the conclusions drawn from this study. Recommendations for further studies are also given.

Chapter 2
Structural Features of the Problem and Literature Review

2.1 Introduction

As will be seen later in this chapter, the research on local scour at bridge piers has had limited interaction with the research on the flow around a cylinder. Local scour has been studied by people whose primary concern was, above all, to find an estimate of the scour depth. Efforts were also made to understand the scouring process, mainly with the help of dimensional arguments and small-scale experiments. However, attempts to study the flow, which is responsible for the scouring, were rather limited.

On the other hand, a large body of knowledge has been accumulated as workers in other branches of fluid mechanics studied the flow around surface-mounted obstacles more closely. Theories were put forward to explain the three-dimensional flow structure. A large number of experiments were also performed to study the complex flow around a variety of cylindrical obstacles.

The interaction between these two disciplines has been very limited. It appears that the two can be combined to get a better insight into the scouring process. The present work was based on this conviction. Thus the scope of the literature search was broadened to include a review of the pertinent knowledge that will be helpful in understanding the flow, and consequently the scouring process, around a circular cylinder. In addition to the past works on scour prediction methods and scouring process, this chapter includes reviews of the theories of three-dimensional turbulent boundary layers and the flow field around a circular cylinder.

2.2 Empirical Relations for Predicting Scour Depth

The study of the scour problem has largely been driven by the need to estimate the maximum scour depth that can occur at a bridge site during the life time of the bridge. The research, therefore, is directed to find the equilibrium scour depth d_{se} under certain design hydraulic conditions. A large number of equations for finding d_{se} as a function of other known parameters have been devised in the past. No attempt is made to list all of them here because a number of reviews are available (Neill 1964b; Melville 1973, 1975;

Dargahi 1982). The emphasis here is to highlight the underlying concepts behind the formulas.

Figure 2.2.1 shows different types of pier shapes and a definition sketch of the scour depth d_s. The scour can take place under two conditions depending upon the state of bed material movement in the undisturbed approach flow. *Live-bed* scour occurs when there is bed load transport in the approach flow and sediment is fed into the scour hole. In the absence of bed load transport and sediment feeding, so-called *clear-water* scour occurs. Other terms are defined when they are first used in the text.

The available formulas are grouped into four broad categories based on the nature of their underlying concepts as discussed in the following pages.

2.2.1 Experimental approach

Most of the early prediction methods were based upon experiments and model studies in the laboratory environment. These studies gave rise to a number of empirical formulas relating scour depth to pier geometry and approach flow.

Based on model studies under live-bed conditions, Laursen and Toch (1956) provided a graphical relationship between scour depth d_{se} and depth of approach flow y_0 both normalized by pier width b. Neill (1964a, b) fitted the following equation to the curve.

$$\frac{d_{se}}{b} = 1.5\left(\frac{y_0}{b}\right)^{0.3} \qquad [2.2.1]$$

The data were described well by this curve for a wide range of velocity (0.30-0.61 m/s), flow depth (60-275 mm) and sand size (0.44-2.25 mm). This led them to argue that the velocity and sediment size were of no consequence, which is inconsistent with recent studies. Further experiments were done under a standard (constant) flow condition (y_0 = 92 mm, U_0= 0.38 m/s, D_{50} = 0.58 mm, and b = 60 mm) to determine the effect of pier shape and alignment on the scour. The results were expressed in a chart giving the value of a multiplying factor $K_{\alpha L}$ as a function of l/b and α which was extensively used later by others.

Coleman (1971) based his analysis on the principle that in a problem of flow around an immersed body, the dependent variable (a pressure drop or a head loss, or d_{se} in the pier problem) may be best correlated to the Reynolds number, Froude number or both. He successfully correlated pier Froude Number, $F_p = U_0 / \sqrt{gb}$, to what he called the scour Euler number ($U_0 / \sqrt{2gd_{se}}$) in the following way

$$\frac{U_0}{\sqrt{2gd_{se}}} = 0.6\left(\frac{U_0}{\sqrt{gb}}\right)^{0.9} \qquad [2.2.2a]$$

using his own and Shen *et al.*'s (1969) data. This equation can be reduced to

$$\frac{d_{se}}{b} = 1.39\left(F_p\right)^{0.2} \qquad [2.2.3b]$$

He noted that Shen *et al.*'s (1969) data for a large (3 ft or 0.91 m) pier did not agree with this formula.

2.2.2 Regime approach

The regime theory of alluvial rivers was empirically formulated from observed data of the stable irrigation canals in the Indian subcontinent. This theory correlates different parameters which describe the conditions under which alluvial canals are stable. Efforts were made to extend the regime theory to scour problems. The essence of this approach is to express the scour depth in terms of the regime depth of a channel which is proportional to the 2/3 power of unit discharge.

Inglis (1949) gave the following equation (in SI units), now commonly known as the Inglis-Poona equation, which relates the total scour depth D_{se} $(= d_{se} + y_0)$ measured from the water surface to the unit discharge q in $m^3/s/m$ and pier width b in m.

$$\frac{D_{se}}{b} = 2.32\left(\frac{q^{2/3}}{b}\right)^{0.78} \qquad [2.2.3]$$

This was based on model studies carried out at the Poona Research Station. No distinction was made between clear water scour and live bed scour, although Thomas (1962) indicated that the experiments were run without sediment load. Chitale (1962) stated that the Inglis-Poona equation is not dimensionally correct and hence cannot be used in a general way.

Another regime equation, *i.e.*, the Inglis-Lacey equation, gives the scour depth simply as twice the Lacey's regime depth

$$D_s = 2 \times 1.55\left(\frac{Q}{f}\right)^{1/3} \qquad [2.2.4]$$

where Q is the total discharge in m^3/sec and f is the silt factor given by $1.76\sqrt{D}$, where D is the sediment size in mm. This equation was based on prototype data from 17 bridge sites in India. Arunachalam (1965) found that this equation could be in error as much as 50% when applied to other prototype data.

Blench (1962) used the following formula for rectangular rounded nose piers

$$\frac{D_{se}}{y_r} = 1.8\left(\frac{b}{y_r}\right)^{1/4} \qquad [2.2.5]$$

where the regime depth, $y_r = 1.48(q^2 / F_b)^{1/3}$ with q in $m^3/s/m$ and the bed factor, $F_b = 1.9\sqrt{D}$. He claimed that this formula fits reasonably well some Poona experiments with low sediment load.

Ahmad (1962) proposed a simple formula

$$D_{se} = Kq^{3/2} \qquad [2.2.6]$$

where the coefficient K is a function of boundary geometry, pier shape, bed material and velocity distribution. Based on field data, he suggested the value of K in the range of 1.7 to 2.0. For sites with severe flow curvature, higher values are to be used which are obviously difficult to estimate.

Arunachalam (1965) observed the difference in approach between regime equations which predict the total depth D_{se} as a function of discharge and Laursen's equations which relate the scour depth d_{se} to pier geometry and flow depth y_0. He argued that d_{se} depends only on y_0 and y_0 depends only on the discharge or velocity. In other words, velocity affects scour depth only through the flow depth. On this basis he was able to show that the equations of these two types can be converted to each other and, drawing heavily from various regime relationships, modified the Inglis-Poona equation to Laursen's form as:

$$\frac{d_s}{y_0} = 1.95\left(\frac{b}{y_0}\right)^{1/6} - 1 \qquad [2.2.7]$$

where $y_0 = 4.39(q^2 / f)^{1/3}$, and the silt factor, $f = 1.76\sqrt{D}$ with the sediment diameter D in mm. This equation was meant for rectangular piers under live-bed conditions. He verified his equation using prototype data from 11 railway bridge sites in India and found a mean deviation of 10%.

2.2.3 Theoretical approach

A number of efforts have been made to attack the problem on a more rational basis. The changes in the river flow induced by the presence of a pier and later the role played by the horseshoe vortex system in the scouring process were appreciated, and these facts were used to derive the prediction equations.

Laursen (1960) thought that the contraction due to a bridge pier could be considered a special case of the long contraction situation in rivers with a very short contraction length, and he modified the theoretical solution of long contraction to fit the bridge pier problem. For live-bed conditions, the following formula was derived where $m = 11.5$ gave the best correlation with experiments.

$$\frac{b}{y_0} = 5.5\frac{d_s}{y_0}\left[\left(\frac{1}{m}\frac{d_s}{y_0}+1\right)^{1.7} - 1\right] \qquad [2.2.8a]$$

This equation can be conveniently simplified as reported by Melville (1975) to

$$\frac{d_s}{b} = \sqrt{0.107m\left(\frac{y_0}{b}\right)} \qquad [2.2.8b]$$

Coefficients accounting for pier shapes and modes of bed load transport were also suggested along with the alignment coefficient $K_{\alpha L}$ introduced earlier by Laursen and Toch (1956).

Later Laursen (1963) generalized the long contraction analogy for clear water condition with the assumption that at equilibrium stage the bed shear stress in the scoured area is equal to the critical stress of the bed material τ_c. He used the Manning-Strickler relations to approximate the bed shear stress τ_{00} in the upstream region. He derived the following equation.

$$\frac{b}{y_0} = 5.5\frac{d_s}{y_0}\left[\frac{\left(\frac{1}{m}\frac{d_s}{y_0}+1\right)^{7/6}}{\left(\frac{\tau_{00}}{\tau_c}\right)^{1/2}} - 1\right] \qquad [2.2.9]$$

Laursen validated his equations with data from different sources. The validation was generally satisfactory. In particular, he demonstrated the difference between live-bed and clear-water scouring processes by using Chabert and Engeldinger's (1956) data.

Carstens (1966) applied similarity principles to different types of local scour. He hypothesized that the sediment transport rate could be functionally related to the forces acting on a particle and the geometry of scour hole. Assuming that the shape of the scour hole around a circular pier remains that of an inverted frustum of a cone during all the time, he analytically derived the following formula for live-bed condition

$$\frac{d_{se}}{b} = 0.546\left(\frac{N^2 - 1.64}{N^2 - 5.02}\right)^{5/6} \qquad [2.2.10]$$

where the sediment number, $\mathbf{N} = U_0 / \sqrt{(S_s - 1)gD}$. Only a few experimental data of Chabert and Engeldinger (1956) were used to derive the above equation. For clear-water condition, his analysis indicates no termination of the scouring process, and hence d_{se} cannot be predicted. This analysis was different from traditional ideas.

Shen *et al.* (1966) tried to estimate the scour depth in a more analytical fashion. With certain assumptions, they found that the reduction in circulation $\Delta\Gamma$ on the stagnation plane due to the presence of the pier of diameter b was proportional to bU_0. They reasoned that the scour depth depends on the strength of the horseshoe vortex system which in turn depends on $\Delta\Gamma$. Therefore d_{se} is a function of the pier Reynolds number, $\mathbf{R}_p$ (= bU_0 / ν). From regression analysis of their own data as well as those of Chabert and Engeldinger (1956), they found the following correlation for d_{se} in mm.

$$d_{se} = 0.0588 \left(\mathbf{R}_p\right)^{0.512} \qquad [2.2.11a]$$

This equation is not dimensionally homogeneous. They showed with certain assumptions that it can be approximated to the following form which they recommended for design purposes.

$$\frac{d_{se}}{y_0} = 2\left[\mathbf{F}^2\left(\frac{b}{y_0}\right)^3\right]^{0.215} \qquad [2.2.11b]$$

Equation [2.2.11a] was a best fit line. Later an enveloping line represented by the following equation was proposed (Shen *et al.* 1969) for estimating d_{se} in mm.

$$d_{se} = 0.2225 \left(\mathbf{R}_p\right)^{0.619} \qquad [2.2.12]$$

This relation was shown to satisfactorily match data points from a wide variety of sources and even a field data point. To account for the periodic fluctuation of scour depth associated with dune movement, it was suggested that one half on the dune height be added to the depth computed from the above equation.

For live-bed conditions, Sarma (1971) equated the bed load transport capacities of two sections -- one far upstream and the other at the side of the pier. The Meyer-Peter-Müller bed load function and the Vanoni-Brooks expression for energy slope [$S = 1.125\nu^2\mathbf{F}^{3/2} / gD^3$] were used. This analysis led to the following equation

$$\frac{d_{se}}{b} = f(\text{nose shape})\,\Lambda\left[\frac{y_0}{b}\frac{L_p}{b}\tan\alpha_r\right]^{1/2} \qquad [2.2.13]$$

where

$$\Lambda = \left[\frac{P^{5/12} J\mathrm{F}^{3/2} \frac{y_0}{D}}{J\mathrm{F}^{3/2} \frac{y_0}{D} + 0.188\left(P^{2/3} - 1\right)} \right]^{4/5} - P \quad ,$$

$$P = 1 - \frac{b}{L_p} = \alpha_c \qquad \text{, and}$$

$$J = \frac{8.5}{S_s - 1} \frac{v^2}{gD^3} \qquad .$$

Here L_p is the center to center distance between piers; α_r is the angle of repose; and f was a function of pier nose shape and was found = 1.0 for semi-circular, = 0.9 for 90° and = 0.6 for 60° triangular nose. Three values of L_p / b (7.5, 15 and 30) were used. It was noted that d_{se} becomes infinite for zero contraction and that further studies were required in this regard. This equation was tested only for a limited number of experiments.

Qadar (1981) correlated the characteristics of the horseshoe vortex to the approach flow under rigid bed conditions, and then expressed the mobile bed scour depth under similar conditions in terms of those characteristics. From experiments he found the following expressions for the vortex radius r_0 and the tangential velocity u_0 at a distance r_0 above the vortex center under rigid bed condition.

$$r_0 = 0.1b \qquad (\text{for } b < 0.025\text{m}) \qquad [2.2.14a]$$

$$r_0 = 0.1(b + 0.025) \qquad (\text{for } b \geq 0.025\text{m}) \qquad [2.2.14b]$$

$$u_0 = 0.092 b^{-0.5} U_0^{0.83} \qquad [2.2.14c]$$

Then the equilibrium scour depth on the mobile bed was correlated to the vortex strength, $C_0 = r_0 u_0$, by the following equation (in SI units).

$$d_{se} = 538 \left(C_0\right)^{1.28} \qquad [2.2.14d]$$

In the above equations, b, r_0 and d_{se} are in m, u_0 and U_0 are in m/s and C_0 is in m^2/s. This equation could predict the scour depth in a large number of rivers with good accuracy. It is apparently valid for clear-water conditions.

It was assumed by Baker (1978, 1980b) that the circulation around the vortex core remains constant while the vortex settles into the scour hole and finally reaches an equilibrium state. This assumption was used to express the bottom velocity of the vortex in terms of approach flow and this was then related to the forces acting on a particle

situated on the inclined face of the scour hole. This analysis finally led to the following equation

$$\frac{d_{se}}{b} = (a_1 \mathbf{N} - a_2)\tanh\left(a_3 \frac{y_0}{b}\right) \qquad [2.2.15]$$

where $\mathbf{N} = U_0 / \sqrt{(S_s - 1)gD}$, $a_1 = 4/\mathbf{N}_c$, $a_2 = 2$, $a_3 = 1$, and $\mathbf{N}_c$ is the value of $\mathbf{N}$ when general sediment motion begins. As elaborated later (Baker 1981), the coefficients depend mainly on $\mathbf{G}$ $[= (\rho_s - \rho)gD^3 / \rho\nu^2]$ and y_0 / b. This equation is for clear-water conditions and was validated by Baker's (1978) own and Chabert and Engeldinger's (1956) data.

2.2.4 Correlation approach

The difficulties in analyzing the flow around a pier and the scour mechanism have led some researchers to adopt data correlation or regression analysis techniques. This approach was apparently first used by Chitale (1962) who correlated the scour depth to the Froude number, $\mathbf{F} = U_0 / \sqrt{gy_0}$ and found the following equation for $\mathbf{F} < 0.5$.

$$\frac{d_{se}}{y_0} = -0.51 + 6.65\mathbf{F} - 5.49\mathbf{F}^2 \qquad [2.2.16]$$

Jain and Fisher (1980) did experiments with high velocities covering the higher flow regimes ($\mathbf{F} \approx 0.5$ to 1.5) and observed that the bed level degraded even in areas apparently away from the direct influence of the pier. This was also observed by Holmes (1974) in the case of real bridges. They argued that it is neither possible nor necessary to separate this scour from the local scour adjacent to the pier. The equilibrium under a live-bed condition is reached when the scouring power of the vortices equals the capacity of upstream flow to supply sediment into the scour hole. The latter is proportional to a power of $(\mathbf{F} - \mathbf{F}_c)$, where $\mathbf{F}_c$ $(= U_{0c} / \sqrt{gy_0})$ is the value of $\mathbf{F}$ corresponding to critical condition of sand movement. A multiple linear regression analysis on their data yielded:

$$\frac{d_{se}}{b} = 1.86\left(\frac{y_0}{b}\right)^{0.5}(\mathbf{F} - \mathbf{F}_c)^{0.25} \qquad [2.2.17]$$

This equation with a coefficient of 2.0 instead of 1.86 envelops most of the data points. This method tends to overestimate d_{se} for higher values of y_0 / b.

For clear-water conditions, Jain (1981) noted that maximum scour occurs when $\mathbf{F} \approx \mathbf{F}_c$ or at the threshold condition and therefore $\mathbf{F}$ becomes redundant. A regression analysis on the experimental data from different sources led to:

$$\frac{d_{se}}{b} = 1.41\left(\frac{y_0}{b}\right)^{0.3}(F_c)^{0.25} \qquad [2.2.18]$$

This equation with a coefficient of 1.84 instead of 1.41 forms an envelope to all data.

Kothyari *et al.* (1992a) argued that for clear-water conditions the excess shear stress near the pier that would be responsible for scour can be considered to be proportional to $\tilde{U}_{0c}$ where $\tilde{U}_{0c}$ is the critical value of U_0 that would initiate the scour near the pier. Regressing data from a wide variety of sources, they found that $\tilde{U}_{0c}$ is given by

$$\frac{\tilde{U}_{0c}^2}{\frac{\rho_s - \rho}{\rho} g D_{50}} = 1.2\left(\frac{b}{D_{50}}\right)^{-0.11}\left(\frac{y_0}{D_{50}}\right)^{0.16} \qquad [2.2.19a]$$

and the ultimate scour depth d_{se} is given by

$$\frac{d_{se}}{b} = 0.66\left(\frac{b}{D_{50}}\right)^{-0.25}\left(\frac{y_0}{D_{50}}\right)^{0.16}\left(\frac{U_0^2 - \tilde{U}_{0c}^2}{\frac{\rho_s - \rho}{\rho} g D_{50}}\right)^{0.4}\alpha_c^{-0.3} \qquad [2.2.19b]$$

where α_c is the contraction ratio. This equation is applicable when $U_0 > \tilde{U}_{0c}$; d_{se} is zero when $U_0 \le \tilde{U}_{0c}$. It gave less than 50% error for data from almost all available sources. It forms an enveloping curve if the coefficient 0.66 is replaced by 1.0.

For live-bed conditions, the following relation for d_{se} was found in a similar way (Kothyari *et al.* 1992b).

$$\frac{d_{se}}{b} = 0.99\left(\frac{b}{D_{50}}\right)^{0.67}\left(\frac{y_0}{D_{50}}\right)^{0.4}\alpha_c^{-0.3} \qquad [2.2.20]$$

All laboratory as well as field data used were within ±40% of it.

Froehlich (1988) assembled a large number of field data from various sources. The measurements were taken during sustained high floods and were assumed to represent equilibrium conditions. A linear regression analysis led to

$$\frac{d_{se}}{b} = 0.32 f(\text{shape})\left(\frac{b'}{b}\right)^{0.62}\left(\frac{y_0}{b}\right)^{0.46}F^{0.2}\left(\frac{b}{D_{50}}\right)^{0.08} \qquad [2.2.21]$$

where f = 1.0 for round-nosed, = 1.3 for square-nosed and = 0.7 for sharp-nosed piers; b' (= $b\cos\alpha + l\sin\alpha$) is the pier width projected normal to the approach flow. This equation is valid for live-bed conditions. For the design purpose, it was recommended that b be added to the d_{se} calculated from the above equation.

2.2.5 Design methods

After an extensive literature survey, Breusers *et al.* (1977) suggested the following design procedure.

$$\frac{d_{se}}{b} = f_1\left\langle\frac{U_0}{U_{0c}}\right\rangle\left[2\tanh\left(\frac{y_0}{b}\right)\right]f_2\langle\text{shape}\rangle f_3\left\langle\alpha,\frac{l}{b}\right\rangle \qquad [2.2.22]$$

in which $f_1 = 0$ for $U_0 / U_{0c} < 0.5$, $= (2U_0 / U_{0c}\text{-}1)$ for $0.5 < U_0 / U_{0c} < 1.0$, and $= 1$ for $U_0 / U_{0c} > 1.0$; f_2 is 1.0 for circular and rounded piers, 0.75 for stream lined piers, and 1.3 for rectangular piers; and $f_3\langle\alpha, l / b\rangle$ is the same as Laursen and Toch's $K_{\alpha L}$.

Baker (1981) tried to improve the above formula by introducing $[k_1 \tanh(k_2 y_0 / b)]$ in place of $[2\tanh(y_0 / b)]$. Analyzing Chabert and Engeldinger's (1956) data. it was found that k_1 and k_2 are functions of **G** $[= (\rho_s - \rho)gD^3 / \rho\nu^2]$.

$$k_1\langle\mathbf{G}\rangle = 1.625\left(3.55 - \log\left(\frac{\mathbf{G}}{10^3}\right)\right)\left(50\frac{D}{y_0} + 0.35\right) \qquad (\mathbf{G} < 355\times10^3) \quad [2.2.23a]$$

$$k_1\langle\mathbf{G}\rangle = 1.625\left(50\frac{D}{y_0} + 0.35\right) \qquad (\mathbf{G} > 355\times10^3) \quad [2.2.23b]$$

$$k_2\langle\mathbf{G}\rangle = 0.26\log\left(\frac{\mathbf{G}}{10^3}\right) + 0.32 \qquad (\mathbf{G} < 355\times10^3) \quad [2.2.23c]$$

$$k_2\langle\mathbf{G}\rangle = 1 \qquad (\mathbf{G} > 355\times10^3) \quad [2.2.23d]$$

Based on laboratory experiments, a fourth function f_4 was proposed by Elliot and Baker (1985) to account for the presence of other piers when a number of piers are used at a bridge site.

$$f_4\left\langle\frac{L_p}{b}\right\rangle = 1 + 1.79\left[\frac{L_p}{b} - 1\right]^{-0.695} \qquad (L_p / b < 4) \quad [2.2.24a]$$

$$f_4\left\langle\frac{L_p}{b}\right\rangle = 4.34 - 0.62\frac{L_p}{b} \qquad (7 < L_p / b < 4) \quad [2.2.24b]$$

$$f_4\left\langle\frac{L_p}{b}\right\rangle = 1 \qquad (L_p / b > 7) \quad [2.2.24c]$$

where L_p is the center to center distance between piers.

Melville and Sutherland (1988) proposed a design procedure based on the envelope curves drawn to data mostly from laboratory experiments. Local scour depth estimation was based upon the largest possible scour depth that can occur at a bridge pier, which was found from experiments to be 2.4 times the pier diameter. According to this method, this depth is reduced by using multiplying factors. These factors are designed to take into account the effect of velocity, depth of flow, sediment size, sediment gradation, pier shape and alignment, *etc.* Conservative estimates of scour depth are possible with this method. This method states

$$\frac{d_{se}}{b} = K_I K_y K_D K_\sigma K_S K_{\alpha L} \qquad [2.2.25]$$

where K_I is the flow intensity parameter and is a function of $[U_0 - (0.8U_{0ac} - U_{0c})] / U_{0c}$; U_{0ac} is the critical velocity beyond which armoring of the channel bed is impossible; K_y is the depth parameter and is a function of y_0 / b; K_D is the sediment size parameter and is a function of b / D_{50}; K_σ is the sediment gradation parameter and is a function of σ_g; K_S is the pier shape parameter and is given in a table; and $K_{\alpha L}$ is the pier shape and alignment parameter. All the functional relations were given. The function of K_σ is to replace D_{50} by D_{50a} when calculating K_D where D_{50a} is the mean size of the armoring coat assumed equal to D_{90}. The $K_{\alpha L}$ function of Laursen and Toch (1956) was recommended.

This widely used function $K_{\alpha L}$ does not always give correct results. Varzeliotis (1960) found that it grossly overestimated the alignment effect and the curve he found from experiments was concave upwards as opposed to Laursen and Toch's curve which is convex upwards. Recently, Mostafa *et al.* (1993) found that the general trend of this curve as originally proposed by Laursen and Toch is right although it can underestimate the scour in certain cases. For the design purpose, they proposed the following equation to compute $K_{\alpha L}$ which forms an envelope to all experimental data.

$$K_{\alpha L} = \left[\frac{l}{b}\sin\alpha + \cos\alpha\right]^{0.8} \qquad [2.2.26]$$

Recently Richardson *et al.* (1993) recommended an equation developed at the Colorado State University (CSU) which can be expressed as

$$\frac{d_{se}}{b} = 2\left(\frac{y_0}{b}\right)^{0.35} \mathrm{F}^{0.43} f_1\langle\text{bed condition}\rangle f_2\langle\text{shape}\rangle f_3\left\langle\alpha, \frac{l}{b}\right\rangle \qquad [2.2.27]$$

where f_1 = 1.1 for clear-water scour, plain bed, antidune flow and small dunes, = 1.1 to 1.2 for medium dunes, and = 1.3 for large dunes; f_2 = 1.0 for circular and round-nosed,

= 1.1 for square-nosed, and 0.9 for sharp-nosed piers; and f_3 was given in a table. The details of the derivation were not given.

2.2.6 Field applications

Most of the scour estimation methods were either derived from or in some other way checked against small-scale laboratory experiments. It is well documented (Melville 1975, Jain 1981, Dargahi 1982, Jones 1984) that the formulas give widely different values and cannot be depended upon to give reasonable estimates outside the parameter range within which they were first derived. No wonder, about 50% of the agencies surveyed by Highway Research Board (1970) indicated that they rely on "engineering judgment" rather than using any prediction formula. Neither it is surprising that Holmes (1974), after noting that none of the formulas was satisfactory, devised a new way to estimate scour at the bridge sites he was interested in.

It appears from the review of Breusers *et al.* (1977), who summarized the published field data available at that time, that the field application of the scour formulas has been hampered by the paucity of data which is a direct result of the difficulties of scour measurement under flood conditions. Furthermore the irregularities of natural rivers make it more difficult to measure/estimate other parameters. There is now a renewed interest in the USA, and to a lesser extent in other countries, in collecting field data. In the near future, this will provide the researchers with the much needed field data.

It is instructive to look at a few real world examples to appreciate the difficulties in scour prediction. Figure 2.2.2, based on Melville's (1975) calculations for bridges in New Zealand, shows how inaccurate predictions can be. Figure 2.2.3, taken from Ahmed *et al.* (1993) for a bridge over the South Saskatchewan river in Canada, shows that the scour depth may be different for different piers of the same bridge and that taking local flow conditions at different piers into consideration does not seem to improve the prediction.

There are very few published information about the suitability of scour formulas. Jain and Modi (1986) tested different formulas for 27 bridge sites in the Indian subcontinent. Surprisingly, Laursen and Toch's (1956) formula gave better results than even the regime equations. Posada and Nordin (1989) used 104 cylindrical pier data from the USA and the USSR and found that the design method of Melville and Sutherland (1988) is the best with no recorded scour depth more than 80% of the predicted value. The method of Froehlich (1988) also gave good estimates but consistently overestimated scour for larger piers. Generally not much confidence is placed on the formulas even

when they give good results, the reason being that, in the absence of sufficient field verification, it is difficult to separate actual performance from coincidence.

2.3 Mechanism of Local Scour

In this section, the scouring process will be described. Only the part of the flow structure which has been recognized as a scouring agent will be described here. More details will be presented in Section 2.5. Influence of different parameters on the local scour will also be discussed.

2.3.1 Scouring process

A bridge pier (or any other obstruction for that matter) placed in a flowing stream will change the flow, usually increasing the local sediment transport capacity of the flow near the pier and initiating local scouring of the bed. The sediment continuity equation applied to a control volume coinciding with the scour hole geometry will assume the following form.

$$\frac{d\forall\langle d_s\rangle}{dt} = Q_{s,out} - Q_{s,in} \qquad [2.3.1]$$

Here $\forall$ is the volume of the scour hole and is a function of scour depth d_s; $Q_{s,in}$ and $Q_{s,out}$ are the rates at which the sediment is being transported into and out of the scour hole respectively. This provides a basis for classifying local scours. When $Q_{s,in} = 0$, the scour is called *clear-water* scour. It occurs when the ambient flow is incompetent to move bed material and hence no bed material enters the scour hole from upstream. A scour is known as *live-bed* scour when the ambient flow is able to move bed materials and hence $Q_{s,in} \neq 0$. In theory, an *equilibrium state* is defined as a condition when $[Q_{s,out} - Q_{s,in}]$ is infinitely small and therefore d_s is essentially invariant with time. However, in reality this state is attained only asymptotically for clear-water scour. In the case of live-bed scour, due to the passage of bed forms over the scour holes, a time-averaged value of d_s has to be used to define the equilibrium state.

A bridge pier changes the flow in several ways (Figure 2.3.1). The unidirectional approach flow becomes strongly three dimensional. A re-distribution of velocity, pressure and shear stress takes place. Two principal vortex systems are created, namely the horseshoe and wake vortex systems. There also exist a downflow component along the upstream face of the pier and a upflow component along the downstream face. It is believed that the horseshoe vortex system and the downflow form the mechanism

necessary for loosening bed material, and that the arms of the horseshoe vortex system, the wake vortices and the upflow are responsible for transporting the loosened material out of the scour hole.

This picture of the flow structure and scouring process is generally accepted by those who have studied the pier scour problem. The description of the scouring process given by Melville (1975) is by far the most complete and comprehensive one so far. Moreover it does not contradict other studies on any important aspect. Therefore his ideas will be presented here with remarks by others when necessary.

When the approaching boundary layer separates as a result of the pressure gradient induced by the pier, the horseshoe vortex is created. This vortex system derives its vorticity from the vorticity already present in the approaching shear flow. The open ends of the vortex filaments stretch downstream for several diameters before becoming part of the general turbulence. The arms extending around the flanks of the pier oscillate with a frequency that was found to be the same as that of the shedding of the wake vortices by Melville (1975), which led him to the conclusion that these two vortex systems were not totally uncoupled. For the Reynolds number range of practical interest, the horseshoe vortex is shed periodically. Both Shen *et al.* (1969) and Melville (1975) noticed that this shedding is observable during scouring as slugs of sediments are being pulsed around the pier. The bed shear stress caused by the horseshoe vortex system in the reverse direction in front of the pier is responsible for eroding bed material. This stress was found to be at least 12 times the ambient bed shear in the experiments conducted by Hjorth (1975).

The horseshoe vortex is initially small in cross-section and comparatively weak. With the formation of the scour hole, however, the vortex rapidly grows in size and strength as additional fluid attains a downward component and the strength of downflow increases. Contours of bed shear stress, mean flow magnitudes and directions, and turbulent intensities on the bed of scour hole remains remarkably similar throughout its development after its initial formation. This is a direct result of the similarity of shape of the scour hole which is also apparent during its growth. As the scour hole enlarges, the circulation associated with the horseshoe vortex increases due to its expanding cross-sectional area, but with a decreasing rate. At the same time the magnitude of the downflow near the bottom also decreases. The armor coat, if it develops, helps to limit erosion. Ultimately an equilibrium is reached which for clear-water conditions signifies that the combination of the temporal mean bed shear and the turbulent agitation near the bed is no longer able to remove bed material from the area ahead of the cylinder and in the lower portion of the scour hole. For live-bed conditions, the equilibrium means that

the flow is just able to remove the sediment that is fed into the scour hole by the approach flow in a time-averaged sense.

The equilibrium defined in the above way does not necessarily mean a termination of the scouring activities downstream. Erosion may continue in the pile-up of bed materials downstream of the pier. This mound is progressively flattened and extended downstream by the flow out of the scour hole. This flow is directed into and out of the scour hole parallel to the downstream bed, and curves slightly inwards behind the cylinder.

There is difference in opinion as to where the initial scour begins. For example, Nakagawa and Suzuki (1975) stated that the scour begins at the sides of a circular pier and then gradually moves towards upstream face and finally to the stagnation plane. Bonasoundas (1973) found that it starts at a region located at 40° with the upstream stagnation plane. Melville (1975) found it around 100°. Earlier it was thought to begin right at the stagnation plane. One thing is clear, however, that irrespective of where the scour begins first, the maximum scour depth ultimately occurs in the upstream stagnation plane.

According to Baker (1980b), the vortex circulation remains more or less constant during the scouring process. He stated that Melville (1975) calculated the circulation based on the scour hole dimensions in equilibrium condition which is greater than the vortex core dimensions, and thus came to the wrong conclusion. Instead the vortex dimensions should have been used.

The scouring is facilitated also by the downflow component, which was apparently first measured by Shen *et al.* (1966). The magnitude of the downflow seems to be greater inside the scour hole. For small pier diameters, the downflow does not seem to affect the local scour in a direct manner (Tanaka and Yano 1967). The downflow may or may not penetrate into the horseshoe vortex but in either case the vorticity near the bed is intensified (Carstens and Sharma 1975). As the size of the horseshoe vortex increases, the tangential velocity and the shear stress exerted by the vortex on the bottom of the hole decrease.

Under the equilibrium condition of a scour hole, the shedding of wake vortices occurs at a value of the Strouhal number varying from 0.229 to 0.238; this is an increase of about 15% from that for the two dimensional case (Melville 1975). Individual vortices are convected downstream at a speed initially less than the approach velocity but becoming nearly constant and equal to the approach velocity at about eight cylinder diameters downstream. Each of the vortices acts with its low pressure center as a "vacuum cleaner" in removing bed material. During the initial period of scour activity,

bursts of sediment transporting away from the bed can be noticed with the generation of each vortex.

The wake vortex system is related to the so-called upflow component behind the pier. These two form an additional mechanism for scour behind the pier. For sharp-nosed piers with a relatively weak horseshoe vortex, the wake vortex system can even become the dominant erosion mechanism. This fact was demonstrated by the experiments of Shen *et al.* (1966). However when this occurs, the local scour develops to lesser depths than when the horseshoe vortex plays the dominant role (Ettema 1980).

2.3.2 Dimensional analysis

The parameters on which the scour depth (or any other characteristic of the scouring process) depends are as follows.

Fluid properties:
- density of water (ρ),
- kinematic viscosity of water (ν), and
- acceleration due to gravity (g).

Sediment properties:
- representative size (D_{50}),
- size distribution (σ_g),
- density of sediment (ρ_s),
- critical shear stress (τ_c) or critical shear velocity (u_{*c}),
- angle of repose (α_r), and
- other grain properties and cohesion of material.

Flow properties:
- approach flow depth (y_0),
- average velocity (U_0),
- bed shear stress (τ_{00}) or friction velocity (u_{*0}),
- angle of attack (α), and
- longitudinal and transverse distribution of velocity.

Pier properties:
- representative size (b),
- shape (both above and under bed level),
- surface condition and roughness,
- contraction ratio (α_c), and
- any protection device.

Time:
- time since the scour starts (t).

The above list is by no means complete. One can always think of other potential situations that will introduce new variables to it such as unsteady flow, layered bed material, presence of other piers and abutments, and so on.

Obviously so many variables can make the interpretation of a dimensional analysis exceedingly difficult. Therefore, a pragmatic way is to consider only a minimum number of variables so that the essential physics of the scouring process can be studied under the simplest but reasonably representative conditions possible. The following assumptions allow such an approach.

- The sediment is uniform, round and cohesionless.
- The approach flow is fully developed rough turbulent in nature and the resistance is due only to the grain roughness so that the flow can be fully described by y_0, U_0 and τ_{00}. There is no variation of the approaching velocity in the transverse direction.
- Only a solitary circular pier in a wide channel is considered so that α_c is negligible. The pier is perfectly smooth. No protection device is considered.

Then the scour depth can be expressed functionally as:

$$d_s = f\langle \rho, \nu, g, D_{50}, \rho_s, u_{*c}, \alpha_r, y_0, U_0, u_{*0}, b, t \rangle \qquad [2.3.2]$$

Taking ρ, D_{50} and u_{*0} as the repeating variables, a dimensional analysis leads to the following.

$$\frac{d_s}{D_{50}} = f\left\langle \frac{D_{50}u_{*0}}{\nu}, \frac{u_{*0}^2}{gD_{50}}, \frac{\rho_s - \rho}{\rho}, \frac{u_{*c}}{u_{*0}}, \alpha_r, \frac{y_0}{D_{50}}, \frac{U_0}{u_{*0}}, \frac{b}{D_{50}}, \frac{u_{*0}t}{D_{50}} \right\rangle \qquad [2.3.3]$$

It seems reasonable to assume that for natural sands, ρ_s and α_r are approximately constant; so these terms may be omitted from the above equation. Further, the dimensionless terms may be combined and rearranged so that their physical significance becomes more apparent. Thus we get

$$\frac{d_s}{b} = f\left\langle \frac{D_{50}u_{*c}}{\nu}, \frac{u_{*c}^2}{\frac{\rho_s - \rho}{\rho} gD_{50}}, \frac{u_{*0}}{u_{*c}}, \frac{y_0}{b}, \frac{U_0 b}{\nu}, \frac{b}{D_{50}}, \frac{tD_{50}\nu}{b^3} \right\rangle \qquad [2.3.4]$$

This may be considered as the basic functional form for scour depth; the following explains the choice of this particular set of parameters. As pointed out by Breusers *et al.* (1977), the first two terms on the RHS of this equation are the classical parameters of bed load transport phenomenon. These are also related by the Shields' diagram; so one of them may be dropped. The third parameter indicates the competence

of the approach flow to move bed material, which influences the scouring process. This is often replaced by U_{0c} / U_0. It may be noted that if u_{*c} is considered as a function only of D_{50} then two of the first three parameters may be dropped.

The structure of the local flow around the pier depends primarily on the ratio of the boundary layer thickness (herein the depth of flow) to the pier diameter (y_0 / b) and the pier Reynolds number ($U_0 b / \nu$). These include the dimension, oscillation and shedding frequency of the horseshoe and wake vortex systems; the dimensions and characteristics of the wake and the approaching skewed flow; and the flow inside the scour hole.

The ratio of the pier diameter to sand size (b / D_{50}) has been found to be a parameter of influence in the scouring process (Ettema 1980; Raudkivi and Ettema 1983, 1985). Ettema (1980) has shown with partial success that $tD_{50}\nu / b^3$ may be used as a non-dimensional time. It has been difficult to find a suitable time scale for local scours. In the cases of jet and groyne scours, the time to reach the equilibrium condition, the time when the $d_s - \log t$ plot deviates from a straight line, and the time to reach a certain percentage of d_{se} have been used with varying degrees of success (*e.g.*, Rajaratnam and Berry 1977; Rajaratnam and Beltaos 1977; Rajaratnam and Nwachukwu 1983b). It is unknown what would work for a pier scour. However, Ettema's (1980) ideas may be tentatively used.

Thus Equation [2.3.4] contains the most important parameters for pier scour. Other parameters that were dropped as a result of simplifying assumptions and that are necessary for accounting for special circumstances may be added to this equation as the need arises. Functional relations derived by others (*e.g.*, Breusers *et al.* 1977; Baker 1978) may be considered as special cases of it. Baker (1978) has pointed out some drawbacks and mistakes in the dimensional analyses of others. It should be noted that a different choice of repeating variables and subsequent manipulation can lead to a very different set of dimensionless parameters. The functional relation for d_{se} most used is as follows for circular piers:

$$\frac{d_{se}}{b} = f\left(\frac{U_0}{U_{0c}}, \frac{y_0}{b}, \frac{b}{D_{50}}\right) \qquad [2.3.5]$$

For more common rectangular piers, Laursen and Toch's (1956) shape and alignment parameter $K_{\alpha L}$ is widely used with it. As will be explained in the following sections, whether a sand forms ripples or not is of fundamental importance in the scouring process. So this characteristic of a sand should be included in the above equations. In the bridge scour literature, sands with $D_{50} < 0.6$ to 0.7 mm are generally assumed to be ripple-

forming. On the other hand, many sets of parameters have been proposed to mark the delineation of different bed forms, although none has been accepted at the exclusion of others (Raudkivi 1990, pp. 80-109). Therefore, the D_{50} criterion may be used for the time being.

2.3.3 Effect of approach flow

The velocity, depth, bed shear stress, and the angle of attack are the main components of the approach flow. The effects of the angle of attack are usually taken care of by empirically determined coefficients such as Laursen and Toch's $K_{\alpha L}$. The flow in rivers generally follows the law of the fully turbulent rough flow regime; hence its effect should not vary much from one river to another. The effect of the turbulence in the approach flow on scour is unknown and is generally assumed to be of secondary importance. The effects of longitudinal and transverse variation of velocity have not been investigated so far. The effects of velocity (U_0), shear stress (τ_{00}) and depth (y_0) on the equilibrium scour depth (d_{se}) have been studied in detail and will be described here briefly.

The bed shear stress determines the mode of bed load transport and the bed forms. Hence it affects the scouring process in a fundamental way, so much so that local scour classification is generally based on it (clear-water and live-bed scours, as defined earlier). As shown in Figure 2.3.2(a), d_s develops slowly with time and reaches the equilibrium value d_{se} only asymptotically under clear-water conditions. For live-bed conditions, it reaches d_{se} very quickly but the scour depth keeps on fluctuating in response to the passage of bed forms over the scour hole. Thus a time-averaged value of d_s is necessary to determine d_{se} over a time period large compared to the time taken by the bed forms to travel a distance equal to their wavelength.

The variation of d_{se} with U_0 is shown in Figure 2.3.2(b). Since the experiments of Chabert and Elgeldinger (1956), if not earlier, it has been known that d_{se} increases with U_0 and reaches the peak at around $U_0 = U_{0c}$, where U_{0c} is the critical velocity corresponding to the initiation of sediment motion. The reduction in d_{se} after the peak was about 10% of the maximum d_{se} at the peak in the experiments conducted by Shen *et al.* (1966). This led many to believe that the maximum possible scour occurs just before the general sediment transport begins. Later with more data at higher velocities, Melville (1984) demonstrated that two maxima are in fact possible. The first is the *threshold peak* corresponding to the threshold of sediment motion as discovered earlier; and the second is the *transition flat bed peak* associated with the transition flat bed condition. For *ripple-forming* sand (finer sand with $D_{50} < 0.6$ to 0.7 mm), the second peak is higher than the

first one, but the first peak is higher in the case of coarser *non-ripple-forming* sand (Figure 2.3.2(b)). Earlier Chee's (1982) data showed a similar trend. Later Chiew (1984) and Chiew and Melville (1987, 1989) provided further experimental evidence for both uniform and non-uniform sands.

The lower first peak for ripple-forming sands may be explained by the fact that ripples start forming well before the threshold condition, at about when $U_0 \approx 0.6U_{0c}$. This initiates the bed load transport and hence the sediment feeding into the scour hole. Thus the material removed from the hole is replenished to a certain extent, resulting in a smaller scour depth. Immediately after the threshold condition, this replenishment starts for the non-ripple-forming sands and becomes larger for ripple-forming sands. This causes d_{se} to go down slightly.

Melville (1984) explained the formation of the second peak in terms of the variation of bed load transport and bed form movement with increasing velocity. The formation of bed features (ripples and dunes) is associated with a large increase in bed shear stress which in turn is responsible for an increase in the amount of sediment fed into the scour hole with the effect of reducing the scour depth. The transportation of the bed material into the hole can be considered to have a steady and a fluctuating components with the periodicity of the fluctuating component being related to the wavelength of bed features. With increasing velocity, the scour depth eventually reaches a minimum value. This minimum probably occurs at the stage of the minimum dune wavelength when the scour hole is subjected to frequent avalanches of sediment and there is insufficient time for the removal, from the scour hole, of the sediment dumped into it during one avalanche, before the next avalanche arrives. Thereafter, the dune wavelength increases and the frequency of avalanches decreases. The form drag also starts diminishing. As a result, the scour depth increases and finally reaches the second peak when the form drag vanishes, *i.e.*, at the transition flat bed peak. It is called a peak because the limited amount of data available in this range of velocity indicates a decreasing trend afterwards. More data are needed, however, to establish it on a firm basis.

The general effect of the depth of flow is shown in Figure 2.3.2(c). As shown by Raudkivi and Ettema (1983), at shallow flow depths, d_{se} / b increases with y_0 / b but as y_0 / b increases, d_{se} / b eventually becomes independent of y_0 / b, generally at $y_0 / b \approx 3$ (≈ 1 for fine sands and ≈ 6 for course sands). Raudkivi and Ettema (1983) offered the following explanation:

> "The presence of the pier causes a surface roller around the pier, like a bow wave to a boat, and a horseshoe vortex at the base of the pier. These two rollers have opposite sense of rotation. In principle, as long as the two rollers do not interfere with each other, the local scour depth in insensitive to depth of flow. With decreasing depth of flow the surface roller becomes the more dominant and finally eliminates the horseshoe vortex altogether, *i.e.*, the vortex at the base of the pier changes direction of rotation for small depth."

It is not clear whether they actually observed this phenomenon or were speculating about what might happen. However a much simpler explanation can be inferred from Baker's (1980a, 1985) observation that the size of the horseshoe vortex (and hence its scouring potential) increases with cylinder height up to about three times the cylinder diameter before becoming independent of it.

2.3.4 Effect of the pier

Among the different parameters describing the size and shape of a pier, the width of it (b) normal to the approach flow influences the scour depth the most. Smooth, circular, uniform cylinders have been used most frequently in the experiments and are taken as a standard. Effects of other shapes are generally taken care of by experimentally determined coefficients. The following discussion pertains to circular cylindrical piers unless otherwise stated.

The pier width b affects the time required for d_s to reach the equilibrium depth d_{se}. The amount of sediment removed from a scour hole is proportional to the cube of the pier diameter. Therefore the larger the pier, the larger the scour volume and the longer the time required to scour it. Ettema (1980) used $tD_{50}v / b^3$ as a non-dimensional time.

The effect of the flow depth to pier width ratio y_0 / b has been discussed earlier. The effect of pier to sediment size, b / D_{50}, is shown in Figure 2.3.2(d). In this figure K is the ratio of scour depth affected by the relative size b / D_{50} to that independent of it. It may be seen that the scour depth becomes independent of sediment size for $b / D_{50} > 50$. For smaller ratios the scour depth decreases because the sediment becomes too large relative to the width of the groove excavated by the downflow. The coarser grains which accumulate on the bed of the groove also make it more porous and allow more of the downflow to penetrate and dissipate its energy in the bed (Raudkivi 1986). This effect would be rare in natural rivers but appears quite frequent in laboratory flumes.

2.3.5 Effect of bed material

The effect of ripple-forming and non-ripple-forming uniform sediments on the scouring process has already been discussed earlier. Here the effect of size and gradation will be discussed. The effects of armoring and layered layers have been extensively studied by Ettema (1980) [also Raudkivi and Ettema (1982, 1985)], and cannot be described adequately in a short space; the original papers may be consulted.

The effect of grain size relative to pier diameter is shown in Figure 2.3.2(e). It can be seen that d_{se} / b is unaffected by particle size as long as $b / D_{50} > 50$. For smaller values the grains are large compared to the scour hole. Consequently the erosion process is impeded. The initial phase of scour develops similarly for most values of b / D_{50}, but the principal erosion phase and the equilibrium depth are affected by the ratio of b / D_{50}. Raudkivi and Ettema (1983) identified four regions in their experimental results as follows.

[1] $b / D_{50} > 130$: The sediment is fine relative to the pier diameter. The sediment is entrained from the groove by the downflow and from the slope by the horseshoe vortex until an equilibrium state is reached.

[2] $130 > b / D_{50} > 30$: The sediment is of an intermediate size. The sediment is entrained mainly from the groove with only a limited entrainment under the horseshoe vortex. The supply of sediment to the groove is accomplished by sliding down the slope.

[3] $30 > b / D_{50} > 8$: The sediment is coarse relative to the pier diameter and relative to the downflow. A significant proportion of energy of the downflow is dissipated in the coarse bed material at the base of the scour hole.

[4] $b / D_{50} < 8$: The sediment grains are so large that the erosion phase does not develop. The scour is mainly due to the entrainment at the flanks of the pier.

This distinct trend is apparent only for non-ripple-forming sediments. For ripple forming sediments, the scour depth tends to be lower and the results are more scattered.

The general effect of the sediment gradation measured in terms of the geometric standard deviation $\sigma_g = \sqrt{D_{84.1} / D_{15.9}}$ on d_{se} is shown in Figure 2.3.2(f). The scour depth decreases dramatically with the non-uniformity of sediments because armors form

in the case of non-uniform sediments and prevent further scouring. The gradation affects only d_{se}, not the time to reach it (Raudkivi 1991). Ettema and Raudkivi (1983) stated that three straight line segments on a $d_s - \log t$ plot define the scouring process. The first segment is associated with the rapid scouring by the downflow. The middle segment describes the phase when the horseshoe vortex grows in size and strength. The last segment indicates the near-equilibrium state. However, as the value of σ_g increases, the middle segments gradually vanish, indicating that the armor formation limits the growth of horseshoe vortex and that most of the scouring is done by the downflow in the case of well graded sediments.

2.3.6 Time evolution of scour

The general pattern the scour depth development with time as shown in Figure 2.3.2(a) is more or less universally accepted. However, despite several attempts, a suitable time scale that would collapse data from different experiments has yet to be found. A detailed discussion of earlier works is presented by Ettema (1980). Recently, more work has also been done to devise computational schemes that would describe the temporal development of d_s. Here more emphasis will be given to recent works.

Ettema (1976, 1980) identified three phases in the development of scouring. During the *initial phase*, the bed material at the flanks of the pier is eroded by the accelerated flow. The second phase starts when the horseshoe vortex starts to dominate the scouring process and the main erosion occurs at the pier front. This is known as the *principal eroding phase*. It is followed by the *transition to final equilibrium phase* as the horseshoe vortex ceases to excavate further and an equilibrium is reached. Each of the phases can be represented approximately by a straight line in a $d_s - \log t$ graph.

Shen *et al.* (1963) found empirically that d_s / d_{se} can be expressed as

$$\frac{d_s}{d_{se}} = f\left\langle \frac{t}{t_e}, \mathbf{F} \right\rangle \qquad [2.3.6]$$

where t_e is the time required to reach the equilibrium state. This was based on experiments in the subcritical range ($\mathbf{F}$ = 0.105 to 0.935). Another empirical relation proposed later by Shen *et al.* (1966) may be written as

$$\frac{d_s}{y_0} = 2.5\mathbf{F}^{0.4}\left(\frac{b}{y_0}\right)^{0.6}\left[1 - \exp\left(aE^2\right)\right] \qquad [2.3.7]$$

where $a = 0.026\exp(-2.932 y_0)$ with y_0 in feet,

and $$E = \left(\frac{b}{y_0}\right)^{1/3} \mathbf{F}^{1/3} \ln\left(\frac{U_0 t}{y_0}\right) \quad .$$

Both of these equations are for both clear-water and live-bed conditions. Other empirical equations include

$$\frac{d_s}{d_{se}} = 1 - \exp\left[-0.028\left(\frac{tU_0}{b}\right)^{1/3}\right] \qquad [2.3.8]$$

of Franzetti *et al.* (1982); and

$$\frac{d_s}{d_{se}} = \left(\frac{t}{t_e}\right)^a \qquad [2.3.9]$$

of Breusers (1965) with $a = 0.38$ and Davies and Davis (1980) with $a = 0.1$

Carstens (1966) assumed the shape of the scour hole to be similar to that of a inverted frustum of a cone with a slope equal to the angle of repose of the bed material (α_r) so that for clear water condition

$$Q_{s,out} = \frac{d\forall}{dt} = \frac{\pi}{\tan\alpha_r}\left(\frac{d_s}{\tan\alpha_r} + b\right) d_s \frac{dd_s}{dt} \qquad [2.3.10a]$$

From the data of Chabert and Engeldinger (1956), the following empirical relation for bed material transport was found.

$$\frac{Q_{s,out}}{U_0\left(\frac{b+2d_s}{\tan\alpha_r}\right)D_{50}} = 1.3\times10^{-5}\left[\mathbf{N}^2 - \mathbf{N}_c^2\right]^{5/2}\left(\frac{d_s}{b}\right)^{-3} \qquad [2.3.10b]$$

Eliminating $Q_{s,out}$ between these two equations and integrating with respect to time and letting $d_s = 0$ when $t = 0$, the following relation was obtained.

$$\begin{aligned} 4.14\times10^{-6}\left[\mathbf{N}^2 - \mathbf{N}_c^2\right]^{5/2}\left(\frac{D_{50}}{b}\right)\left(\frac{U_0 t}{b}\right) &= \frac{1}{\tan\alpha_r}\left(\frac{d_s}{b}\right)^5 \\ &+ \frac{1}{16}\left(\frac{d_s}{b}\right)^4 - \frac{\tan\alpha_r}{24}\left(\frac{d_s}{b}\right)^3 + \frac{\tan\alpha_r}{32}\left(\frac{d_s}{b}\right)^2 \\ &- \frac{\tan^3\alpha_r}{32}\left(\frac{d_s}{b}\right) + \frac{\tan^4\alpha_r}{64}\ln\left(\frac{2}{\tan\alpha_r}\frac{d_s}{b} + 1\right) \end{aligned} \qquad [2.3.10c]$$

This equation gave good results for some of Chabert and Engelinger's experiments. This analysis can be extended to the case of live-bed condition if a relation similar to Equation

[2.3.10b] for $Q_{s,in}$ can be found. However, necessary data were not given by Chabert and Engeldinger; so Carstens could not derive the equation for live-bed conditions.

Nakagawa and Suzuki (1975) applied the concept of sediment continuity in the scour hole with the assumption that all sediment is removed from the hole via the groove (the nearly flat bottom of the hole adjacent to the pier) and that all sediment is fed into the groove by sliding down the sloping sides of the hole. A simple geometry of the hole that remains similar throughout the scour development was also assumed. The amount of the sediment sliding down was related to dd_s / dt while the amount removed through the groove was related to the local bed shear stress by Paintal's (1971a, b) stochastic bed load model. The local shear was related to the approach flow through the vorticity conservation principle and a few assumptions about the size and shape of the horseshoe vortex. The following equation was finally derived.

$$\frac{d_s}{b}+\frac{1+2K}{2(1+K)\tan\alpha_r}\left(\frac{d_s}{b}\right)^2+\frac{\varepsilon}{3(1+K)\tan^2\alpha_r}\left(\frac{d_s}{b}\right)^3=\frac{K}{1-\lambda}\frac{A_2}{A_1}p_s\frac{D}{b}t \quad [2.3.11]$$

Here p_s is the probability that a sand grain would move under the action of a certain dimensionless shear stress as given by Paintal (1971a, b) and λ is the porosity. The following values of the constants were used: $K = 0.25$, $A_1 = \pi/4$, $A_2 = \pi/6$, and $\varepsilon = 1.0$. This equation described the principal erosion phase quite well but deviated substantially near the equilibrium stage. This model is apparently for clear-water conditions.

Another scheme was proposed by Hjorth (1976) with very similar assumptions but using Einstein's (1950) probabilistic bed load theory. The rate of scour was further assumed to be proportional to $Q_{s,in} / Q_{s,out}$. This model was meant for both clear-water and live-bed conditions. However, the computational procedure does not seem very clear and its validation by Chabert and Engeldinger's (1956) data was somewhat incomplete.

Falcón and Uribe (1987) assumed that the sediment concentration C_s in the scour hole is the same everywhere and that it varies with time as

$$C_s(t) = (C_{s0} - C_{se})[1 - d_s / d_{se}]^p + C_{se} \quad [2.3.12a]$$

where C_{s0} is its initial value assumed equal to that of the bed; C_{se} is its value at the final equilibrium state; and p is a constant to be determined experimentally. For clear-water conditions, $C_{se} = 0$. The rate of change of the scour volume was related to the sediment in suspension in the hole and the sediment that leaves the hole with a characteristic velocity $\bar{W}$ which, from dimensional considerations and regression analysis on

experimental data under clear-water conditions, was correlated in the following functional form.

$$\frac{\tilde{W}}{U_0} = f\left\langle \mathbf{F}, \frac{y_0}{b}, \frac{D_{50}}{b}, \mathbf{R}_p = \frac{U_0 b}{\nu} \right\rangle \qquad [2.3.12b]$$

The correlation coefficient of this equation was 0.65. The temporal variation of scour depth was finally expressed as

$$\frac{\tilde{W}t}{d_s} = f\left\langle \frac{C_{se}}{C_{s0} - C_{se}}, \frac{d_s}{d_{se}}, \alpha_r, \frac{d_s}{b} \right\rangle \qquad [2.3.12c]$$

which is valid for clear-water conditions only. It was noted that the success of this scheme depends heavily on the accuracy in the estimation of $\tilde{W}$. It gave good results when $\tilde{W}$ was estimated accurately. Accurately estimating the value of d_{se} beforehand is also a problem.

Yanmaz and Altinbilek (1991) used the sediment pickup function of LeFeuvre *et al.* (1970) with a variable K to obtain the following equation.

$$\frac{Q_{s,out}}{u_d D_{50}\left(\frac{2d_s}{\tan\alpha_r} + b\right)} = K\Lambda \qquad [2.3.13a]$$

where $\Lambda = \left[\frac{C_D \mathbf{N}^2}{8.2\tan\Phi} - \tan\Phi - \tan\alpha_r\right]^{2.5}$;

Φ is the bed inclination; C_D is the coefficient of drag on sand grains; u_d is the velocity at the particle level; K is a coefficient that decreases with time and was experimentally found to be a function mainly of $u_d t / D_{50}$. Applying the sediment conservation principle to the scour hole, the following first-order non-linear differential equation was obtained for a circular pier.

$$\frac{dd_s}{dt} = \frac{K\Lambda D_{50}\tan\alpha_r}{\pi}\left(\frac{2d_s + b\tan\alpha_r}{d_s^2 + bd_s\tan\alpha_r}\right) \qquad [2.3.13b]$$

This was solved by a second-order Runge-Kutta method. Melville (1992) later pointed out that an analytical solution also exists. Corresponding equations were also given by Yanmaz and Altinbilek (1991) for square piers. The solution was shown to be in reasonable agreement with their short-duration experiments. However, the model's behavior near the equilibrium state remains to be checked.

Kothyari *et al.* (1992a, b) presented a model for the temporal development of the scour depth considering the horseshoe vortex as the main scouring agent. The initial size of the horseshoe vortex was related the b / y_0 using experimental data, and the initial shear stress near the pier was assumed to be equal to $4\tau_{00}$. The time to scour until a depth equal to D_{50} was then calculated from Paintal's (1971a, b) stochastic bed load theory. The horseshoe vortex was assumed to occupy this additional area available as a result of scouring and the shear stress near the pier was assumed to decrease inversely with the total area occupied by the horseshoe vortex. Using this new shear stress, the time required to remove one more layer of grains was again calculated. The scour depth in each time step was given by the sum of total grain layers removed at that point in time. This procedure generated d_s as a function of time until it was stopped when the shear stress becomes less than the critical shear stress of the sand. This model was verified for both steady and unsteady flows under clear-water conditions; the prediction is generally good in the principal erosion phase, with overestimation of d_s near the equilibrium state. This model does not seem to simulate adequately the quick increase in d_s during the early stage in the case of live-bed scours as can be seen the figures presented by Kothyari *et al.* (1992b). This happens in spite of the fact that the bed load transport into the scour hole under live-bed conditions has not been taken into account. If incorporated into this model, it would tend to slow down the scour development even more.

2.4 Three-Dimensional Boundary Layers

The flow approaching a bridge pier (Figure 2.4.1) exhibits the characteristics of what is called a skewed boundary layer in aeronautical engineering. In the case of a 2DTBL, only the magnitude of the velocity vector changes continuously with the distance from the wall; the direction remains the same. When viewed from the top, projections of the velocity vectors will fall on a single line. In other words, the vectors are contained in the same plane and are called *coplanar*, and the boundary layer is called *collateral*. When the direction as well as magnitude of the vectors change with the distance from the wall, the boundary layer is called *skewed* (Taylor 1959). In this case, the projections of the vectors will radiate from a common point. It is interesting to note that a 2DTBL would appear skewed to an observer moving in the transverse direction. By the same token, a boundary layer which is skewed to a stationary observer may appear collateral to a observer moving with a suitable velocity. Such a skewed boundary layer which could be resolved into a collateral boundary layer by viewing from a moving coordinate system is called *quasi-collateral*.

As shown in Figure 2.4.1, the approach flow turns under the influence of the lateral pressure gradient which is determined by the potential flow outside the boundary layer or by the outer portion of the boundary layer when such a potential flow is absent. In most of the studies on 3DTBL, there exists a potential flow above the boundary layer. However in a channel flow, the boundary layer often hits the free surface; thus there is no potential flow region. In both the cases, the slower-moving fluid near the wall with less momentum turns more than the faster-moving outer fluid. This causes the skewing of the boundary layer. In the above discussion, it is implicitly assumed that the vertical velocity component is negligibly small. This assumption will not be true near the obstruction. However, a certain distance away from the obstruction, the vertical velocity component can be neglected without any serious error. In what follows, this will be assumed unless otherwise stated.

In addition to the usual Cartesian coordinate system, the so-called *streamline coordinate system* is frequently used in 3DTBL studies. The principal reason for using this seemingly complicated system is that, when experimentally determined velocity profiles are viewed in this system, certain regularities can be discerned. Moreover, when the momentum integral equations are written in the streamline coordinate system, physical meanings may be assigned more easily to various terms of the equations.

Figure 2.4.2(a) shows the Cartesian coordinate system (x,y,z) with velocity components (u_x,u_y,u_z) and the streamline coordinate system (ξ,η,ζ) with velocity components (u,v,w). It should be noted that the streamline coordinate system is a right-handed, orthogonal system generated by the projections of the streamlines at the outer edge of the boundary layer on the ζ = constant planes and their orthogonal trajectories, where $\zeta = 0$ represents the surface of the body. This figure also shows the typical streamwise and cross flow profiles and defines some relevant parameters. Here $\mathbf{q}$ denotes the velocity at a certain distance y (or η) from the wall. For a flat wall, η will be equal to y. The value of $\mathbf{q}$ at the edge of the boundary layer is denoted by $\mathbf{q}_e$. Note that by the very definition of the streamline coordinate system, the transverse component of $\mathbf{q}_e$ is zero. The deflection of $\mathbf{q}_e$ from the direction of the original 2D approach flow (assumed along x-axis) is α. It is customary to measure the angle of everything else relative to the direction of $\mathbf{q}_e$. The angle made by any velocity vector $\mathbf{q}$ with $\mathbf{q}_e$ is γ and that made by the wall shear stress vector $\vec{\tau}_w$ is γ_w. Components of the velocity vector $\mathbf{q}$ along both the coordinate systems are shown in Figure 2.4.2(b). A typical hodographic representation or polar plot of the velocity vectors in the boundary layer is shown in Figure 2.4.2(c), where the velocity components in the streamline coordinate system normalized by q_e (magnitude of $\mathbf{q}_e$) are plotted. Here each point denotes the tip of the velocity vector at a

certain distance from the wall. Very close to the wall, the magnitudes are small and the directions tend to coincide with that of the wall shear stress. As the distance from the wall increases, the magnitude increases as expected and the direction changes continuously towards that of q_e. Polar plots like this are very useful in the study of 3DTBL.

The research on 3DTBL is of relatively recent origin and although a number of theories have been put forward, none of them has yet been accepted at the exclusion of others. Thus the subject has competing theories as well as controversies. A good introduction to this emerging discipline is given by Nash and Patel (1972). In the absence of a more recent review, one has to wade through the original, scattered papers. However, a couple of papers (Pierce, McAllister, and Tennant 1983a; Ölçman and Simpson 1992) give useful perspectives of recent developments.

2.4.1 Equations of motion

Following the work of Nash and Patel (1972), the Navier-Stokes and continuity equations for 3DTBL have been rigorously derived in the streamline coordinate system starting from the general form in orthogonal curvilinear coordinate system. The appropriate equations for the outer potential flow are also derived. The momentum and energy integral equations are obtained. The simplified form of equations on the plane of symmetry is also derived in both the streamline and the Cartesian coordinate systems. These derivations are presented in Appendix A. Whenever possible, the equations were checked against those available in other published works (Nash and Patel 1972; Johnston 1960a, b; and Pierce 1964).

These equations would describe very closely the upstream and surrounding flow around a symmetrical obstacle sitting on a flat wall. In the immediate neighborhood of the obstacle where the vertical component of velocity is pronounced, these equations will not be valid. Thus only certain parts of the flow around a bridge pier will be governed by these equations. The wake, the separated flow including the horseshoe vortex, the downflow at the nose of the pier and the flow inside the scour hole will not be described by this set of equations.

2.4.2 Cross-flow models

The existence of cross-flow is a direct result of the lateral pressure gradient, $\partial p / \partial \zeta$, associated with the curvature of the external flow streamlines. Since the pressure gradient remains constant across the boundary layer, the slowly moving fluid near the wall is imparted larger lateral velocity, w, than the faster moving fluid in the outer part of the boundary layer. Of the various models that have been proposed for the entire cross-

flow profile, none is capable of taking into account all the possible shapes that can occur in real flow situations. In fact, most models attempt to treat only the simplest case in which the cross-flow does not change direction through the boundary layer, *i.e.*, they exclude the S-shaped and other "cross-over" profiles.

2.4.2.1 Prandlt's model

The first model is due to Prandtl (1946) who suggested the following equations for the main and cross flows respectively:

$$\frac{u}{u_e} = G\left\langle \frac{y}{\delta} \right\rangle \qquad [2.4.1a]$$

$$\frac{w}{u_e} = eG\left\langle \frac{y}{\delta} \right\rangle g\left\langle \frac{y}{\delta} \right\rangle \qquad [2.4.1b]$$

where $e = \tan \gamma_w$ (see Figure 2.4.2(a)) and η has been replaced by y for convenience. In this model, G and g are supposed to be universal functions of (y / δ) as shown in Figure 2.4.3. Different functional forms of g were proposed by those who tried to apply this model, but only with limited success. In fact, as was shown conclusively by Johnston (1960a), who was probably the last one to test Prandtl's model, it was grossly inconsistent with experiments. Its failure is mainly due to the fact that it does not incorporate the influence of the main flow on the skewing of the velocity vector in the boundary layer. Further, the dependence of the main flow solely on the outer variables (presumably, even near the wall) is contradictory even to the accepted theories of 2DTBL.

2.4.2.2 Coles' model

The second model is due to Coles (1956) who extended his well-verified 2D model to the vector form

$$\mathbf{q} = \mathbf{q}_{\text{wall}} + \mathbf{q}_{\text{wake}} \qquad [2.4.2a]$$

for 3DTBL, where $\mathbf{q}_{\text{wall}}$ is the wall component along the direction of the wall shear stress vector $\vec{\tau}_0$ given by the familiar law of the wall

$$\frac{q_{\text{wall}}}{q_*} = f\left\langle \frac{yq_*}{\nu} \right\rangle \qquad [2.4.2b]$$

where q_* is the shear velocity, and $\mathbf{q}_{\text{wake}}$ is the wake component given by the law of the wake

$$\frac{q_{wake}}{q_*} = \frac{1}{\kappa}\Pi\omega\left\langle\frac{y}{\delta}\right\rangle \qquad [2.4.2c]$$

where Π is a profile parameter dependent on the outer flow and $\omega\langle y/\delta\rangle$ is the Coles' universal wake function. Figure 2.4.4 shows the concept of this model. For the few 3D experiments that Coles applied his model to, it was found that the wake components were nearly parallel to the direction of the pressure gradient. He was not sure whether this was merely a coincidence or it indicated an intrinsic property of skewed flows. Later workers determined the wake direction by evaluating Equation [2.4.2a] at the outer layer of the boundary layer where the direction of $\mathbf{q}$ is known from experiments.

Coles (1956) demonstrated the validity of his model by using the limited swept airfoil data available at that time. Johnston (1960a) and later Hornung and Joubert (1963) tested Coles' model without success. However, as Pierce (1966) pointed out, the measuring stations in the experiments of Hornung and Joubert were close to the separation line and hence based on these measurements it was wrong to discredit Coles' model which, like all other models, was intended for flows away from separation.

Pierce (1966) compared Coles' model to the experimental data of an expanding diffuser flow, and confirmed that Coles' model was valid for the plane of symmetry in a collateral 3D flow. However, the validity of the model off the plane of symmetry in such a collateral flow and, of course, for a general skewed 3D flow is yet to be verified experimentally.

2.4.2.3 Johnston's model

This model was proposed by Johnston (1960a) and takes into account the deflection of the main flow (α) as well as the relative skewing of the limiting streamline (γ_w). As shown in Figure 2.4.5(b), the cross-flow in this model is given by

$$\frac{w}{u_e} = e\frac{u}{u_e} \qquad [2.4.3a]$$

in Region I, and

$$\frac{w}{u_e} = A\left(1-\frac{u}{u_e}\right) \qquad [2.4.3b]$$

in Region II, where $e = \tan\gamma_w$. This model is essentially empirical in the sense that it was based on the polar plots of experimental data. Based on the assumption of a nearly inviscid flow in the outer portion of the boundary layer and a small cross flow, A was related to the outer potential flow through the parameter α by

$$A = -2u_e^2 \int_0^{\alpha} \frac{d\alpha}{u_e^2} \qquad [2.4.3c]$$

which reduces to $A = -2\alpha$ when u_e is constant along a streamline. Figures 2.4.5(a) shows the model in 3D perspective. The projections of the velocity vector tips are shown in Figure 2.4.5(b). The data points are supposed to fall on two straight lines. The model divides the boundary layer into collateral (Region I) and skewed (Region II) portions at $y = y_p$. The projections of the velocity vectors on the wall (Figure 2.4.5(c)) shows it clearly. However, to an observer moving with the outer flow, the inner region would appear skewed and the outer region collateral. Thus, Johnston's model divides the boundary layer into two quasi-collateral regions.

Johnston observed that Region I constituted only a small fraction of the total boundary layer thickness and that the apex of the triangle occurs at about $y^+ \approx 12\text{-}16$ and thus was within the viscous sublayer. This was found in the range of 15 to 80 in the "region of forward flow" in the experiments of Hornung and Joubert (1963). Values as high as 150 were found in the "region of backflow", *i.e.*, downstream of the separation line. Nash and Patel (1972) observed that this disagreement could be overcome if the apex location is defined in terms of u^+ $(= u/q_*)$ rather than y^+ and the value of u^+ at the apex is around 12-16.

Johnston verified his model with his own data of an impinging jet on a flat surface and other airfoil data available at that time with good correlation. Hornung and Joubert (1963) also confirmed the triangular shape of the model. However, later experiments of Francis and Pierce (1966), Pierce and East (1972), Prahlad (1973) and many others have demonstrated that there are situations when it is difficult to define the apex of the triangle and when straight lines cannot adequately represent the locii of the velocity vector tips (both in Region I and II). Several attempts have been made to overcome these difficulties by adopting higher order polynomials instead of straight lines (*e.g.*, Shanebrook and Hatch 1972). The problem with this approach, however, is that the whole process becomes essentially a data fitting exercise and that the parameters (or, more specifically, the coefficients of the polynomial) cannot be attributed any physical meaning.

2.4.2.4 Perry and Joubert's model

This model was formally introduced by Perry and Joubert (1965) although some of the ideas had already been used earlier by Hornung and Joubert (1963). This model may be described as the three-dimensional counterpart of the velocity defect law for 2DTBL and applies to only the outer part of the boundary layer. It was derived by a first-

approximation analysis of the boundary layer equations and by neglecting viscous effects. Mathematically it may be expressed as follows:

$$\frac{\mathbf{q}_e - \mathbf{q}}{q_*} = \bar{\Pi}'(x,z)\varphi\left(\frac{y}{\delta}\right) \qquad [2.4.4a]$$

Here, $\varphi(y/\delta)$ is the velocity defect function of the undisturbed upstream flow and $\bar{\Pi}'$ is a factor similar to Coles' Π and is determined by the outer flow. The defect function for a 2DTBL flow without a wake component on both smooth and rough surfaces is given by:

$$\frac{q_e - q}{q_*} \equiv \varphi\left(\frac{y}{\delta}\right) = 5.75\log\left(\frac{y}{\delta}\right) \qquad [2.4.4b]$$

According to this model, the magnitude of $\bar{\Pi}'$ (or Π') provides the necessary stretching to fit the defect function while its direction gives the direction of $(\mathbf{q}_e - \mathbf{q})$. These are approximately correct in the outer part of the boundary layer (y/δ > 1/4 to 1/3), as shown in Figure 2.4.6(a). The projections of the velocity vector tips are supposed to fall on a straight line (Figure 2.4.6(b)), just like Region II of Johnston's model. However, the difference is that Johnston's model does not relate the velocities with the distance from the wall while Perry and Joubert's model specifies this relation through the defect law.

Perry and Joubert offered an interesting physical interpretation of their model. Relative to an observer moving with the outer flow at the boundary layer edge, the outer part of the velocity profile in the skewed flow lies on a single plane (Figure 2.4.6(c)), thus making the outer portion quasi-collateral. Closer to the wall, it will continuously turn towards the wall shear vector in a way left unspecified by them. The opposite appears to a stationary observer whose observation can be expressed best by Johnston's model.

Perry and Joubert successfully tested their model with Hornung and Joubert's (1963) data on the skewed flow around a tear-drop cylinder. Good correlation was obtained for flows with a wide range of pressure gradient and skewing. Further analyses were presented later (Joubert, Perry and Brown 1967) in support of this model. However, a comparison with Johnston's data showed poor correlation.

2.4.2.5 Comments on Cross-Flow Models

The four models described above are the only ones proposed to date that describe the entire cross-flow profile (in contrast to the near-wall similarity models which correlate the cross-flow only in the inner part of the boundary layer). Out of these, Prandtl's model has been shown to lack a theoretical basis as well as experimental support. Each of the other three has a better physical basis. Although Johnston's model does not apply in every situation, the idea of polar plot has nevertheless become a popular

way to represent the cross-flow graphically. Coles' model has been shown to give good results on the plane of symmetry in 3DTBL. However, no evidence is yet presented to test the validity of Coles' model off the plane of symmetry. Perry and Joubert's model has been successfully applied off the plane of symmetry.

It appears that only a few attempts have been made to develop or verify the cross-flow models. Almost no work has been done after the late sixties. It is interesting to note that Pierce and his co-workers, who have performed many experiments to study the flow around a cylinder and probably have collected all the data necessary to test cross-flow models, have apparently not done so.

2.4.3 Near-wall similarity models

Near-wall similarity refers to the experimentally determined "sameness" of velocity profiles in the wall region of a broad class of TBL flows when these are plotted in suitably non-dimensionalized coordinates. For 2DTBL the concept of similarity is expressed by the well accepted law of the wall. For the 3D case the concept of near-wall similarity is still in its developing stage. Recently Pierce, McAllister and Tennant (1983a) have given an excellent review of the eleven near-wall similarity models proposed so far for 3DTBL flows. Since this review covers the models quite extensively, only their essential features are given here. Six models are classified as scalar and the remaining five as complex. It may be noted that all of them have been proposed for smooth walls only. Apparently no work has been done to incorporate the roughness effect in a 3DTBL.

2.4.3.1 Scalar Models

These models consider only one velocity component and express the 3D similarity in the form of

$$q^+ = \frac{\hat{q}}{\hat{q}_*} = \frac{1}{\kappa}\ln\left(\frac{y\hat{q}_*}{\nu}\right) + C \qquad [2.4.5]$$

where $\hat{q}$ is the component of velocity that has been non-dimensionalized by an equivalent shear velocity $\hat{q}_*$. Note that it is essentially the familiar 2D law of the wall. Pierce, McAllister and Tennant (1983a, b) noted that the difficulties in making direct measurement of the wall shear in a 3D flow have prevented an experimental verification of the relation between $\hat{q}_*$ and τ_0. It may be possible for $\hat{q}_*$ to collapse data without being related to τ_0. The equivalent quantities are defined for the six scalar models in Table 2.4.1.

Table 2.4.1 Scalar Similarity Models for 3DTBL

Model	$\hat{q}$	$\hat{q}_*$
Coles (1956)	$q\cos(\gamma_w - \gamma)$	$\sqrt{\tau_0/\rho}$
Johnston (1960a)	$u/\cos\gamma_w$	$\sqrt{\tau_0/\rho}$
Hornung and Joubert (1963)	u	$\sqrt{\tau_0/\rho}$
Pierce and Krommenhoek (1968)*	u	$\sqrt{\tau_0\cos\gamma_w/\rho}$
Prahlad (1968)	q	$\sqrt{\tau_0/\rho}$
East and Hoxey (1969)†	$q/\cos\alpha_1$	$\sqrt{\tau_0/\rho}$

† α_1 = a complicated function of reference velocities and streamwise and transverse displacement thicknesses.
*original reports not seen; quoted from Pierce, McAllister and Tennant (1983a).

2.4.3.2 Complex Models

The complex models tend to become more complicated and while not all are in vector form, they explicitly treat the vector nature of the 3DTBL velocity profiles. These will now be described in order of ascending complexity.

In the first model proposed by Chandrashekhar and Swamy (1976), both the streamwise and cross-flow components are expressed by logarithmic functions separately.

$$u^+ = \frac{u}{u_*} = 5.4\log\left(\frac{yu_*}{\nu}\right) + 4.9 \qquad [2.4.6a]$$

$$w^+ = \frac{w}{w_*} = 1.0\log\left(\frac{yw_*}{\nu}\right) + 11.8 \qquad [2.4.6b]$$

where $u_* = \sqrt{\tau_0\cos\gamma_w/\rho} = q_*\sqrt{\cos\gamma_w}$,

and $w_* = \sqrt{\tau_0\sin\gamma_w/\rho} = q_*\sqrt{\sin\gamma_w}$.

This model is empirical in the sense that it was based on experimental data.

The next three models were derived in a way similar to the derivation of the 2DTBL law of the wall as outlined by Cebeci and Smith (1974, pp. 113-115). The essence of this method is to evaluate the momentum equation near the wall region where

velocities become almost zero and to assume a suitable expression for the turbulent stress in terms of the mean flow. An integration then leads to the law of the wall. Prandtl's mixing length theory is often used to relate the turbulent stress to the mean flow which, according to Townsend (1956), represents the equilibrium between production and dissipation of turbulent energy in the vicinity of the wall.

White, Lessmann and Christoph (1975) used Prandtl's mixing length to approximate the turbulent stress and included the effect of the streamwise pressure gradient. Their model may be expressed as

$$u^+ = \frac{u}{u_*} = \frac{1}{\kappa}\left[2(S - S_0) + \ln\left(\frac{S-1}{S+1}\cdot\frac{S_0+1}{S_0-1}\right)\right] \qquad [2.4.7a]$$

and

$$w^+ = \frac{w}{u_*} = u^+ \tan\gamma_w \left[1 - \frac{y^+}{\delta^+}\right]^2 \qquad [2.4.7b]$$

where $u_* = \sqrt{\tau_0 \cos\gamma_w / \rho}$,

$S = \sqrt{1 + \alpha_\xi y^+}$,

$S_0 = \sqrt{1 + 0.1108\alpha_\xi}$,

$\alpha_\xi = \frac{\nu}{\rho u_*^3}\frac{1}{h_1}\frac{\partial p}{\partial \xi}$,

and $\delta^+ = \delta u_* / \nu$.

The cross flow equation is that given earlier by Mager (1952). The equations show the additional complexities of incorporating the effect of pressure gradient. No comparison with experimental data was given.

The third complex model was developed by Perry and Joubert (1965) using similarity arguments and treating the near-wall region as an equilibrium layer. Effects of pressure gradients both in the direction of main and cross flows were included. The turbulent stress was assumed isotropic and was approximated by a modified Prandtl's mixing length model. According to this model

$$\frac{q_d}{q_*} = \frac{1}{k}\int_0^{y^+} \frac{1}{y^+}\left[1 - 2w\cos\theta + w^2\right] dy^+ + C \qquad [2.4.8]$$

where $q_* = \sqrt{\tau_0 / \rho}$,

$$\omega = \frac{y^+ \alpha_p \nu}{q_*^3} \quad ,$$

$$\alpha_p = \frac{1}{\rho}\left[\left(\frac{\partial p}{\partial \xi}\right)^2 + \left(\frac{\partial p}{\partial \zeta}\right)^2\right]^{1/2} ,$$

$$q_d = \int_0^u \left[1 + \left(\frac{\partial w}{\partial u}\right)^2\right]^{1/2} du \quad ,$$

and θ is the angle between the wall shear stress and the pressure gradient vectors. It may be noted that the "developed velocity" q_d is equal to the arc from the origin in a polar plot. Perry and Joubert tested this model against the data of Hornung and Joubert (1963) but the result was inconclusive for the lack of sufficient data.

In his model, van den Berg (1975) used a coordinate system along and normal to the local shear stress direction (x', z'). It was assumed that the direction of the shear stress coincides with that of the maximum deformation of a fluid element and that both the main and cross flows are functions only of the wall distance and the wall shear stress vector. The effects of pressure gradients as well as the fluid inertia were taken into account. This is the only model that accounts for the inertia terms. This model states that

$$u_{x'}^+ = \frac{u_{x'}}{q_*} = \frac{1}{\kappa}\left[\ln y^+ + \kappa C + \frac{1}{2}\alpha_{x'} y^+ + \frac{1}{2}\beta_{x'}\frac{1}{\kappa^2}\left(\ln y^+\right)^2 y^+\right] \qquad [2.4.9a]$$

and

$$w_{z'}^+ = \frac{w_{z'}}{q_*} = \frac{1}{\kappa}\left[\alpha_{z'}\left(y^+ + b\right) + \beta_{z'}\frac{1}{\kappa^2}\left(\ln y^+\right)^2 y^+\right] \qquad [2.4.9b]$$

where $\alpha_{x'} = \dfrac{\nu}{\rho q_*^3}\dfrac{\partial p}{\partial x'}$,

$$\alpha_{z'} = \frac{\nu}{\rho q_*^3}\frac{\partial p}{\partial z'} \quad ,$$

$$\beta_{x'} = \frac{\nu}{q_*^2}\frac{\partial q_*}{\partial x'} \quad ,$$

$$\beta_{z'} = \frac{\nu}{q_*}\frac{\partial \phi}{\partial z'} \quad ,$$

and $\phi = \alpha + \gamma_w$ and $b = 13$.

The model is restricted to either small pressure gradients and shear gradients or to relatively small y^+ values. A good match with experimental data was reported.

The last complex model was proposed by East (1972) which consists of six differential and two algebraic equations. As pointed out by Pierce, McAllister and Tennant (1983a), the practical difficulties of some of the parameters prohibits the application or testing of this model.

2.4.3.3 Comments on near-wall models

In general, the specific y^+ range of applicability of the six scalar models was not given. However considering the fact that in the limit of a vanishing cross-flow, all of them become identical to the 2D law of the wall, a first look for similarity in the 3D case would focus on the range of y^+ from approximately 50 to 300, with the upper limit being influenced by both the magnitude and direction of the pressure gradient (Pierce, McAllister and Tennant 1983b). Of the complex models, the one of Chandrashekhar and Swamy takes no account of the pressure gradient effect and it results from the empirical fitting of data. The models of White, Lessmann and Christoph, Perry and Joubert, and van den Berg require explicit input of pressure gradient information. These three models are also based on some sort of mixing length or eddy viscosity hypothesis. At this point, not enough experimental data is available to determine the benefit of pressure gradient information.

The pressure-driven 3DTBL experiments of Pierce, McAllister and Tennant (1983b) indicate the better predictive ability of these three models and confirms that pressure gradient parameters are needed to accurately predict the near-wall behavior. The scalar models and the model of Chandrashekhar and Swamy failed to give good results when the skew angles were larger than 15° and when steep pressure gradients were present. Similar conclusions were also drawn in the case of shear-driven 3DTBL experiments (Pierce and McAllister 1983). Recently, Ölçman and Simpson (1992) have appraised the models against nine sets of data from different sources. They indicated that the main flow is best predicted by Johnston's model. None of the models really worked for the cross flow. However, it was pointed out that slightly better results were given by Mager's (1952) cross-flow relation (used in White, Lessmann and Christoph's model) for pressure driven flows and by Chandrashekhar and Swamy's model for shear-driven flows.

However it would be premature to generalize these findings without further reliable experimental data, especially a substantial amount of directly measured wall shear stress data.

Another noteworthy point concerns collateral velocity profiles very close to the wall since both Coles' and Johnston's model suggest their existence. Some measurements, although not all, have suggested no region of collateral flow. According to Prahlad (1973), there is reason to expect significant variation in the direction of the velocity vectors even within the viscous sublayer, especially when a large lateral pressure gradient is present. Apart from these experimental observations, the numerical solutions of East and Pierce (1972) and Klinksiek and Pierce (1973) indicated turning of the velocity vector right down to the wall and they concluded that the existence of collateral flow is not consistent with the boundary layer equations themselves. Therefore the overall verdict at present appears to be against the existence of a collateral region in 3DTBL.

2.4.4 Wall shear under skewed flow

In the case of 2DTBL, the wall shear stress and hence the shear velocity can be determined either by Clauser chart, Ludwieg-Tillmann formula, Thompson chart, *etc.* or from the velocity profile data in the logarithmic region. Moreover, direct force measurements are not unduly difficult. However, in the case of 3DTBL, the determination of shear stress is much more difficult because, on one hand, no universally accepted near-wall similarity model exists and, on the other hand, direct force measurements are extremely difficult since the direction has to be determined as well.

Pierce and Zimmerman (1973) devised a method in which velocity data right from the wall up to a region where the wake component becomes significant can be used to obtain a better estimate of τ_0 for both 2D and 3D boundary layers. They manipulated Spalding's (1961) single formula law of the wall to derive

$$\frac{\hat{q}y}{\nu} = \left(q^+\right)^2 + q^+ \exp(-\kappa C)\left[\exp\left(\kappa q^+\right) - 1 - \kappa q^+ - \frac{1}{2}\left(\kappa q^+\right)^2 - \frac{1}{6}\left(\kappa q^+\right)^3\right] \quad [2.4.10]$$

where $q^+ = \hat{q} / \hat{q}_*$.

These equivalent quantities are defined in Table 2.4.1 for the models of Coles, Johnston, Pierce and Krommenhoek, and Prahlad. These models were used along with that of Perry and Joubert for which q_d and $\sqrt{\tau_0 / \rho}$ were used.

Now given a measured velocity profile, for each pair of y and $\hat{q}$, equation [2.4.10] can be solved for q^+ and hence for $\hat{q}_*$. Thus it is possible to construct a table or

graph of $\hat{q}_*$ versus y from which the most appropriate value of shear velocity (and shear stress) can be chosen by giving more weight to the points closer to the wall. Pierce and Zimmerman (1973) obtained encouraging results consistent with experiments by using all the five models, but could not reach any conclusion as to which one is best suited for inferring wall stress in 3DTBL. A drawback of this method is that the direction of $\bar{\tau}_0$ must be known to compute its magnitude.

To overcome this difficulty, Chandrashekhar and Swamy (1976) proposed the use of their logarithmic expressions for velocity components (Equations [2.4.6a, b]) to determine both the magnitude and direction of wall stress. The Clauser scheme was also extended to calculate both $\tau_{0\xi}$ and $\tau_{0\zeta}$ which requires some prior analysis of the cross-flow profile and, of course, fitting the logarithmic expressions first. They also extended the Ludwieg-Tillmann formula for $\tau_{0\zeta}$ where the displacement and momentum thicknesses are to be calculated only from the inner region of the boundary layer (the exact extent was not given). For a particular data set, these three methods gave good and consistent results.

The basic equations of 3DTBL in streamline coordinate system (Equations [A.25] to [A.28] as given in Appendix A) were manipulated by White, Lessmann and Christoph (1975) along with their velocity profile equations ([2.4.7a, b]) to obtain two complex and lengthy differential equations for the two components of $\bar{\tau}_0$. Numerical solutions of these equations require complete information of the outer potential flow and values of τ_0 at some initial boundary. Reasonably good agreement was obtained with the experiments of Johnston (1960a) and Klinksiek and Pierce (1970).

2.4.5 Three-dimensional separation

The classical definition of two dimensional and axisymmetric flow at zero incidence identifies separation of flow by the inception of reverse flow and zero shear stress at the wall. However, in a three dimensional flow, separation can occur without flow reversal and without zero friction. Therefore a more generalized approach is needed to describe and define separation in 3D flows.

There are two types of flow separation in 3D flow, namely ordinary and singular. Ordinary separation is more common and is described here first. Maskell (1955) observed that separation occurs at a point only when two distinct surface stream lines, lying on the solid surface, converge and meet at that point. Then they combine and leave the surface in the form of a single separation stream line. At the separation point the two stream lines are tangent to each other on the wall forming a cusp. Furthermore they must be tangent to the wall at the separation point and hence the line of separation is also an envelope of the

separation stream lines. This kind of separation is ordinary. It should be noted that vanishing wall shear is not a necessary condition of ordinary separation.

In case of a singular separation, the shear stress becomes zero at the wall and the surface flow direction can become discontinuous and multi-valued. In other words, at a singular point, the surface stream lines can meet in other than a cusp. Points of singular separation occur on the plane of symmetry in 3DTBL. The line of singular separation has never been observed and perhaps it does not exist (Chang 1970; p. 32).

2.5 Flow Around a Cylinder

Elegant analytical solutions have been available for a long time for the potential flow around a circular cylinder placed in a uniform, two-dimensional, steady flow. During the last hundred years, numerous experiments have been performed on the flow past a cylinder in real fluids. In particular the wake, with all its beautiful regularity in slow flows and challenging irregularity in faster flows, has fascinated experimenters. Then the secondary flow generated in front of a cylinder in shear flow began to draw attention. Finally researchers began to perform experiments to map the flow field, to explain it in terms of theories, and to develop numerical models to simulate the flow. In the mean time several attempts were made to tackle certain aspects of the flow analytically with simplifying assumptions.

Most of these works were done by people who had no direct interest in the flow around bridge piers and the associated scour problem. Although attempts were made from time to time to apply this knowledge to the pier problem, none persisted for long. Here the studies on the flow around a cylinder are reviewed and the possibility of their potential use in the pier scour problem is pointed out.

Menna and Pierce (1988) divided the flow field around a tear-drop cylinder on a smooth rigid surface into four arbitrary regions. These regions have different flow characteristics and thus it is easier to study each of them separately. A similar approach may be applied to the flow around a bridge pier with due recognition of the bed deformation in the case of sand beds.

(1) **Skewed flow region**: It consists of the three-dimensional turbulent boundary layer-like flow upstream and around the cylinder but excluding the separated flow. This is basically the 2D upstream flow deflected and skewed under the influence of the pressure gradient generated by the pier.

(2) **Separated flow region**: It consists of the 3D separated flow including the separation sheet/envelope and the horseshoe vortex system in front of and at the sides of the pier. The trailing ends of the horseshoe vortex are also parts of this region before they enter the near-wake region. In the presence of a scour hole, the flow inside it may be considered a part of the separated flow region.

(3) **Near-wake region**: This consists of the flow immediately behind the pier. It starts with the separation of unstable shear layers on the two sides of the pier. The vortices generated in this way are mixed vigorously with the trailing ends of the horseshoe vortex and the upflow. The boundary between near- and far-wakes is, to a large extent, arbitrary. In the case of a sand bed, the reattachment point of the separated flow at the lee side of the sand bar may arbitrarily be considered the end of the near-wake region.

(4) **Far-wake region**: In this region the complex turbulent flows of the near-wake region continues to mix and homogenize to some extent toward a more boundary layer-like downstream flow. Eventually the far-wake loses its separate identity and regains the properties of a 2D boundary layer.

It is impossible to separate the different flow components completely in a complex flow situation. Thus the above division is only rough.

2.5.1 Upstream and surrounding flow

As shown in Figure 2.4.1, the 2D boundary layer turns continuously towards the lateral direction under the influence of the pressure gradient induced by the cylinder. The slow-moving fluid near the wall with lower momentum turns more than the fast-moving fluid near the top. This causes skewing of the boundary layer. During the last thirty years, many experiments have been performed to study this skewed flow in front of a cylindrical obstacle (*e.g.*, Hournung and Joubert 1963; Shabaka and Bradshaw 1981; McAllister *et al.* 1982; Moore and Forlini 1984; Kubendran *et al.* 1986; Menna 1984; Menna and Pierce 1988; Devenport and Simpson 1990; Chang and Gessner 1991; Eckerle 1985; Eckerle and Awad 1991; Agui and Andreopoulos 1992; Flemming *et al.* 1993). Some of the recent experiments have been offered as standard test cases for numerical models. None of them, however, was motivated directly by the bridge scour problem.

The existence of secondary flows around struts and airfoils in shear flows was theoretically deduced by the inviscid analyses of Squire and Winter (1951) and

Hawthorne (1954). These analyses gave good results only for sharp-nosed cylinders; and thus have limited utility for the bridge pier problem.

Toomre (1960) assumed that the shear flow is small and uniform such that the fluid moves almost precisely in a 2D manner along planes imagined drawn perpendicular to the cylinder, although for each of these laminae the upstream velocity $U_\infty\langle y\rangle$ is a function of y. The flow in each of these laminae was calculated from the potential flow theory. The vertical flow near the cylinder was assumed viscous inside the boundary layer developed along the cylinder surface and inviscid outside it. His analysis led to an ordinary differential equation for the inner region for which a numerical solution was given and to an algebraic equation for the outer region which could be solved readily. The matching point of these two regions was somewhat subjective or arbitrary. For a circular cylinder, his solutions show that the position of the maximum downflow varies from 0.01 to 0.0025 diameters upstream from the cylinder surface and its magnitude varies from 1.75 to 2 times $b\partial U_\infty\langle y\rangle / \partial y$ for the Reynolds number ($= bU_\infty / \nu$) range from 10^4 to 10^5. This may be used as a rough estimate for the strength of downflow in front of a pier if a part of the velocity profile $U_\infty\langle y\rangle$ can be assumed to vary linearly with depth.

A more simplified analysis was presented by Moore and Masch (1963), who neglected the viscous effects altogether and assumed that the downflow is driven solely by the stagnation pressure gradient along the cylinder front. Their analysis gave the downflow as equal to $\sqrt{U_{top}^2 - U^2\langle y\rangle}$ where U_{top} is the approach velocity at the free surface and $U\langle y\rangle$ is the velocity at any height y. This method predicts a downward velocity equal to U_{top} near the bottom which, of course, will be prevented by the bed. The downflow would more likely behave like an impinging jet.

Menna (1984) carried out extensive measurements of the upstream and surrounding flow around a tear-drop-shaped cylinder, part of which was presented later by Menna and Pierce (1988). This was presented as a standard test case for numerical models. Measurements included extensive mean velocity, Reynolds stresses, turbulent kinetic energy (TKE), floor pressure and wall shear stress. The pressure field away from the separated region resembled that given by a potential flow analysis. It was observed that the boundary layer thickness did not change significantly around the cylinder; the fluid accelerated around the body approximately within the undisturbed boundary layer thickness. The velocity vector was observed to continuously turn down to the wall and its direction nearest to the wall differed significantly from that of the wall shear stress inferred from oil streak visualization.

Menna (1984) observed that the $\overline{u'v'}$ stress is dominant at stations with collateral or nearly collateral flow. A growth in the magnitude of $\overline{w'u'}$ and $\overline{v'w'}$ stresses occurs as the secondary flow develops in response to the transverse pressure gradient following the outer flow curvature. It was inferred that $\partial(\overline{w'u'}) / \partial z$, which is generally neglected in the x-momentum equation, may be significant in flows with large skewing; thus all three components of Reynolds stress may have to be taken into account to model this type of flow. Along the plane of symmetry, where the flow encounters a steep adverse pressure gradient before separation, there is an increase in normal stresses, with $\overline{u'u'}$ stress increasing most rapidly. This results in an increase in TKE of the flow along this plane. Off the plane of symmetry and downstream from the leading edge, Reynolds stress profiles show two maxima. This apparently occurs when the transverse pressure gradient changes direction.

In the absence of an universally applicable near-wall similarity model for 3D TBL, the use of any indirect method of wall shear stress measurement (such as a Preston tube technique using a 2D calibration) assumes, *a priori* and without a firm basis, that the near-wall flow is identical for 2D and 3D boundary layers. To date most of the evidence is against this assumption, which was first suggested by Johnston (1960a). This means that direct force measurement of wall shear stress is essential for studying the nature of and the theories about 3DTBL. McAllister, Pierce and Tennant (1982) developed a floating element omnidirectional direct force sensing wall shear meter and used it to measure the wall shear stress around the same cylinder used by Menna (1984). Their measurement shows that the direction of the velocity vector nearest to the wall differs from that of the wall shear, more so when the skewing is large. The difference recorded was as high as 10° when the velocity was measured with a probe with a 0.25 mm external diameter, indicating that the velocity vector turned 10° along a vertical distance of 0.125 mm. The results of this study were later used to test the near-wall similarity models by Pierce, McAllister and Tennant (1983b).

Chang and Gessner (1991) studied the secondary flows on the transverse (y-z) planes. An airfoil was used in their experiments. The horseshoe vortex, after being generated on the plane of symmetry, bends and crosses these transverse planes almost perpendicularly. Another secondary vortex, rotating in the opposite direction, develops above the horseshoe vortex. It becomes more prominent further downstream which may be due to the absence of any solid surface inhibiting its growth, while the horseshoe vortex becomes weaker. The general flow is directed inwards in such transverse planes and feeds both the vortices. The distribution of Reynolds stresses and TKE is complex on these planes, that of $\overline{w'u'}$ being most distorted. It was inferred that the conventional form

of k-ε turbulence model is not adequate for this type of flow and that closure at the full Reynolds stress transport equation level may be required. This second vortex was, however, observed neither by Kubendran *et al.* (1986) who used a wing-fuselage-type configuration nor by Moore and Forlini (1984) who used a Rankine half-body. This has not been observed for circular cylinders so far.

2.5.2 Separated flow and horseshoe vortex

The boundary layer upstream of the cylinder on a flat surface is subjected to an adverse pressure gradient, and some distance ahead of the cylinder this boundary layer undergoes a three-dimensional separation. The separated boundary layer rolls up in a complex way downstream of the separation line to form a system of vortices. This vortex system is then swept around the base of the cylinder to form the horseshoe vortex system (HVS). The composition and behavior of the HVS have been found to be complex and in general functions of the Reynolds number.

The laminar HVS was studied in detail by Baker (1978, 1979). The HVS is steady for small Reynolds numbers; then it exhibits a regular oscillatory motion at a higher Reynolds number; and at still higher Reynolds numbers it shows irregular unsteady motion. The time-averaged pressure distribution on the upstream plane of symmetry (POS) shows a minimum at the location of the HVS in case of a steady HVS. No such minimum was detected for the unsteady HVS. The oscillatory behavior of the HVS was found to be complex. With increasing Reynolds number, it began to oscillate intermittently and randomly at two different Strouhal frequencies (0.26 and 0.40 increasing to 0.60 for higher Reynolds number). Baker (1979) maintains that these oscillations were not caused by the wake vortex shedding or any other disturbances in the wind tunnel. They were determined solely by the values of $U_\infty b / \nu$ and b / δ^* where δ^* is the displacement thickness of the boundary layer and U_∞ is the freestream velocity. The wall skin friction beneath the HVS was found to be as large as five times that at an upstream location.

A similar study was presented for turbulent HVS by Baker (1978, 1980a). The pressure distribution shows a low flat portion whose position roughly coincides with the HVS center. The pressure distribution was invariant with Reynolds number. The distances of the separation point and the HVS from the cylinder center were found to decrease with increasing $U_\infty b / \nu$ and to increase with increasing b / δ^*. The Reynolds number at which transition from laminar to turbulent HVS takes place appears to be about 4×10^3. The locations of the HVS and the separation line were also analyzed by

Baker (1985) and were found to be functions mainly of $U_\infty b / \nu$ and cylinder height to diameter ratio.

Dargahi (1987, 1989) visualized the turbulent HVS in a water channel by means of the hydrogen bubble method. These studies also revealed the complex structure of the HVS. The interaction of the individual vortices was qualitatively described by considering the effect of a single vortex on the others. These vortices were found to be shed with a lower frequency which was different from that of wake vortices. A unique finding of Dargahi was that the flow around the separated region including the HVS satisfies the topological law given by Hunt *et al.* (1978), which relates the numbers of the nodal, half-nodal, saddle and half-saddle points. It was also concluded that there is no closed region of separated flow known as bubble-type separation. The wall shear stress under the HVS was found to be about 1.5 times that at the upstream point.

The reverse flow in the separated flow was measured by both Baker (1978) and Dargahi (1987). Earlier, Utami (1975) made similar measurements and tried to compute the velocity distribution across a HVS analytically. He approximated the HVS by a single circular vortex and assumed another image vortex beneath the wall. Then the velocity field induced by the vortex pair roughly simulated the velocity distribution inside the HVS. The results were crude, indicating that the HVS is too complicated to be computed by such a simple model.

Harsh (1985) made extensive flow measurements in the separated flow region using the same tear-drop cylinder at the same Reynolds number as Menna (1984). Some of the results are presented by Pierce and Harsh (1988). Measurements included static pressure on the floor and cylinder surface, velocity field, and pressure distribution. A five-hole probe was used for flow measurement. The flow separation on the floor as well as on the cylinder surface was visualized. The development of the secondary boundary layer along the cylinder surface was calculated by integral methods and compared to the visualized pattern. Secondary flows were shown for the 43 and 100 percent cord transverse planes (y-z planes). The vorticity field was also calculated by numerical differentiation of velocity data. Only one vortex (HVS) can be seen on such planes and the secondary flow was inward everywhere, in contrast to the findings of Chang and Gessner (1991). The velocity map on the POS also shows only one vortex (of the HVS) and no upward flow was observed.

Continuing the works of Menna (1984) and Harsh (1985), more accurate and detailed measurements on the POS were taken by Tree (1986) using a two-color LDV system. These measurements on a finer grid suggested, but did not show conclusively, the existence of a smaller counter-rotating vortex at the corner of the cylinder-wall junction.

Vortices of this type develop as a result of the separation of the secondary boundary layer developed on the cylinder surface by the downflow. This shows that the complex composition and behavior of the HVS, which can be rather easily observed in a flow visualization, do not easily show up in quantitative measurements. Tree (1986, p. 130) cites a smoke visualization study by Pierce, Kim and Frangistas (private communication) of the HVS around the same cylinder over a wide range of Reynolds number. At lower Reynolds number, clear but fleeting views of multiple vortex structures were observed with significantly smaller vortices upstream of the dominant vortex structure. Even at the lowest Reynolds number values, the vortex system was characterized as highly time variant. As the Reynolds number was increased, these secondary vortices became smaller and more difficult to observe. Comparing his LDV data with Harsh's five-hole probe data, Tree concluded that, in general, good agreement could be found in the regions away from the wall. Near the wall, the LDV data consistently indicated lower velocities. These differences near the wall increase for stations closer to the cylinder and could be attributed to turbulence effects, wall proximity, velocity gradient effects on mechanical probes, and the probe-induced flow field alterations. Tree also points out the difficulty in measuring small vertical velocities near the separation region and its effect on measurement uncertainty. For data points near the singular separation point, the uncertainty in pitch angle was found to be as high as 55°. Turbulence level (r.m.s. velocity) in the separated region was found to be several times higher than that found in the upstream region. Moreover the turbulence level in the horizontal direction was consistently higher than that in the vertical direction. It was found to reach a maximum value near the core of the vortex. Some of Tree's results have been reported by Pierce and Tree (1990).

Pierce and Shin (1992) analyzed further the data of Menna (1984), Harsh (1985) and Tree (1986) and some additional measurements they took in the downstream region to study how the HVS travels around the tear-drop cylinder. The small corner vortex on the POS becomes larger and more easily detectable as it wraps around the cylinder. Both the primary and corner vortices move away from the wall as well as from the cylinder body as they travel downstream. The peak value of the vorticity, the mean flow secondary kinetic energy per unit mass and the circulation of the principal vortex were found to decrease in the downstream direction.

Agui and Andreopoulos (1992) found that there are certain regions in the flow around a circular cylinder which are characterized by large r.m.s. pressure fluctuations. The peak values (as large as three times the normal value) are associated with HVS and the upstream flow separation of the oncoming boundary layer. It is the reattachment of

the separated shear layers and the unsteady "wandering" of the HVS which produced largest pressure fluctuations. At this point the p.d.f. of the pressure fluctuation is bimodal, indicating a highly intermittent or periodic flow. The p.d.f. of the pressure fluctuations near the separation point was slightly skewed, so that negative pressure fluctuations have higher probability of appearance. These two peaks in p.d.f. were thought to be related to two separate phenomena: the unsteady boundary layer separation off the plate and the quasi-regular vortex shedding from the cylinder.

Although there are many versions of the HVS observed in different experiments, only one study (Eckerle 1985; Eckerle and Awad 1991) claimed that there was no vortex formed at the POS at high Reynolds number but only a reversed flow going outward, off this plane. A dimensionless parameter $[(bU_\infty / \nu)^{1/3}(b / \delta^*)]$ was identified; for a value of this parameter greater than 1000, no vortex was created on the POS. After extensive visualization of the POS illuminated by a laser sheet, Agui and Andreopoulos (1992) concluded that Eckerle and Awad's observation could be due to a substantial "wandering" of the HVS.

From their measurement of a wing-body junction with an LDA, Davenport and Simpson (1990) found that the turbulent stresses become very large near the HVS. The $\overline{v'v'}$ and $\overline{u'v'}$ stresses reach peak values in an area of high mean-velocity gradient close to the center of the mean vortex. The maximum of $\overline{u'u'}$ occurs much closer to the wall in the region of intense reverse flow. These large stresses are associated with bimodal p.d.f. of u- and v-velocities that occur over a region encompassing most of the mean vortex. The velocity variation with time that produces this type of p.d.f. is bistable and switches between two states, one of large negative u (reverse flow mode) and one of near-zero u (zero flow mode).

Belik (1973) derived a relationship, mainly from dimensional considerations, for the distance of the separation point from a circular cylinder (x_v). It was found to depend mainly on what he called the vortex Fourier number $\mathbf{Fo}_v$ ($= 0.5\nu / U_\infty \delta$) and weakly on the Reynolds number $\mathbf{R}_p$ ($= bU_\infty / \nu$).

2.5.3 Wake flow

In the wake region behind a cylinder, the separated HVS and the wake vortices shed from the cylinder surface interact in a complex way. The presence of the wall and the free-surface, if any, introduces further complexities.

Coutanceau and Defaye (1991) has given an extensive review of the wake visualization. It shows, with an impressive array of photographs, the evolution of the

wake over a large range of Reynolds number (from less than 0.1 to over 10^6). The idealized 2D wake flow was classified into ten regimes.

For the simplest 2D case, where a uniform shearless incident flow approaches a smooth circular cylinder at a right angle, much research has been done. As a result the general variation of the drag coefficient C_D and Strouhal number $\mathbf{S}$ (= $f b / U_\infty$) with the Reynolds number $\mathbf{R}_p$ (= bU_∞ / ν) is now known. Here f is the frequency of wake vortex shedding. There is a sharp drop in the value of C_D in the $\mathbf{R}_p$ range from 2×10^5 to 5×10^5. This is generally known as the *lower transition*. The regions before and after it are called *subcritical* ($C_D \approx 1.2$) and *supercritical* ($C_D \approx 0.3$) respectively. There is another *upper transition* at $10^6 < \mathbf{R}_p < 3.5\times10^6$, to a new plateau known as the *transcritical* region ($C_D \approx 0.7$). Roshko (1961) explained that in the lower transition the wake width b_w decreases from values larger than cylinder diameter b to values smaller than b, as the separation point moves from the front to the back of the cylinder (Figure 2.5.1). In the upper transition, indications are that the wake "opens" again, the separation point moving a little bit upstream. According to Roshko's free-streamline model as shown in Figure 2.5.1, the pressure on the wake boundary remains constant ($C_p = C_{pb}$) from the separation point to the section AA' where the wake boundary becomes parallel to the free stream. Here C_{pb} is the base pressure coefficient. Beyond this section the wake width remains constant while the pressure recovers to the free stream value. Type A is characteristic of the subcritical region, and Type B is characteristic of supercritical and transcritical regions.

Roshko speculated that there must be a universal Strouhal number, defined by $\mathbf{S}^*$ = $f b_w / V_w$, which is independent of the body producing the wake. Here V_w = $U_\infty(1-C_{pb})^{1/2}$. For subcritical and transcritical regions, $\mathbf{S}^*$ was found equal to 0.16 and 0.27 respectively. In the supercritical regions, attempts to find a value of $\mathbf{S}^*$ were not successful. Roshko was not sure whether it was due to errors in the experimental data or that the free streamline model simply does not apply in this region. Griffin (1981) observed that the universal characteristics of wakes can be better expressed in the following way. He defined a wake drag coefficient, $C_D^* = C_D / (b_w / b)(1-C_{pb})^{1/2}$ and found that the product $\mathbf{S}^* C_D^*$ has a constant value of 0.073 ± 0.005 for a $\mathbf{R}_p$ range from 100 to 10^7. There are indications that this relationship is not valid when there are appreciable three-dimensional or secondary flow effects in the wake (Griffin 1985).

The wake has a different structure under shear flow, *i.e.*, when the approach velocity $U_\infty\langle y\rangle$ is a function of y. The main difference is the presence of vorticity vectors along the transverse direction in the approaching shear flow. As the flow

approaches the cylinder, these vorticity vectors turn continuously until they become more or less parallel to the main flow velocity. The interaction of this vortices with wake vortices is believed to be responsible for the changes in the wake flow (Maull and Young 1973). The most prominent effect of a shear flow is the division of the wake into a number of cells. The vortex shedding frequency varies from cell to cell in such a way that the Strouhal number based on the local velocity ($f b / U_{\infty}\langle y\rangle$) remains more or less constant along the whole vertical length, but decreases slightly in the direction of increasing $U_{\infty}\langle y\rangle$ within a cell. The Strouhal number based on a constant reference velocity increases in the direction of increasing $U_{\infty}\langle y\rangle$, but remains constant within a cell. The boundary of these cells is marked with a change in slope of the base pressure coefficient C_{pb}.

The cellular characteristic described by Maull and Young (1973) was later confirmed by other studies as reviewed by Griffin (1985). It is now known that the number of cells is strongly dependent upon the height to width ratio of the cylinder (h / b) and the end configurations. For short cylinders, the tendency of strong cells to form is usually highest near the ends. The length of the cells usually vary between 4 to 6 times the cylinder diameter. The general trend of the cell length is to decrease with increasing shear and to increase with increasing roughness of the cylinder surface. Gerich and Eckelmann (1982) found experimentally that the vortex shedding frequency in a region close to an end plate (ranging from 6 to 15 diameters) is 10-15% less than regular Strouhal frequency. A third frequency in between these two was observed along the whole cylinder length bounded by two end plates less than 20-30 diameters apart.

Dargahi (1987, 1989) observed that close to the bed vortices are shed at different frequencies. The turbulent character of the wake is found to increase near the bed and the width of the wake decreases. This latter effect can also be due to the acceleration of flow near the bed, towards the wake center where the pressure is low. The position of the separation line at the sides of the cylinder surface moved downstream near the bed. Dargahi (1989) observed that different flow patterns may exist at a particular Reynolds number. For instance, at a Reynolds number of 39×10^3, three different patterns were observed, which were believed to be created as packets of low or high pressure migrated from one region to another. Flow visualization by Dargahi (1987) as well as the five-hole probe measurements of Eibeck (1990) indicates a vertically upward flow at the back of the cylinder.

It appears that the wake behind a bridge pier in a sand bed would be very different from the wakes discussed above. The main reasons are a low h / b ratio, presence of the

free surface, scour hole configuration, the sand bar behind the hole, and strong three-dimensional effects.

2.5.4 Measurements inside scour hole

Only a few attempts were made to measure the flow with or inside the scour hole. Shen *et al.* (1966) measured the downflow and the reverse flow inside the scour hole by aligning a Pitot tube parallel to the cylinder surface and the scour hole slope respectively. As the direction of the velocity vector was not taken into consideration, these measurements should be interpreted with caution.

Melville's (1975) study was perhaps the most detailed one, part of which was presented later by Melville and Raudkivi (1977). The measurements were carried out for three scour conditions: initial flat bed before scouring, intermediate scoured bed and final equilibrium condition bed. Concrete replicas of scour holes under these conditions coated with appropriate sand served as rigid models that allowed prolonged measurements. The aim was to obtain information on flow patterns, turbulence intensity distributions, boundary shear stress distribution in the scour zone, and the interaction of the wake vortices with the horseshoe vortex. The results were shown as contour plots. General similarity was observed in the flow pattern with the development of the scour hole. The downflow reaches a maximum near the original bed level which is about 75% of the average velocity of the approach flow. The shear decreases with time inside the hole while the turbulent agitation increases. This led Melville and Raudkivi (1977) to conclude that these two factors along with the weight of a sand grain add up everywhere to the threshold condition for sediment transport.

Ettema (1980) measured the downflow in front of a cylinder placed in a wind tunnel. The pier Reynolds number was kept similar to that of the hydraulic models. Wooden replicas of scour holes were used to study the effect of the scour hole dimension on the downflow. The direction of the flow at a point was first determined by smoke and cotton tufts. Then a total head and a static head tube were used in succession. The difference of these two readings gave the velocity. The overall variation of the downflow with height above the bed and the size of scour hole was shown by these measurements.

2.6 Discussion

In this chapter, a detailed survey of the available literature on the scour problem and of some other branches of fluid mechanics that might be relevant to this problem has been presented.

In presenting the scour prediction methods in Section 2.2, no attempt was made to describe them all. Rather the emphasis was put on the various concepts behind the methods. The simplest of all is perhaps the regime concept, which estimates the scour depth simply as a multiple of the regime depth. Similar simplicity was also observed in Laursen and Toch's experimental curve. This began to change as researchers started to base their methods on various sorts of theory. Coleman introduced the scour Euler number. Laursen introduced the long contraction analogy. Carstens based his analysis on the similarity principle. Shen *et al.* related the circulation to the scour. Sarma took into account the bed load transport capacity. And finally Qadar and Baker utilized the characteristics of the horseshoe vortex. Chitale and Froehlich introduced purely correlation based methods. The methods of Jain and Fisher, Jain, and Kothyari *et al.* were mainly correlation based, although the bed load transport was taken into the analysis to some extent. Melville and Sutherland based their design method on enveloping curves while those of Breusers *et al.* and Richardson *et al.* were more empirical in nature. It appears that although a rich variety of concepts were conceived, the overwhelming complexities of the phenomenon compelled researchers to accept some sort of empiricism at the end in order to devise a working "formula" to predict scour depths.

In Section 2.3, the scouring process, a dimensional analysis and the effect of different parameters have been described. Developments occurring roughly after the extensive review of Breusers *et al.* (1977) were given more emphasis. Systematic experiments were conducted at this time in New Zealand, the principal contribution of which is our present knowledge regarding the dependence of the scour depth on other parameters. The effect of individual parameters on the scour depth is now more or less well established. However, the combined effect of all parameters on the scour depth, *i.e.*, the determination of scour depth when other parameters are known, is yet to be fully understood. Various concepts on the time evolution of scour were synthesized here. The logic and philosophy behind these temporal models shed much light on the scouring phenomenon. They may in future serve as the basis of computational schemes for the simulation of the flow and scour.

The theories of three-dimensional turbulent boundary layers are presented in Section 2.4. It should be noted that these theories, unlike those for 2DTBL, are not well accepted, allowing many contradictions and controversies. However, it is desirable, and

possible too, to analyze the flow around a bridge pier in the light of 3DTBL theories. The cross-flow models will help us understand the overall approach flow. The near-wall similarity models, on the other hand, may be expected to expose the details of the flow structure near the bed and their implications on the transport of sediment.

In Section 2.5, different features of the flow around a cylinder are described. The analysis of the secondary flow (downflow) by Toomre is valid only for a weak shear flow and away from the presence of any wall. Moore and Masch assume that the downflow is driven solely by the pressure gradient which leads to an absurd downflow equal to the free stream velocity at the wall. Obviously the downflow in front of a pier, with the horseshoe vortex and possibly a scour hole, is too complex to be described by either of these models. The measurements by various researchers have shown the complex nature of the mean and fluctuating flow fields, especially the increase in turbulent stresses. A much more complex nature of the separated flow region and horseshoe vortex system was also revealed by detailed measurements. The Reynolds number dependent composition and oscillation of the horseshoe vortex system are noteworthy. The cellular nature of the wake, which depends on the Reynolds number and cylinder size, presents further difficulties.

As much as the above paragraphs show the complex nature of the flow, they also give us an idea about so many things that are known. They also help us to appreciate the importance of the flow and its influence on the scouring process.

The knowledge surveyed in this chapter leads to the following conclusion. The study of local scour would benefit greatly from the analysis of the flow structure. And the accumulated knowledge in other branches of fluid mechanics may be fruitfully utilized in this endeavor.

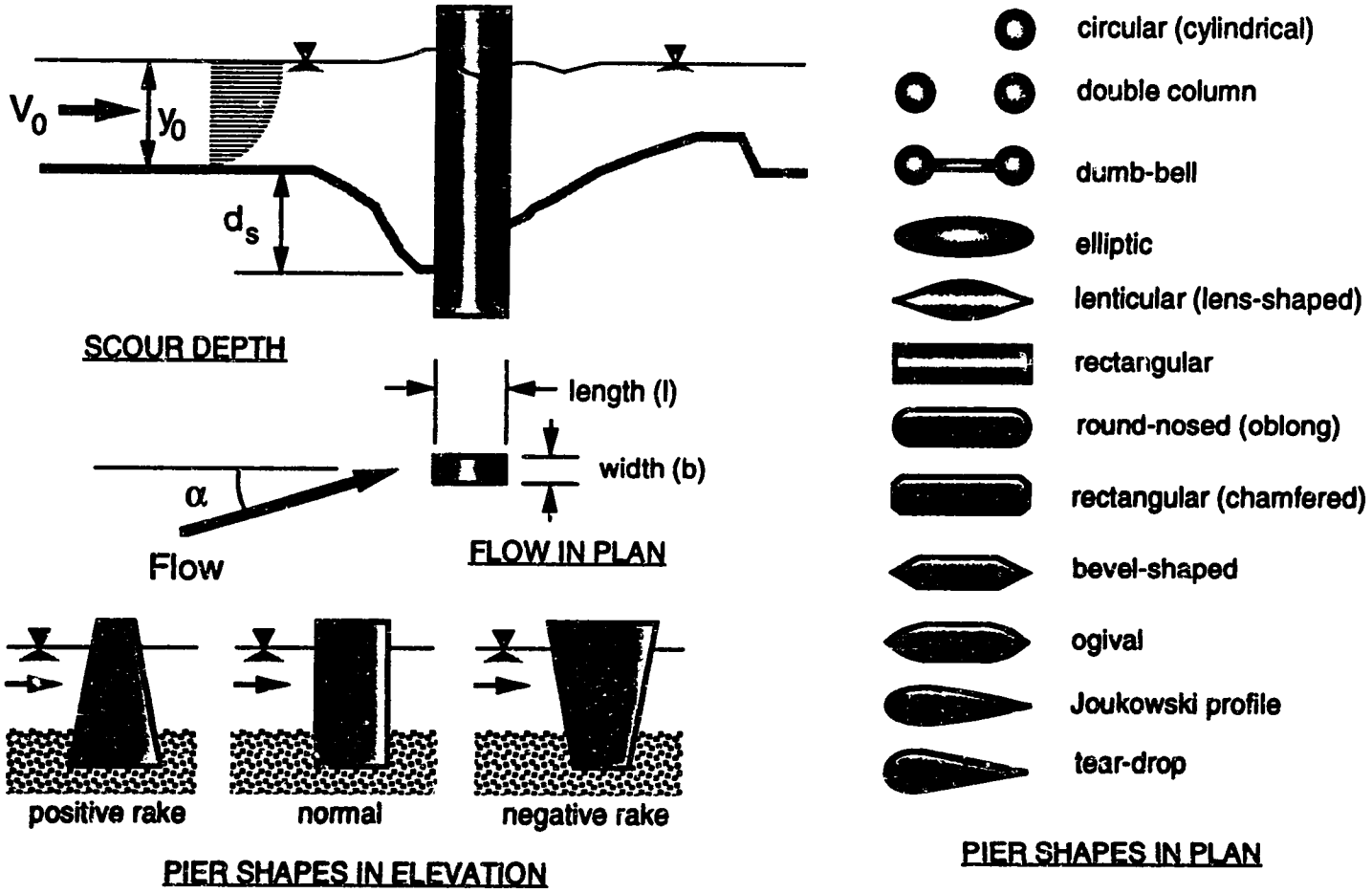

Figure 2.2.1 Bridge pier shapes and local scour

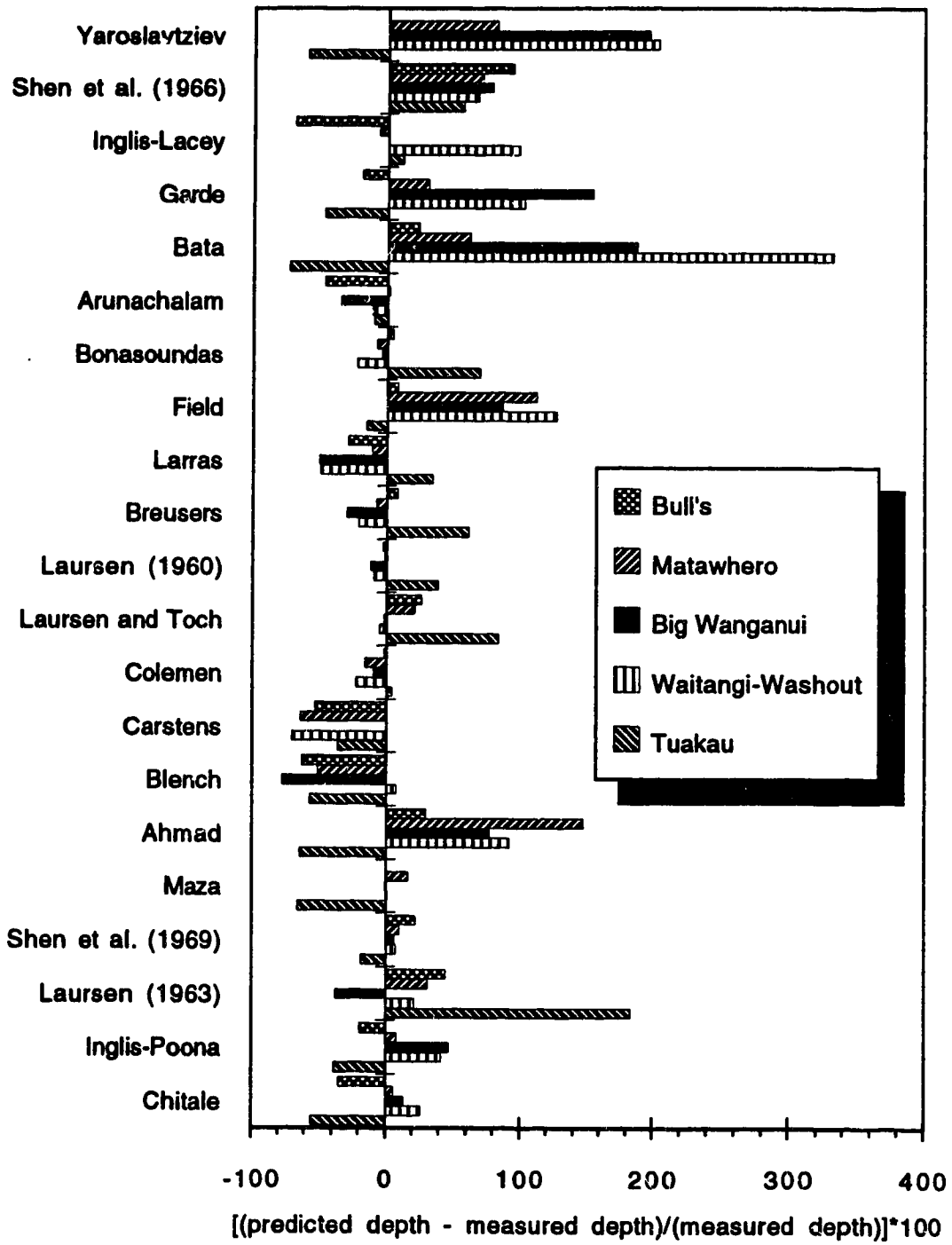

Figure 2.2.2 Scour prediction for some New Zealand bridges (based on the calculations of Melville 1975)

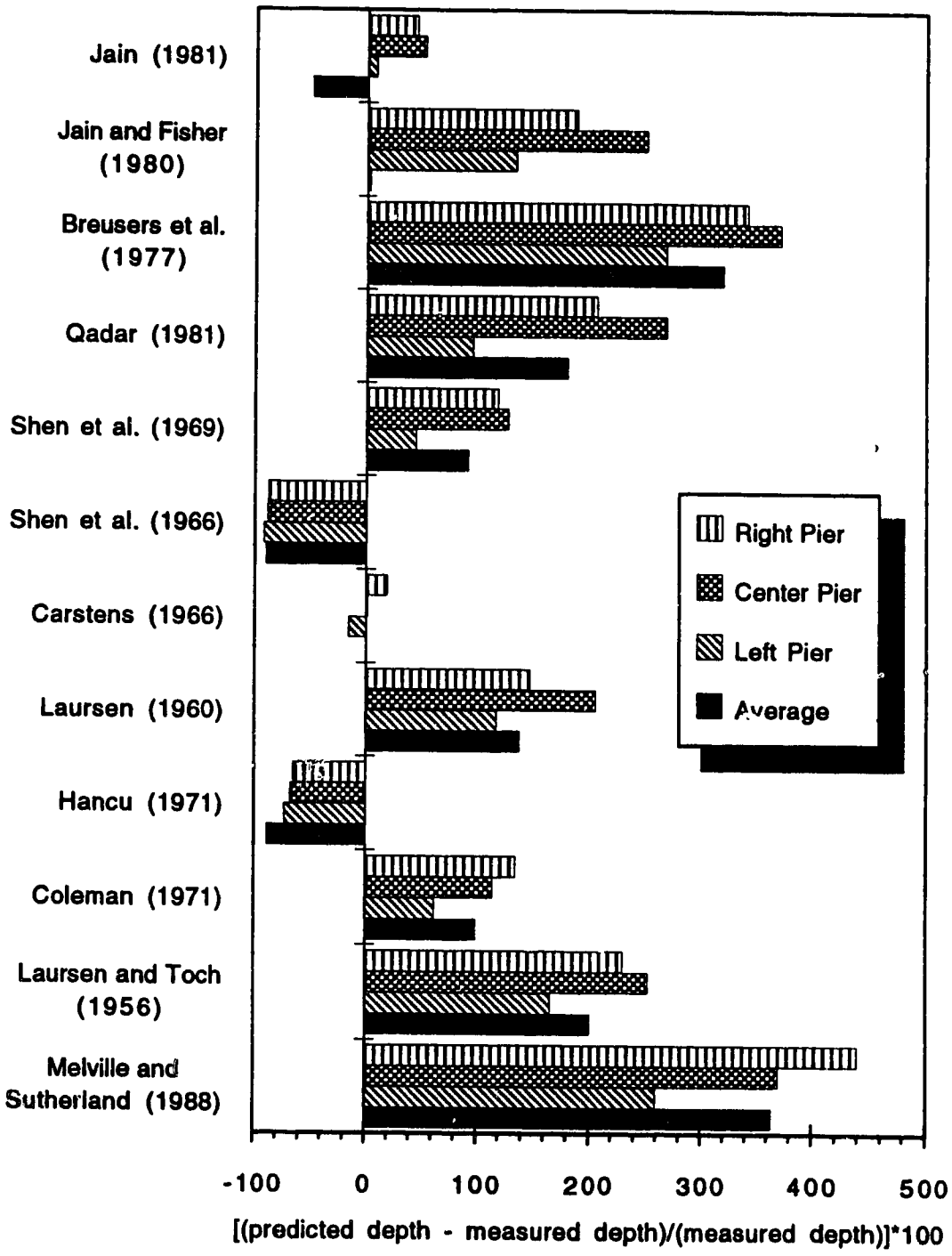

Figure 2.2.3 Scour prediction for South Saskatchewan river at Hwy 41 bridge (adapted from Ahmed et al. 1993)

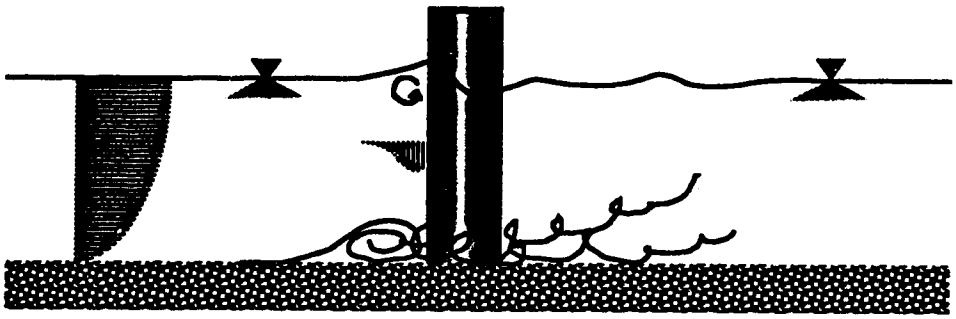

BEFORE SCOURING

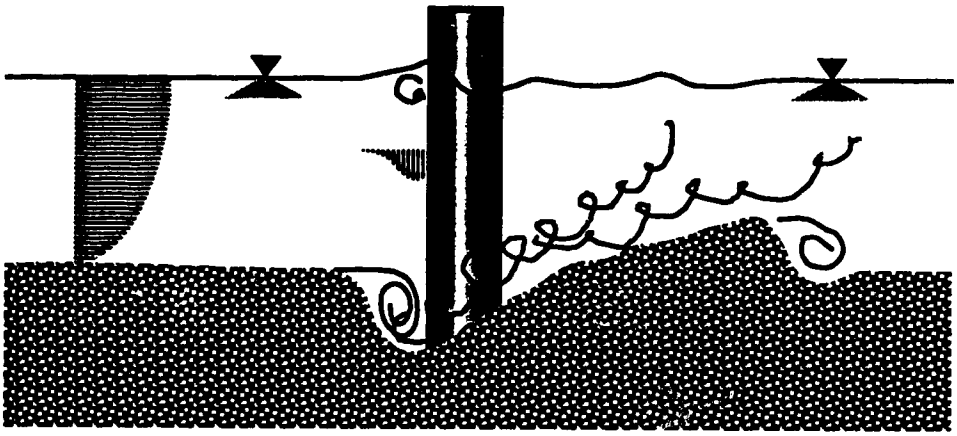

WITH SCOUR HOLE

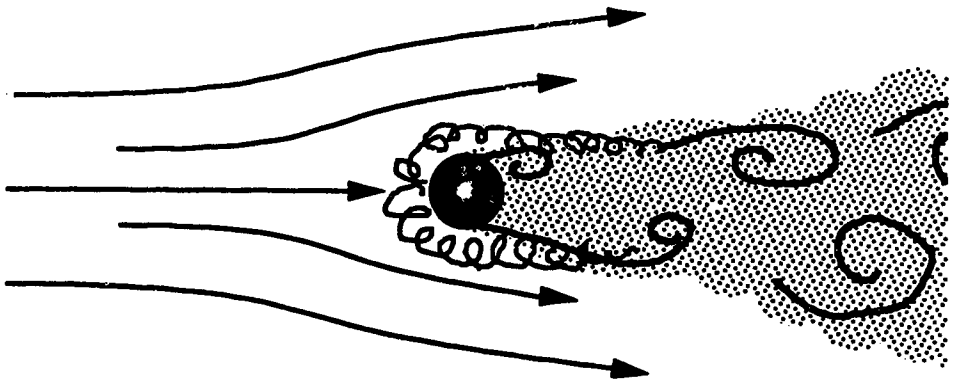

FLOW IN PLAN

Figure 2.3.1 Flow pattern around a bridge pier

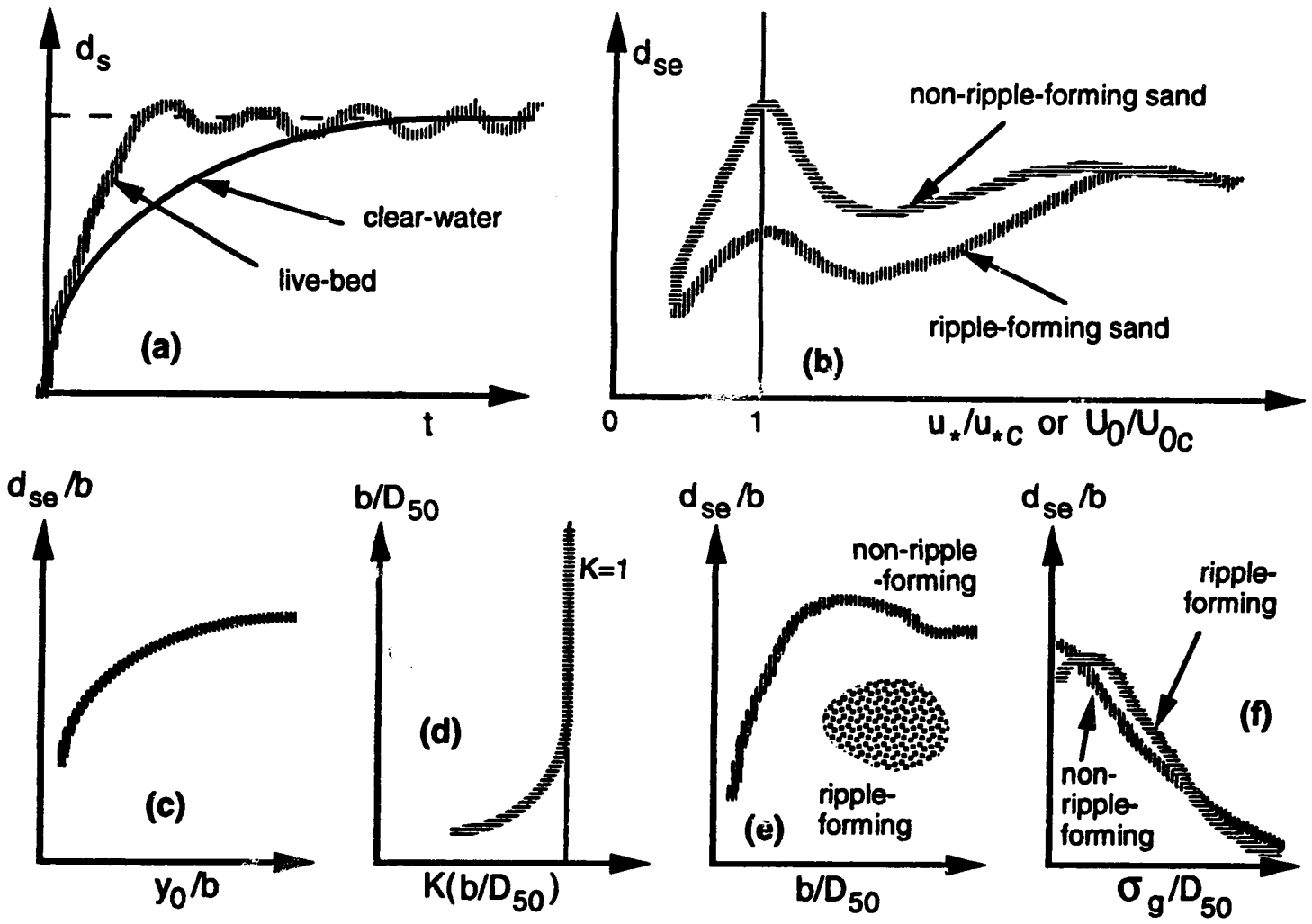

Figure 2.3.2 Functional trends of scour depth

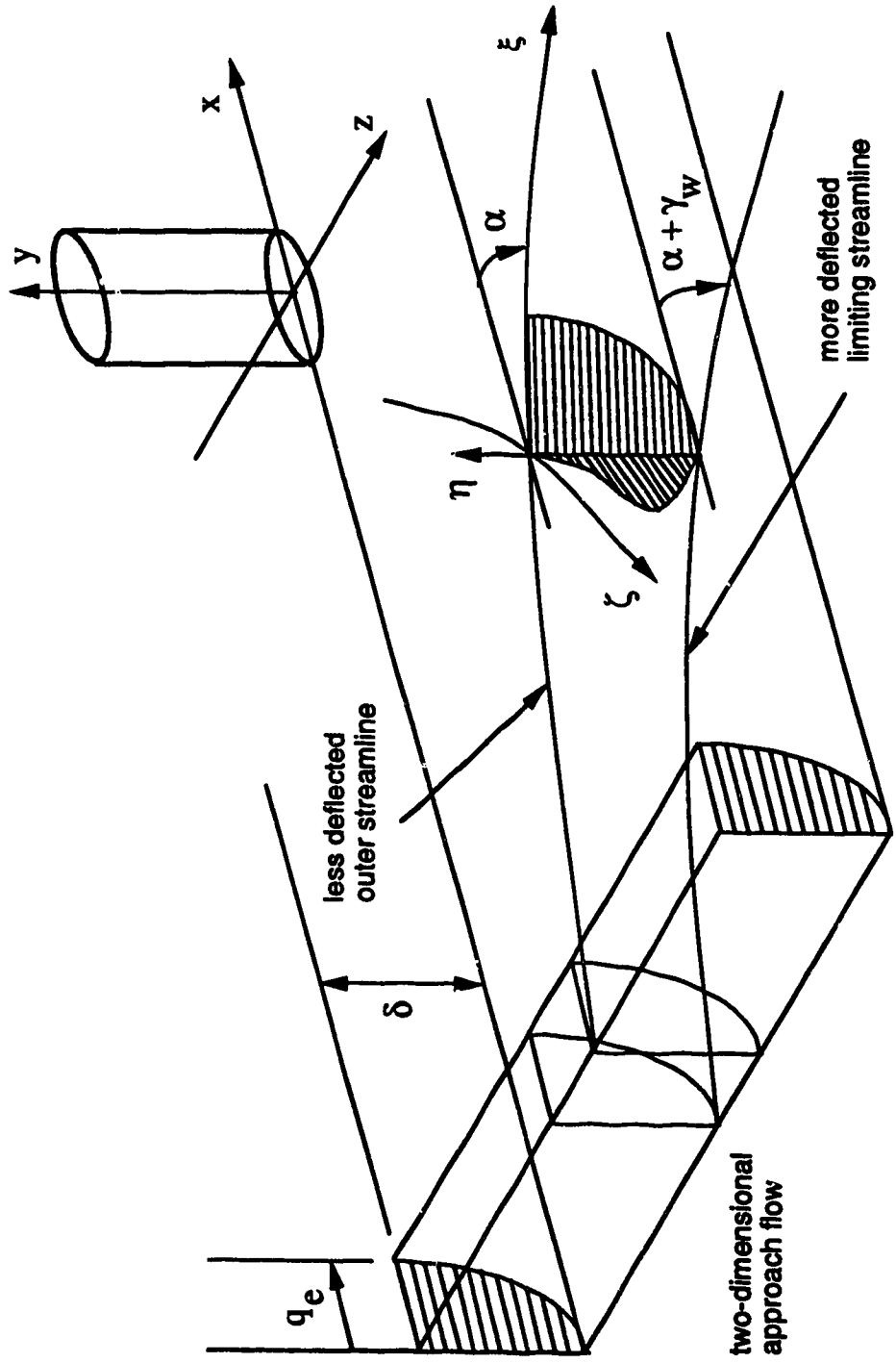

Figure 2.4.1 Typical skewed boundary layer

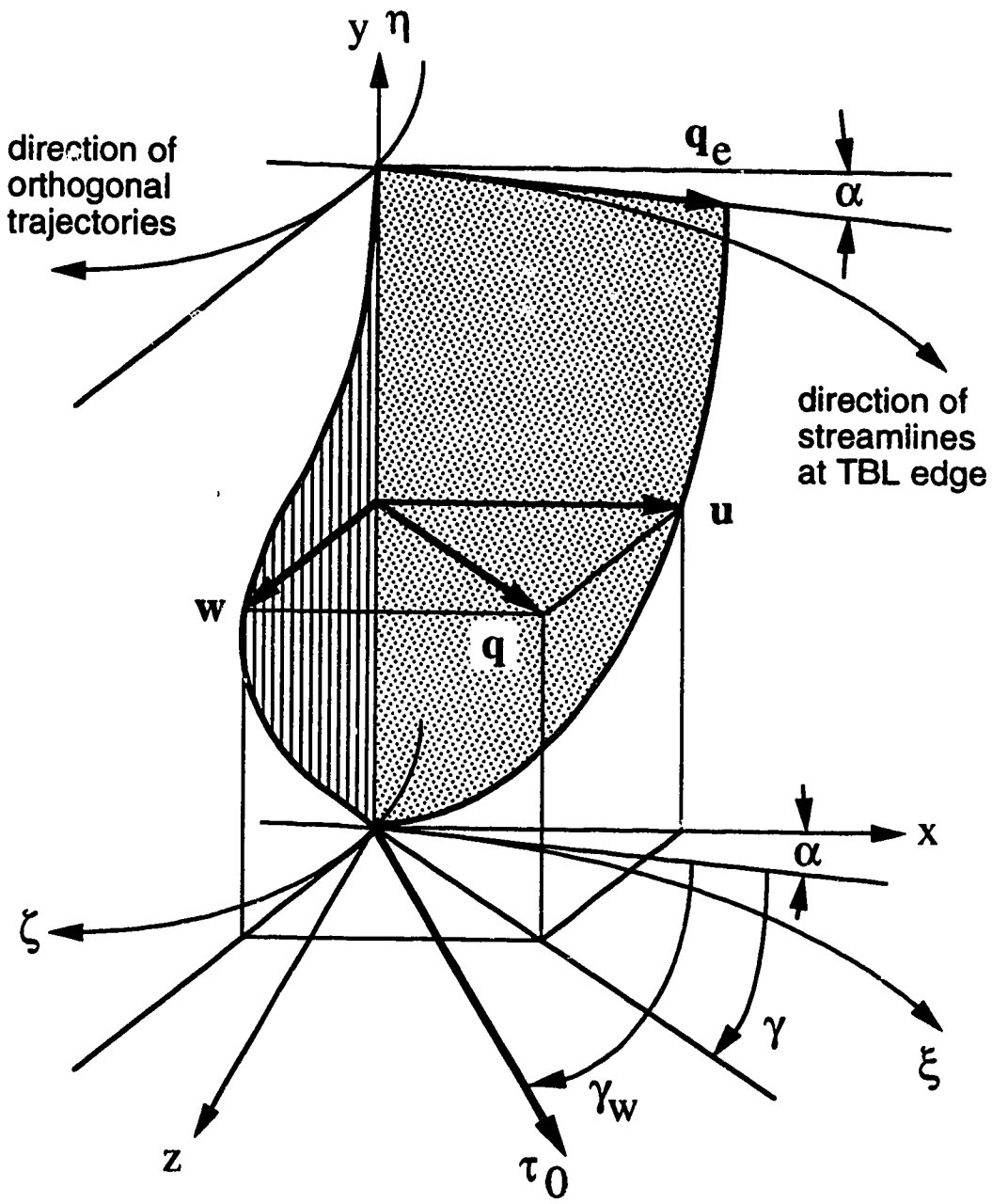

(a) coordinate systems and notations

Figure 2.4.2 Three-dimensional boundary layer

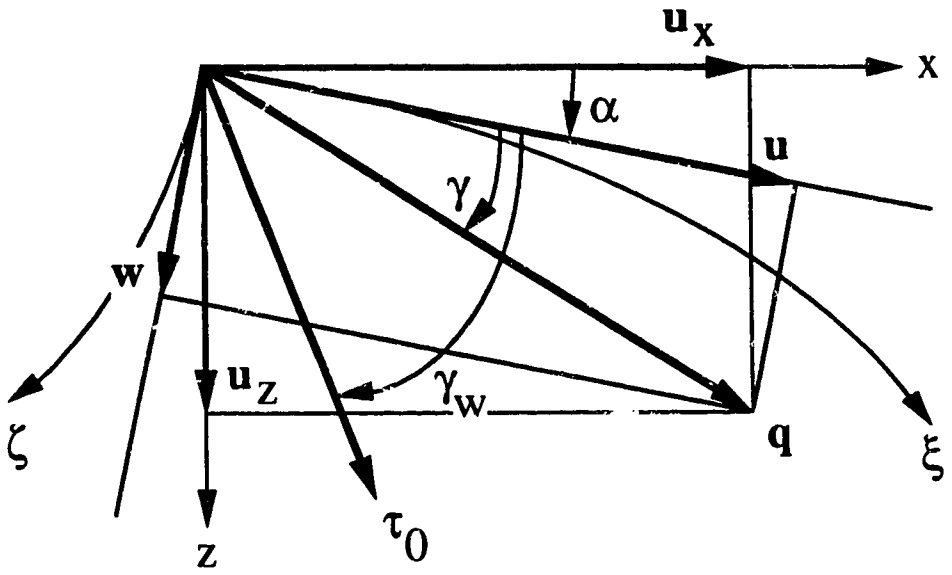

(b) components of velocity vector

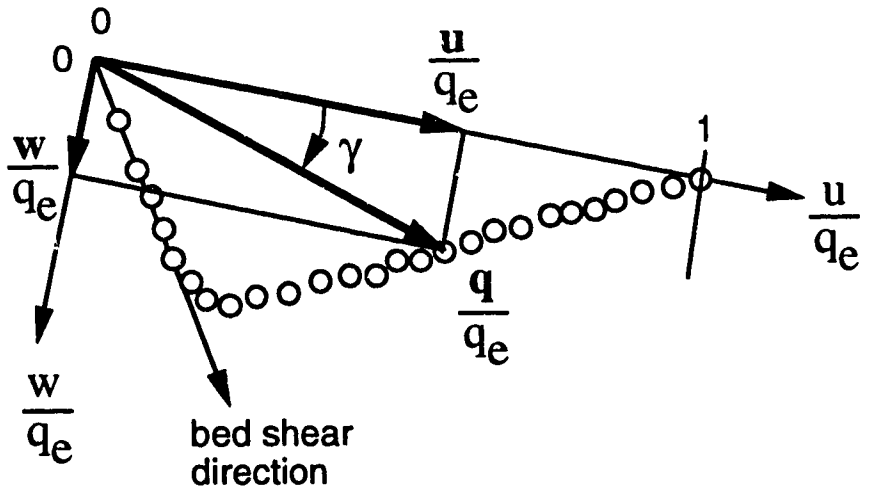

(c) hodographic representation

Figure 2.4.2 Three-dimensional boundary layer

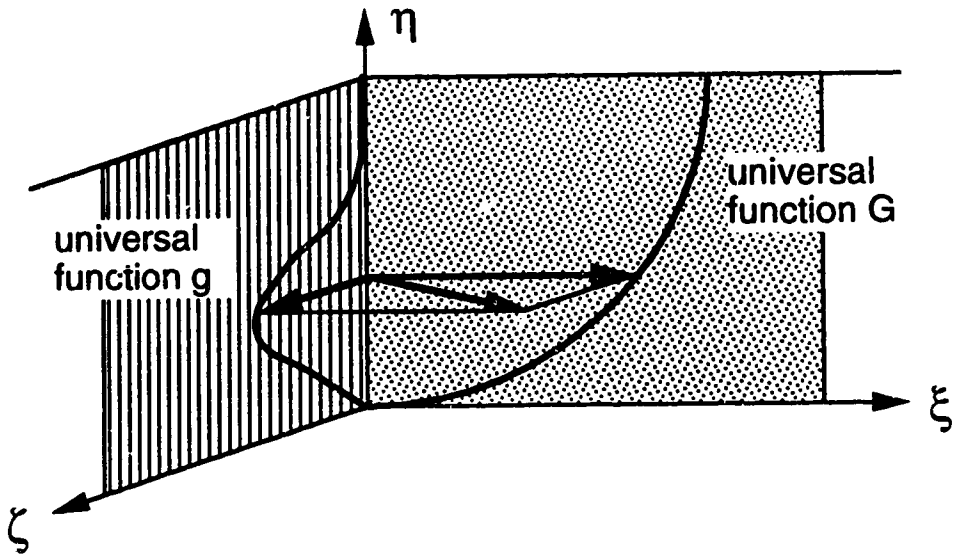

Figure 2.4.3 Prar nodel

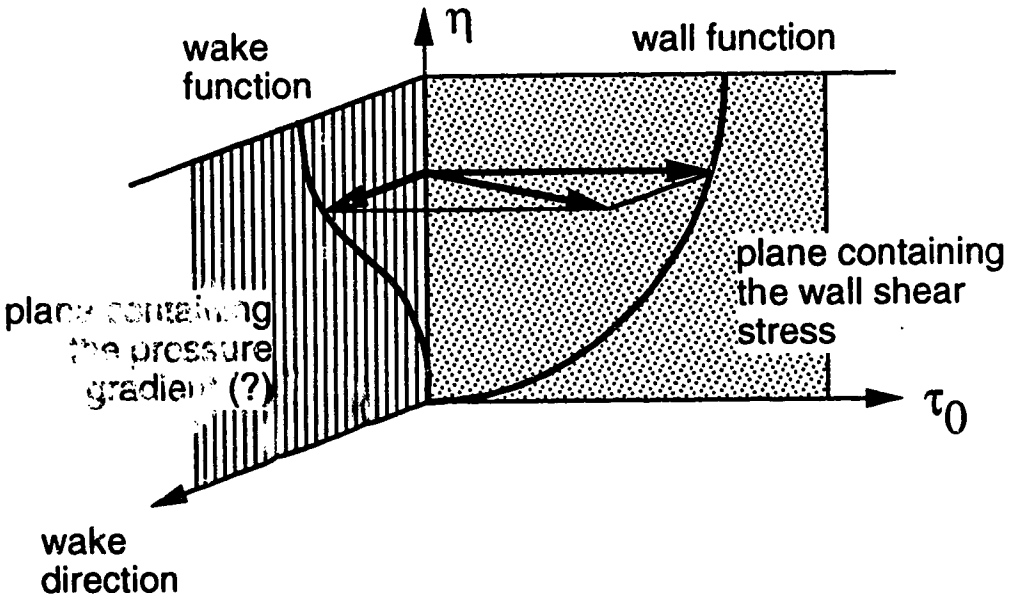

Figure 2.4.4 Coles' model

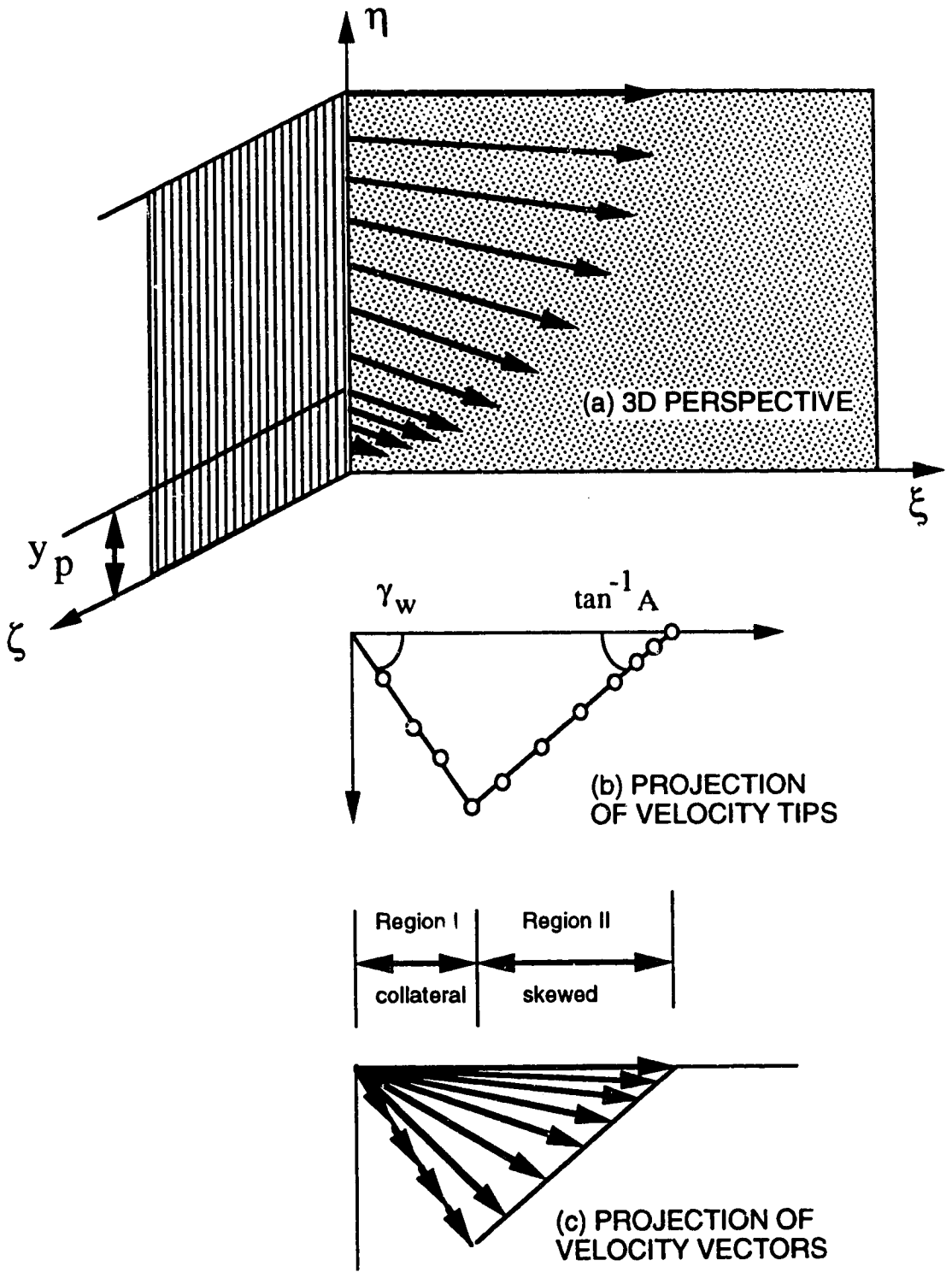

Figure 2.4.5 Johnston's model

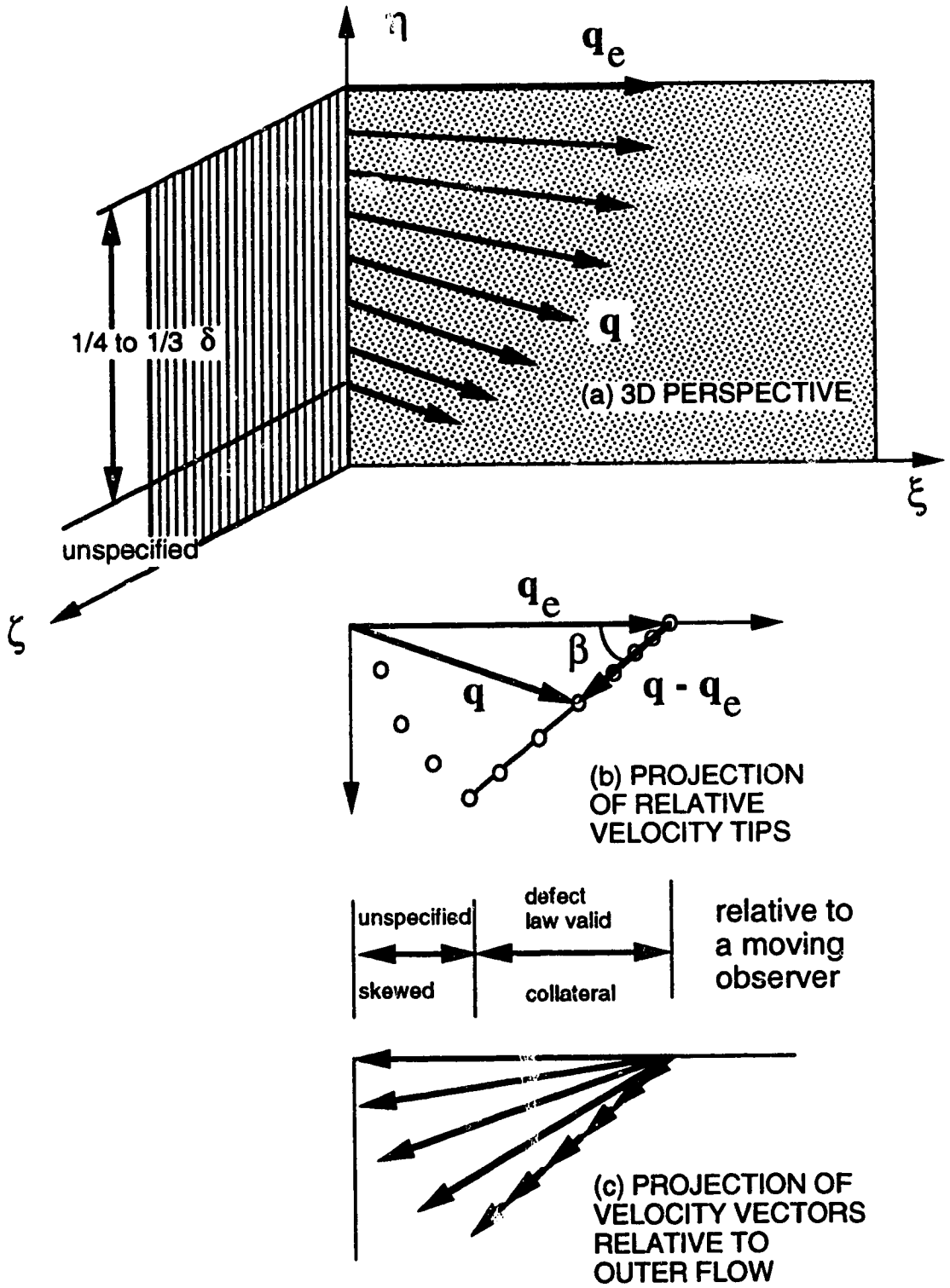

Figure 2.4.6 Perry and Joubert's model

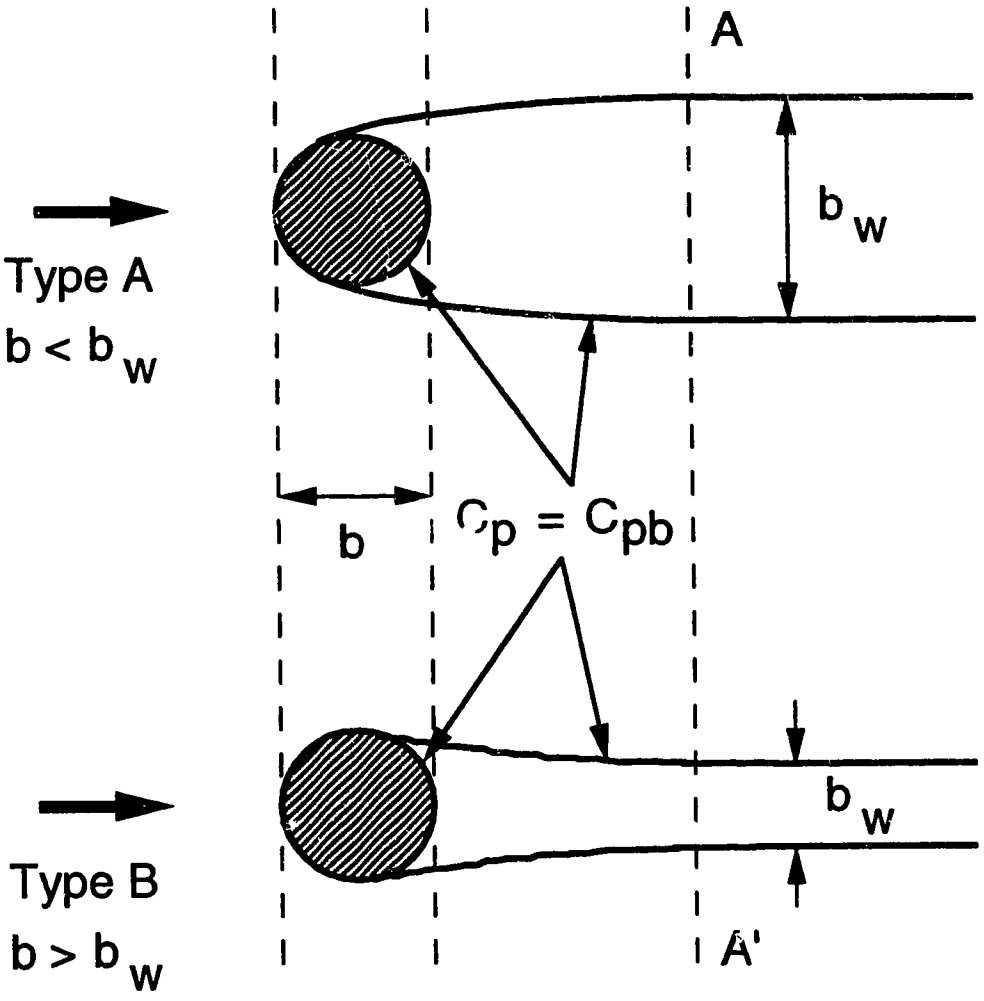

Figure 2.5.1 Roshko's free streamline model

Chapter 3
Equipment and Experimental Procedures

3.1 Introduction

In this chapter the experimental arrangement and other related facilities are described. First of all, the nature of the velocity profile over rough surfaces is described which is related to the measurement of wall shear stress. A couple of methods devised to avoid trial and error procedures in velocity profile analysis and Patel's calibration of Preston tube are given. Then the test procedures are described. Finally experimental errors are described and uncertainty estimates are given.

3.2 Velocity Profile over Rough Surfaces

The general form of the equation describing the 2D velocity profile over rough surfaces is

$$\frac{u}{u_*} = \frac{1}{\kappa}\ln\left(\frac{y}{k}\right) + B \qquad [3.2.1]$$

where u is the (time-averaged) velocity at a normal distance y from an appropriate datum; k is the characteristic length scale of the roughness elements; B is a function of the roughness Reynolds number k^+ ($= u_* k / \nu$); and κ is the von Karman constant ($\approx$ 0.4).

The experiments of Nikuradse (1933) with pipes roughened with uniform sand grains provided the necessary framework for evaluating B as a function of $u_* k / \nu$. The velocity profile over a wall with any arbitrary roughness can now be expressed in terms of Nikuradse's equivalent sand roughness as

$$\frac{u}{u_*} = \frac{1}{\kappa}\ln\left(\frac{y}{k_S}\right) + B_S \qquad [3.2.2]$$

where k_S is the equivalent sand roughness; and B_S is the corresponding value of B and is a function of k_S^+ ($= u_* k_S / \nu$).

Given a measured velocity profile, it is possible to determine u_* and then the value of B if k is known. In case of open channel flow over a sand bed, k can be taken as equal to D_{50} without any loss of generalization. However, it is a common practice to

express the velocity profile in terms of k_s and B_s. Equating Equations [3.2.1] and [3.2.2] it can be shown that

$$\frac{k_s}{k} = \exp\left[\kappa(B_s - B)\right] \qquad [3.2.3]$$

With k and B already known, k_s can be determined if the relation between k_s and B_s is known. This rela as determined by Nikuradse (1933) as shown in Figure 3.2.1. It takes a trial and edure to find out both k_s and B_s simultaneously. This trial and error procedure ca avoided by manipulating Equations [3.2.1] and [3.2.2] in a different way to get

$$B - \frac{1}{\kappa}\ln\left(\frac{ku_*}{\nu}\right) = B_s - \frac{1}{\kappa}\ln\left(\frac{k_s u_*}{\nu}\right) = B_s' \qquad [3.2.4]$$

The variation of the newly defined variable B_s' with u_*k_s / ν can be easily determined from the known values of B_s. This is also shown in Figure 3.2.1. Now from a known value of B_s' we can find u_*k_s / ν and then k_s and B_s from Figure 3.2.1. It may be noted that Equations [3.2.3] and [3.2.4] are equivalent statements.

The curves of Figure 3.2.1 were derived from the original equations suggested by Nikuradse. According to Nikuradse, when $u_*k_s / \nu \leq 3.5$ the roughness elements are totally submerged within the viscous sublayer and the flow is hydraulically smooth and

$$B_s = \frac{1}{\kappa}\ln\left(\frac{u_*k_s}{\nu}\right) + 5.5 \qquad [3.2.5]$$

which, when substituted in Equation [3.2.2], reduces it to the well-known smooth boundary law of the wall

$$\frac{u}{u_*} = \frac{1}{\kappa}\ln\left(\frac{yu_*}{\nu}\right) + 5.5 \qquad [3.2.6]$$

When $u_*k_s / \nu \geq 70$, the roughness elements protrude out of the viscous sublayer and the sublayer is completely destroyed; the flow is completely rough and B_s maintains a constant value of 8.5. Thus Equation [3.2.2] takes the following form.

$$\frac{u}{u_*} = \frac{1}{\kappa}\ln\left(\frac{y}{k_s}\right) + 8.5 \qquad [3.2.7]$$

In the transitional region ($3.5 \leq u_*k_s / \nu \leq 70$), some roughness elements protrude out of the viscous sublayer and the sublayer is partially destroyed. In this range B_s varies continuously with u_*k_s / ν and was approximated by Nikuradse as follows:

for $3.5 \leq u_*k_s / \nu \leq 7.1$

$$B_S = 6.59 + 3.5 \log\left(\frac{u_* k_S}{\nu}\right) \qquad [3.2.8a]$$

for $7.1 \le u_* k_S / \nu \le 14.1$

$$B_S = 9.58 \qquad [3.2.8b]$$

for $14.1 \le u_* k_S / \nu \le 70$

$$B_S = 11.5 - 1.62 \log\left(\frac{u_* k_S}{\nu}\right) \qquad [3.2.8c]$$

3.3 Physical Facilities

3.3.1 The flume

The experiments were conducted in a straight rectangular flume 18.4 m long, 1.22 m wide, and 0.67 m deep. It had a smooth aluminum bed and the side walls were made of smooth transparent Plexiglas. The flume was mounted on three pairs of synchronized screws which were driven by an electric motor for slope adjustment. A tailgate installed at the downstream end of the flume was used to adjust the depth of flow. A traverse system was also mounted on the flume. It could hold the probes and point gauges in place. The traverse system could also be moved manually in any direction (longitudinal, transverse or vertical).

Water was supplied to the head tank of the flume from an underground sump network by a Fairbanks-Morse propeller pump through a 200 mm diameter pipe. The maximum discharge of the pumping system was about 72 L/s. The discharge was measured by a 200 mm diameter Foxboro magnetic flowmeter and was displayed in a Fluke 8000A digital multimeter which showed up to one tenth of a L/s. When the experiments were run for several days, the discharge fluctuation as shown by the multimeter was about 0.2 to 0.6 L/s.

The head tank was 2.44 m long and 1.8 m wide, and had smooth semi-circular contractions from the side walls and the floor into the flume. The turbulent agitation caused by the delivery pipe was first intercepted by a weir of masonry brick. Then the water was guided through a flow straightener consisting of a number of 1 m long pipes with a diameter of 100 mm. Furthermore, 50 mm thick mattresses of synthetic hair-like material were placed both upstream and downstream of the flow straightener to suppress surface waves and turbulence.

The experimental arrangement for the mobile bed runs is shown in Figure 3.3.1. In these runs the scour hole was allowed to develop in the sand bed. A wooden frame,

165 mm high and 10 m long, was constructed on the flume bed and was covered with a 15 mm thick layer of the desired sand. At the upstream end a 5 ramp covered with rough sand paper was constructed to provide smooth transition of water depth. A 0.78 m by 0.78 m sediment recess was constructed in the wooden frame at a distance of 7.5 m from the start of sand bed. The cylinder of desired size was placed vertically inside the sediment recess. The size of the recess was found adequate for containing the scour holes. The coordinate system adopted is also shown in the figure.

In the case of rigid bed runs, the scour hole was not allowed to develop. This was achieved by wholly covering the sediment recess with a wooden plank. The cylinder was then placed on this plank and sand was glued to it to simulate the roughness but at the same time not allowing any scour hole to develop. This is shown in Figure 3.3.2 along with the arrangement for smooth bed runs in which case the original flume bed was used.

3.3.2 Sand types

Two types of natural sand of specific gravity 2.65 were used. The sands are shown against a 2 mm by 2 mm grid in Figure 3.3.3. It may be noted that the finer sand consists of quartz grains most of which are well rounded. The coarser sand probably contains a variety of minerals, and some grains were angular. Their grain size distributions are shown in Figure 3.3.4. The mean diameters (D_{50}) of them were 0.88 mm and 1.84 mm. In this work the sands will be designated by their D_{50} values. Other properties are given in Table 3.3.1.

Table 3.3.1 Sand characteristics

	0.88 mm sand	1.84 mm sand
mean diameter, D_{50} (mm)	0.88	1.84
$D_{84.1}$ (mm)	1.11	2.14
$D_{15.9}$ (mm)	0.75	1.48
geometric standard deviation, σ_g	1.22	1.20
Specific gravity, S_s	2.65	2.65
angle of repose, α_r (degree)	28	30
critical shear stress, τ_c (Pa)	0.420	1.214

3.3.3 Pressure transducers

Velocity and pressure were measured by using Validyne DP45-16 variable reluctance differential pressure transducers. The range of these transducers was ±1.4 inches (35.56 mm) of water or ±348.84 Pa. Thus these were capable of measuring a maximum velocity of about 0.83 m/s. The accuracy as given by the manufacturer was ±0.25% of the full scale which is equivalent to ±0.1778 mm of water or ±1.7442 Pa. The readings of the pressure transducers were displayed on Validyne CD379 portable transducer indicators in digital form. The signals from the indicators were then fed into a computer for further analysis.

The transducers were calibrated by applying known heads of ±1 inch (25.4 mm) of water with 0.1 inch (2.54 mm) increments. The indicators were adjusted to show readings of +1 volt for a +1 inch (25.4 mm) head and to show a zero reading for a zero pressure head. A typical calibration is shown in Figure 3.3.5. The tests shown were done at different times over a period of two months. Good repeatable responses were found and they were almost linear. However, a polynomial of order three was fitted for each transducer. The calibration were checked from time to time to ensure the proper functioning of the transducers.

3.3.4 Data acquisition system

A data acquisition system was developed and was available at the T. Blench Hydraulics Lab. This system consisted of a Macintosh fx II computer and several programs written in LabView language. The programs were fed with appropriate calibration data of the probes and pressure transducers, and then they could compute the velocity magnitude, its direction and piezometric pressure as the case may be using the inputs received from appropriate probes. The programs also enabled the user to set the total number of samples and the time interval between two consecutive samples (sampling frequency). The real time values were shown graphically on the computer screen. The arithmetic average and the standard deviation of all quantities measured were then saved on a disk.

Usually 2000 samples were taken for velocity measurement at a frequency of 10 Hz. Thus a value acquired in this way was the time-averaged one over a period of 200 seconds (3.33 minutes). For pressure measurement 4000 samples were taken at the same frequency over a period of 6.67 minutes.

3.4 Velocity Measurement

3.4.1 Pitot-static tube

Pitot-static tubes were used to measure velocity when the direction of flow was known, *e.g.*, the undisturbed 2D flow at the center plane of the flume without the cylinder in place. Tubes of two sizes were used, with external diameters of 1/8 inch (3.2 mm) and 1/16 inch (1.6 mm). These were commercially available from United Sensors.

3.4.2 Yaw and pitch probes

However, in most of the flow situations, the flow direction was unknown. With the cylinder in place, the flow even on the plane of symmetry had unknown direction because it had both longitudinal and vertical components. Pitch probes were used in this case. The skewed flow around the cylinder was measured by a yaw probe.

A set of yaw and pitch probes developed and available at the T. Blench Hydraulics Laboratory were used when both magnitude and direction of the velocity vector were unknown but the plane containing the velocity vector was known (exactly or approximately).

They were fabricated and calibrated by Rajaratnam and Muralidhar (1967) and have since been successfully used by a number of researchers. Some of the probes were made of three lengths of stainless steel tube of 3 mm external diameter and 1.8 mm internal diameter. Others were made of smaller tubes of 1.3 mm external diameter and 0.8 mm of internal diameter. The three tubes were rigidly soldered together. The nose of the probe was machined so that the face of the central tube was perfectly flat and the side tubes were chamfered at an angle of 45° (Figure 3.4.1).

The working principle as given by Rajaratnam and Muralidhar (1967) is as follows. If a yaw probe is placed in a 2D flow, as shown in Figure 3.4.1(a), at an angle θ with the velocity vector, then the piezometric heads sensed by the three probes may be written as

$$h_1 = h_0 + K_1 \frac{V^2}{2g} \qquad [3.4.1]$$

$$h_2 = h_0 + K_2 \frac{V^2}{2g} \qquad [3.4.2]$$

$$h_3 = h_0 + K_3 \frac{V^2}{2g} \qquad [3.4.3]$$

where h_0 is the static piezometric pressure head at the point under consideration; and K_1, K_2 and K_3 are calibration coefficients and are functions of only θ. Manipulating the above equations it can be shown that

$$\frac{h_2 - h_3}{h_2 - h_1} = \frac{K_2 - K_3}{K_2 - K_1} = K_4 \qquad [3.4.4]$$

and

$$V = \frac{\sqrt{2g(h_2 - h_1)}}{\sqrt{K_2 - K_1}} = K_5\sqrt{2g(h_2 - h_1)} \qquad [3.4.5]$$

where two new coefficients K_4 and K_5 have been defined and introduced.

By rotating the yaw (and pitch) probes through known angles in the potential core of a plane turbulent jet produced by a deeply submerged sluice gate, Rajaratnam and Muralidhar (1967) determined the calibration curves for K_1 through K_5 as a function of θ. The range was zero to 60° and the calibration curves were symmetrical for the other side (zero to -60°). It was found that the same calibration curves could be used for both yaw and pitch probes of either size. The calibration curves are shown in Figure 3.4.1(a).

Computation of the magnitude (V) and direction (θ) of the velocity vector V consisted of the following steps. These were executed by a computer program. Only discrete experimental points were fed into the computer; and points in between were calculated by linear interpolation.

1. measure $(h_2 - h_3)$ and $(h_2 - h_1)$ with differential pressure transducers;
2. find K_4 from Equation [3.4.4];
3. find θ as a function of K_4 from Figure 3.4.1(a);
4. find K_5 as a function of θ from Figure 3.4.1(a); and finally
5. compute V from Equation [3.4.5].

The yaw probe was used when the velocity vector was on the a horizontal (or x-z) plane. Since the working principle and the calibration of the pitch probes are exactly the same, it could be used when the vertical (or x-y) plane contained the velocity vector.

3.5 Pressure Measurement

In the present study, pressure was measured only on the plane of symmetry and hence the pitch probes could be readily used. The working principle is as follows. In addition to $(h_2 - h_3)$ and $(h_2 - h_1)$, if $(h_2 - h_{ref})$ is also measured where h_{ref} is a known

reference head, then h_2 can be readily found and the static piezometric pressure head h_0 can be computed from Equation [3.4.2] as

$$h_0 = h_2 - K_2 \frac{V^2}{2g} \qquad [3.5.1]$$

3.6 Bed Shear Measurement

3.6.1 Velocity profile method

A measured velocity profile, when plotted on a semi-log paper, can be used to calculate the shear velocity and thus the wall shear stress. The data points usually fall on a straight line in the log-law region, and a best fit straight line can be drawn. The slope of this line is the shear velocity and may be calculated as

$$\sqrt{\frac{\tau_0}{\rho}} \equiv u_* = \frac{u_2 - u_1}{5.75 \log\left(\frac{y_2}{y_1}\right)} \qquad [3.6.1]$$

from any two points on the fitted line (assuming $\kappa = 0.4$). In the case of rough surfaces, it is important to determine a correct datum for y. Based on earlier research (*i.e.*, Einstein and El-Samni 1949; and Hollingshead 1972), this datum was assumed to be at 0.2 times sand diameter below the tops of the sand grains.

This method was used in the undisturbed 2D flow with no cylinder in place. It uses data points of most of the velocity profile and usually gives more accurate values of bed shear both on smooth and rough beds than other methods described below.

3.6.2 Preston tube technique

From similarity considerations and based on the existence of the law of the wall, Preston (1954) found that the dynamic pressure Δp (difference of the total pressure sensed by a total head tube resting on the wall and the static pressure) can be expressed as a function of wall shear stress τ_0 (or friction velocity u_*), density (ρ) and kinematic viscosity (ν) of the fluid, and a length scale (external diameter of the tube, d). A dimensional analysis leads to the following expression where $\Delta p_* = \Delta p d^2 / 4\rho\nu^2$ and $\tau_{0*} = \tau_0 d^2 / 4\rho\nu^2$.

$$\Delta p_* = F_s\langle \tau_{0*} \rangle \qquad [3.6.2]$$

Several attempts were made by different researchers to find out the function F_S. The calibration of Patel (1965) is believed to the definitive one and it has been used for smooth walls in this study. However it may be noted that the original equations of Patel did not always make variables explicitly expressible in terms of others (Table 3.6.1). This required a trial and error procedure. To avoid this inconvenience, explicit expressions were derived from the original equations as shown in Table 3.6.1, along with the ranges in terms of different variables. This facilitated a quick determination of shear stress from the dynamic pressure, which was measured by the Pitot-static tubes described earlier.

In the case of rough walls, an additional length scale k_s has to be included and the expression for wall shear stress takes the following form.

$$\frac{\Delta p}{\tau_0} = F_r\left\langle \Delta p_*, \frac{d}{k_s} \right\rangle \qquad [3.6.3]$$

The analytical form of this relation was worked out by Hollingshead and Rajaratnam (1980) based on the validity of the law of the wall for rough surfaces (Equations [3.2.7] and [3.2.8]). The datum for y was also assumed to be at 0.2 times the sand diameter below the tops of the sand grains. This analytical calibration was found to be in reasonably good agreement with the available experimental data.

It may be noted that for fully rough flow ($u_* k_s / \nu \geq 70$), F_r becomes independent of Δp_* and thus F_r assumes a constant value for a particular value of d / k_s. This idea could be conveniently used to simplify the computation of bed shear as described below. For the sand bed experiments (Series C and D) where bed shear were extensively measured, the flows were fully rough and thus F_r had constant values for each experiment. In the 2D undisturbed flow τ_0 was carefully calculated from the velocity profile and Δp was measured by taking a large number of samples (10,000). From these, an accurate numerical value of F_r was calculated which was later used to measure the bed shear around the cylinder. Moreover, F_r calculated in this way is also expected to absorb, at least to some extent, the displacement effect, just like the original function F_S for smooth beds.

3.6.3 Yaw probe used as Preston tube

The Preston tube technique using Pitot-static tubes could not be used where the direction of bed shear was unknown. Rajaratnam and Muralidhar (1968) devised a way of using the yaw probe as a Preston tube. The working principle is as follows. If a yaw probe, made of the same size of tube as a Preston tube, is placed on the wall (Figure

3.4.1(b)) at an angle θ with the direction of the shear stress, then the total pressures sensed by the tubes may be expressed as

$$p_1 = p_0 + K_{10}\Delta p \qquad [3.6.4]$$

$$p_2 = p_0 + K_{20}\Delta p \qquad [3.6.5]$$

$$p_3 = p_0 + K_{30}\Delta p \qquad [3.6.6]$$

where p_0 is the static pressure and K_{10}, K_{20} and K_{30} are calibration coefficients and are functions of θ only. The above equations can be used to show that

$$\frac{p_2 - p_3}{p_2 - p_1} = \frac{K_{20} - K_{30}}{K_{20} - K_{10}} = K_{40} \qquad [3.6.7]$$

and

$$\frac{p_2 - p_1}{K_{20} - K_{10}} = \frac{p_2 - p_1}{K_{50}} = \Delta p \qquad [3.6.8]$$

where two new coefficients K_{40} and K_{50} have been defined and introduced. The variation of these coefficients with θ was found out from known flow conditions. These are shown in Figure 3.4.1(b).

Computation of the magnitude (τ_0) and direction (θ) of the bed shear vector $\vec{\tau}_0$ consisted of the following steps. These were executed by a computer program. Only discrete experimental points were fed into the computer; and points in between were calculated by linear interpolation.

1. measure ($p_2 - p_3$) and ($p_2 - p_1$) with differential pressure transducers;
2. find K_{40} from Equation [3.6.7];
3. find θ as a function of K_{40} from Figure 3.4.1(b);
4. find K_{50} as a function of θ from Figure 3.4.1(b);
5. find Δp from Equation [3.6.8]; and finally
6. compute τ_0 from Equation [3.6.2] for smooth beds and from Equation [3.6.3] for rough beds.

3.7 The Experiments

3.7.1 Choice of experiments

The experiments performed in this study are listed in Table 3.7.1 along with the important parameters. Each series has different flow conditions. The first character (A, B, C, D, E, or F) in a experiment number denotes the series to which it belongs. The second character (1, 2, 3, or 4) indicates the size of the cylinder used (radius = 54, 44.5, 32, or 21.1 mm). Smooth, transparent acrylic cylinders were used. A zero (0) indicates no cylinder, and thus the undisturbed 2D flow. A third character (M = mobile, R = rigid, or S = smooth) describes both the nature of the bed and whether a scour hole was allowed to develop. In the case of mobile beds, the scour hole was allowed to develop. But for a rigid bed case, the sediment recess was wholly covered with a wooden plank. A cylinder of the desired size was placed on it and the base of the cylinder was sealed water-tight. Then, one layer of sand of the desired size was glued on the plank and left to dry. The plank was large enough to cover the area which was vulnerable to bed deformation either by scouring or deposition. The rigid bed thus provided the roughness of a sand bed but did not allow bed deformation around the cylinder. It is, therefore, expected to simulate the condition just prior to scouring in a sand bed. Smooth bed runs were made on the original smooth aluminum bed of the flume.

The selection of experiments was guided by the following considerations:

(a) **Flow conditions**: The flow had to be fully developed at the test section. This was verified by comparing several measured velocity profiles at the test section. The width/depth ratio (W / y_0) was made as large as possible to ensure the two-dimensionality of the approach flow. Two ratios of 6.7 and 8.7 were achieved. The ratio of flow depth to pier diameter ($y_0 / 2r$) varied from 1.3 to 4.3, and the ratio of pier diameter to sand size ($2r / D_{50}$) ranged from 23 to 123. It was intended to keep the flow conditions as simple as possible. Therefore, only uniform sands ($\sigma_g < 1.35$) were used and the shear ratio (τ_{00} / τ_c) was kept low enough not to cause any general bed load transport and not to produce any bed form on its own.

(b) **Ease of measurement**: Since the principal objective of this study was to investigate the flow pattern in detail, care was taken to produce flow conditions which made flow measurement easier. This was particularly crucial in the case of mobile bed runs. The larger (1.84 mm) sand was more suitable for this purpose, and flow measurements were conducted only with this sand (Series C and D). The larger yaw probe (with 3 mm tubes) was used to measure bed shear and skewed velocity profiles on sand beds. Measurements could be done without any problem even in Series D with a shear ratio of 0.88.

(c) **Comparison of flows**: A better perspective of a flow as complicated as the one around a bridge pier with a changing bed configuration can be gained if we start with a simpler condition and then move towards more complex situations. That is why two smooth bed runs were done in addition to mobile and rigid bed runs. It was hoped that this would allow us to see the how the roughness and then the scour hole affect the flow pattern. The effect of roughness can be seen by comparing two pairs of experiments (C2R & E2S; and D2R & F2S) and that of scour hole by comparing four pairs of experiments (C1M & C1R; C2M & C2R; D2M & D2R; and D3M & D3R)

3.7.2 Test procedures

For each series of experiments, the undisturbed flow (A0, B0, *etc.*) was first established. For a particular discharge, the flume slope and depth were adjusted to produce uniform flow conditions. The flow depth was measured along the flume center line with a manual point gauge. Uniform flow was assumed when the flow depth was within ±1 mm of the mean value in the test section (1.5 m upstream and downstream from the cylinder location). Velocity profiles were then taken at the cylinder location, 1 m upstream and 1 m downstream sections, all on the flume center line. An increase of velocity with depth throughout the flow depth indicated that the boundary layer extended up to the free surface. Further support was provided by a good collapse of these profiles as shown in Figure 3.7.1 which also indicated that the flow was invariant in the longitudinal direction.

After establishing the test flow condition, the flume was dried and the cylinder installed in place. The lower end of the cylinder was sealed water-tight. For mobile bed runs, the sand bed was carefully leveled and the flume was slowly filled with water from the tail end so that the sand bed was not disturbed. This was continued even when the water spilled over the tailgate. After some time all the water supplied into the flume was spilling over. The water depth in the flume at this stage was lower than the desired depth but was the closest to it that could be achieved without disturbing the sand bed. Then the pump was started and the controlling valve was opened as quickly as possible to reach the desired discharge. It took less than a minute. For series A and B where flow was not measured, the flow was run until the increase in the scour depth was less than 1 mm in 24 hours. It usually took 10 to 13 days to attain this stage. One experiment (A1M) was run for 22 days. For mobile bed runs of Series C and D, the flow measurement was started after 7 to 9 days when the rate of scour was considered very low. And the flow was stopped after all the measurements were finished, usually after 15-18 days. The

measurements were expected to give an approximate picture of the flow pattern at the equilibrium stage.

In the case of rigid bed runs, the flow was started the same way, the only difference being that flow measurements could be started after a few minutes. In all mobile and rigid bed runs, after the completion of one experiment, the flume was carefully drained so as not to disturb the sand bed. For smooth bed runs, there was no need to fill or drain the flume slowly. The pump was just started and measurements were taken.

3.7.3 Characteristics of undisturbed flows

The velocity profiles in the test section collapsed together as shown in Figure 3.7.1, indicating a fully developed flow that remains the same in the longitudinal direction. The velocity profiles were analyzed to derive other parameters as shown in Table 3.7.2. These parameters gave further insight into the nature of flow. Displacement and momentum thicknesses were calculated numerically from the measured velocity profiles. As mentioned earlier, the velocity at a point was computed as the arithmetic average of 2000 samples. The standard deviation (σ_u) was also calculated automatically, as shown in Figure 3.7.2. This value at a point gives a crude indication of the turbulent agitation. It can be seen from Figure 3.7.2 that σ_u is greater in the case of fully rough flows (Expt. C0 and D0), with the maximum at about 20-30 mm above the bed. In case of smooth flows (E0 and F0), this maximum is less pronounced and the overall agitation seems somewhat less. It is still less in the case of Expt. A0 and B0. These flows were transitionally rough and finer sand was used. The smaller value of σ_u may be due to low velocities. The velocity profiles are shown in Figures 3.7.3 along with the fitted log law equations.

An attempt was made to compute the boundary layer development length (L) theoretically. For a boundary layer growing on a smooth flat plate, the local skin friction coefficient c_f at any point may be expressed as a function of the Reynolds number based on the distance of this point from the leading edge of the plate (x) and the outer potential velocity U_∞ (Schlichting 1968, pp. 597-603):

$$c_f \equiv \frac{\tau_0}{\frac{1}{2}\rho U_\infty^2} = \left[2\log\left(\frac{xU_\infty}{\nu}\right) - 0.65\right]^{-2.3} \qquad [3.7.1]$$

If it is assumed that the skin friction changes with x in a water channel until the growing boundary layer hits the free surface and that beyond this point the flow remains invariant for uniform flows, then the above equation can be used to compute the development

length. The bed shear and the surface velocity at a uniform flow section may be taken as the bed shear and U_∞ respectively at this point ($x = L$) and L can be readily computed.

For a boundary layer growing on a rough plate, c_f depends on k_s also, so that the function takes a more general form (Schlichting 1968, pp. 610-611):

$$c_f \equiv \frac{\tau_0}{\frac{1}{2}\rho U_\infty^2} = f\left(\frac{xU_\infty}{\nu}, \frac{x}{k_s}\right) \qquad [3.7.2]$$

or

$$c_f \equiv \frac{\tau_0}{\frac{1}{2}\rho U_\infty^2} = f\left(\frac{xU_\infty}{\nu}, \frac{k_s U_\infty}{\nu}\right) \qquad [3.7.3]$$

For fully rough flow, Equation [3.7.3] takes the following functional form:

$$c_f \equiv \frac{\tau_0}{\frac{1}{2}\rho U_\infty^2} = \left[2.87 + 1.58\log\left(\frac{x}{k_s}\right)\right]^{-2.5} \qquad [3.7.4]$$

But for the transitionally rough regime, no simple expression is available. Instead the function is given in a graphical form (Figure 21.7 of Schlichting 1968, p. 611). With the known value of k_s, L can be computed from Equation [3.7.4] or the graph for a rough channel. It may be noted that Yalin (1977, pp. 42-46) modified Equation [3.7.4] to make it expressible in terms of flow depth y_0 instead of τ_0.

Development lengths were computed by Schlichting's equations and are presented in Table 3.7.2. The boundary layer hit the free surface well before the test section for all experiments except B0 for which the computed value of L was very large (12.4 m). Velocity profiles of B0 were also unique in showing a marked wake component (Figure 3.7.3(b)). On a more careful scrutiny, the B0 profiles show a slight slowing down with x (Figure 3.7.1). This might have been caused by a backwater effect that escaped detection at the time of Series B experiments.

3.8 Experimental Errors and Uncertainties

3.8.1 Basic concepts

From the point of view of reliability estimates, experiments fall into two categories: single-sample and multiple-sample experiments. When a sufficiently large number of measurements are taken using various methods and instruments so that the reliability of the results can be evaluated statistically, then the experiment is called

multiple-sample. On the other hand, an experiment in which the uncertainties are not found from such repetition is called *single-sample*. Most engineering experiments, including the present one, are single-sample. A very useful and practical way of describing uncertainties in engineering experiments was introduced by Kline and McClintock (1953) which has since been widely used by experimenters in the field of fluid mechanics. Their idea of describing the uncertainties in basic variables and of how they propagate into other variables dependent on them will be presented briefly in this section.

An *error* is defined as the difference between the true and measured values of a variable. The *uncertainty* associated with this measurement is defined as what one thinks the probable error might be with a certain degree of confidence.

Errors may be classified into three types:

1) Random (or accidental or precision) error;
2) Fixed (or bias or systematic) error; and
3) Mistakes (or blunders).

Random errors are those varying errors which occur without any apparent reason. These arise from instrument friction and time lag, personal observation power and many other incorrectable sources. *Fixed errors* are those which cause repeated readings to be in error by the same amount without apparent reason. Known reasons, such as a dent on the probe, causing a fixed error can be fixed and the error removed. Some fixed errors are sometimes known and accepted, such as the wall effects on the Pitot tube readings. It is the undetected reasons for which fixed errors remain in the measurement. Some of these can be detected by using different instruments or checking simply related variables, and suitable corrections can be made without physically removing the cause of error. Other fixed errors which are not detected at all, of course, creep into the measurement in the guise of random errors. *Mistakes* are completely erroneous readings of scales, watches, and so on. These are usually detectable on inspection as "way out" and are discarded. In error analysis, it is assumed that all the fixed errors and mistakes have been detected and removed. So only the random errors are considered.

Most of the observed random errors have a normal frequency distribution although non-normal distributions have been exhibited by some. For general engineering purposes, random errors are generally assumed to have normal distribution. However, in a single-sample experiment, no measure of error is obtained, let alone the information sufficient to construct a distribution. Consequently, the experimenter must rely on his/her past experience and judgment. The best he/she can do is to make a statement of what

he/she thinks would happen if the experiment was repeated an infinitely large number of times. A good and concise way to describe the uncertainty in a variable is to specify the most likely value (usually the arithmetic mean of several readings) and an uncertainty interval with a specified confidence level, such as

$$\text{Pressure} = 123.4 \pm 0.5 \text{ Pa (95\%)} \ .$$

This means that the experimenter believes that 123.4 Pa is probably the true value and that, if a large number of observations were taken, 95% of the them would fall within ±0.5 Pa of that mean value.

Kline and McClintock (1953) also described a method to compute the propagation of uncertainty into a result which is a function of n independent variables $V_1, V_2, ..., V_n$, with respective uncertainty intervals of $W_1, W_2, ..., W_n$, all with the same confidence level. Let the function be

$$R = R(V_1, V_2, ..., V_n) \qquad [3.8.1]$$

The uncertainty interval W_R with the same confidence level is given by the following relation.

$$W_R = \left[\left(\frac{\partial R}{\partial V_1} W_1 \right)^2 + \left(\frac{\partial R}{\partial V_2} W_2 \right)^2 + ... + \left(\frac{\partial R}{\partial V_n} W_n \right)^2 \right]^{1/2} \qquad [3.8.2]$$

Over the decades, this method has been widely accepted and used for uncertainty analysis by the fluid mechanics community. Often Equation [3.8.1] takes the form of

$$R = V_1^{m_1} V_2^{m_2} ... V_n^{m_n} \qquad [3.8.3]$$

and then Equation [3.8.2] may be expressed in the following more useful way.

$$\frac{W_R}{R} = \left[\left(m_1 \frac{W_1}{V_1} \right)^2 + \left(m_2 \frac{W_2}{V_2} \right)^2 + ... + \left(m_n \frac{W_n}{V_n} \right)^2 \right]^{1/2} \qquad [3.8.4]$$

3.8.2 Sources of error and estimate of uncertainty

All the uncertainty estimates were made with a confidence level of 95% (or 19 to 1 odds or 1 in 20 chance). The possible sources of errors are described for all measured variables. These along with the estimated uncertainties are given below.

Flume dimensions were measured with scales with millimeters on them. Therefore the uncertainty was ±0.5 mm. For cylinder measurement it was ±0.1 mm since

a more accurate scale was used. The uncertainty in measuring the flume bed was ±0.5 mm and that of the water surface was ±1 mm (relatively less accurate because of waves and fluctuation of the surface). Therefore the uncertainty of flow depth was ±1.12 mm, as may be calculated from Equation [3.8.2].

The uncertainty in discharge measurement was estimated at ±0.5 L/s. From the uncertainties in flume width W, flow depth y_0 and discharge Q, the uncertainty in average velocity U_0 ($= Q / Wy_0$) may be computed.

For example, in the case of Expt. A0

$Q = 50 \pm 0.5$ L/s,

$W = 1220 \pm 0.5$ mm,

$y_0 = 182 \pm 1.12$ mm.

Therefore, $$U_0 = \frac{Q}{Wy_0} = \frac{50\,\text{L/s}}{1220\,\text{mm} \times 182\,\text{mm}} = 0.2252\,\text{m/s} \quad .$$

The uncertainty from Equation [3.8.4] is given by

$$\frac{W_{U_0}}{U_0} = \left[\left(1 \cdot \frac{0.5}{50}\right)^2 + \left(-1 \cdot \frac{0.5}{1220}\right)^2 + \left(-1 \cdot \frac{1.12}{182}\right)^2\right]^{1/2}$$

or

$$\frac{W_{U_0}}{U_0} = \left[1 \times 10^{-4} + 1.68 \times 10^{-7} + 3.78 \times 10^{-5}\right]^{1/2} = 0.0117 \quad .$$

With $U_0 = 0.2252$ m/s, the uncertainty in velocity computation W_{U_0} is equal to 1.17% of U_0 or 0.0026 m/s. A benefit of uncertainty analysis is that it points out exactly where improvements are necessary and fruitful. In the calculations above, it is obvious that improved accuracy in discharge and flow depth would improve the accuracy of the average discharge. However, at the same time it is also clear that improving only one of them would make little difference.

The uncertainty of the pressure transducer was taken as 0.5% of the full scale (manufacturer's accuracy 0.25%). This was based on the accuracy of the calibration procedure and the transducer's response. The response was found to be almost linear and no hysterisis effect was detected. On this basis the uncertainty in the differential pressure measurement was about ±0.35 mm of water or ±0.2832 Pa.

The accuracy of the velocity measurement with a Pitot-static tube depends mainly on the alignment, turbulence and wall effects. The alignments were made accurate to ±2° and no correction was made for turbulence and wall effects. Therefore, errors arising only from the pressure transducer were accounted for in the uncertainty estimate. The

uncertainty calculated this way is 34% for 0.1 m/s which was about the lowest velocity recorded, and decreased rapidly with increasing distance from the bed (8.6% for 0.2 m/s, 3.8% for 0.3 m/s, 2% for 0.4 m/s, and 1.3% for 0.5 m/s). However, the averaging of 2000 samples over a period of 3.33 minutes tended to improve the accuracy but it is difficult to estimate how much. From the velocity and its fluctuation profiles (Figures 3.7.1 to 3.7.3), it appears that the uncertainty close to the bed is about 10% and decreases very quickly to about 2% at 20 mm above the bed and about 1% at higher levels.

The accuracy of the velocity measurements with the yaw and pitch probes are more difficult to quantify. Errors may result from velocity and pressure gradients across the three holes, calibration curve fitting, probe misalignment, the presence of the velocity component perpendicular to the plane containing the probe. Less error is likely in the pitch probe measurements on the plane of symmetry, except close to the cylinder which induced pressure gradient around it. More error has probably occurred in the yaw probe measurements at the 3DTBL stations. Here, the effect of the continuously turning velocity vector on the probe reading is unknown. This effect was more acute near the bed and decreased rapidly with the distance away from the bed. However the effect of the vertical component of velocity increased with the vertical distance. In the measurement of divergent flows at the sides of the cylinders, there was a significant gradient of velocity and its direction. The effects of all these are unknown; any investigation of them will involve a considerable amount of work. Considering the complexities, it seems reasonable only to make a very rough statement about their accuracy. The accuracy in velocity magnitude is probably as good as Pitot-static tube measurements for small yaw or pitch angle (< 15°). For higher angles, the uncertainties may be more. The misalignment uncertainty could be reduced within ±0.5° and the overall uncertainty in angle measurement is believed to be ±2° when the angle was less than 30° and the point of measurement was above 15 mm from the bed. Closer to the bed it was probably in the order of 2-8°. At the sides of the cylinder, with the angle of yaw greater than 30° and a steep gradient of both velocity and angle, the uncertainty in angle measurement was about ±2-5°. These estimates are based on flow visualization, inspection of final profiles, *etc.*, and as such should be considered only as a rough guide.

The sources of error in bed shear measurement with the yaw probe are similar to the ones described above and also include the followings. The effect of rapidly changing yaw angle near the bed is considered the source of largest error since the calibration was done in 2D flows. The effect of this error is unknown. There was some error in placing the probe on both the mobile and rigid sand beds. Generally the effect of this was an underestimate for mobile beds and an overestimate for the rigid beds. The uncertainty in

the angle of yaw is estimated at ±4° in the case of smooth bed runs where a smaller probe was used. It is about ±8° on the sand beds where the larger probe was used. The uncertainty in bed shear magnitude was 10% for Expt. E0 and 5% for Expt. F0 (higher shear). For sand bed experiments, it was about 10-15%. The Pitot-static tube used as a Preston tube gave similar accuracy, if not better.

The uncertainty in pressure measurement by pitch probes using Equation [3.5.1] is difficult considering the uncertainties in other variables. An indirect method was employed for its estimation. Vertical piezometric pressure profiles (which are supposed to be constant along the vertical) were measured in unobstructed channels using the same pitch probes. From these measurements, the general uncertainty of pressure measurement was estimated to be ±0.25 mm of water (±2.45 Pa). Closer to the cylinder it is more due to the pressure gradient effects on the probe, probably about ±0.5 mm (±4.5 Pa).

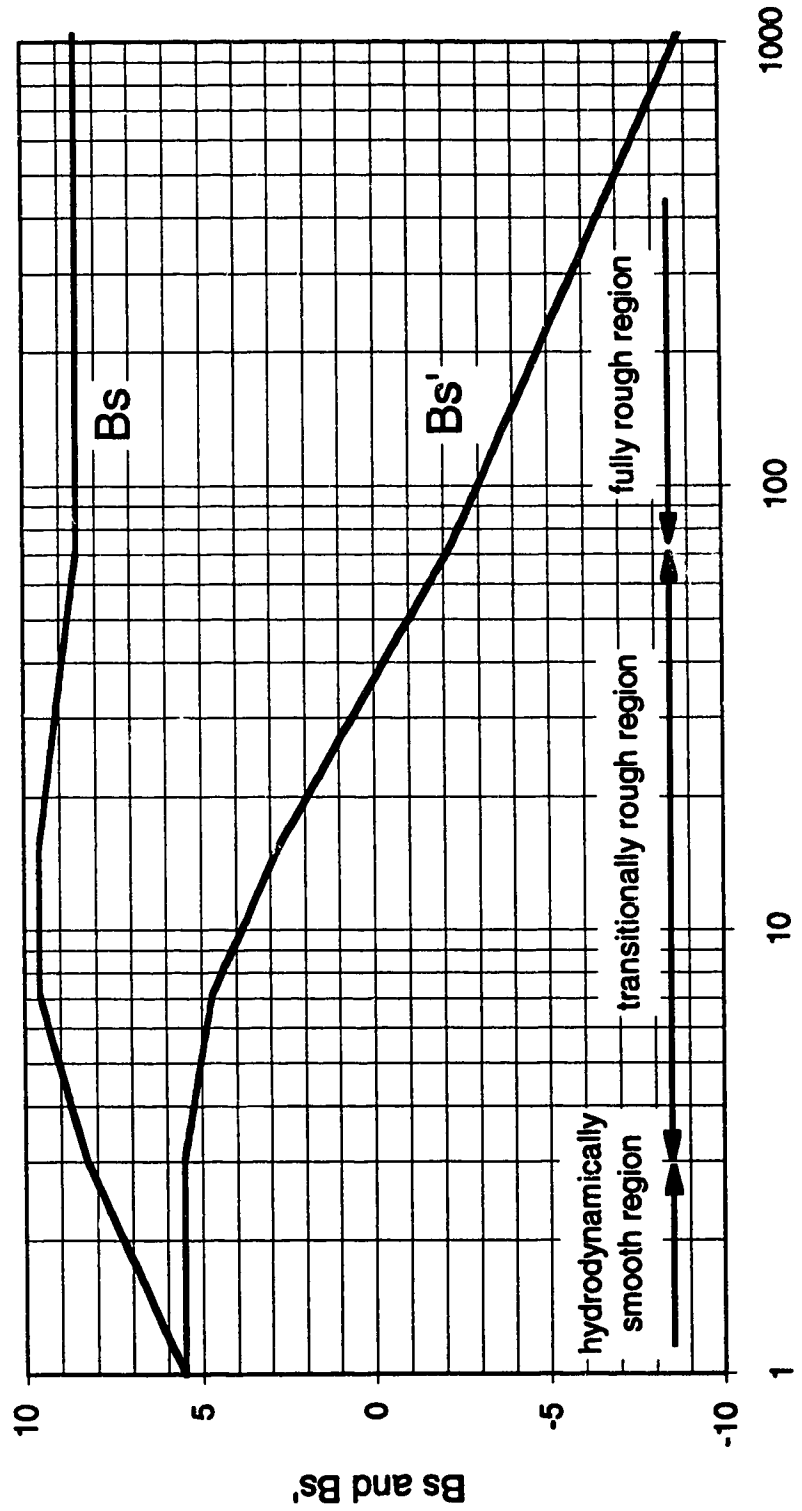

Figure 3.2.1 Variation of Bs and Bs' with roughness Reynolds number

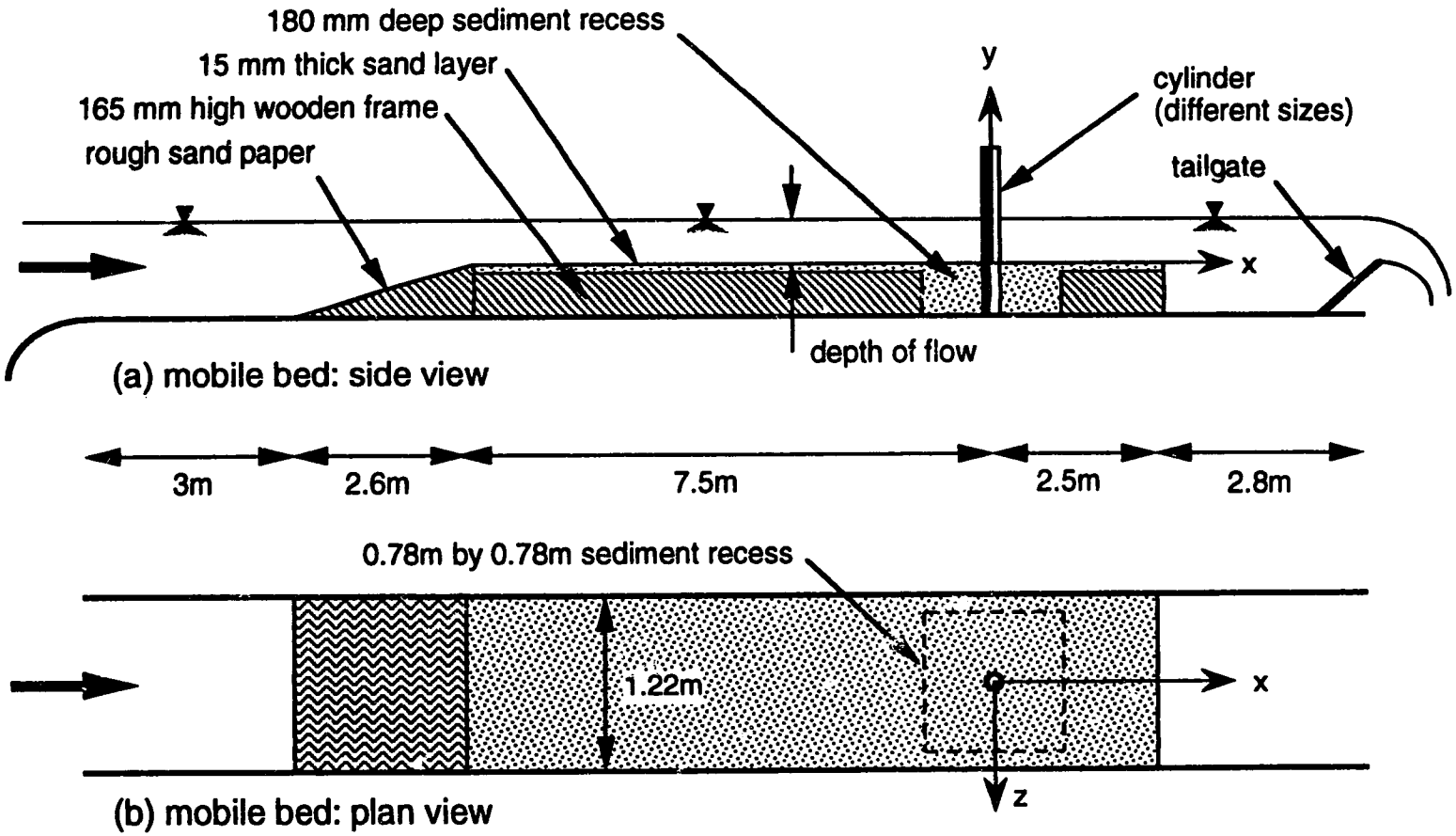

Figure 3.3.1 Experimental arrangement for mobile bed runs

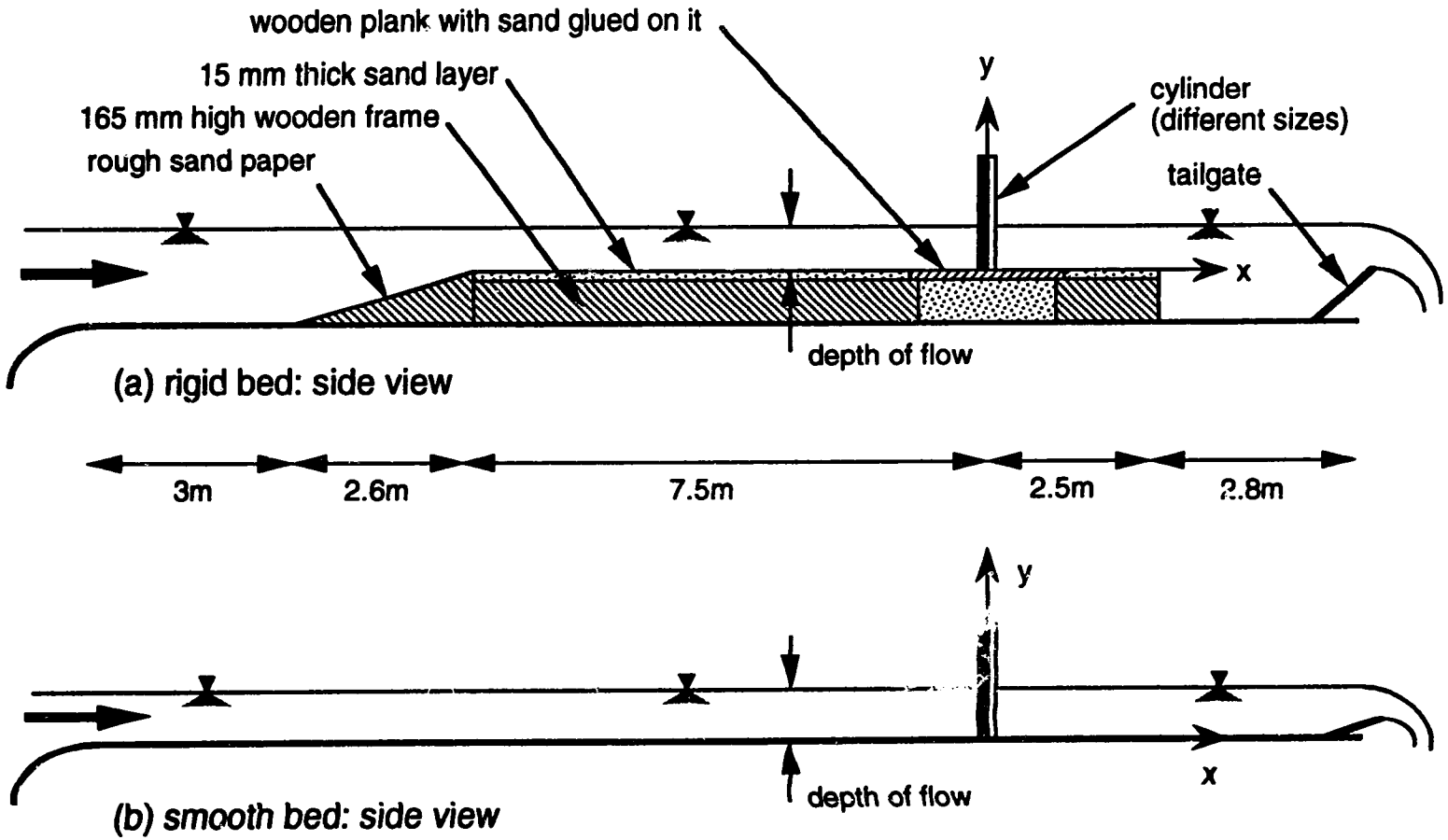

Figure 3.3.2 Experimental arrangement for rigid and smooth bed runs

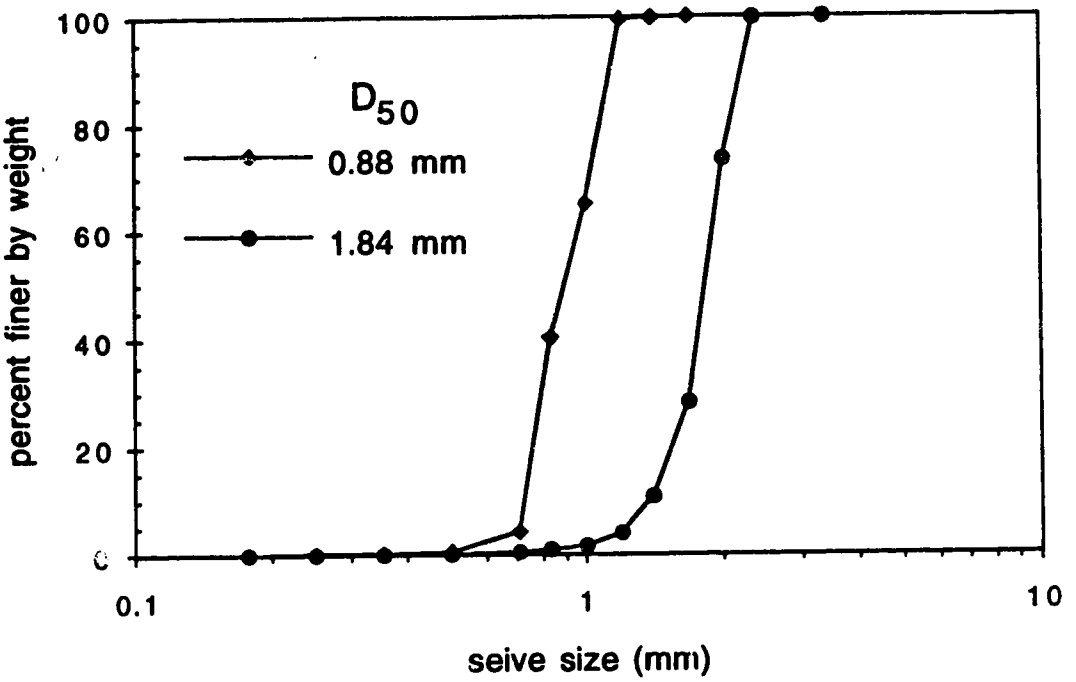

Figure 3.3.4 Grain size distribution of sands

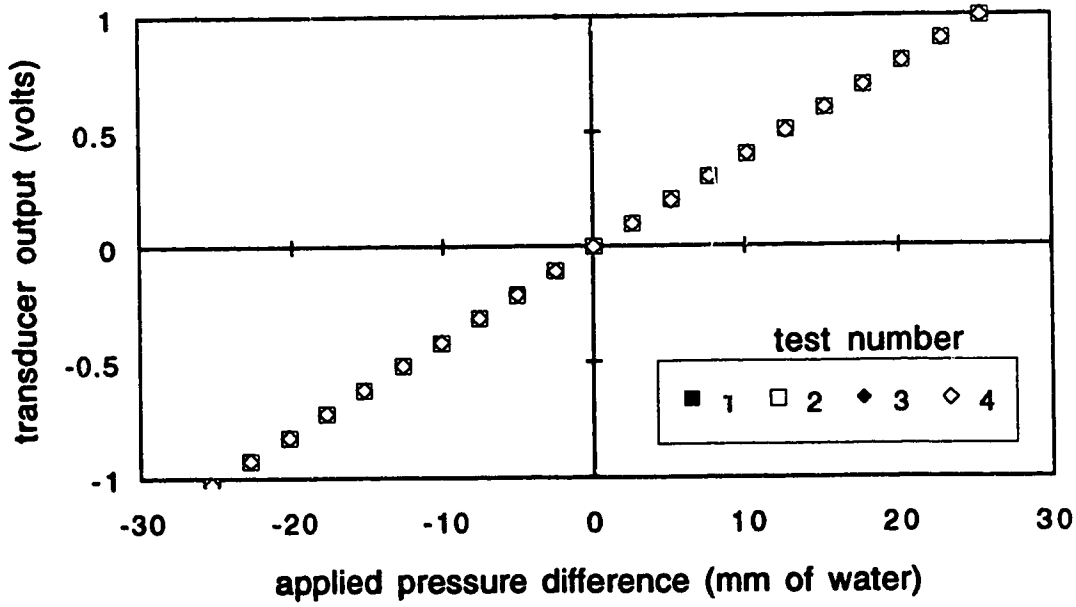

Figure 3.3.5 Typical calibration of a pressure transducer

(a) D_{50} = 0.88 mm ⇑ (b) D_{50} = 1.84 mm ⇓

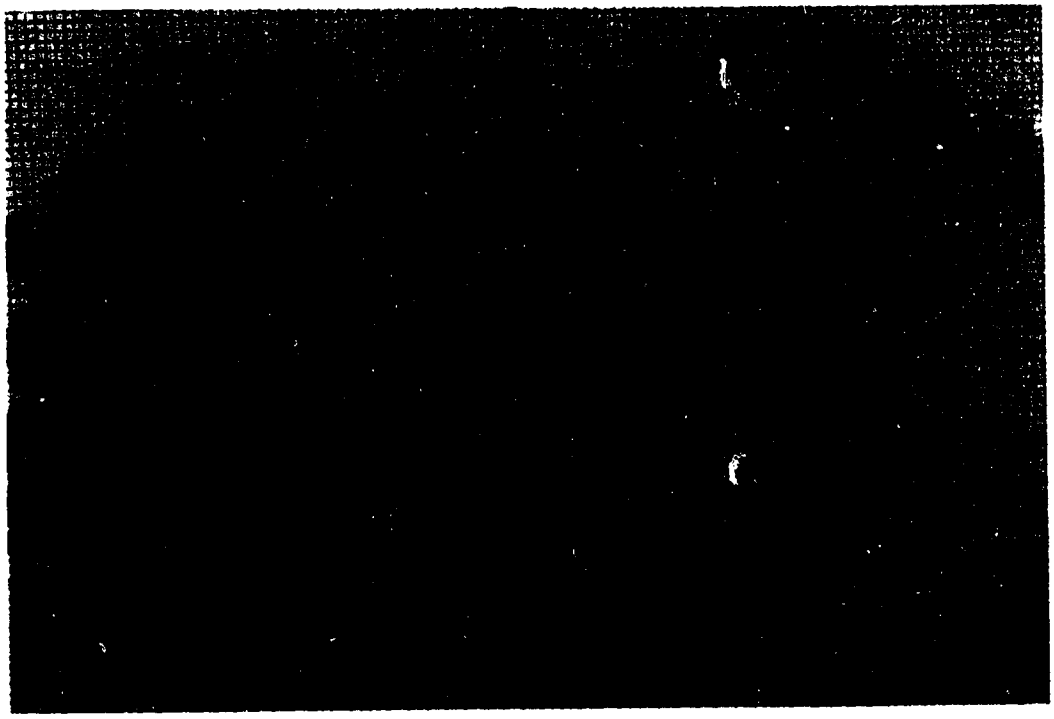

Figure 3.3.3 (a-b) Photograph of sands (2 mm x 2 mm grid)

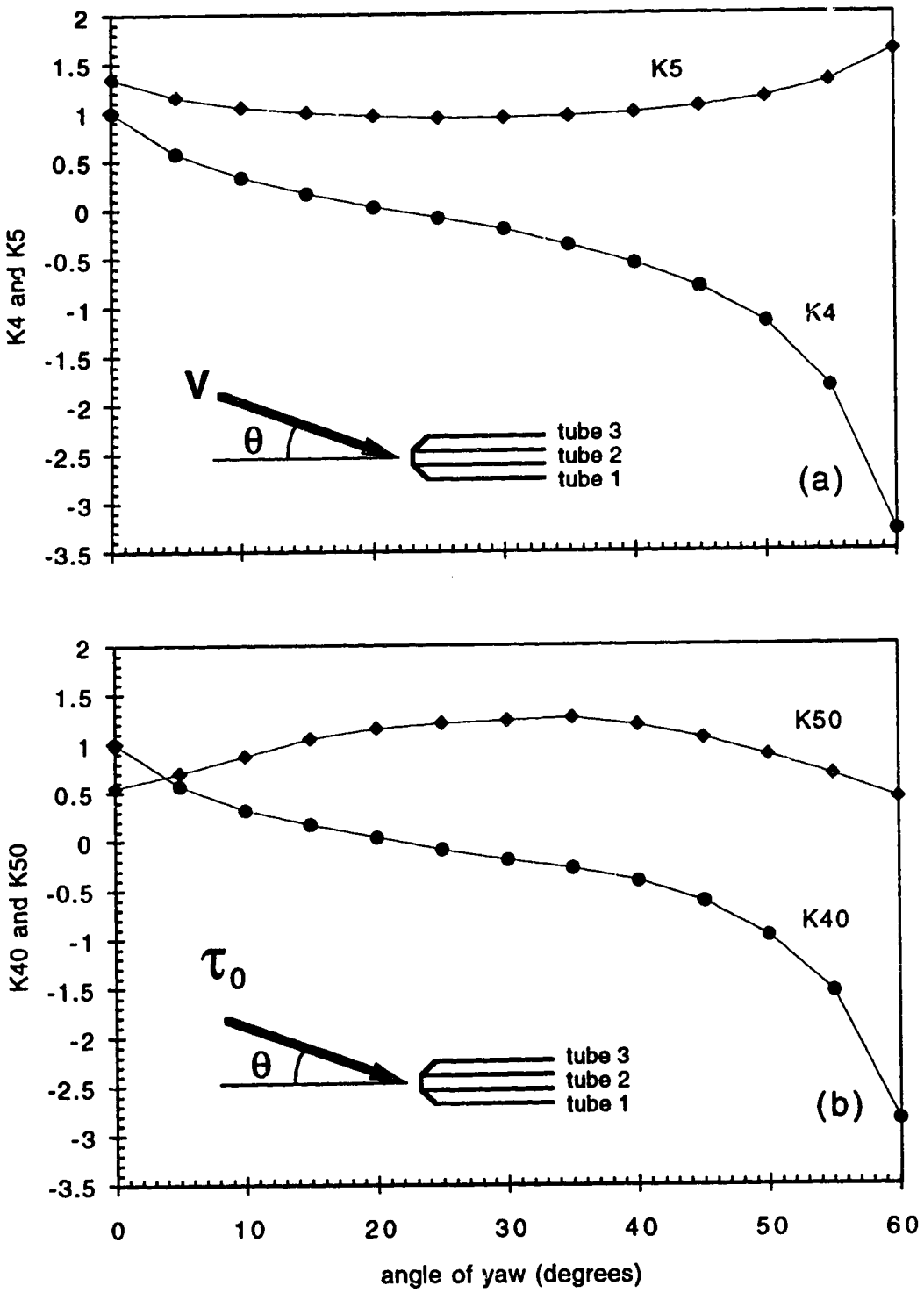

Figure 3.4.1 Yaw probe and its calibration curves; for (a) velocity and (b) wall shear measurement

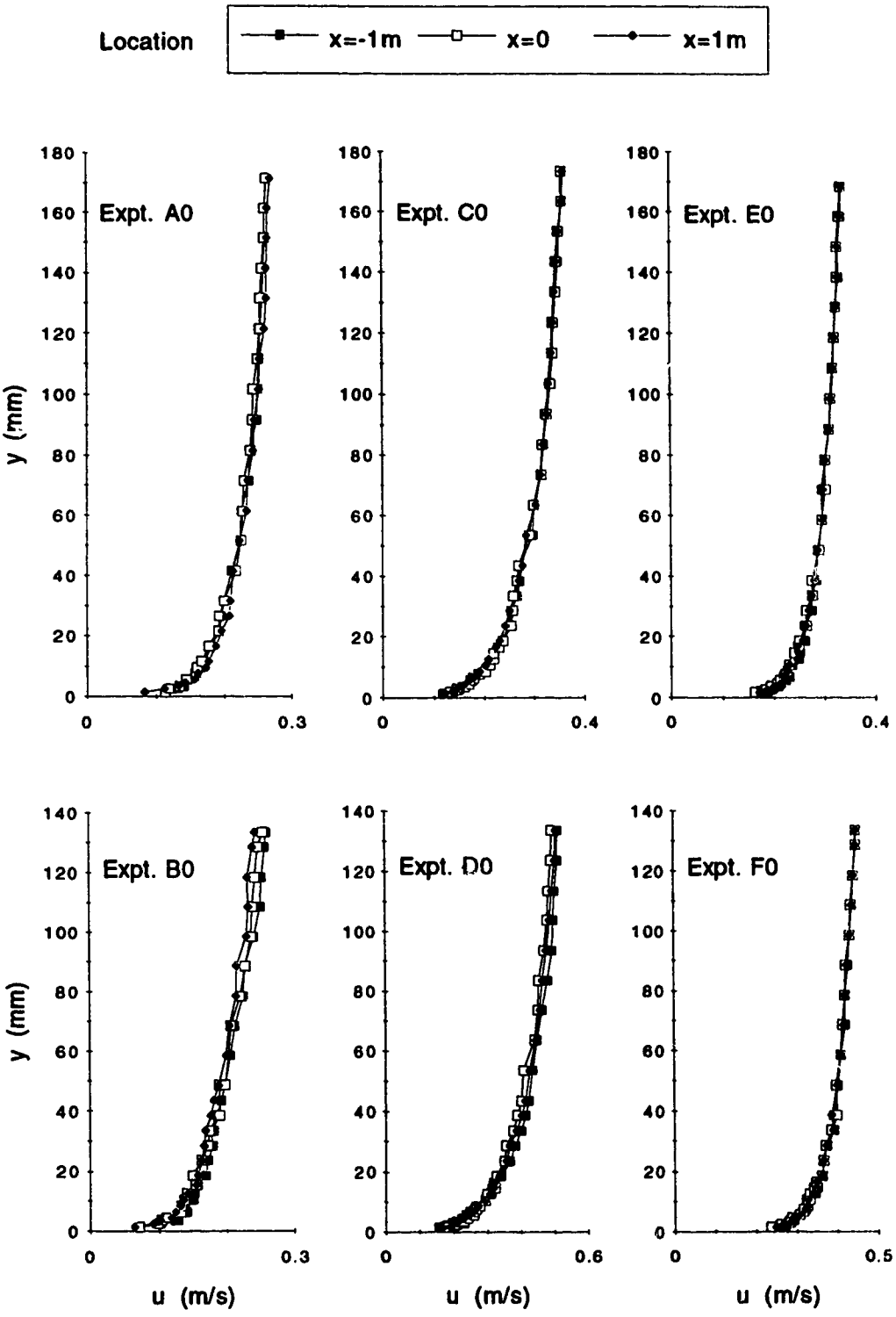

Figure 3.7.1 Velocity profiles of undisturbed flows

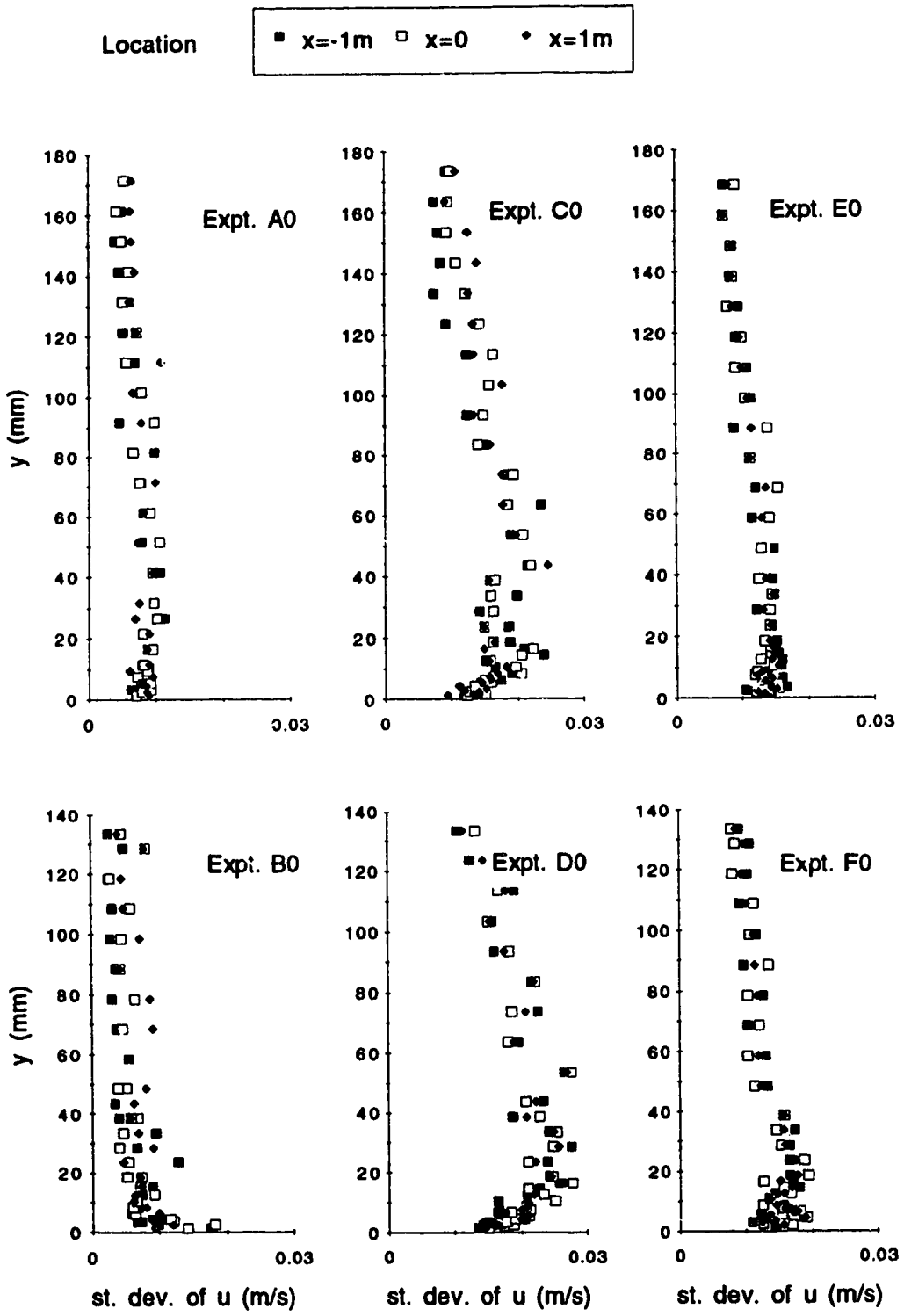

Figure 3.7.2 Velocity fluctuation of undisturbed flows

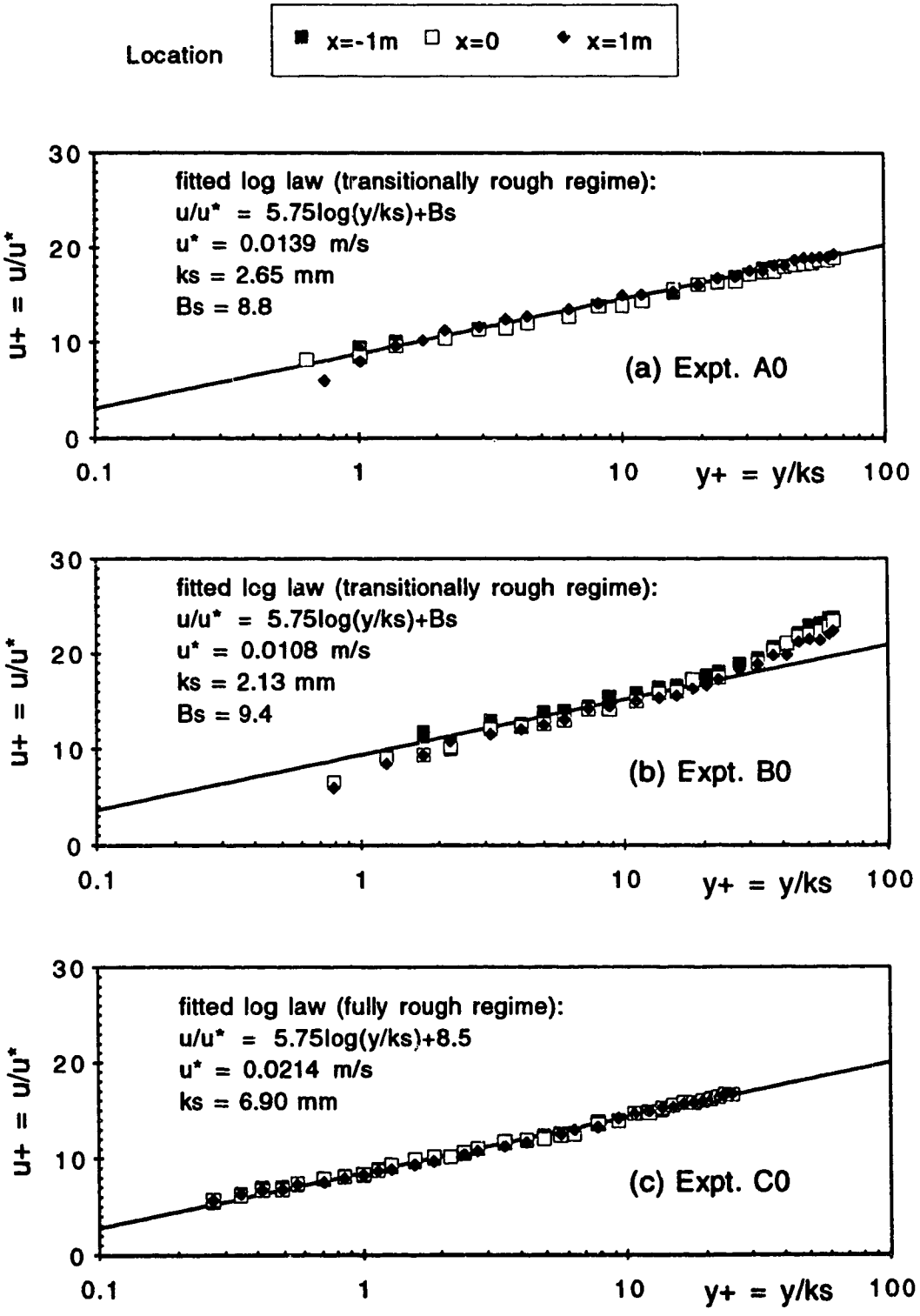

Figure 3.7.3(a-c) Velocity profiles compared with log law

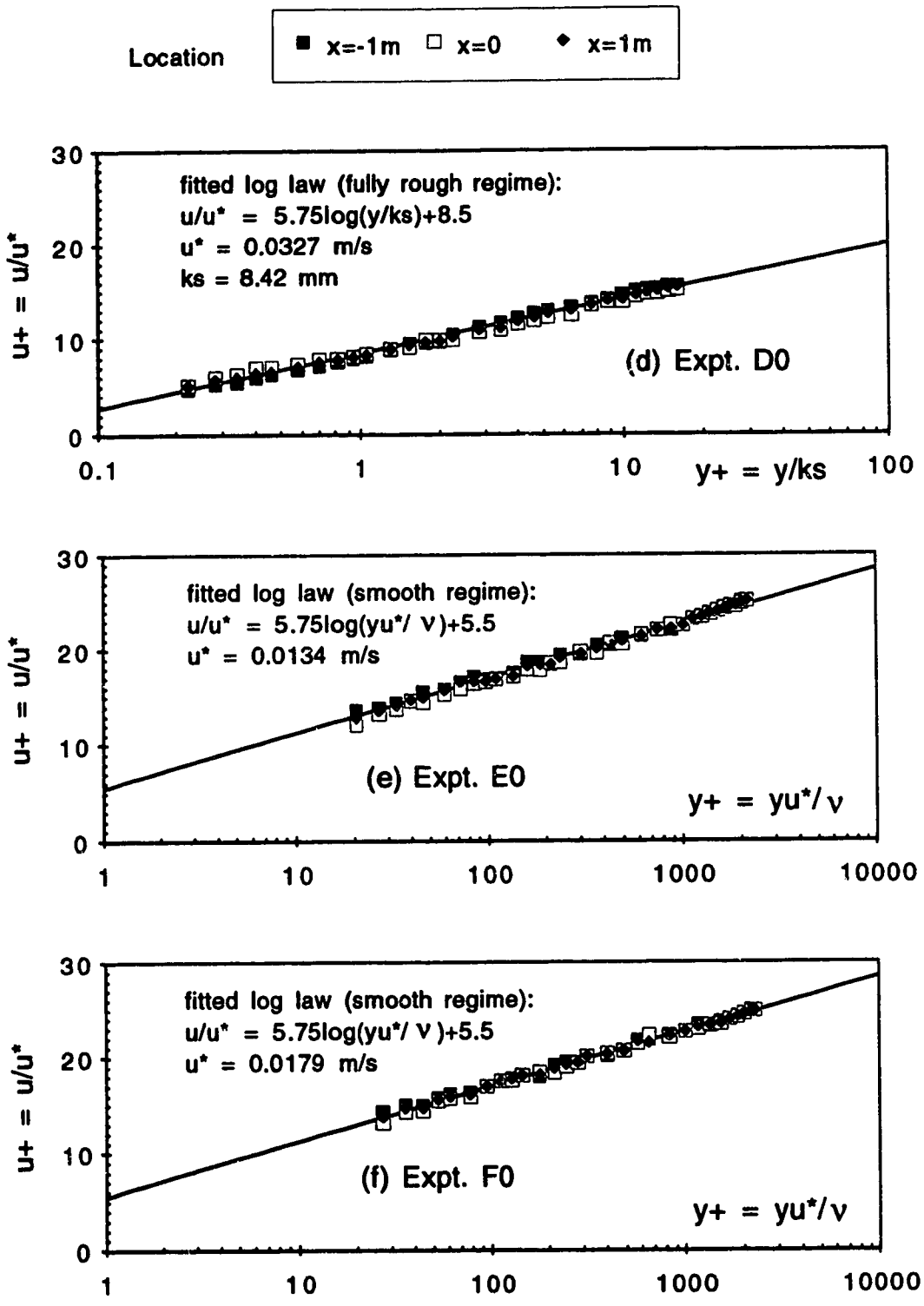

Figure 3.7.3(d-f) Velocity profiles compared with log law

Table 3.6.1 Rearrangement of Patel's calibration curves for Preston Tube

	Region 1	Region 2	Region 3
Original equations as given by Patel	$y_* = 0.5x_* + 0.037$	$y_* = 0.8287 - 0.1381x_* + 0.1437x_*^2 - 0.006x_*^3$	$x_* = y_* + 2\log(1.59y_* + 4.1)$
Range given by Patel	$y_* < 1.5$	$1.5 < y_* < 3.5$	$3.5 < y_* < 5.3$
Range in terms of τ_{0*}	$\tau_{0*} < 32$	$32 < \tau_{0*} < 3{,}162$	$3{,}162 < \tau_{0*} < 199{,}526$
y_* in terms of x_*	$y_* = 0.5x_* + 0.037$	$y_* = 0.8287 - 0.1381x_* + 0.1437x_*^2 - 0.006x_*^3$	$y_* = -0.96562 + 0.71911x_* + 0.017594x_*^2 - 0.00053x_*^3$
x_* in terms of y_*	$x_* = -0.074 + 2y_*$	$x_* = -0.61306 + 3.0882y_* - 0.57057y_*^2 + 0.055727y_*^3$	$x_* = 1.3272 + 1.2866y_* - 0.024433y_*^2 + 0.00106y_*^3$
Range in terms of x_*	$x_* < 2.926$	$2.926 < x_* < 5.59$	$5.59 < x_* < 7.619$
Range in terms of Δp_*	$\Delta p_* < 843$	$843 < \Delta p_* < 389{,}045$	$389{,}045 < \Delta p_* < 41{,}591{,}061$
$\Delta p / \tau_0$ in terms of x_*	$\Delta p / \tau_0 = -21.848 + 35.705x_* - 17.775x_*^2 + 3.8403x_*^3$	$\Delta p / \tau_0 = 55.869 - 58.619x_* + 20.378x_*^2 - 1.2946x_*^3$	$\Delta p / \tau_0 = 10.699 + 2.751x_* + 2.8804x_*^2 + 0.021509x_*^3$

Note: $x_* = \log\left(\frac{\Delta p d^2}{4\rho\nu^2}\right) = \log(\Delta p_*)$ and $y_* = \log\left(\frac{\tau_0 d^2}{4\rho\nu^2}\right) = \log(\tau_{0*})$ by definition.

Table 3.7.1 List of Experiments

Expt. Series	Expt. No.	Radius of cylinder r (mm)	Nature of bed	Discharge Q (L/s)	Depth of water y_0 (mm)	Average approach velocity U_0 (m/s)	Froude Number F	Approach bed shear stress τ_{00} (Pascal)	Mean sand diameter d_{50} (mm)	Critical stress of sand τ_c (Pascal)	Shear ratio τ_{00}/τ_c	Pier Reynolds Number R_p ($=2U_0r/\nu$)	Remarks on measurement
A	A0	--	mobile	50	182	0.2252	0.1685	0.1931	0.88	0.420	0.46	--	SCOUR: scour profiles with time; length scales with time; detailed scour profiles at equilibrium condition FLOW: flow visualization with dye
	A1M	54.0	mobile									23,163	
	A2M	44.5	mobile									19,088	
	A3M	32.0	mobile									13,726	
	A4M	21.1	mobile									9,050	
B	B0	--	mobile	40	140	0.2342	0.1998	0.1174	0.88	0.420	0.28	--	SCOUR: length scales with time; detailed scour profiles at equilibrium condition FLOW: same as A
	B1M	54.0	mobile									24,089	
	B2M	44.5	mobile									19,851	
	B3M	32.0	mobile									14,275	
	B4M	21.1	mobile									9,412	
C	C0	--	mobile	65	182	0.2927	0.2191	0.4584	1.84	1.214	0.38	--	SCOUR: same as B for mobile bed runs FLOW: detailed velocity, pressure and bed shear at near-equilibrium condition; flow visualization with dye
	C1M	54.0	mobile									30,106	
	C1R	54.0	rigid									30,106	
	C2M	44.5	mobile									24,809	
	C2R	44.5	rigid									24,809	
D	D0	--	mobile	65.5	140	0.3835	0.3272	1.0705	1.84	1.214	0.88	--	SCOUR: same as B for mobile bed runs FLOW: same as C
	D2M	44.5	mobile									32,506	
	D2R	44.5	rigid									32,506	
	D3M	32.0	mobile									23,375	
	D3R	32.0	rigid									23,375	
E	E0	--	smooth	65	182	0.2927	0.2192	0.1796	--	--	--	--	FLOW: same as C
	E2S	44.5	smooth									17,840	
F	F0	--	smooth	65.5	140	0.3835	0.3272	0.3204	--	--	--	--	FLOW: same as C
	F2S	44.5	smooth									23,375	

Table 3.7.2 Characteristics of undisturbed flows

Expt. No. (Expt. Series)	A0 (Series A)	B0 (Series B)	C0 (Series C)	D0 (Series D)	E0 (Series E)	F0 (Series F)
Channel width, W (m)	1.22	1.22	1.22	1.22	1.22	1.22
Nature of bed	sand bed	sand bed	sand bed	sand bed	smooth	smooth
Sand size, d_{50} (mm)	0.88	0.88	1.84	1.84	--	--
Sand gradation, σ_g	1.22	1.22	1.20	1.20	--	--
Critical stress of sand τ_c (Pascal)	0.420	0.420	1.214	1.214	--	--
Discharge, Q (L/s)	50	40	65	65.5	65	65.5
Water depth, y_0 (mm)	182	140	182	140	182	140
Average velocity, U_0 (m/s)	0.2252	0.2342	0.2927	0.3835	0.2927	0.3835
Froude Number, F	0.1685	0.1998	0.2191	0.3272	0.2191	0.3212
Bed shear stress, τ_{00} (Pascal)	0.1931	0.1174	0.4584	1.0705	0.1796	0.3204
Shear ratio, τ_{00}/τ_c	0.46	0.28	0.38	0.88	--	--
Boundary layer thickness, δ (mm)	182	140	182	140	182	140
Displacement thickness, δ^* (mm)	22.78	28.41	26.39	21.80	19.76	14.65
Momentum thickness, θ (mm)	16.62	18.77	18.35	14.78	15.19	11.38
BL Shape parameter, H ($=\delta^*/\theta$)	1.37	1.51	1.43	1.47	1.30	1.29
Estimated surface velocity, U_{top} (m/s)	0.2634	0.2541	0.3565	0.4958	0.3365	0.4471
Mass flux/unit width, Λ_0 (kg/m/s)	41.95	28.35	55.48	58.61	54.60	56.04
Momemtun flux/unit width, Ω_0 (kg/s^2)	9.90	5.99	17.45	25.43	16.65	22.78
Clauser's delta, Δ^* (mm)	431.76	666.14	439.41	330.35	496.15	365.92
Skin friction coefficient, c_f	0.005564	0.003635	0.007212	0.008708	0.003172	0.003205
Shear velocity, u_* (m/sec)	0.013897	0.010837	0.021412	0.032718	0.0134	0.0179
Nature of turbulent flow	transitional	transitional	fully rough	fully rough	smooth	smooth
Particle Reynolds Number ($d_{50}u_*/v$)	12	9	38	57	--	--
Roughness Renolds Number ($k_s u_*/v$)	35	22	141	263	--	--
Roughness hieght, k_s (mm)	2.65	2.13	6.90	8.42	--	--
k_s/d_{50}	3.01	2.42	3.75	4.58	--	--
Estimated BL development length, L (m)	2.8	12.4	3.7	2.2	8.3	5.9

Chapter 4
Results, Analyses and Discussions

4.1 Introduction

In this chapter, the results obtained from all the experiments are presented. Analyses of the results and discussions are also presented. Frequently the results are compared to the potential flow solution (PFS). Details of this method and computational procedures are given in Appendix B.

A Cartesian coordinate system as shown in Figures 3.3.1 and 3.3.2 will be used throughout this chapter unless otherwise stated. The angles of yaw θ and pitch ϕ made by a general velocity vector **V** is shown in Figure 4.4.1(a). The magnitude of **V** is denoted by V. Components of **V** in the (x,y,z) directions are denoted by (u,v,w) respectively. Measurements in the present experiments were limited to two-dimensional velocities only. The planes containing the velocity vectors were the plane of symmetry (POS) and horizontal planes at different distances from the bed. The pitch and yaw angles for velocity vectors on these planes are shown in Figures 4.1.1(b-c) respectively.

4.2 Velocity Distribution

4.2.1 Flow pattern in the plan

Velocity measurements were taken on three horizontal planes at different heights from the bed (y / y_0 = 0.2, 0.5 and 0.8) to investigate the overall flow pattern in plan view. A typical example is shown in Figure 4.2.1 for Expt. F2S. Since large pitch angles introduce errors in the measurement of yaw angles measured by the three-hole yaw probes, the measurement points were chosen in such a way that the flow was predominantly on a horizontal plane, *i.e.*, the vertical component could be neglected. This condition could not be satisfied, especially at the y / y_0 = 0.2 level, in some experiments in Series C and D with large scour holes. These figures show the overall flow pattern very well. But the data, plotted in this way, do not reveal the way in which the flow pattern varies from one depth to another or from one experiment to another. This is because the difference in magnitude and angle of yaw varies only slightly, which is hard to detect in a vector plot.

The same data was therefore plotted along longitudinal lines parallel to the POS and was compared to the potential flow solutions (PFS). Typical plots are shown in Figures 4.2.2 (a-c) and 4.2.3 (a-c) for Expt. C2M, C2R and E2S. The magnitude V of the velocity vector V has been normalized by the ambient velocity U_y at the appropriate height y from the bed. These figures and similar ones not shown here led to the following observations.

In the upstream region (Figures 4.2.2 (a-c)), the magnitude V was smaller than that given by the potential flow theory, with the discrepancy increasing near the cylinder (smaller z/r). This means that the fluid retarded more than what the potential theory predicts. This effect was more pronounced near the POS and gradually diminishes away from it. Here effects of two phenomena are present. One is the global effect of placing the cylinder in a subcritical flow and the other is the effect of the local flow modification by the cylinder. Using the measured U_y at $x/r = -10$ instead of U_y of undisturbed flow, these effects can be separated to some extent. These type of plotting, not shown here, indicates that the flow did not retard much far upstream. Only very near the cylinder ($x/r > 2$), the retardation was evident. In the lower level ($y/y_0 = 0.2$), the flow actually accelerated slightly, especially away from the cylinder (larger z/r). The yaw angle was slightly higher than that given by the PFS, with the discrepancy decreasing near the cylinder and near the bed (smaller y/y_0), as can be seen in Figures 4.2.3 (a-c). Since the flow was slower near the bed, the lateral pressure gradient was able to cause more skewing near the bed. The agreement was better in the upper layers ($y/y_0 = 0.8$ and 0.5), which is not unexpected as the pressure field was determined largely by the upper portion of the flow.

In the downstream region, the presence of the wake prevented the flow from following the PFS closely. Thus both the magnitude and yaw angle exhibited different trends there. The magnitude continued to increase to a certain value of x/r where it reached a peak value, then gradually decreased again (Figures 4.2.2 (a-c)). The peak occurred somewhere in between $x/r = 2$ to 3 and reached a value in the range from about 1.15 to 1.4, with higher values achieved near the bed and near the POS. Since the wake (at least immediately behind the cylinder) is a recirculating zone without contributing much to the net transport of fluid in the downstream direction, the flow in the region adjacent to the wake tends to accelerate in order to transport the extra fluid. That is why the velocity was higher in the downstream region. In general the yaw angle was also positive in this region (Figures 4.2.3 (a-c)), as the flow was prevented by the wake from converging towards the POS.

The scour hole, when present, accommodated a certain amount of flow through it, thus relieving somewhat the accelerated flow at the sides of the cylinder. Thus one would expect smaller velocities and less skewing in experiments with scour holes (mobile bed runs). This is exactly what was observed in the present experiments. As can be seen in Figure 4.2.2 (a) and 4.2.3 (a) respectively, the velocity and yaw angle for Expt. C2M is always lower than those for Expt. C2R. It may also be observed that this effect was more pronounced near the bed and near the POS (Figures 4.2.2 (a-c) and 4.2.3 (a-c)). This effect became more amplified in the downstream region, indicating that the fluid that entered into the scour hole at the front of the pier eventually exited through the wake relieving the flow outside the wake. The effect of the rear bar on the flow is evident in Figures 4.2.3 (a-c). The bar prevented the flow from converging towards the POS. This was more pronounced near the bed.

4.2.2 Defl flow

The f ted as it approached the cylinder. This deflected flow was measured at an ion (x/r = -5 for Series C and E and x/r = -7 for Series D and F) and at the e cylinder (x/r = 0 plane for all series). Measurements were taken at different ghts from the bed (y/y_0 = 0.8, 0.5 and 0.2). Additional measurements inside the scour hole were taken in the case of mobile bed runs.

4.2.2.1 Upstream of the pier

Figures 4.2.4 (a-b) and 4.2.5 (a-b) show the magnitude and the yaw angle of the velocity vectors at an upstream section located at x/r = -5 for Series C and E and at x/r = -7 for Series D and F. Due to larger size of the scour holes, measurements were taken further upstream for Series D and F. These figures in general lend further support for the observations noted in the previous section.

The measured magnitude (Figures 4.2.4 (a-b)) was smaller than PFS values near the POS and gradually recovered the deficiency far away from the POS, confirming the earlier conclusion that the flow retarded more than that predicted by the potential flow theory. This deficiency was found to be more or less same for the rigid bed and mobile bed runs within the experimental uncertainty. However, indications are there that a smaller amount of fluid is displaced from the POS in case of runs with scour holes. In the case of smooth bed runs, the deficiency was more near the POS but recovered very quickly at about z/r = 3 to 4, especially near the bed. Then it became larger than the PFS values, indicating the passage of more fluid away from the POS.

The yaw angle as shown in Figures 4.2.5 (a-b) led to the following conclusions. In the upper layers the skewing was very close to PFS, but near the bed indications of more skewing was apparent. The skewing for mobile bed runs was always smaller than that for the rigid bed runs. In case of Expt. D2M with a large scour hole, the skewing assumed small negative values (less than 0.5°) indicating that the fluid turned towards the POS. This convergence towards the POS even at the upper levels was rather unexpected. However more support for this observation from other measurements was available as will be discussed later.

4.2.2.2 Side of the pier

The deflected flow at the side of the pier ($x = 0$ plane) is shown in Figures 4.2.6 (a-b) and 4.2.7 (a-b). As can be seen from Figures 4.2.6 (a-b), the velocity did not increase as much as the potential theory predicts, less so at the upper layers. Very near the cylinder surface the velocity fell very quickly, as expected of any real viscous fluid. The velocity for mobile bed runs was always smaller than that of rigid bed runs, indicating that the scour hole accommodated a certain amount of fluid moving through the $x = 0$ plane. This effect is more pronounced in Expt. D2R with large scour hole, where unlike other experiments, the velocity never recovered to the PFS line.

The variation of yaw angle as shown in Figures 4.2.7 (a-b) indicates that the flow deflected outward for the most part. However very close to the cylinder surface, the flow actually moved inward by angles as large as 30° to 50°. Away from the cylinder, the outward flow gradually became aligned with the x-axis. The skewing of the flow was large at the upper layers and diminished near the bed. The skewing was smaller for the mobile bed runs, more so near the bed.

In the upstream region the standard deviations of velocity (σ_u) and yaw angle (σ_θ) was less than 5% of the average velocity (U_0) and 1° respectively, indicating a level of velocity fluctuation the same as that for the undisturbed approach flow. On the $x = 0$ plane, the same level prevailed, except very close to the cylinder where σ_u and σ_θ assumed values as large as 10-20% of U_0 and 8° respectively. As expected, slightly higher fluctuations were observed near the bed ($y / y_0 = 0.2$).

4.2.2.3 Inside the scour hole

Attempts were made to measure, with yaw probe, the deflected flow (on the $x = 0$ plane) inside the scour holes of all mobile bed experiments. Although the longitudinal and transverse components (u and w) of the velocity vector were much larger than the vertical component (v), the flow field was complex and the effect of the flow (especially

the vertical velocity component and the spiral motion of the vortices) on the measurement were unknown. No estimate of error and uncertainty was therefore assigned to the measurements presented in this section. The results are only approximate and should therefore be interpreted with caution.

Figures 4.2.8 (a-e) and 4.2.9 (a-e) show the deflected flow in the scour holes for Expt C2M and D2M respectively. In these figures, different levels where the data were taken are shown by different symbols in (a), with the same symbols in (b-e) denoting measured quantities at corresponding levels.

From these figures, the following observations may be made. The velocity near the cylinder was high but diminished very quickly away from it, especially near the bottom of the hole. The angle of yaw assumed small negative values close to the cylinder and gradually increased to small positive values away from it. This happened at the upper levels of the scour hole. Closer to the bottom, the yaw angle increased rapidly to large positive values, indicating strongly outward flow. The broad conclusion is that the flow was more or less aligned along the longitudinal direction at the upper portion of the hole, but at the lower portion it quickly turned outward.

Coming to the behavior of velocity fluctuations, the variation of σ_u was similar to that at the upper levels (y / y_0 = 0.8, 0.5 and 0.2 on the $x = 0$ plane). But the value of σ_θ showed a sharp rise away from the cylinder, especially near the bottom of the hole. The maximum value recorded was about 5° for Expt. C2M and about 12° for Expt. D2M. This showed the highly unsteady and agitated nature of the flow inside the scour holes.

The above characteristics of the deflected flow inside the scour hole are consistent with the observation that the horseshoe vortex system (HVS) was observed to settle down close to the bottom, leaving the larger upper area for accelerated flow past the cylinder. The flow near the bottom was therefore more complex, with all of its complicating implications for sediment transport. This leads one to the unfortunate conclusion that the scouring mechanism is intimately connected to the complex vortex flow near the bottom and that a better understanding of scouring has to await a more detailed investigation of this vortex flow.

4.2.3 Velocity on the plane of symmetry

The velocity vector on the plane of symmetry (POS) had a zero transverse component, *i.e.*, $w = 0$. Therefore the pitch probe could be used to measure it. Detailed measurement was taken both upstream and downstream of the cylinder for all experiments. A typical example of the velocity distribution in the vector form for Expt.

C1M is shown in Figure 4.2.10 (a-b). Further analyses are presented below for each region and for the downflow in front of the pier.

4.2.3.1 Upstream region

All measurements in the upstream region except the downflow are presented in this section. The stations were located at distances ranging from x/r = -10 to about -2.25.

As pointed out by Johnston (1960b), the flow on the POS is not two-dimensional although it appears to be so, because it is completely immersed in a truly three-dimensional flow. The momentum integral equation takes the following form on the POS (see Appendix A):

$$\frac{\partial}{\partial \xi}\left(\theta_{\xi\xi}\right)+\left(2\theta_{\xi\xi}+\delta^*_{\xi}\right)\frac{1}{u_e}\frac{\partial}{\partial \xi}\left(u_e\right)+\frac{1}{h_3}\frac{\partial}{\partial \zeta}\left(\theta_{\xi\zeta}\right)+\theta_{\xi\xi}\frac{1}{h_3}\frac{\partial \alpha}{\partial \zeta}=\frac{\tau_{0\xi}}{\rho u_e^2} \qquad \text{[A.44]}$$

Note that this equation is written in the streamline coordinate system. Use of this system permits a simple physical interpretation of various terms of these equation. It differs from its 2D counterpart by the last two terms on the LHS. The first of them $[(1/h_3)\cdot(\partial\theta_{\xi\zeta}/\partial\zeta)]$ represents the rate of change, with respect to ζ-direction, of the transport of the free stream direction momentum in the lateral direction. The other term $[(\theta_{\xi\xi}/h_3)\cdot(\partial\alpha/\partial\zeta)]$ accounts for the free stream direction momentum which, while being transported downstream, is also being distorted laterally, not by a lateral velocity but by the spreading of the flow. The lateral direction referred to above denotes a direction (ζ) normal to the free streamline direction (ξ) and has a curvature on the horizontal plane. It is not to be confused with the z-direction. These ideas were first pointed out by Johnston (1960b) and were further clarified by Pierce (1964). They studied the POS of a jet impinging on a flat wall and the POS of a diffuser respectively.

The momentum integral equation takes the following form when written in the Cartesian coordinate system (as shown in Appendix A):

$$\frac{\partial}{\partial x}\left(\theta_{xx}\right)+\left(2\theta_{xx}+\delta^*_{x}\right)\frac{1}{u_e}\frac{\partial}{\partial x}\left(u_e\right)-\theta_{xx}\frac{1}{u_e}\frac{\partial}{\partial x}\left(u_e\right)=\frac{\tau_{0x}}{\rho u_{xe}^2} \qquad \text{[A.50]}$$

The last term on the LHS of Equation [A.50], *i.e.*, $[-(\theta_{xx}/u_e)\cdot(\partial u_e/\partial x)]$ which is also equal to $[\partial\theta_{xz}/\partial z]$, is equivalent to the two terms in the streamline coordinate system discussed above. Thus this term reflects the combined effect of both skewing and spreading without showing their individual contribution. The advantage of the streamline coordinate system is evident here.

The data of the present experiments were analyzed in the laboratory coordinate system (x,y,z) with velocity components (u,v,w) respectively. The momentum, momentum integral, and the continuity equations on the POS (Equations [A.49] to [A.51] of Appendix A) are written below in the laboratory coordinate system, which will be used in the analyses that follow.

$$u\frac{\partial u}{\partial x}+v\frac{\partial u}{\partial y}=-\frac{1}{\rho}\frac{\partial p}{\partial x}+\frac{1}{\rho}\frac{\partial}{\partial y}\left(\mu\frac{\partial u}{\partial y}-\rho\overline{u'v'}\right) \qquad [4.2.1]$$

$$\frac{\partial}{\partial x}(\theta_{xx})+\left(2\theta_{xx}+\delta_x^*\right)\frac{1}{V_{top}}\frac{\partial}{\partial x}\left(V_{top}\right)-\theta_{xx}\frac{1}{V_{top}}\frac{\partial}{\partial x}\left(V_{top}\right)=\frac{\tau_{0x}}{\rho V_{top}^2} \qquad [4.2.2]$$

$$\frac{\partial u}{\partial x}+\frac{\partial v}{\partial y}+\frac{\partial w}{\partial z}=0 \qquad [4.2.3]$$

The following thicknesses were used in the above equations.

$$\delta_x^*=\frac{1}{V_{top}}\int_0^{\delta}\left(u_{top}-u\right)dy \qquad [4.2.4]$$

$$\theta_{xx}=\frac{1}{V_{top}^2}\int_0^{\delta}\left(u_{top}-u\right)u\,dy \qquad [4.2.5]$$

Here δ may be replaced by the local flow depth. The velocity was extrapolated to the surface to get an estimate of V_{top} and the vertical component was assumed equal to zero so that $V_{top}=u_{top}$. The BL parameters (δ_x^*, θ_{xx} and $H\equiv\delta_x^*/\theta_{xx}$) were calculated numerically from the measured velocity profiles. It should be noted that only the longitudinal component of the velocity vector has been used in the computation of BL parameters; the vertical component did not enter the computation.

Clauser (1956) suggested an integral parameter defined as

$$\Delta^*\equiv\int_0^{\delta}\left(u_{top}-u\right)/u_*\,dy \qquad [4.2.6a]$$

to normalize y in a defect type similarity scheme. Here this will be referred to as Clauser's scheme and the integral parameter Δ^* will be referred to as Clauser's thickness parameter. This parameter can be shown to be related to other BL parameters by the following identity

$$\Delta^*\equiv\delta_x^*V_{top}/u_* \qquad [4.2.6b]$$

which was used to compute Δ^* instead of numerical integration.

Figures 4.2.11 (a-i), 4.2.12 (a-i) and 4.2.13 (a-i) show the raw data on the POS and how they fit the log law, defect law and Clauser's scheme for Expt. C2M, C2R and E2S respectively. Similar plots were also made for all other experiments. The following observations refer to these figures although further support came from plots not shown here for other experiments unless otherwise stated. The magnitude V and the pitch angle ϕ of the velocity vector V are shown in (a) and (b) of these figures. Their fluctuation in terms of the standard deviations, σ_V and σ_ϕ, are shown in (c) and (d) while (e) and (f) show the longitudinal and vertical components of V (u and v respectively). V and ϕ diminished gradually as the cylinder was approached, *i.e.*, the flow retarded and turned downward at the same time. Near the bed, V diminished steadily for rigid and smooth bed experiments (C2R and E2S), but the flow was allowed to enter the scour hole with considerable velocity in the case of the mobile bed experiment (C2M). The velocity near the bed was, in general, higher for mobile bed runs compared to that for rigid and smooth bed runs, showing the effect of the scour hole on the flow. The pitch angle ϕ was within -3° in the upper part in Expt. E2S, although very near the bottom it assumed values as small as -8°. In case of rough beds (Expt. C2R), ϕ was about -7° in the upper part and about -18° near the bed. This shows the effect of roughness, which makes the velocity profile less uniform, thus resulting in a steeper pressure gradient along the cylinder surface and a correspondingly stronger downflow. ϕ exhibited much smaller values especially near the cylinder in the case of mobile bed runs as the flow entered the scour hole. The variation of v as shown in (f) of these figures lend further support to the above observation. The variation of u as shown in (e) exhibited a trend generally similar to that of V. The fluctuations of velocity σ_V showed a trend similar to that of the approach flow (see Figure 3.7.2) but with somewhat higher values. This is probably due to the disturbance created by the cylinder. This higher value of σ_V was slightly mitigated in the presence of scour holes. The fluctuation in pitch angle σ_ϕ was less than 1.5° for the upper part in Expt. E2S and increased rather sharply to about 5° near the bed. In case of the rough rigid bed (Expt. C2R), the increase was more gradual and took place over a larger portion of the depth, and σ_ϕ reached values as high as 14°. This indicated that the roughness increased the unsteadiness of the flow. The variation of σ_ϕ for the mobile bed case (Expt. C2M) is similar to that of Expt. C2R except the peak value attained by σ_ϕ, which was much less (about 5°, a value equal to that of Expt. E2S). This indicated that the scour hole had a stabilizing influence on the flow.

The longitudinal velocity component u and the measured bed shear stress τ_0 were used to see how the velocity profiles match the log law, defect law and Clauser's scheme. These are shown in (g-i) of Figures 4.2.11 to 4.2.13. In the case of Expt. E2S, the

data fell below the log law line for most of the stations away from the cylinder, indicating that the bed shear did not diminish as much as the velocity did. A small wake component appeared to be there, which became more prominent as the cylinder was approached. The opposite happened just ahead of the separation point where the bed shear assumed very small values. The same thing was observed for Expt. C2R, but the effects were more amplified. Expt. C2M showed the same trend except that the wake component was less visible. The velocity data followed the defect law well only for the stations far away from the cylinder for Expt. E2S. It was worse for Expt. C2R and C2M. The data from all stations fell on a close band when plotted according to Clauser's scheme for Expt. E2S and C2R. This was also observed by Dargahi (1987, 1989). In general the scheme also worked reasonably well for mobile bed runs, although the band took a different shape. However, the scheme did not work well for the particular case of Expt. C2M.

The velocity data on the POS was further utilized to estimate the flux of mass and momentum in the longitudinal direction on this plane. The mass flux Λ across the entire BL thickness δ (same as the flow depth y_0) per unit time per unit width is given by:

$$\Lambda \equiv \int_0^{\delta} \rho u \, dy \qquad [4.2.7a]$$

Similarly the momentum flux is defined as:

$$\Omega \equiv \int_0^{\delta} \rho u^2 \, dy \qquad [4.2.7b]$$

These quantities were computed numerically from the measured velocity profiles, and were normalized by their values in the undisturbed approach flow without the cylinder in place (denoted by Λ_0 and Ω_0). The dimensionless fluxes thus obtained are called mass and momentum flux ratios. Their formal definitions are as follows.

$$\hat{\Lambda}\langle x\rangle \equiv \frac{\Lambda\langle x\rangle}{\Lambda_0} \qquad [4.2.8a]$$

$$\hat{\Omega}\langle x\rangle \equiv \frac{\Omega\langle x\rangle}{\Omega_0} \qquad [4.2.8b]$$

Note the dependence of Λ, $\hat{\Lambda}$, Ω and $\hat{\Omega}$ on x on the POS. Analytical expressions for $\hat{\Lambda}$ and $\hat{\Omega}$ may be derived from potential flow theory as given below.

$$\hat{\Lambda}\langle x\rangle = \left(\frac{u\langle x\rangle}{U_\infty}\right) \qquad [4.2.9a]$$

$$\hat{\Omega}(x) = \left(\frac{u(x)}{U_\infty}\right)^2 \qquad [4.2.9b]$$

Uniform (as opposed to shear) flow of infinite extent was assumed in the potential flow.

Experimentally determined values of $\hat{\Lambda}$ and $\hat{\Omega}$ for smooth, rigid and mobile bed runs were compared to each other and to the PFS, as shown in Figure 4.2.14 (a-b) and 4.2.15 (a-b). The adverse pressure gradient induced by the cylinder in front of it is largely determined by the upper part of the flow. As a result, the fluid near the bed with less momentum is more susceptible to the retarding and skewing effects. Thus, the mass and momentum flux across the entire depth of a shear flow like the present one will always be smaller than that given by the potential flow theory. This is in fact the case for the present experiments, as all the experimental points were below the PFS lines (Figure 4.2.14 and 4.2.15). Mass and momentum fluxes of the mobile bed runs were always greater than those of rigid bed runs, indicating the passage of more fluid with more momentum made possible by the presence of the scour hole. In case of Expt. D2M with a large scour hole, the fluxes showed even a slightly increasing trend towards the cylinder. This showed the effect of the scour hole on the flow approaching the cylinder on and around the POS. The effect of roughness is more complicated. The non-uniformity of velocity profile, which is characteristic of the flow over rough beds, would tend to lower the values of $\hat{\Lambda}$ and $\hat{\Omega}$ because the velocity in the lower level will be much smaller than smooth bed case and will be more susceptible to the retarding and skewing effects. On the other hand the amount of fluid actually subjected to these effects will be less than for the smooth bed case due to lower velocities in the lower level. This would tend to increase $\hat{\Lambda}$ and $\hat{\Omega}$. The net effect of roughness will depend on the relative strengths of these opposing trends. In the present experiments, the net effect of roughness was an increase in the values of $\hat{\Lambda}$ and $\hat{\Omega}$, as can be seen in Figures 4.2.14 (a-b) and 4.2.15 (a-b). The present experiments indicates that the effects of the presence of the cylinder, the roughness and the scour hole propagate far upstream (beyond $x/r = -10$).

Typical variation of the different BL parameters along the POS is shown in Figure 4.2.16 (a-d). The thickness parameters (δ_x^*, θ_{xx} and Δ^*) have been normalized by their ambient values ($\delta_{x,0}^*$, $\theta_{xx,0}$ and Δ_0^*) determined from the measured velocity profiles without the cylinder in place. It can be seen that under the influence of adverse pressure gradient, δ_x^* increased gradually by about 15% before dropping rather sharply just before the separation for both smooth and rigid bed runs while δ_x^* decreased monotonously by about 15% for the mobile bed run (Figure 4.2.16 (a)). A similar trend was exhibited by θ_{xx} as shown in Figure 4.2.16 (b). The combined effect of these two can be seen in the

variation of shape parameter $H \equiv \delta_x^* / \theta_{xx}$ (Figure 4.2.16 (c)). For all experiments, H was slightly higher than the ambient value H_0, even far away from the cylinder, pointing to the far reaching influence of the cylinder. For smooth bed runs, H increased slightly, but the trend was steady and monotonous. For rough bed runs, the increase was more but the trend was slightly undulatory, probably due to errors in numerical integration. This is in keeping with the expected rise in H as separation is approached, although the highest values of H were nowhere near ≈2.5, at which separation was thought to occur by earlier researchers. However, as Clauser (1956) has pointed out, a number of experiments indicate otherwise. It is interesting to observe the behavior of H for Expt. C2M with a scour hole. Far upstream H assumed smaller values than that of rigid bed run, indicating that the presence of the scour hole worked against the tendency towards separation. Very near the edge of the hole, H actually shows a decreasing trend, due to the acceleration of fluid into the hole. Lastly, the variation of Δ^* ($= \delta_x^* V_{top} / u_*$) can be seen in Figure 4.2.16 (d). This parameter increased monotonously by about 20% for smooth bed run, increased by about 70% to a peak before decreasing again for rigid bed run, and exhibited a somewhat undulatory pattern for the mobile bed run. Its behavior was largely dependent on the local bed shear stress, which showed similar patterns as can be seen in Figure 4.4.2 (a-b). The behavior of other parameters (δ_x^* and V_{top}) on which Δ^* depends was more stable. Irrespective of what caused such a behavior of Δ^*, it also caused the Clauser's scheme work better than the defect law, as discussed earlier.

4.2.3.2 Downflow

The downward flow in front of the pier was measured with a small three-hole probe. This probe was originally a yaw probe which was bent and placed in front of the cylinder from one side so that it acted as a pitch probe and measured the velocity vector **V** on the plane of symmetry. Due to probe configuration, a clear distance of about 50 mm had to be allowed between the local bed level and the lower end of the probe. No measurement could therefore be taken closer than 50 mm to the bed. The closest measurement point to the cylinder surface was 1.5 mm.

Typical downflow measurements and subsequent analyses are shown in Figure 4.2.17 (a-h) for Expt. C2M. The lines on the POS along which measurements were taken are shown with different symbols in (g) along with the scour profile. The same symbols have been used to plot the measured or derived quantities corresponding to these lines in (a-f). The magnitude V and pitch angle ϕ of the velocity vector **V** are shown in (a) and (b). These show how **V** decreased in magnitude and turned gradually as the cylinder

surface was approached. At all levels, ϕ assumed values very close to -90° near the cylinder surface, *i.e.*, **V** was almost vertically downward. The fluctuation of velocity magnitude and direction is shown in (c) and (d) in terms of their standard deviations (σ_V and σ_ϕ). Close to the cylinder, σ_V diminished gradually from its free stream value to reach a minimum at a distance of about $0.1\,r$ from the cylinder surface. It rose again closer to the surface, but not to the free stream level. σ_ϕ increased slowly from very small values (about 1°) as the cylinder was approached and reached a peak at a distance that varied at different levels. The peak value also varied from one level to another. Close to the free surface, σ_ϕ was as high as 15°. This fluctuation in angle was observed to be coupled with the unsteady oscillation of the free surface just in front of the cylinder. The longitudinal and vertical components (u and v) of **V**, both normalized by the average velocity U_0, are shown in (e) and (f). It is interesting to see how u from all levels fell on a narrow band, suggesting a rather uniform character of the velocity in front of the pier. This was probably due to the scour hole, which allowed in front of it relatively higher velocities near the bed. The vertical component v assumed large negative values close to the cylinder surface. The downflow reached about 75% of U_0 at the ambient bed level. If the downflow is denoted by $\tilde{v}$ and if the maximum value of $\tilde{v}$ attained at any particular level is denoted by $\tilde{v}_{max}$, then Figure 4.2.17 (h) shows the variation of $\tilde{v}_{max}$ with depth. Also shown is the curve derived from the analyses of Moore and Masch (1965) and Shen *et al.* (1966) based on the assumption that the downflow is dependent only on the stagnation pressure gradient, as discussed in Section 2.5.1. The agreement was not good, not only near the bed where the downflow is affected by the bed and the horseshoe vortex, but at upper levels also. Similar conclusions was also drawn by Ettema (1980) from measurements in a wind tunnel.

The downflows for Expt. C2R are shown in Figures 4.1.18 (a-f), where the symbols are the same as those for Expt. C2M in Figure 4.2.17. There was little difference in the upper levels between these two experiments. The differences are expected to become pronounced near the bed due to the presence or absence of the scour hole. Unfortunately, the experimental techniques used did not allow us to take data below $y/r < 1.5$ in rigid and smooth bed runs. Therefore the effect of the scour hole on the downflow could not be studied in the lower level. Very near the top ($y/r = 4$), some differences could be seen. For Expt. C2R, V was slightly higher and ϕ changed gradually away from the cylinder surface. The downflow characteristics of the smooth bed runs were very similar to those of rigid bed runs and are not shown here.

The variation of $\tilde{v}_{max}/U_0$ with y/y_0 for different experiments is shown in Figure 4.2.19 (a-b). In the upper part of the flow, the variation of $\tilde{v}_{max}/U_0$ was milder

for the smooth bed runs, which is probably due to the gentler variation of the approach velocity with the depth. In the region $0.4 < y / y_0 < 0.75$, no distinction could be made between rigid and mobile bed runs. Above this region, $\tilde{v}_{max}$ assumed slightly larger values for rigid bed runs. This observation is only tentative since the velocity was small, fluctuations were large, and thus the experimental uncertainty was large. As the limited number of data showed (Figure 4.2.19 (a)), $\tilde{v}_{max} / U_0$ reached a maximum value of about 0.38 at about $y / y_0 = 0.35$ in the absence of a scour hole. The scour hole allows the downflow to grow even below the ambient bed level. Values of $\tilde{v}_{max} / U_0$ as high as 0.8 were recorded for different experiments. Similar values were also reported by Ettema (1980). The highest value of about 0.95 was observed for Expt. D2M which had a very large scour hole (Figure 4.2.19 (b)). At the ambient bed level ($y / y_0 = 0$), $\tilde{v}_{max} / U_0$ varied from 0.55 to 0.7 depending on the pier size and the extent of scour.

The downflow and the scouring caused by it in the front of the pier bear many similarities to an impinging jet and the corresponding scouring. There are, however, some fundamental differences which prevent application of the elegant mathematical analyses of jets (Rajaratnam 1976) to the downflow. The jet is formed inside the nozzle and after exiting, diffuses as it entrains ambient fluid and forms the shear layer. The downflow is more complex. It is driven by the pressure gradient as it develops along the curved cylinder surface. It, therefore, forms and diffuses at the same time. Moreover, unlike the inert fluid around a jet, the approach flow carries both mass and momentum into the downflow. It is easy to see the mass and x- and y-momentum on the POS being contributed to the downflow. However, the effects of skewing, spreading and the z-momentum (on and off the POS) are very difficult even to visualize. A prospect of a theoretical or even an semi-theoretical analysis of the downflow seems remote. In the mean time, detailed and accurate measurements (by non-intrusive methods like LDA) might be useful in understanding the physics of this complex phenomenon.

4.2.3.3 Downstream region

The velocity distribution downstream of the cylinder was measured with a pitch probe. Measurements were taken only on the POS. In some cases the pitch angle fluctuated beyond the range of probe ($\pm 60^\circ$). In other cases the velocity was small but the fluctuation was large, causing the velocity to fall below zero from time to time. Data could not be recorded when any of these happened. In certain regions, especially just behind the cylinder in rigid and smooth bed runs, the data profiles exhibited undulatory characteristics, which appeared to be due to the highly turbulent eddy motion in the wake. In spite of this and the relatively high experimental uncertainty, the broad flow features

could be examined in sufficient details to discern the effects of scouring on the wake flow. The rigid and smooth bed runs showed very similar characteristics, and the effect of the roughness on the wake flow appeared to be negligible. Therefore, the smooth bed runs are not discussed here any further. Thus the principal emphasis of the present section is to study the effect of the scouring on the wake.

Measurements were taken along several horizontal lines at different heights from the bed and along several vertical lines at different distances from the cylinder. This allows one to see the variation of flow characteristics along the downstream direction and across the depth. Typical plots are presented for a mobile and a rigid bed run (Expt. C2M and C2R). Figures 4.2.20 (a-g) and 4.2.21 (a-f) show the flow variation along horizontal lines for Expt. C2M and C2R respectively. Figure 4.2.20 (g) shows the location of these measurement lines by different symbols. The same symbols have been used in Figures 4.2.20 (a-f) and 4.2.21 (a-f) to represent different parameters along these lines. Similarly the measurements along vertical lines are presented in Figures 4.2.22 (a-g) and 4.2.23 (a-f) and the location of the vertical lines are shown in Figure 4.2.22 (g).

Let us consider Figures 4.2.20 and 4.2.21 first. Comparing (a) of these figures, it can be seen that the velocity magnitude V in general assumed higher values in Expt. C2M. Particularly notable was the large increase in V just behind the cylinder. Even at the bed level ($y/r = 0$), V attained about 70% of U_0. The existence of the so called upflow is confirmed for both rigid and mobile bed runs (b). The pitch angle ϕ was about 70° near the cylinder surface for Expt. C2R; then it reached its peak value at $x/r \approx 2.5$ to 4.5 depending on the level; then ϕ gradually went down to zero. The effect of the scour hole in Expt. C2M was to move the peak closer to the cylinder ($x/r \approx 1.5$) and to make the fall of ϕ steeper. The scour hole concentrated the upflow into a smaller region and thus increased its intensity. The components of V (u and v) as shown in (e) and (f) indicated that the scour hole caused the flow to pick up u velocity rapidly and at a point closer to the cylinder. Reverse flow as indicated by negative values of u was confined in a relatively smaller region in Expt. C2M. The increase in v is also noticeable, especially closer to the cylinder. The scour hole also reduced the fluctuation (σ_V and σ_ϕ) to a large degree (c-d).

Now let us consider Figures 4.2.22 (a-g) and 4.2.23 (a-f). The quality of data at $x/r = 3$ was poor due to large fluctuations in Expt. C2R and so this profile has not been shown here. A comparison of V indicates that more fluid was passing on the POS in Expt. C2M (a). The variation of ϕ was more or less similar except near the bed (b). The u profile for Expt. C2M indicated a jet-like shape which diffused in the downstream direction (e). This may be traced back to the accelerated flow at both sides of the cylinder

which combined just downstream of the cylinder. This effect was also observed in Expt. C2R, but in a less noticeable way. The scour hole increased v as can be seen in (f). It also suppressed both σ_V and σ_ϕ (c-d).

4.3 Pressure Distribution

Piezometric pressure was measured with yaw and pitch probes only on the POS. There were certain regions where the probes could not be physically placed or where the velocity was too small to measure. This left the measurement somewhat incomplete.

The piezometric pressure P at a point is the sum of the pressure p and $\rho g y$, where y is the height of the point from a suitable datum (ambient bed level). The pressure coefficient C_p is defined in the following way.

$$C_p = \frac{P - P_{00}}{\frac{1}{2}\rho U_y^2} \qquad [4.3.1]$$

Here, P_{00} is the ambient piezometric pressure at the cylinder position ($x = 0, z = 0$) without the cylinder in place, *i.e.*, $P_{00} = \rho g y_0$ where y_0 is the depth of flow. U_y is the approach velocity at a level y above the bed at the cylinder position ($x = 0, z = 0$) without the cylinder in place and obviously varies with y.

4.3.1 Upstream region

The pressure was measured along the x-axis at two levels from the bed ($y = r/2$ and $y = 54$ mm). At the $y = r/2$ level, the measurement with pitch probe could not be taken closer than about 50 mm to the cylinder surface. For this reason the second level was chosen, where measurement close to the cylinder surface was taken with a special yaw probe converted into a pitch probe to measure the pressure along with the downflow. The raw data is presented in Figures 4.3.1 (a-b) in terms of the piezometric pressure in millimeters above the flume bed. As expected, the pressure gradually rose as the cylinder was approached. Several remarks can be made from these figures. First, the pressure seemed to rise at $x/r \approx -5$ for Series C and E and at $x/r \approx -7$ for Series D and F, suggesting that the presence of the pier was felt further upstream for experiments with higher velocity. Second, the maximum rise in pressure was generally higher for larger cylinders. Third, no systematic effect of the level of measurement was found. Neither was any systematic distinction found between smooth, rigid and mobile bed runs within the experimental accuracy.

The same data was presented in Figures 4.3.2 (a-d) in terms of the pressure coefficient C_p as defined in Equation [4.3.1] and was compared to the potential flow solution (PFS). The experimental points seemed to follow the PFS closely. No apparent effect of the horseshoe vortex system (HVS) was found. This effect was reported in the form of a dip in the pressure distribution on the bed by Baker (1978, 1980a) and Dargahi (1987, 1989). The measurements in the present study were taken above the HVS. One might therefore speculate on the disappearance of the dip effect in the upper layers, although the present data are not adequate to put this on a firm basis.

The pressure was also measured at a distance of 3 mm from the front surface of the cylinder along the vertical. The raw pressure data are shown in Figures 4.3.3 (a-b). The pressure in excess of y_0 was higher at higher levels and diminished gradually at lower levels, right down into the scour hole in case of mobile bed runs. The vertical pressure gradient was milder in smooth bed runs, indicating the effect of approach flow velocity gradient. For Expt. D2M, the pressure seemed to increase slightly again near the bottom of the scour hole. This may be due to the rising stagnation pressure as the downflow hit the bottom. The data was again plotted in terms of C_p in Figures 4.3.4 (a-b). Note that C_p at or below the flume bed could not be evaluated because of the particular definition of C_p adopted here. For smooth bed runs, C_p maintained a nearly constant value of about 0.7 across the entire depth except very near the bed where it increased slightly. The same trend was shown in Dargahi's (1987) measurement except a different constant value of about 0.9, which is probably due the fact that he measured the pressure right on the cylinder surface. For rigid bed runs, C_p exhibited some scatter but remained within a fairly narrow band (0.85 to 0.95). In case of mobile bed runs, C_p increased continuously near the bed and the very high values at the lowest levels were probably due to small velocities used for normalizing C_p. For want of data, the behavior of C_p near the bed for rigid bed runs and thus the effect of the scour hole on C_p near the bed could not be determined.

4.3.2 Downstream region

The pressure and C_p in the downstream region at $y / y_0 = 0$ are shown in Figures 4.3.5 (a-b) and 4.3.6 (a-b) respectively. The pressure drop behind the cylinder is remarkable. The point of minimum pressure was located somewhere between $x / r \approx 2$ to 3 for all experiments. The pressure then rose quit rapidly up to a distance of $x / r \approx 6$ to 8, after which the rise was very gradual. The lowest C_p for smooth and rigid bed runs were in the range of -1 to -1.3. All these were in good agreement with Dargahi's (1987) observations. In case of mobile bed runs with scour holes, the fall in pressure was

smaller, more so for larger cylinders. This is because the scour hole guided the accelerated flows on either side of the cylinders smoothly into the wake. When these two jet-like flows intersected on the POS, the pressure rose. Another reason may be the weakening of the recirculating eddies in the presence of scour holes. In the case of Expt. D2M with large scour hole, the pressure seemed to rise slightly above the ambient level. This may be due to very strong jet-like flows with a large upward component.

Lastly, the pressure at a distance of 3 mm away from the cylinder surface along the back of the cylinder is presented in Figures 4.3.7 (a-b). For smooth and rigid bed runs, the minimum pressure was attained at a level away from both the bed and the free-surface where the pressure increased sli[illegible]. This observation led Dargahi (1987) to the conclusion that the flow immediately behind the cylinder was from the bed upwards and from the free-surface downwards, which he was able to confirm by hydrogen bubble visualization. In the present experiments, the upward flow was easily observable with dye visualization. This flow was stronger near the bed and became weaker near the free-surface. However no downward flow was ever observed.

The effect of scour holes can be seen in Figure 4.3.7 (b). The pressure drop was again smaller for larger cylinders. The pressure increased near the free-surface and near the bed. In fact, for Expt. D3M, the pressure was almost equal to y_0 near the scour hole bottom, indicating the effect of intersecting jet-like flows in the near wake. Another rise in pressure was observed at $y / y_0 \approx 0.3$ to 0.5 for all mobile bed experiments. As the bulk of the fluid rushed through the large scour hole, the velocity at the sides of the cylinder at this level ($y / y_0 \approx 0.3$ to 0.5) reduced substantially (see, for example, Figure 4.2.6 (b) for Expt. D2M) leading to a smaller pressure drop (thus a rise in pressure).

The variation of pressure, when plotted in terms of C_p as shown in Figures 4.3.8 (a-b), became smoother and showed a trend roughly opposite to that observed at the cylinder front (Figure 4.3.4 (a-b)). The effect of scour hole was still visible. However, this type of plotting masked to some extent the observations made earlier about the pressure peaks at different levels.

4.4 Bed Shear Distribution

4.4.1 Overall shear field

Extensive shear stress measurements were taken around the cylinder as shown in Figures 4.4.1(a-j). In each of the experiments, the number of measurement points varied from approximately 100 for mobile bed runs to nearly 300 for rigid and smooth bed runs. Generally, a square grid with spacing equal to the cylinder radius (r) was used; however

closed to the cylinder, where the shear stress varied rapidly in terms of magnitude or yaw angle or both, smaller spacing ($r/2$ and $r/4$) were used. These figures give an idea about the overall shear distribution around a cylinder in case of smooth, rigid and smooth beds.

The shear stress amplification (τ_0 / τ_{00}), where τ_{00} is the upstream bed shear, was about 10-12 in the case of rigid bed runs, which were representative of the condition prior to the initiation of scour. As expected, the maximum amplification was found at the sides of the cylinder. What is rather unexpected is the large amplification in the wake region. Another startling finding is that in the case of Expt. D2M and D3M, which had large scour holes extending roughly $6r$ upstream from the cylinder center, the direction of shear stress was towards the POS in the region in front the cylinder (figures 4.4.1(e, g)). Several checks were made during the experiments to make sure that it was really the case; further confirmation came from the measurements at the 3DTBL stations. Flow visualization indicated that the flow very near the bed was in fact going inwards. The scour holes were so large that it was easier for the approach flow to dive into the scour hole rather than diverging out around the cylinder.

The shear stress amplification on the smooth beds was much smaller than that on the rough beds and was confined to a smaller region close to the cylinder. It appears that the roughness increases the area of influence of the cylinder.

Measurements on mobile beds with scour holes indicate that all the high shear stress area fell on the scour hole. The deflection of the shear stress vectors became smaller compared to rigid bed values. However the shear stress increased a little bit in the region upstream of the cylinder, as water rushed towards the scour hole. On the other hand, the shear stress decreased substantially at the region to the side of the cylinder across the scour hole. This was a result of the extra passage provided by the scour hole for the water to flow through.

4.4.2 Bed shear on the POS

Shear stress along the POS was measured in more detail (Figures 4.4.2(a-b)). A negative value in these figures indicates a bed shear in a direction opposite to the main flow (negative x-direction). This type of negative shear was measured with the probe facing upstream (Figure 4.4.3). This figure also shows the overlapping region of data in opposite directions. From this sort of raw data, certain data points had to be omitted to make the transition smooth. Figure 4.4.2(a) shows the final results.

It is clear that the shear stress gradually decreased as the separation point was approached beyond which the shear direction changed by 180°. The maximum shear

stress amplification in the separated region for smooth bed runs were about 1.25-1.5, which was in excellent agreement with Dargahi's (1987) measurement. Amplification for rough rigid bed runs were about 2.75-3.25. In the case of mobile bed runs with scour holes, the shear stress remained unchanged on the average upto the edge of the scour hole (Figure 4.4.2(b)). However, the shear showed a sharp increasing trend near the scour hole edge for Expt. C1M and C2M, which had relatively smaller scour holes. This indicates that the approaching water rushed into the scour holes. Expt. D3M with large hole did not show this trend.

4.4.3 Bed shear on the $x = 0$ plane

Further detailed shear measurement was made at the side of the cylinders (on the $x = 0$ plane). The magnitude of the shear stress vector τ_0 normalized by the upstream value τ_{00}, the yaw angle θ it makes with the x-axis, and the fluctuation of this angle in terms of the standard deviation σ_θ are shown in Figures 4.4.4(a-b) through 4.4.6(a-b). For rigid and smooth bed runs the shear stress increased rapidly as the cylinder was approached; however very near the cylinder surface the shear decreased a little (Figure 4.4.4(a)). The trend was clearly different for the smooth and the rough rigid beds. The shear amplification (Figure 4.4.4(a)) and the fluctuation of yaw angle (Figure 4.4.6(a)) were smaller for smooth bed runs, while the variation of yaw angle was very similar (Figure 4.4.5(a)) although with more scatter. A closer look very near the cylinder surface (Figure 4.4.5(a)) showed that the shear vector turned less in the case of rough beds. This is explained by the larger resistance offered by rough beds on the limiting streamlines as they turn outwards under the influence of pressure gradient.

For mobile bed runs with scour holes, the shear stress increased gradually as the cylinder was approached, reaching a value close to the critical shear stress τ_c of the sand near the edge of the scour hole (Figure 4.4.4(b)). The yaw angle (Figure 4.4.5(b)) showed a variation similar to rigid beds except for the absence of the rising tendency near the cylinder. This indicates that the scour hole made the yaw angles smaller near at the edge of scour holes. The yaw angle showed slightly larger fluctuation than rigid bed runs (Figure 4.4.6(b)), indicating that the scour holes somewhat relaxed the rigidity of flow conditions prevailing in the case of rigid and smooth bed runs.

4.4.4 Shear in the scour hole

Some measurements of shear stress inside the scour hole and on the sand bar developed behind the cylinder were taken. It was difficult to place the Pitot-static tube at certain locations and aligning it with the local bed topography. The Preston tube

technique was based on the assumption of a 2DTBL flow a flat wall. The effect of the complex 3D flow and irregular boundary on measurement accuracy is not known. The primary objective, therefore, was to obtain an approximate picture of the shear field, at least in a qualitative way. Data was collected for Expt. C1M and C2M. The shear inside the scour hole was too small to measure in Expt. D2M and D3M with larger scour holes.

Typical results for Expt. C2M are shown in Figures 4.4.7 (a-c). The shear stress on the POS caused by the deflected downflow and horseshoe vortex system (HVS) is shown in Figure 4.4.7 (a). The direction was upwards and upstream. The downflow hit the bed and was deflected upstream. The shear was low near the stagnation point and increased away from it. The spiral formed by the downflow was swept away by the flow, and it separated from the bed approximately at the intersecting point of the upper and lower slopes of the scour hole. The shear stress diminished gradually near this separation point and probably went to zero. All these took place at the lower slope near the cylinder. The shear on the upper slope was too small too measure, suggesting the rather stall-like nature of the degenerated HVS. The present measurements are in qualitative agreement with that of a plane impinging jet (Beltaos 1974). The only difference is that the fall of shear after the peak was as rapid as the rise in the present experiments while Beltaos' measurements show a gradual decrease. This may be due to the fact that the downflow is swept downstream quickly.

The accelerated flow at the sides of the cylinder, combined with the HVS, imparted a complex shear field on the scour hole boundary. On the $x = 0$ plane, the shear stress was largely in the downward direction. This shear was large at the bottom of the hole and decreased rapidly away from the cylinder and up the slope, as shown in Figure 4.4.7 (b). The shear was too small to measure in the upper portion. This shear pattern indicates that the erosion occurred mainly at the bottom of the hole and the sand from the upper portion slid down only when the slope became too steep. This was consistent with visual observations.

The shear was small just downstream of the cylinder and increased rapidly as the two jet-like flows from both sides of cylinder combined on the POS. The maximum shear was recorded on the sloping side of the bar. It was slightly greater than the critical shear stress of sand (τ_c), probably due to the extra resistance offered by the slope. As the slope of the bar became gentler, the shear fell and then maintained a more or less constant value up to the crest of the bar. This trend, with higher values at the peak, is different from the monotonically decreasing wall shear pattern exhibited by a wall jet. This might be due to the uneven bed topography and the superimposition of the wake on the jet-like flows. The

present pattern is also different from the continuously increasing shear stress on a classical dune (Raudkivi 1963).

4.5 The Skewed Boundary Layer

The nominally 2D approach flow was found to skew under the influence of the pressure gradient induced by the cylinder. In order to analyze the behavior of this skewed flow in the light of 3DTBL theories, data were taken at ten stations for Series C and E and at five stations for Series D and F. Large scour holes in Series D did not allow more stations to be included. The stations were selected in such a way that the velocity vectors across the vertical remained in approximately horizontal planes, *i.e.*, the vertical velocity component could be neglected. The number of data points across a vertical varied from 30 to 40.

4.5.1 Analysis of cross-flow

4.5.1.1 Prandtl's model

First of all, Prandtl's model was tested. The free surface velocity $\mathbf{V}_{top}$ and its angle of yaw θ_{top} was estimated from the measured velocity profiles. This gave the direction of the free streamline, which along with the direction normal to it gave the local directions of the streamline coordinate system (see Figure 2.4.2). The magnitude of the cross-flow in this coordinate system was then determined, which when divided by $|\mathbf{V}_{top}|\tan\gamma_w$ or $V_{top}\tan\gamma_w$ yields the experimentally determined value of $g(y/\delta)G(y/\delta)$. Here γ_w is the angle between $\mathbf{V}_{top}$ and the local shear stress vector $\vec{\tau}_0$. Typical plots of $g(y/\delta)G(y/\delta)$ as it varies across the BL thickness δ (= flow depth y_0 in the present experiments) are shown in Figures 4.5.1(a-c). It is clear that $g(y/\delta)G(y/\delta)$ is not an universal function of (y/δ) since its magnitude and shape vary widely from station to station and from experiment to experiment. Data from other experiments not shown here also lend support to this conclusion.

4.5.1.2 Polar plots and Johnston's model

Next, the polar plots were prepared for all the experiments (Figures 4.5.2(a-f)). In these figures, the velocity components along and perpendicular to $\mathbf{V}_{top}$ were plotted against each other. Both were normalized by $V_{top} \equiv |\mathbf{V}_{top}|$. The location of the stations and the extent of the scour hole are also shown. Any support for the validity of Johnston's (1960a) triangular model is difficult to find in these plots, even for the smooth bed runs.

However, a few profiles such as at Station 5 of Expt. C1R and Station 4 of Expt. C2R (Figure 4.5.2(a, c)) showed some resemblance to a triangle. The position of the apex in terms of y^+ in these two cases were 165 and 182 respectively (or $0.78k_s$ and $0.93k_s$ in terms of bed roughness). Johnston estimated a y^+ value of about 12-16 for smooth walls which means an apex within the viscous sublayer. The higher values for the rough bed runs may or may not be due to roughness effects because values as high as 300 were reported for smooth walls by Hornung and Joubert (1963), Nwachukwu (1979), and Rajaratnam and Nwachukwu (1983a).

Irrespective of the validity of Johnston's triangular model, the polar plots can be used to gain valuable insight into the flow structure. If it is assumed that the pressure field is determined by the outer flow and that it remains constant across the entire flow depth, then the magnitude of the cross-flow at a certain depth is an indication of the momentum deficit at that depth due to lower velocity. The pressure gradient force will skew the flow while the inertial force will try to retain it in the direction of the free streamline. The velocity and the inertial force diminish continuously as the bed is approached, thus offering progressively less resistance to the pressure gradient force. As a result the skewing increases near the bed. The effect of roughness will probably be to limit the extent of skewing near the bed; however roughness effects on skewed flow are yet to be studied.

The effect of the scour hole on the flow is vividly illustrated in the polar plots. In general, the presence of the scour hole caused a decrease in the cross flow, especially in the upstream region (Figures 4.5.2(a-f)). This effect took place only below a certain depth (compare, for example, Expt. C1M and C1R in Figure 4.5.2(a, b)). The depth was higher for the stations closer to the scour hole, as can be seen by comparing Stations 2 and 3 in Figure 4.5.2(a). The cross flow at these stations was affected by the scour hole below $y/\delta \approx 0.31$ and 0.64 respectively and deceased roughly by 60% and 70% near the bed. This effect was more pronounced in experiments with larger scour holes. Similar trends in the upstream regions were also found for other experiments (Figure 4.5.2(c, e, f)).

The cross flow at Stations 1, 2 and 3 was negative near the bed in the case of Expt. D2M (Figures 4.5.2(e)). This means that the flow near the bed was towards the POS, as were the shear stress vectors as discussed in Section 4.4.1. At Station 1, this inward flow near the bed persisted up to 6 mm above the bed (equal to a y^+ value of 176 or $0.71k_s$). In case of Expt. D3M negative cross flow was found only at Station 1 (Figure 4.5.2(f)). This observation shows that a very large scour hole tends to draw water from an area wider than the width of the hole.

In the downstream region, the velocity profile generally turned inward near the bed. This was consistent with, and was probably caused by, the tapered shape of the wake which was narrower near the bed. In case of mobile bed runs, this tendency was substantially reduced (Figures 4.5.2(b, d, e, f)). It appeared that the presence of the rear bar partially prevented th cross flow from turning towards the POS. This effect was more pronounced for the stations closer to the bar.

The polar plots for some smooth bed runs in Series E showed a different behavior (Figure 4.5.2(c-d)). They showed negative cross flows in the upper part of the boundary layer, which then gradually increased to positive values near the bed. No explanation was found to account for this behavior. In Series F as shown in Figure 4.5.2(e), only Station 1 exhibited this behavior. In other stations the cross flow for smooth bed was positive and was found to be smaller than that of rough rigid bed. This is consistent with the fact that close to the bottom the velocity is higher for the smooth bed compared to that for a rough bed. Thus it offers more resistance to the skewing effect and hence the cross flow is smaller.

4.5.1.3 Coles' model

The performance of this model was evaluated using both wall and wake components. The wake direction was first determined by evaluating Equation [2.4.2a]

$$\mathbf{q} = \mathbf{q}_{wall} + \mathbf{q}_{wake} \qquad [2.4.2a]$$

at the free surface level. Here $\mathbf{q} = \mathbf{V}_{top}$; the magnitude of $\mathbf{q}_{wall}$ was given by the law of the wall evaluated at $y = \delta$; and its direction was given by the measured direction of $\bar{\tau}_0$. Then $\mathbf{q}_{wake}$ could be determined completely from Equation [2.4.2a]. With $\omega\langle y/\delta\rangle$ equal to 2 at $y = \delta$, the value of Π was given by $\kappa q_{wall} / 2q_*$ where $q_* = \sqrt{\tau_0 / \rho}$. Now it was possible to decompose the velocity vector at any distance from the bed into wall and wake components, which were then plotted in separate graphs along with the theoretical curves (Figures 4.5.3(a-j)). Some wildly oscillating values can be found in some of these figures, which happened when wall and wake directions were nearly parallel. These points will be disregarded in the following discussion.

The present experiments lend only limited support to Coles' model. Both the wall and wake functions showed poor agreement with data, though in some cases the wall function appeared more reasonable. So much scatter was never observed by Hornung and Joubert (1963) who studied the flow around a circular cylinder very much like the present experiments. Their wake function data did not match with Coles' wake function but fell within a narrow band. The band formed by the data of Stations 1, 2 and 3 in Expt. D2R

(Figure 4.5.3(f)) is very similar to Hornung and Joubert's band. Data at most of the stations at the upstream region showed this trend. Nwachukwu's (1979) experiments on the flow around groynes showed a similar but separate band. All these point to the possibility of another form of wake function that might be valid for a certain class of flow which includes the flow in the upstream region.

4.5.1.4 Perry and Joubert's model

First of all, $(\mathbf{q}_e - \mathbf{q})$ was calculated at every level at a particular station; $\mathbf{q}_e$ and $\mathbf{q}$ were given by $\mathbf{V}_{top}$ and $\mathbf{V}$ respectively. Then the point $y = y_{max}$ where $|\mathbf{q}_e - \mathbf{q}|$ was maximum was found. Usually y_{max} turned out to be the closest point to the bed except in a few sand bed experiments it was the second closest point. The direction of $|\mathbf{q}_e - \mathbf{q}|_{max}$ (expressed as β, see Figure 2.4.5) was the direction of $\bar{\Pi}'$ and its magnitude is given by Equation [2.4.4a]

$$\frac{\mathbf{q}_e - \mathbf{q}}{q_*} = \bar{\Pi}'\langle x,z\rangle \varphi\left\langle \frac{y}{\delta} \right\rangle \qquad [2.4.4a]$$

evaluated at $y = y_{max}$ and the defect function was given by Equation [2.4.4b].

$$\varphi\left\langle \frac{y}{\delta} \right\rangle = 5.75 \log\left(\frac{y}{\delta}\right) \qquad [2.4.4b]$$

Now it was possible to compute the experimental defect function ($|\mathbf{q}_e - \mathbf{q}|$) at all points. The angular deviation $\Delta\beta$ of an experimental velocity defect vector $|\mathbf{q}_e - \mathbf{q}|$ from the vector ($|\mathbf{q}_e - \mathbf{q}|_{max}$) was determined as ($\beta_{expt} - \beta$) and was another indicator of the validity of this model. A positive value of $\Delta\beta$ indicates more skewing than that prescribed by the model. Similarly a negative value indicates less skewing. The experimental defect function and the angular deviation were plotted separately as shown in Figures 4.5.4(a-j).

Among the four cross-flow models, Perry and Joubert's model performed best. It should be kept in mind that a large value of $\Delta\beta$ in the outer portion of the BL ($0.5 < y/\delta < 1$) does not necessarily mean poor performance since the measured velocity vectors were nearly equal to each other. Therefore large values of $\Delta\beta$, which is an angular measure, could result.

The model gives best results for Series D (Figure 4.5.4(e-h)), both with and without scour hole. The performance was reasonably good for other series also. In the case of Series C, the result was better for Expt. C2M and C2R with smaller cylinder than Expt. C1M and C1R with larger cylinder (Figure 4.5.4(a-d)). The stations closer to the wake usually showed poor result in this series. The superior performance of the model for

Series D, even at stations closer to the wake, is probably due the greater distance of the stations from the cylinder. It is surprising that the smooth bed runs did not show better match with this model which was originally proposed for smooth beds. The present attempt to apply this model to rough beds was based on the assumption that the defect function should be equally applicable in the region away from the wall. However, the model showed good results even for the points closest to the rough bed.

4.5.2 Near-wall similarity

As noted earlier, all the near-wall similarity models were intended for smooth walls. Therefore, testing of their applicability was limited only to smooth bed runs in the present study.

The following comments by Pierce, McAllister and Tennant (1983a) are highly relevant in interpreting the results presented in this section.

> "The direct force measurement of local shear stress is an absolute requirement in any serious study of the near-wall similarity question in three-dimensional flows. This is an essential requirement since the several near-wall similarity models proposed in the literature for the 3DTBL case all require the local wall shear stress (or some component of it) in the necessary nondimensionalizing of experimental data. While the use of indirect wall shear devices has been reported in some 3DTBL flows (*e.g.*, see references [12-19]), all such devices reported to date have used only two-dimensional calibrations in three-dimensional flows. This, in effect, assumes *a priori* and without proof the validity of the two-dimensional near-wall similarity law in three-dimensional flow -- and this is wholly unacceptable in any attempt at a definitive study of near-wall similarity in a three-dimensional flow. The use of a two-dimensional calibration in a three-dimensional flow presumes far more than is acceptable in a near-wall similarity study in 3DTBL flows."

The principle of the yaw probe, which was used to measure the bed shear stress in the present experiments, is based on this very *a priori* assumption, thus casting some doubt as to the soundness of the 3DTBL similarity analysis presented below. Nevertheless, the following considerations seemed to justify it.

In the present experiments, the measurement stations were far away from the cylinder and the yaw angle γ_w of the wall shear vector $\bar{\tau}_0$ relative to the free-surface velocity vector V_{top} was rather small (usually less than 10°). Thus the expected error

introduced due to a ±5° error in γ_w measurement would be less than ±1% in the coordinates of all of the scalar similarity models tested here. Similar inaccuracy would also be introduced in the main flow component of Chandrashekhar and Swamy's model, the only complex model to be tested here. However, inaccuracies as high as ±30% may result in the cross flow component of this model. The later inaccuracy would be less than ±10% for a ±2° inaccuracy in γ_w. The use of the smaller yaw probe (the outer diameters of each tube was 1.3 mm) ensured minimum turning of the velocity vector over the 0.65 mm distance from the probe center down to the wall. The uncertainty in this turning angle, and thus in γ_w, was estimated to be less than 2-5°. As much as these errors show the limitations of a near-wall similarity analysis, they also show the viability of the same. There are only a very few direct force measurements of the wall shear stress, and indirect measurements are still used in near-wall similarity analysis (*e.g.*, the experiments discussed by Ölçmen and Simpson 1992). Moreover, this would probably be the first application of the 3DTBL similarity models to a free-surface flow problem (without the overlying potential flow layer usually found in wind tunnel tests).

All of the scalar models except that of East and Hoxey and one of the complex models, that of Chandrashekhar and Swamy, were tested. The velocity profile and local bed shear stress were all that were needed for testing these models. Other models required as direct input explicit pressure gradient data, which could not be measured using available experimental facilities. Therefore they could not be tested.

The scalar models postulate that a particular component of the velocity ($\hat{q}$) and a particular quantity ($\hat{q}_*$) related to the local shear stress as shown in Table 2.4.1 would together satisfy the 2DTBL law of the wall. Note that the quantities are in streamline coordinate system (x,y,z) with velocities (u,v,w). This will also be used in the present section and associated figures and is not to be confused with the laboratory coordinate system. The 2D law of the wall with the following constants was found to describe the 2D approach flow adequately and was taken as the theoretical curve for the scalar near-wall similarity models.

$$q^+ \equiv \frac{\hat{q}}{\hat{q}_*} = 5.75 \log\left(\frac{y\hat{q}_*}{\nu}\right) + 5.5 \qquad [2.5.1]$$

For brevity, $y\hat{q}_* / \nu$ is often replaced by y^+. At each station, γ_w and $\hat{q}_*$ were first determined. Then for every point in the particular station, the yaw angle γ of the velocity vector $\mathbf{q}$, $\hat{q}$, q^+ and y^+ were computed. The results were then plotted in q^+-y^+ coordinate system.

For the model of Chandrashekhar and Swamy, the main and cross flow components of $\mathbf{q}$ (u and w) and of $\bar{\tau}_0$ ($u_* \equiv q_* \sqrt{\cos\gamma_w}$ and $w_* \equiv q_* \sqrt{\sin\gamma_w}$) and then u^+ ($\equiv u / u_*$) and w^+ ($\equiv w / w_*$) were computed for all points at a station. The wall units were defined as $yu_* / \nu \equiv y^+ u_* / q_*$ and $yw_* / \nu \equiv y^+ w_* / q_*$. The results were then plotted in $u^+ - y^+ u_* / q_*$ and $w^+ - y^+ w_* / q_*$ coordinate systems for the main and cross flow components respectively. The data were compared to the theoretical curves given by Equations [2.4.6a, b].

The performance of the scalar models are shown in Figures 4.5.5 (a-b) though 4.5.9 (a-b). It is interesting to note that the experimental points in the coordinate system of all the scalar models gave very similar values and thus exhibited almost identical behavior in terms of trend and range of applicability. This may be directly traced to the low skewing of flow at most of the stations, *i.e.*, the small values (generally less than 5° across the BL thickness) of the yaw angle γ of $\mathbf{q}$ relative to $\mathbf{V}_{top}$ and to small values of γ_w. This suggests that the further turning of the velocity vector from the probe center down to the wall is small and therefore leads to small error in the measurement of γ_w. This further confirms our earlier argument that the effect of the error in measuring γ_w in the present experiments would be very small (less than 2-5°) and thus the similarity models could be tested with good accuracy.

In Figure 4.5.5 (a), it can be seen that Coles' model did not perform well at any station in Expt. E2S. The scatter in the data was substantial and apparently did not show any systematic dependence on the location of station, the degree of skewing or the distance from the bed. The data fell on a wide band. On the other hand, the data fell on a narrow band for all stations in Expt. F2S (Figure 4.5.5 (b)), suggesting the existence of a near-wall similarity. The best consistency in data from all stations was achieved in the y^+ range from 30 to 700, after which the data for downstream stations showed somewhat greater deviations. The data points below $y^+ \approx 30$ showed a deviation similar to that observed in 2DTBL, suggesting the possibility of another similarity relation in the viscous sublayer region. Coles' theory was closest to the data points at $30 < y^+ < 80$; then it remained parallel to the data band but overestimated q^+. This continued up to $y^+ \approx$ 700 when the data started to fall suggesting a rather uniform upper layer flow.

The same comments can be made about other scalar models, namely those of Johnston, Hornung and Joubert, Pierce and Krommenhoek and Prahlad (Figures 4.5.6 (a-b) through 4.5.9 (a-b)). As noted already, this is the result of small cross flows. The reason for the better performance of scalar models in Expt. F2S than in Expt. E2S is not obvious, except that the stations in Expt. F2S were located further away from the cylinder

and thus were subjected to smaller skewing. This is also consistent with the fact that all similarity models degenerate, in the limit of vanishing skewing, into the 2D law of the wall.

Both the main and cross flow components of Chandrashekhar and Swamy's model are shown in Figures 4.5.10 (a-d). The model overpredicted the main flow component u^+ across the entire BL thickness at all stations in Expt. E2S. Again no apparent correlation could be found with other parameters. In case of Expt. F2S, the results were good at all stations up to $y^+ \approx 900$, after which the data points started to fall below the theoretical line. The cross flow component (w^+) data points fell far below the theoretical line and this discrepancy could not be wholly accounted for even by the relatively large uncertainty in γ_w. The cross flow at certain data stations in the downstream region, where γ_w assumed negative values, could not be computed, as may be noted in Figures 4.5.10 (c-d). From the plots of present experiments as well as those presented by Pierce, McAllister and Tennant (1983b) and Ölçmen and Simpson (1992), it may be noted that the cross flow gradually become zero near the BL edge, as it should in a streamline coordinate system. The cross flow model of Chandrashekhar and Swamy, however, not only shows a poor match with data, but also shows a obviously wrong trend (increasing continuously with $y^+ w_* / q_*$). The data from several stations of Expt. E2S fell on a narrow band, indicating the possibility of the existence of a near-wall similarity in w^+-$y^+ w_* / q_*$ coordinate system. However, the data of Expt. F2S showed no such band.

4.6 Scour Depth and Scour Profiles

4.6.1 Measurement of scour profiles

The scour profiles in the front (on the POS and $x < 0$), at the back (on the POS and $x > 0$) and on the lateral side (on the $x = 0$ plane) of the cylinders were taken using a manual point gauge. The smallest division on the scale was 1 mm; thus the nominal uncertainty in measurement on a flat bed was 0.5 mm at a 95% confidence level. The uncertainty in the depth measurement inside the scour hole with inclined bed was estimated to be at 1 mm. Since the scour depth at any level was calculated as the difference between these two measurements, the uncertainty in scour depth was about 1.12 mm, as given by Kline and McClintock's (1953) method. The measurement points were 5 mm apart for the front and side profiles. They were generally 5 mm apart in the back profiles also, but when the bed level variation was small, larger spacings (10-20 mm) were used. The measurement of a single profile took about 5 to 15 minutes depending on its length, and the middle point of the time period was taken as the

representative measurement time of that profile. The operation of the point gauge did not disturb the flow or scour profile in any noticeable way.

For Series A, the scour profiles were taken many times during the mobile bed runs. Figure 4.6.1 shows and defines the special points in the scour profiles and the geometric scales that can be derived from these profiles. For other series (B, C and D), only the length scales were measured instead of the whole profile during the experiments. After the equilibrium stage was reached, the flow was stopped and the water was slowly drained, and the scour profiles were taken for all experiments of all series. In addition a cross-section of the rear bar at the point of maximum height was also taken for all experiments. Typical measured profiles are shown in Figures 4.6.2(a-c) for Expt. A3M.

4.6.2 Similarity of scour profiles

The scour hole has been observed by earlier researchers to maintain a similar shape for most of the time of scour development and most of the models of scour development (see Section 2.3.3.4) are based on this assumption. However, so far no experimental data have been published to establish this observation on a firm basis. The scour profile measured in the present experiments were used for this purpose.

For a front profile, the linear scales in the horizontal and vertical directions (Figure 4.6.1) were defined as

$$S_{fx} = |x_{\min} - x_{1/2}| \quad ,$$

and $$S_{fy} = |y_{\min}| \quad ,$$

where the subscripts min and 1/2 denote the deepest point (point B in Figure 4.6.1) and the point where $y = y_{\min} / 2$. The coordinates were normalized by these scales and the origin was shifted to point O' as shown in Figure 4.6.1. The new dimensionless coordinates for the front side were defined as follows:

$$\bar{x} = \frac{x - x_{\min}}{S_{fx}} \quad ,$$

and $$\bar{y} = \frac{y}{S_{fy}} \quad .$$

The scour profiles in front of the cylinders are shown in Figures 4.6.3 (a-d) in the normalized coordinate system $(\bar{x},\bar{y})$. The following curve is also shown in these figures.

$$\bar{y} = -\exp\left[\ln\left(\frac{1}{2}\right)\bar{x}^2\right] + \sin(-\pi\bar{x})\left\{C_1 \exp\left[\ln\left(\frac{1}{2}\right)(2\bar{x}+1)^{20}\right]\right.$$
$$\left. + C_2 \exp\left[\ln\left(\frac{1}{2}\right)(2\bar{x}+3)^{20}\right]\right\} \qquad [4.6.1]$$

The first term of this equation represents an exponential curve which was used by Rajaratnam and Beltaos (1977) to describe the scour profile dug by an impinging jet. Observing the similarity between the downflow in front of the cylinders and an impinging jet, the exponential function was first tried. But it did not fit the data adequately and the discrepancy showed a sine curve-like variation in a certain region ($-2 < \bar{x} < 0$). After a few trials, it was found that a combination of an exponential and a sine curve describes the data well. The influence of the sine curve was confined within two separate regions ($-2 < \bar{x} < -1$ and $-1 < \bar{x} < 0$) by multiplying it with two square wave-like functions. The constants C_1 and C_2 were found to be equal to 0.07. Figures 4.6.3 (a-d) shows how this equation fits the data. The fit is very good everywhere except for the region where $\bar{x} < 2$. The approximate position of the cylinder surface is at $\bar{x} \approx 0.25$ and the scour extends to a point approximately at $\bar{x} \approx -2.25$. The experimental error relative to the scour hole size increases for smaller cylinders and hence the scatter around the fitted line also increases. Similar dimensionless profiles for other experiments at equilibrium state could also be described by this equation equally well.

The scales for the side profiles were found in a similar way and similar normalizations were adapted to get

$$S_{sz} = |z_{min} - z_{1/2}| \quad ,$$

$$S_{sy} = |y_{min}| \quad ,$$

$$\bar{z} = \frac{z - z_{min}}{S_{sz}} \quad ,$$

and $$\bar{y} = \frac{y}{S_{sy}} \quad .$$

The results for Expt. A1M and A3M are shown in Figures 4.6.4 (a-b) along with the fitted line which is same as Equation [4.6.1] except for a change necessary for the fact that, unlike x and $\bar{x}$, z and $\bar{z}$ were in the same direction. The equation is as follows.

$$\bar{y} = -\exp\left[\ln\left(\frac{1}{2}\right)\bar{z}^2\right] + \sin(\pi\bar{z})\left\{C_1 \exp\left[\ln\left(\frac{1}{2}\right)(2\bar{z}-1)^{20}\right]\right.$$
$$\left. + C_2 \exp\left[\ln\left(\frac{1}{2}\right)(2\bar{z}-3)^{20}\right]\right\} \qquad [4.6.2]$$

The scatter of data, especially in the early stage, is evidently more than that in the case of front profiles. This indicates that it takes relatively more time to attain the similarity at the sides of the cylinder. The position of the cylinder surface is slightly nearer ($\bar{z} = -0.2$) than the front side and the scour extends a little bit more ($\bar{z} \approx 2.5$). These differences reflect of the different flow patterns prevailing at the front and at the side. Profiles of other experiments at equilibrium state showed very similar characteristics.

The profiles at the back of the cylinders were analyzed in a slightly different way. First the points of minimum and maximum elevation (point C and D in Figure 4.6.1) were identified. Then the scales were defined as

$$S_{bx} = |x_{max} - x_{min}| \quad ,$$

and $$S_{by} = |y_{max} - y_{min}| \quad .$$

The dimensionless coordinates were defined as

$$\bar{x} = \frac{x - x_{min}}{S_{bx}} \quad ,$$

and $$\bar{y} = \frac{y - y_{min}}{S_{by}} \quad .$$

Dimensionless plots of the back profiles are shown in Figures 4.6.5 (a-b) for Expt. A1M and A3M. Figure 4.6.5 (b) is typical of other experiments not shown here. The back profiles seem to grow in a self-similar way and the upstream side of the rear bar roughly follows a sine curve. The equation may be written as:

$$\bar{y} = \frac{1}{2}\sin(\pi\bar{z} - \pi/2) + 0.5 \qquad [4.6.3]$$

The cylinder surface was found to be at $\bar{x} \approx -0.125$ on the average and the lee side of the bar extended to a point at about $\bar{x} \approx 1.3$. Expt. A1M was run for more than 20 days and during the later stage the flow was not strong enough to carry the sand scoured from the scour hole all the way up to the crest of the rear bar. Thus the sand accumulated on the bar and made its curvature more prominent as shown in Figure 4.6.5 (a). A few small ripples formed on the bar too, which was not observed in other experiments.

4.6.3 Time development of scour

Attempts to find similarity in the development of the scour depth d_s with time (t) were made with the following quantities as potential time scale:

- the time to reach the equilibrium state, *i.e.*, d_{se} (t_e),
- the time when the data points deviate from the straight line in a $d_s - \log t$ plot (t_{dev}),
- the time to reach 75% of d_{se} (t_{75}),
- the time to reach 90% of d_{se} (t_{90}), and
- the time to reach 95% of d_{se} (t_{95}).

The results were not good. However, the best among these was obtained for t_{95}, which is shown in Figure 4.6.6 (a). A mean line fitted through the data points from all experiments is shown Figure 4.6.6 (b). The equation of this line is:

$$\frac{d_s(t)}{d_{se}} = 1 - \exp\left[\ln(1-0.95)\left(\frac{t}{t_{95}}\right)^{0.65}\right] \qquad [4.6.4]$$

The equilibrium scour depth d_{se} is generally reached at around $t / t_{95} \approx 1.5$, but the range varies from 1.3 to 2.3. Some of the time scales listed above were used for jet scour (Rajaratnam and Beltaos 1977; Rajaratnam and Berry 1977) and for groyne scour (Nwachukwu 1979; Rajaratnam and Nwachukwu 1983b) with a moderate to good degree of success. The poor performance of these in collapsing the present set of data is probably due to the relatively more complex nature of the pier scour mechanism.

Among the models for the temporal development of scour depth proposed so far, the one of Kothyari *et al.* (1992a, b) is the most recent and is considered to be representative of the latest trend in scour research. It was therefore chosen to be tested against the present experiments. When testing the model against Kothyari *et al.*'s own data, it was found necessary to stretch the model generated time by a factor of 3.16 to fit data, or in other words, a value 3.16 times the reported value (0.05) of the coefficient C_2 gives the correct result. Therefore $C_2 = 0.158$ was used throughout. The performance of the model was found to vary widely from one series to another, but within one particular series its performance was more or less equal for all experiments. This suggests that the coefficients used in this model may be more dependent on the flow parameters than on the cylinder size. Figure 4.6.7 (a) for Expt. A3M shows one of the best matching while Figure 4.6.7 (b) for Expt. B2M shows a poor performance. Kothyari *et al.* recommended that the computation be stopped when the bed shear stress under the horseshoe vortex equals the critical stress of the sand, *i.e.*, when $\tau_{HVS} / \tau_c = 1$. But as can be seen in these figures, this may be premature and the computation may be carried out further to obtain

meaningful results. For Series A, the equilibrium was reached at about when $\tau_{HVS} / \tau_c \approx$ 0.5. It was also found possible to manipulate the coefficients to obtain better match with experiments. An example is shown in Figure 4.6.7 (c) for Expt. B2M with $C_1 = 0.7$ and $C_2 = 0.001$.

4.6.4 Behavior of length scales

An attempt was made to study the behavior of the various length scales defined in Figure 4.6.1. Preliminary analysis indicated that the scour depth $d_s\langle t\rangle$ at a particular time t should be used to normalize the length scales and that the time to reach the equilibrium condition t_e (or any fraction of it such as t_{95} for that matter) should be used to normalize the time. These parameters, as will be seen shortly, did not always bring the data from different experiments into a narrow band, but led to less scattering than other parameters. The temporal development of length scales, normalized in this way, are shown in Figures 4.6.8 (a-l). The development of d_s for different experiments is shown first in Figure 4.6.8 (a).

Some characteristics of the front side of the scour hole can be inferred from the behavior of S_{fx}, X_A and X_B (Figures 4.6.8 (b-d)). The value of S_{fx} / d_s is indicative of the average steepness of the lower slope. It remained in the range of about 0.6 to 0.9 with a mean of about 0.75. In other words, the slope varied within a range from 29° to 40°, with a mean of 34°. This may be compared to the angle repose α_r of the sands used (28° and 30° for 0.88 mm and 1.84 mm sand). The average value of X_A / d_s was about 1.85 and 1.5 for the finer and the coarser sand respectively. The upstream extent of the scour hole was therefore larger for the finer sand, or, stated differently, the coarser sand resisted more before sliding down the slope. This is consistent with the larger value of α_r of the coarser sand. Moreover, at the initial stage, X_A / d_s showed opposite trends for these two sands. Slightly higher values for the finer sand indicates that the slope of the scour hole was initially flatter. The coarser sand, on the other hand, formed a steeper sided hole at the initial stage. Different trends were also exhibited by X_B / d_s. Larger values of about 0.2 for the finer sand indicated a wider groove. The size of the groove was only half of that in the case of the courser sand. This was probably due to the relative ease with which the impinging downflow removed the finer sand.

Figures 4.6.8 (e-f) shows the characteristics of the scour behind the cylinder. The distance X_C of the deepest point from the cylinder generally increased with time. However, the value of X_C / d_s decreased at the initial stage mainly because d_s increased rapidly during this time. Near the later stage, X_C / d_s remained more or less constant for most experiments but for some showed a slightly increasing trend. This indicates that

scouring behind the cylinder continued even after equilibrium was reached in front of it. In general, X_C / d_s was higher for higher shear ratio ($\tau_{\sim 0} / \tau_c$). Interestingly, the relative depth Y_C / d_s was dependent on the sand size, not on τ_{00} / τ_c. For the coarser sand, the absolute value of X_C / d_s was higher.

The height and distance of the crest of the rear bar are shown in Figures 4.6.8 (g-h). For all experiments except D2M, X_D / d_s remained between 3 and 6. For smaller cylinders, X_D / d_s was lower. For larger cylinders, X_D / d_s was higher and showed an increasing trend even after $t / t_e = 1$, indicating that the bar continued to elongate. In case of Expt. D2M, X_D / d_s showed an altogether different trend. The reason, however, is not clear. The relative height Y_D / d_s was higher for the smaller cylinders, probably due to smaller scour in front of the cylinder. The reason for the different trend exhibited by Expt. D2M and D3M is not apparent.

The length scales of the rear bar are shown in Figures 4.6.8 (i-k). The horizontal scale was mainly dominated by the distance of its crest from the cylinder. So the behavior of S_{bx} / d_s was similar to that of X_D / d_s. Similarly, S_{by} / d_s showed a behavior somewhat similar to that of X_D / d_s. Expt. D2M and D3M showed different trends as before. However, influence of any particular parameter could not be discerned. The combined effect of both horizontal and vertical scales is reflected in the variation of S_{by} / S_{bx}, which was also indicative of the average steepness of the bar. The value of S_{by} / S_{bx} generally fell between 0.3 to 0.5, with larger values for smaller cylinders. Expt. D2M and D3M again showed clearly different trends.

4.6.5 Equilibrium scour depth

The scour depth predicted by different formulas was compared to the observed depth for all the mobile bed experiments. The results are shown in Figures 4.6.9 (a-c). Only the equations which have been explicitly recommended for clear-water condition were used. In case of Series C and D, extensive flow measurements were taken at the near-equilibrium stage. This might have disturbed the scouring process and increased the value of d_{se}. Although this effect is considered small, the results of Series C and D should be interpreted cautiously.

Comparing Figures 4.6.9 (a-c) to Figures 2.2.2. and 2.2.3, it may be said that in general, the prediction of scour in laboratory channels was slightly better then that in real rivers. It may be so because most of the equations were based on laboratory data and the parameters can be better defined and measured more accurately in the laboratory.

The prediction was better for Series A than for Series B. For Series C, it was slightly worse than Series A but better than Series B. It was worst for Series D, where

most of the equations underestimated the scour depth. It appears that predictions are better for low Froude number flows and for larger flow depth (compared to cylinder size).

The so-called design methods deserve special attention. The method of Breusers *et al.* (1977), which was based on extensive literature survey, underpredicted the scour depth for almost all experiments in all series. Melville and Sutherland's (1988) method was based on envelope curves. True to its conservative nature, it has overpredicted the scour depth for all experiments including Expt. D2M which had a very large scour hole. The so-called CSU method has been recommended by Richardson *et al.* (1993) as the official US guideline. It overpredicted scour depth for all experiments except Expt. D2M.

It is interesting to compare the performance of older formulas with that of later methods. Different methods are arranged chronologically in Figures 4.6.9 (a-c). Inglis' (1949) equation, the oldest method tested here, gave results comparable to that given by Kothyari *et al.* (1992a) for Series A, by Melville and Sutherland (1988) and Richardson *et al.* (1993) for Series B, C and D.

Laursen's (1963) formula, which was derived analytically based on a long contraction analogy, consistently underestimated scour depth. On the other hand, Chitale's (1962) equation, which was based on a simple correlation on a few data points, gave results comparable to that given by the design methods of Melville and Sutherland (1988) and Richardson *et al.* (1993). This makes it more difficult to judge the benefits of so-called theoretical approach. It would be interesting to see the performance of a method based solely on field data, such as that of Froehlich (1988) which is applicable to live-bed condition only. But so far no such method has been devised for clear-water condition.

No firm conclusion can be made based on the application of various formulas to such a limited number of experiments. The only thing that can be said is that one should not be surprised to see a good (or poor) performance by most of the formulas regardless of their age and basis. The need for further research is obvious.

4.7 Erosion Process

4.7.1 Modes of sand movement

The sand grains were acted upon by the widely varying flow around the pier and as a result were found to exhibit different types of instability and movement at different places. Careful observation of the sand movement during the erosion process led to the following categorization. Different modes of sand movement are now described in the ascending order of instability.

(1) **Vibration**: Most of the time individual sand grains were found to vibrate while remaining in position. The intensity of vibration varied, sometimes making it difficult to distinguish it from other modes of sand movement. So the line was drawn based on the contribution to the bed material transport. Thus the movement was categorized as vibration until it began to contribute to the transport. At the initial stage of scouring, grains near the pier flanks, in the near wake and the far wake exhibited this behavior. As the scouring progressed, the sand vibration was observed on almost the entire area of the scour hole, especially at the sides. The grains on the sand bar developed downstream of the pier were also in a state of vibration. This type of sand movement was clearly captured in the videos. The latitude of the vibration varied widely, starting from very small values to 2-3 times the grain diameter. In the case of larger latitude, the movement was called vibration when the grains were found to move around a mean position. This mode probably indicates a state of incipient motion, since a little more instability led to sediment transport. Several authors, particularly Melville (1975) and Melville and Raudkivi (1977), observed that the grains in the scour hole were in a state of incipient motion.

(2) **Suspension**: After the scour hole had reached a certain size, the sand grains excavated by the strongly deflected (almost by 180°) downflow were found to be in a state of suspension at the rim of the lower groove. A certain finer fraction of the sand was found to accumulate here. It appears that the flow was unable to lift heavier grains into suspension and hence to this particular place, and that the lighter grains were washed away by the flow. From time to time, the grains in suspension were buried under avalanches sliding down the upstream slope of the hole. Another place where sand was found in suspension was the area just behind the cylinder. This was observed during the later stage of the scouring process when the flow had made the bed profile more "aerodynamic." The shear exerted by the jet-like accelerated flows along either side of the cylinder and the prevailing low pressure at the back of the cylinder seemed to be responsible for this type of sand movement in the near-wake region.

(3) **Rolling**: Sand grains were found to roll when the disturbing forces were a little bit higher than the stabilizing forces. Generally a number of grains (5 to 25) were found to roll together in long streaks. The distance traveled ranged from a very small value to 20-25 mm, with most of them about 10 mm. At the initial stage, rolling was found mostly at the sides of the pier. With the formation of a scour

hole, rolling was the principal mode of removal of scoured material through the side edges of the hole, continuing on to the crest of the rear bar. The rolling of sand grains, especially in long streaks, and the associated flow pattern as visualized by dye injection are reminiscent of the bursting phenomenon of the TBL which has been found to be closely associated with sand motion and entrainment (Grass 1970, 1971; Jackson 1976; Sumer and Deigaard 1981).

(4) **Somersaulting**: Individual grains as well as small groups of a few grains were found to move in a fashion known as somersaulting. This was found at the sides of the cylinder at the early stage when the bed was more or less flat. With the growth of the scour hole, this kind of movement became rare at this location, although it did not cease altogether. It was observed that the grains underwent three or four somersaults in rapid succession. This mode of transport probably occurred during the lift-up and breakup stages of the low-speed streaks as described by Offen and Kline (1975) in their model of the bursting phenomenon. The movement of sand grains was similar to that observed by Sumer and Deigaard (1981) on rough sand beds.

(5) **Sliding**: The sand on the inclined face of the scour hole was observed to slide down towards the bottom of the hole. This was not a continuous process. It took place from time to time in the form of what Melville (1984) called avalanches of sand. The volume of these avalanches and the distance they traveled varied widely. The volume varied from a few grains to a whole slip-circle-like chunk. Usually not more than two layers of sand grains moved at a time, with the thinner and thicker layers found mostly at the upper and lower portions of the inclined face respectively. The distance traveled varied from a few millimeters (when it resembled rolling) to the whole distance down the sloping face. Away from the POS, the avalanches were found to be smaller in volume and less frequent. The sand grains loosened by the avalanches away from the POS often did not reach the bottom; they were found to follow the curved spiral path of the HVS directly towards the wake region. The shape of the scour hole (especially the upper portion of it) appeared to be shaped mainly by the sliding mechanism which in turn was determined strongly by the angle of repose (α_r) of the sand and the local flow. The upper portion of the inclined face away from the influence of the impinging downflow was at an angle nearly equal to α_r. This sliding was also found at the lee side of the sand bar. The sand carried by the flow to the crest of the bar gradually made the lee side steeper than α_r. From time to time the sand grains

accumulated in this way at the crest slid down the lee face of the bar and made the angle closer to α_r.

(6) **Abortive tornadoes**: Three types of tornado-like swirling flows were identified in the wake region. These tornadoes were probably generated by cast-off wake vortices. They differed only in strength as evidenced by their capacity to transport sand grains. The first type includes only the weakest of all, called abortive tornadoes here. These could initiate the lift-up of a small group of grains (5 to 20) but could not sustain them in a state of suspension long enough. The grains collapsed roughly over the same area from which they were lifted. Thus these tornadoes did not contribute to the net transport but changed the local bed topography. The typical diameter of these were about 15-20 mm and the sand grains were lifted about 10-20 mm above the local bed level. The frequency of occurrence of this type of tornado was pretty high at the beginning but declined slightly at the later stage.

(7) **Weak tornadoes**: The second type of tornadoes, called weak tornadoes here, could lift about 10-30 sand grains to a height of about 10-25 mm for a time long enough to travel a distance of up to 60-80 mm. Then the sand grains collapsed on the bed. The diameter of these were about 10-15 mm. This type of movement changed the bed topography as well as transported sand in the general downstream direction and slightly diverging out from the POS. The frequency of occurrence of weak tornadoes, unlike the other types, increased with time and eventually they became dominant as the rear bar developed. But if the rear bar became too flat, the dominance of the weak tornadoes was lost as the frequency of occurrence of other types increased.

(8) **Strong tornadoes**: The strongest tornadoes, called strong tornadoes here, were similar to weak ones in all respects except that they moved the sand grains over distances up to 300-400 mm. Strong tornadoes were particularly frequent during the initial stage of scouring when the bed in the wake region was almost flat. Their number went down quickly as the rear bar formed and interfered with their formation and movement. Strong tornadoes were observed only for the largest cylinder size (r = 54 mm) used in these experiments.

With different modes of sand movement defined and described above, the scouring process will now be described in terms of them.

4.7.2 Visual observation of the scouring process

The scouring process was carefully observed during the experiments. The local flow close to the cylinder and inside the scour hole was visualized by injecting dye. Moreover about 200 still pictures and a few hours of video were taken. These were studied later to gain further insight into the phenomena that are too fast to see with the naked eye. Several experiments were repeated just for the purpose of observing the mechanism of local scour. The following description of the scouring process is based on these observations.

As shown in Figure 4.7.1(a), the scouring was initiated along the cylinder surface at an location A (and A' on the other side of the POS line) in between 45° and 90° from the upstream face. Almost immediately after this, if not at the same time, scouring started at locations B and B'. These are the regions where the flow accelerated most (Figure 4.2.6 (a-b)) and where the divergence of the bed shear vector ($\nabla \cdot \bar{\tau}_0$) assumed highest values (Figure 4.4.1 (b, d, f, h)). From potential flow analysis, it can be shown that the circumferential pressure gradient is also highest here. The sand grains were rolling and somersaulting along long streaks at this stage and were deposited in the areas marked C and C' in this figure. Within minutes, regions A and B joined to form a long narrow groove, as did regions A' and B' on the other side of the POS (because of obvious symmetry, similar things may be assumed without being mentioned).

The downstream end of these grooves formed a leaf-like pattern (Figure 4.7.2(a)), which later grew into the rear mound or bar. In this region the sand grains could be seen to be in a state of near suspension and to be thrown upwards by the upflow. These grooves become elongated as their upstream ends moved towards the POS. When the ends got close enough to the POS (usually within ±30°), the mechanism of erosion changed from rolling and somersaulting to sliding and the sand grains started sliding down the upstream sloping ends. After a certain amount of time, which varied from 10 to 45 minutes for different experiments, the two grooves finally joined on the POS. From this moment on, the scour depth at the POS continued to grow and the deepest point in the groove continued to move gradually from the cylinder side to the POS for about another 20 to 90 minutes after which the deepest point finally reached the POS. From this moment on, the maximum scour depth persisted to be in front of the cylinder.

From the very beginning, abortive and weak tornadoes (and strong tornadoes for larger cylinders) were observed in the wake region. These tornadoes, which appeared to be linked to the cast off wake vortices, did not make any particular landscape except numerous shallow, curved scars (Figure 4.7.2(b)). These tornadoes reigned uninhibited in

the wake region until the rear bar developed. The formation of this bar in the early stage had nothing to do with the tornadoes; it formed from the sand grains transported from the elongated grooves by the accelerated flow at either side of the cylinder which had a component towards the low pressure near wake region. The growing bar changed the flow pattern in such a way that the number of tornadoes diminished drastically for a certain period (about 4 to 10 hours), after which weak tornadoes returned on the bar itself. These week and a few abortive tornadoes then took part in the transport of sand along the bar surface.

However rolling and somersaulting still carried the bulk of the sand on the surface of the rear bar. These two modes of transport became so intermingled in this region that it was virtually impossible to separate them. The sand grains were transported along with turbulent pulses as shown in Figure 4.7.2(c). The flow in the wake region was very complex and turbulent; so the finer details could not be visualized properly. However, the dominant overall pattern was quite clear as shown in Figure 4.7.1(e). The sand grains (both 0.88 and 1.84 mm sizes) close to the back of the cylinder were always in a state of suspension. This was probably due to the shear force exerted on them by the accelerated jet-like flows on either side of the cylinder and the low pressure in the near wake region. The jet-like flows had a substantial vertically upward component and a slightly inward component towards the POS. These flow components were facilitated by the "aerodynamic" topography of the bed which, after being created by the flow, guided the flow in a natural, smooth way. As a result the wide fluctuation in the direction of velocity vectors characteristics of the wake region in the early stage (Figure 4.2.21 (c-d)) reduced substantially during the later stage (Figures 4.2.20 (c-d)).

The rear bar resembled a classical dune in terms of shape and growth. The sand was transported along the surface of the bar and was deposited on its lee side. The flow separated at the crest of the bar as shown in Figure 4.7.1(e) and a vortex was formed as expected. Several bars of progressively smaller size formed downstream of the rear bar only in case of the smaller sand as can be seen in Figure 4.7.3(a). Dye visualization revealed the existence of two pairs of vortices at a point downstream of the rear bar (Figure 4.7.1(f)). The larger upper pair were most probably the trailing ends of the HVS and the lower pair seemed to be generated somewhere in the lee side of the bar. Sand was observed to accumulate near the POS as a result of the action of the lower pair of vortices, only in the case of smaller sand experiments. Apparently these vortices were unable to move the larger sand. The overall bed topographies after draining the water are shown in Figure 4.7.3(a-b) for smaller and larger sands respectively. These pictures show

equilibrium conditions but the topography remained essentially similar after the formation of the rear bar.

In front of the cylinder, the direct contribution of the HVS and the downflow appeared to be insignificant at the beginning. These are shown in Figure 4.7.1(b-d) as the scour hole grew deeper. The shear stress was small underneath the HVS as shown by the measurements on rough surfaces (Figure 4.4.1 (b, d, f, h)). Only in a small area directly under the impinging downflow was it greater than the upstream value τ_{00}; however it increased rapidly off the POS and along the cylinder edge, indicating large values of $\nabla \cdot \vec{\tau}_0$ which were however not large enough to cause high erosion rate. It appeared that the HVS and the downflow were not strong enough to initiate scouring on their own. Their contribution started to be noticed only when the grooves migrated to the POS and made more room available for the downflow to travel downward (Figure 4.7.1(b)). The separation point S was determined by the approach flow and the HVS was probably pushed a little bit upstream by the downflow, which now started to travel past the HVS into the scour hole. Occasionally some of the bed material dug by the downflow accumulated near the rim of the hole (point A in Figure 4.7.1(b)).

At this initial stage, the slope of the scour hole was steeper than the angle of repose α_r of the sand, and the sand grains soon started to slide down in the form of slip-circles. Thus the scour hole acquired the second upper slope (Figure 4.7.1(c)). The HVS settled down into the hole and the location of the separation point S was dictated by the extent of the scour hole rather than the upstream flow. The slightly upward streamlines above the separation point became almost parallel to the bed. The point A moved to a new position. The downflow entrained more fluid from upstream and its velocity increased near the bed, with an increase in its scouring power. On the other hand the strength of the HVS seemed to remain the same, if not decreased slightly.

From this moment on, the scour hole grew larger but maintained the similarity of shape. As the downflow grew stronger, it dug in more, making the lower slope steeper. At certain point, the upper slope lost the support provided by the lower slope and the sand grains slid down into the lower slope, from where they were removed by the flow. The outer edge of the hole or the separation point S moved away from the cylinder as the hole grew in size. This facilitated the entrainment into the downflow as more fluid started to acquire a downward component in the upstream region (Figure 4.7.1(d)). This, in turn, made the downflow even stronger. This cycle continued until an equilibrium was reached, when the shape of the scour hole in the upstream side became essentially invariant with time. It is interesting to note that the HVS did not play an active role in the scouring process, although it transported most of the loosened bed material inside the

scour hole. Underneath the HVS, $\nabla \cdot \vec{\tau}_0$ was not large enough to cause erosion. However, both the HVS and the downflow brought high velocity fluid from the upper layers towards the accelerated flows on either side of the cylinder, which in turn led to high erosion rate. Their contribution to erosion was thus indirect at the initial stage. The area occupied by the HVS increased and its rotational velocity decreased as the scour hole grew larger. In the case of larger scour holes, the rotational velocity became so small that the HVS on the POS looked more like a stall of dead water.

The term "equilibrium condition" has been used in the sense that the scour hole in front of the cylinder, especially the depth of maximum scour, did not increase with time. The condition prevailing inside the hole might be better described as a dynamic equilibrium of opposing forces (destabilizing and stabilizing forces on the sand grains) which were unsteady in nature. Thus a few grains were sometimes observed to be dislodged and moved around by the flow. In the downstream part of the scour hole, the scouring went on even after this equilibrium stage was attained in the present experiments. As a result, the depth of scour continued to increase at the back of the cylinder and the rear bar continued to move downstream and become flatter as long as the experiments were run. What it would lead to is unknown. But one can speculate on the possibility of the scour depth in the rear side becoming larger than that in the front side, thus destabilizing the equilibrium at the upstream portion of the scour hole.

It was observed that the larger fraction of the sand accumulated near the bottom of the scour hole because the impinging downflow lifted the finer fraction up the lower slope. From there, again a finer fraction was washed away by the flow, leaving a certain fine fraction that was light enough for the downflow to dislodge but heavy enough for the flow to carry away. This was in a state of suspension near point A as shown in Figure 4.7.1(d). After Expt. D2M was stopped, samples of sand accumulated near the bottom and near point A were collected. These are shown in Figure 4.7.2(d) on the left and right sides respectively. The segregation of sand is clear.

4.8 Flow, Scouring and Roughness

4.8.1 Effect of scour hole on flow

It is easy to imagine, even without the benefit of any quantitative measurements such as that presented in this chapter, that a scour hole would accommodate a certain amount of the approach flow. This part of the approach flow would go into the scour hole, would then move through the scour hole in the downstream direction, and would finally emerge into the wake. It would also carry a certain amount of momentum with it.

One would also expect that the accelerated flow around the cylinder would be somewhat relieved and that the skewing of the flow away from the POS would be somewhat less in the presence of a scour hole. In broad terms, the present experiments put this qualitative speculation on a firm, quantitative basis. Some details will now be discussed.

The analyses of the velocity distribution (Section 4.2) showed that the yaw angle θ of the velocity vectors in the upstream region was smaller in the presence of the scour hole. At the side of the cylinder, the velocity magnitude V was smaller. In the downstream region, the rear bar prevented the flow from converging towards the POS. All these effects were in general more pronounced near the bed, near the POS and closer to the cylinder. The fluid moved with high velocity in the scour hole. The highly agitating nature of this flow was clearly evident in large values of σ_V and σ_θ.

On and close to the POS, the flow retarded only to a lesser extent during the mobile bed experiments since it was allowed to enter the scour hole with considerable velocity. V was larger and ϕ was smaller, indicating larger downward velocities. The values of σ_V and σ_ϕ were smaller, suggesting the stabilizing influence of the scour hole on the flow. The wake component in the log-law plot on the POS was less visible in mobile bed experiments. The defect law also worked better. The band on which the data fell in the Clauser's scheme was different. Mass and momentum flux ratios on the POS decreased more slowly in mobile bed runs, even showing a slight increase in case of very large holes. This is because the flow was retarded less and actually accelerated near the bottom into the hole, which also made due impression on the variation of other BL parameters along the POS. Due to lack of data, the influence of the scour hole on the downflow near the bed could not be studied. However, it was found that the downflow reached a peak value of $\tilde{v}_{max} / U_0 \approx 0.38$ at $y / y_0 \approx 0.35$ for rigid bed runs but continued to increase more into the scour hole in mobile bed runs (as much as $\tilde{v}_{max} / U_0 \approx 0.95$).

The effect of scouring was prominent in the downstream region since the jet-like accelerated flows from either side of the cylinder converged on the POS. Both horizontal and vertical velocities were higher. The strength and extend of the reverse flow were diminished. The upward flow became horizontal very quickly. There was large decrease in σ_V and σ_ϕ as the flow became more "aerodynamic."

No distinction was found in pressure distribution in the upstream region (Section 4.3). In the downstream region, the pressure fall was largely mitigated by the presence of the scour holes. Another interesting feature was the pressure rise at $y / y_0 \approx 0.3$ to 0.5, which was traced to the slowing down of the accelerated flow at this level in mobile bed runs.

The scour hole allowed the shear stress vectors ($\bar{\tau}_0$) to deflect less (Section 4.4) in the upstream region but the magnitude increased slightly as water rushed into the hole. In case of very large scour holes, the direction of $\bar{\tau}_0$ was actually towards the POS, as water converged towards the hole. On the POS, the shear did not diminish when the scour hole was present. In some cases with smaller scour hole, the trend was rather increasing. At the side of the cylinder, both the magnitude and yaw angle of $\bar{\tau}_0$ were smaller. The fluctuation of angle (σ_θ) was somewhat larger, showing the effect of scour hole in relaxing the rigidity of flow conditions. The shear also became larger in the wake region.

As discussed in Section 4.5, the polar plots gave valuable insight into the flow. Smaller cross-flows in the case of mobile bed runs were observed. This effect took place only below a certain level, which was higher at stations closer to the scour hole. Larger holes amplified all these effects. In the downstream region, the rear bar prevented the flow from converging towards the POS, thus the negative cross-flow was substantially smaller in mobile bed runs. No systematic effect of the scour hole was found in the performance of various cross-flow models.

4.8.2 Effect of roughness on flow

The roughness increases the non-uniformity of the velocity profile but decreases the slope of the velocity near the bed. Thus the stagnant pressure gradient on the cylinder increases along with the downflow. The unsteadiness of the flow increases. Another important effect of roughness is the increase in resistance to skewing, especially near the bed. All these were manifest in different ways in the flow as discussed below.

The effect of roughness did not significantly affect the flow in plan, the deflected flow and the flow in the wake region (Section 4.2). On the POS, the effect of roughness was evident in larger values of ϕ and downflow component $\tilde{v}$. The increase in σ_ϕ near the bed was over a larger distance from the wall. The wake component was most pronounced in rough bed experiments. The defect law worked better for smooth bed runs. No difference in the performance of Clauser's scheme was found. The roughness increased the mass and momentum flux ratios in the present experiments. However, it was pointed out that roughness can work the other way too. The vertical variation of $\tilde{v}_{max} / U_0$ was milder for smooth beds.

As discussed in Section 4.3, no effect of roughness was found in the pressure distribution in the upstream region except at the cylinder face, where the vertical pressure gradient became steeper for rough bed runs. No systematic difference could be discerned in the downstream region.

The roughness increased the shear amplification (τ_0 / τ_{00}) everywhere and extended the area of influence of the cylinder (Section 4.4). At the side of the cylinder, $\bar{\tau}_0$ turned less for rough rigid bed runs, indicating the resisting effect of roughness to the skewing.

From the polar plots of Section 4.5, it can be seen that the cross-flow was smaller in smooth bed runs, due to the relatively larger velocities near the bed and the resisting tendency of the roughness to skewing forces. The velocity vector turned the most at the free surface for rough bed runs, but the maximum turning was below the free surface at stations closer to the cylinder in smooth bed runs. This caused a negative cross-flow in the polar plots for smooth bed runs. No systematic effect of the roughness was found in the performance of various cross-flow models except Perry and Joubert's model. This model performed better in the rough bed experiments of Series D than the smooth bed Expt. F2S. But, since it performed equally well for Series C and E, it cannot be solely attributed to roughness.

4.8.3 Effect of flow on scouring

The flow and the scouring process influenced each other throughout the run time of all mobile bed experiments. However, it can be said that at the initial stage, the flow could impart more influence on the scouring process and bed topography than was influenced by them. At this time the flow could make the topography more "aerodynamic". And in the later stage when the topography varied only a little, the opposite happened, *i.e.*, the topography controlled the flow pattern.

As discussed in Section 4.6, in front of the cylinder, the flow determined the extend of scour depth, and the overall shape of the hole was scaled accordingly. Two notable exceptions were the width of the groove which varied from sand to sand and the sand grains in suspension which was different for different experiments.

The scenario was clearly different in the downstream region, as various scales exhibited different trends. A single length scale, such as the scour depth or any linear dimension of the rear bar, was not sufficient to describe all of them. Some of the experiments such as D2M and D3M showed altogether different behavior. This suggests the more complex interaction of the flow and scouring in the wake.

The effect of the flow in these two regions seems to be uncoupled to some extent. This is due to the more complex nature of the wake flow with various eddy scales and its cellular structure, which are interfered by the changing bed topography in an unknown way.

4.9 General Discussion

The past research on bridge scour appears to fall into three broad categories. The first category includes all the traditional approaches described in Section 2.2. The main characteristics of them was to estimate of scour depth, without much regard for either the flow or the erosion process. This tradition continues to the present day. Research of the second category concentrated on the influence of isolated parameters on the scour depth. As reviewed in Section 2.3, attention was given mainly to the erosion process. The third, and most recent, category studied the flow field experimentally. The works of Melville (1975) and Dargahi (1987) fall in this category. The present study is a contribution in this direction.

In the present study, a number of systematic experiments have been performed and analyzed to explore the flow structure around a circular cylinder and its relation with the process of local scour. Results from smooth, rigid and mobile bed experiments have revealed how the roughness and then the scour hole affect the flow pattern.

The experimental approach used in this study was considerably different from the earlier ones, not only in the analysis of the flow but in that of the erosion process too. The measurement of the whole scour profile (as opposed to just the maximum scour depth) and the similarity analysis was rather unique. The identification of different modes of sand movement made the study of erosion process more systematic. The study of the length scales gave further insight into it.

Analysis of the velocity, pressure and bed shear revealed different characteristics of the flow and the effect of roughness and scour hole on it. The data allowed a detailed analysis of the flow on the POS in the upstream region. The analysis of the flow in the light of three-dimensional boundary layer theories was very elaborate.

The study had many limitations too, mainly because of the constraints put by the experimental facilities. The horseshoe vortex, turbulence characteristics of the flow, vortex shedding, *etc.* could not be studied. The measurements in the wake region was rather limited. So was the pressure measurement, since no measurement was taken on the bed and on the cylinder surface.

In spite of all these limitations, it is hoped that these experiments will to some extent fill the gap in understanding the flow and scour around bridge piers. Moreover, the broad literature review will place the scour problem in a better perspective.

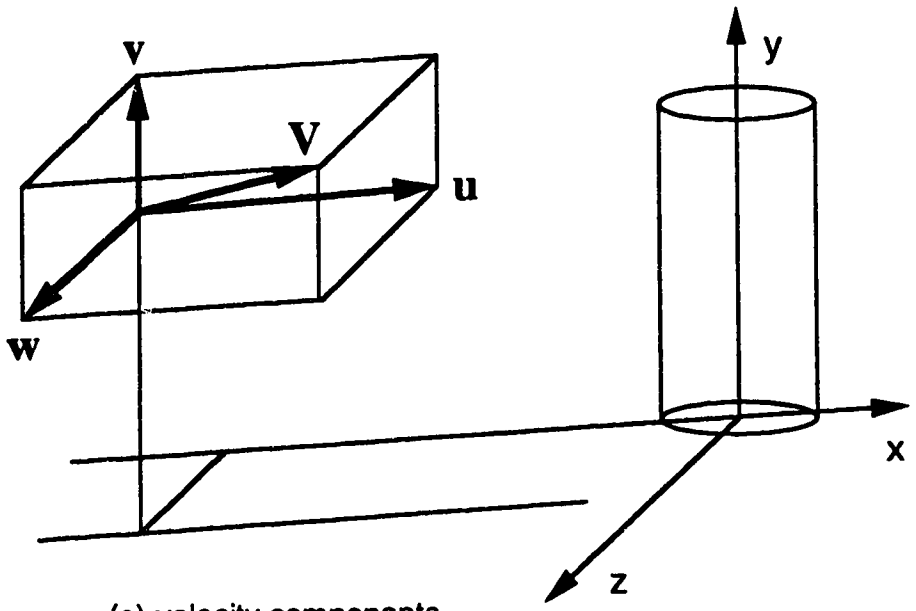

(a) velocity components

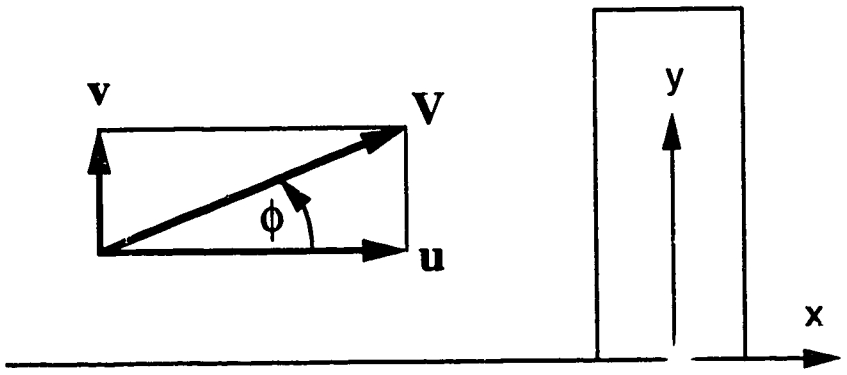

(b) angle of pitch

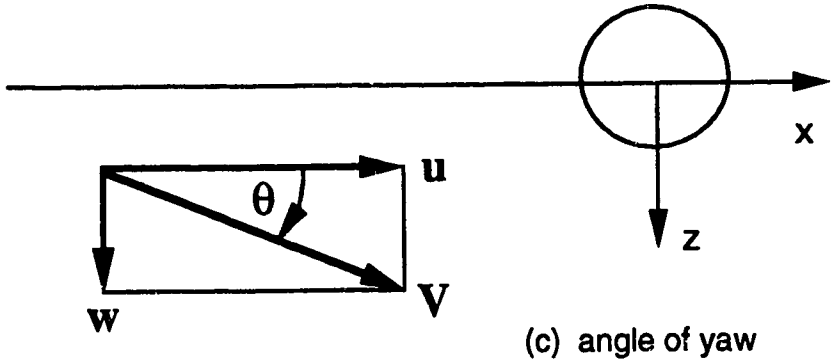

(c) angle of yaw

Figure 4.1.1 Velocity components, yaw and pitch angles

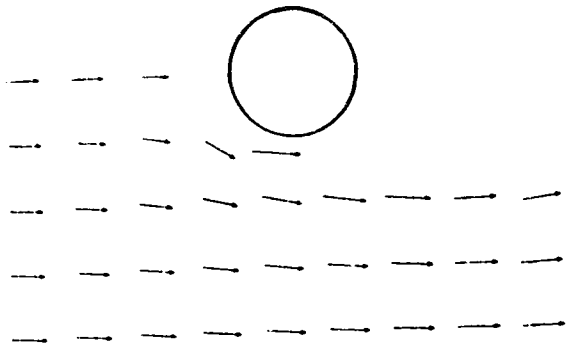

$y / y_0 = 0.8$

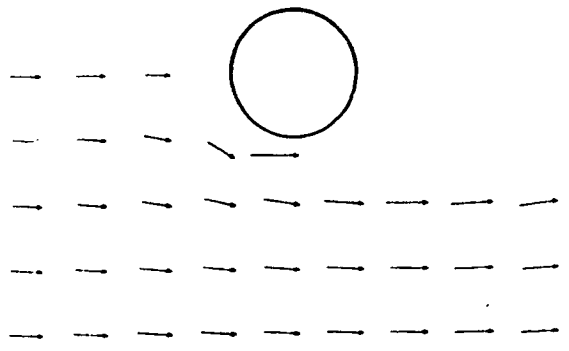

$y / y_0 = 0.5$

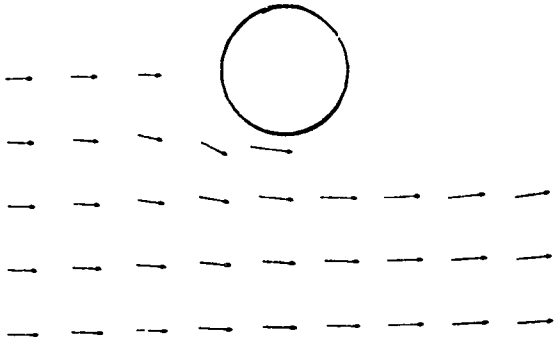

$y / y_0 = 0.2$

Velocity (m/s)

0.6
0.5
0.4
0.3
0.2
0.1

Figure 4.2.1 Overall flow pattern in plan (Expt. F2S)

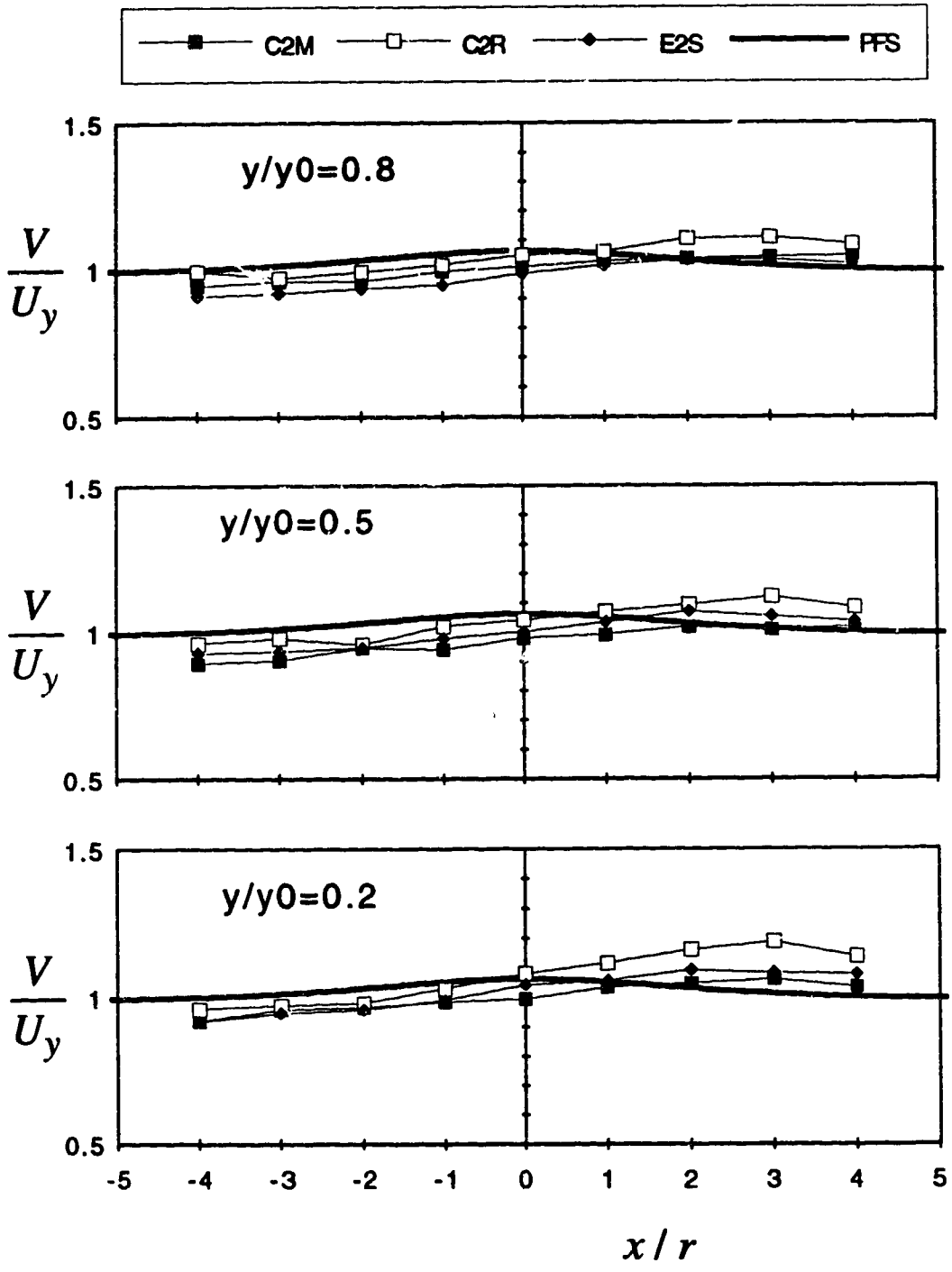

Figure 4.2.2 (a-c) Longitudinal variation of the velocity magnitude of the deflected flow (Expt. C2M, C2R and E2S); (a) z/r=4 plane

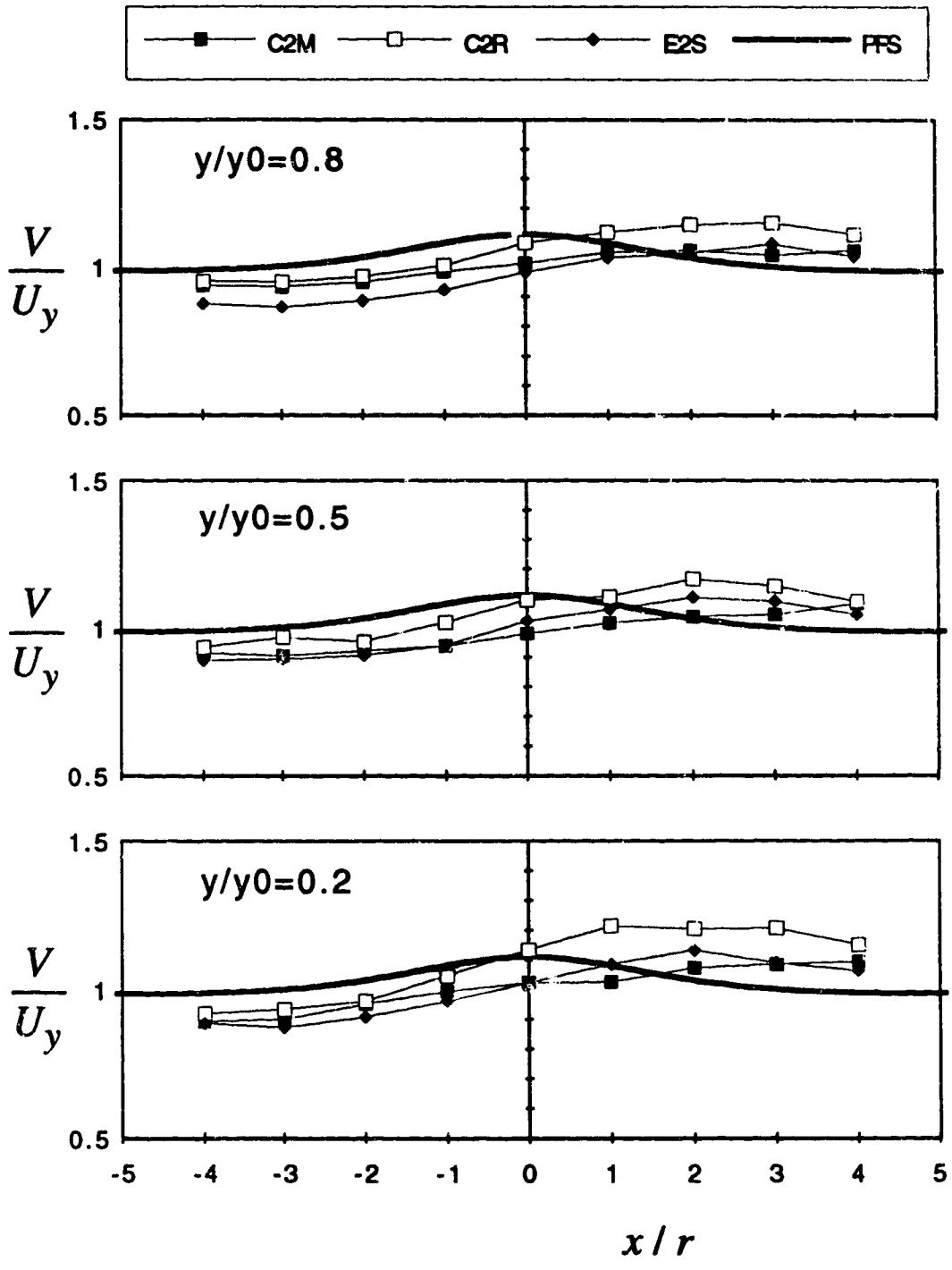

Figure 4.2.2 (a-c) Longitudinal variation of the velocity magnitude of the deflected flow (Expt. C2M, C2R and E2S); (b) z/r=3 plane

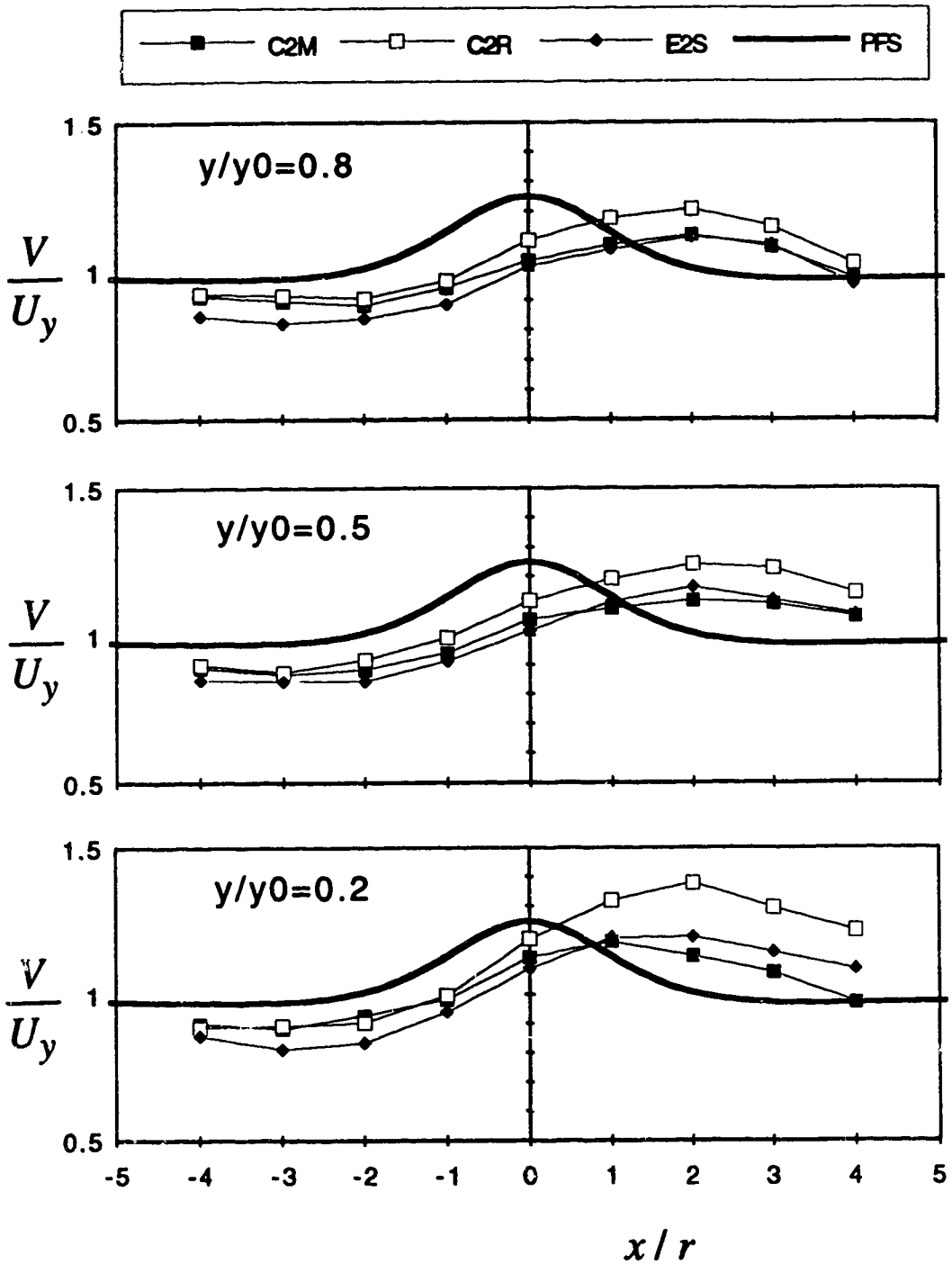

Figure 4.2.2 (a-c) Longitudinal variation of the velocity magnitude of the deflected flow (Expt. C2M, C2R and E2S); (c) z/r=2 plane

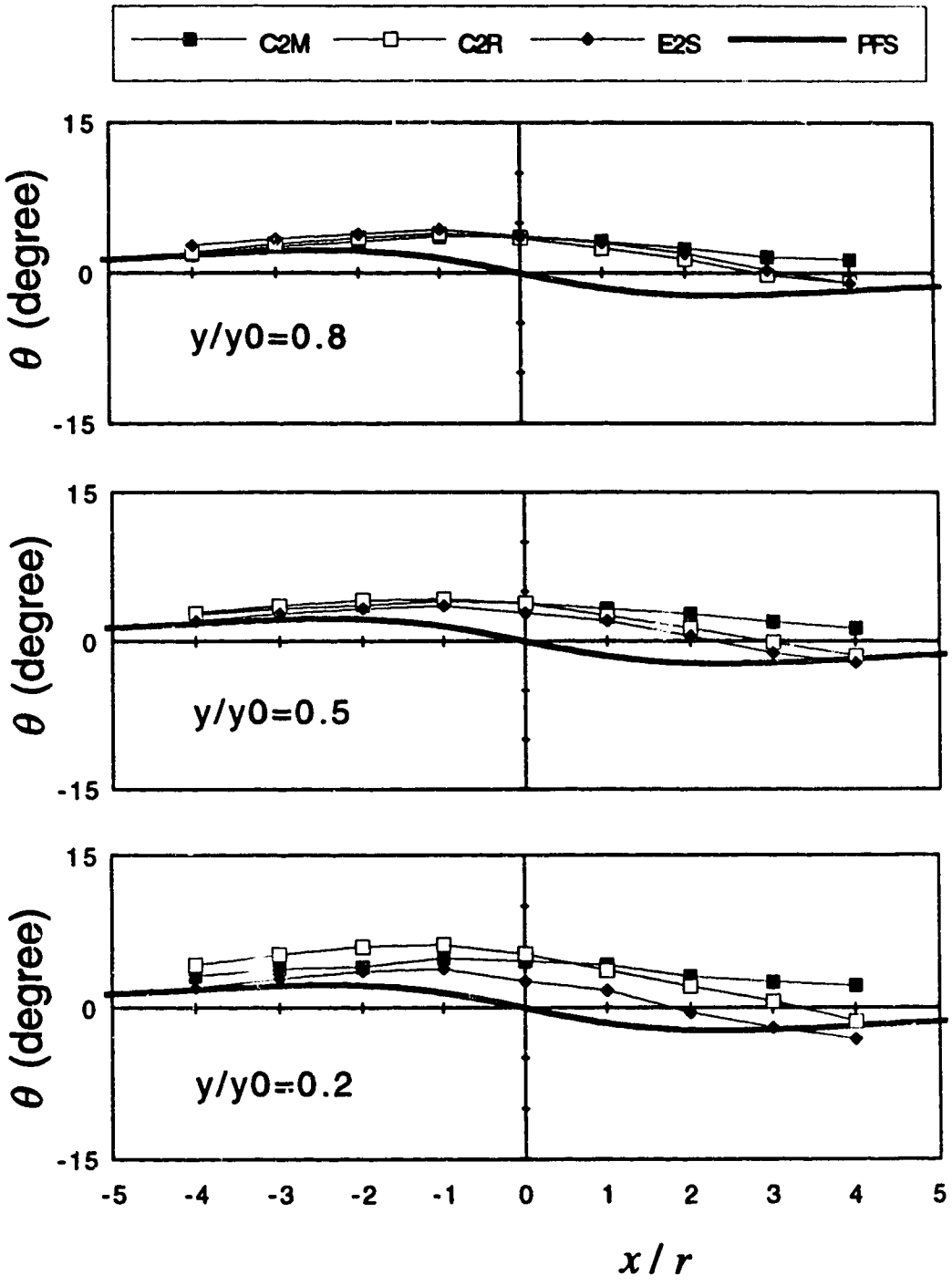

Figure 4.2.3 (a-c) Longitudinal variation of the angle of yaw of the deflected flow (Expt. C2M, C2R and E2S); (a) z/r=4 plane

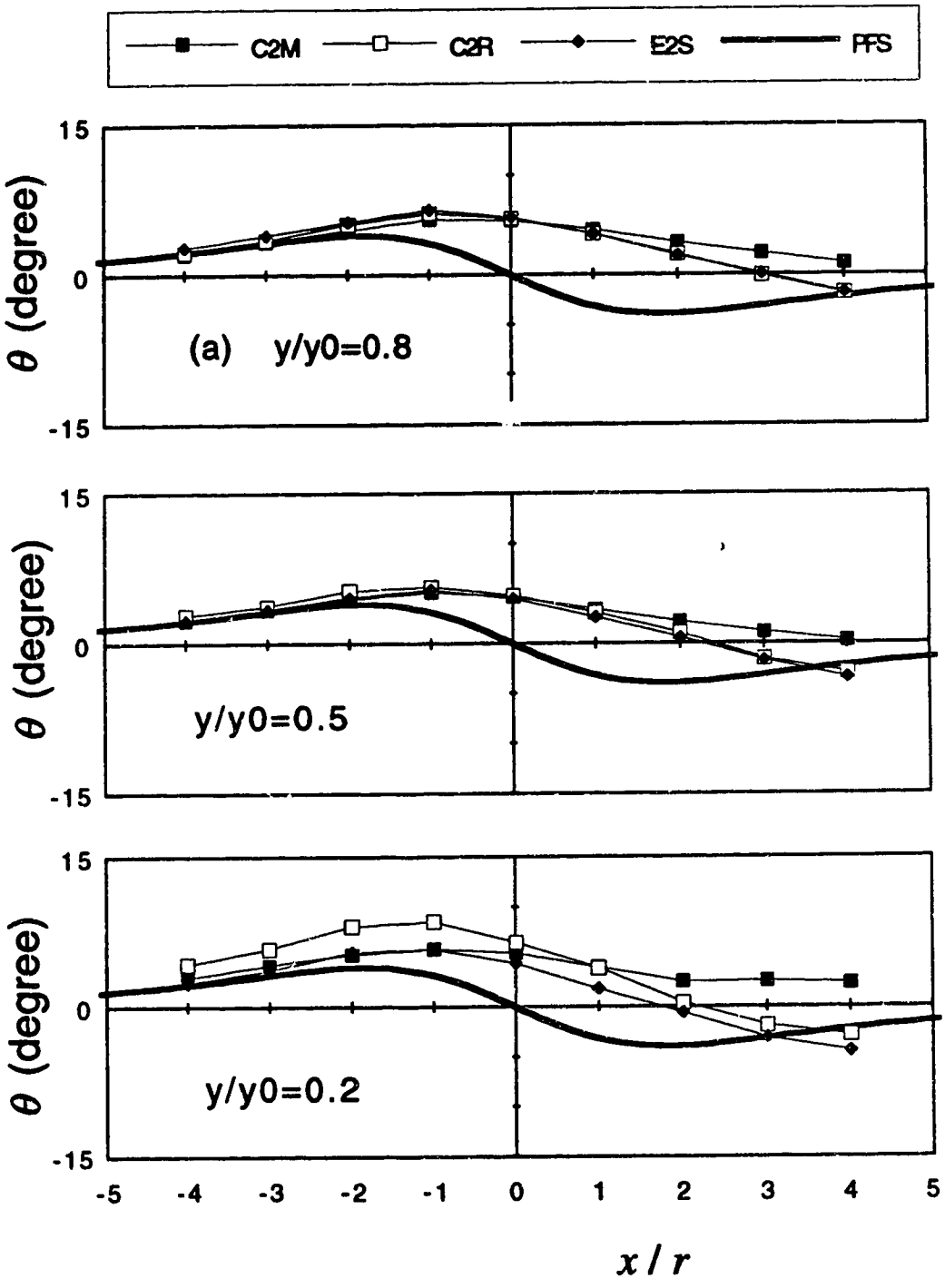

Figure 4.2.3 (a-c) Longitudinal variation of the angle of yaw of the deflected flow (Expt. C2M, C2R and E2S); (b) z/r=3 plane

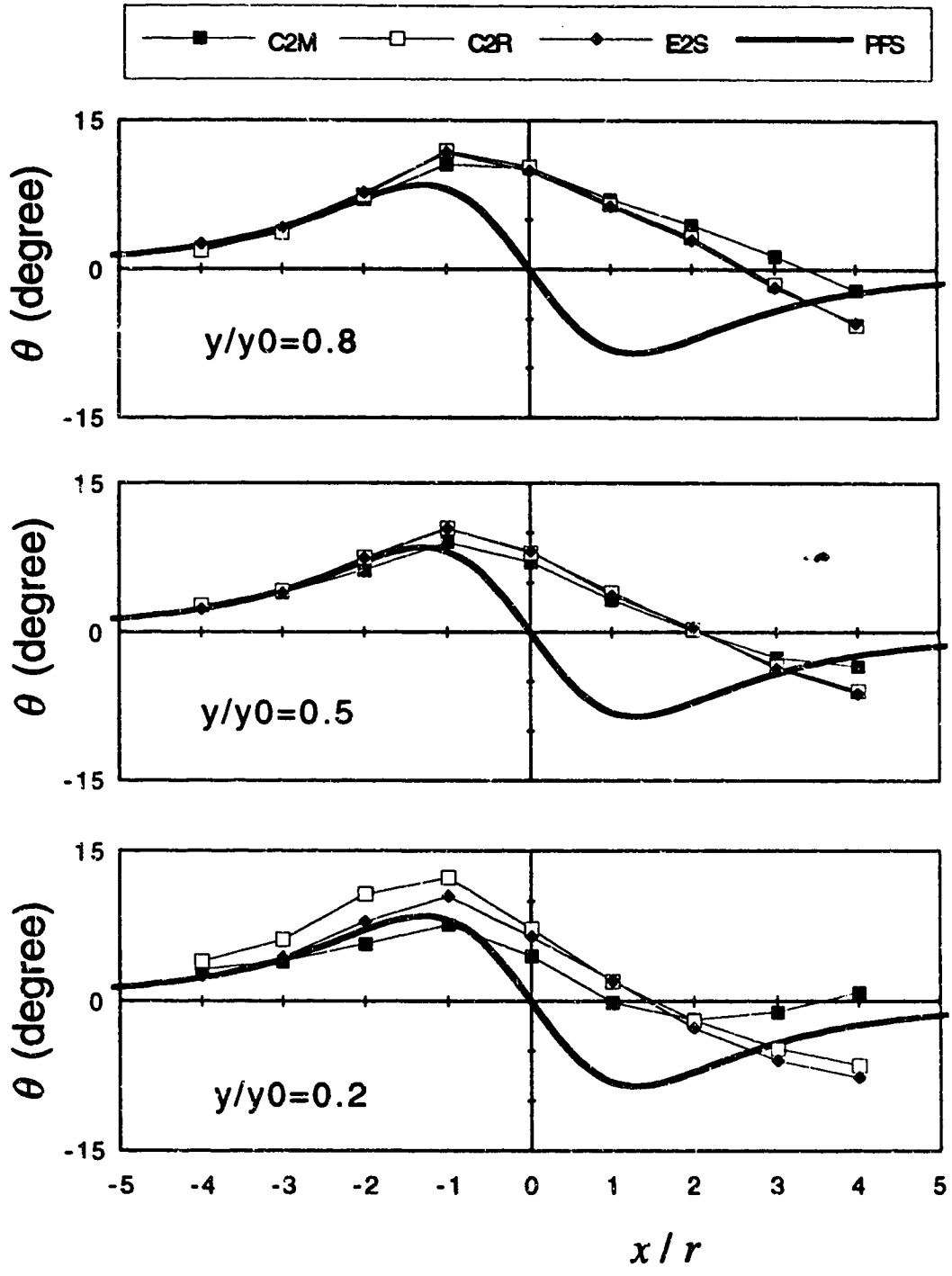

Figure 4.2.3 (a-c) Longitudinal variation of the angle of yaw of the deflected flow (Expt. C2M, C2R and E2S); (c) z/r=2 plane

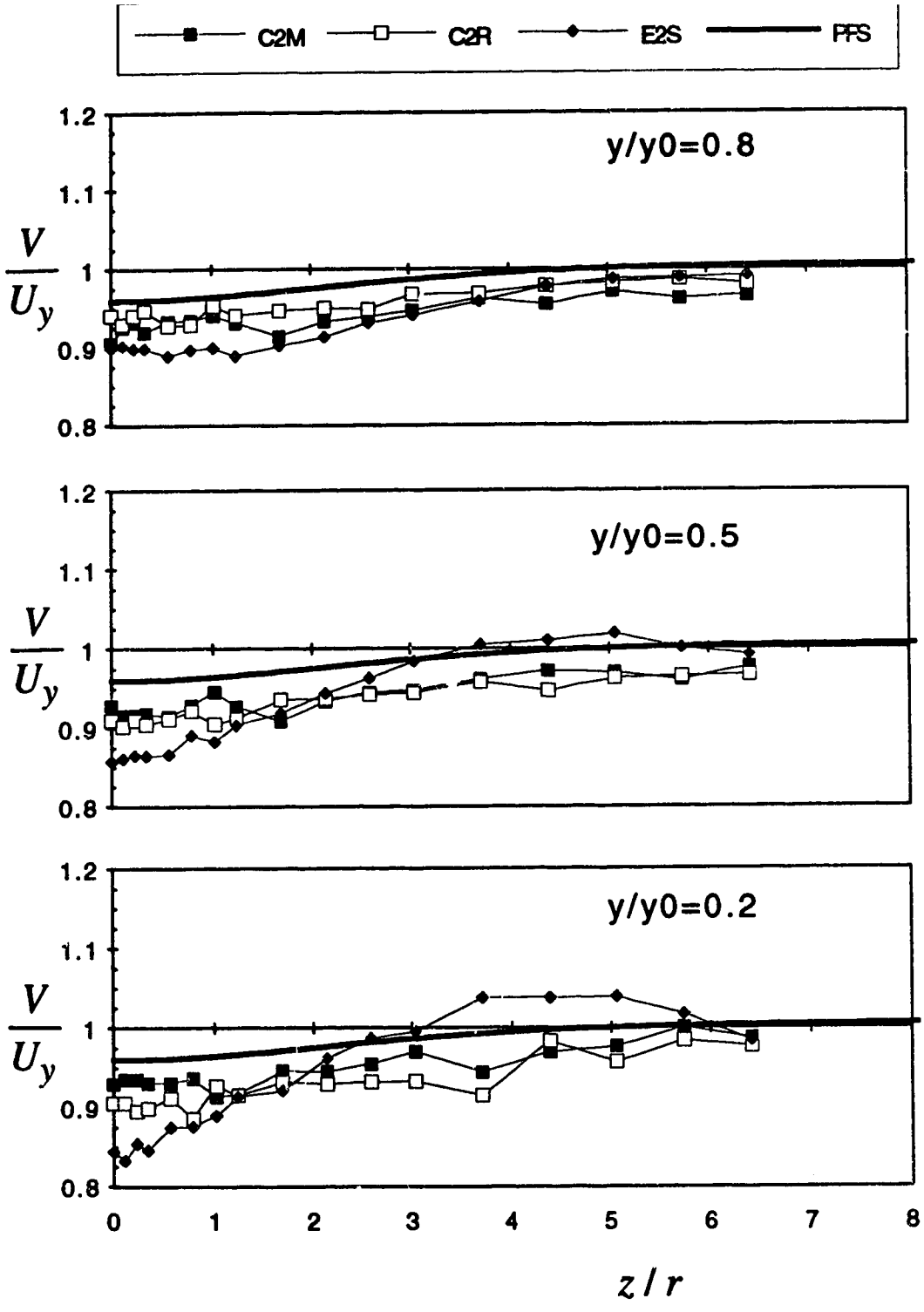

Figure 4.2.4 (a-b) Transverse variation of the velocity magnitude of the deflected flow
(a) Expt. C2M, C2R and E2S; x/r=-5 plane

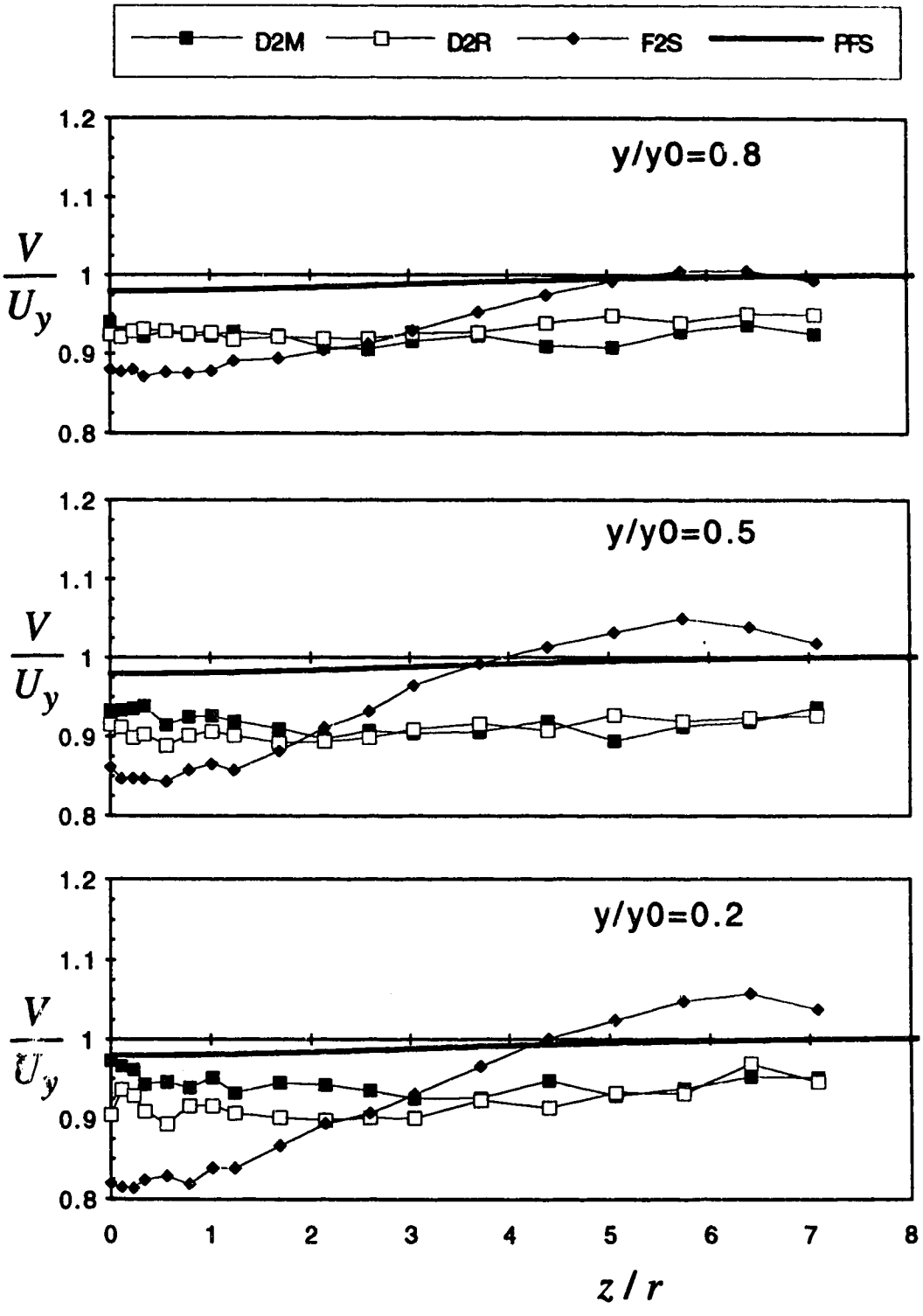

Figure 4.2.4 (a-b) Transverse variation of the velocity magnitude of the deflected flow
(b) Expt. D2M, D2R and F2S; x/r=-7 plane

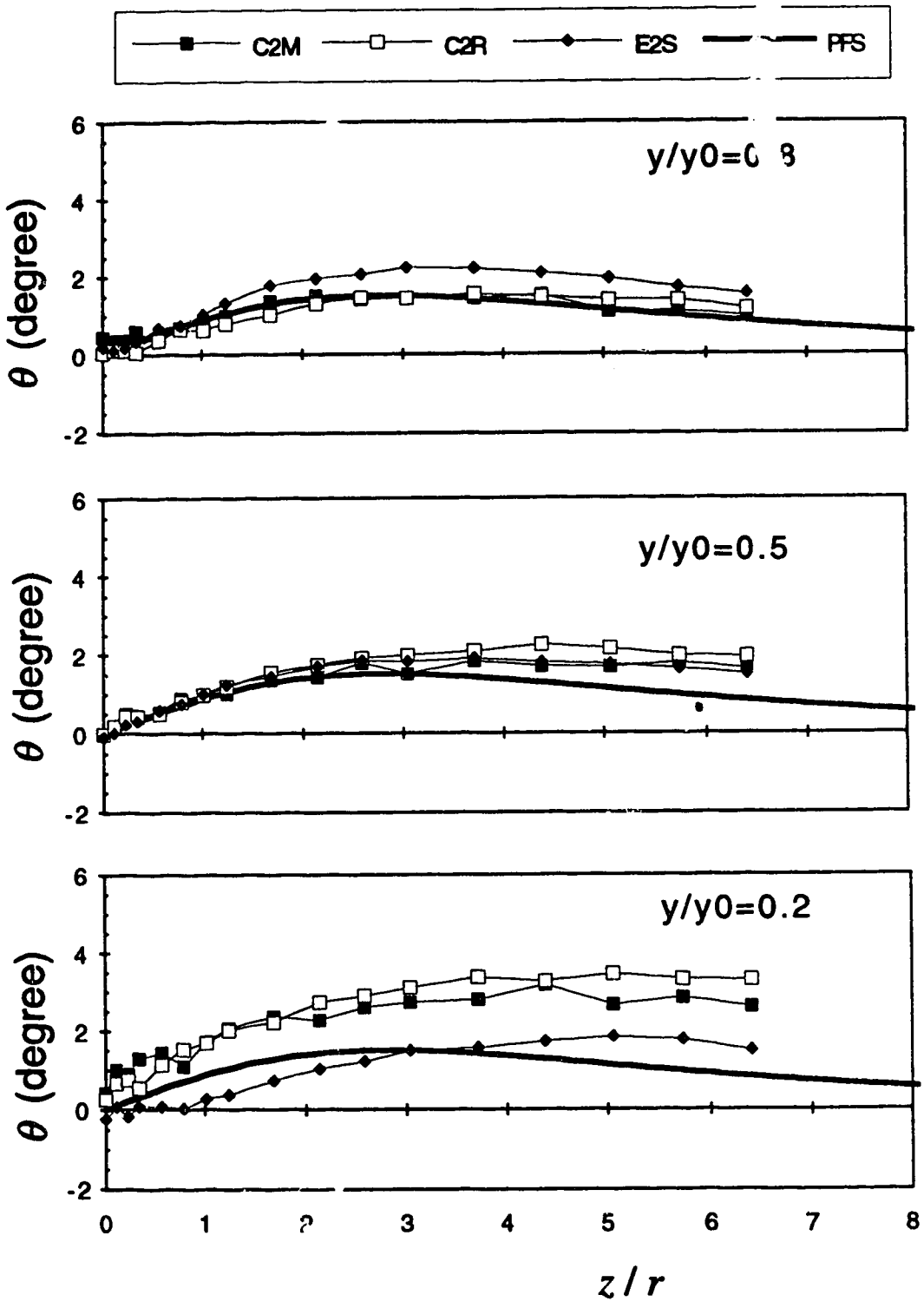

Figure 4.2.5 (a-b) Transverse variation of the angle of yaw of the deflected flow
(a) Expt. C2M, C2R and E2S; x/r=-5 plane

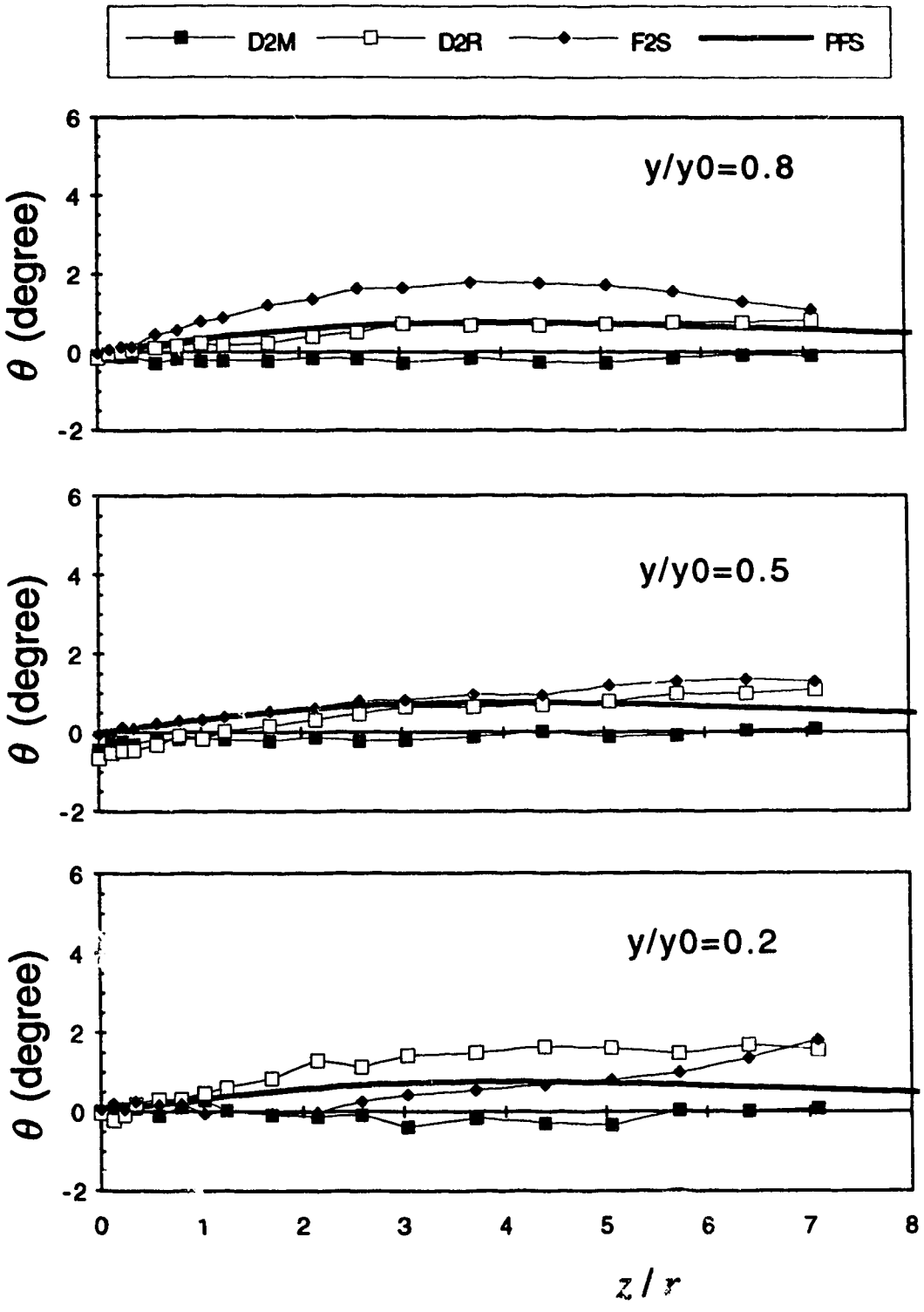

Figure 4.2.5 (a-b) Transverse variation of the angle of yaw of the deflected flow
(b) Expt. D2M, D2R and F2S; x/r=-7 plane

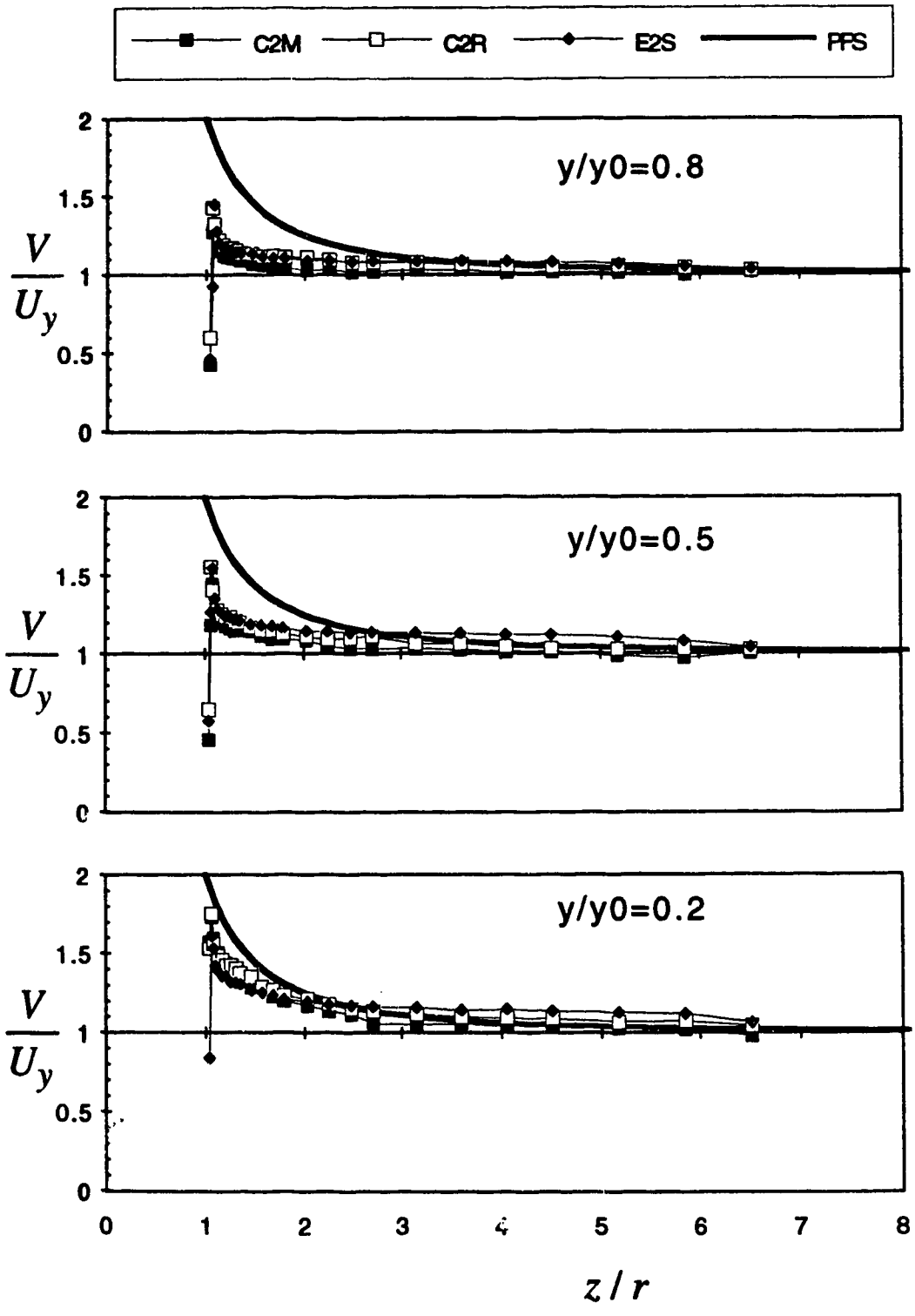

Figure 4.2.6 (a-b) Transverse variation of the velocity magnitude of the deflected flow
(a) Expt. C2M, C2R and E2S; x/r=0 plane

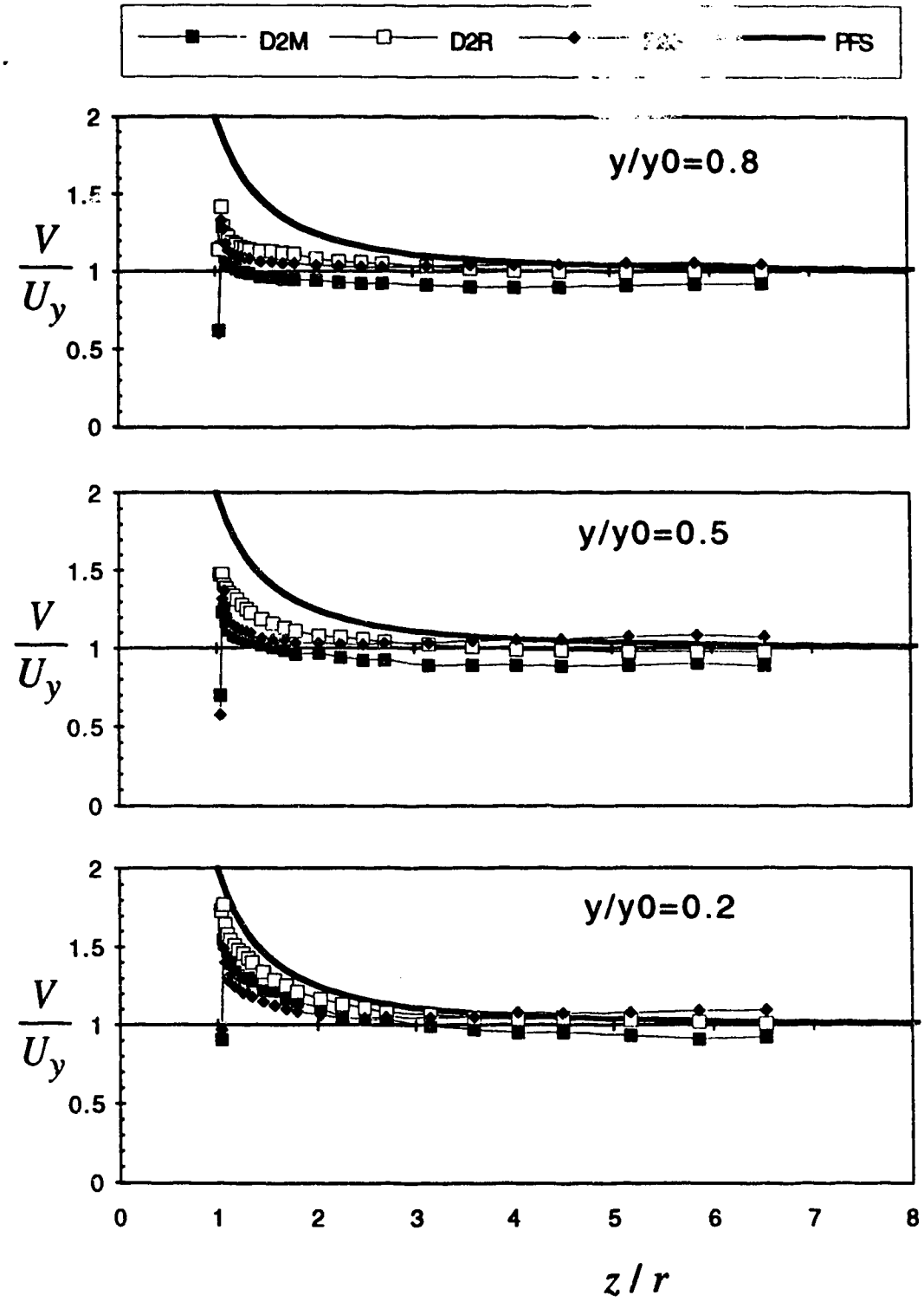

Figure 4.2.6 (a-b) Transverse variation of the velocity magnitude of the deflected flow
(b) Expt. D2M, D2R and F2S; x/r=0 plane

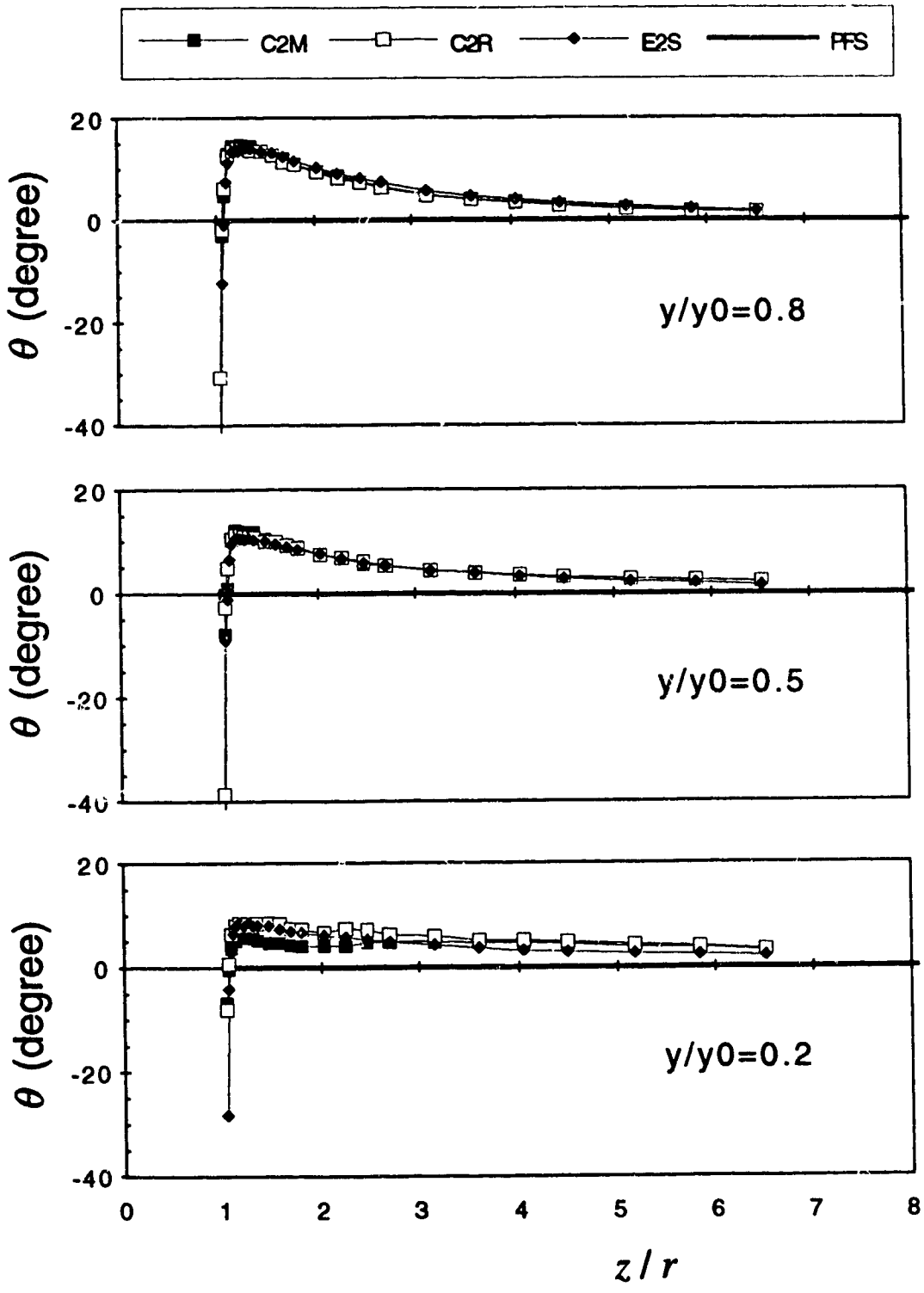

Figure 4.2.7 (a-b) Transverse variation of the angle of yaw of the deflected flow
(a) Expt. C2M, C2R and E2S; x/r=0 plane

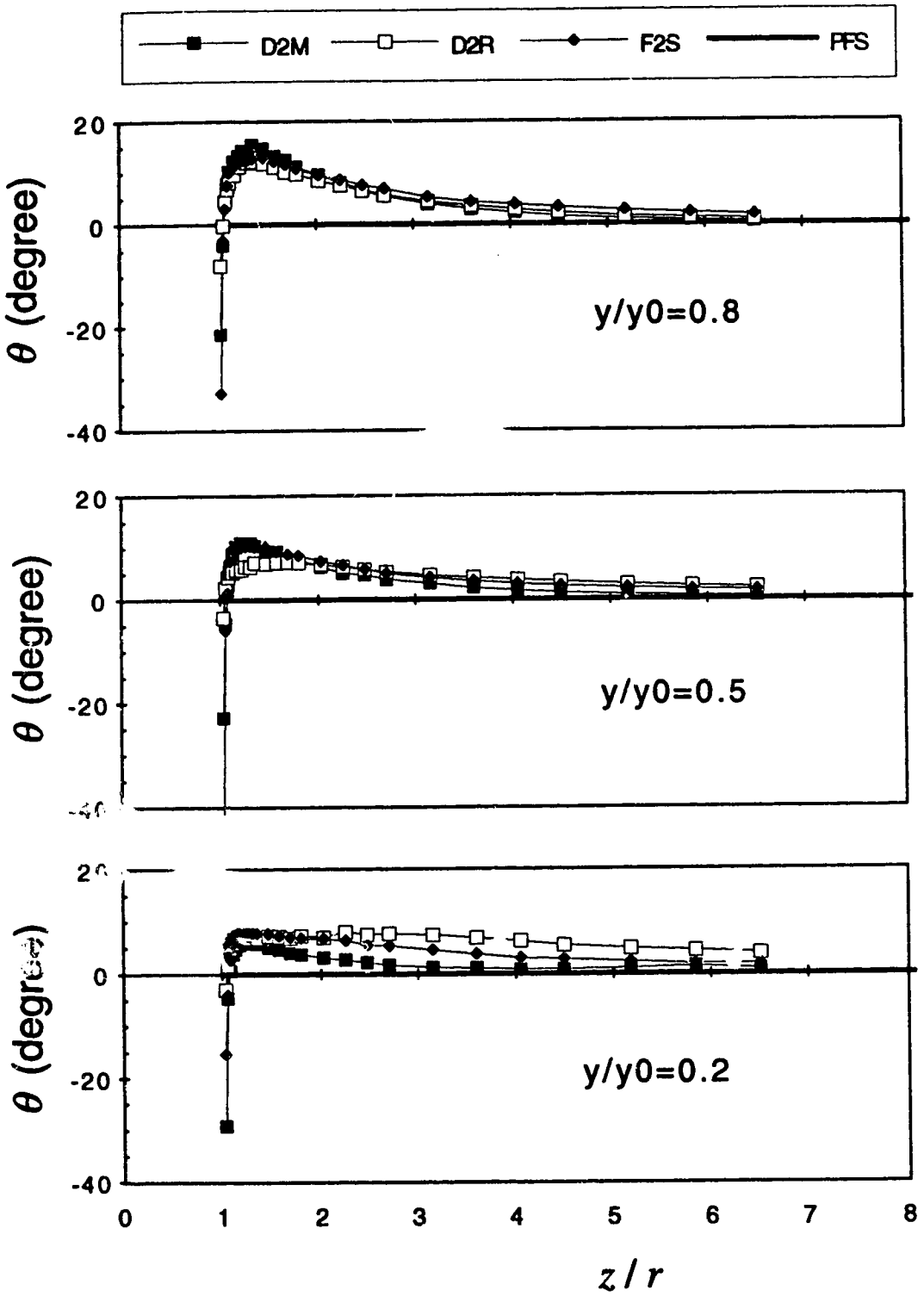

Figure 4.2.7 (a-b) Transverse variation of the angle of yaw of the deflected flow
(b) Expt. D2M, D2R and F2S; x/r=0 plane

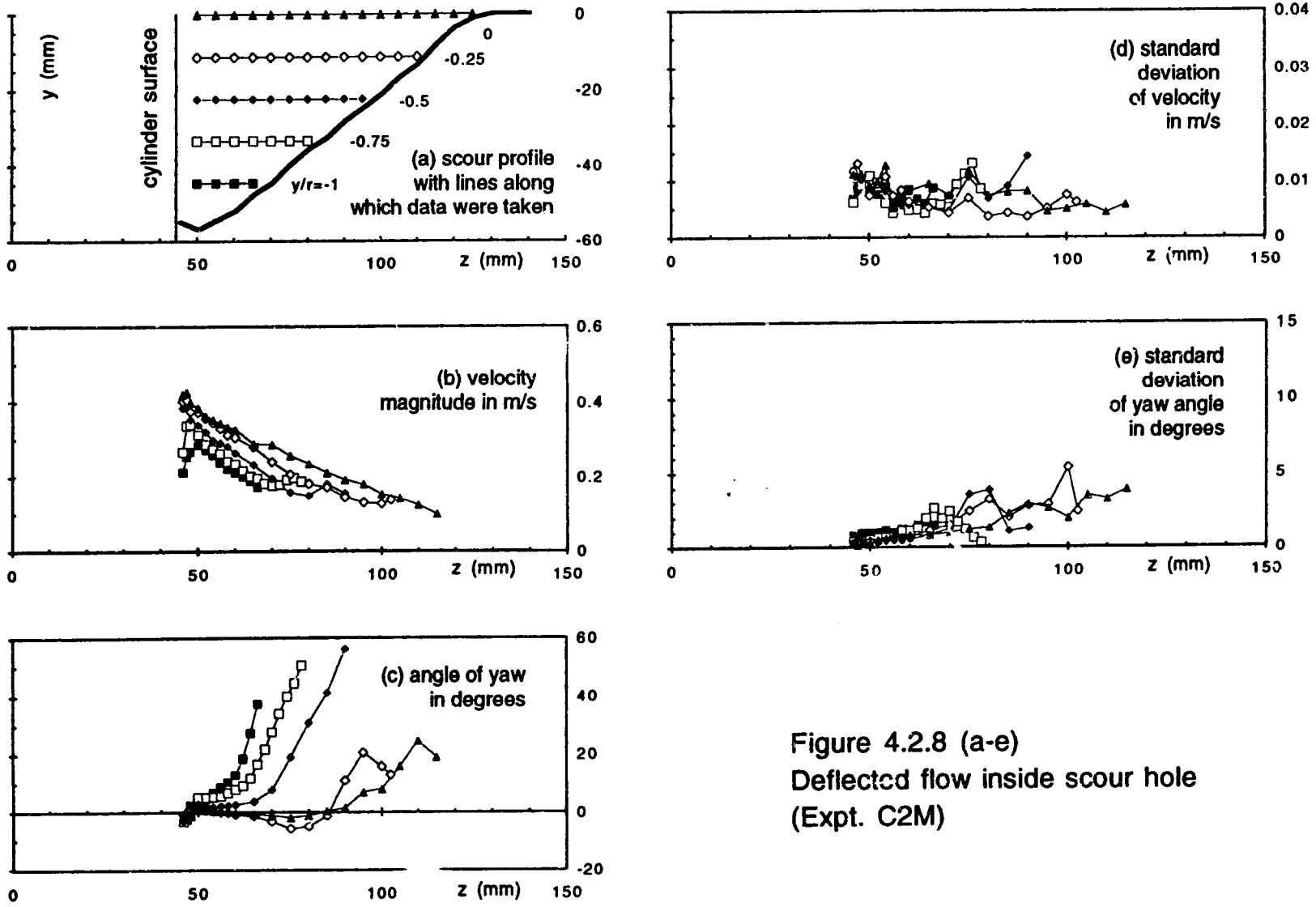

Figure 4.2.8 (a-e)
Deflected flow inside scour hole
(Expt. C2M)

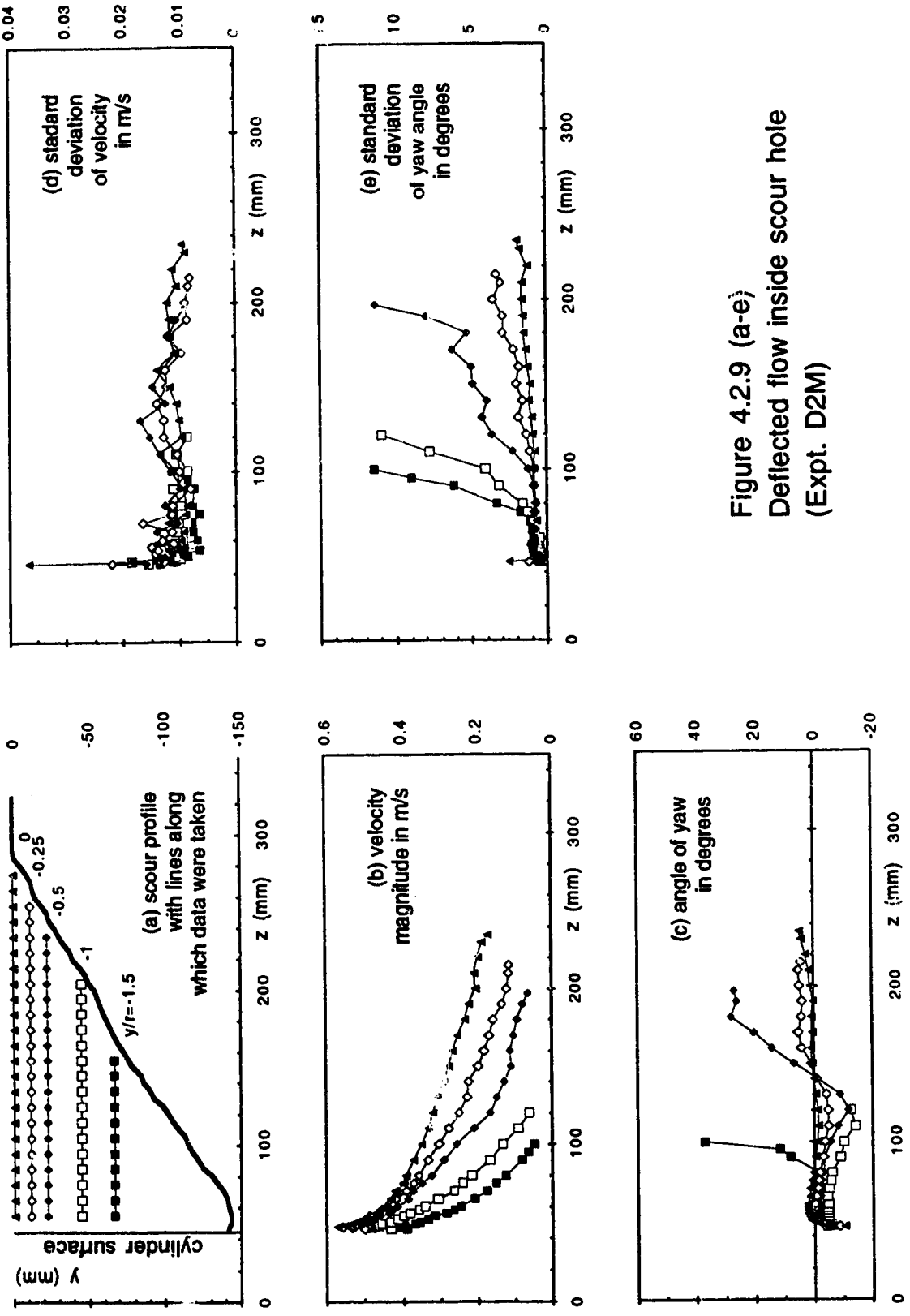

Figure 4.2.9 (a-e)
Deflected flow inside scour hole
(Expt. D2M)

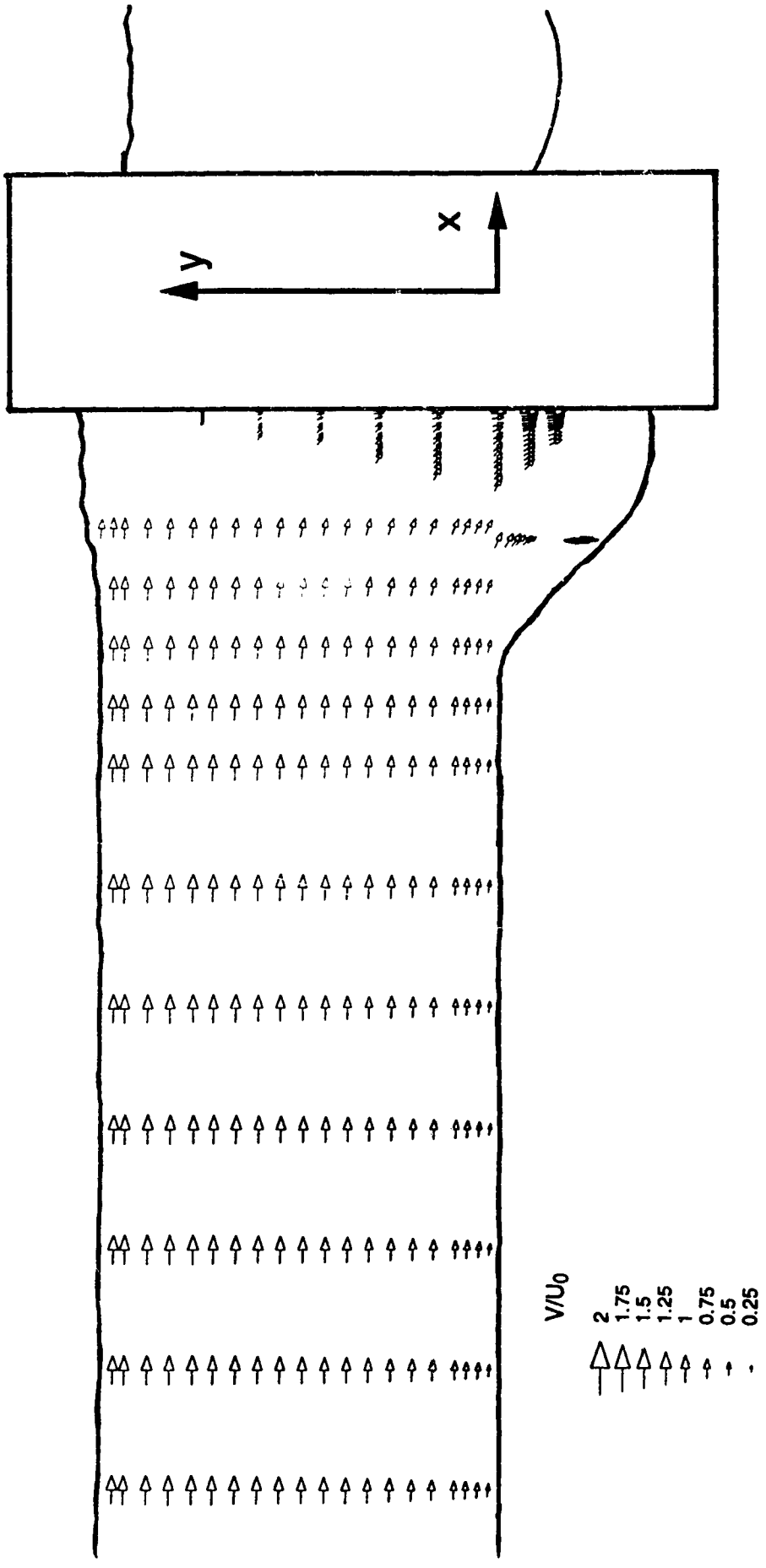

4.2.10 (a-b) Typical vector plot of the velocity distribution on the POS (Expt. C1M); (a) upstream region

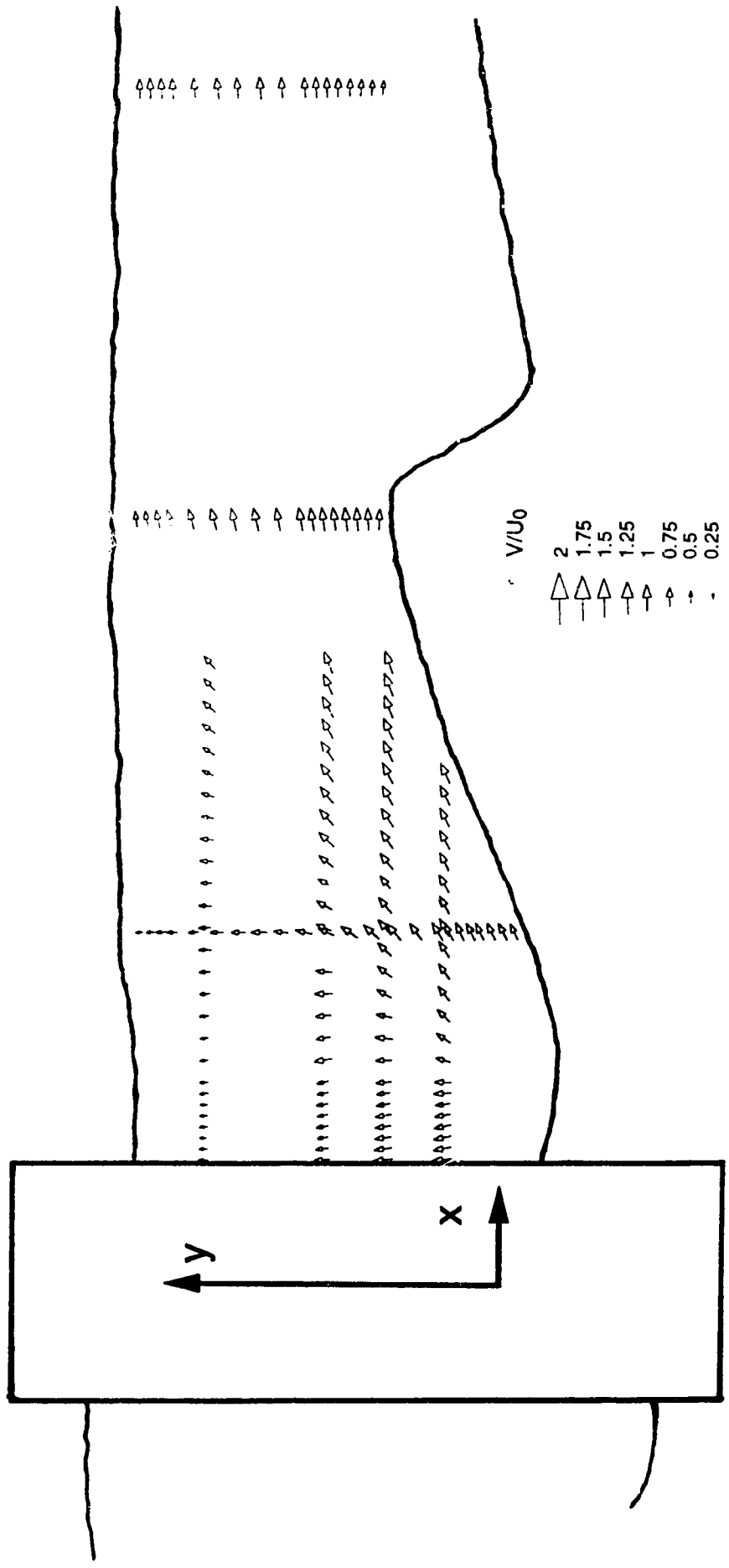

4.2.10 (a-b) Typical vector plot of the velocity distribution on the POS (Expt. C1M); (b) downstream region

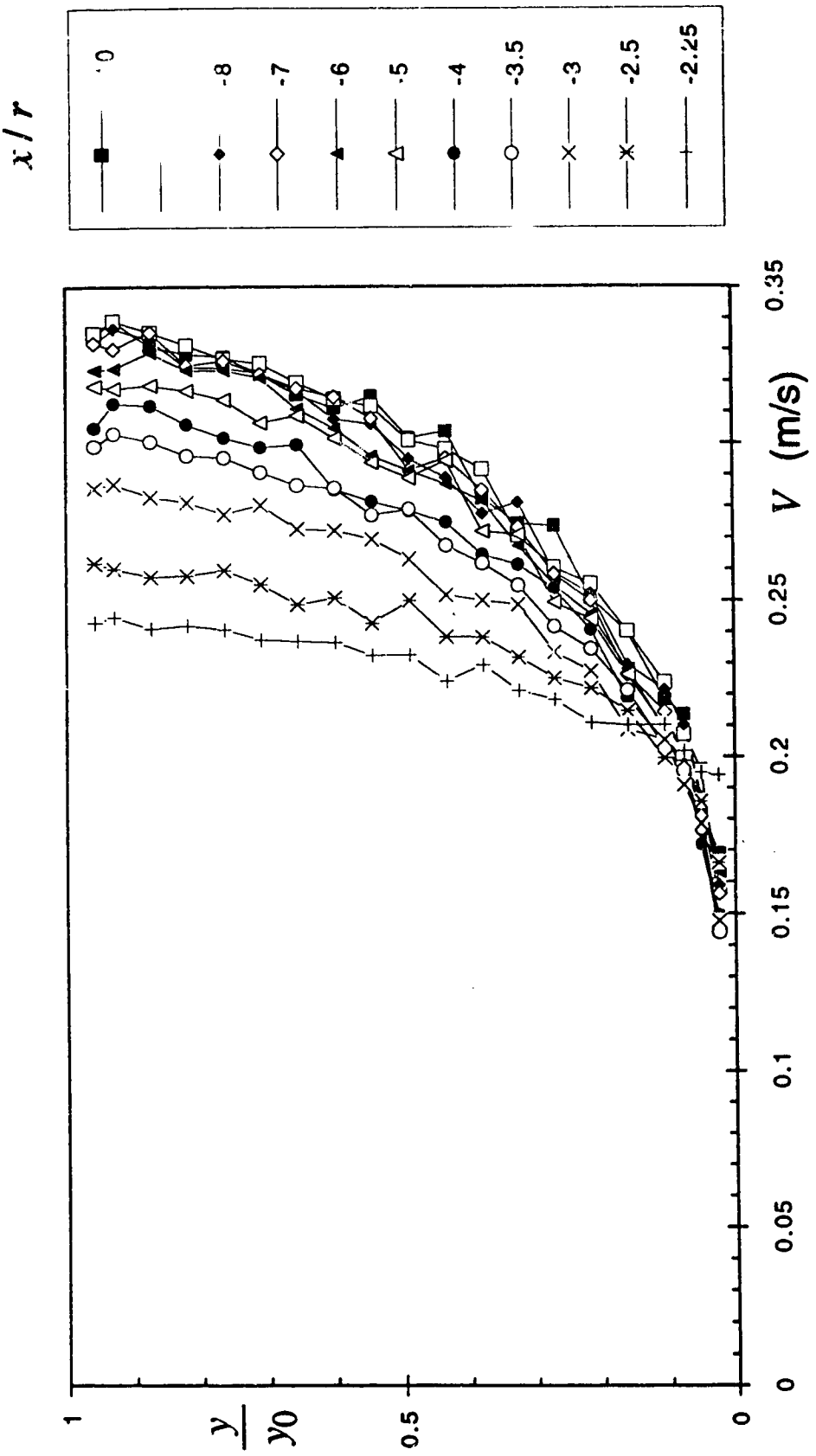

Figure 4.2.11 (a-i) Velocity Distribution on the POS (Expt. C2M)
(a) Velocity magnitude

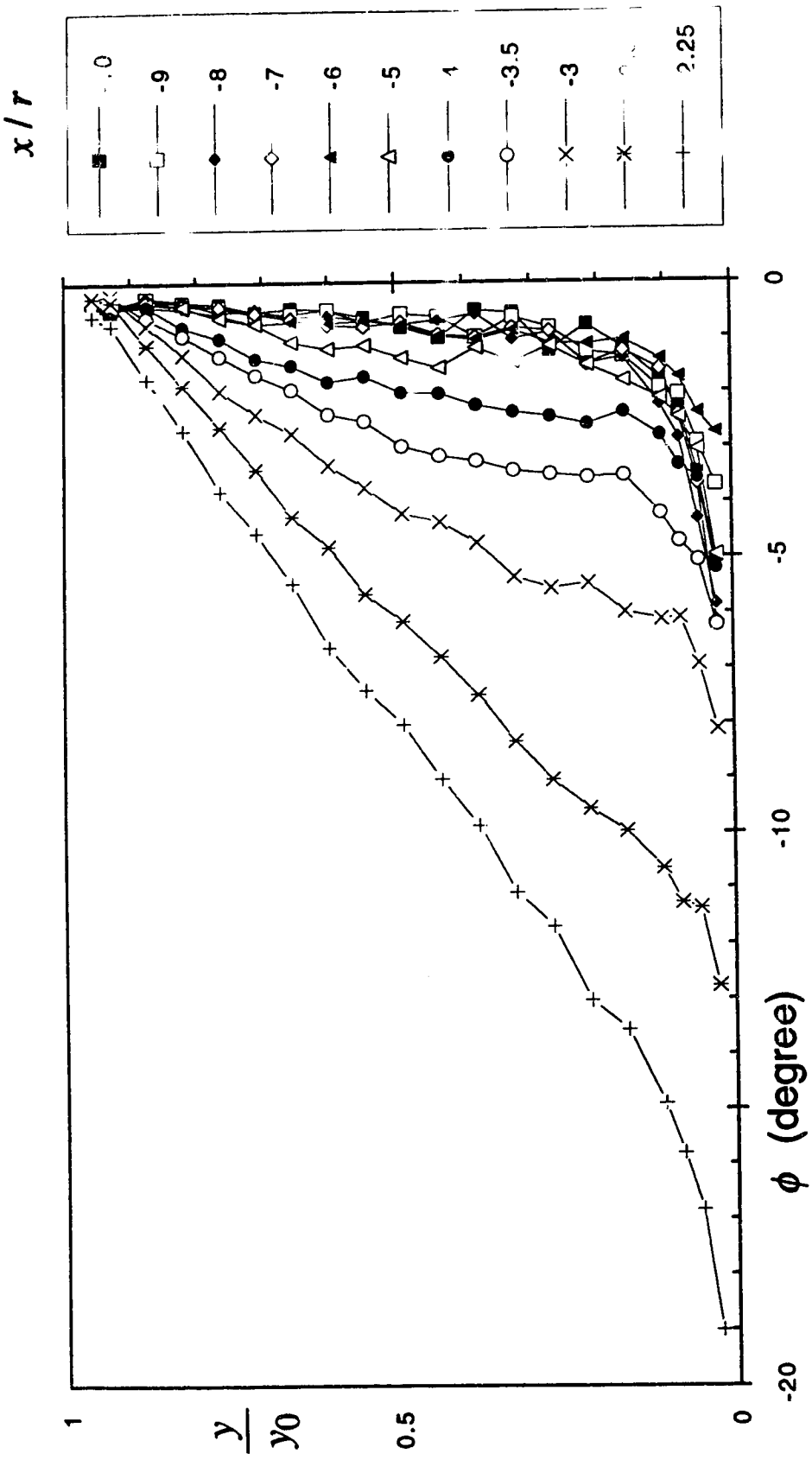

Figure 4.2.11 (a-i) Velocity Distribution on the POS (Expt. C2M)
(b) Angle of pitch

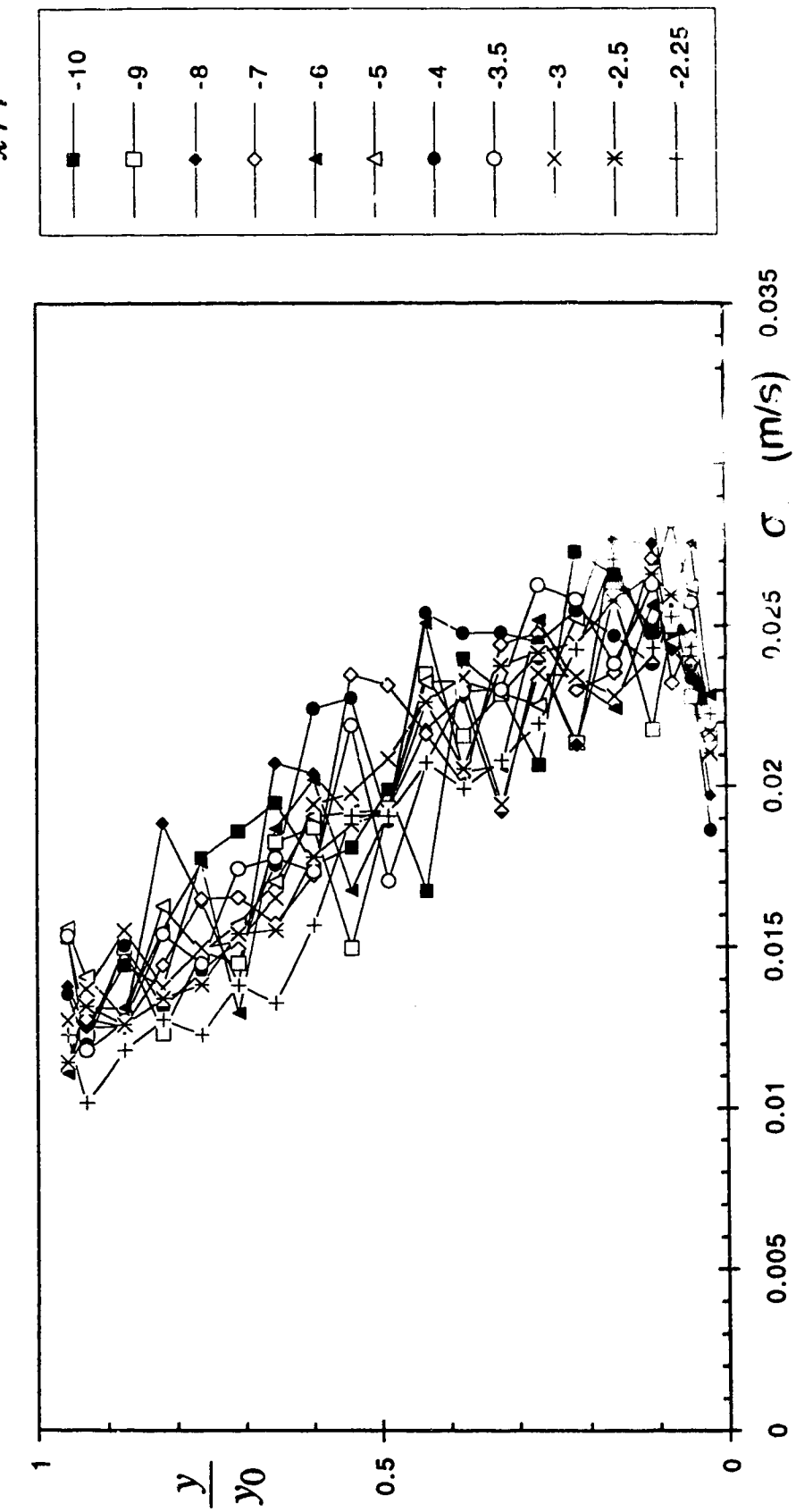

Figure 4.2.11 (a-i) Velocity Distribution on the POS (Expt. C2M)
(c) Standard deviation of the velocity magnitude

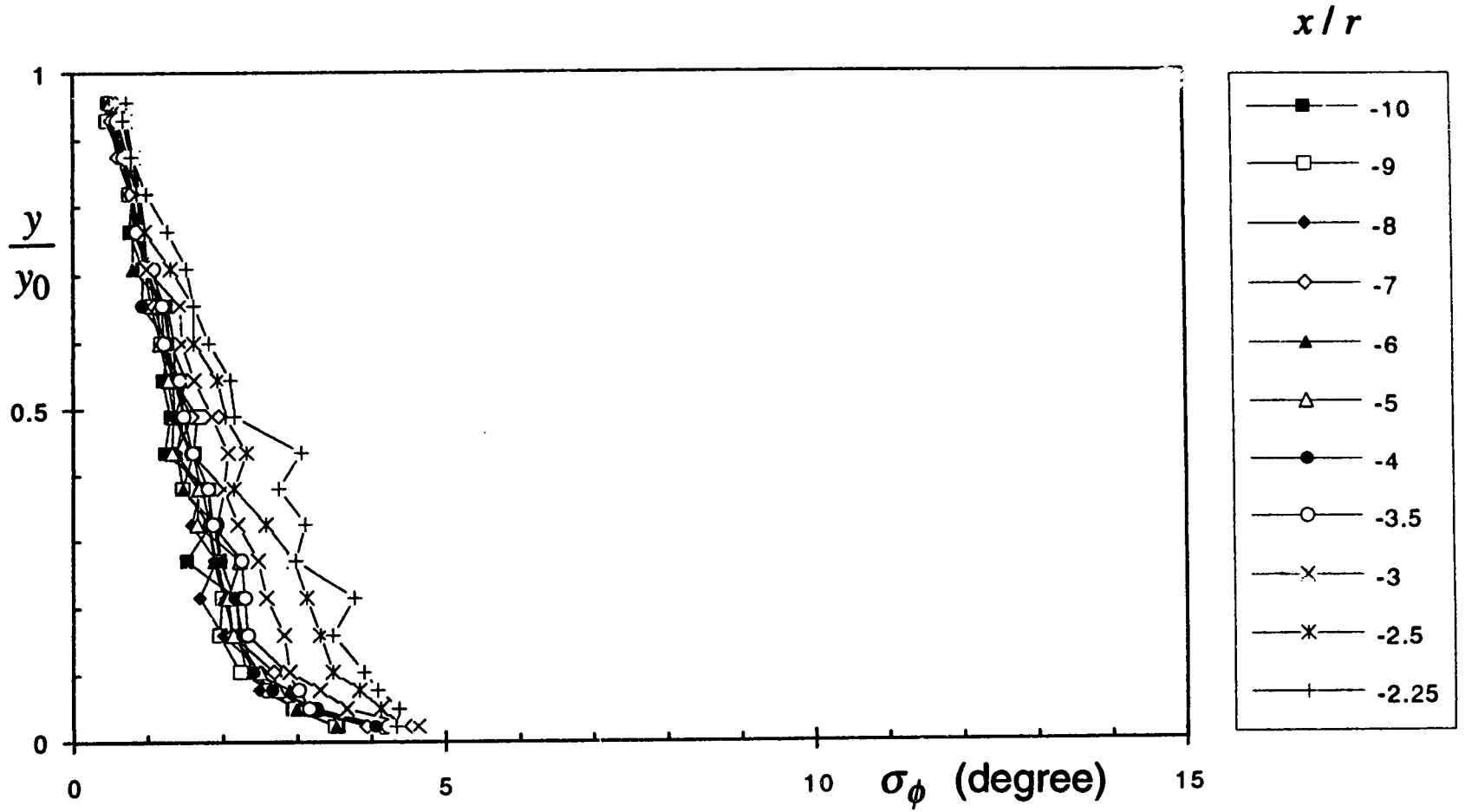

Figure 4.2.11 (a-i) Velocity Distribution on the POS (Expt. C2M)
(d) Standard deviation of the pitch angle

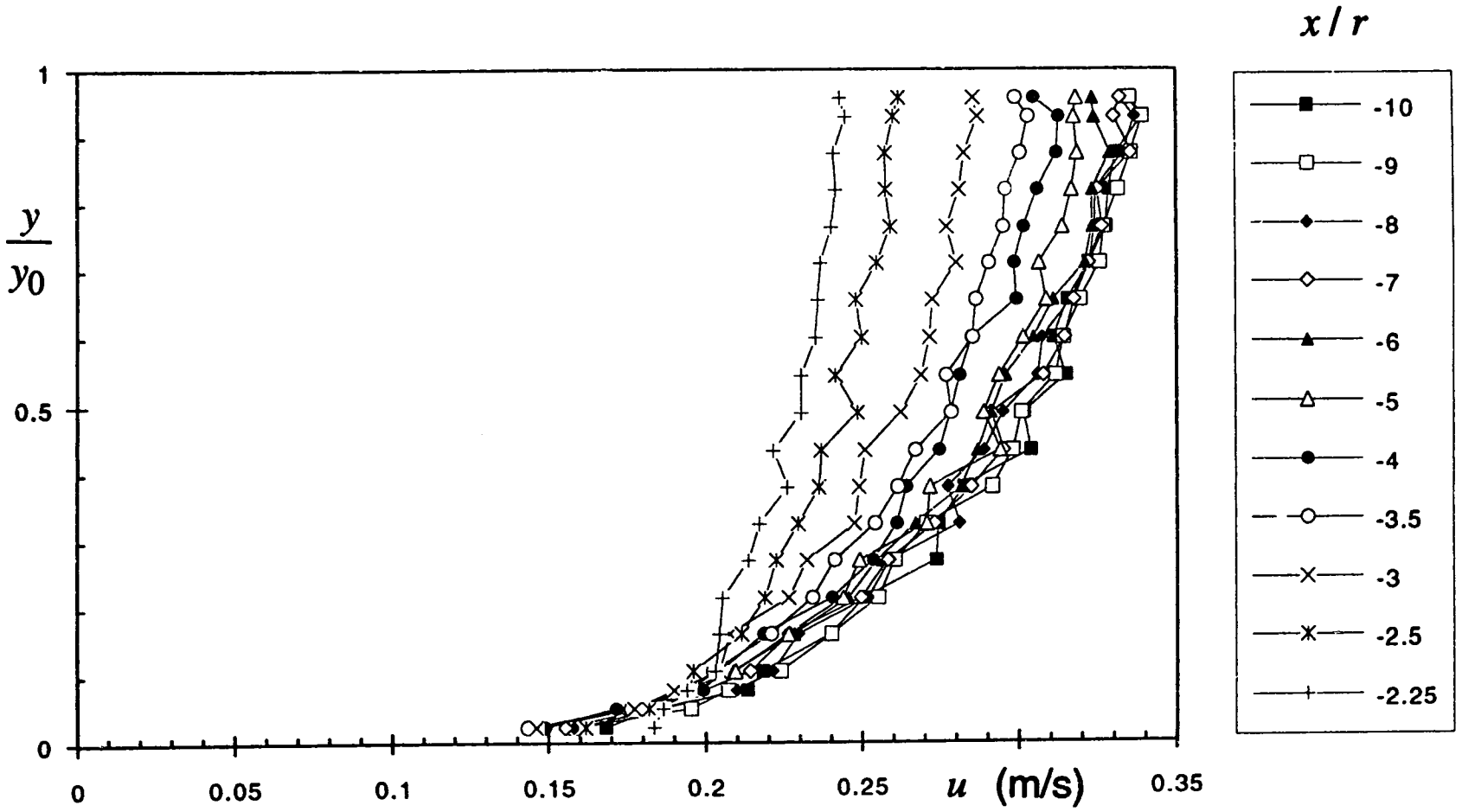

Figure 4.2.11 (a-i) Velocity Distribution on the POS (Expt. C2M)
(e) Longitudinal component of velocity

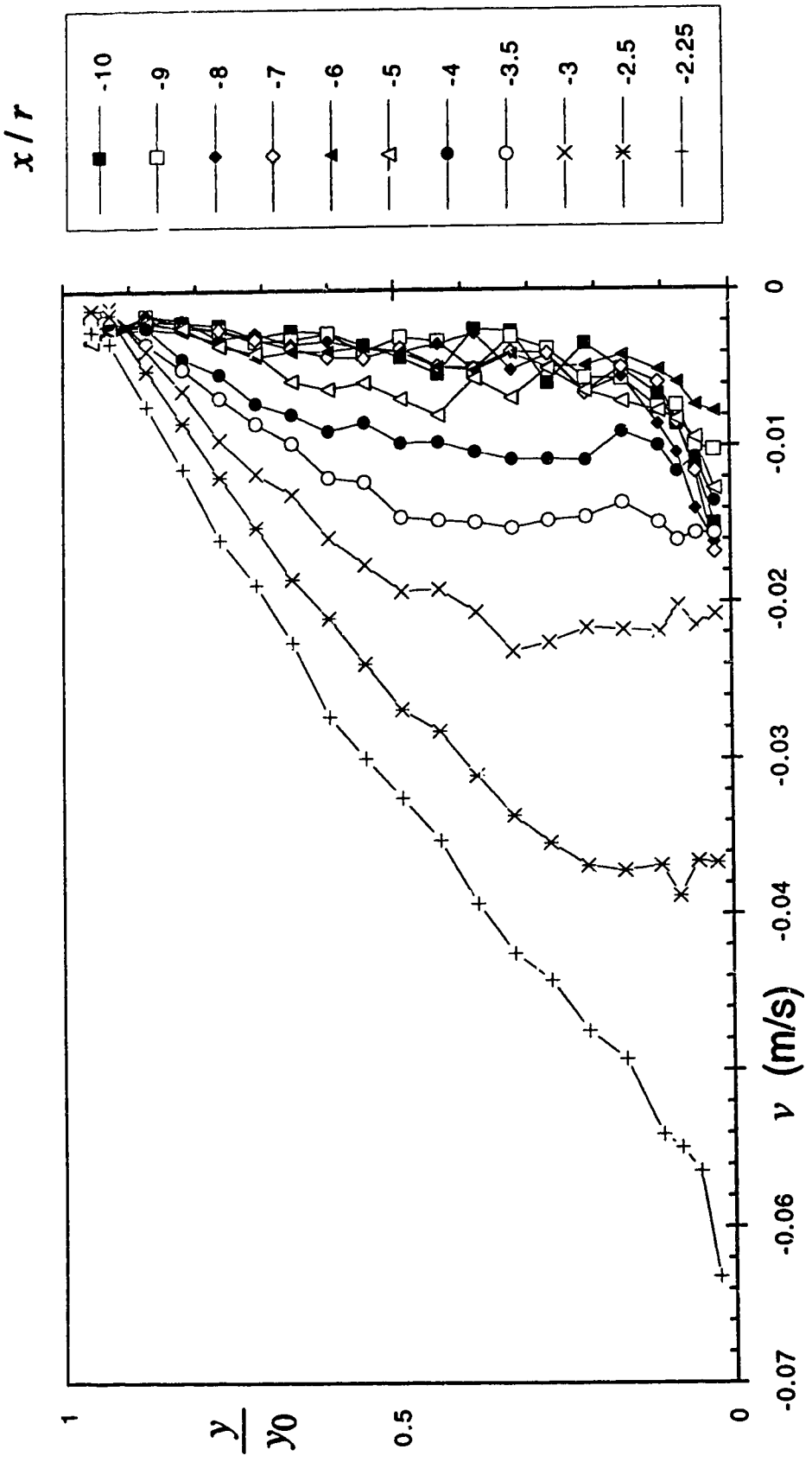

Figure 4.2.11 (a-i) Velocity Distribution on the POS (Expt. C2M)
(f) Vertical component of velocity

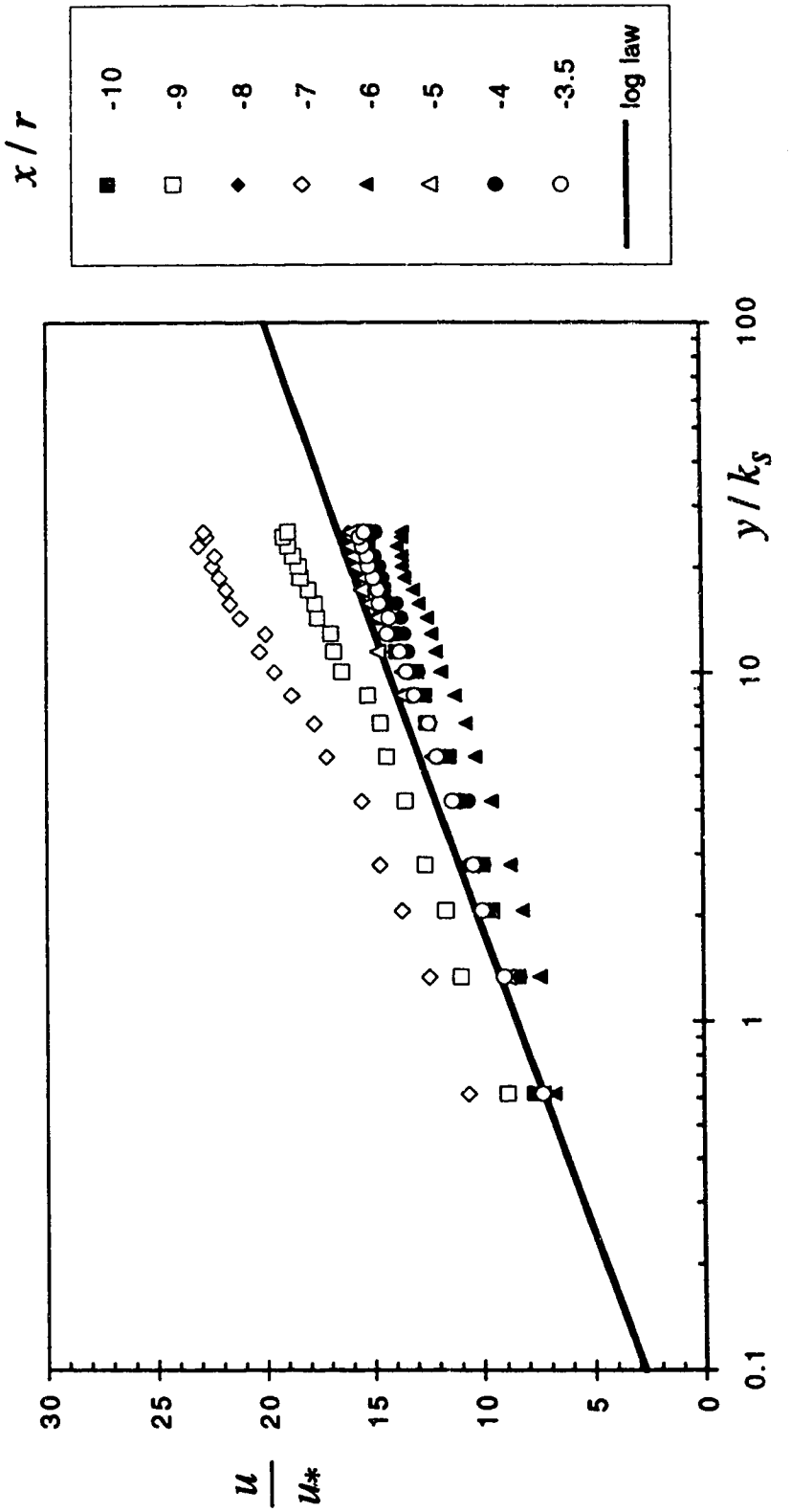

Figure 4.2.11 (a-i) Velocity Distribution on the POS (Expt. C2M)
(g) Comparison with log law

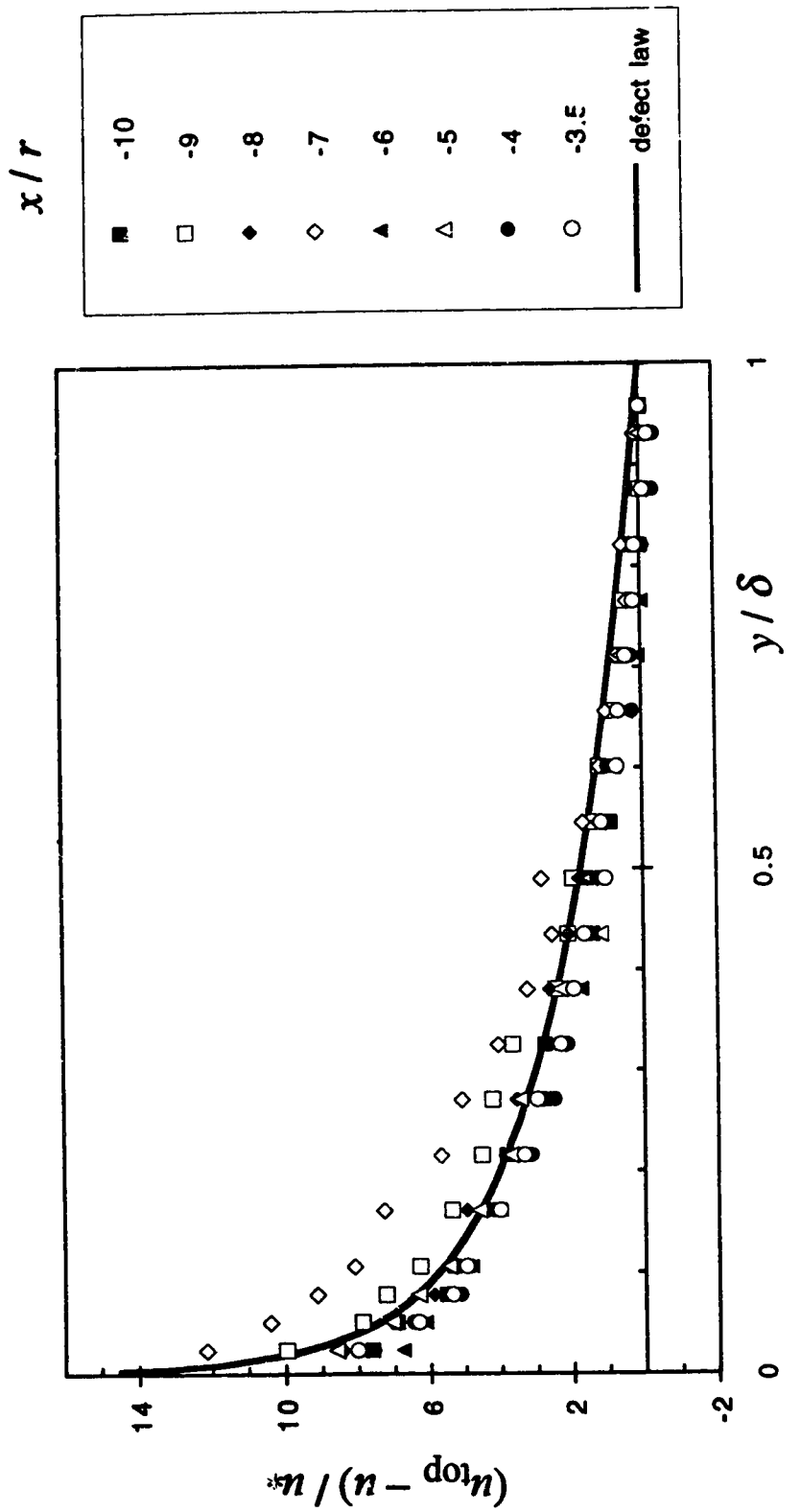

Figure 4.2.11 (a-i) Velocity Distribution on the POS (Expt. C2M)
(h) Comparison with defect law

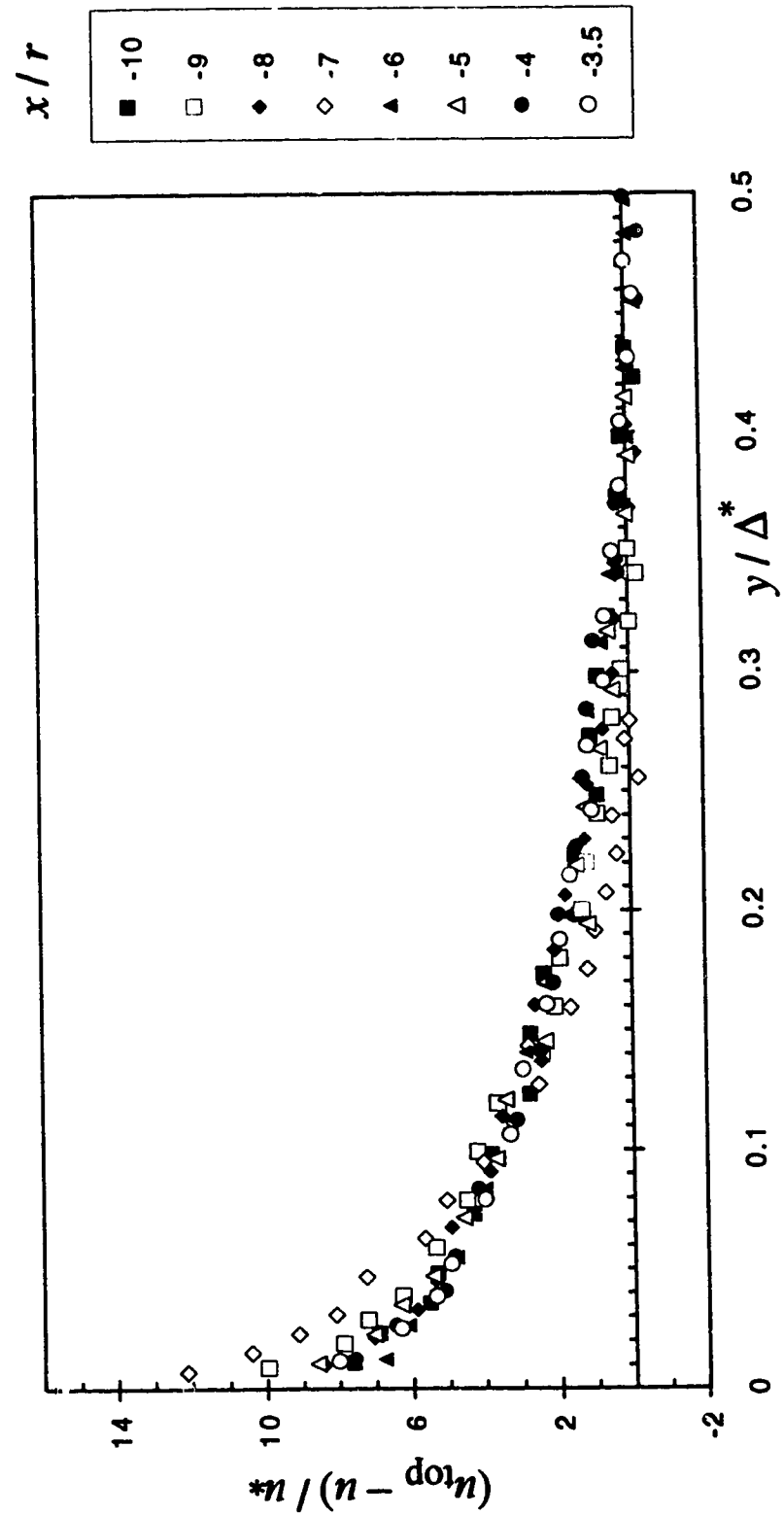

Figure 4.2.11 (a-i) Velocity Distribution on the POS (Expt. C2M)
(i) Comparison with Clauser's scheme

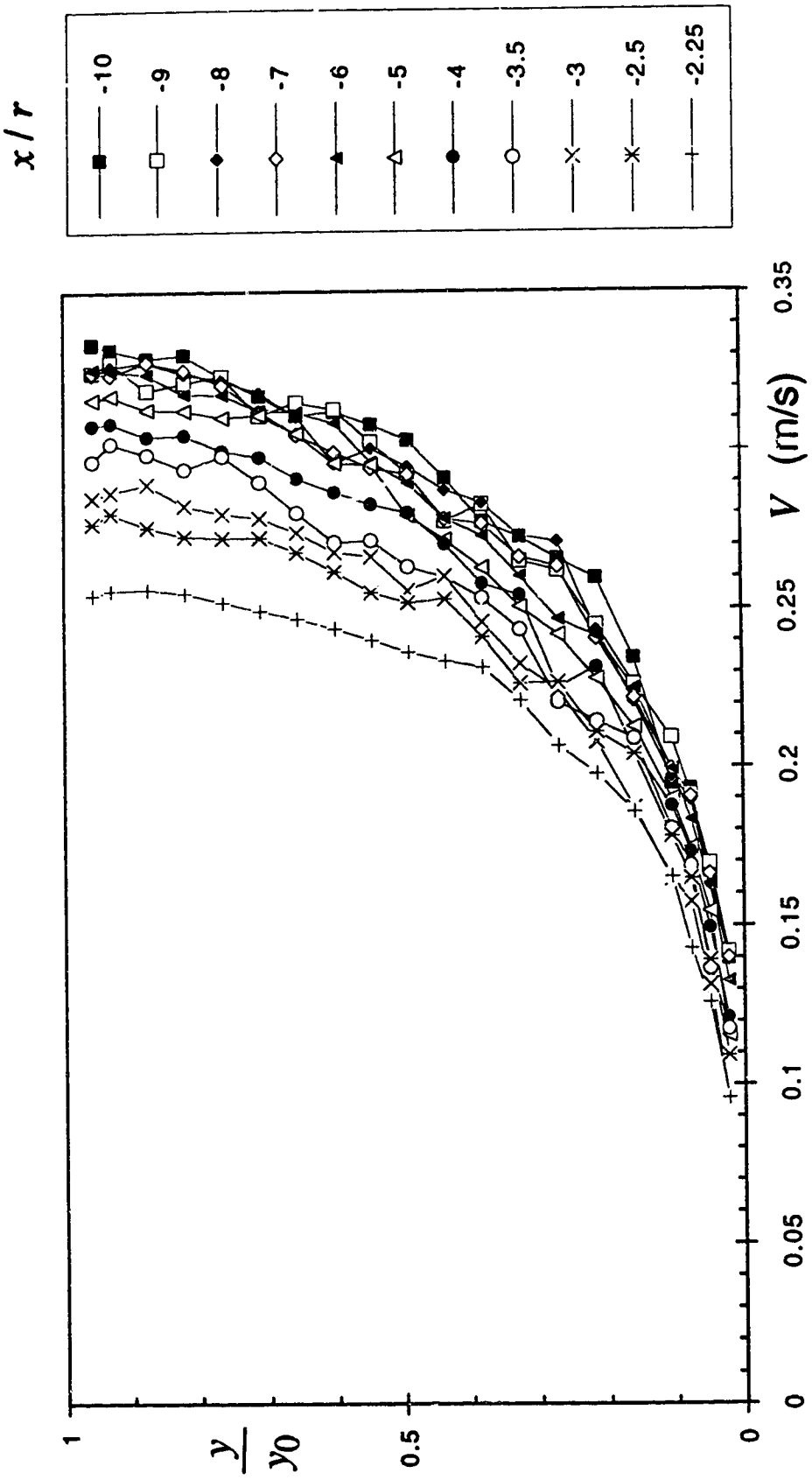

Figure 4.2.12 (a-i) Velocity Distribution on the POS (Expt. C2R)
(a) Velocity magnitude

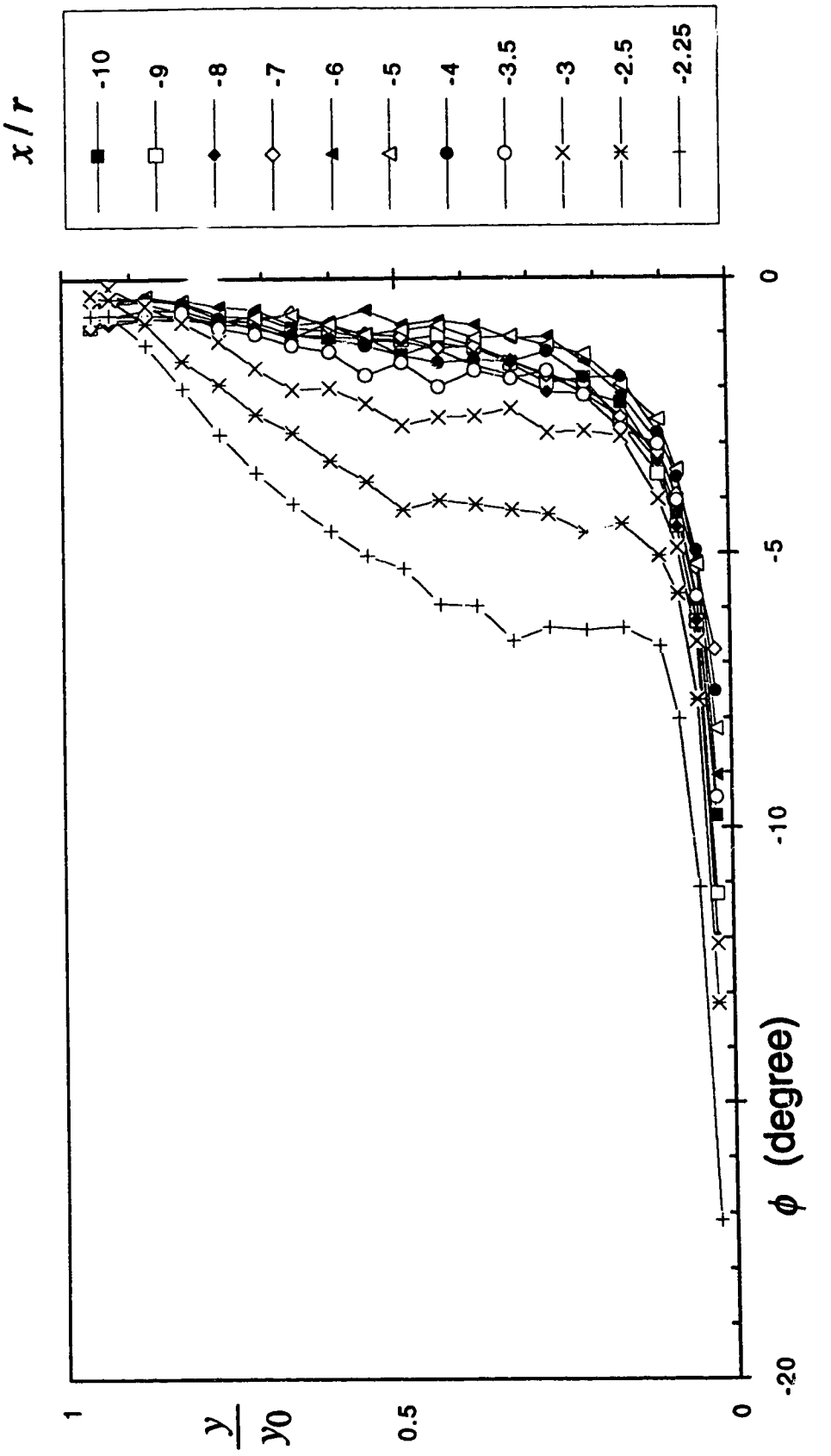

Figure 4.2.12 (a-i) Velocity Distribution on the POS (Expt. C2R)
(b) Angle of pitch

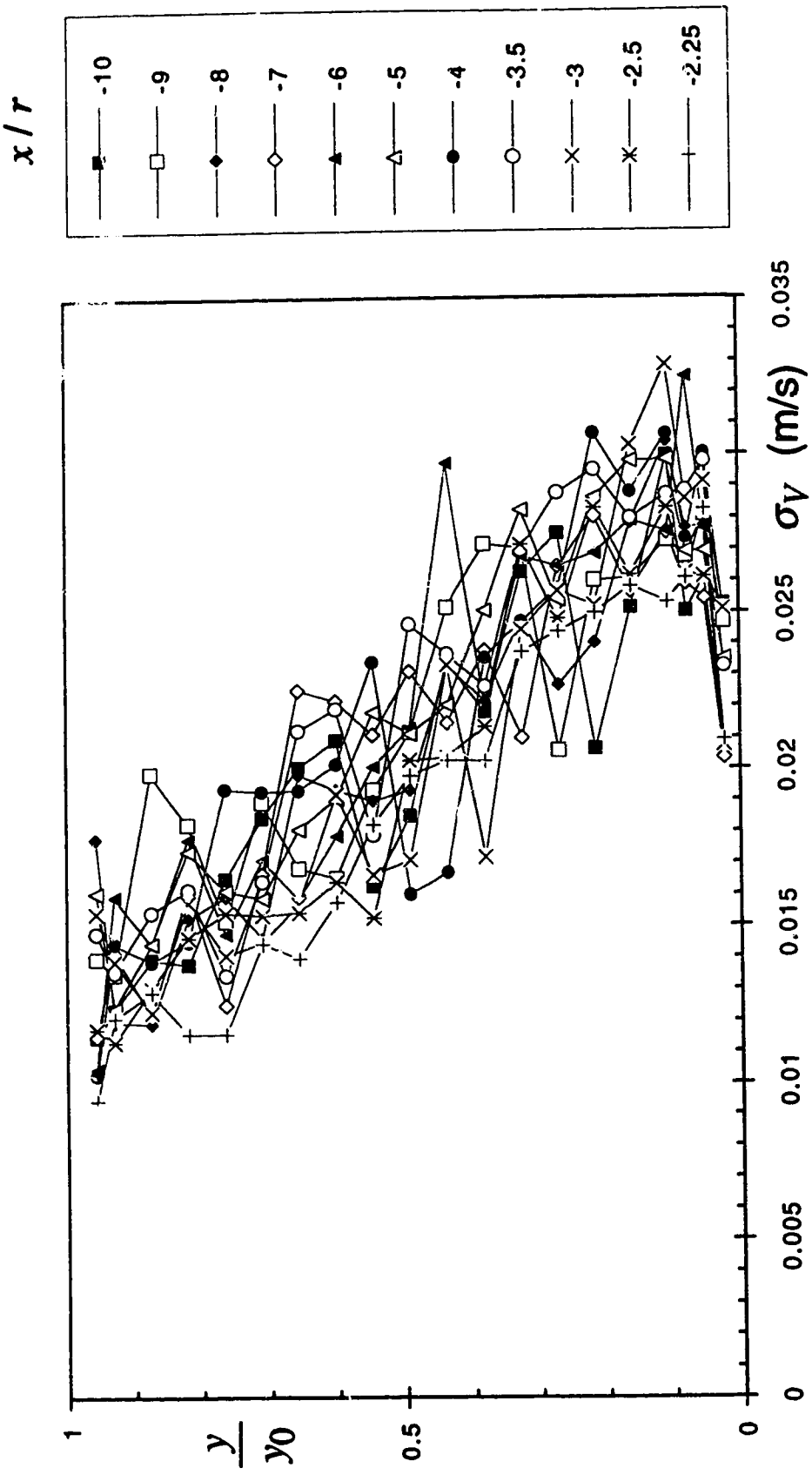

Figure 4.2.12 (a-i) Velocity Distribution on the POS (Expt. C2R)
(c) Standard deviation of the velocity magnitude

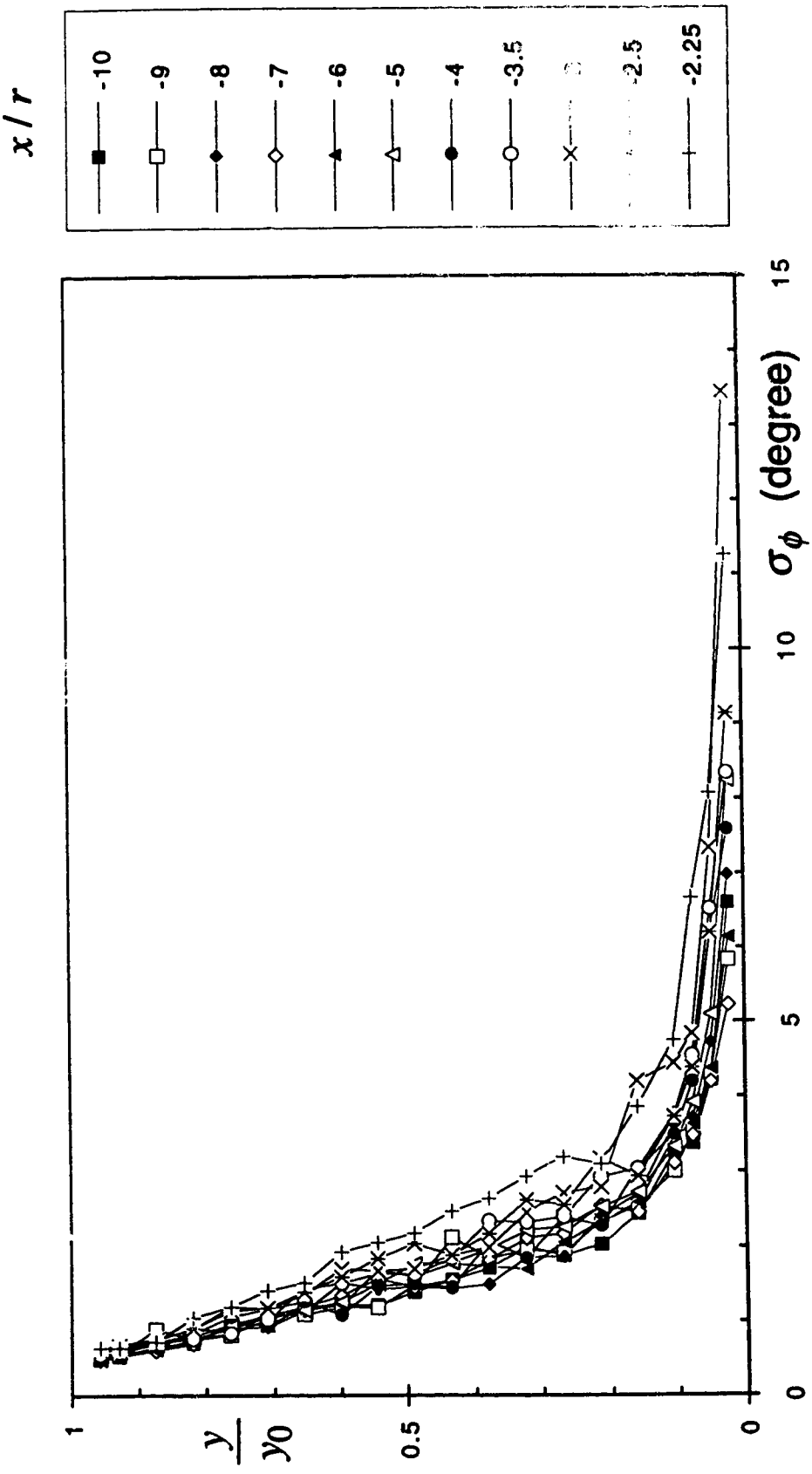

Figure 4.2.12 (a-i) Velocity Distribution on the POS (Expt. C2R)
(d) Standard deviation of the pitch angle

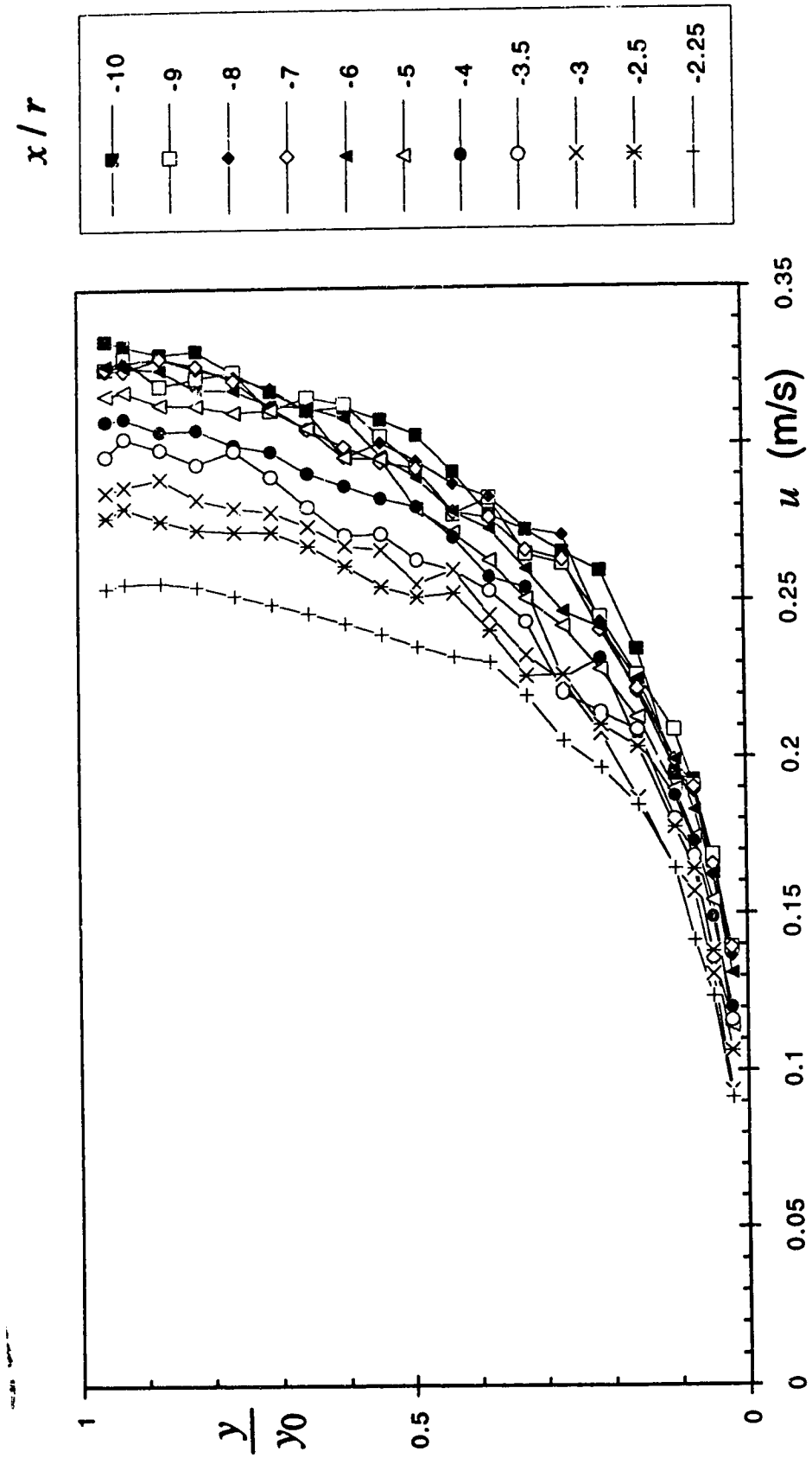

Figure 4.2.12 (a-i) Velocity Distribution on the POS (Expt. C2R)
(e) Longitudinal component of velocity

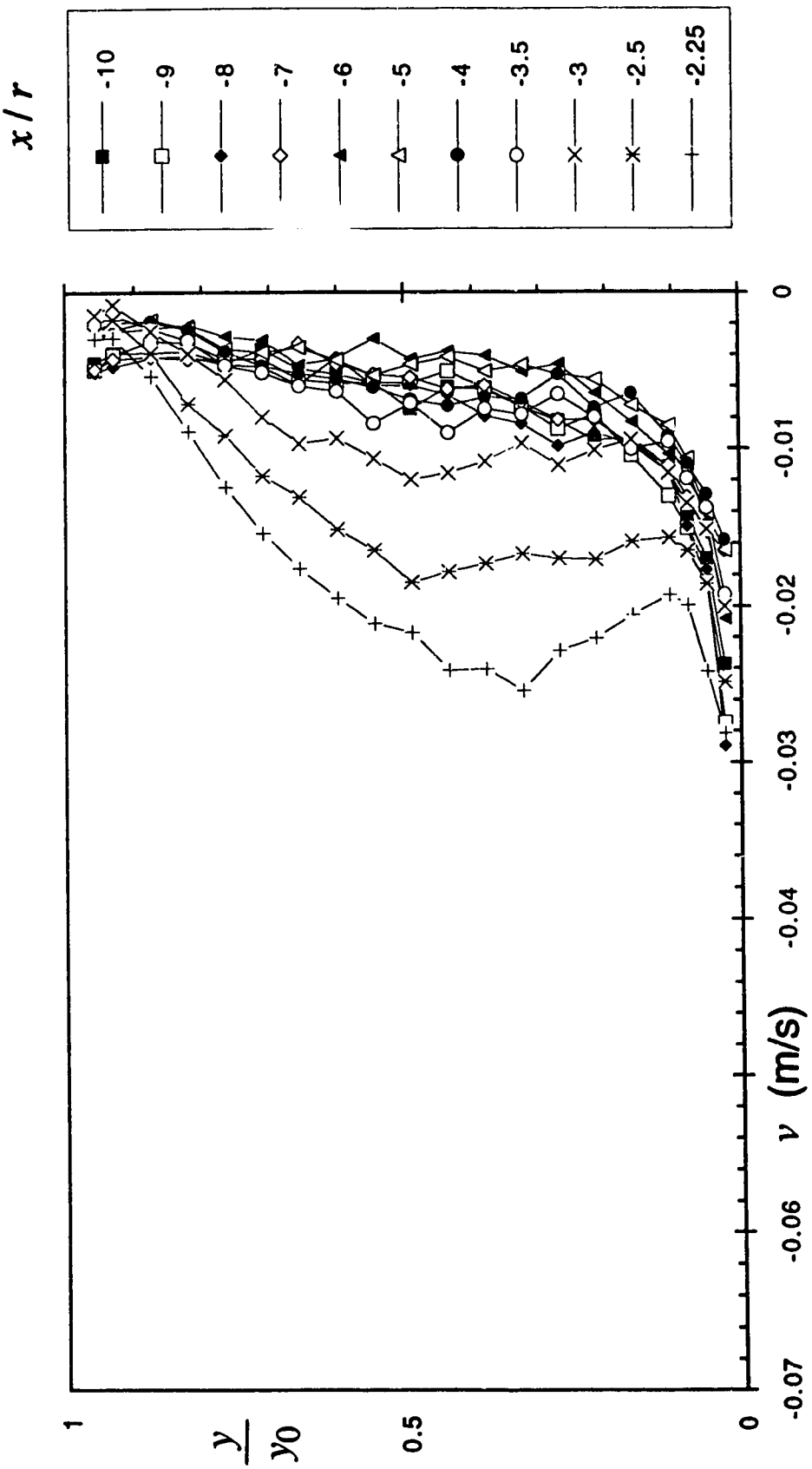

Figure 4.2.12 (a-i) Velocity Distribution on the POS (Expt. C2R)
(f) Vertical component of velocity

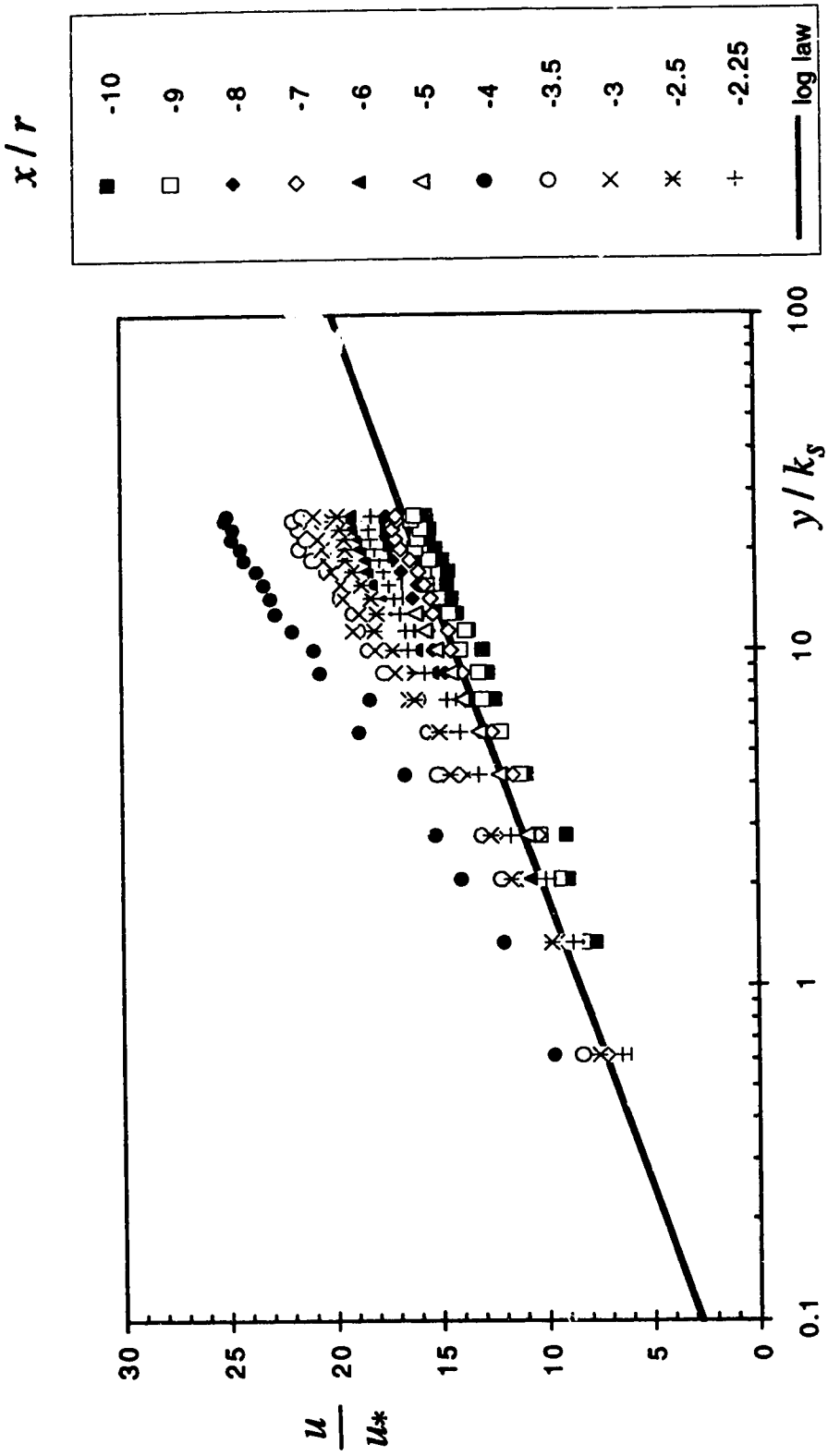

Figure 4.2.12 (a-i) Velocity Distribution on the POS (Expt. C2R)
(g) Comparison with log law

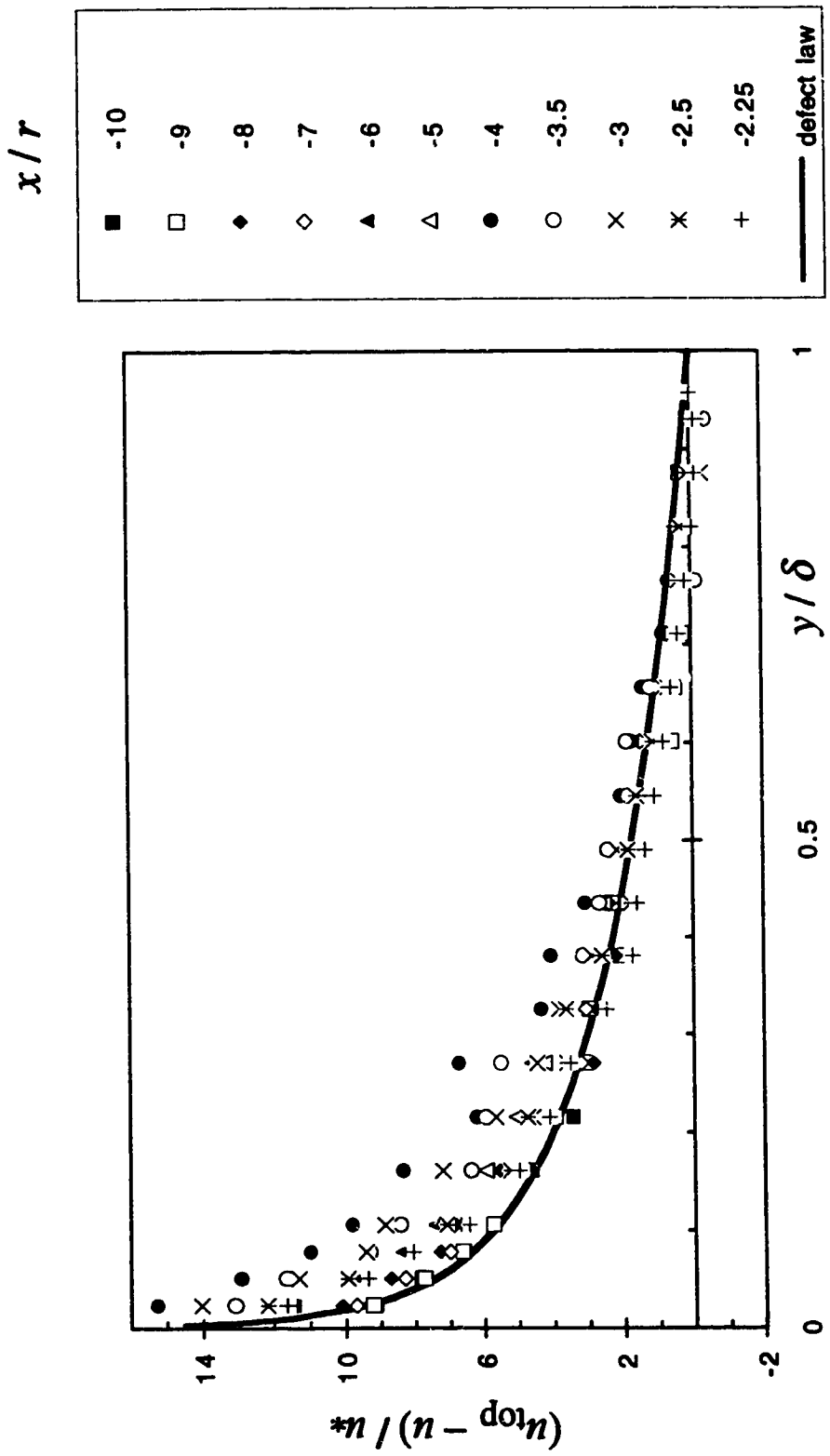

Figure 4.2.12 (a-i) Velocity Distribution on the POS (Expt. C2R)
(h) Comparison with defect law

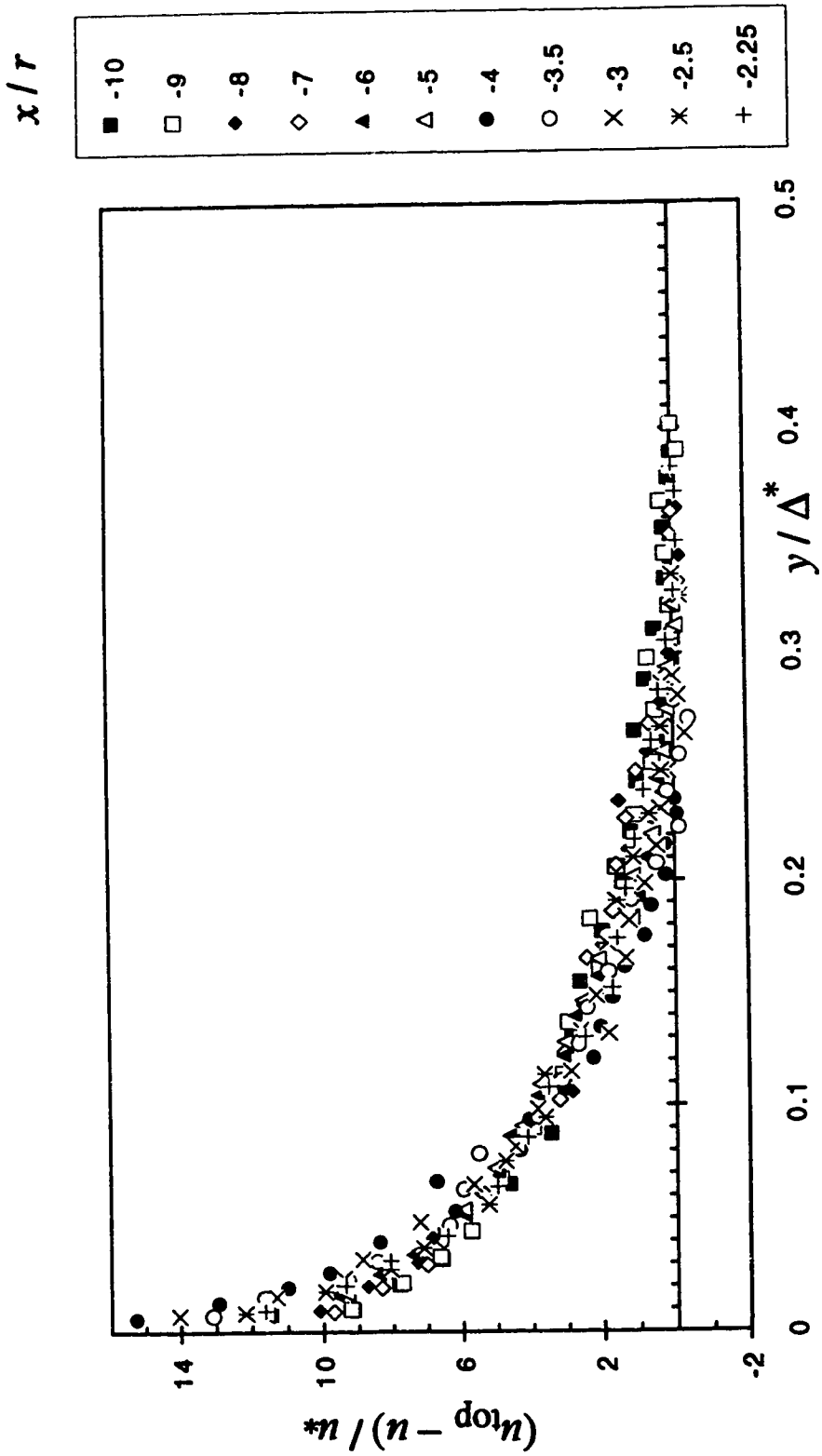

Figure 4.2.12 (a-i) Velocity Distribution on the POS (Expt. C2R)
(i) Comparison with Clauser's scheme

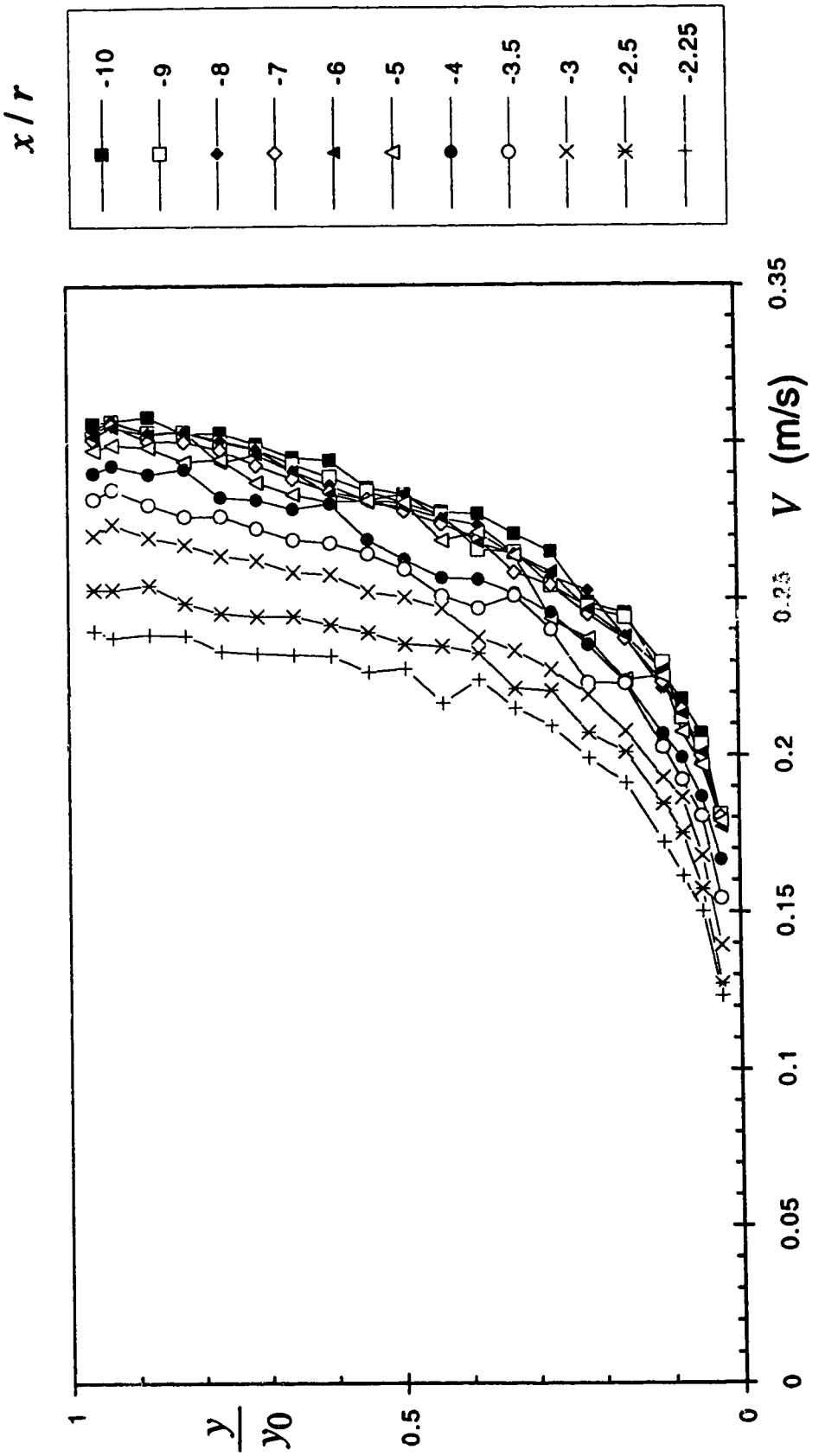

Figure 4.2.13 (a-i) Velocity Distribution on the POS (Expt. E2S)
(a) Velocity magnitude

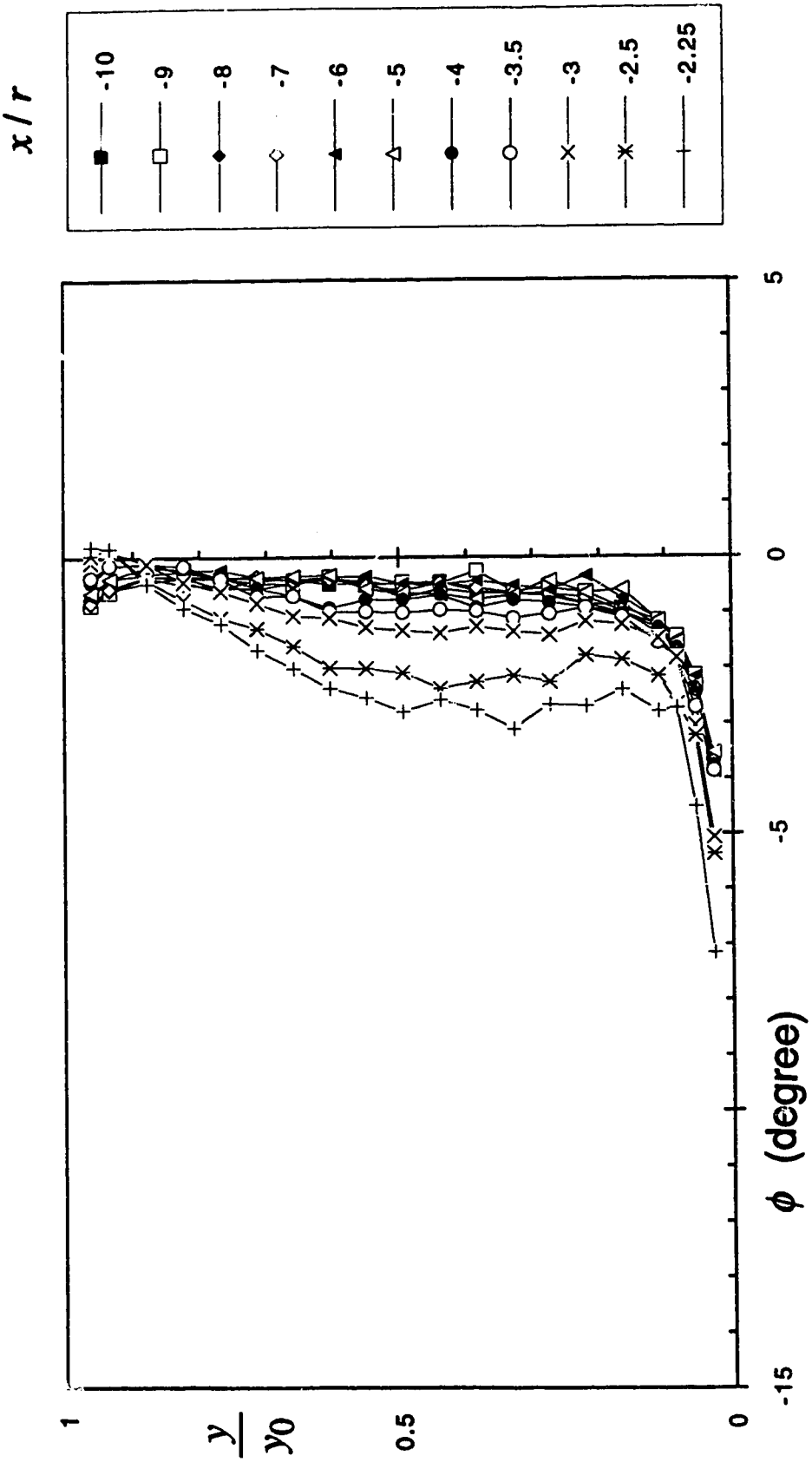

Figure 4.2.13 (a-i) Velocity Distribution on the POS (Expt. E2S)
(b) Angle of pitch

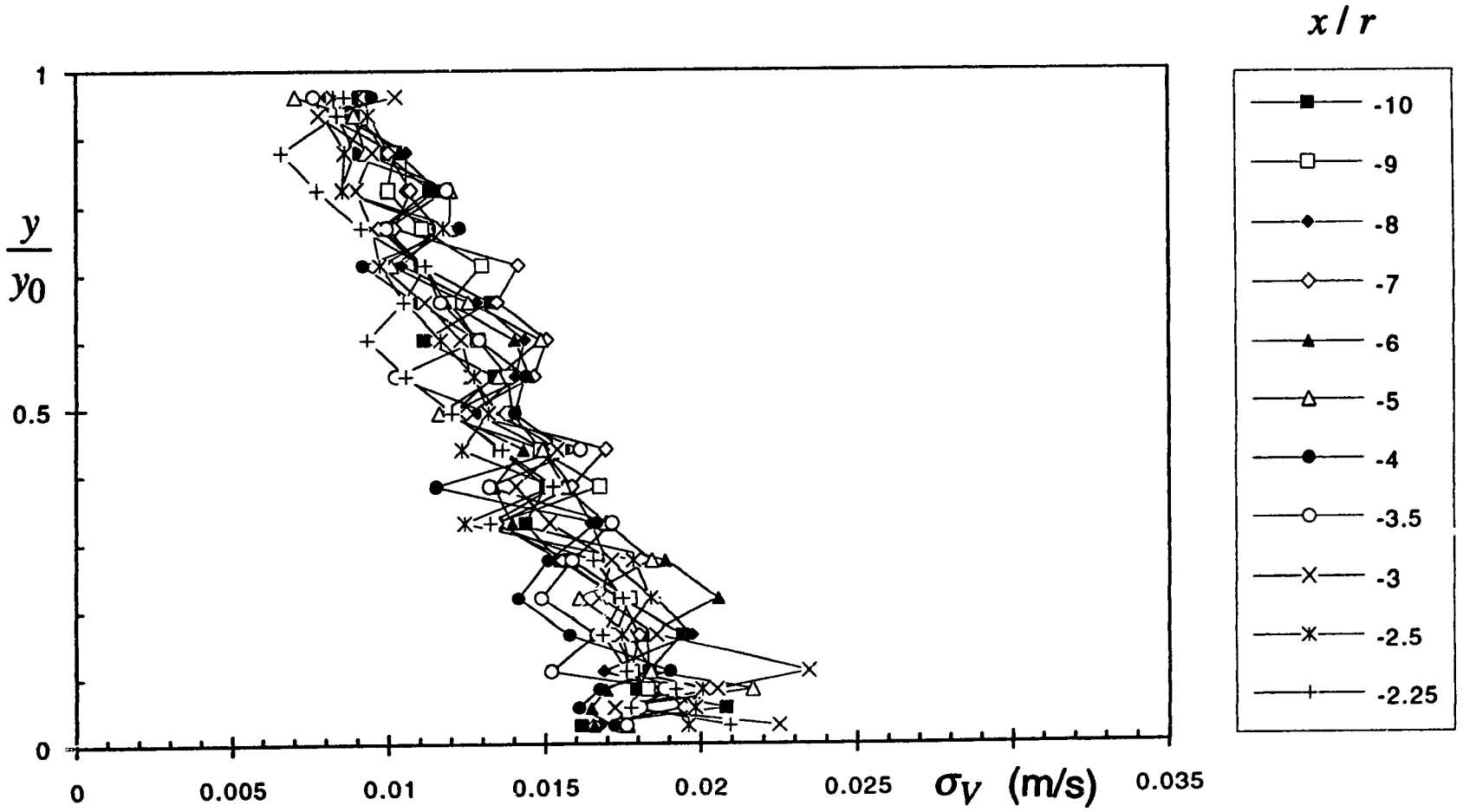

Figure 4.2.13 (a-i) Velocity Distribution on the POS (Expt. E2S)
(c) Standard deviation of the velocity magnitude

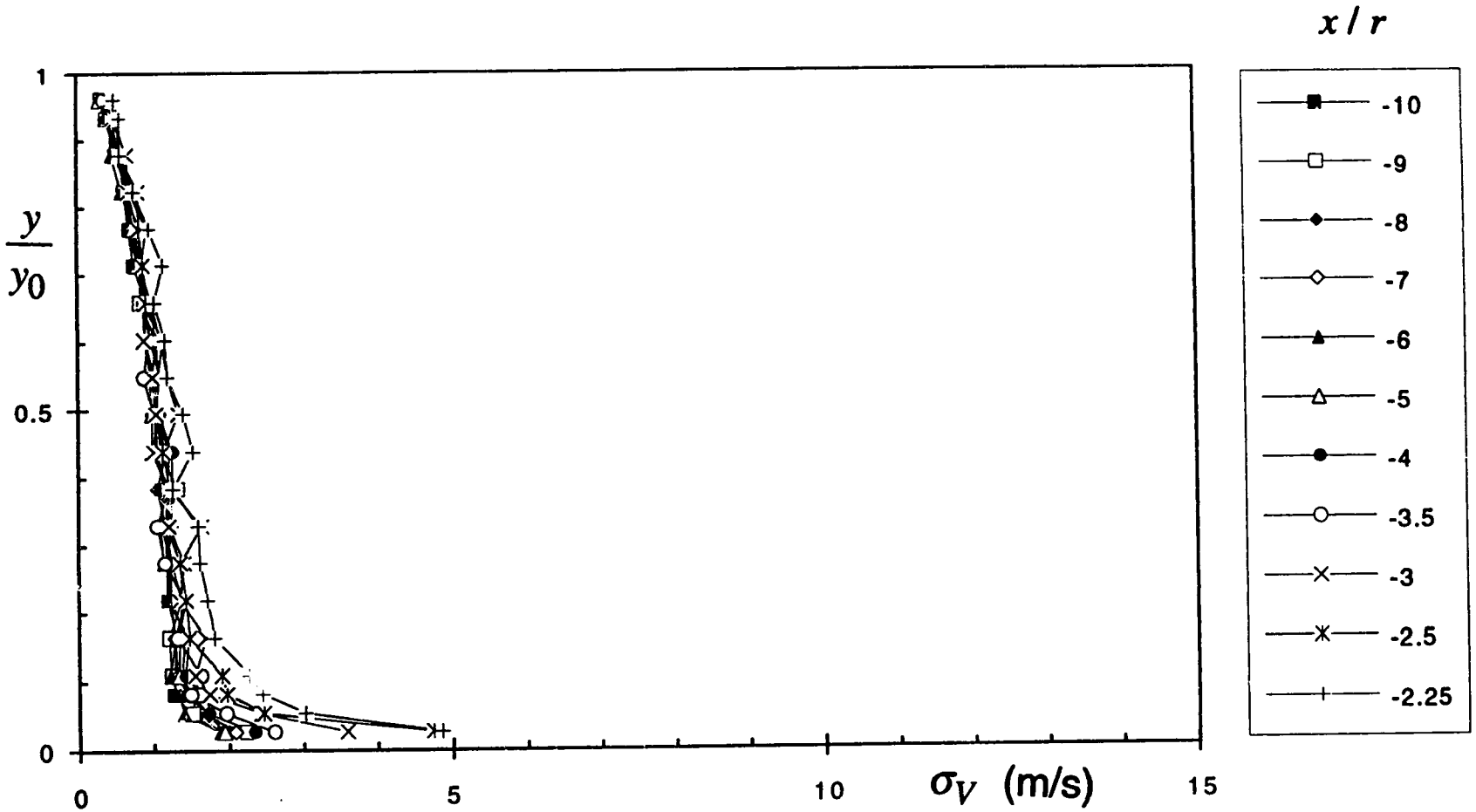

Figure 4.2.13 (a-i) Velocity Distribution on the POS (Expt. E2S)
(d) Standard deviation of the pitch angle

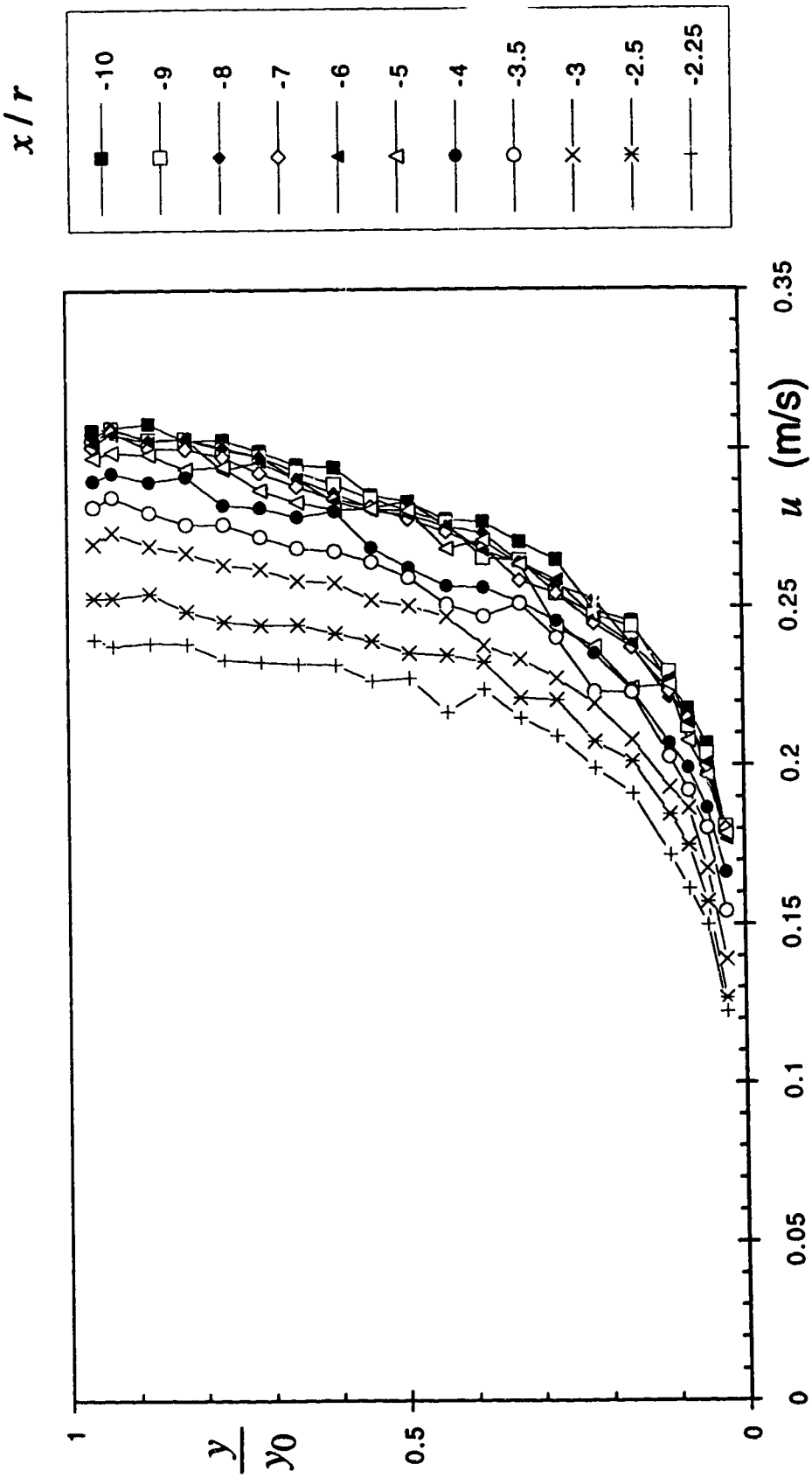

Figure 4.2.13 (a-i) Velocity Distribution on the POS (Expt. E2S)
(e) Longitudinal component of velocity

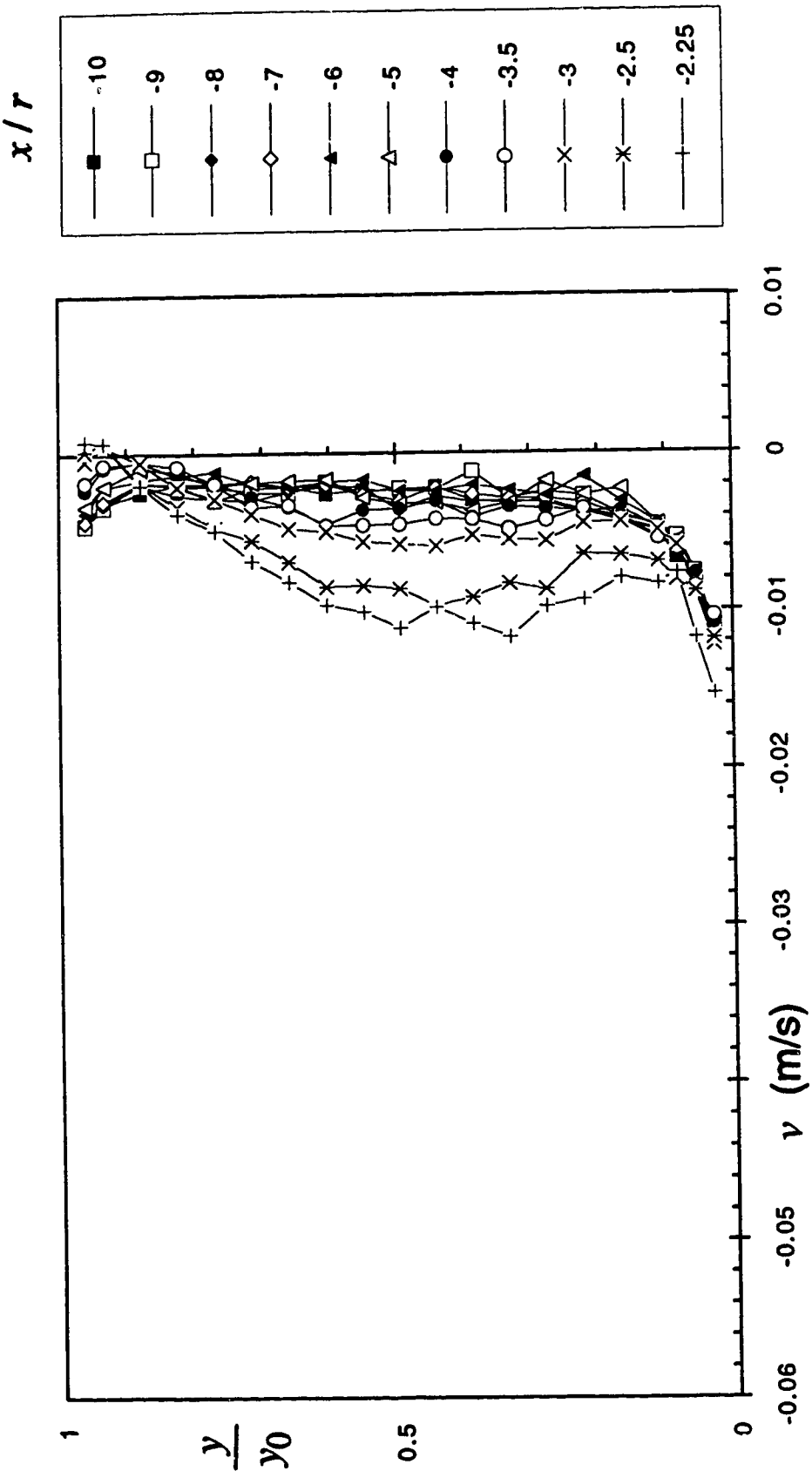

Figure 4.2.13 (a-i) Velocity Distribution on the POS (Expt. E2S)
(f) Vertical component of velocity

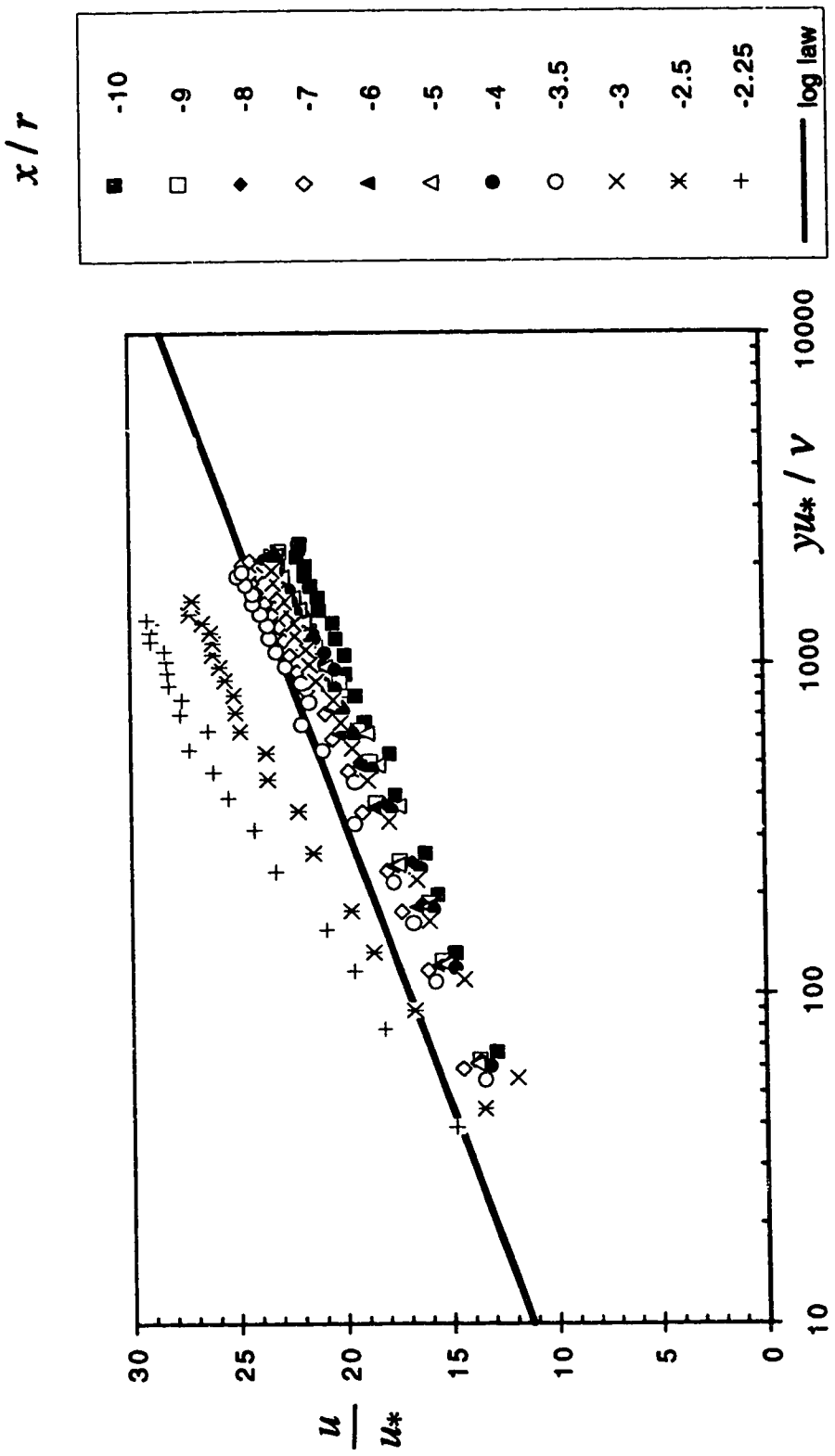

Figure 4.2.13 (a-i) Velocity Distribution on the POS (Expt. E2S)
(g) Comparison with log law

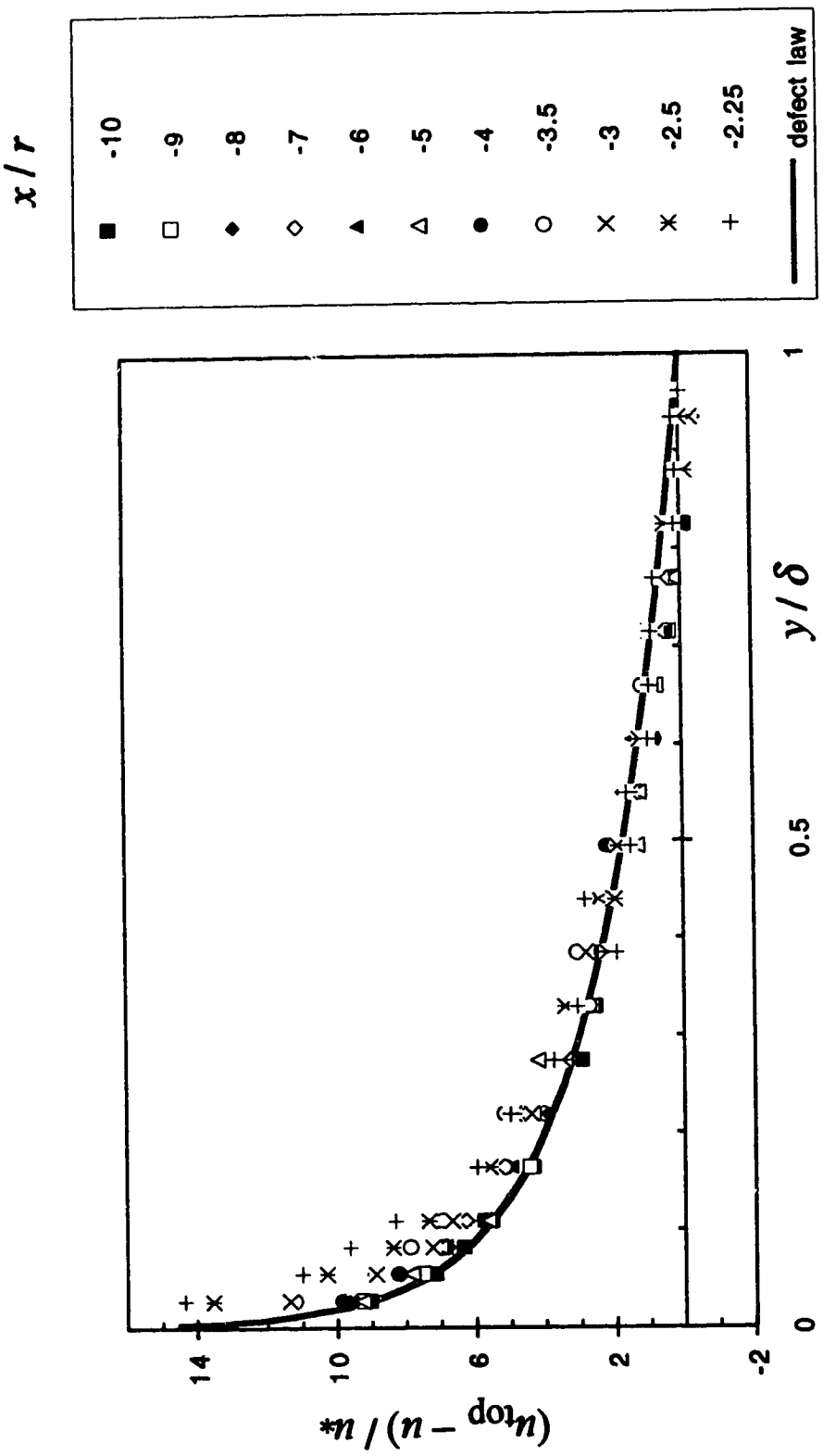

Figure 4.2.13 (a-i) Velocity Distribution on the POS (Expt. E2S)
(h) Comparison with defect law

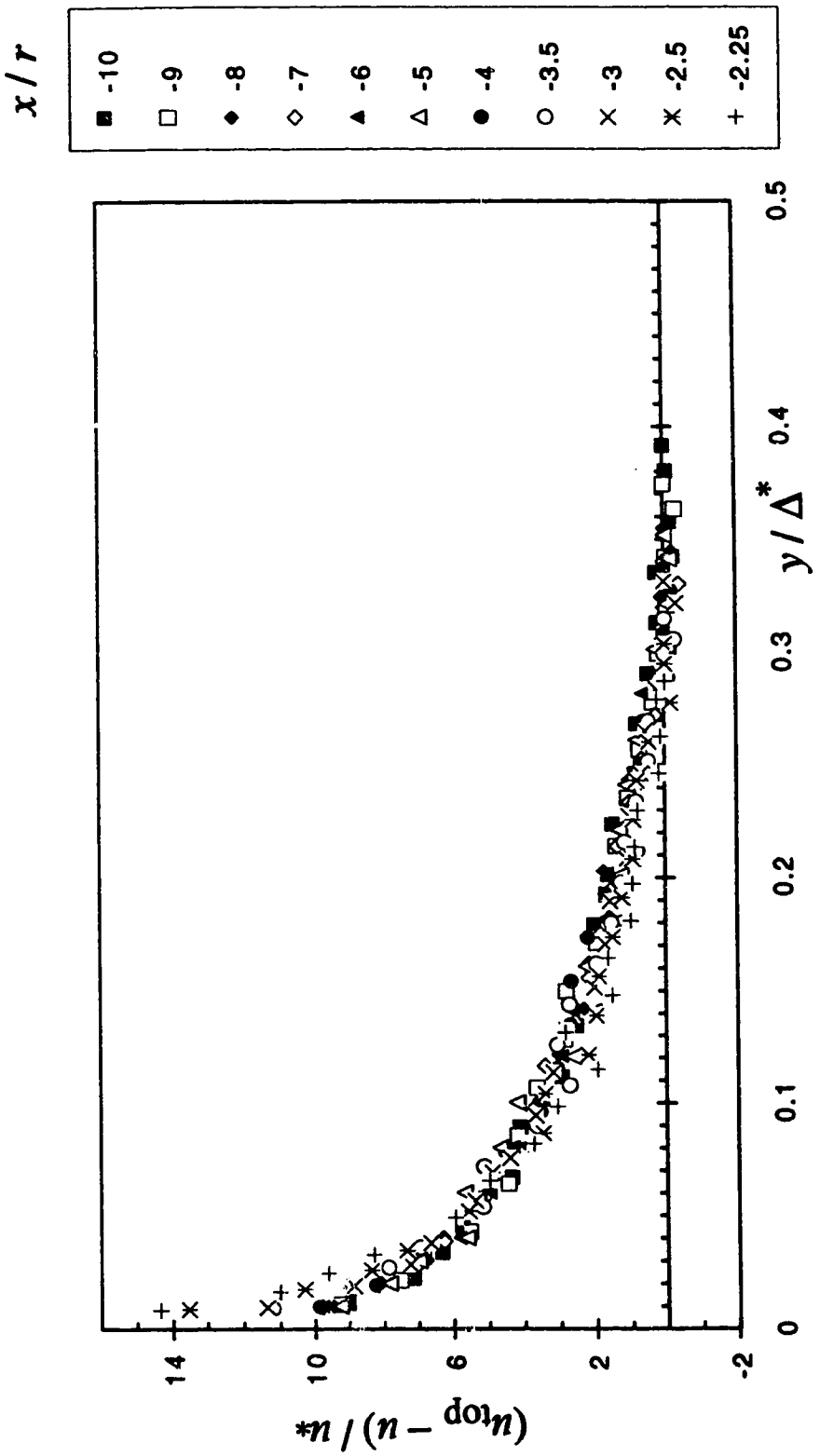

Figure 4.2.13 (a-i) Velocity Distribution on the POS (Expt. E2S)
(i) Comparison with Clauser's scheme

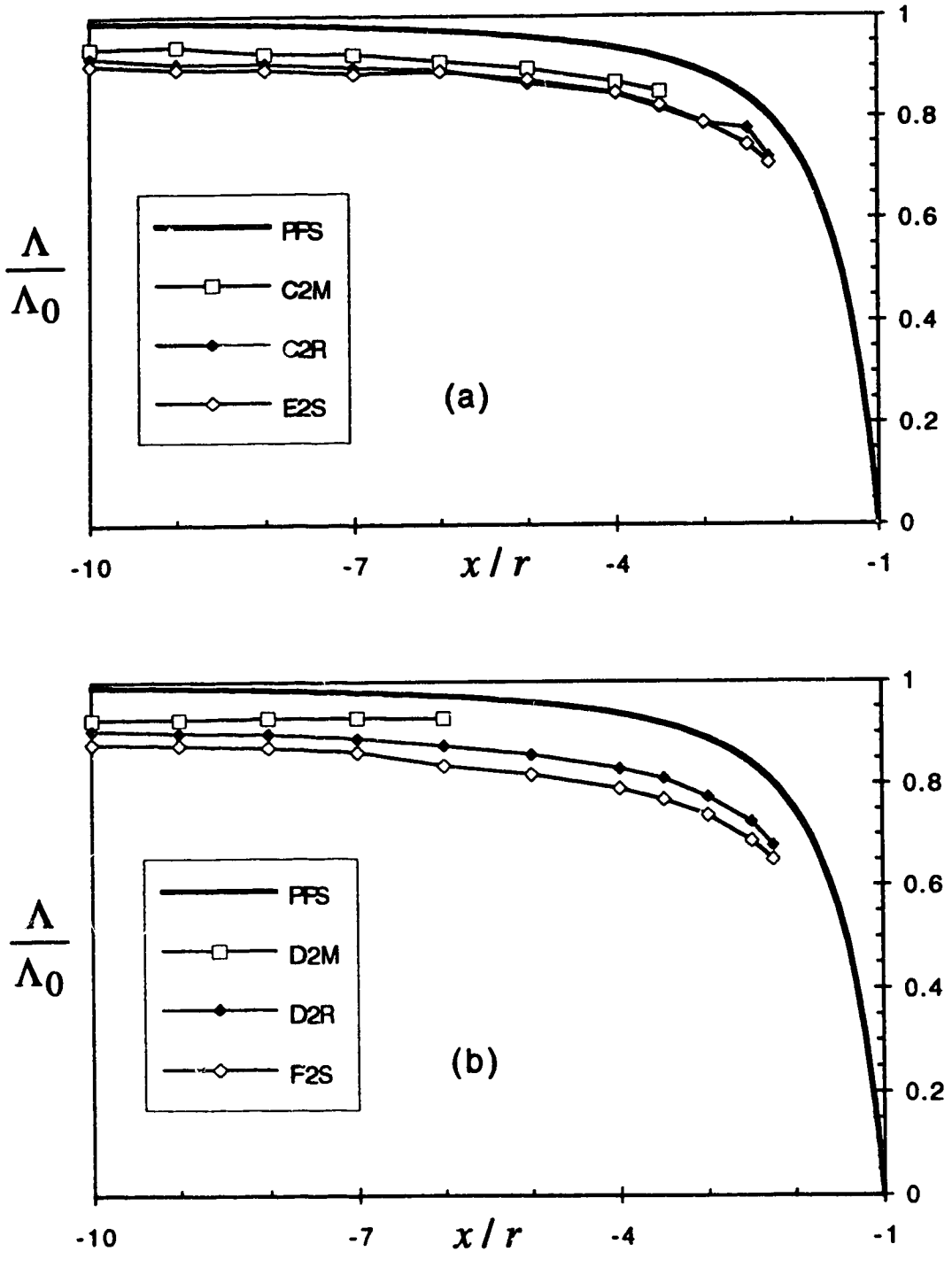

Figure 4.2.14 (a-b) Variation of mass flux on the POS
(a) Expt. C2M, C2R and E2S
(b) Expt. D2M, D2R and E2S

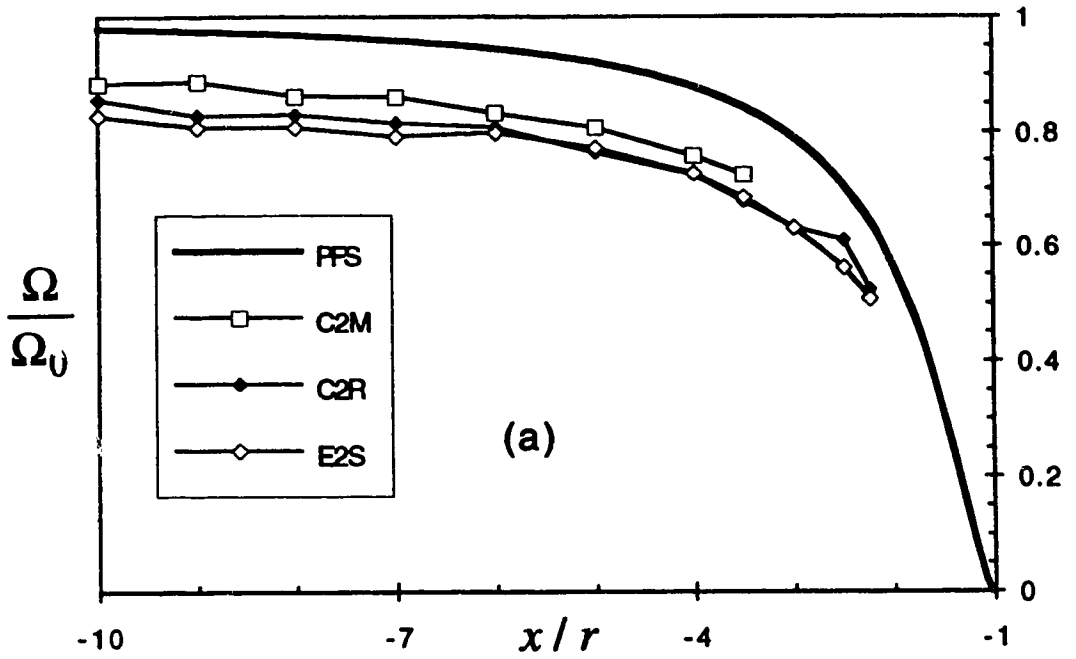

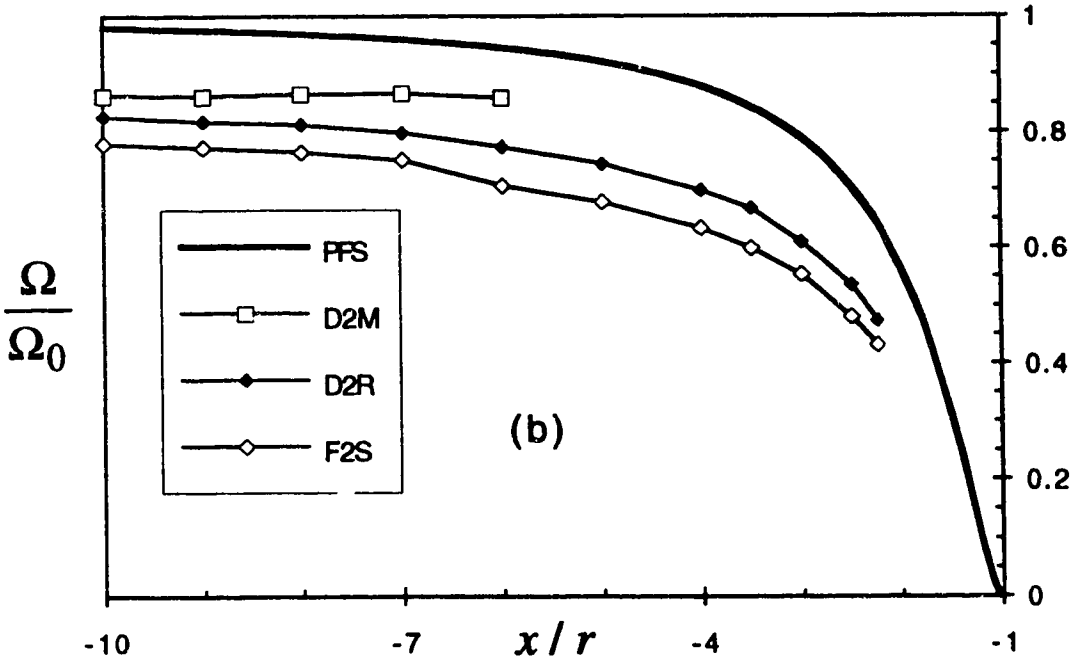

Figure 4.2.15 (a-b) Variation of momentum flux on the POS
(a) Expt. C2M, C2R and E2S
(b) Expt. D2M, D2R and E2S

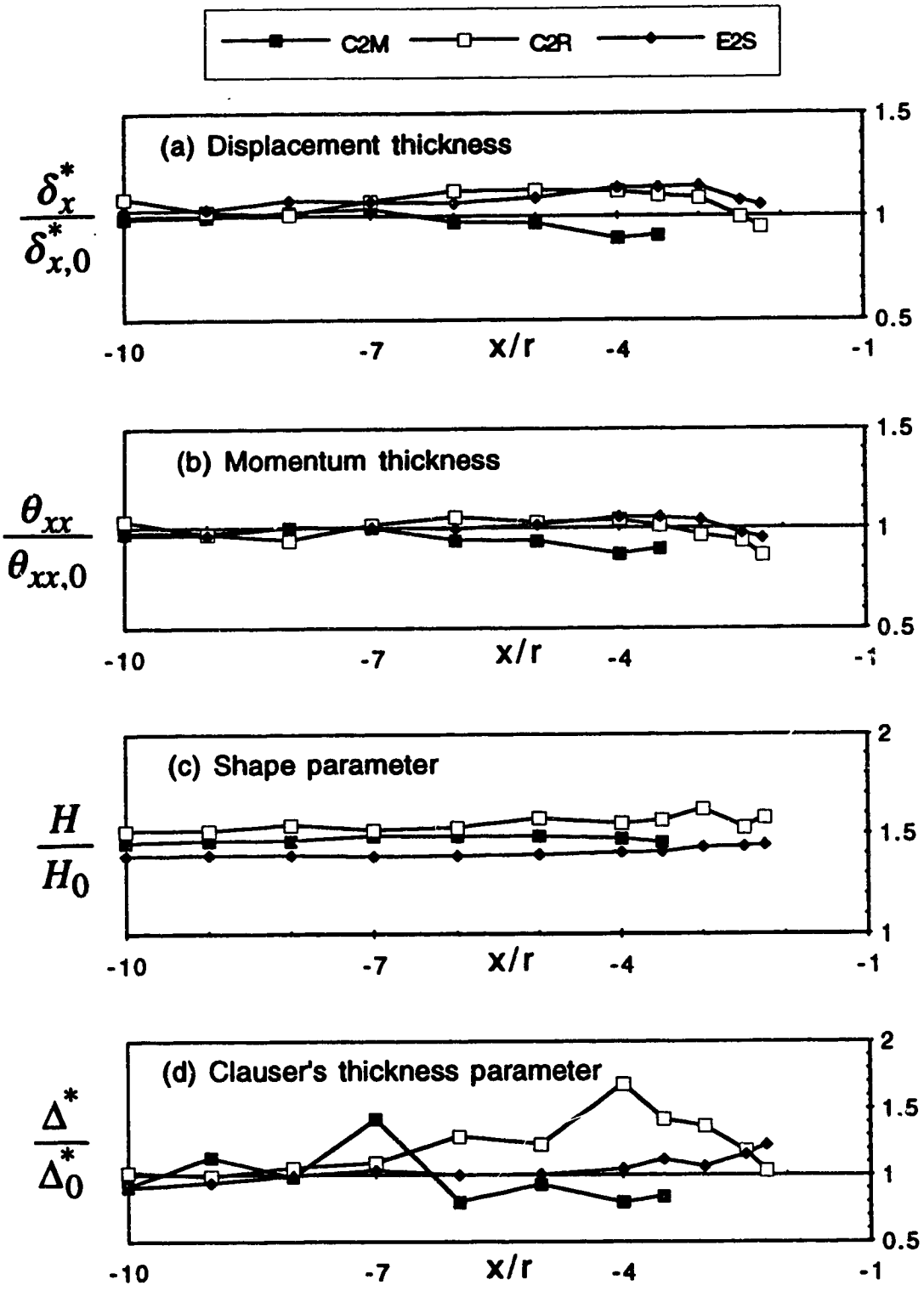

Figure 4.2.16 (a-d) Variation of boundary layer parameters on the POS (Expt. C2M, C2R and E2S)

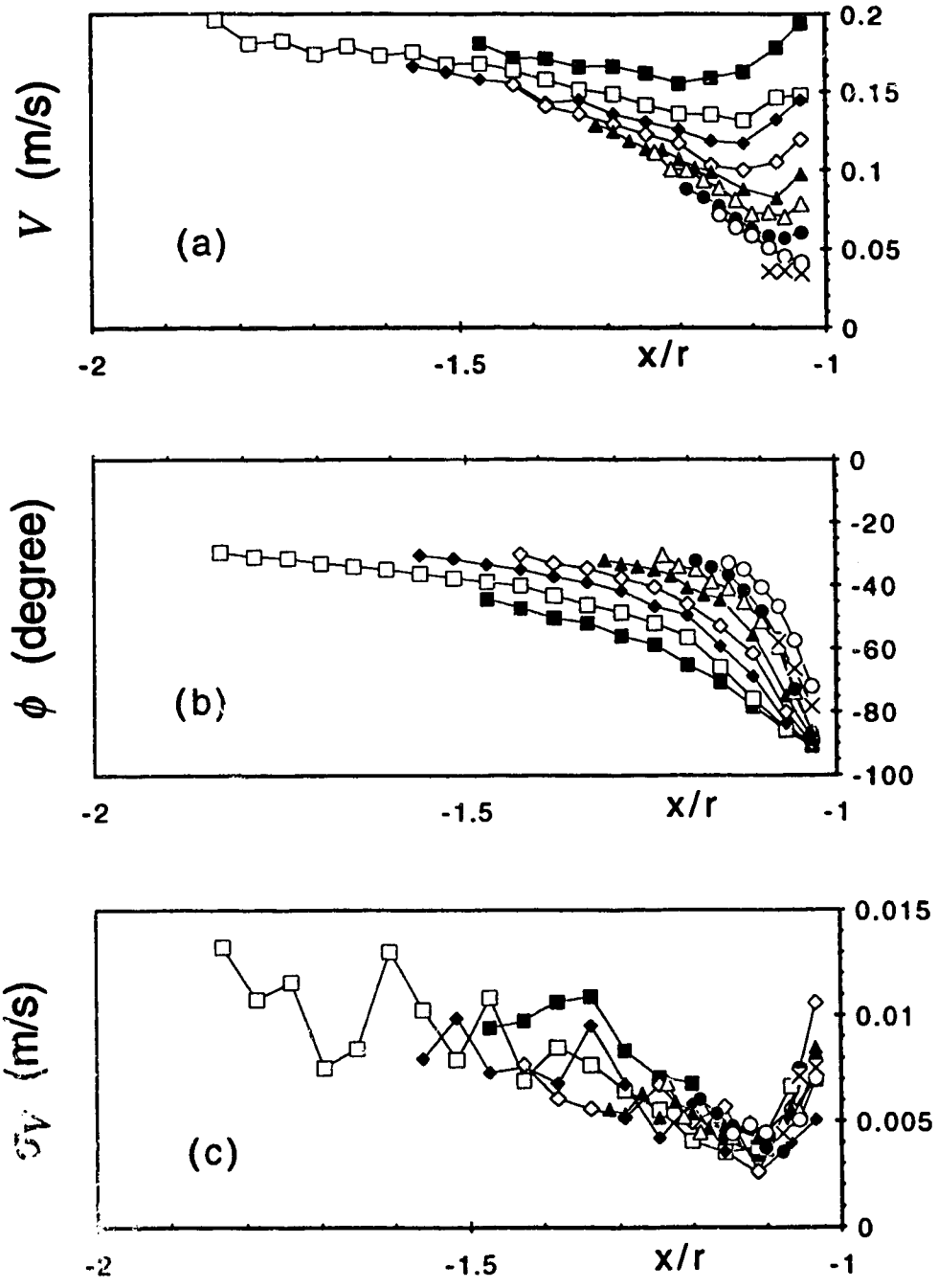

Figure 4.2.17 (a-h) Downflow in front of the pier (Expt. C2M);
(a) velocity magnitude
(b) angle of pitch
(c) fluctuation of velocity

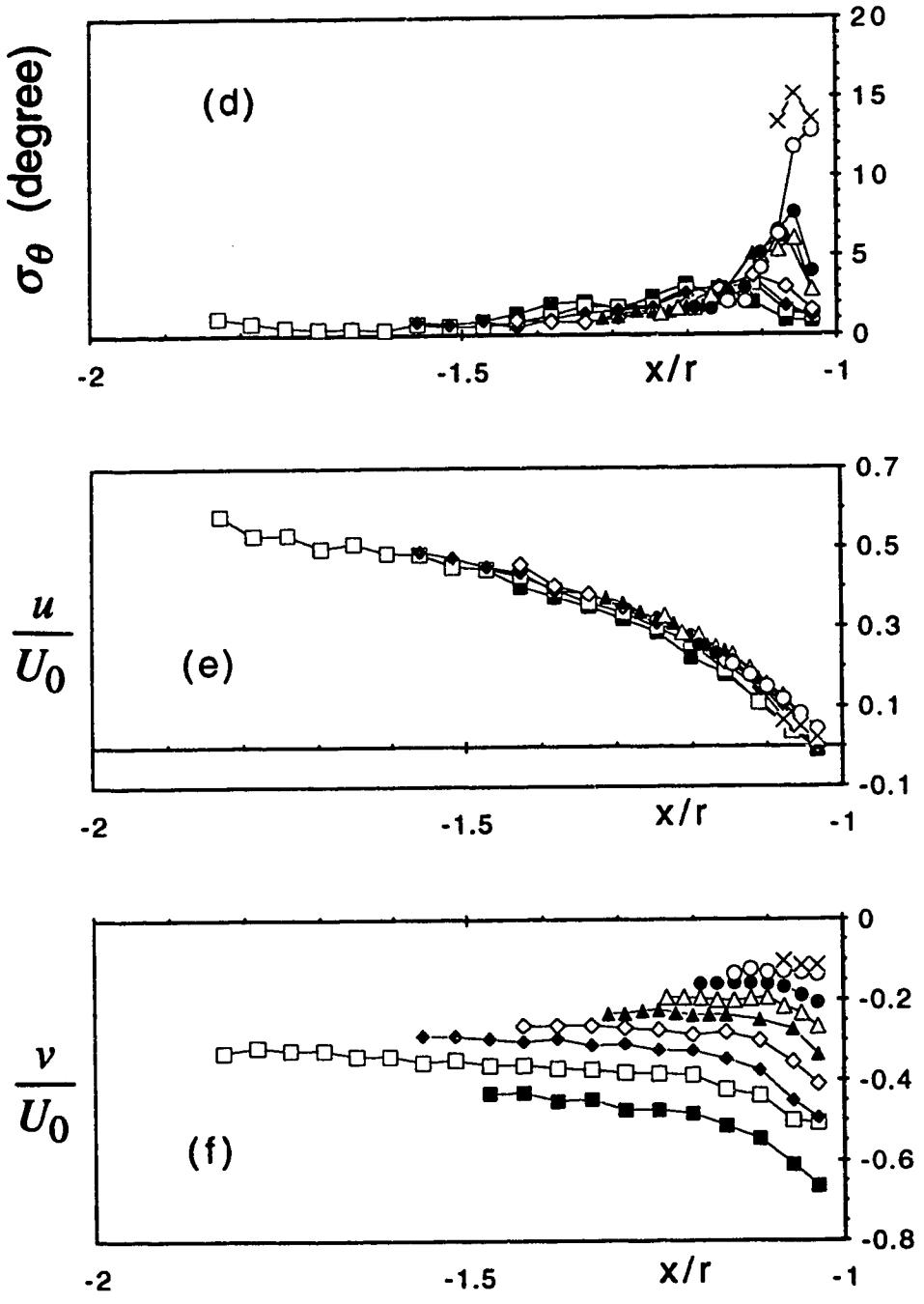

Figure 4.2.17 (a-h) Downflow in front of the pier (Expt. C2M);
(d) fluctuation of pitch angle
(e) longitudinal component of velocity
(f) vertical component of velocity

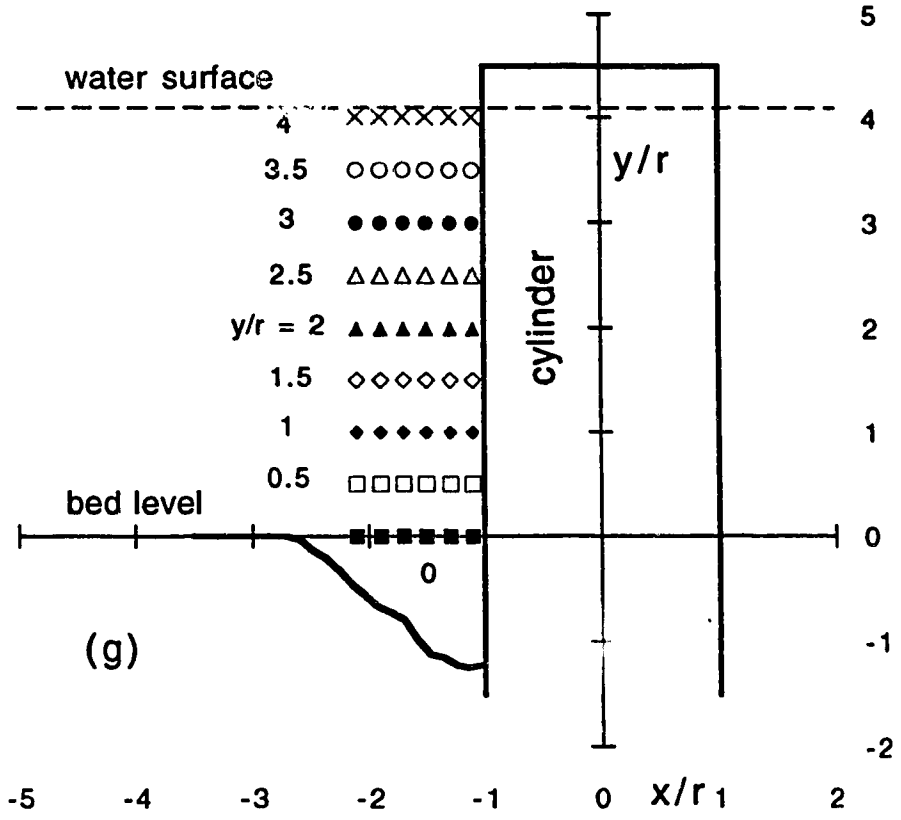

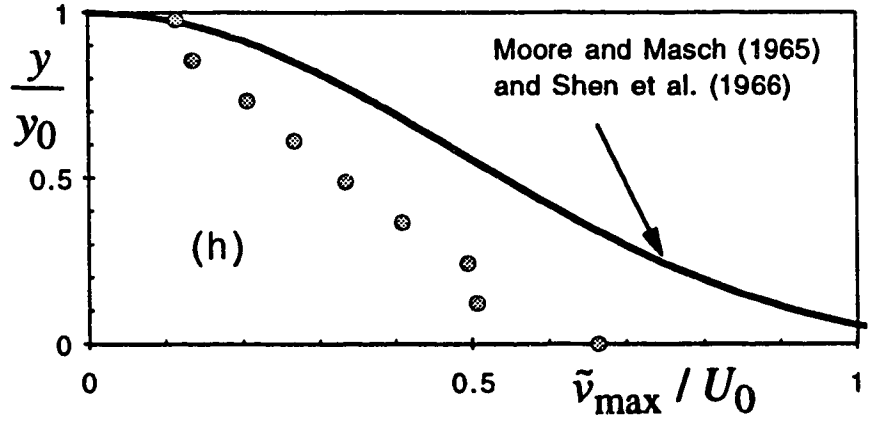

Figure 4.2.17 (a-h) Downflow in front of the pier (Expt. C2M);
(g) location of measurement lines
(h) variation of downflow with depth

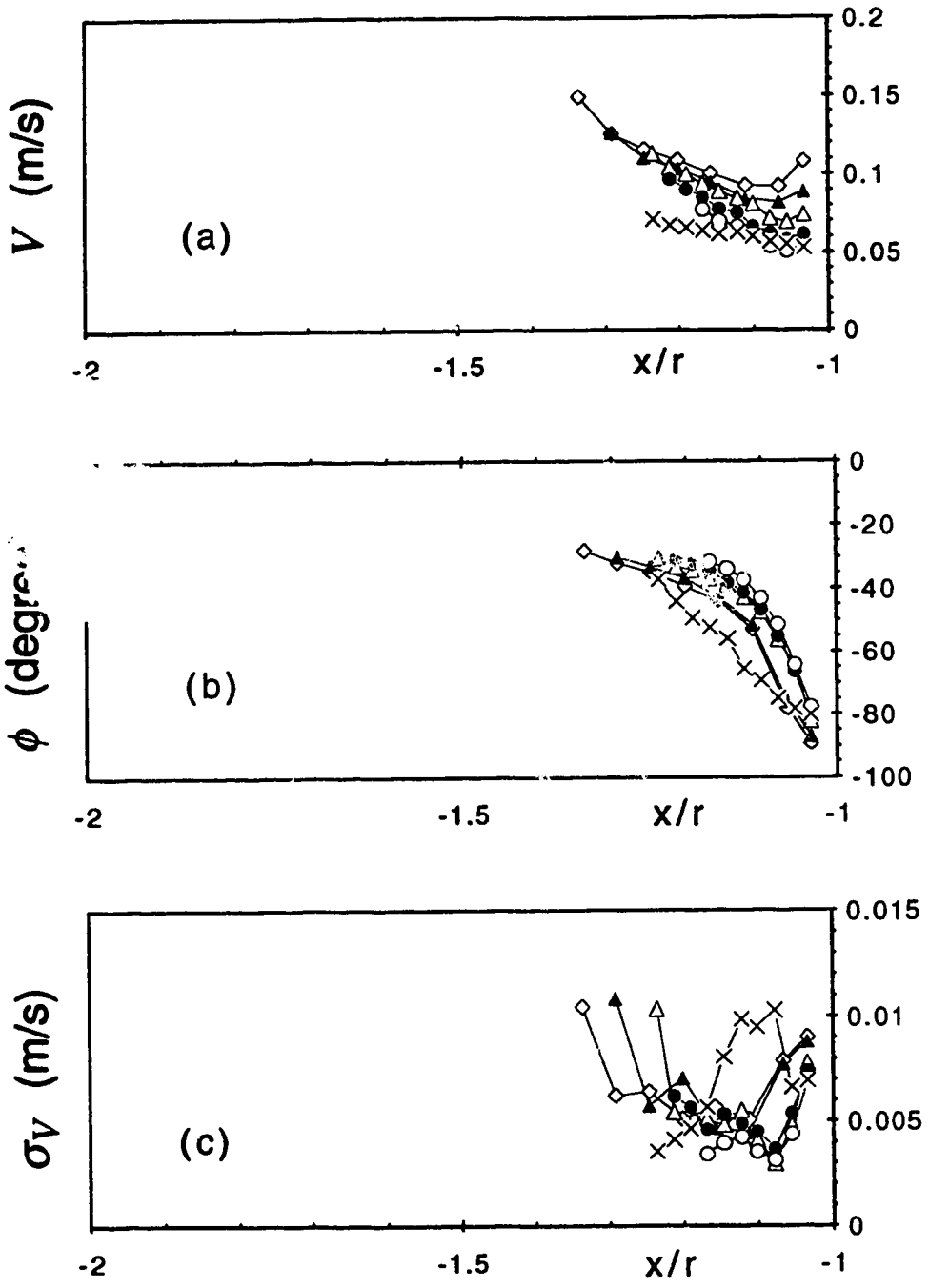

Figure 4.2.18 (a-f) Downflow in front of the pier (Expt. C2R);
(a) velocity magnitude
(b) angle of pitch
(c) fluctuation of velocity
Note: symbols same as Figure 4.2.17

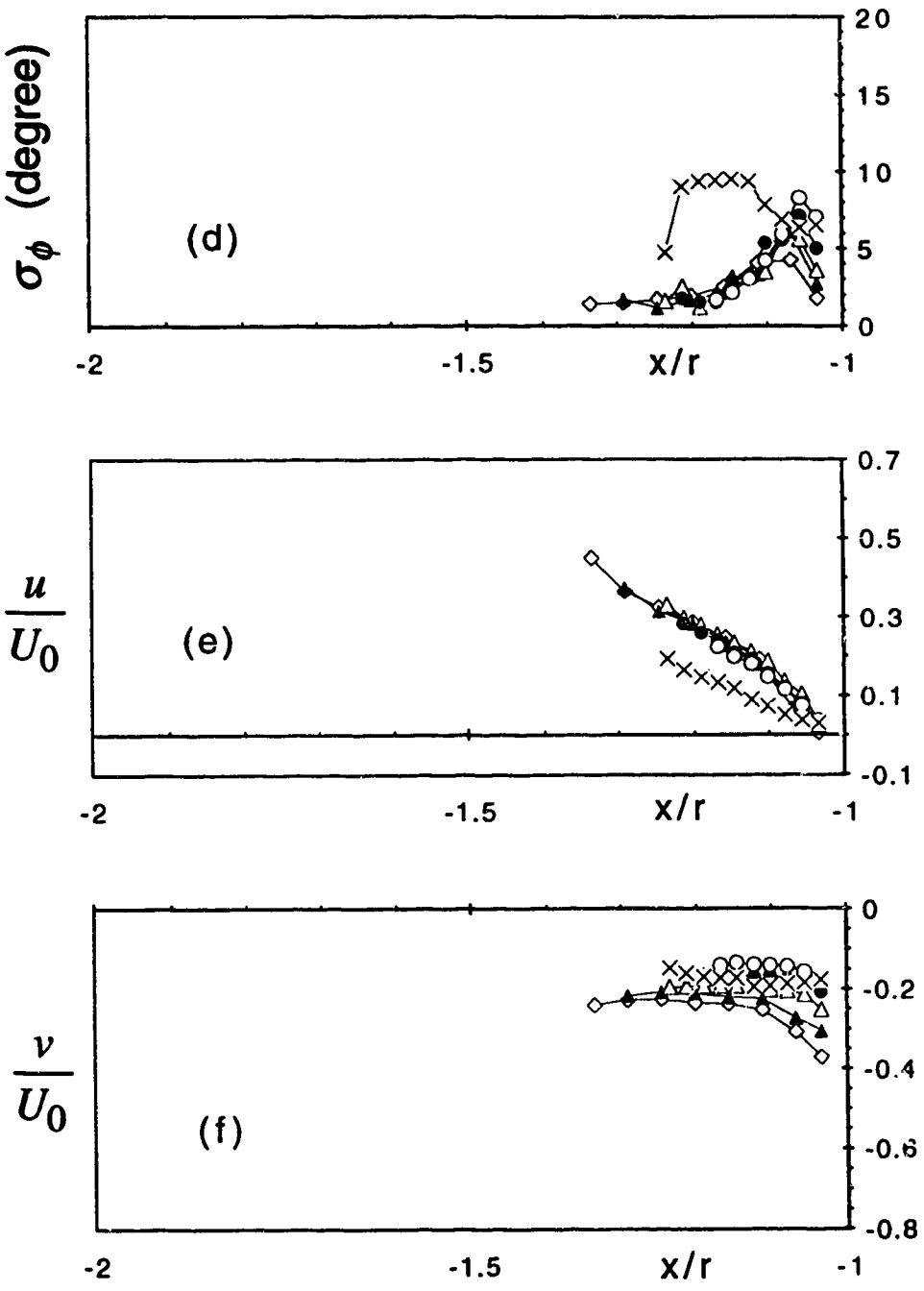

Figure 4.2.18 (a-f) Downflow in front of the pier (Expt. C2R);
(d) fluctuation of pitch angle
(e) longitudinal component of velocity
(f) vertical component of velocity
Note: symbols same as Figure 4.2.17

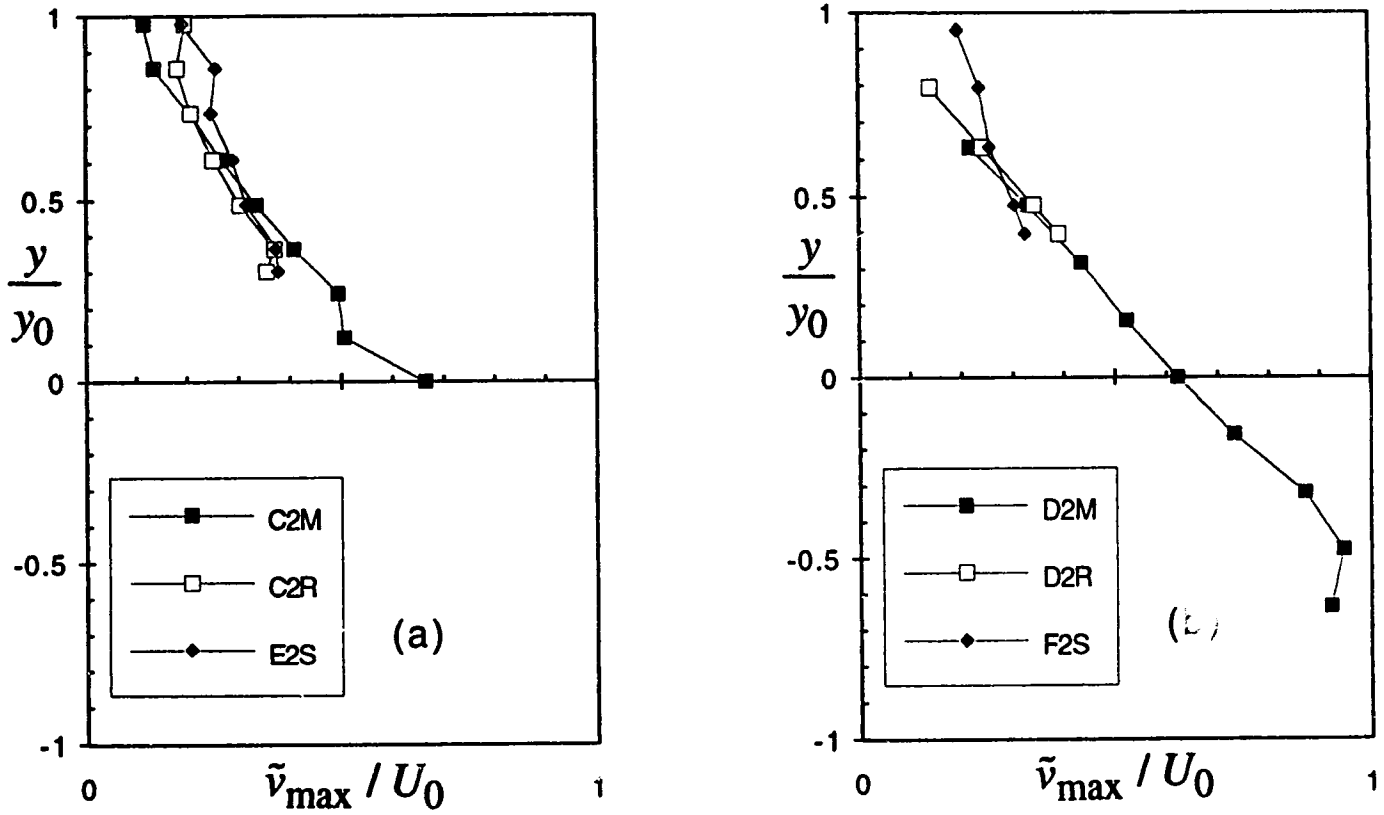

Figure 4.2.19 Variation of maximum downflow velocity with depth
(a) Expt. C2M, C2R and E2S; (b) Expt. D2M, D2R and F2S

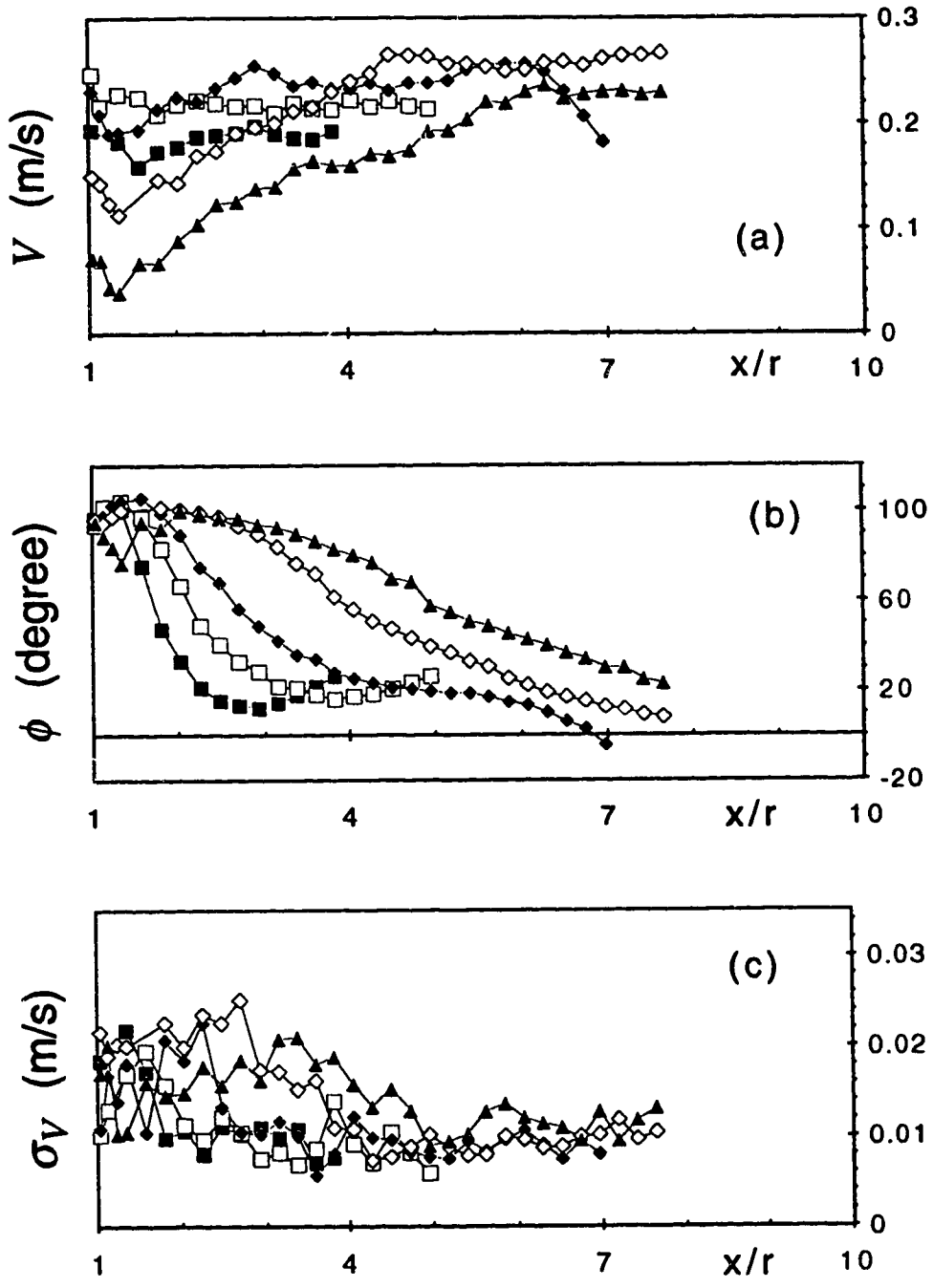

Figure 4.2.20 (a-g) Flow along horizontal lines downstream of the pier (Expt. C2M);
(a) velocity magnitude
(b) angle of pitch
(c) fluctuation of velocity

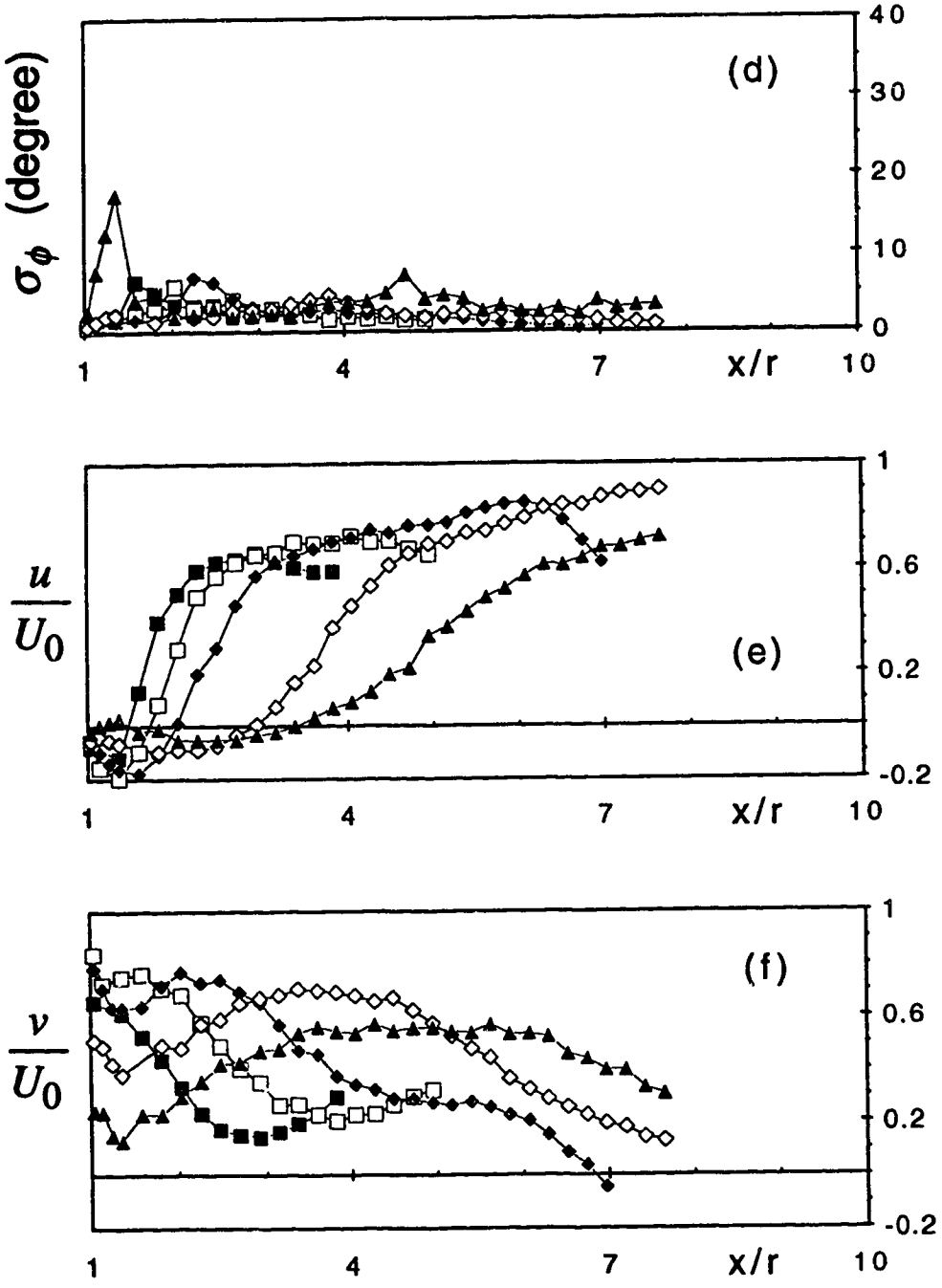

Figure 4.2.20 (a-g) Flow along horizontal lines downstream of the pier (Expt. C2M);
(d) fluctuation of pitch angle
(e) longitudinal component of velocity
(f) vertical component of velocity

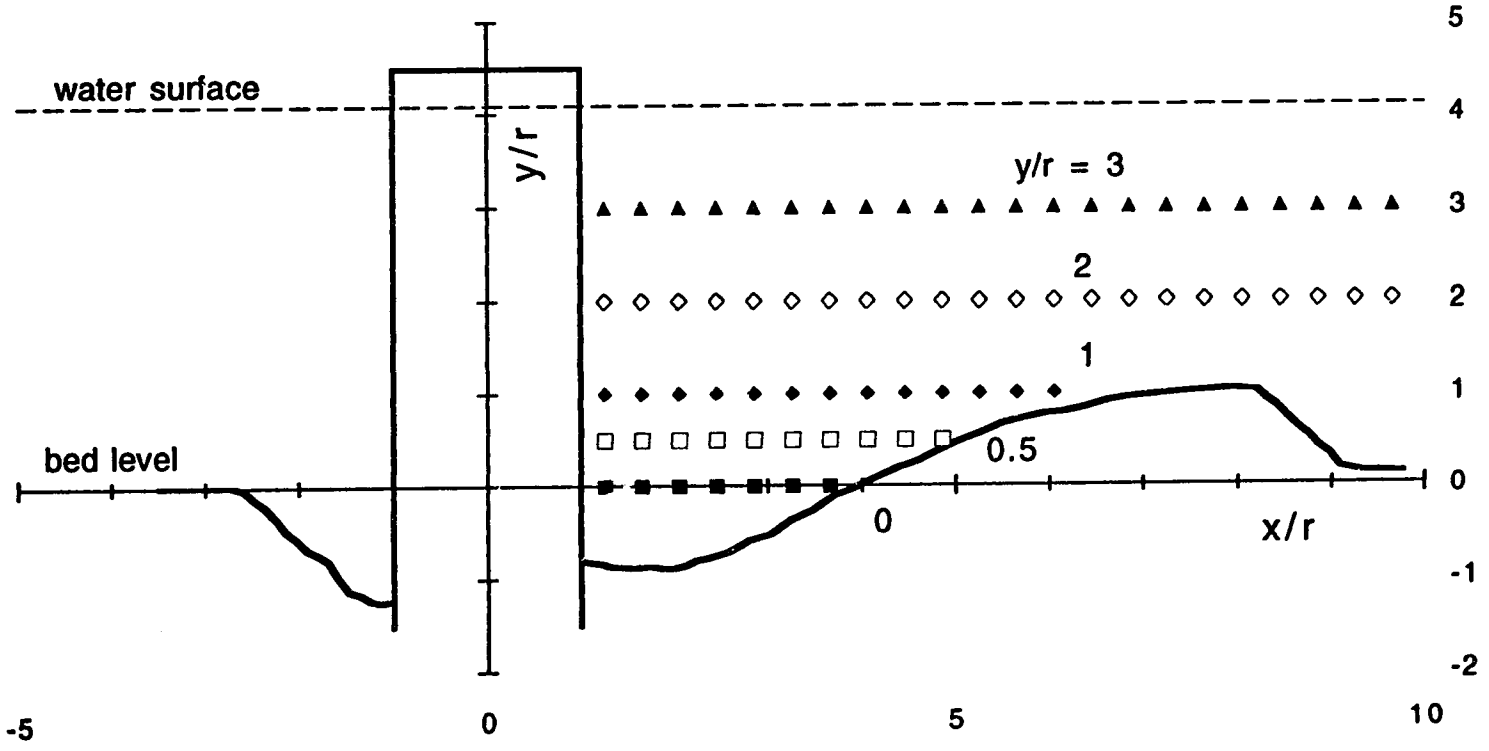

Figure 4.2.20 (a-g) Flow along horizontal lines downstream of the pier (Expt. C2M); (g) location of measurement lines

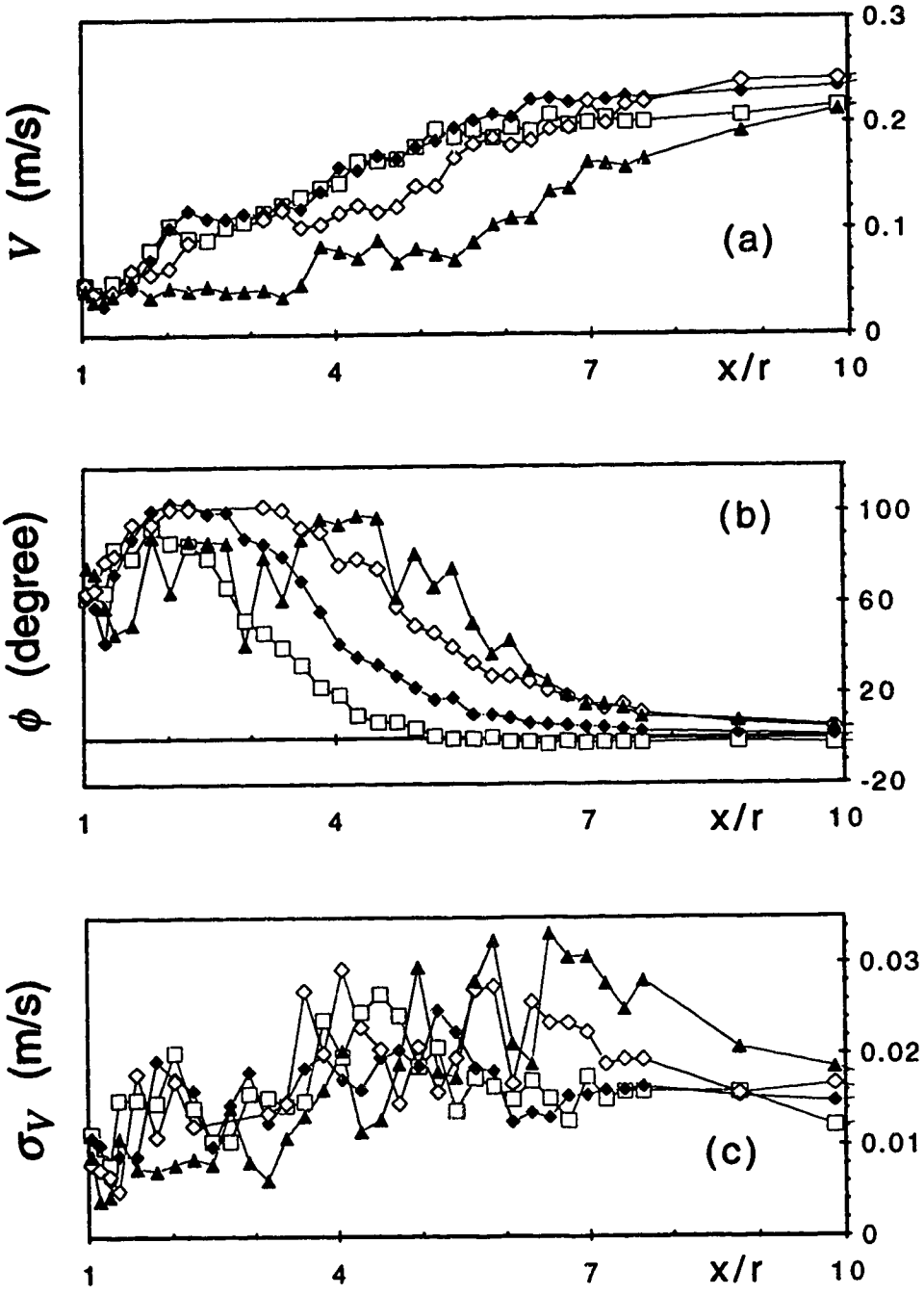

Figure 4.2.21 (a-f) Flow along horizontal lines downstream of the pier (Expt. C2R);
(a) velocity magnitude
(b) angle of pitch
(c) fluctuation of velocity
Note: symbols same as Figure 4.2.20

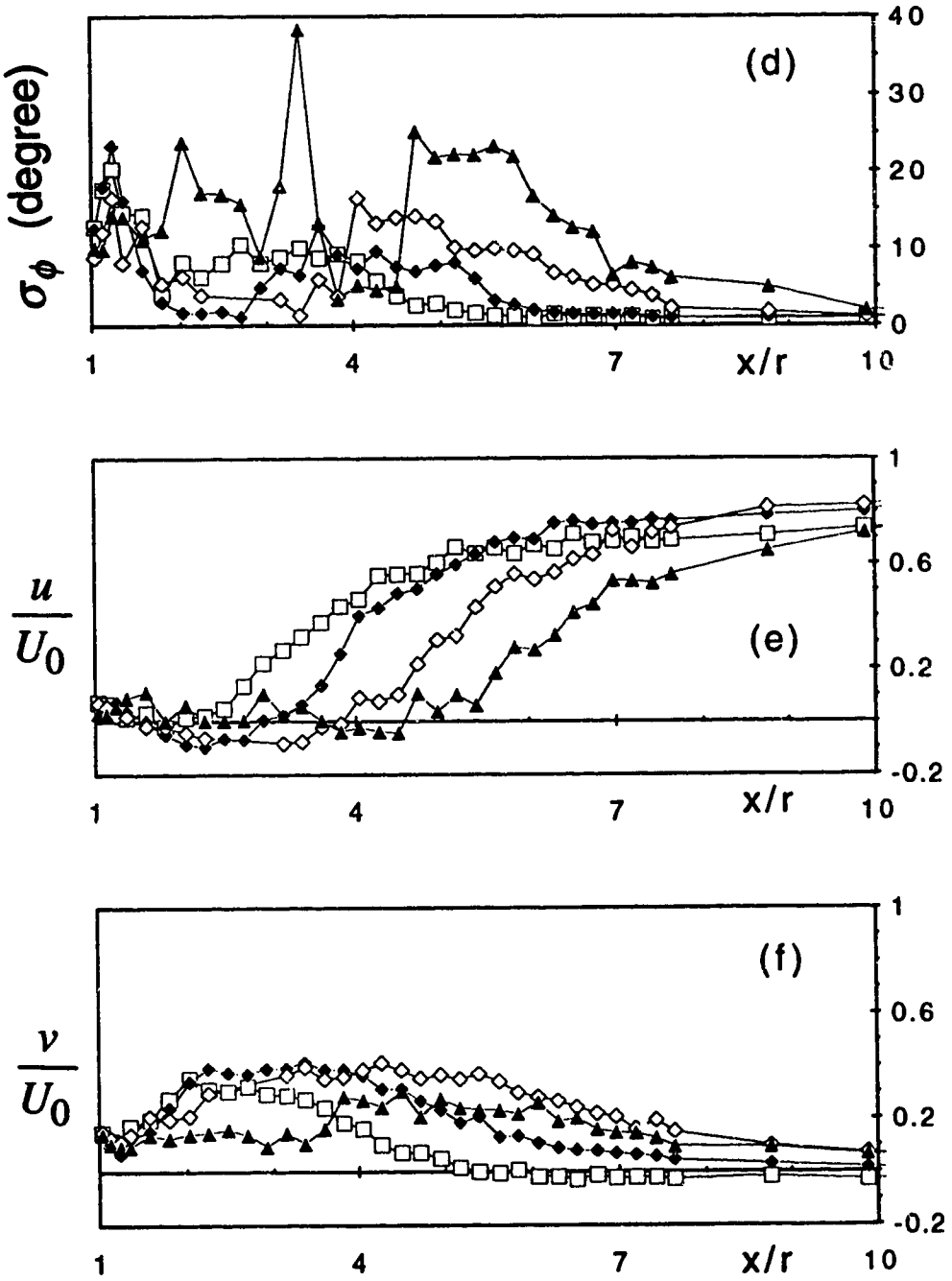

Figure 4.2.21 (a-f) Flow along horizontal lines downstream of the pier (Expt. C2R);
(d) fluctuation of pitch angle
(e) longitudinal component of velocity
(f) vertical component of velocity
Note: symbols same as Figure 4.2.20

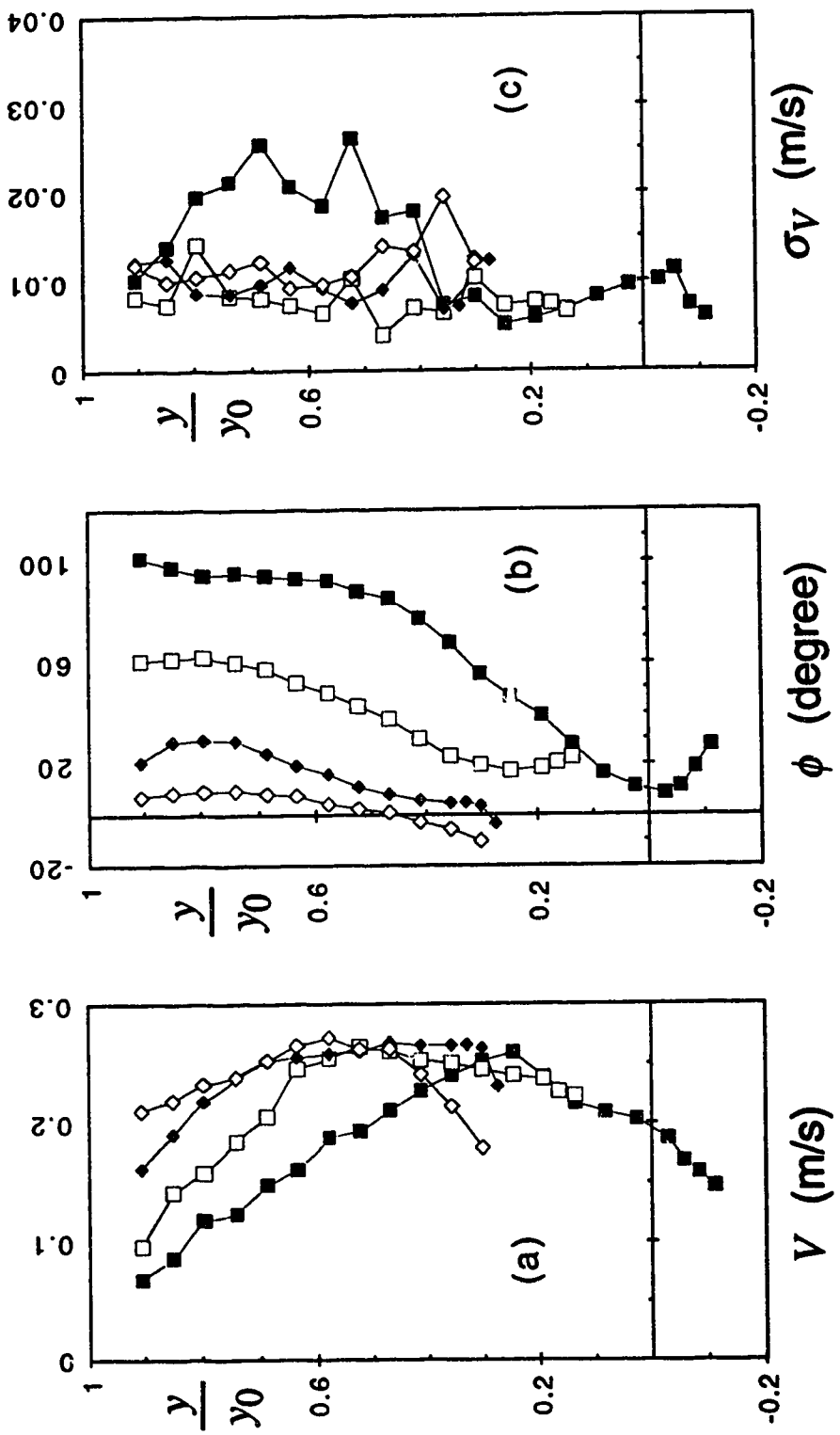

Figure 4.2.22 (a-g) Flow along vertical lines downstream of the pier (Expt. C2M);
(a) velocity magnitude; (b) angle of pitch; (c) fluctuation of velocity

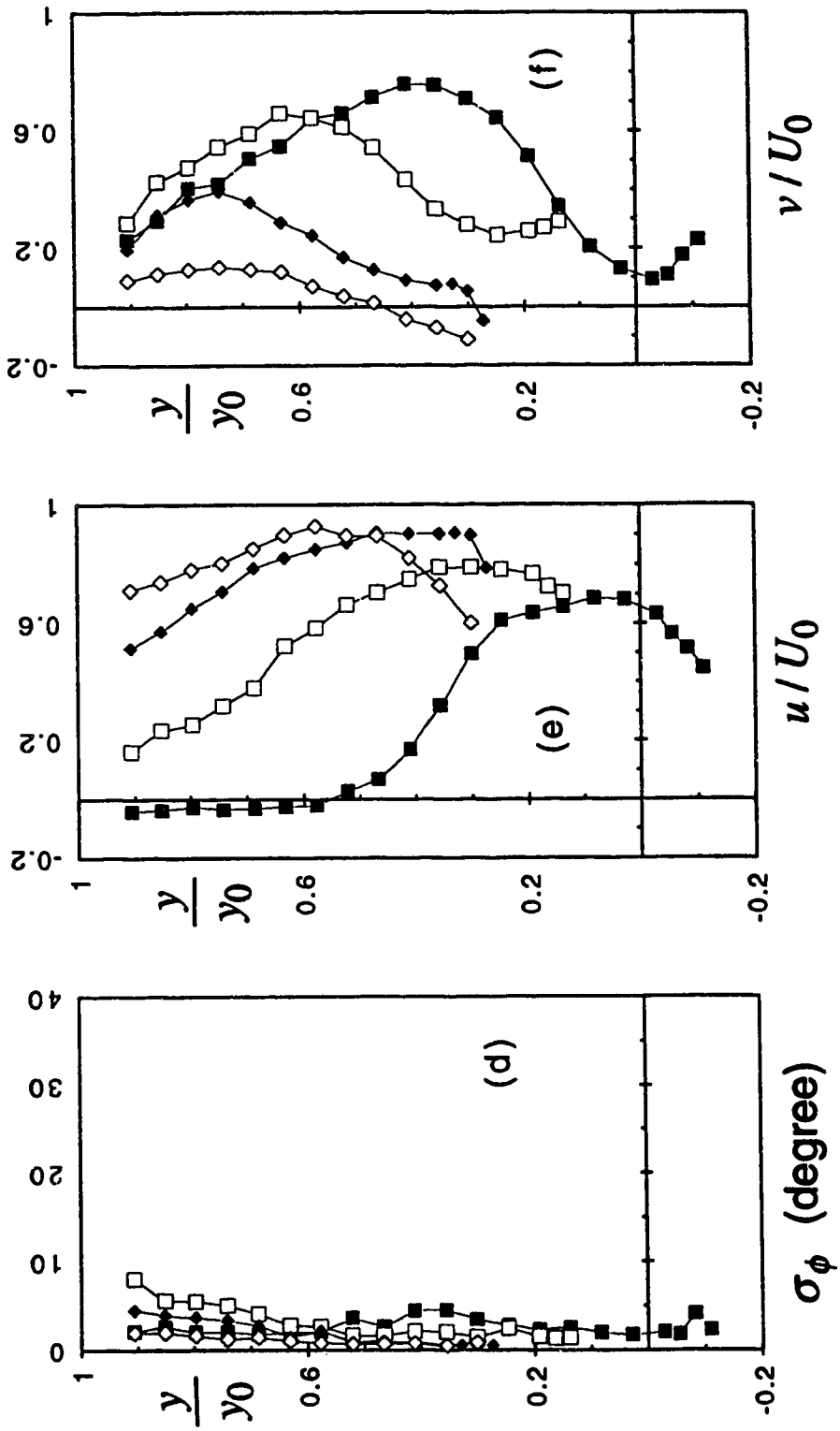

Figure 4.2.22 (a-g) Flow along vertical lines downstream of the pier (Expt. C2M);
(d) fluctuation of pitch angle; (e) vertical component of velocity;
(f) vertical component of velocity

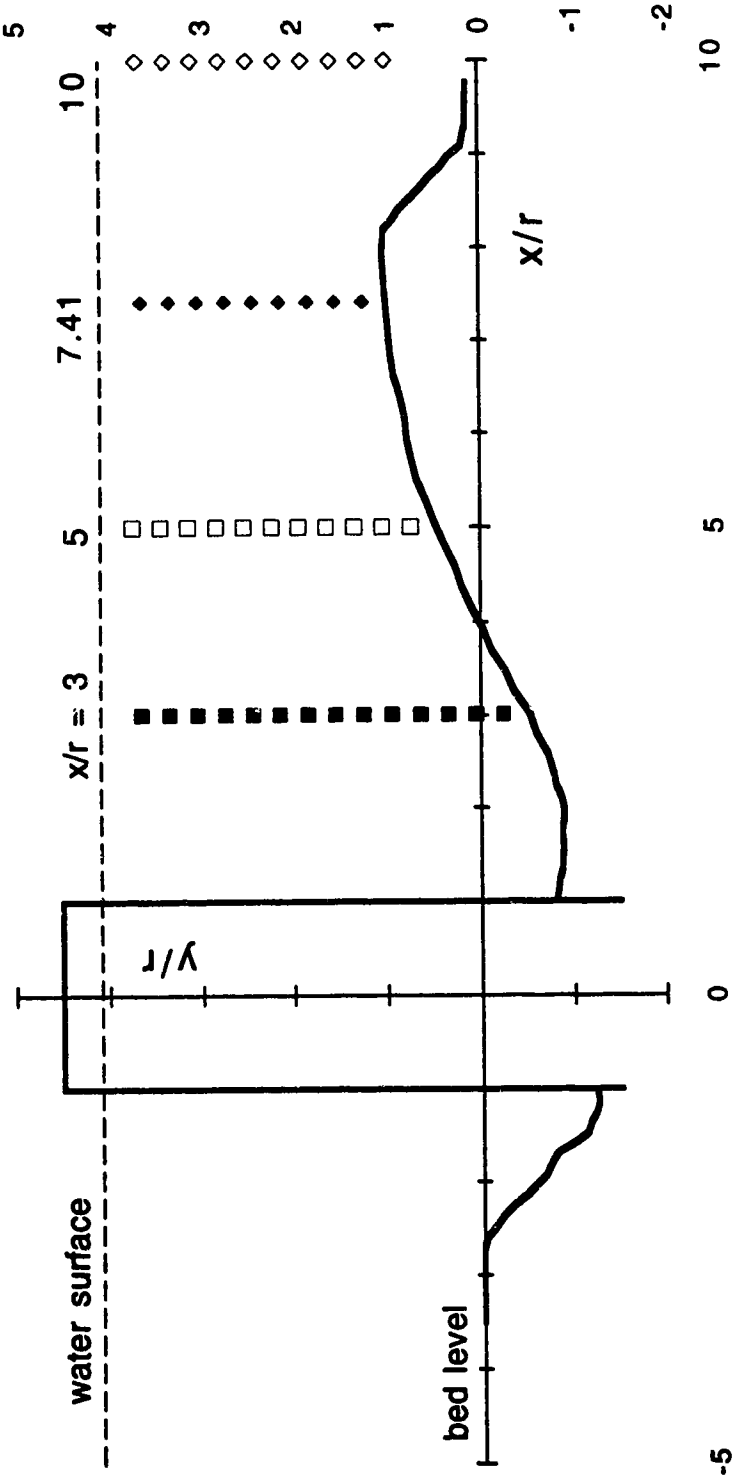

Figure 4.2.22 (a-g) Flow along vertical lines downstream of the pier (Expt. C2M); (g) location of measurement lines

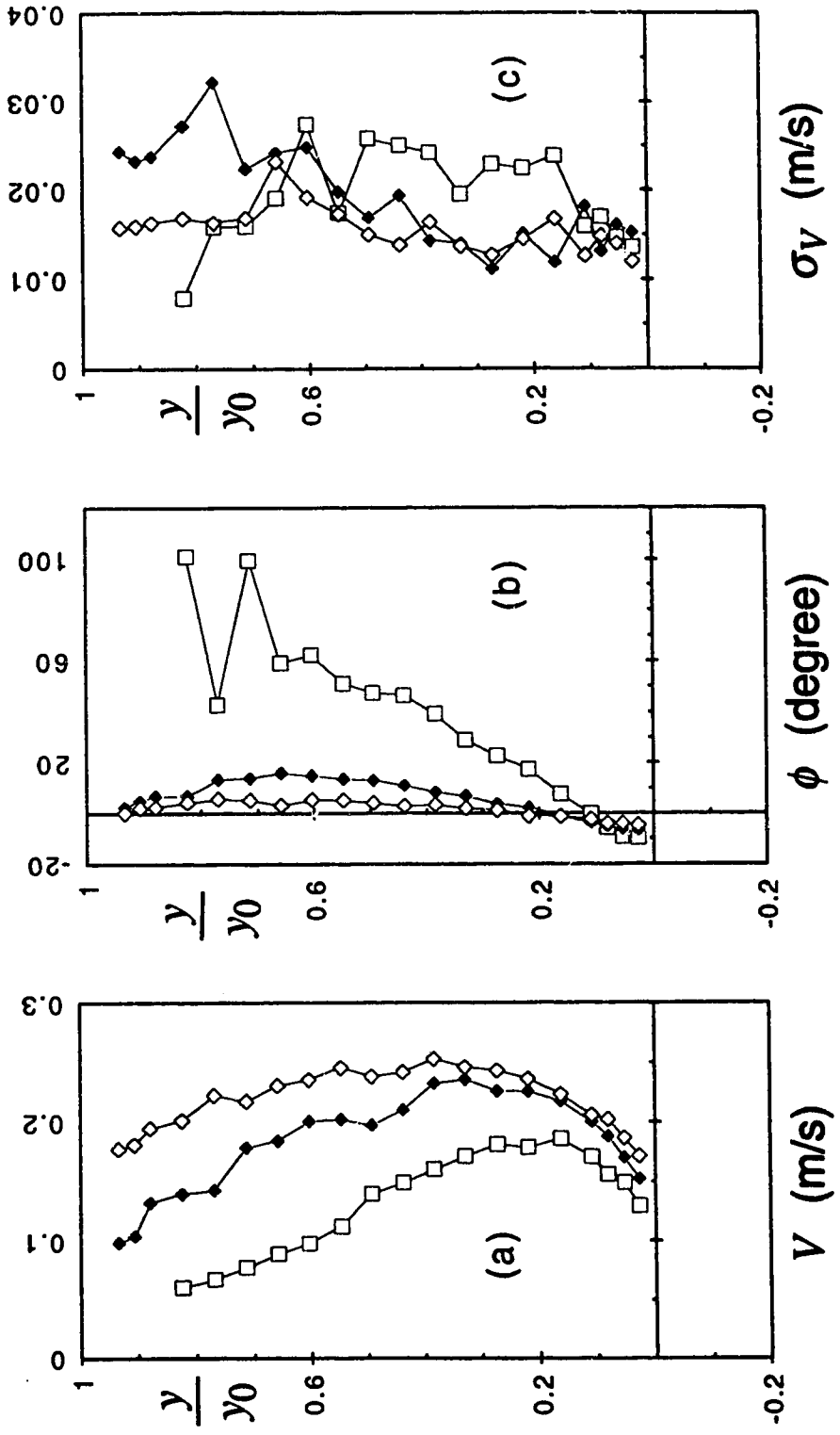

Figure 4.2.23 (a-f) Flow along vertical lines downstream of the pier (Expt. C2R);
(a) velocity magnitude; (b) angle of pitch; (c) fluctuation of velocity
Note: symbols same as Figure 4.2.22

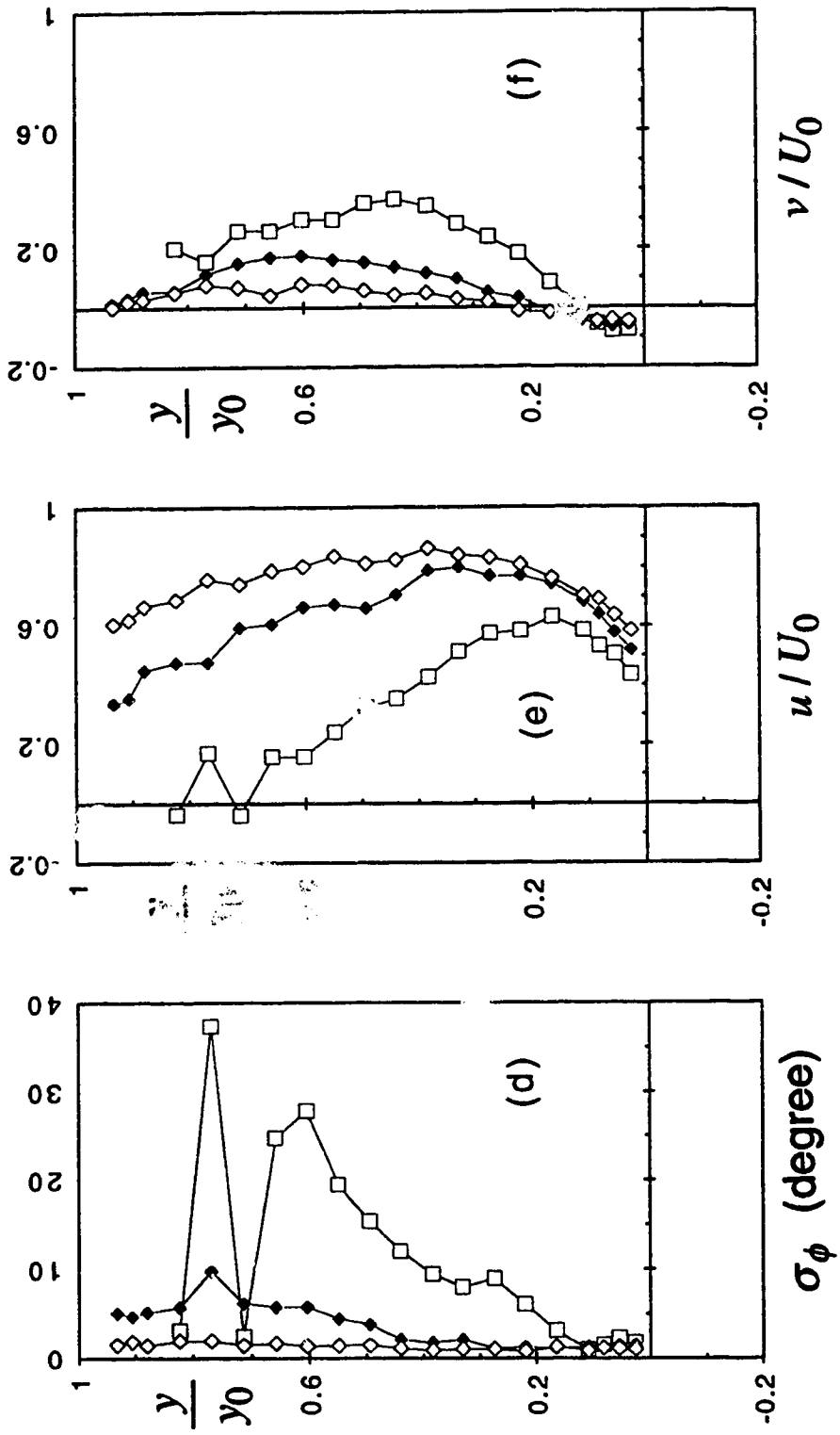

Figure 4.2.23 (a-f) Flow along vertical lines downstream of the pier (Expt. C2R);
(d) fluctuation of pitch angle; (e) vertical component of velocity;
(f) vertical component of velocity
Note: symbols same as Figure 4.2.22

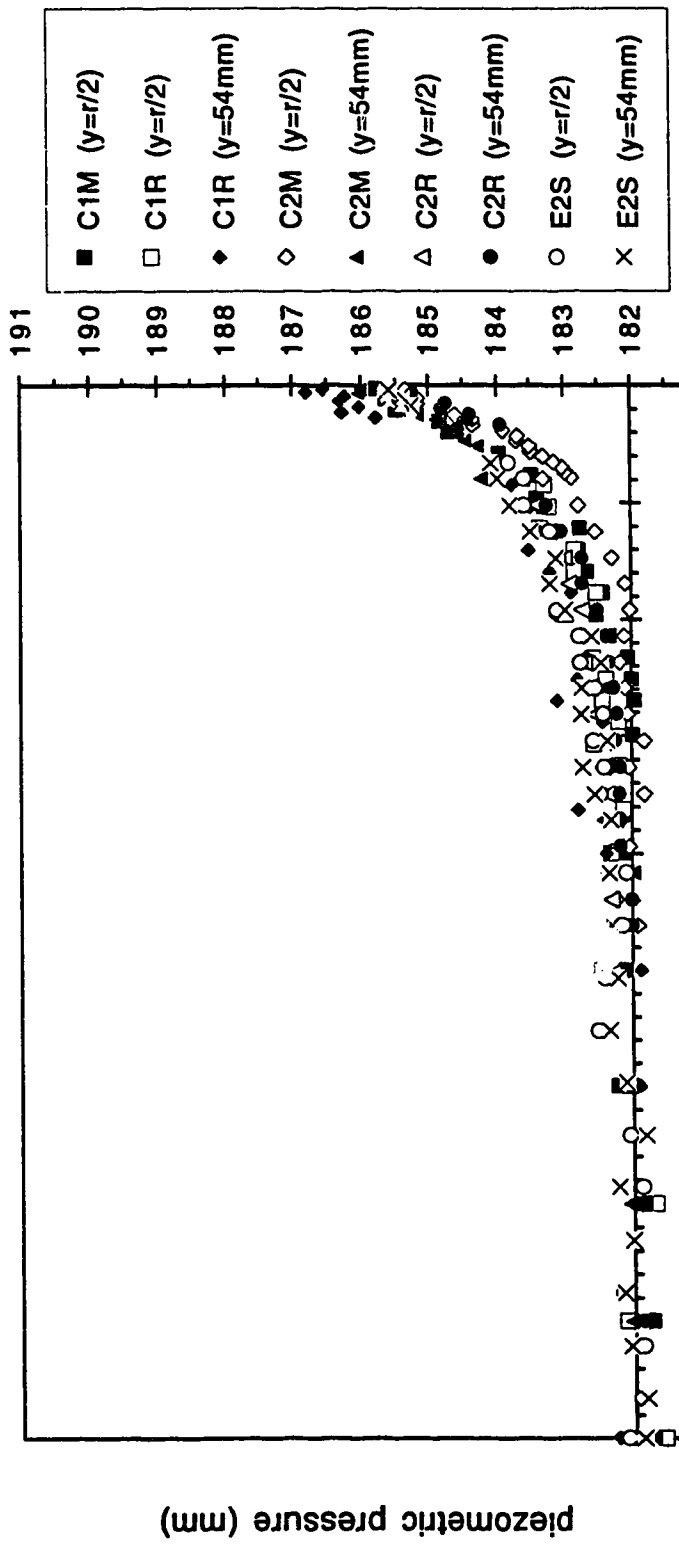

Figure 4.3.1 (a-b) Pressure distribution in the upstream region
(a) Series C and E

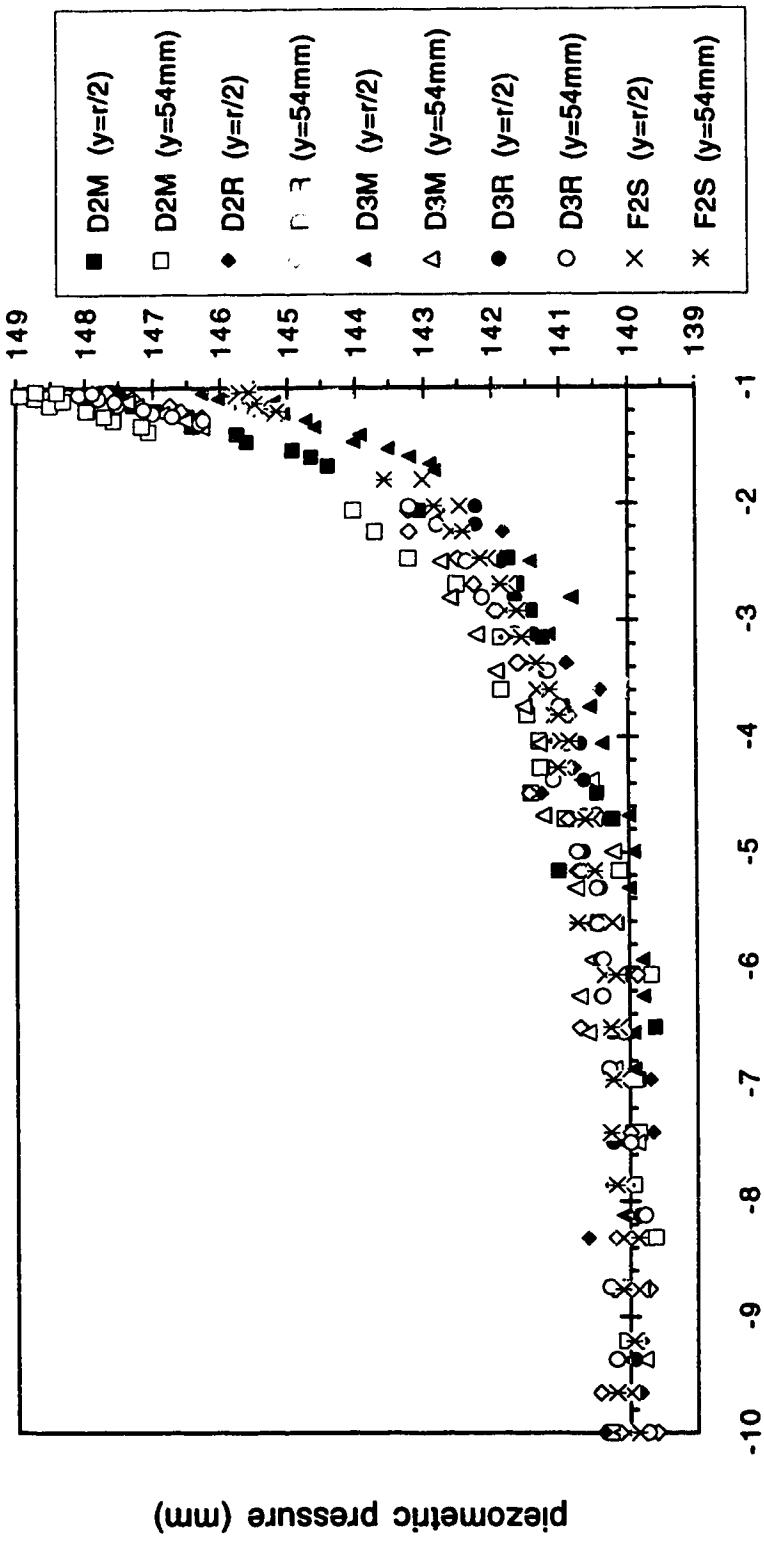

Figure 4.3.1 (a-b) Pressure distribution in the upstream region
(b) Series D and F

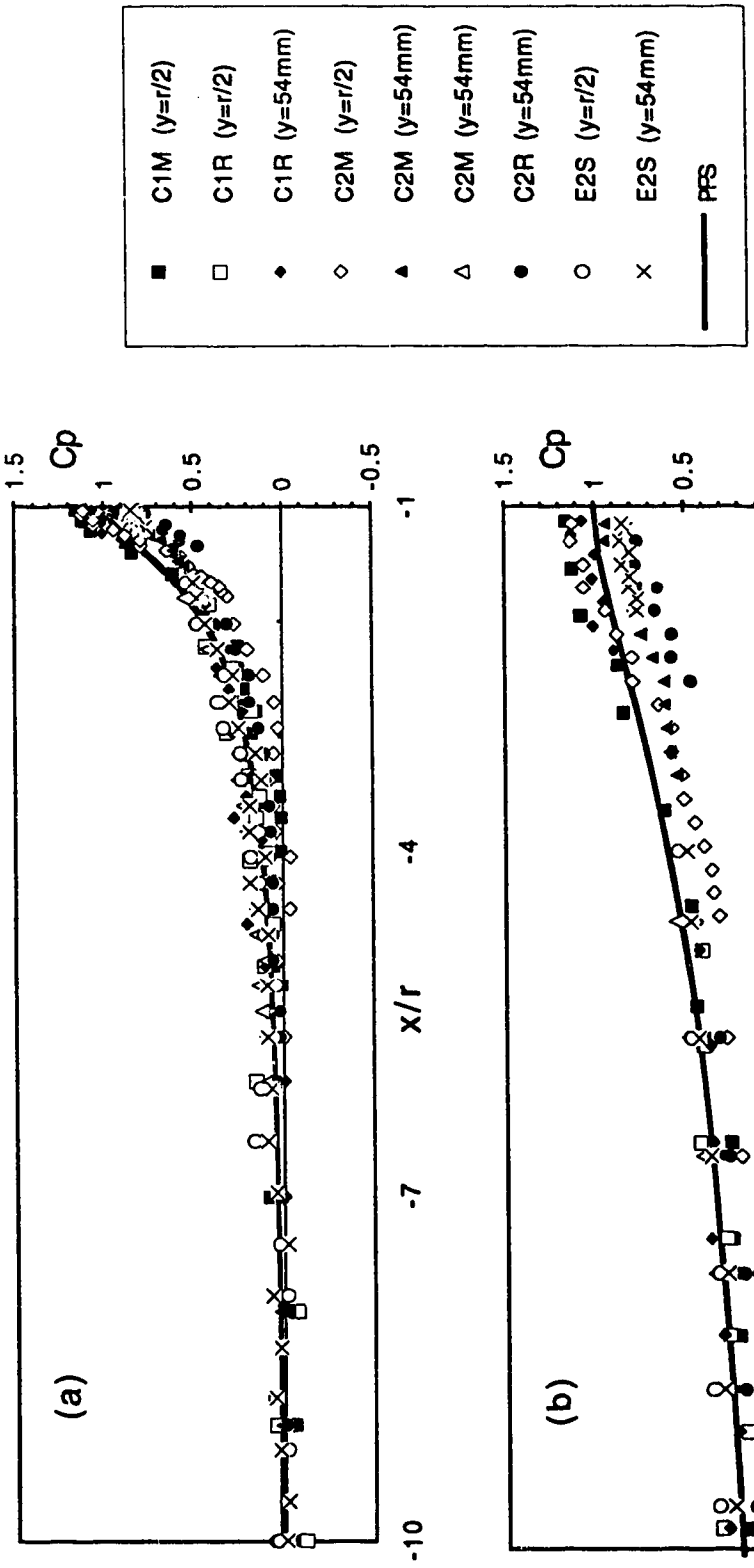

Figure 4.3.2 (a-d) Variation of pressure coefficient in the upstream region
(a) Series C and E; (b) Series C and E (details near the cylinder)

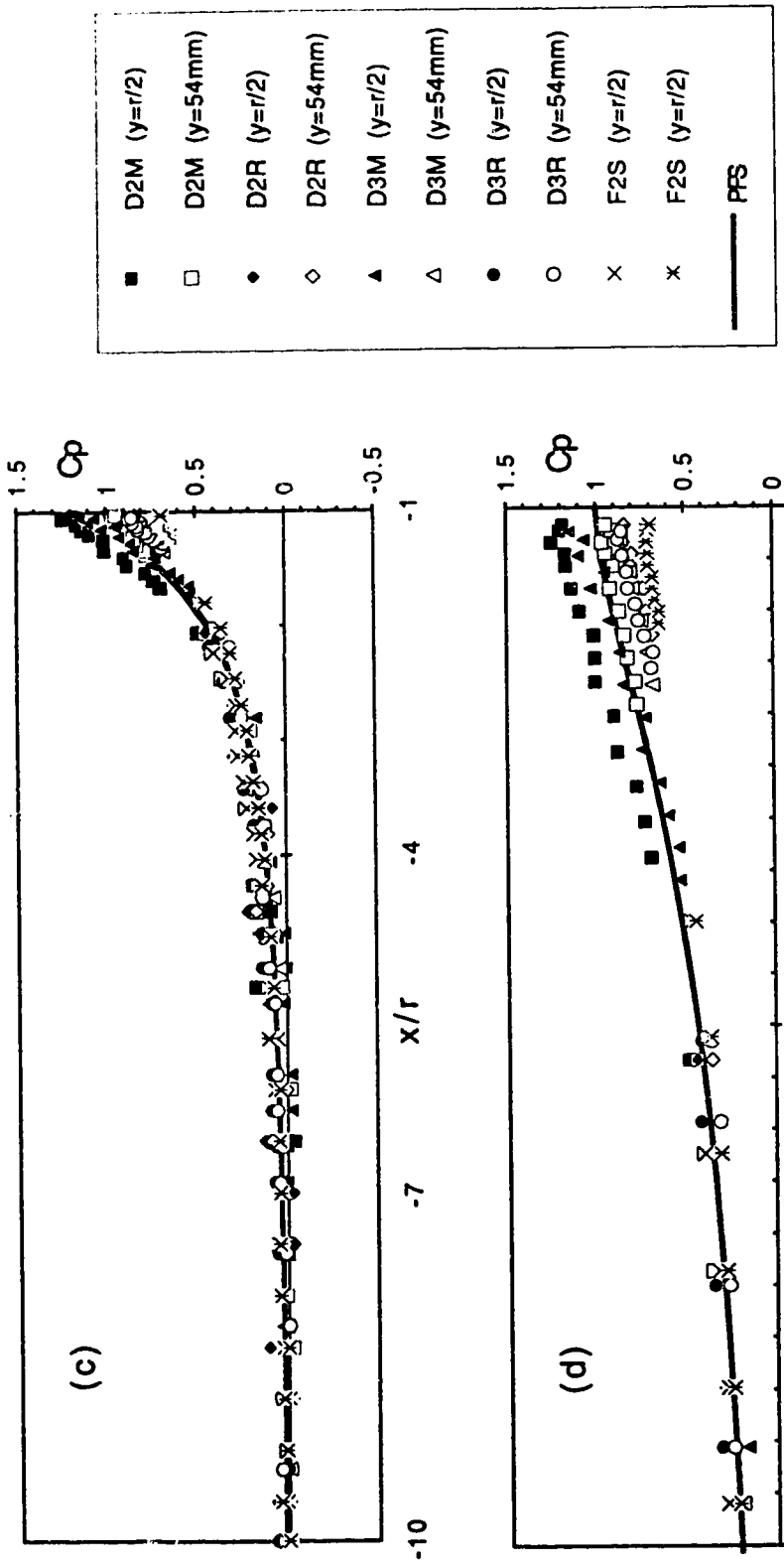

Figure 4.3.2 (a-d) Variation of pressure coefficient in the upstream region
(c) Series D and F; (d) Series D and F (details near the cylinder)

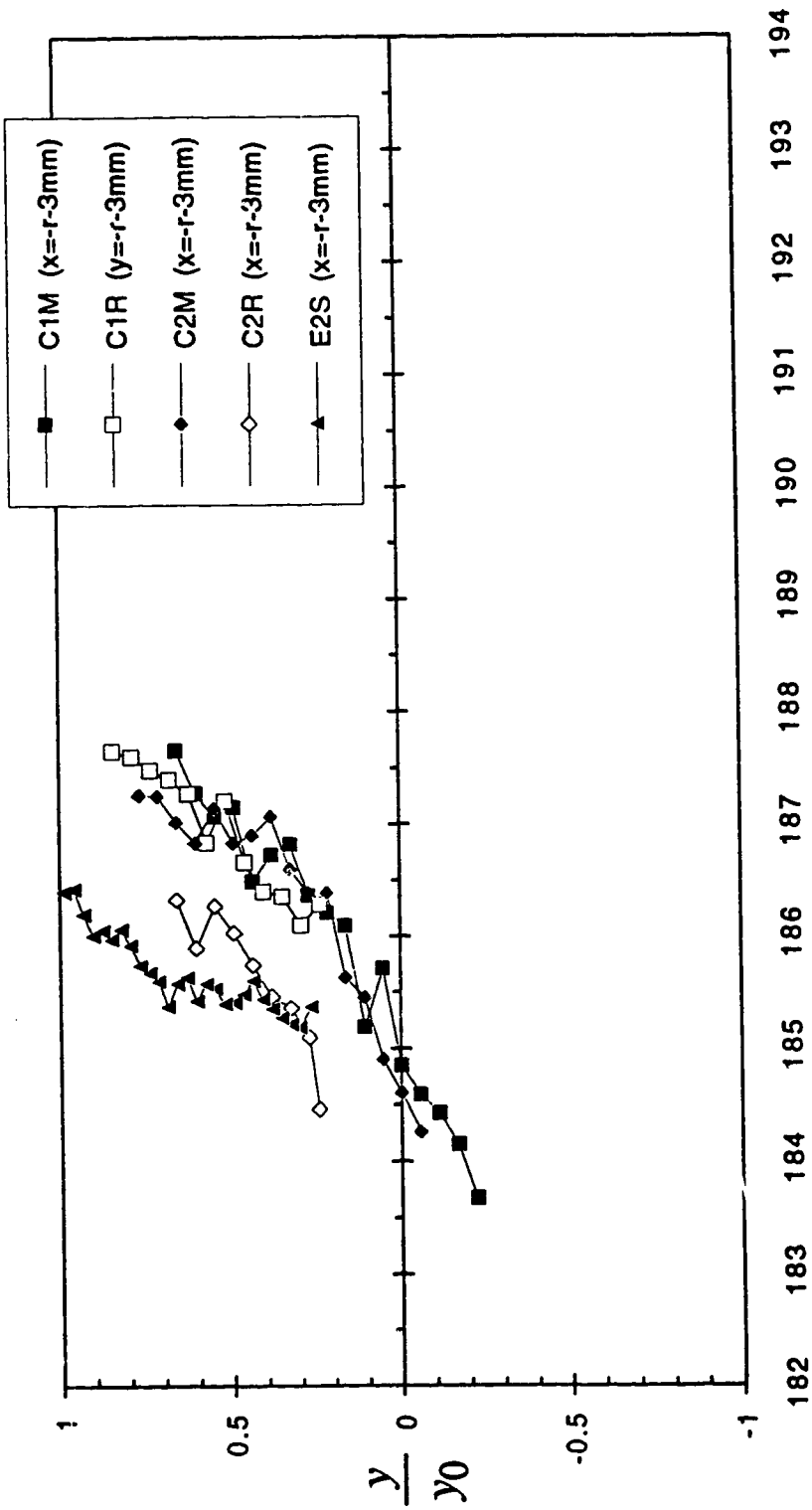

Figure 4.3.3 (a-b) Pressure distribution in front of the cylinder
(a) Series C and E

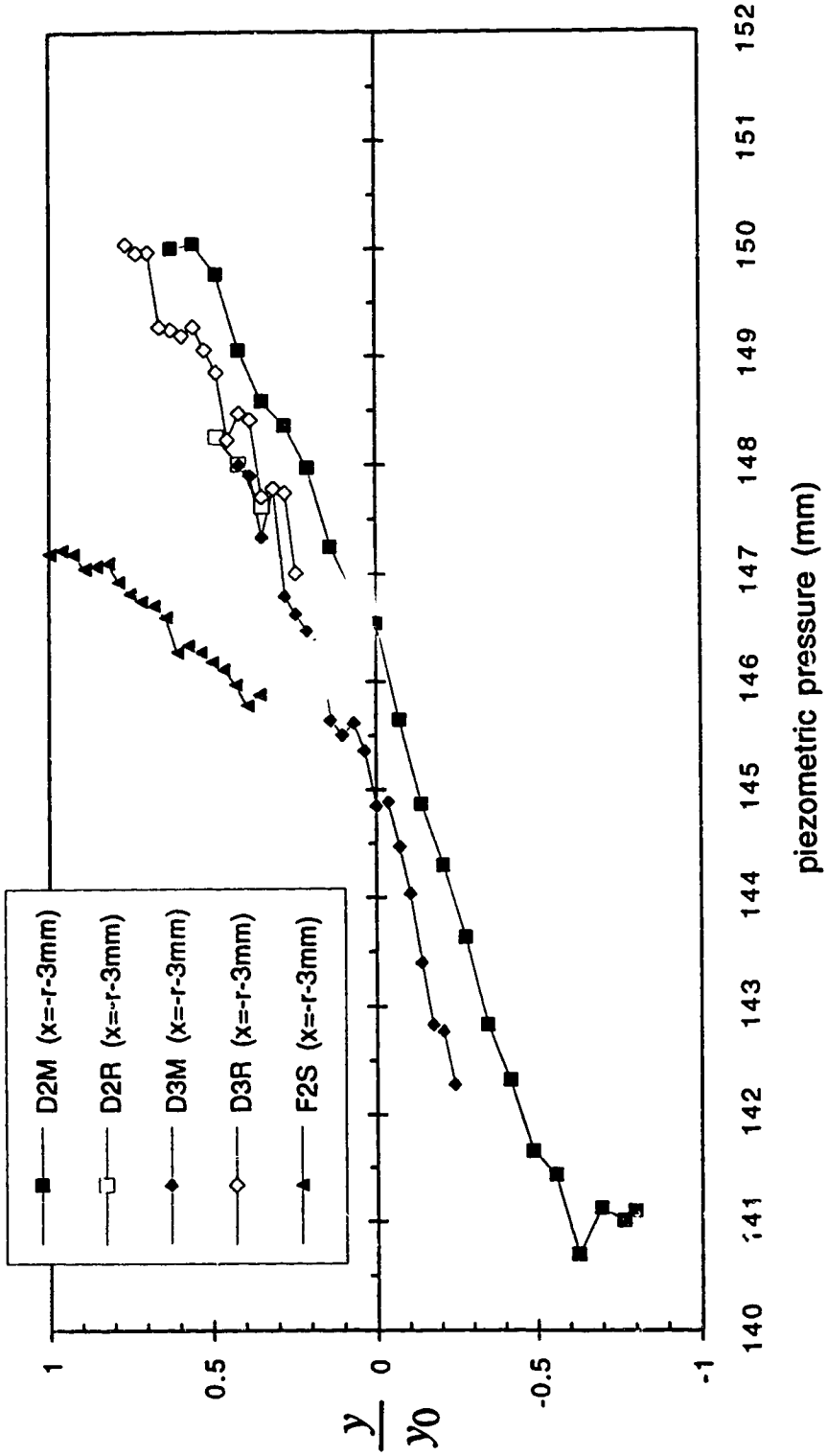

Figure 4.3.3 (a-b) Pressure distribution in front of the cylinder
(b) Series D and F

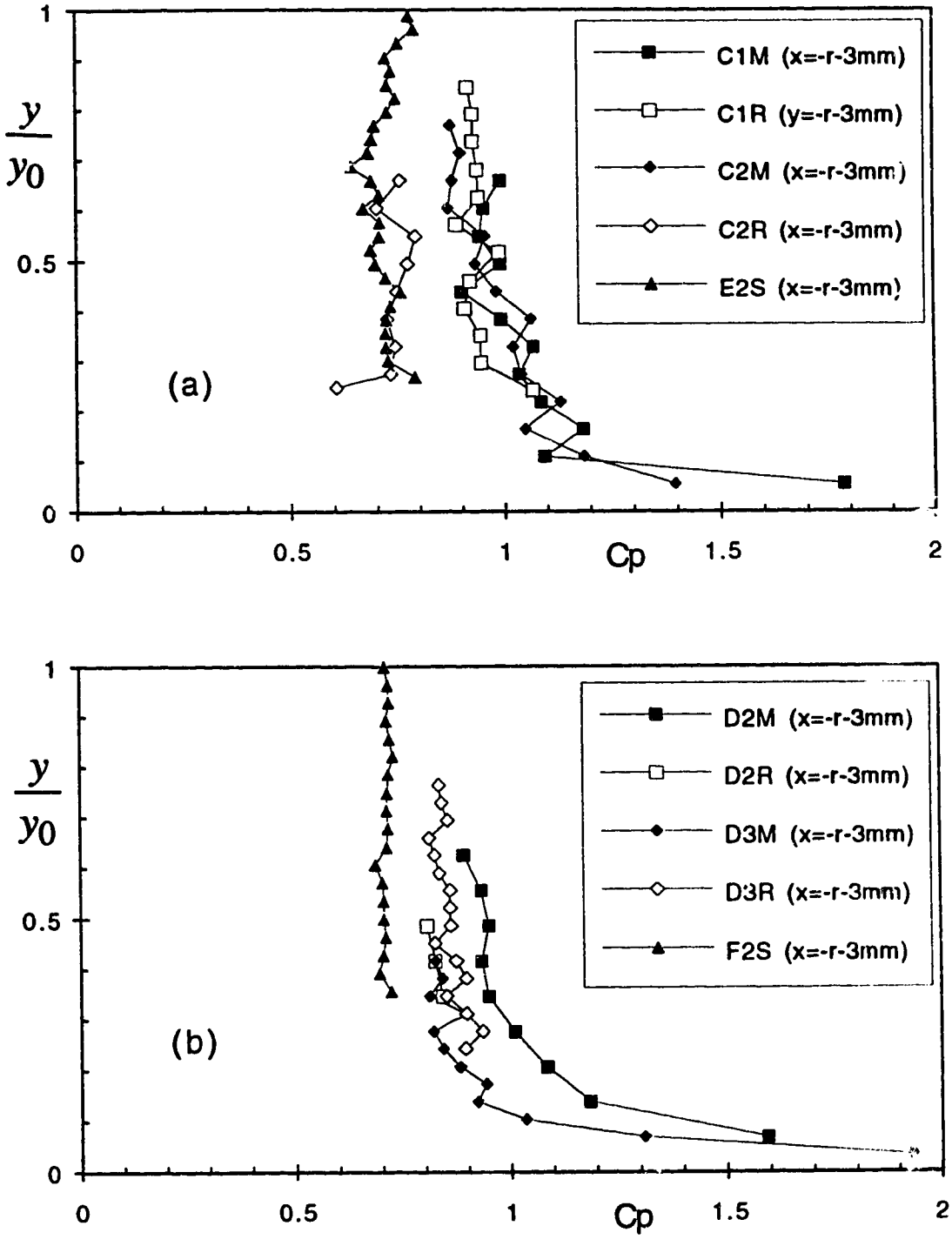

Figure 4.3.4 (a-b) Variation of pressure coefficient in front of the cylinder
(a) Series C and E; (b) Series D a

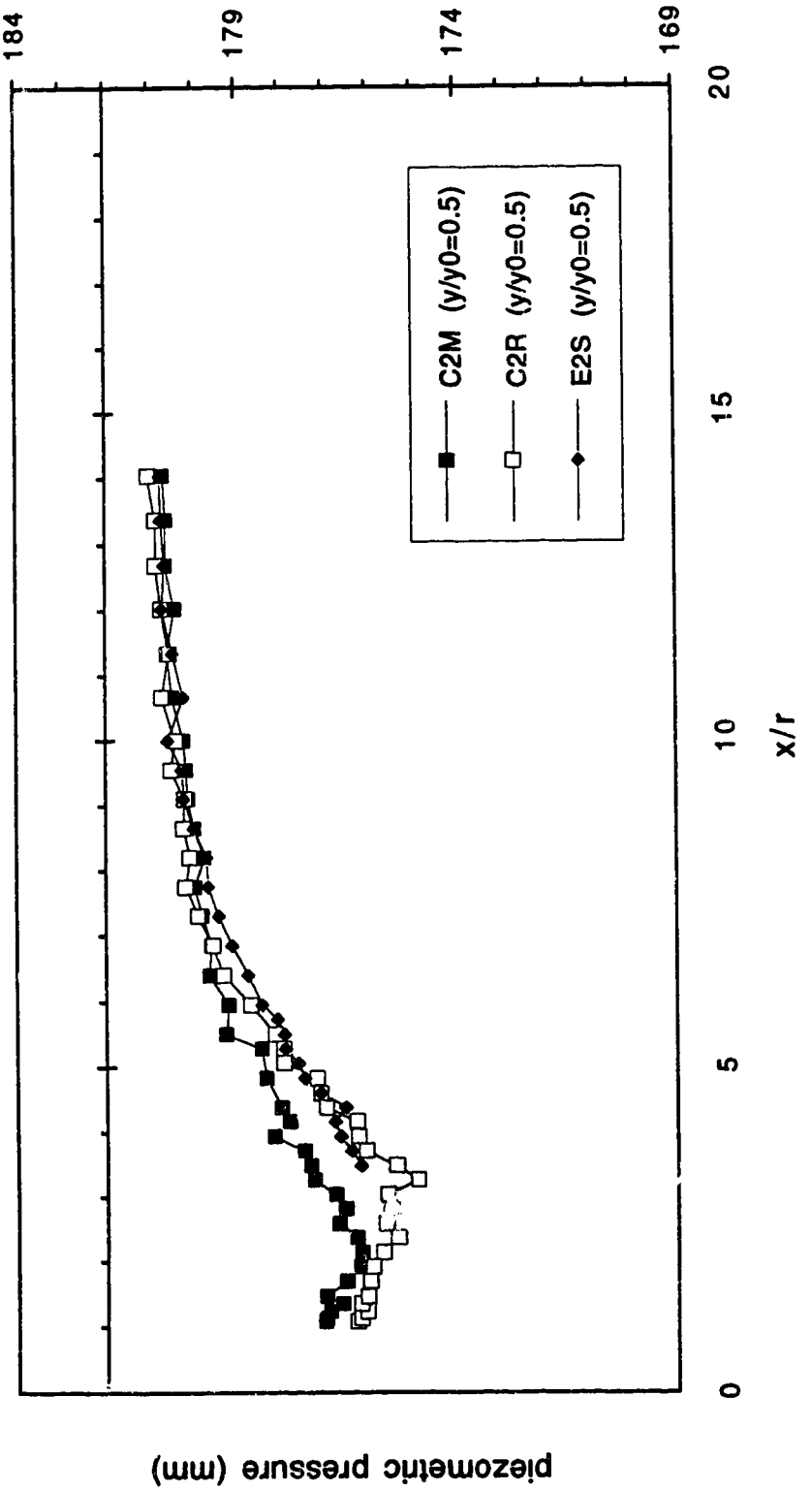

Figure 4.3.5 (a-b) Pressure distribution in the downstream region
(a) Series C and E

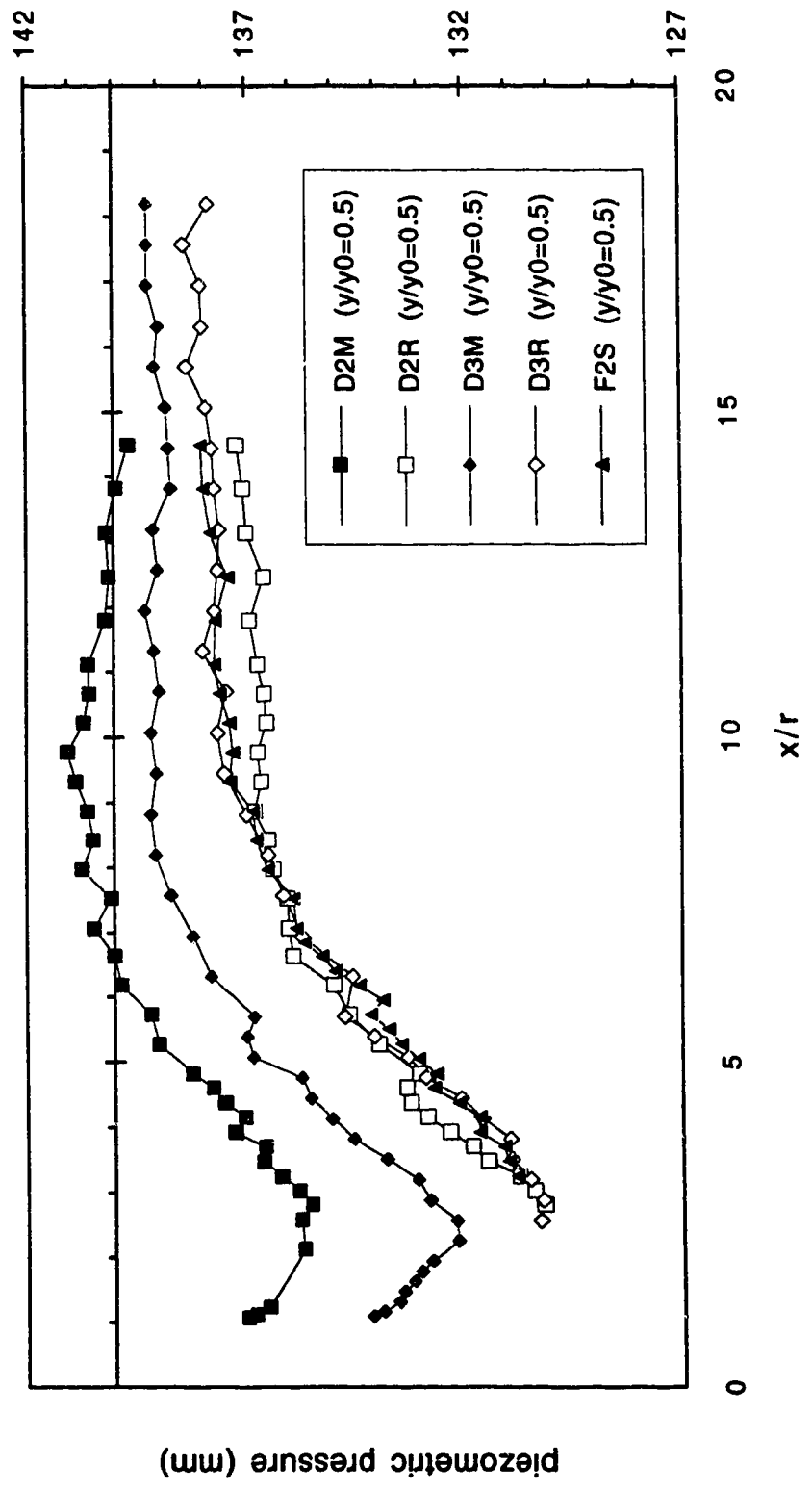

Figure 4.3.5 (a-b) Pressure distribution in the downstream region
(b) Series D and F

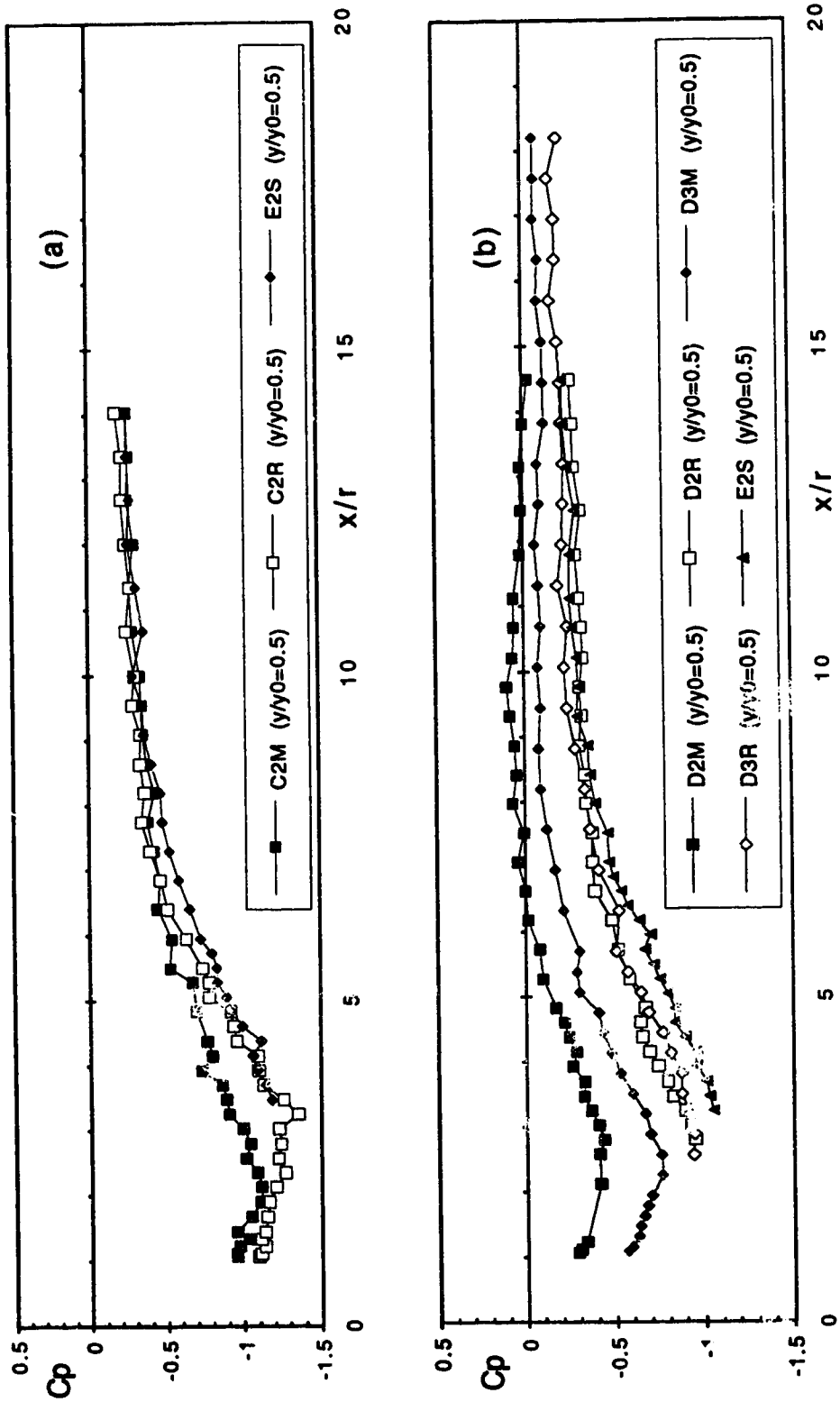

Figure 4.3.6 (a-b) Variation of pressure coefficient in the downstream region
(a) Series C and E; (b) Series D and F

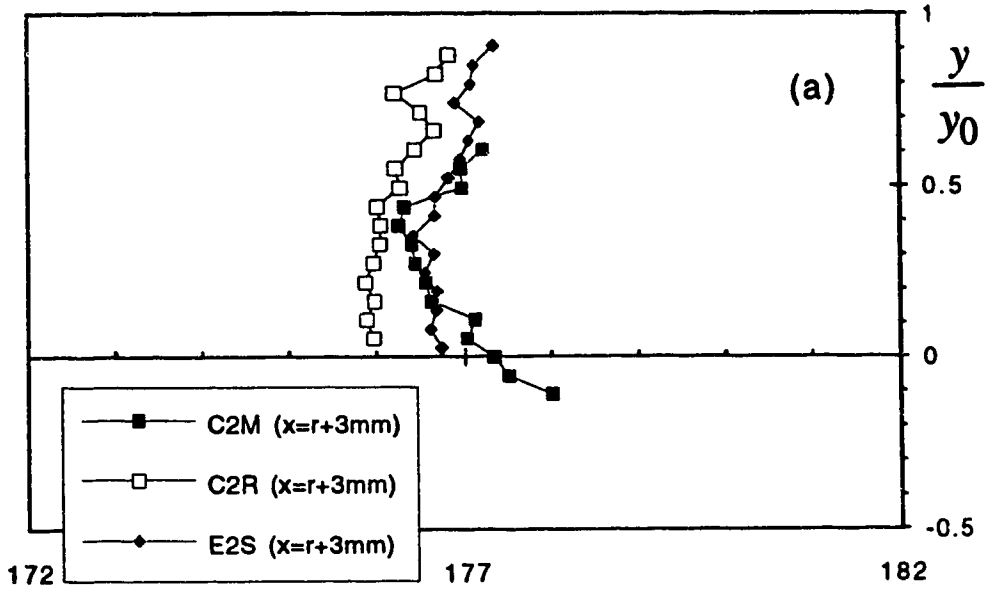

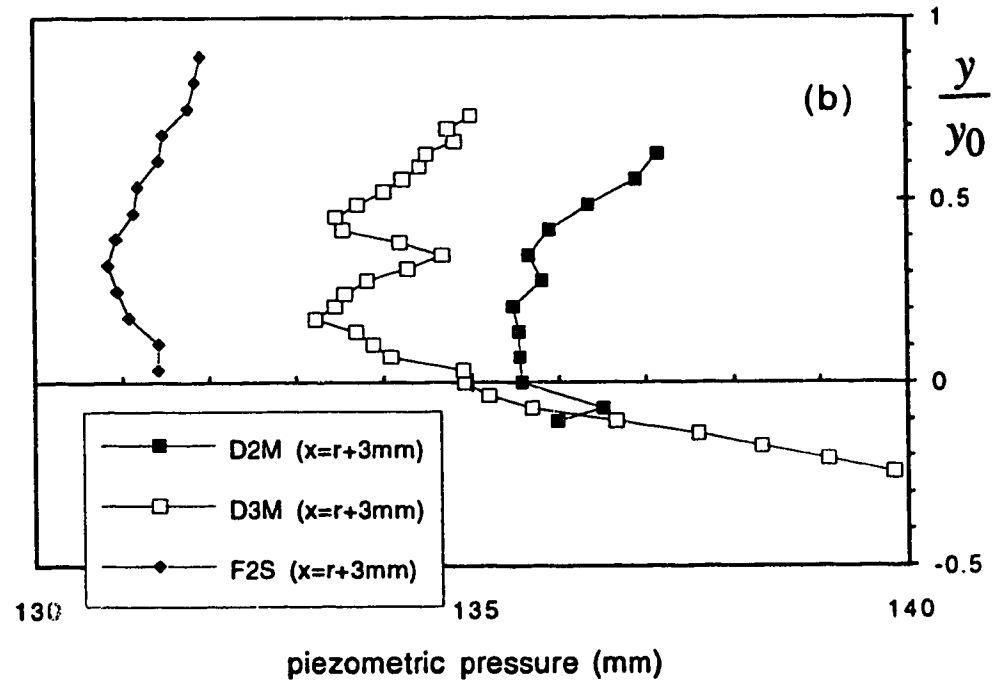

Figure 4.3.7 (a-b) Pressure distribution at the back of the cylinder
(a) Series C and E; (b) Series D and F

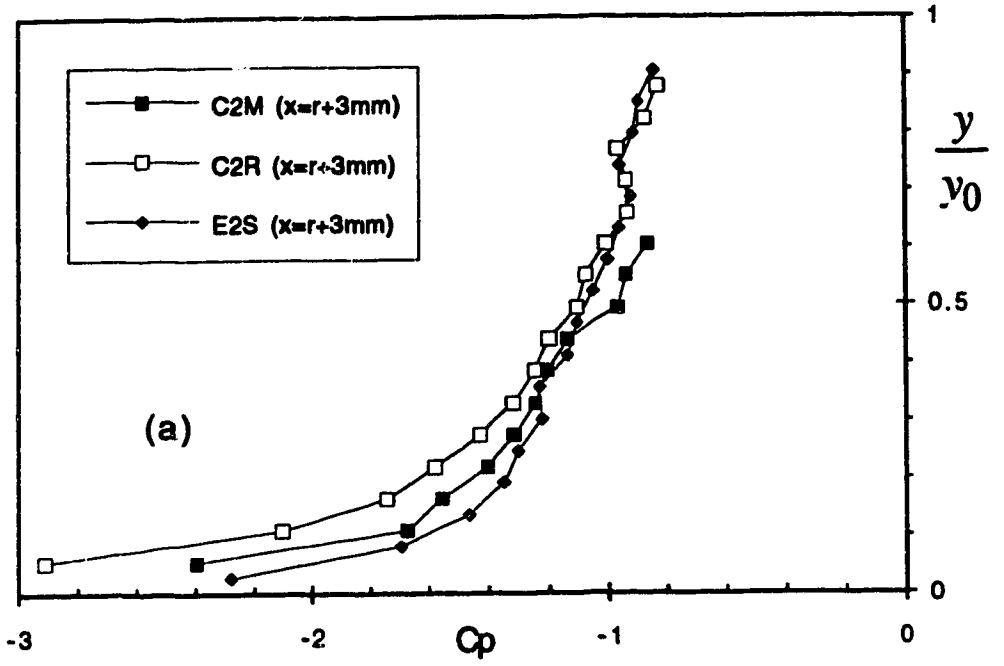

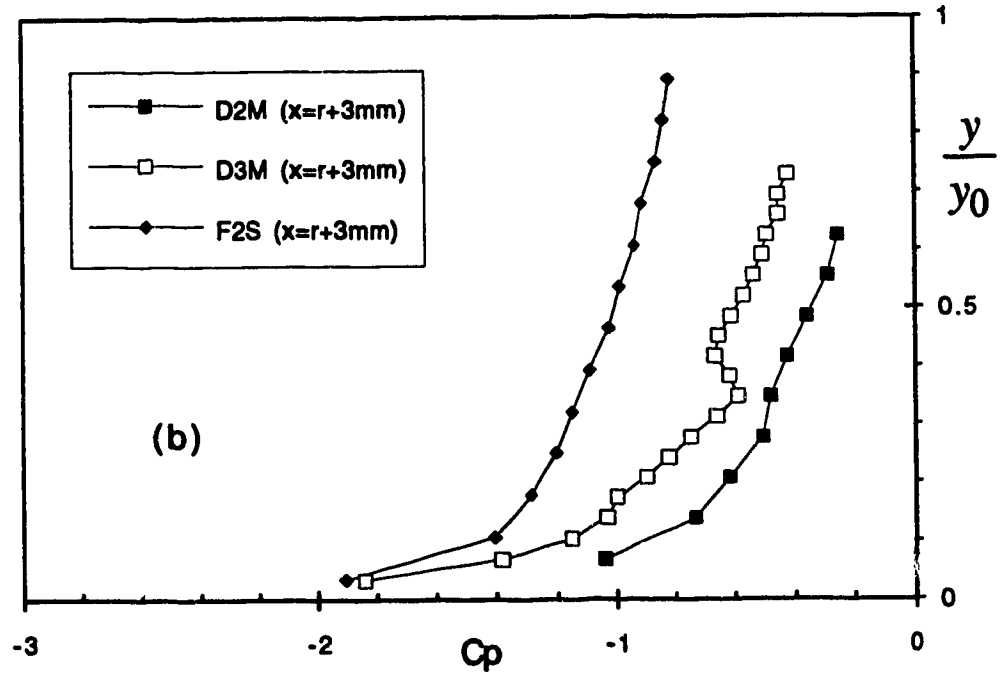

Figure 4.3.8 (a-b) Variation of pressure coefficient at the back of the cylinder
(a) Series C and E; (b) Series D and F

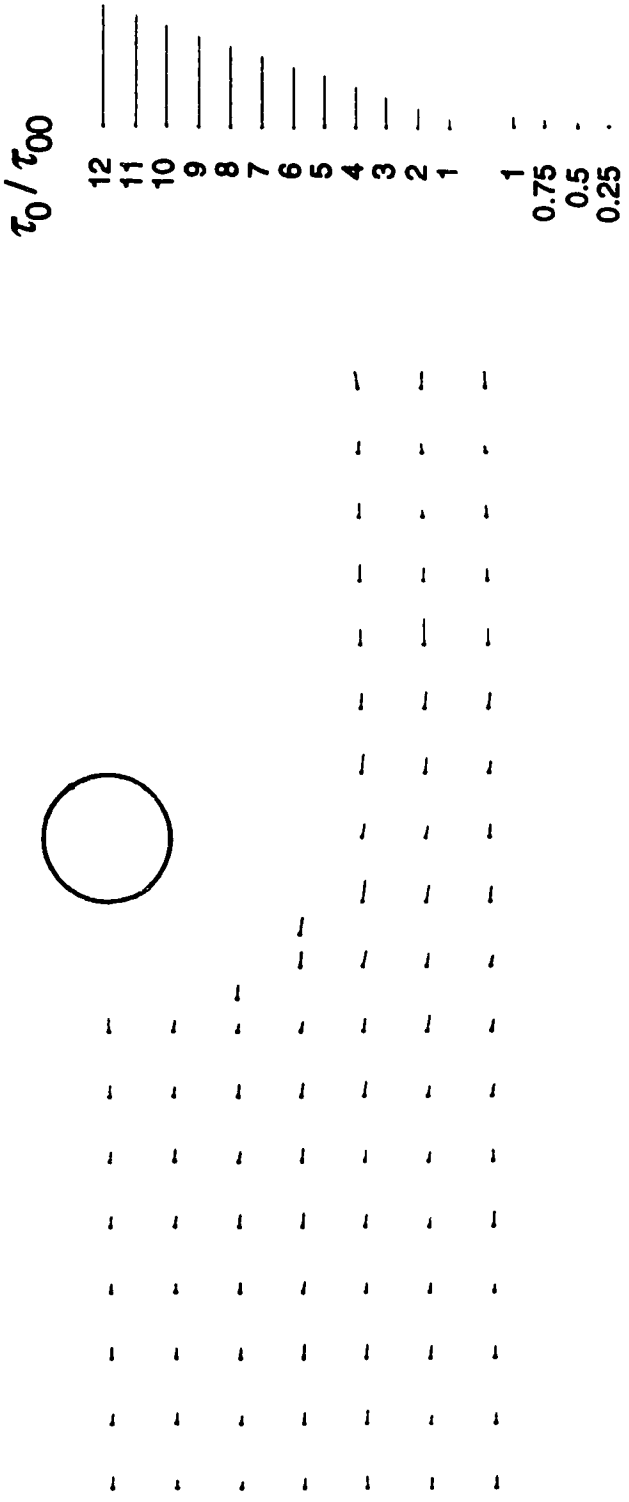

Figure 4.4.1 (a-j) Bed shear stress field (a) Expt. C1M

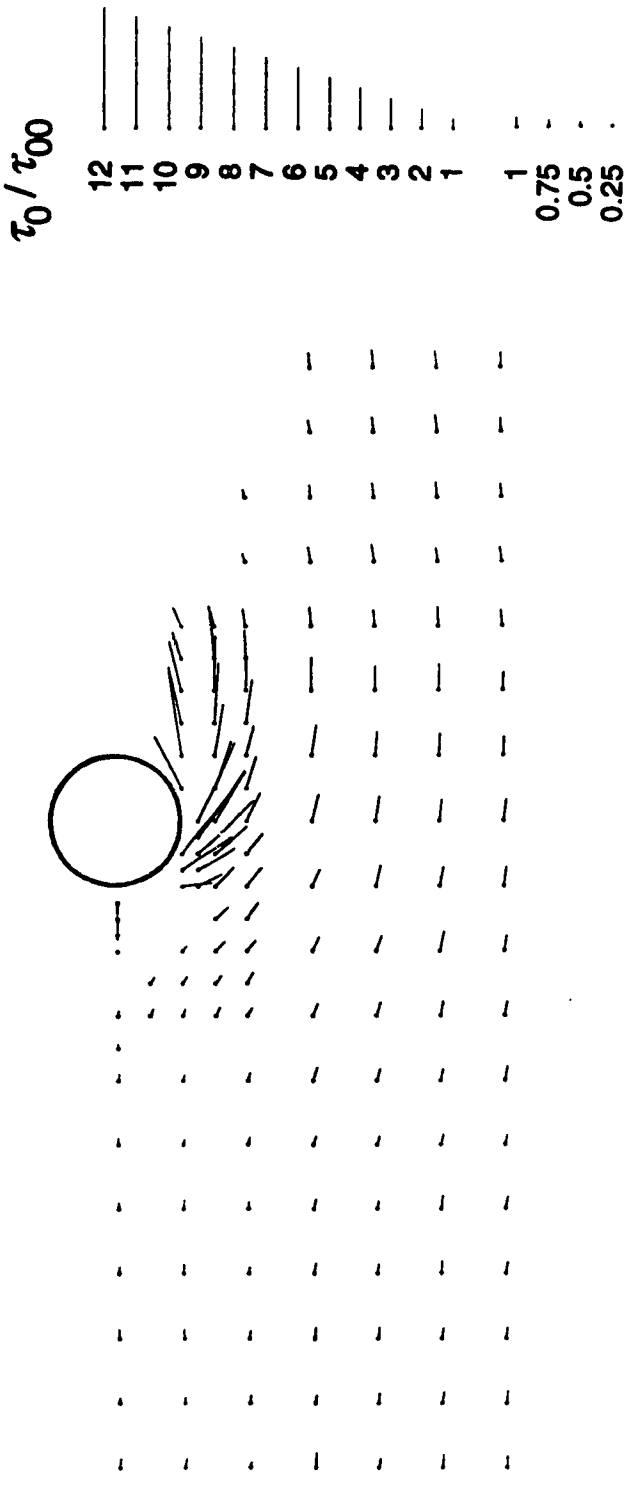

Figure 4.4.1 (a-j) Bed shear stress field (b) Expt. C1R

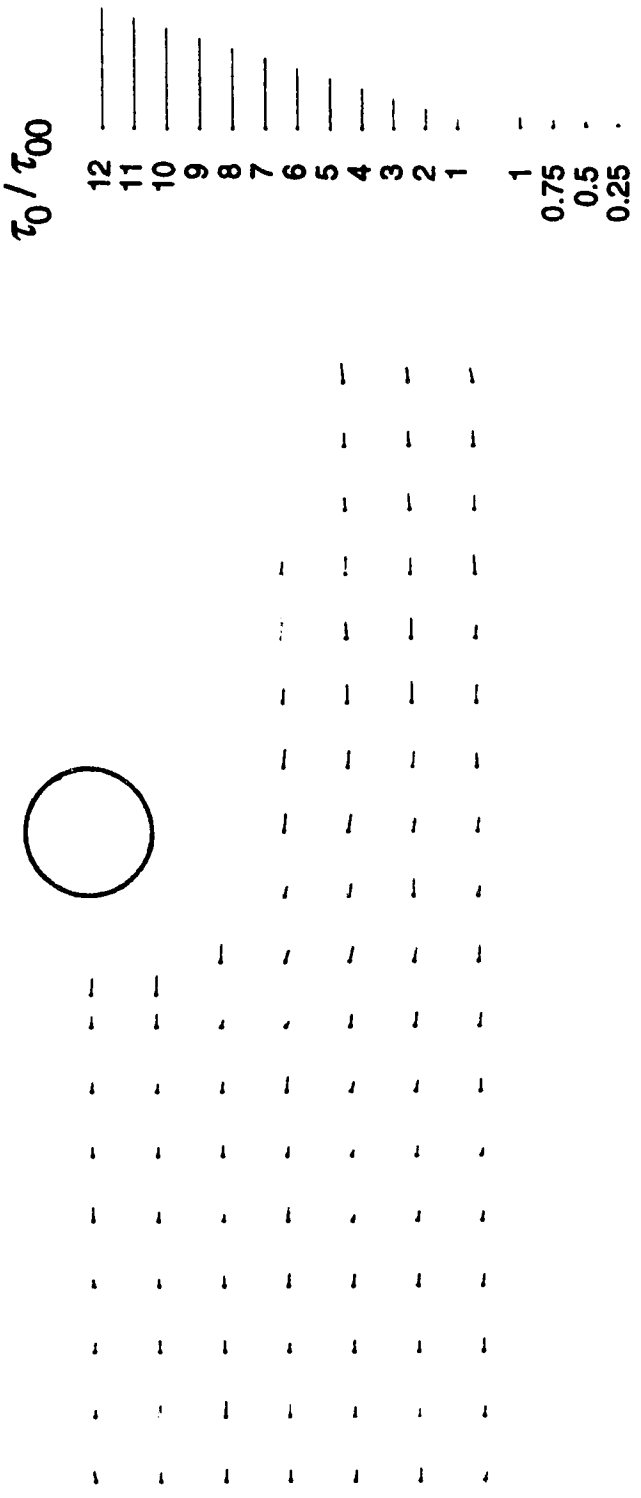

Figure 4.4.1 (a-j) Bed shear stress field (c) Expt. C2M

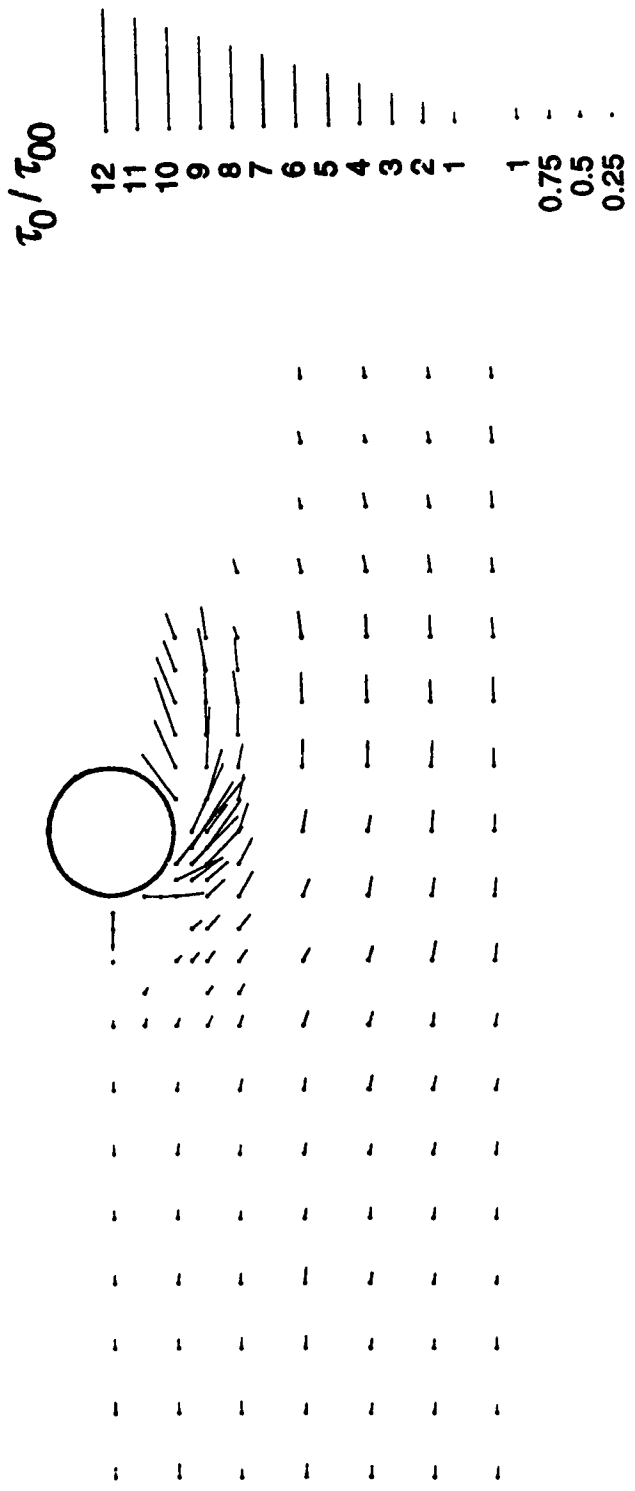

Figure 4.4.1 (a-j) Bed shear stress field (d) Expt. C2R

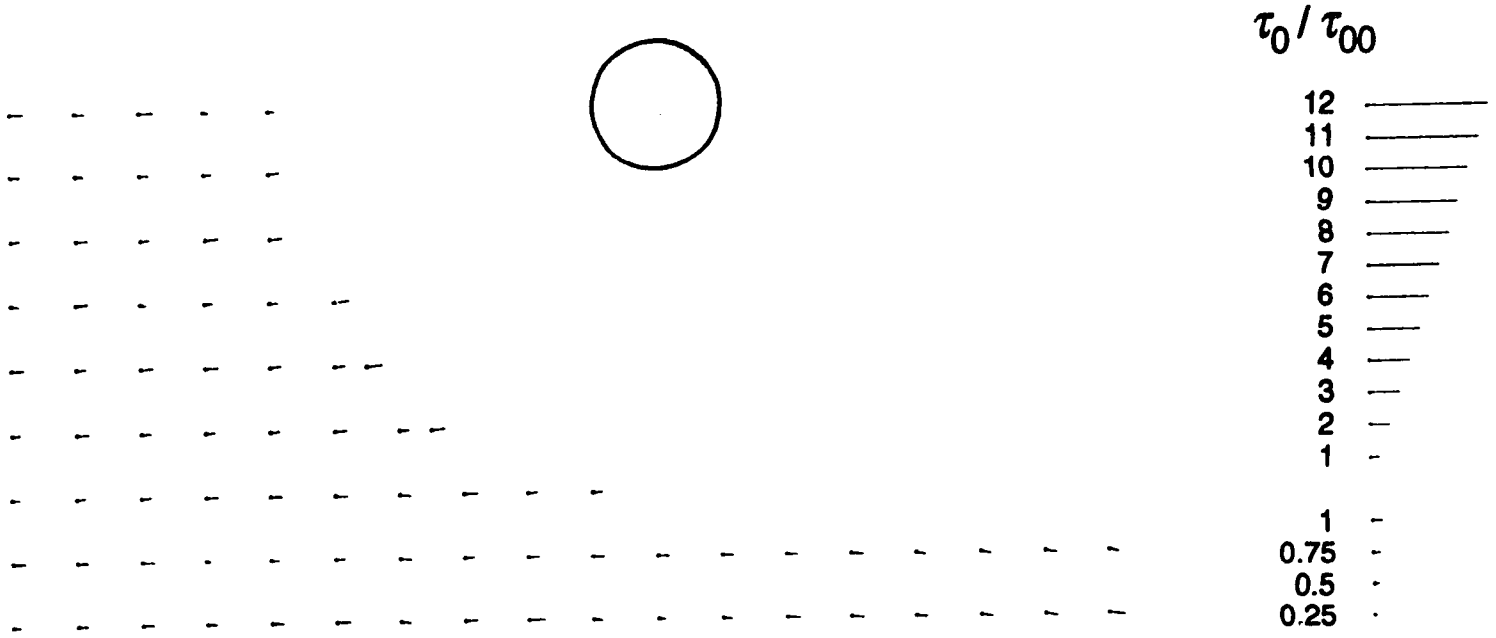

Figure 4.4.1 (a-j) Bed shear stress field (e) Expt. D2M

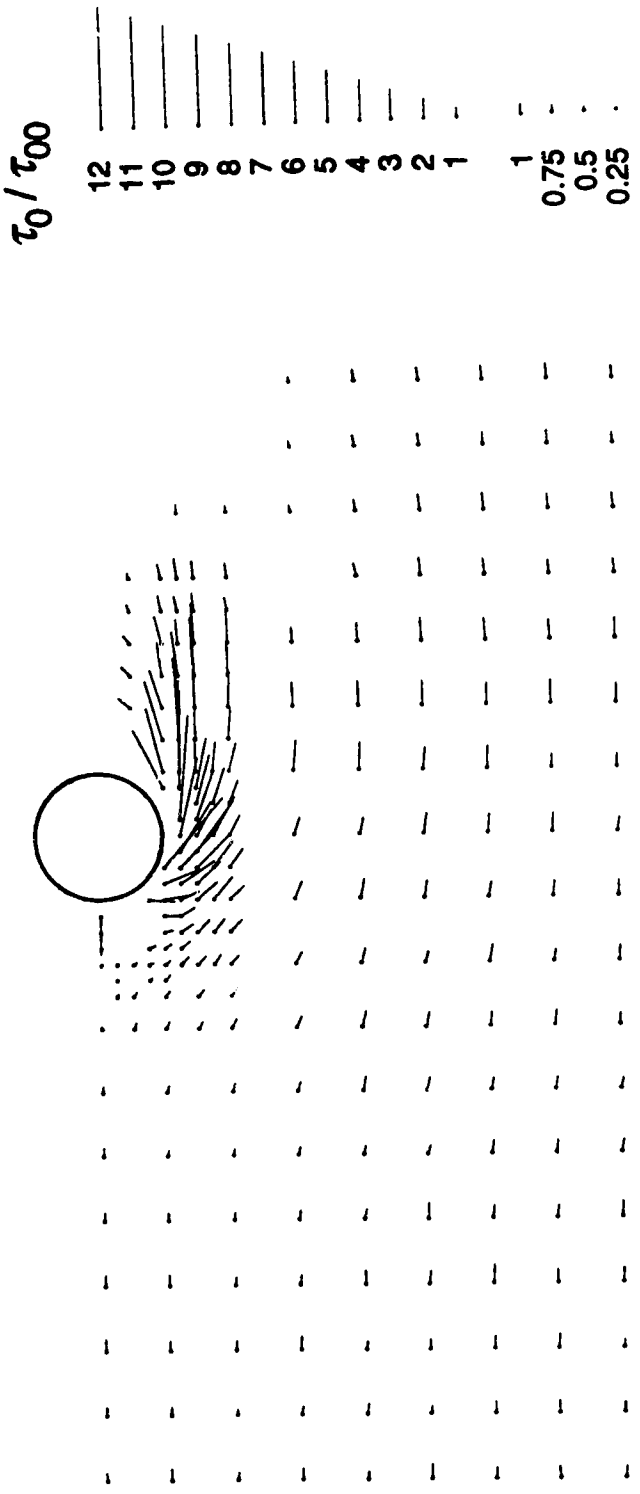

Figure 4.4.1 (a-j) Bed shear stress field (f) Expt. D2R

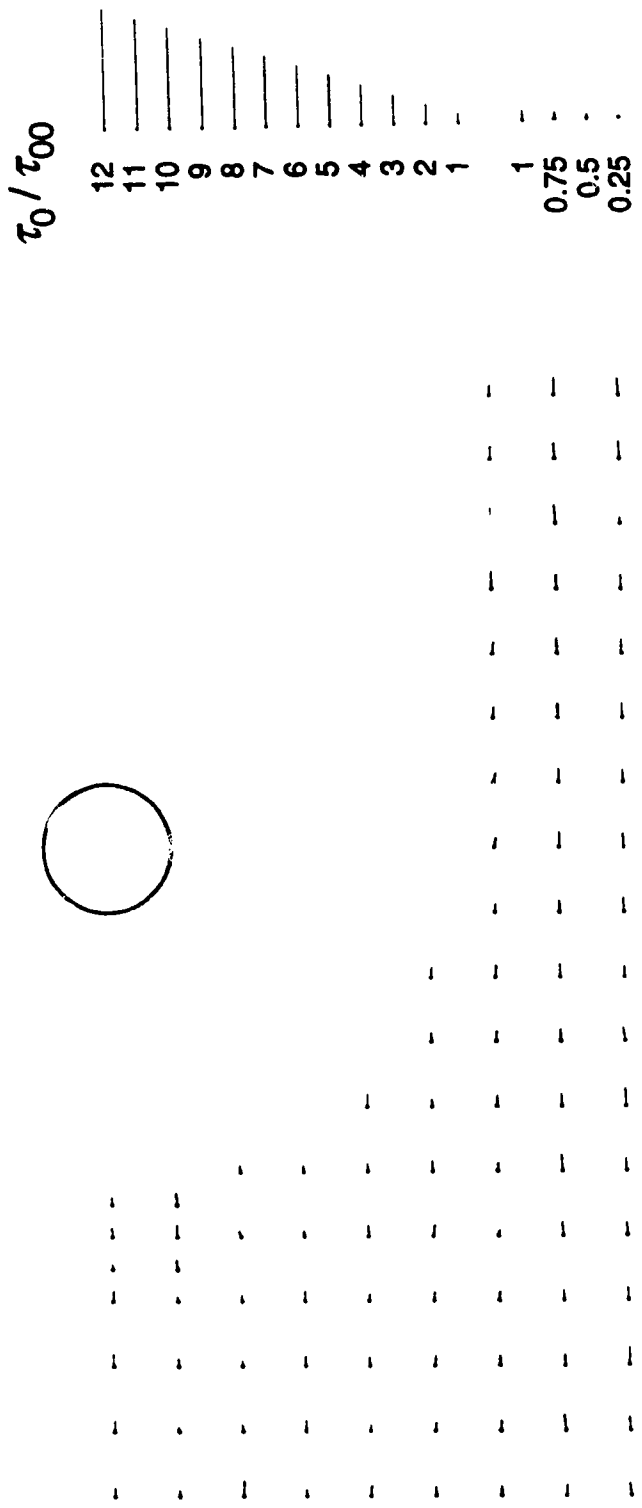

Figure 4.4.1 (a-j) Bed shear stress field (g) Expt. D3M

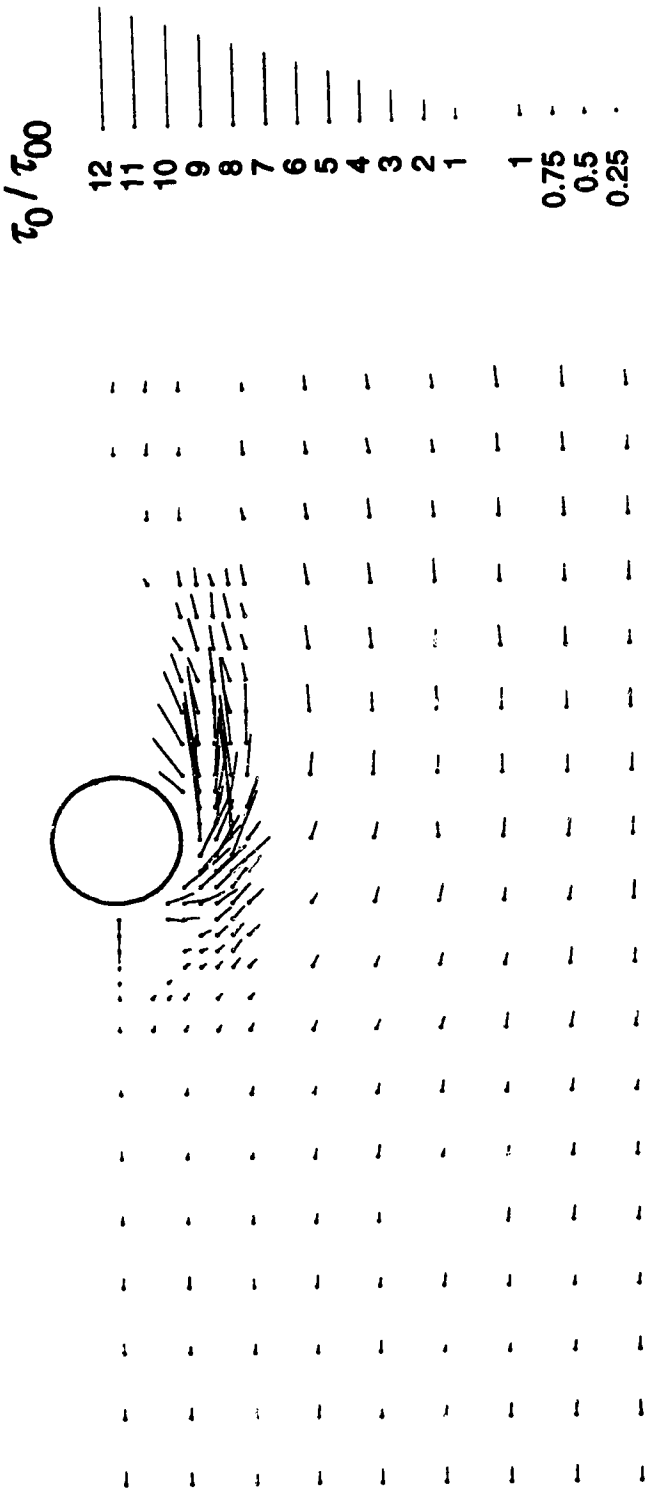

Figure 4.4.1 (a-j) Bed shear stress field (h) Expt. D3R

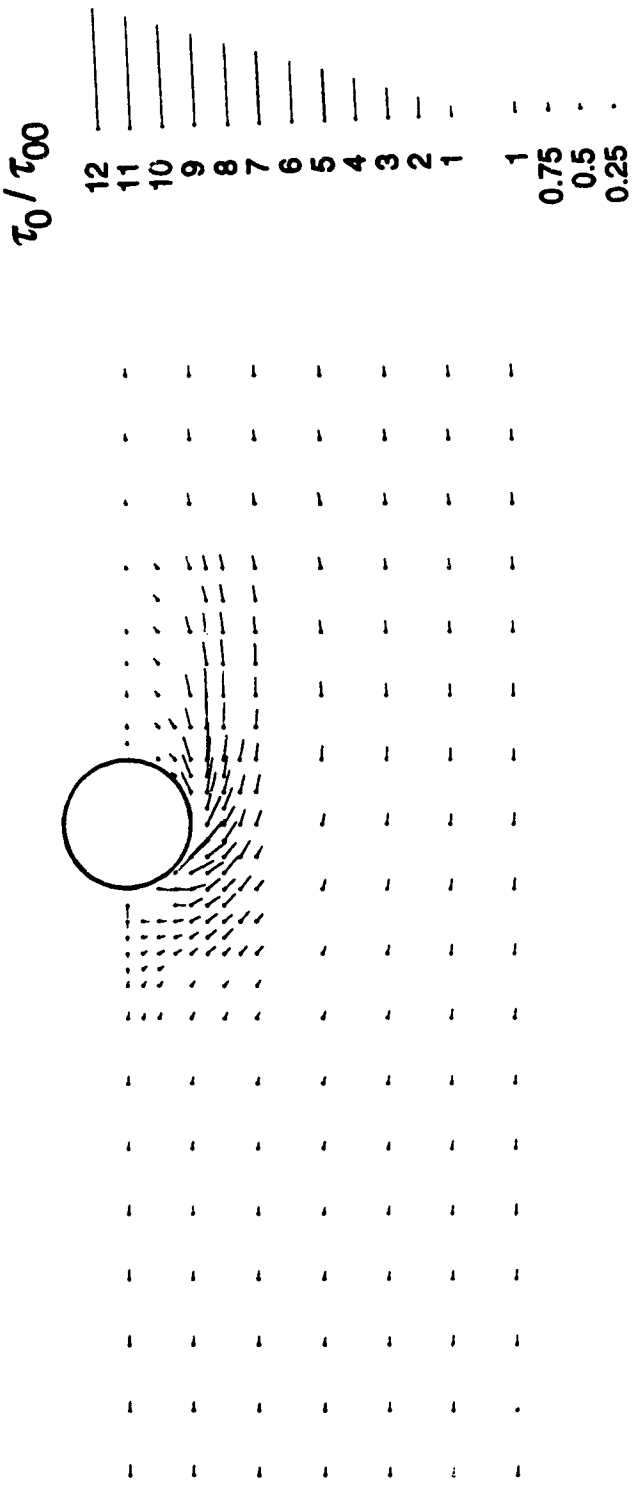

Figure 4.4.1 (a-j) Bed shear stress field (i) Expt. E2S

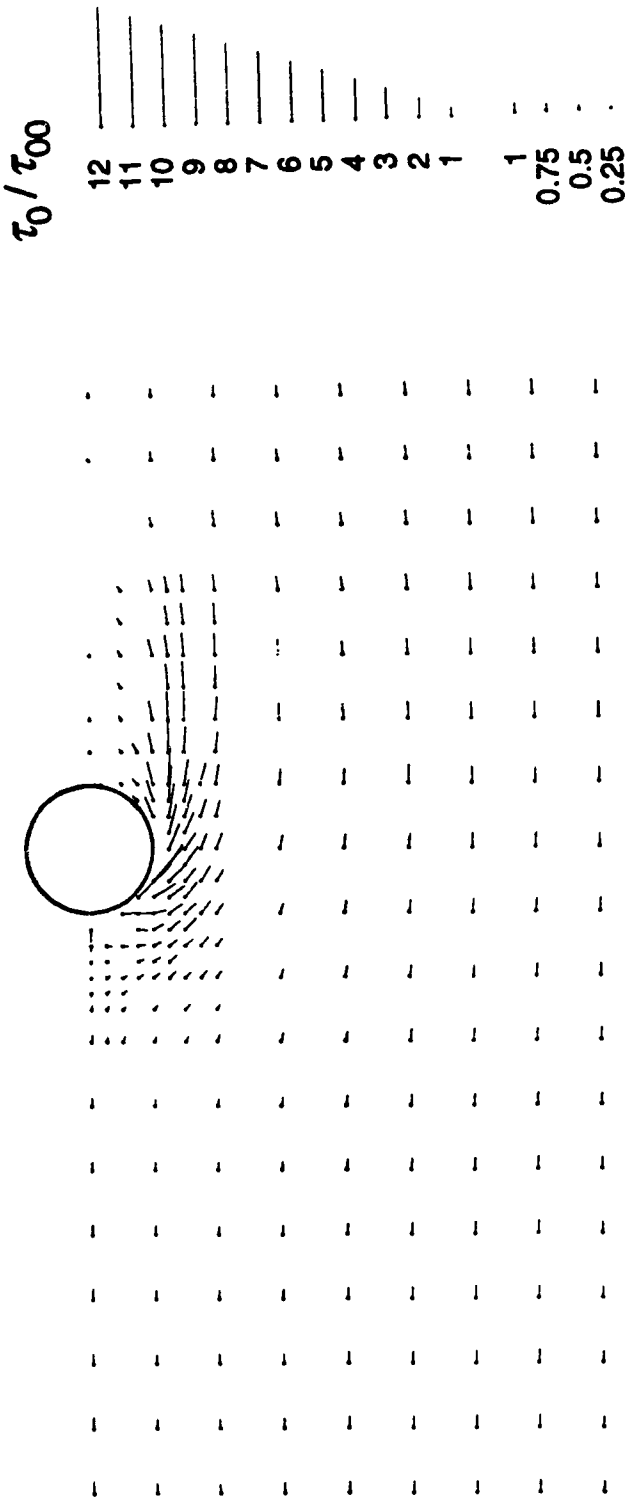

Figure 4.4.1 (a-j) Bed shear stress field (j) Expt. F2S

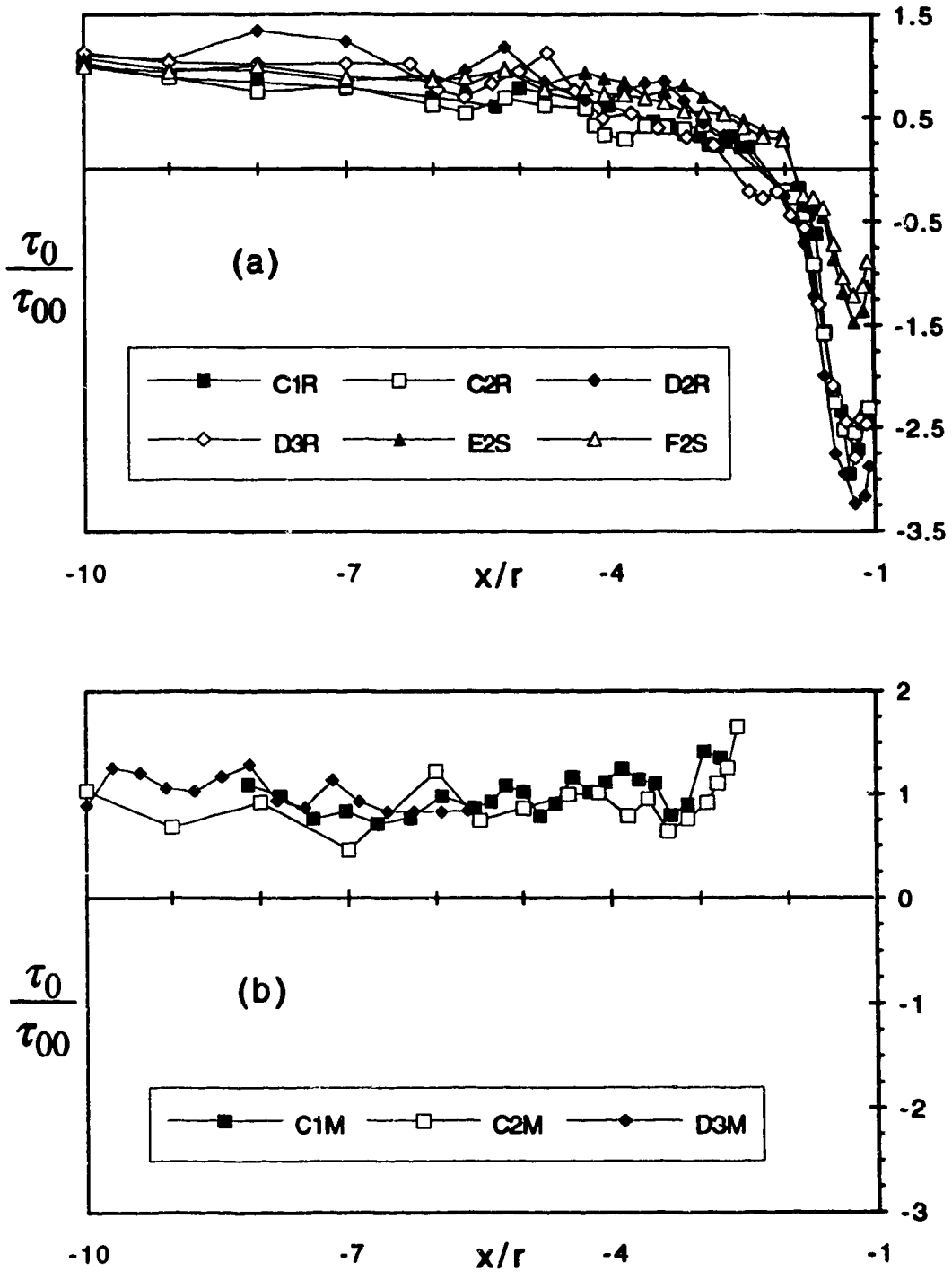

Figure 4.4.2 (a-b) Bed shear stress on the POS
(a) Rigid and smooth bed runs
(b) Mobile bed runs

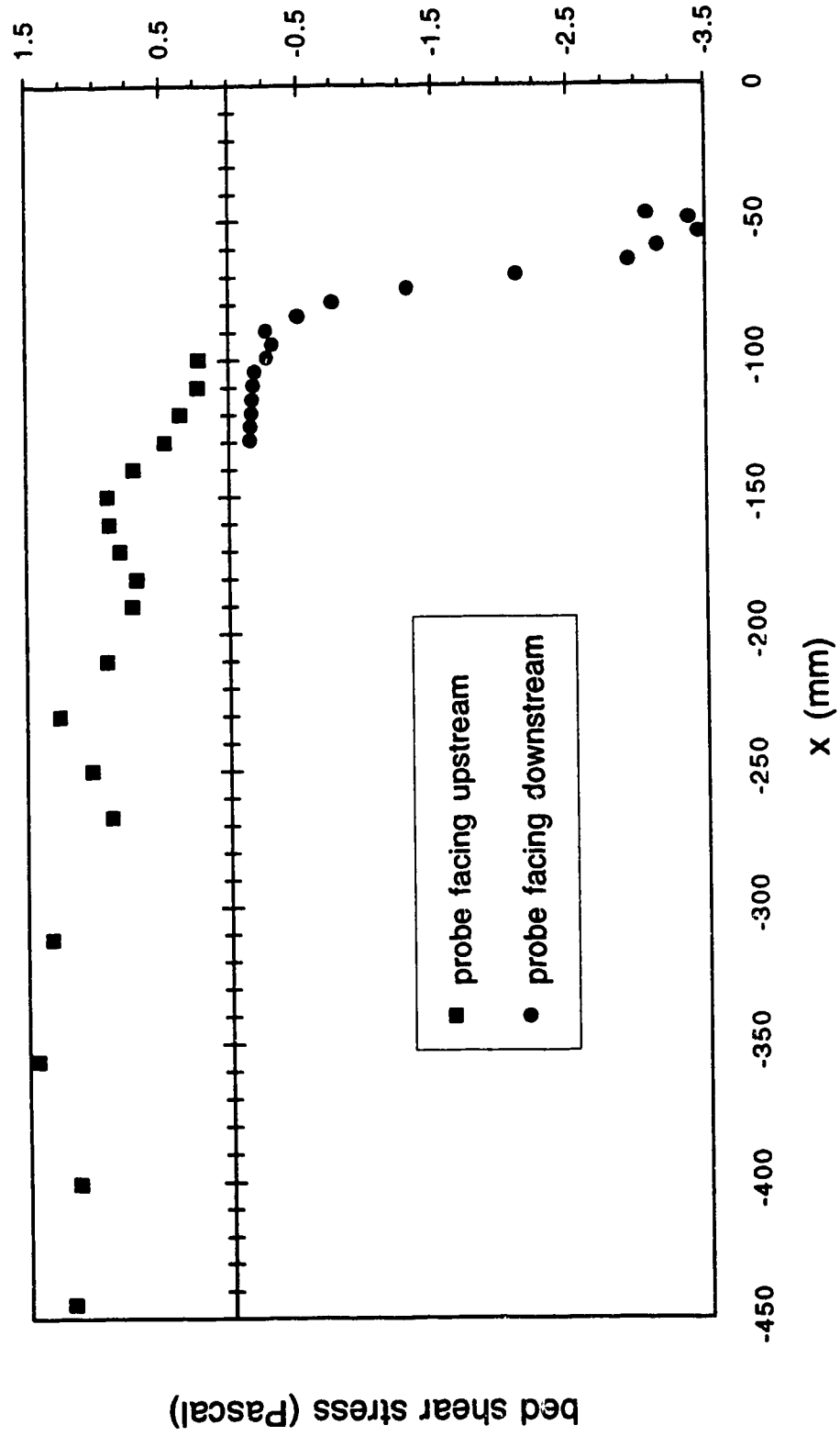

Figure 4.4.3 Typical raw bed shear data on the POS (Expt. D2R)

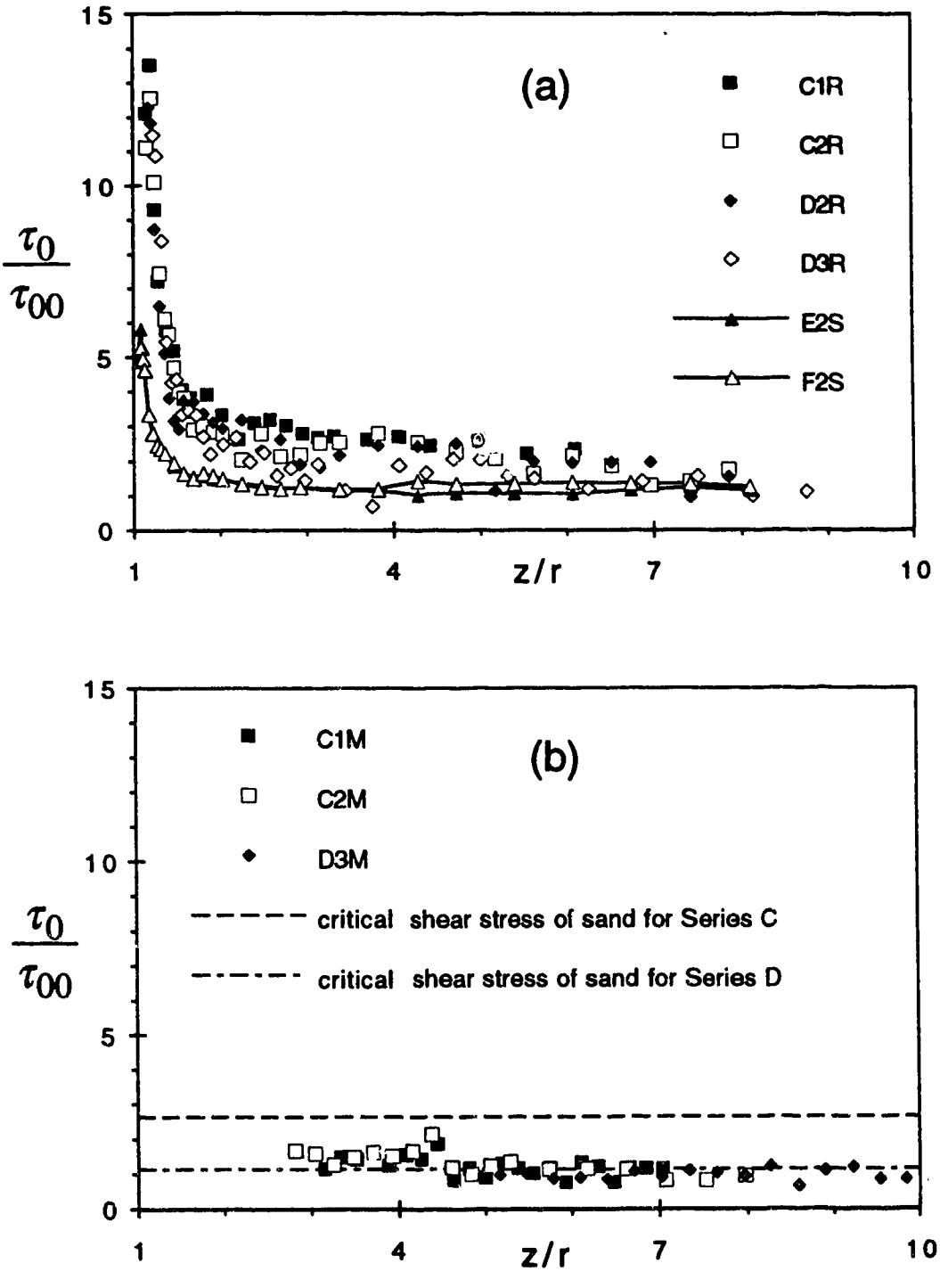

Figure 4.4.4 (a-b) Bed shear stress on the x=0 plane
(a) Rigid and smooth bed runs
(b) Mobile bed runs

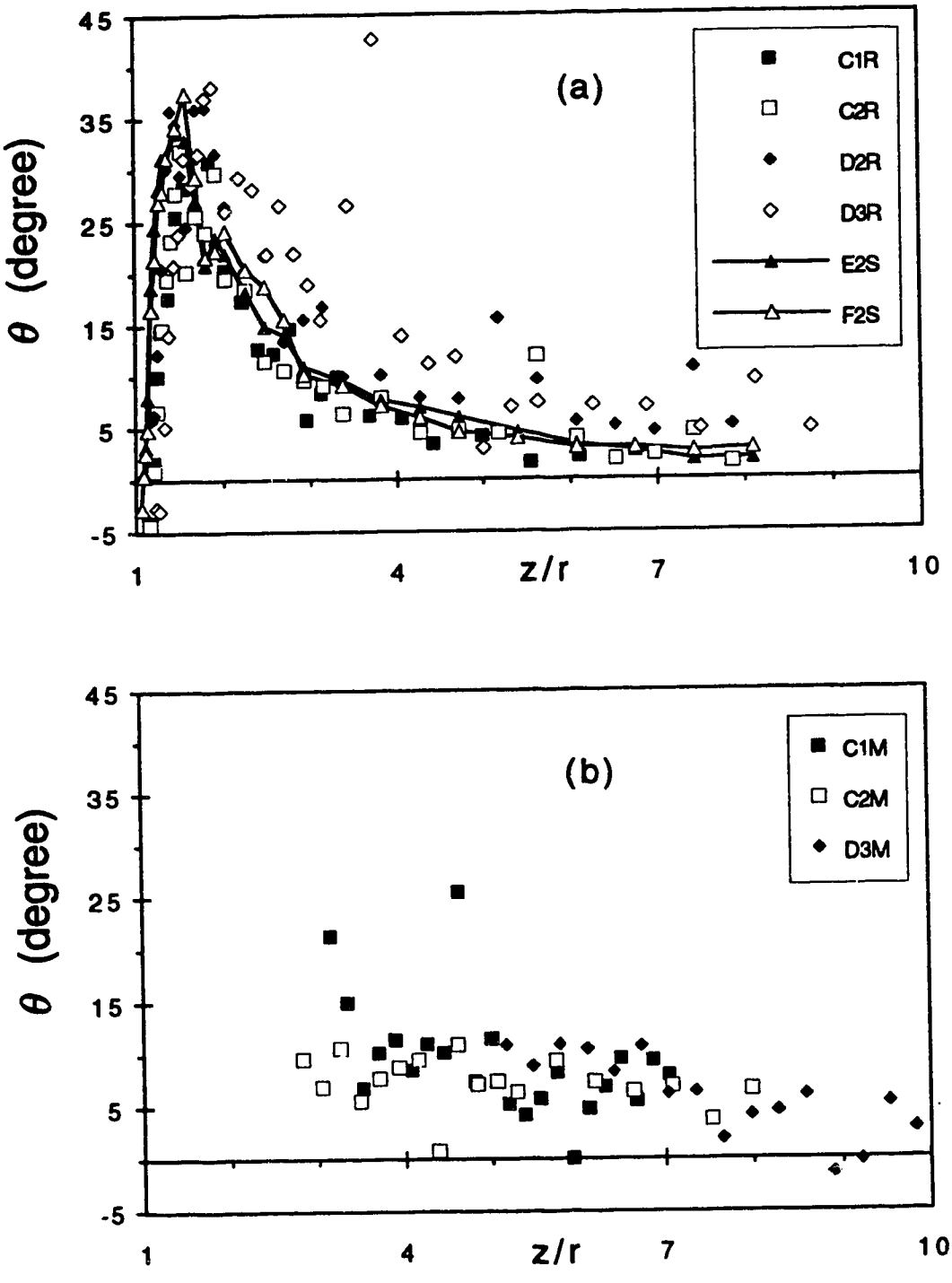

Figure 4.4.5 (a-b) Bed shear angle on the x=0 plane
(a) Rigid and smooth bed runs
(b) Mobile bed runs

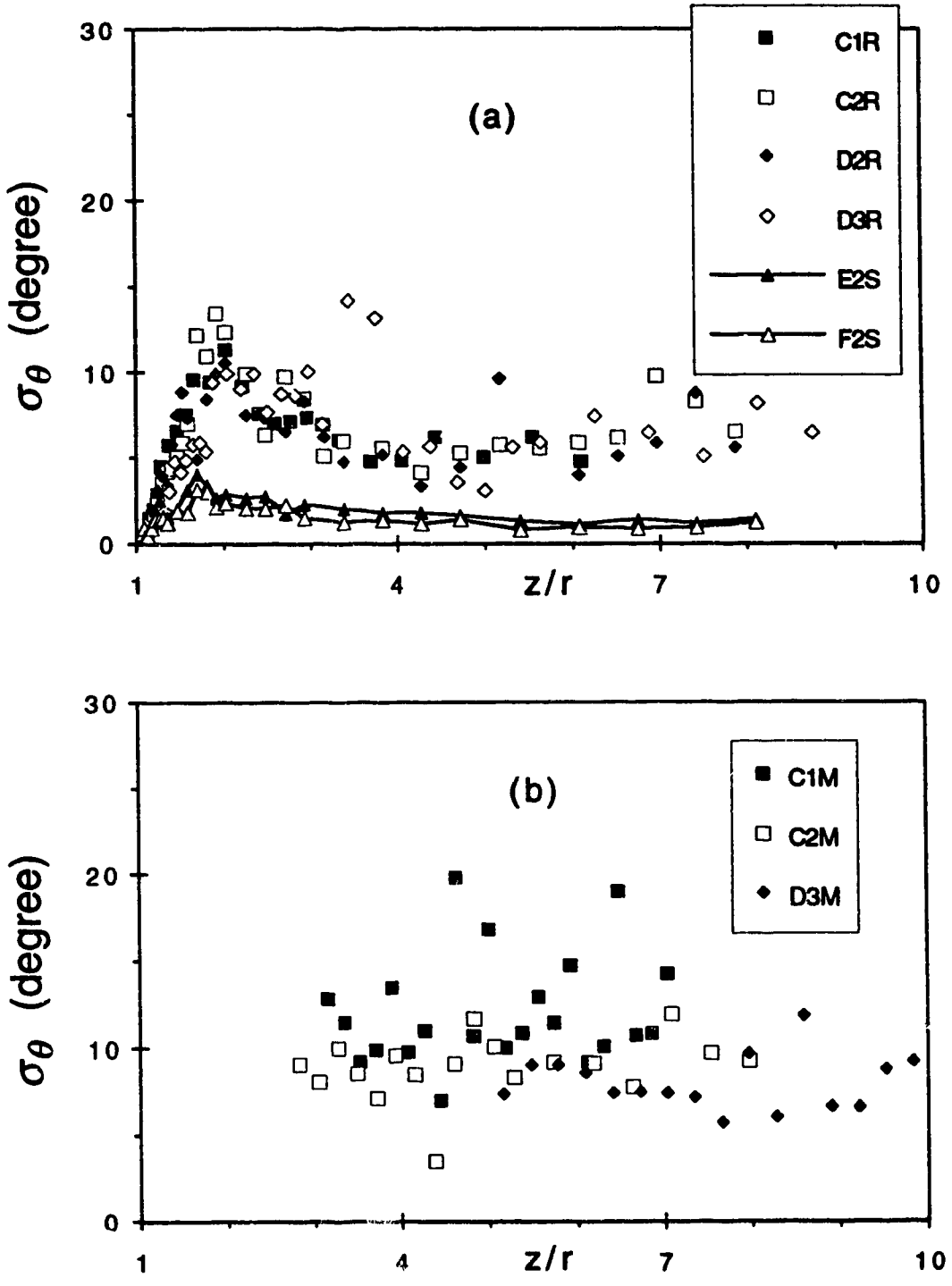

Figure 4.4.6 (a-b) Fluctuation of the bed shear angle on the x=0 plane
(a) Rigid and smooth bed runs
(b) Mobile bed runs

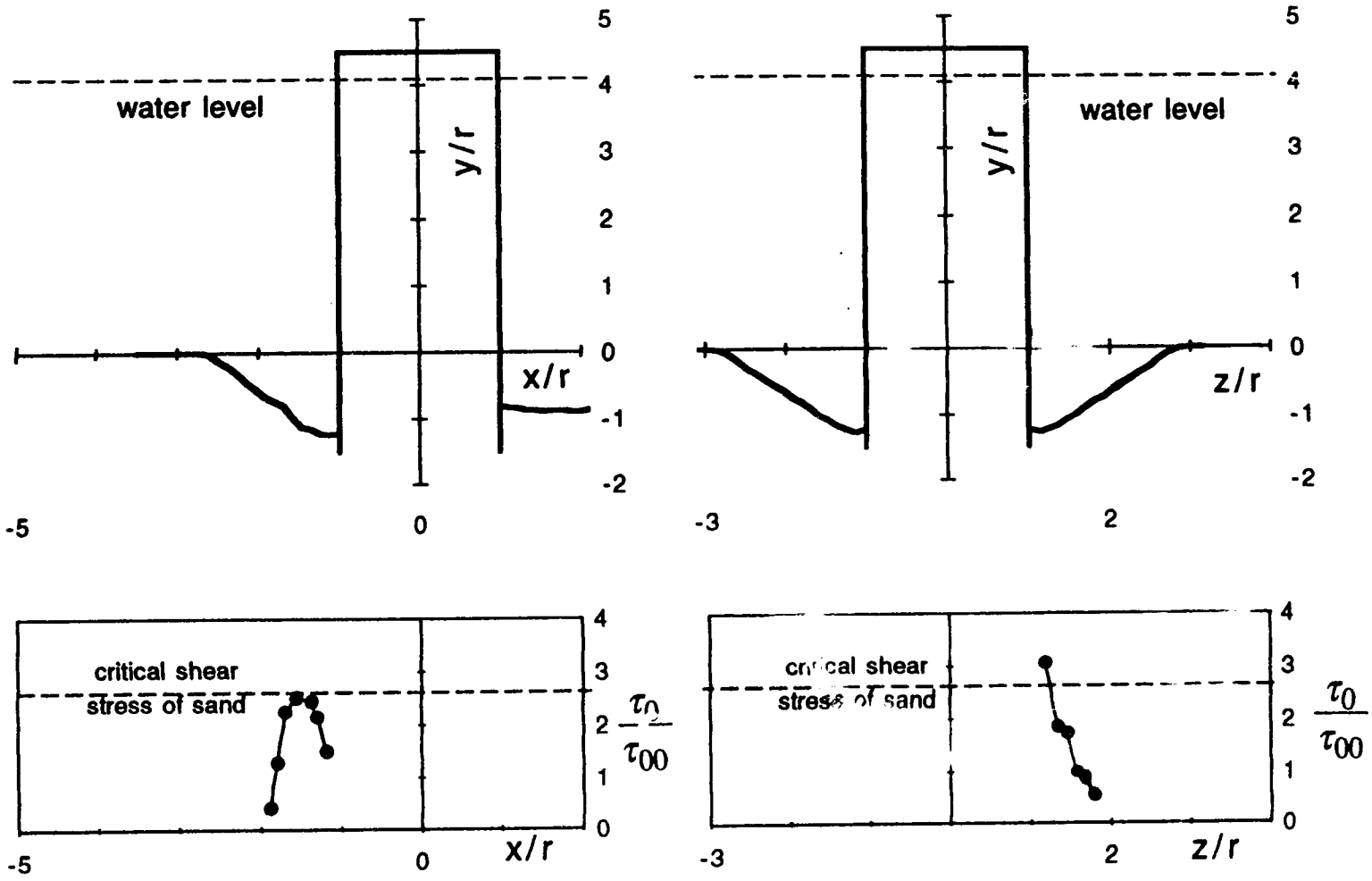

(a) front slope of scour hole

(b) side slope of scour hole

Figure 4.4.7 (a-c) Local shear stress on the deformed channel bed (Expt. C2M)

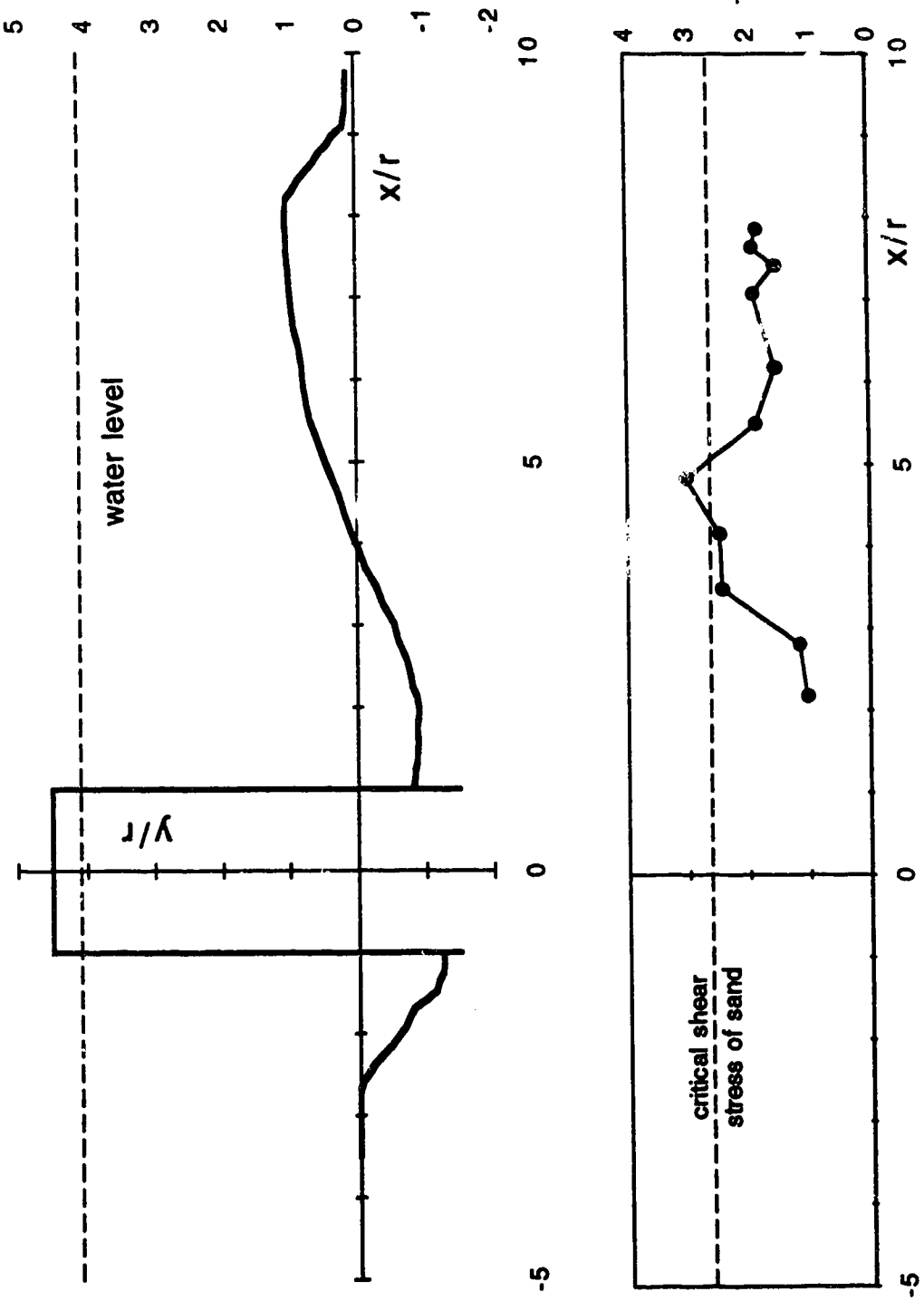

Figure 4.4.7 (a-c) Local shear stress on the deformed channel bed (Expt. C2M); (c) rear bar

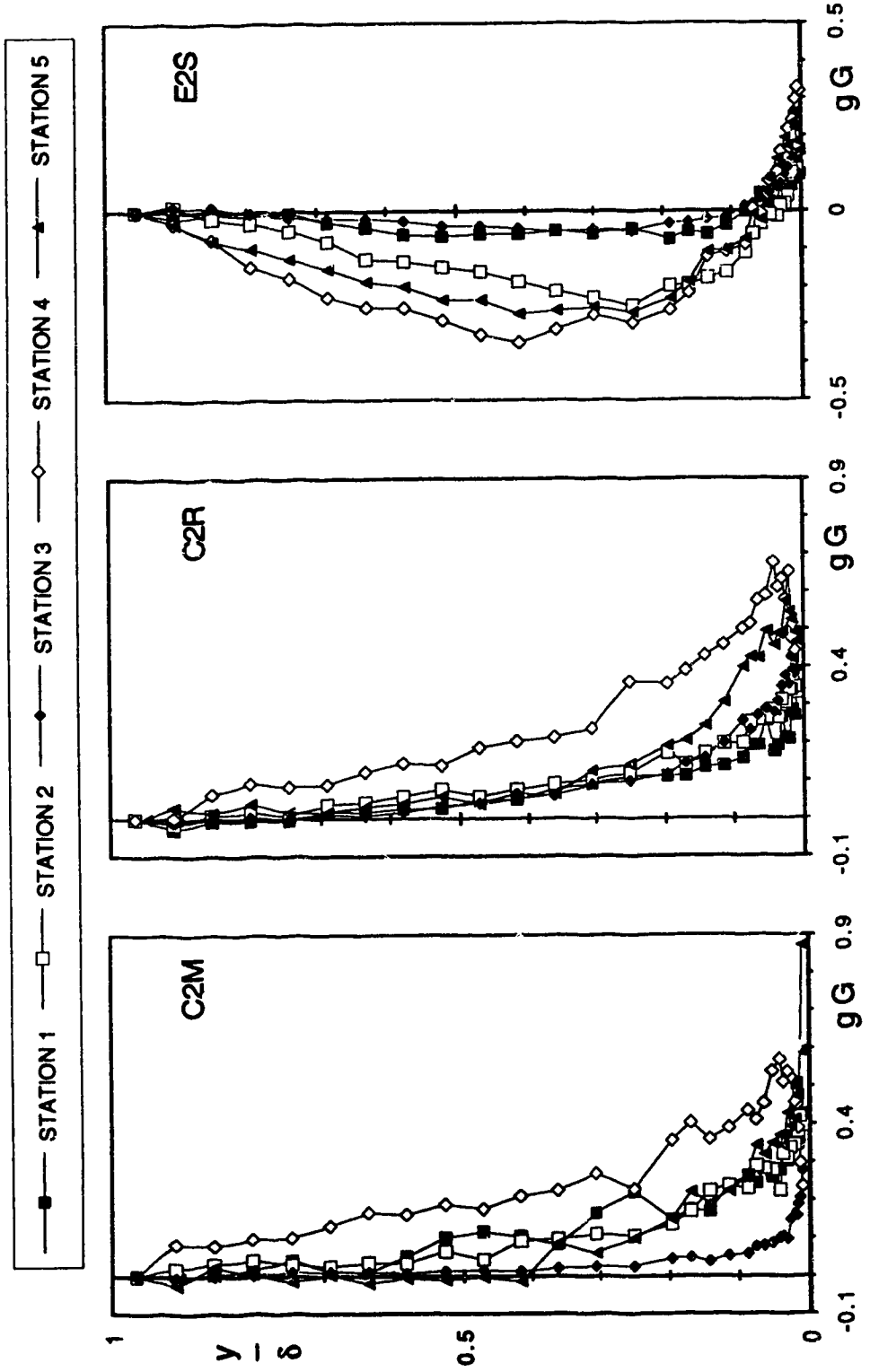

Figure 4.5.1 (a) Applicability of Prandtl's model (Expt. C2M, C2R and E2S; Stations 1 to 5)

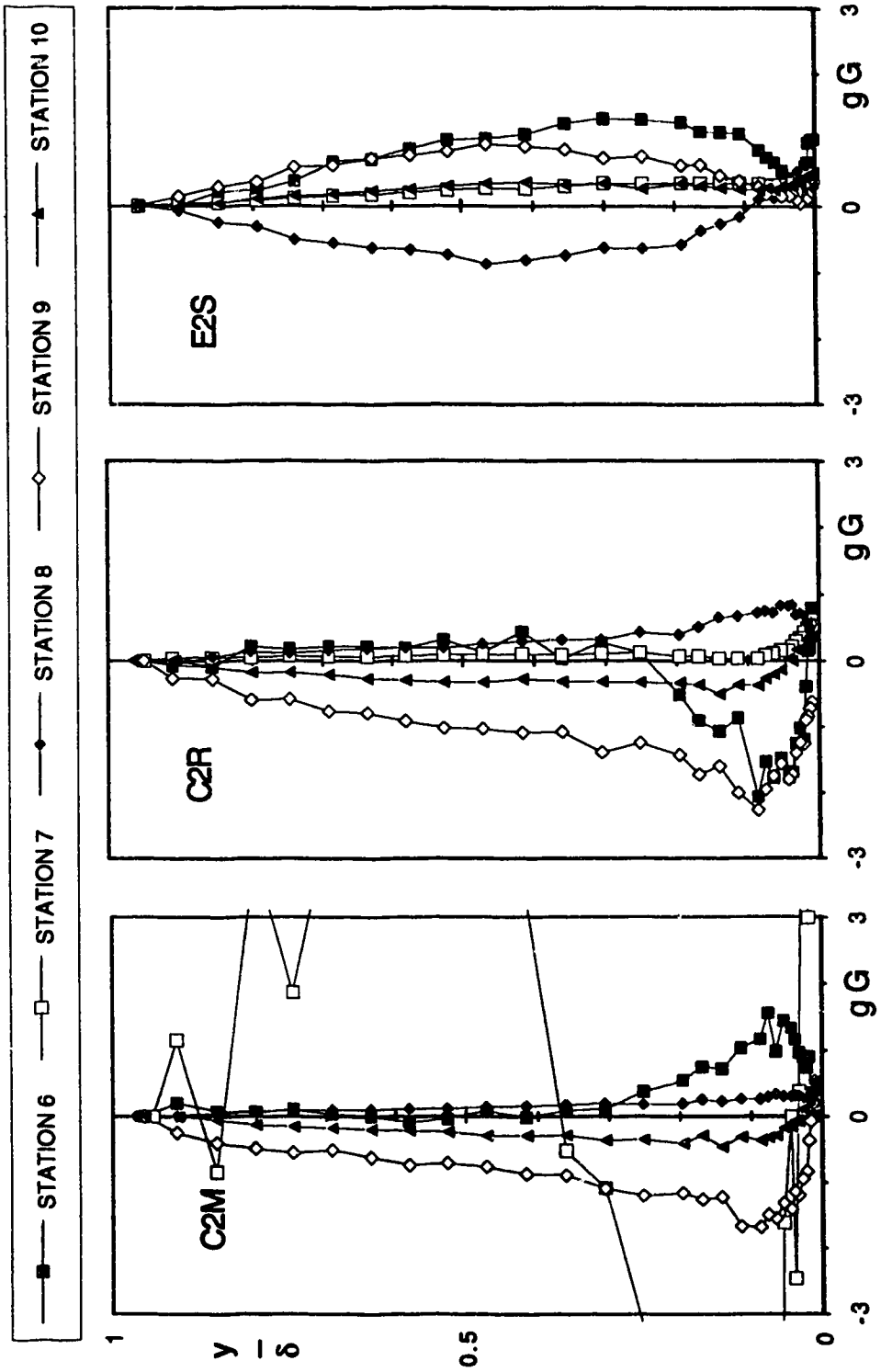

Figure 4.5.1 (b) Applicability of Prandtl's model (Expt. C2M, C2R and E2S; Stations 6 to 10)

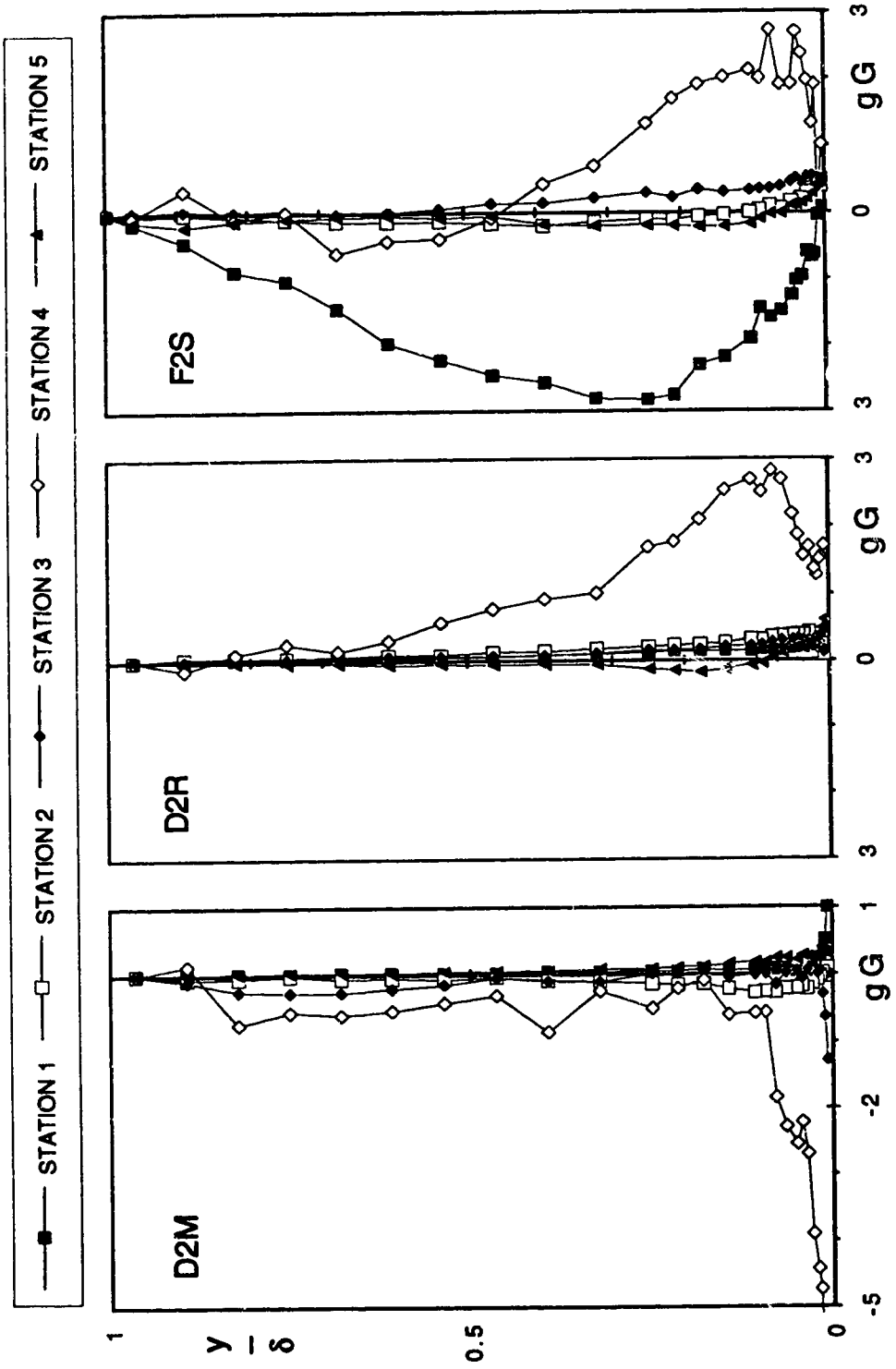

Figure 4.5.1 (c) Applicability of Prandtl's model (Expt. D2M, D2R and F2S; Stations 1 to 5)

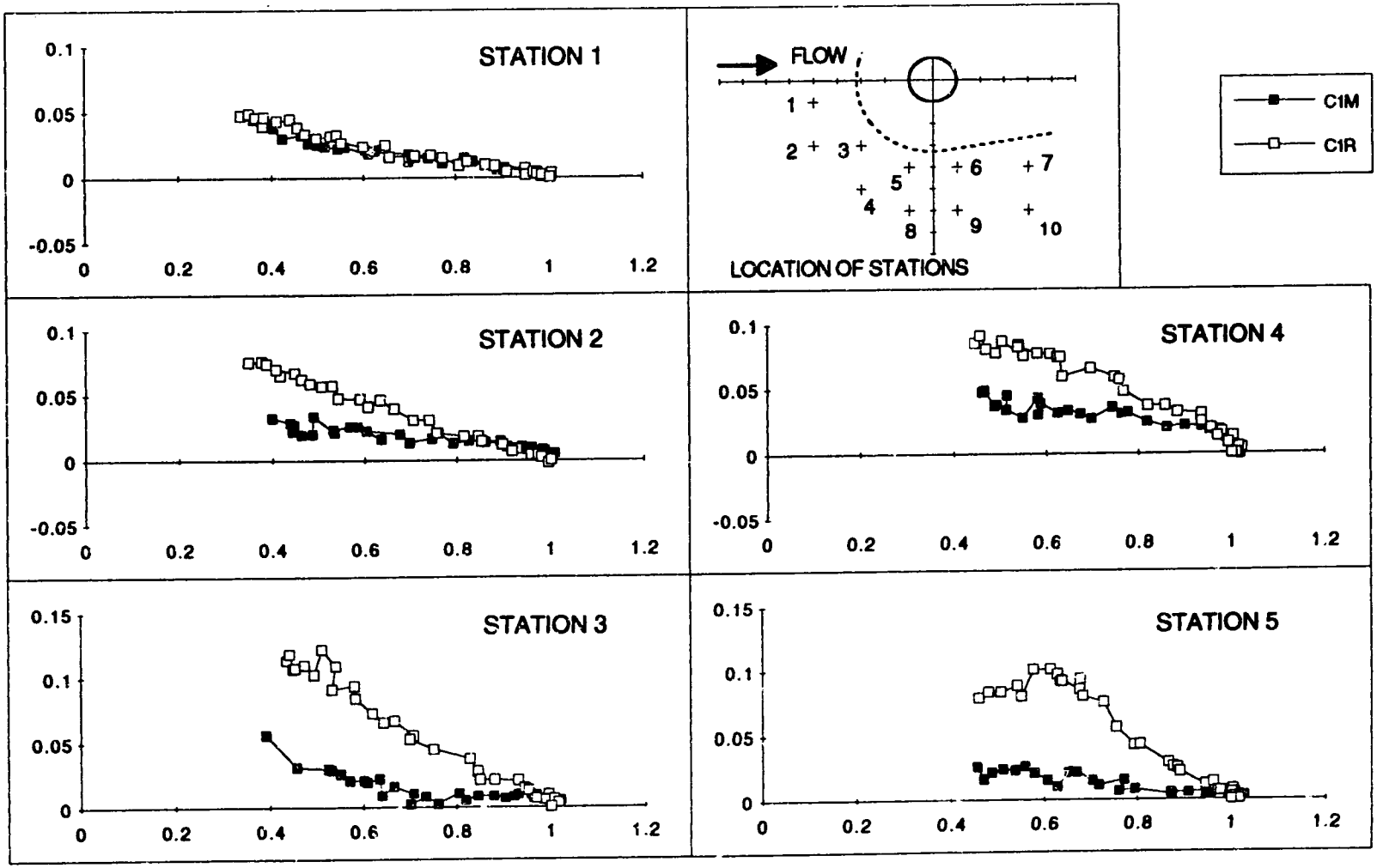

Note: normalized velocity components along and perpendicular to the free streamline direction are plotted on horizontal and vertical axes

Figure 4.5.2 (a) Polar plots of the skewed boundary layer (Expt. C1M and C1R, Stations 1 to 5)

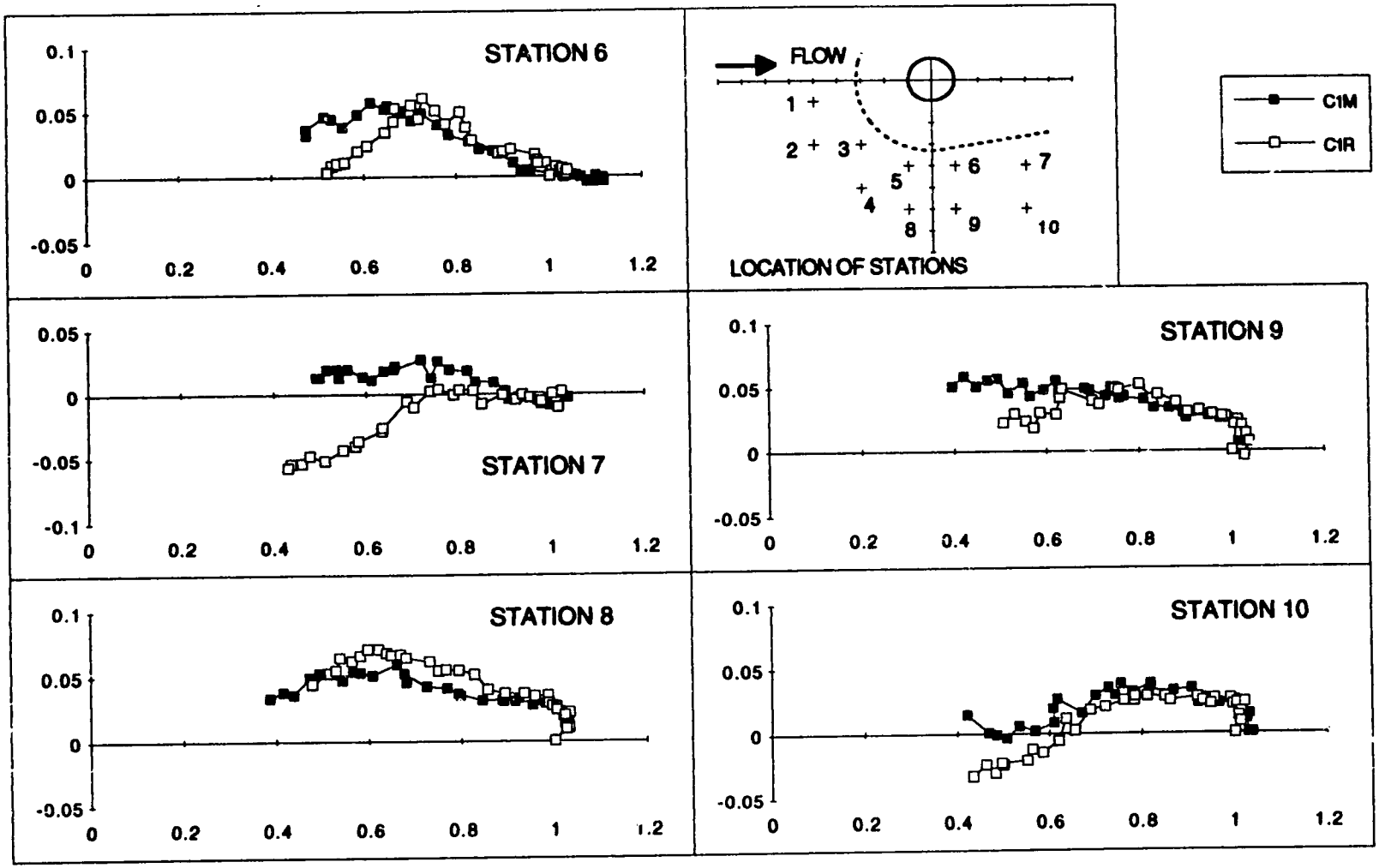

Note: normalized velocity components along and perpendicular to the free streamline direction are plotted on horizontal and vertical axes

Figure 4.5.2 (b) Polar plots of the skewed boundary layer (Expt. C1M and C1R, Stations 6 to 10)

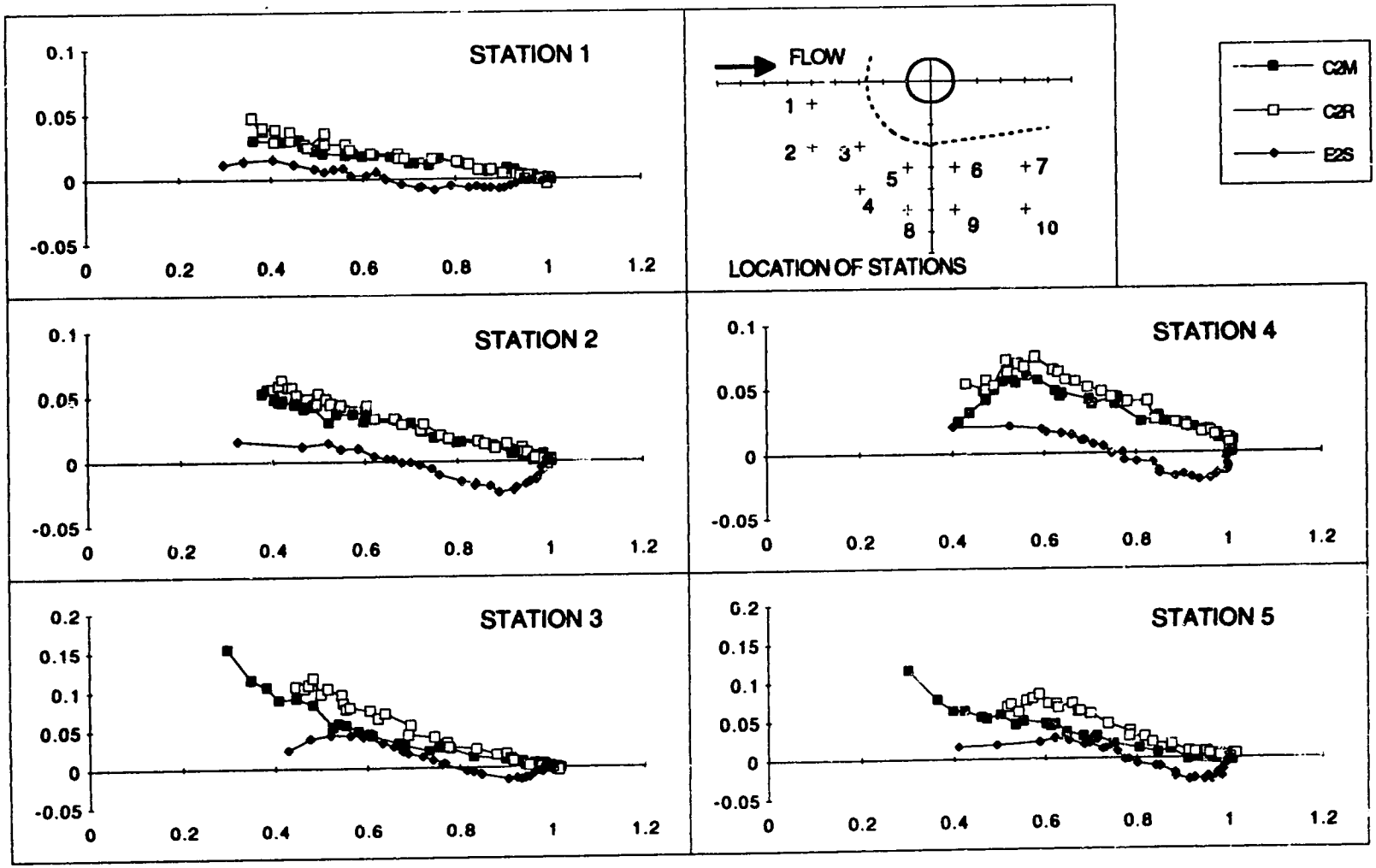

Note: normalized velocity components along and perpendicular to the free streamline direction are plotted on horizontal and vertical axes

Figure 4.5.2 (c) Polar plots of the skewed boundary layer (Expt. C2M, C2R and E2S, Stations 1 to 5)

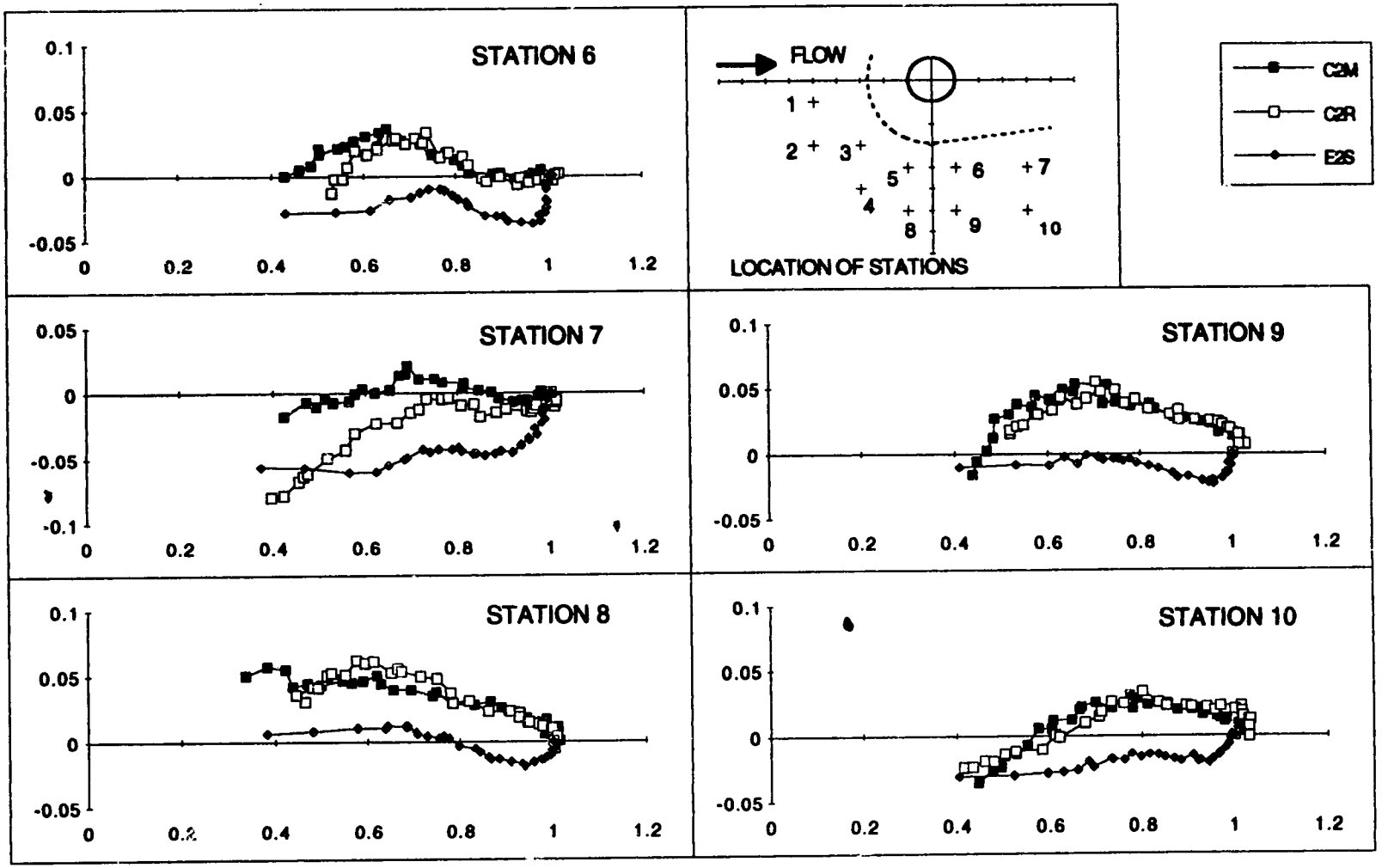

Note: normalized velocity components along and perpendicular to the free streamline direction are plotted on horizontal and vertical axes

Figure 4.5.2 (d) Polar plots of the skewed boundary layer (Expt. C2M, C2R and E2S, Stations 6 to 10)

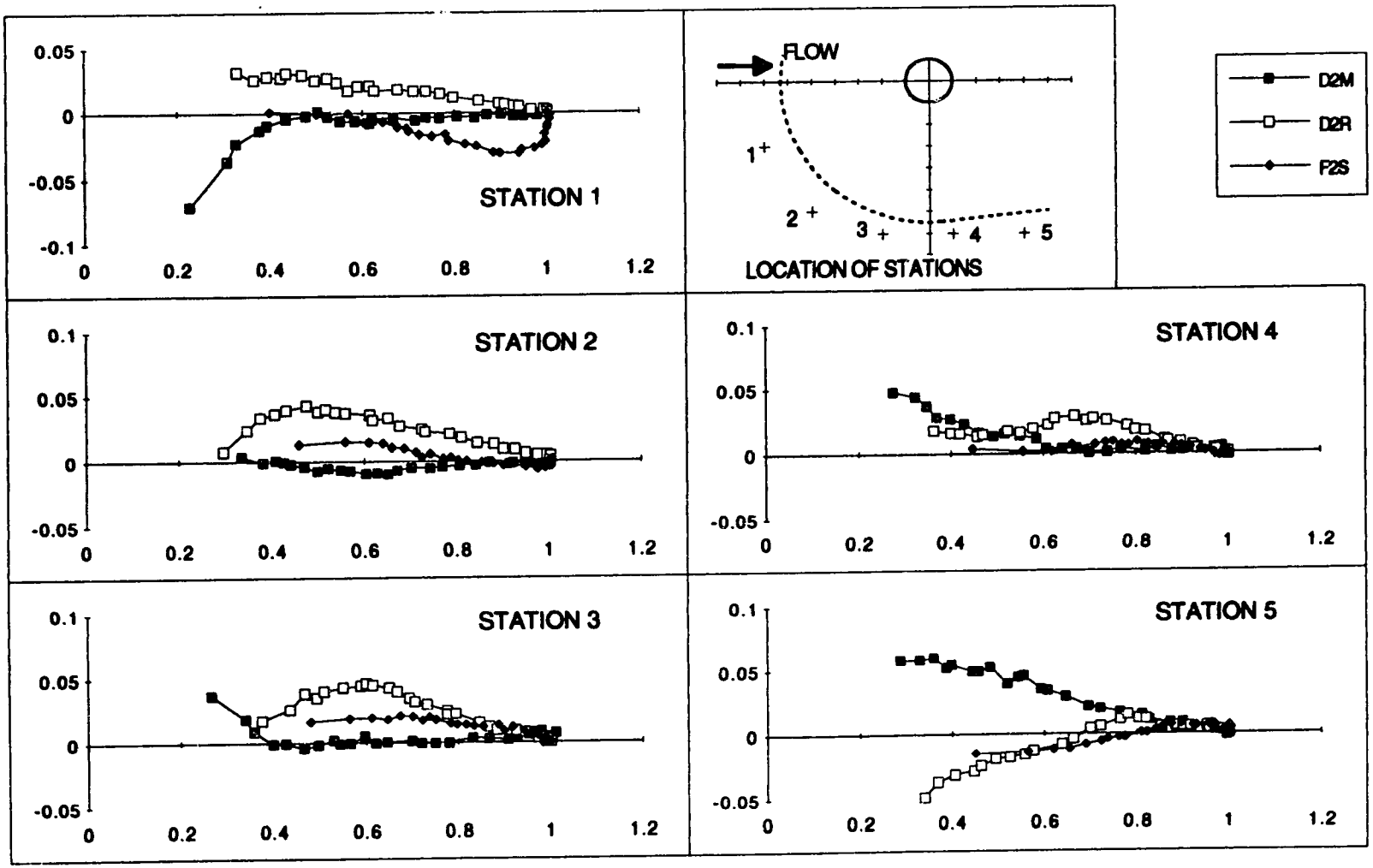

Note: normalized velocity components along and perpendicular to the free streamline direction are plotted on horizontal and vertical axes

Figure 4.5.2 (e) Polar plots of the skewed boundary layer (Expt. D2M, D2R and F2S, Stations 1 to 5)

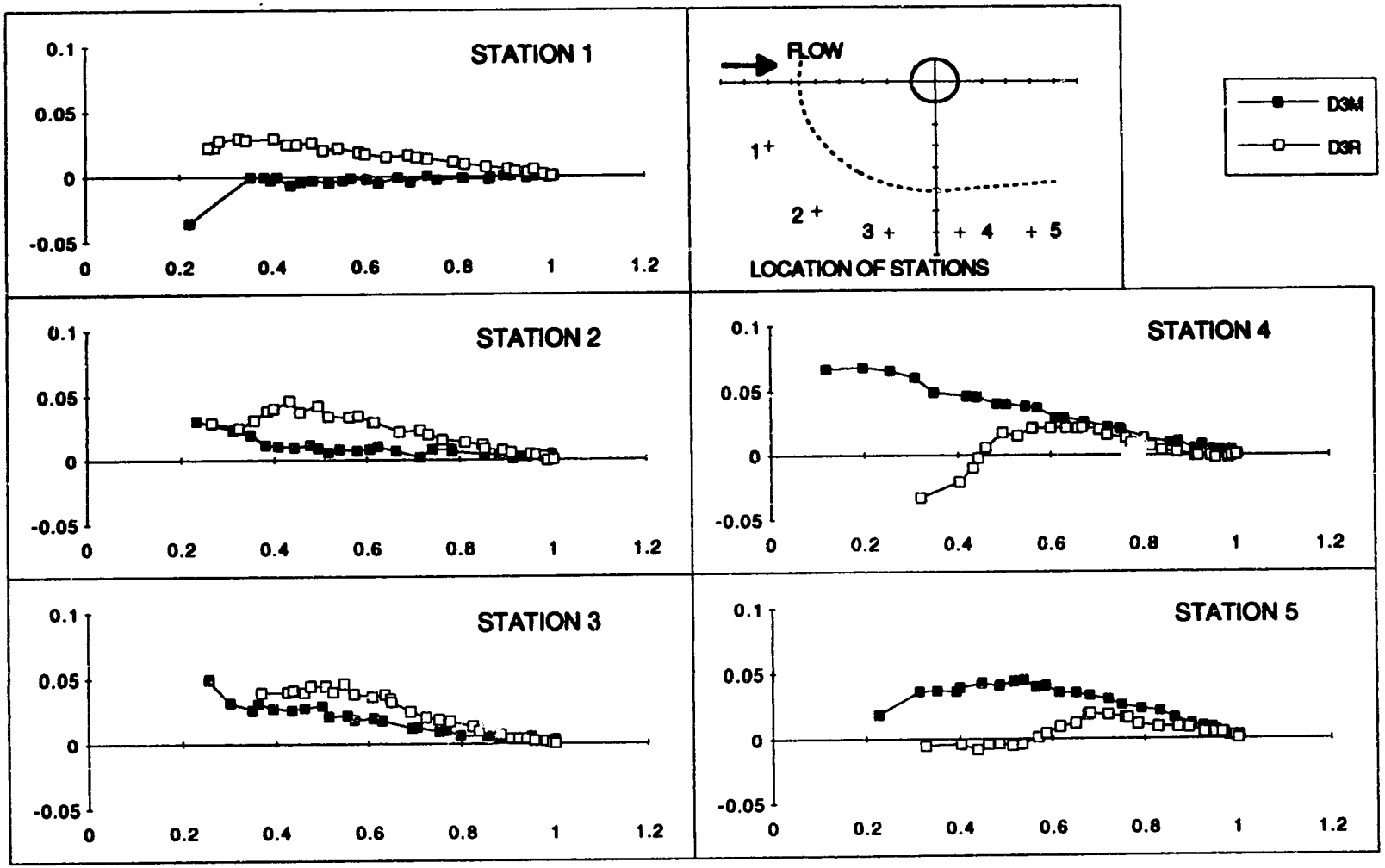

Note: normalized velocity components along and perpendicular to the free streamline direction are plotted on horizontal and vertical axes

Figure 4.5.2 (f) Polar plots of the skewed boundary layer (Expt. D3M and D3R, Stations 1 to 5)

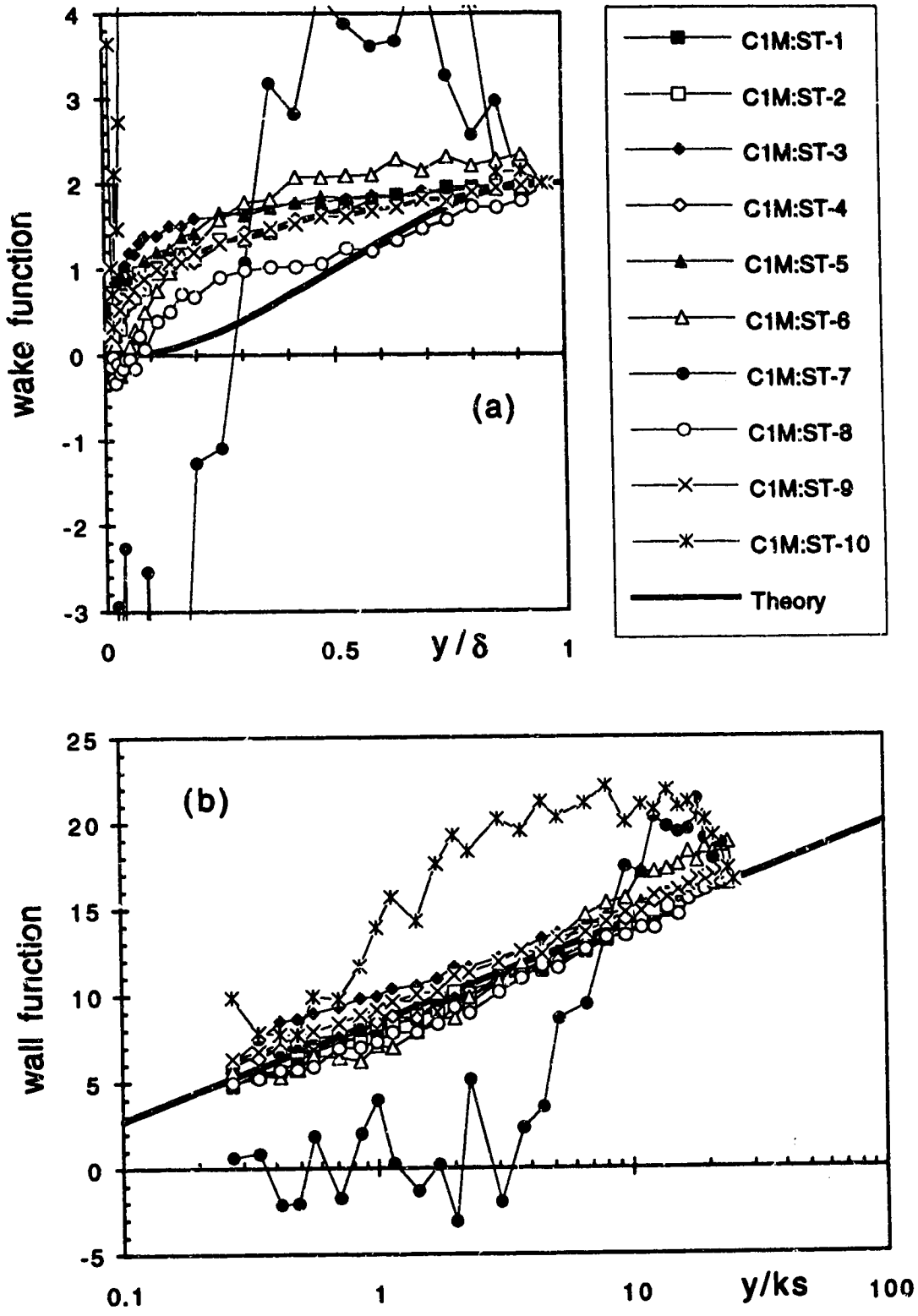

Figure 4.5.3 (a) Applicability of Coles' model (Expt. C1M)

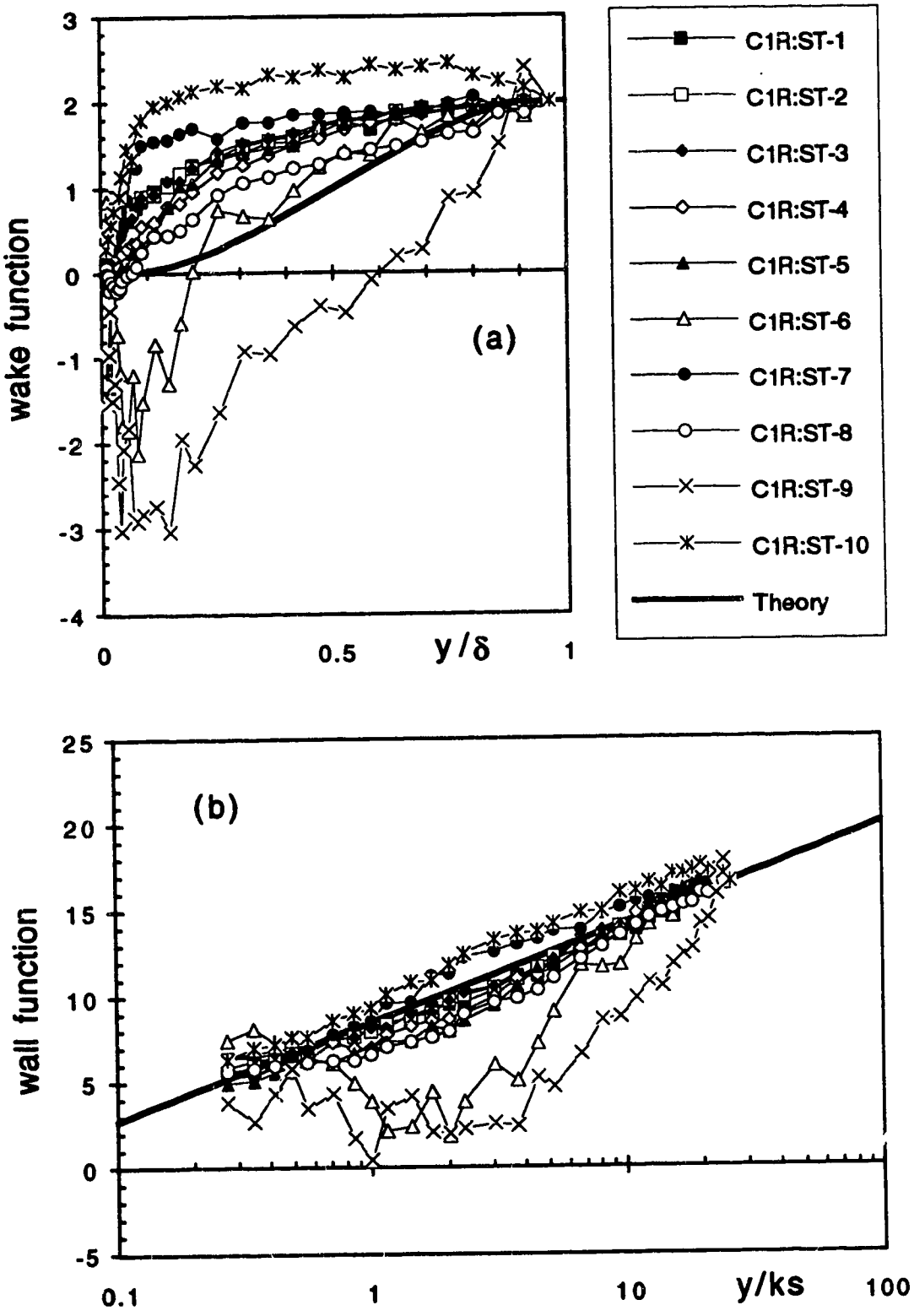

Figure 4.5.3 (b) Applicability of Coles' model (Expt. C1R)

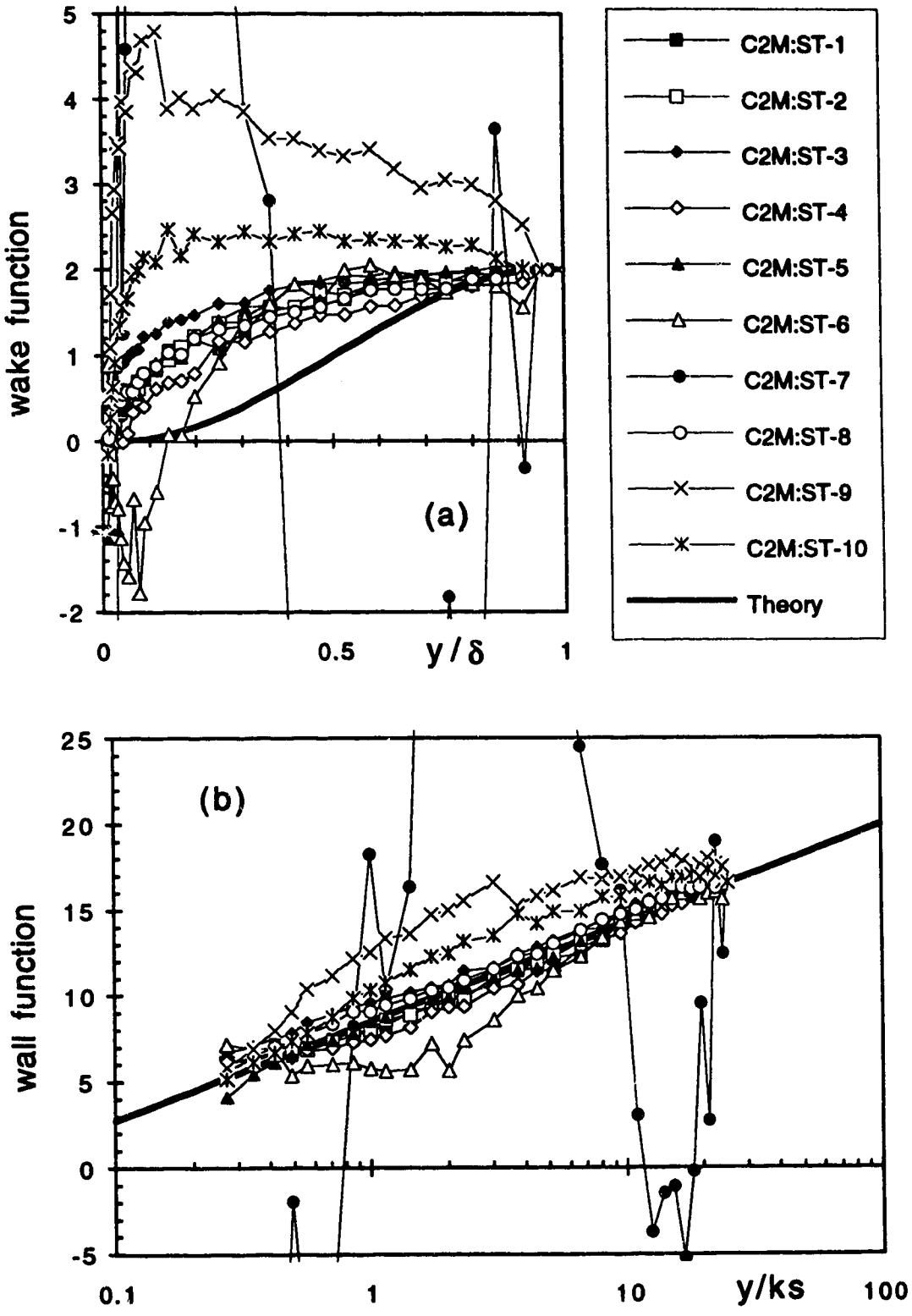

Figure 4.5.3 (c) Applicability of Coles' model (Expt. C2M)

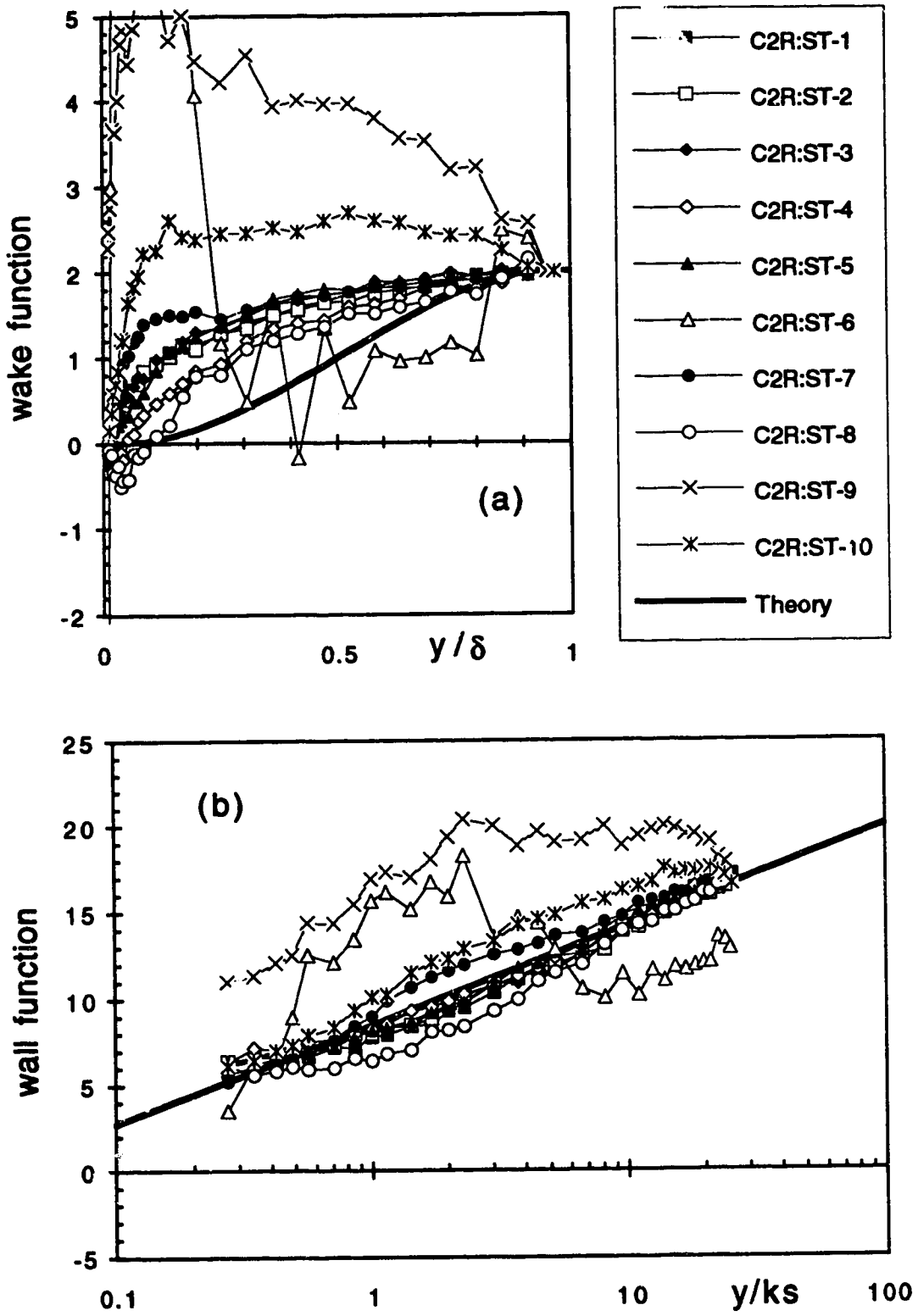

Figure 4.5.3 (d) Applicability of Coles' model (Expt. C2R)

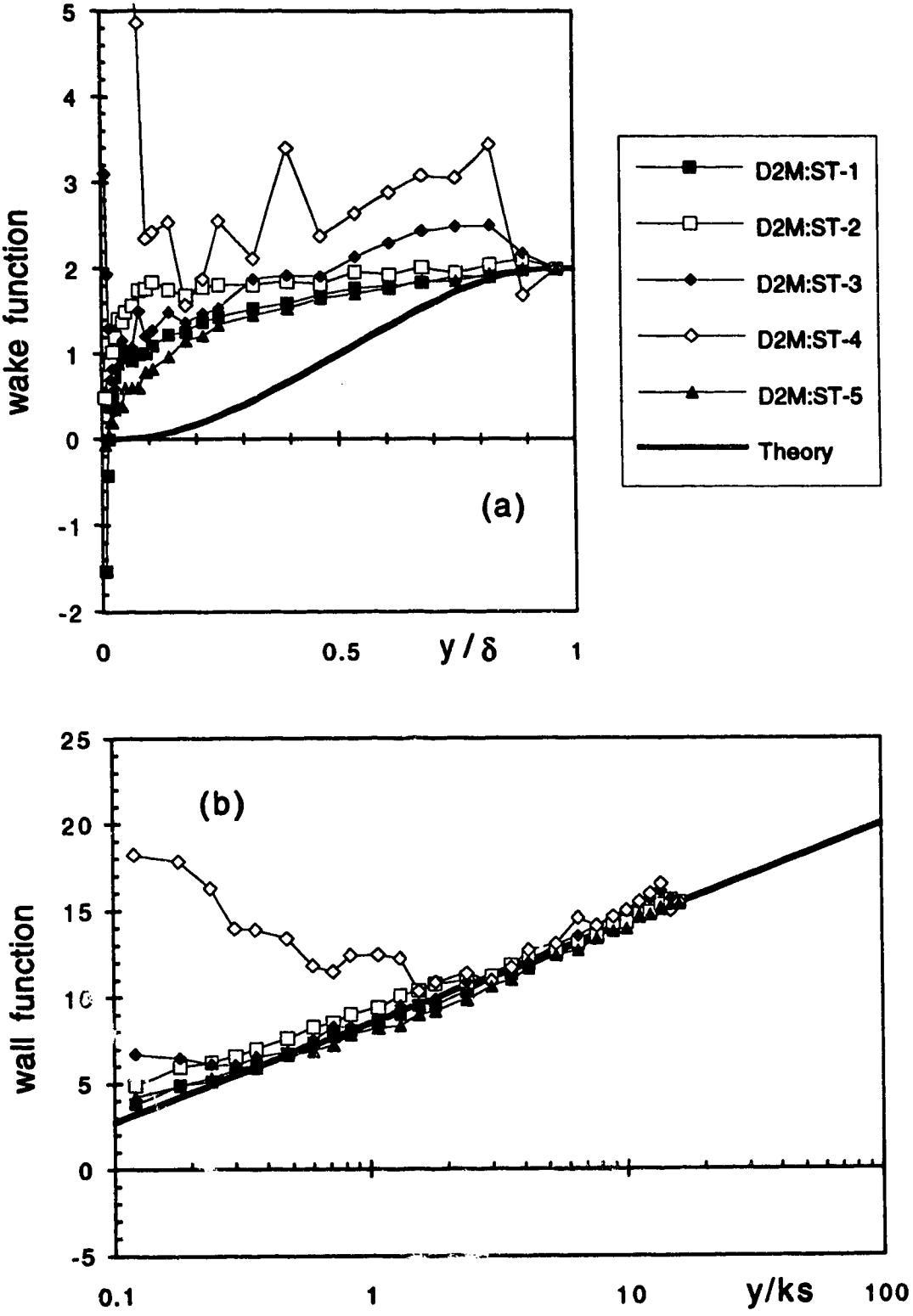

Figure 4.5.3 (e) Applicability of Coles' model (Expt. D2M)

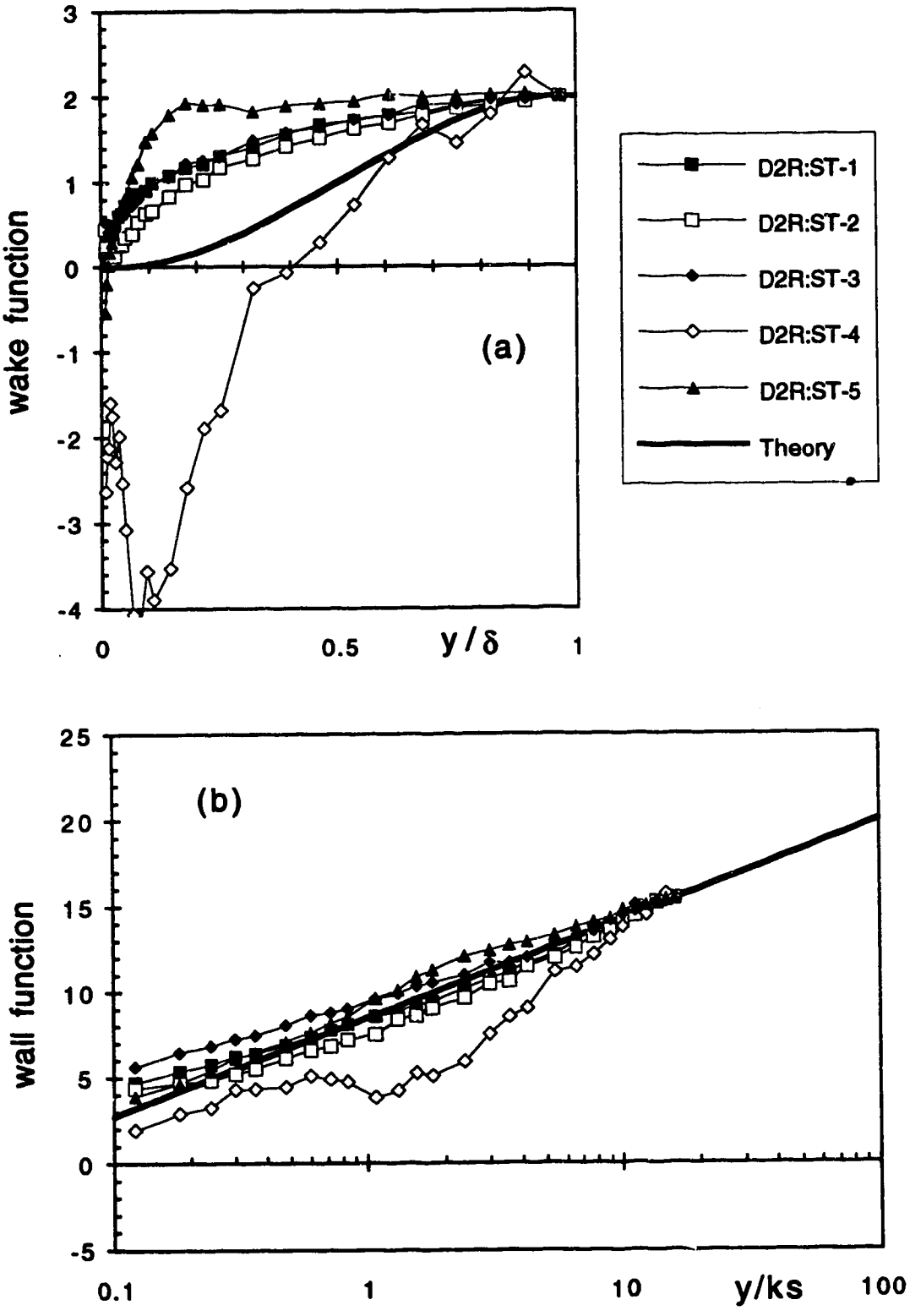

Figure 4.5.3 (f) Applicability of Coles' model (Expt. D2R)

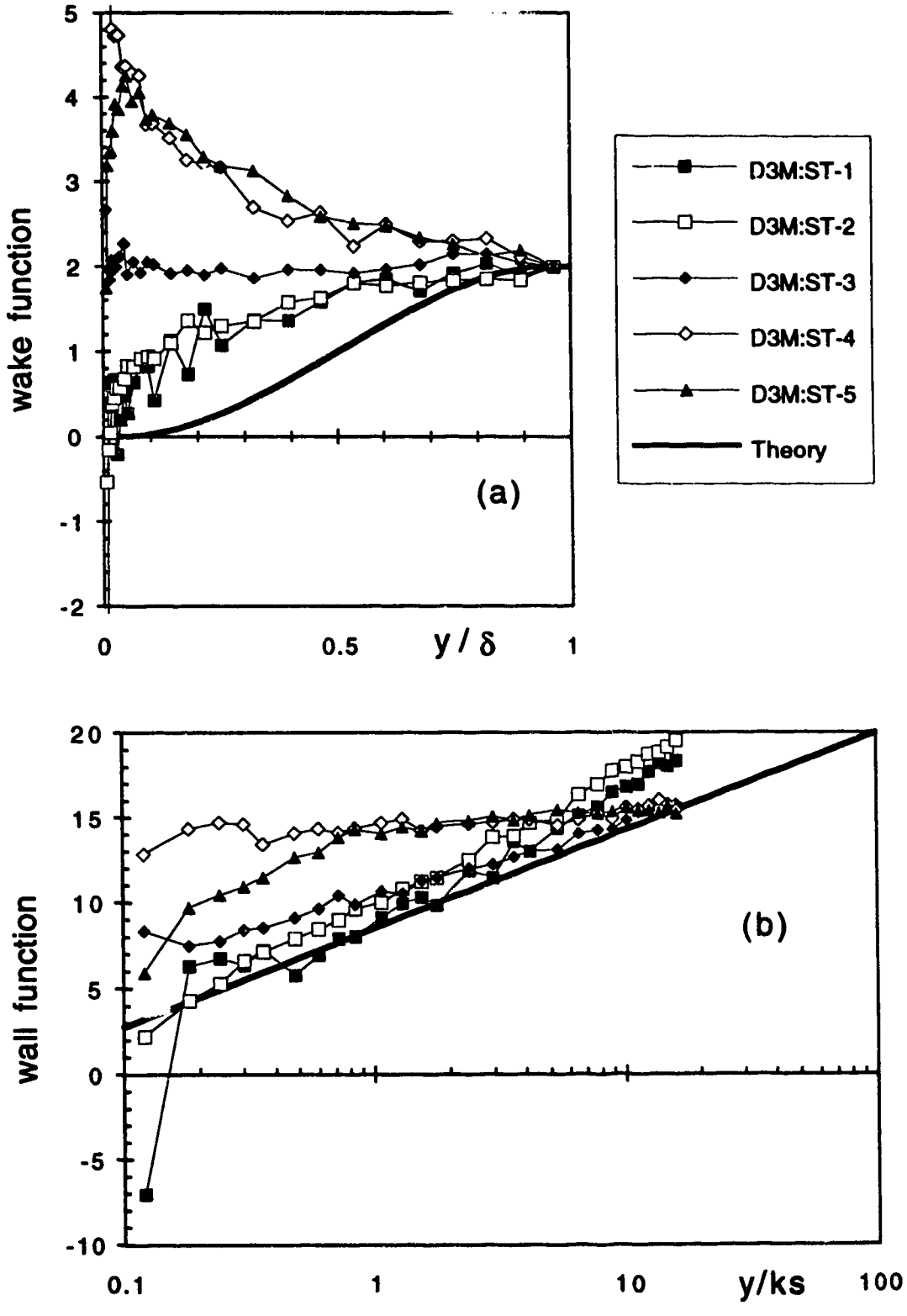

Figure 4.5.3 (g) Applicability of Coles' model (Expt. D3M)

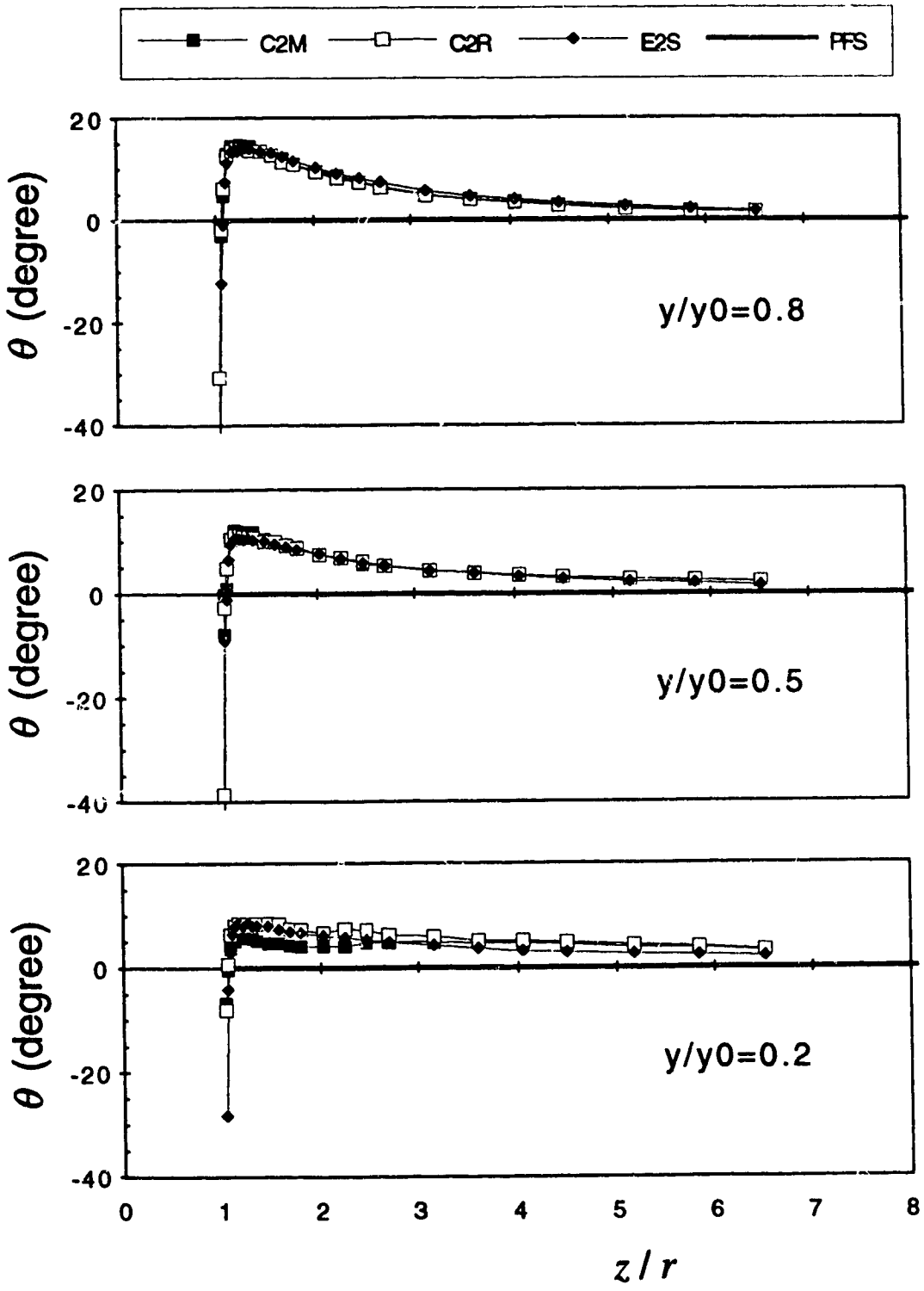

Figure 4.2.7 (a-b) Transverse variation of the angle of yaw of the deflected flow
(a) Expt. C2M, C2R and E2S; x/r=0 plane

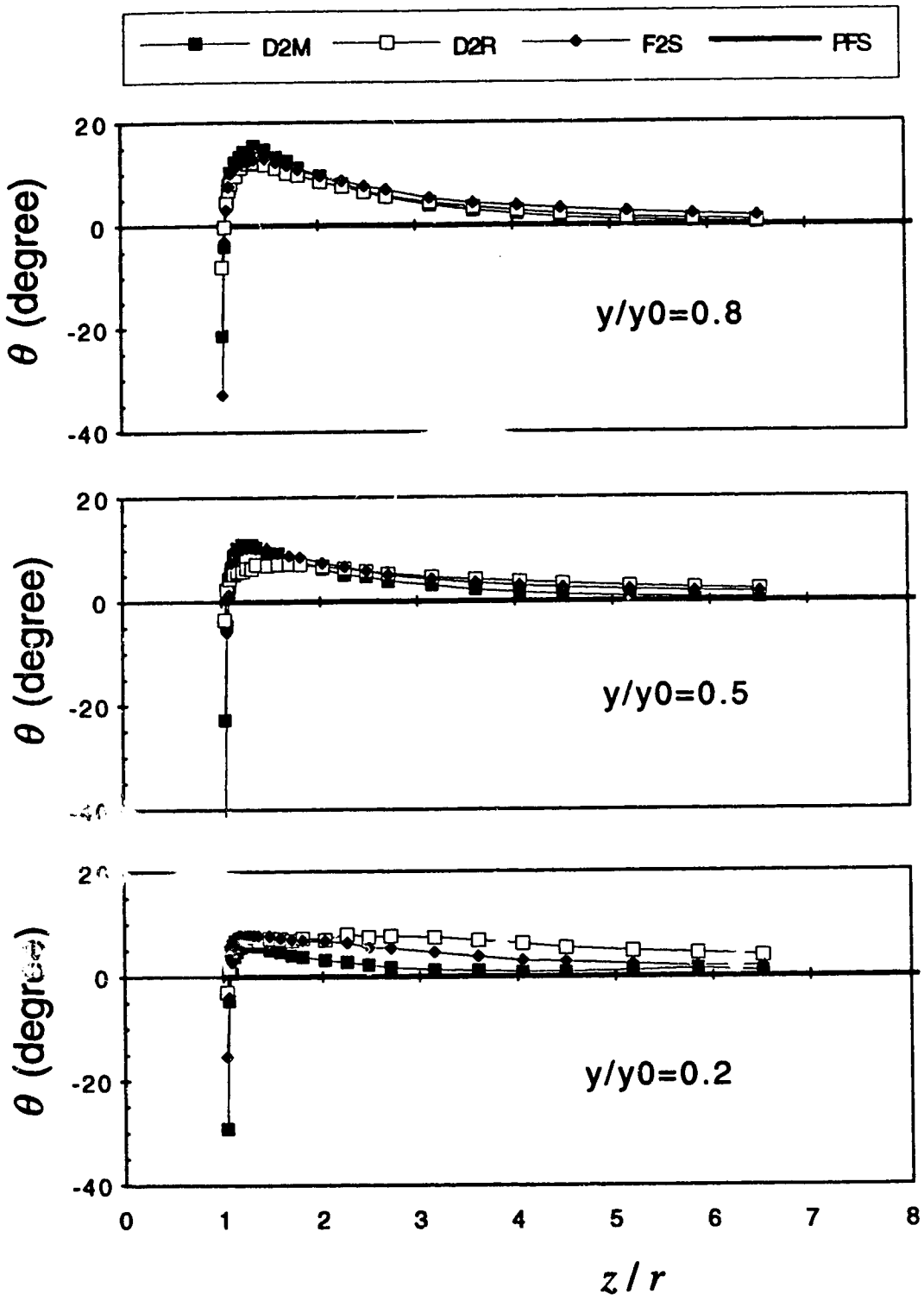

Figure 4.2.7 (a-b) Transverse variation of the angle of yaw of the deflected flow
(b) Expt. D2M, D2R and F2S; x/r=0 plane

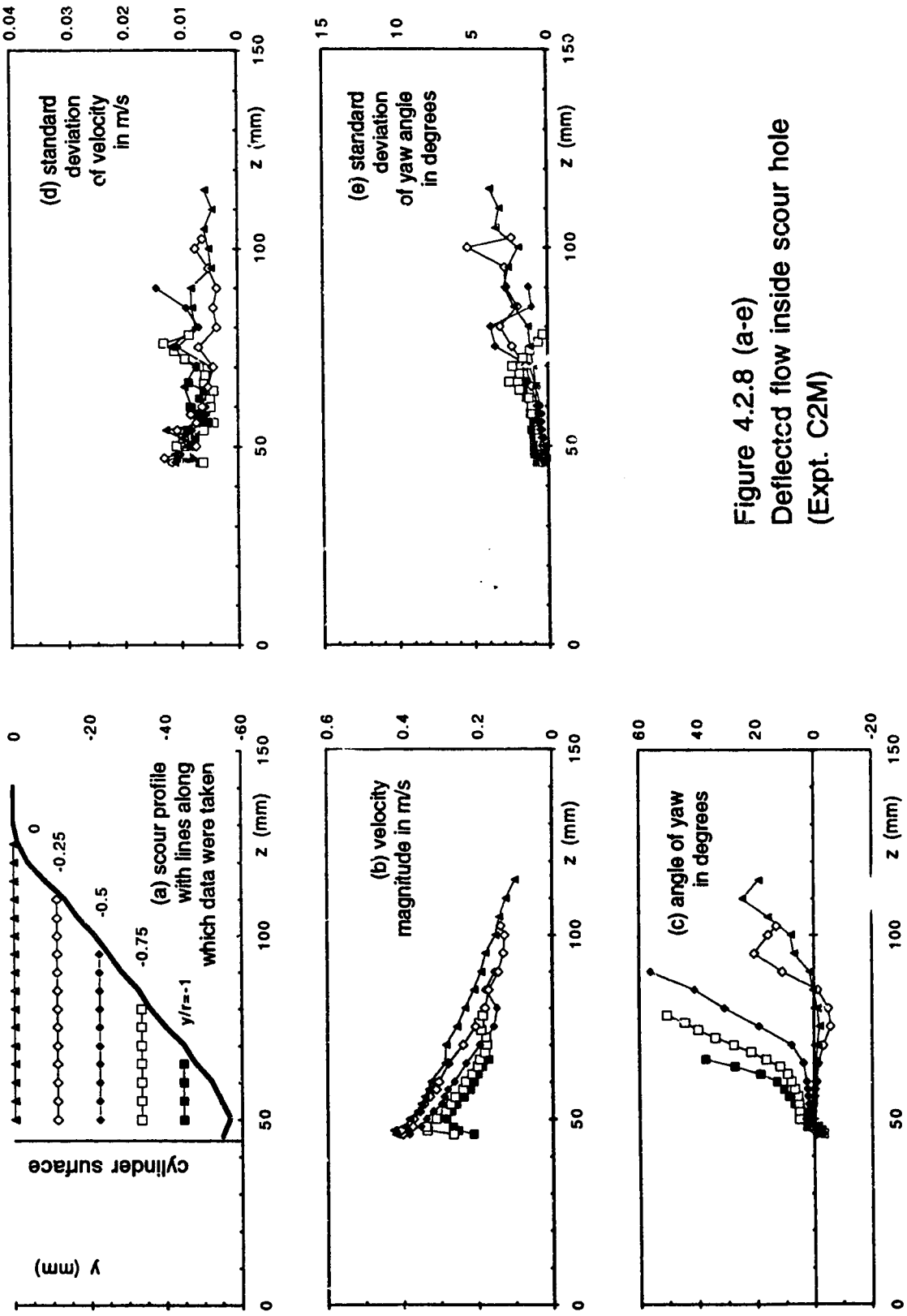

Figure 4.2.8 (a-e)
Deflected flow inside scour hole
(Expt. C2M)

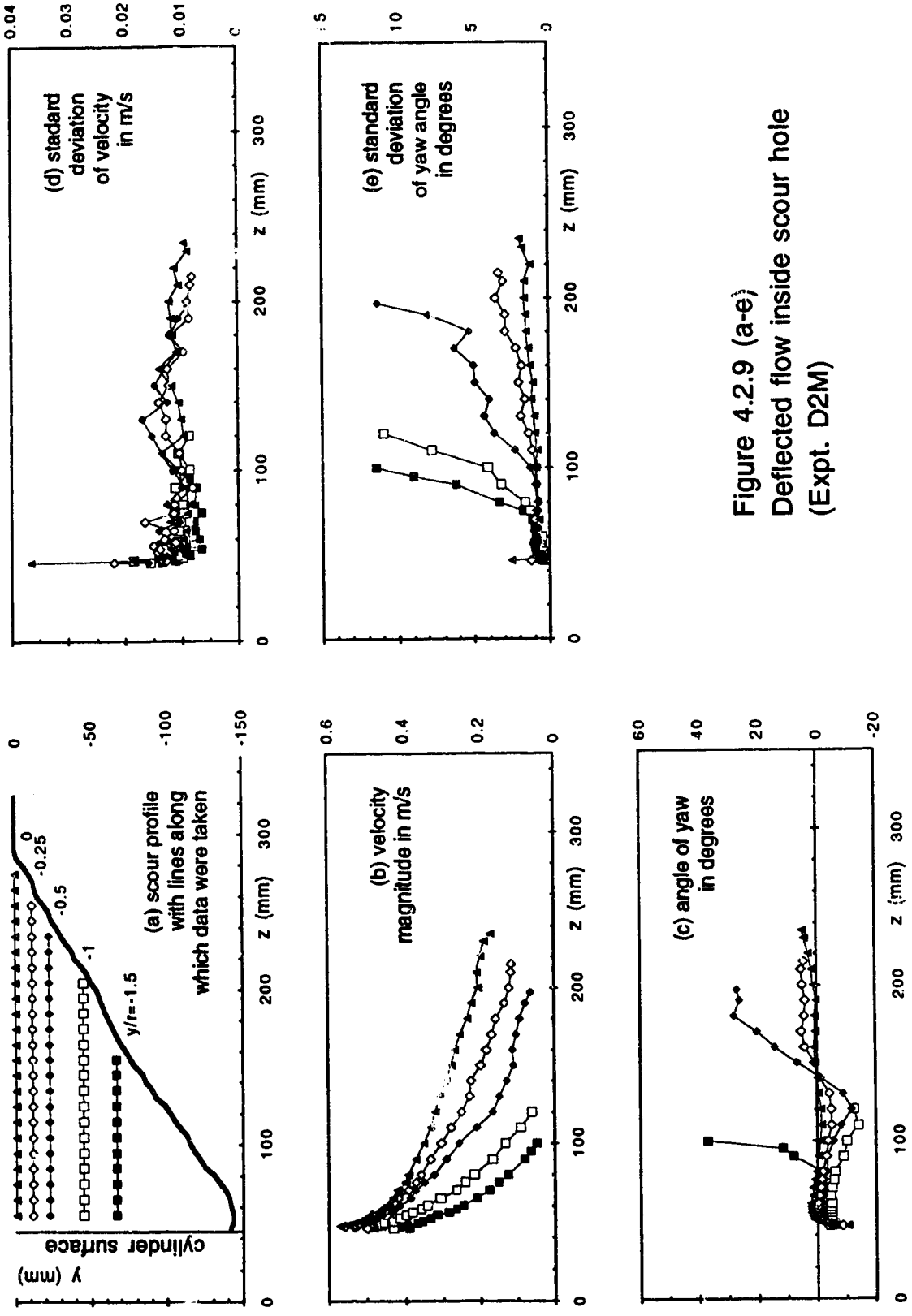

Figure 4.2.9 (a-e)
Deflected flow inside scour hole
(Expt. D2M)

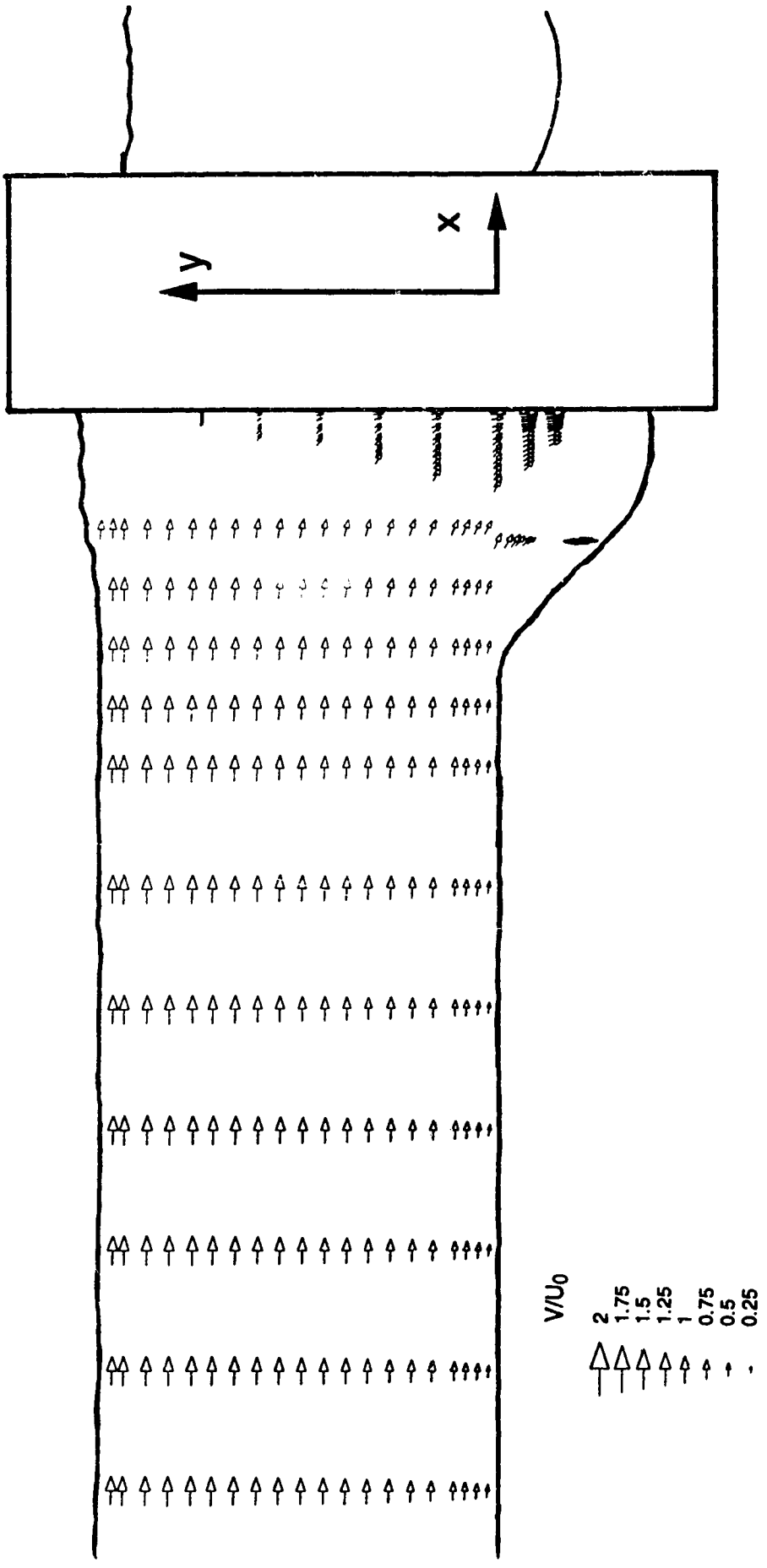

4.2.10 (a-b) Typical vector plot of the velocity distribution on the POS (Expt. C1M); (a) upstream region

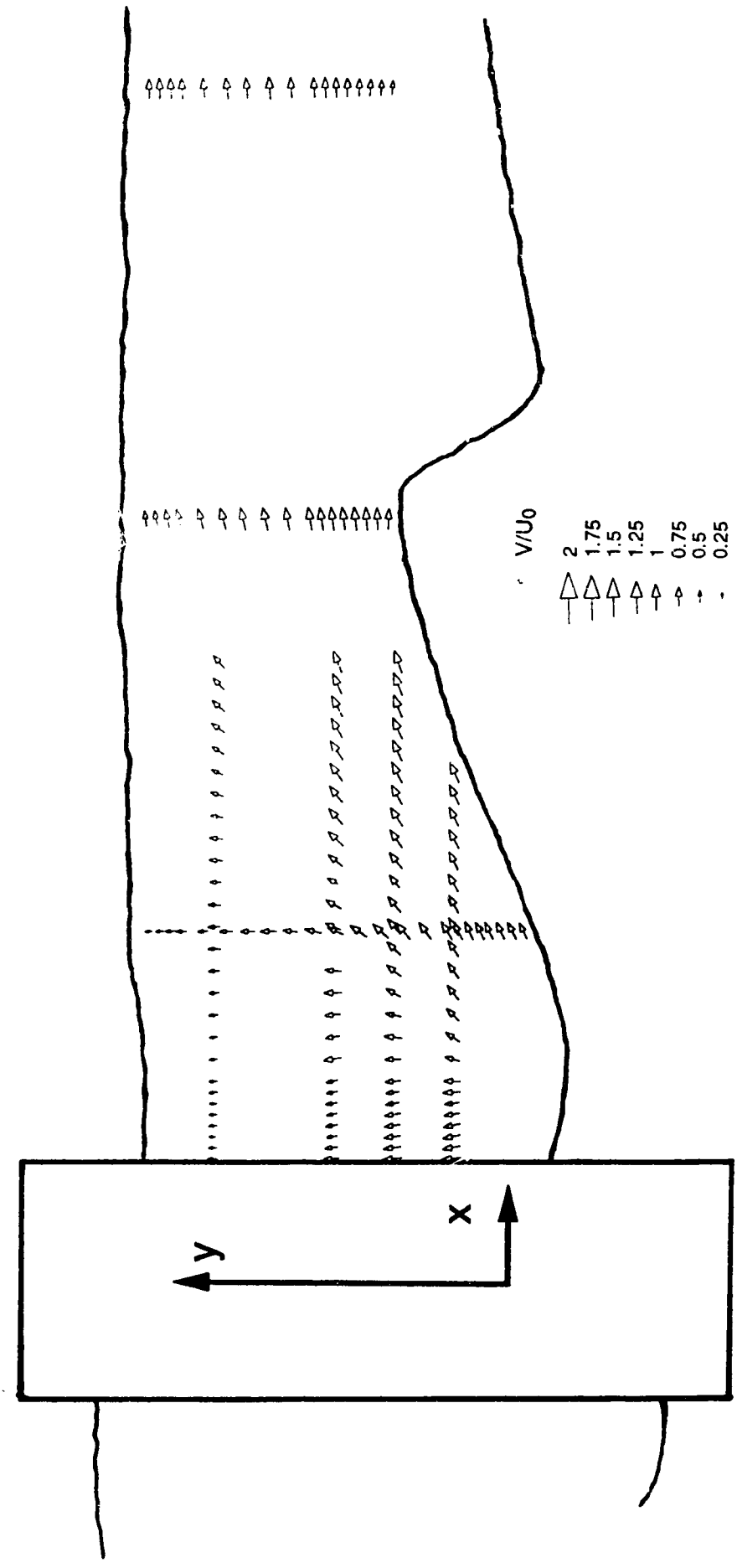

4.2.10 (a-b) Typical vector plot of the velocity distribution on the POS (Expt. C1M); (b) downstream region

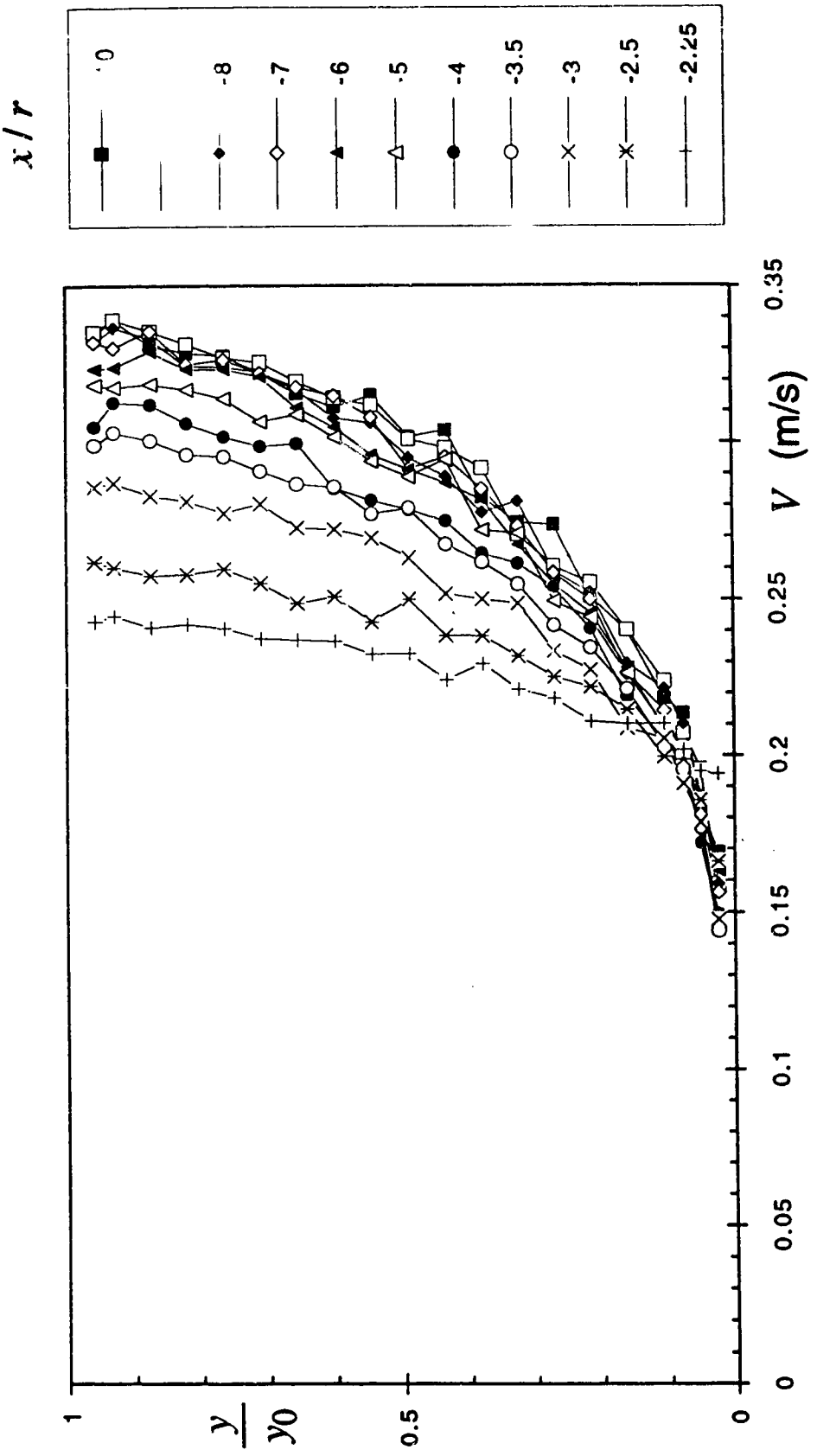

Figure 4.2.11 (a-i) Velocity Distribution on the POS (Expt. C2M)
(a) Velocity magnitude

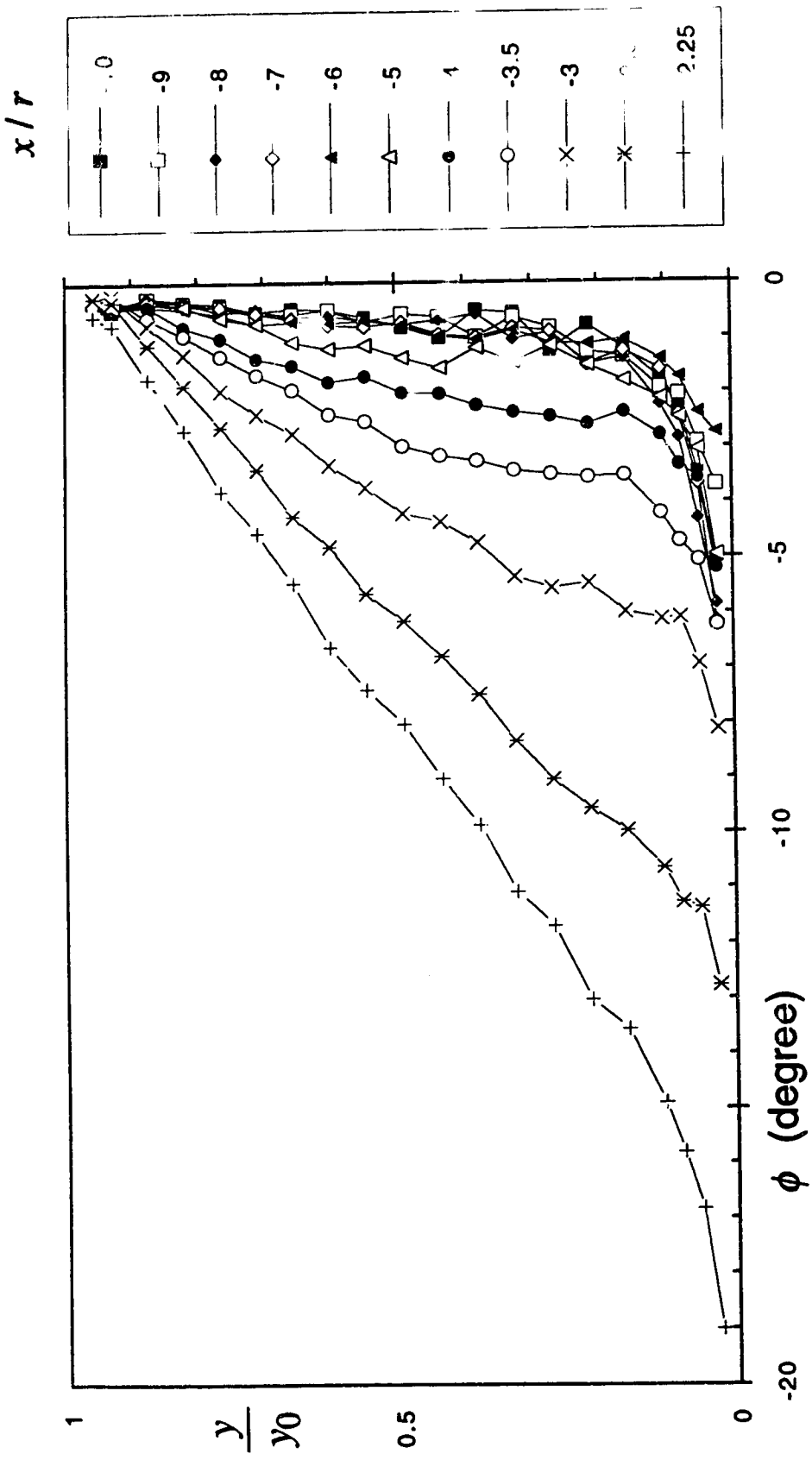

Figure 4.2.11 (a-i) Velocity Distribution on the POS (Expt. C2M)
(b) Angle of pitch

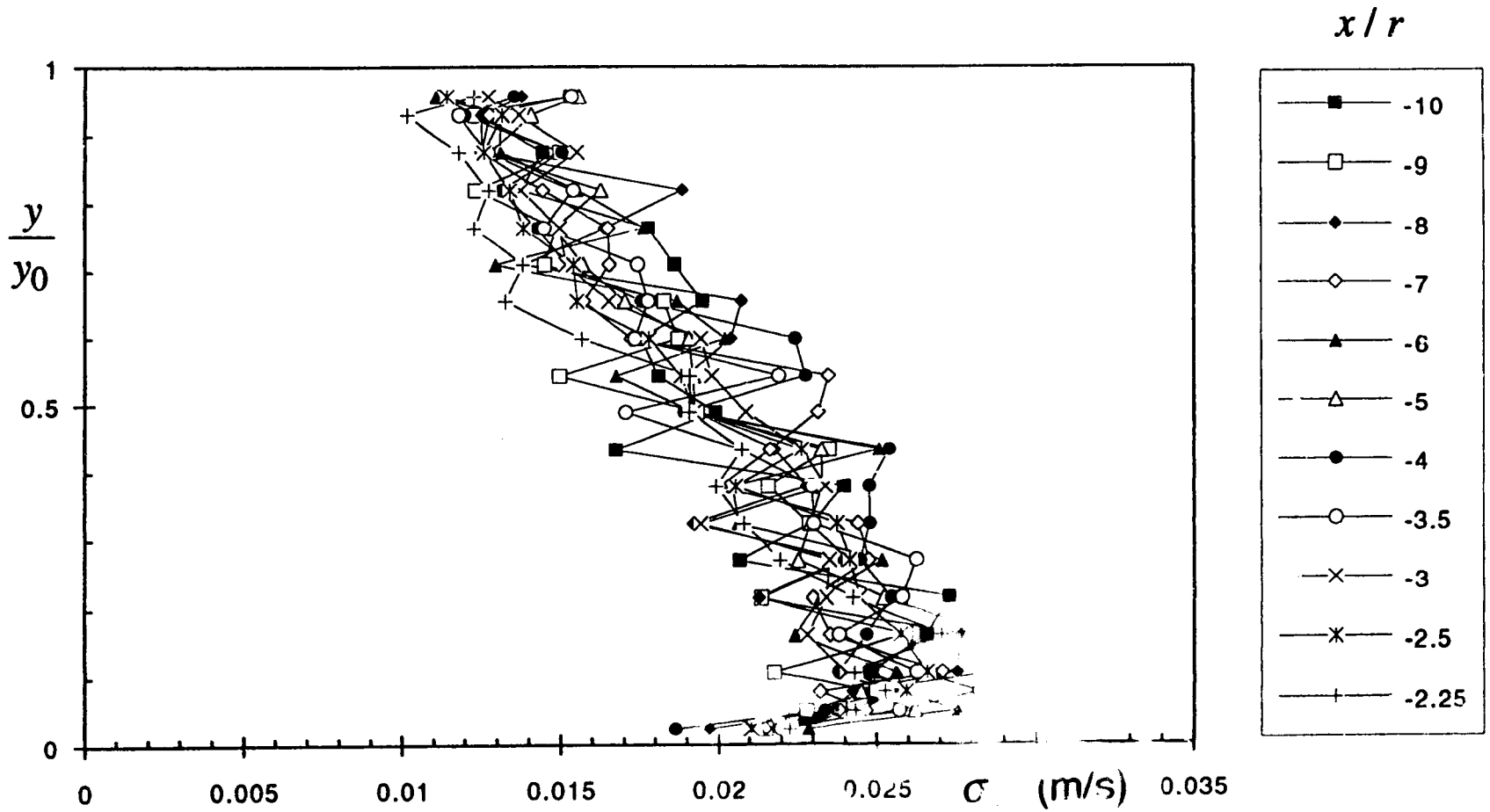

Figure 4.2.11 (a-i) Velocity Distribution on the POS (Expt. C2M)
(c) Standard deviation of the velocity magnitude

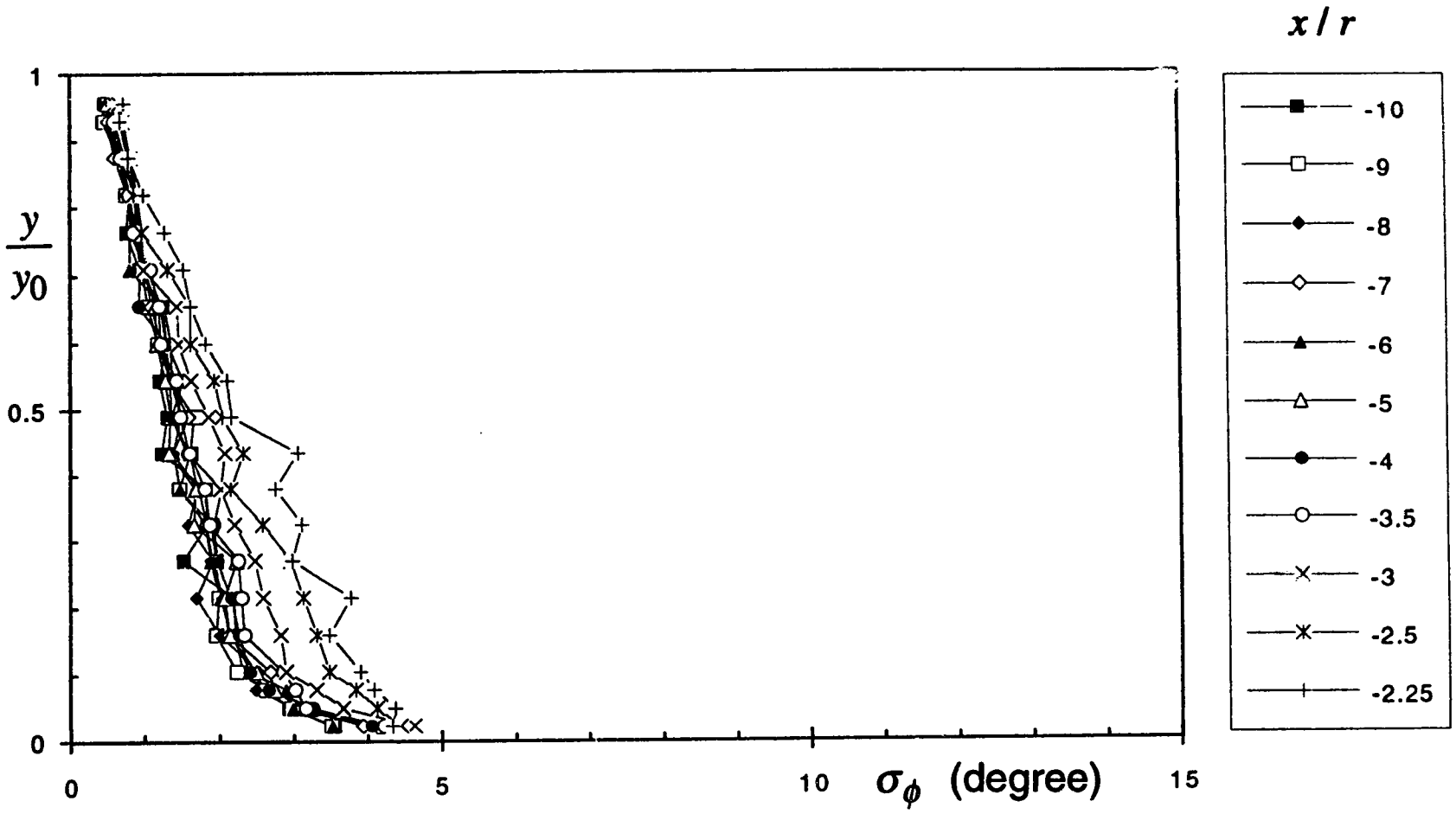

Figure 4.2.11 (a-i) Velocity Distribution on the POS (Expt. C2M)
(d) Standard deviation of the pitch angle

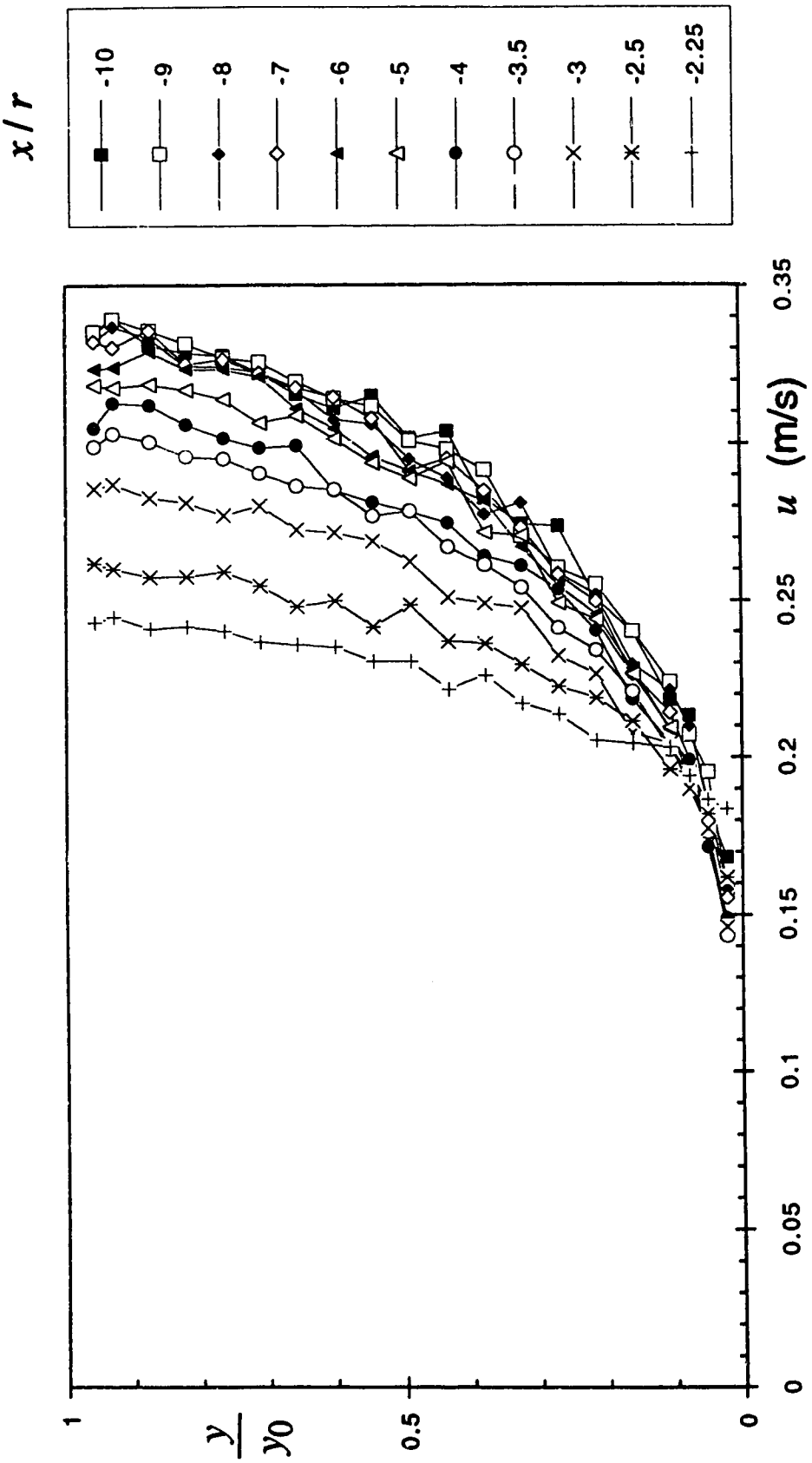

Figure 4.2.11 (a-i) Velocity Distribution on the POS (Expt. C2M)
(e) Longitudinal component of velocity

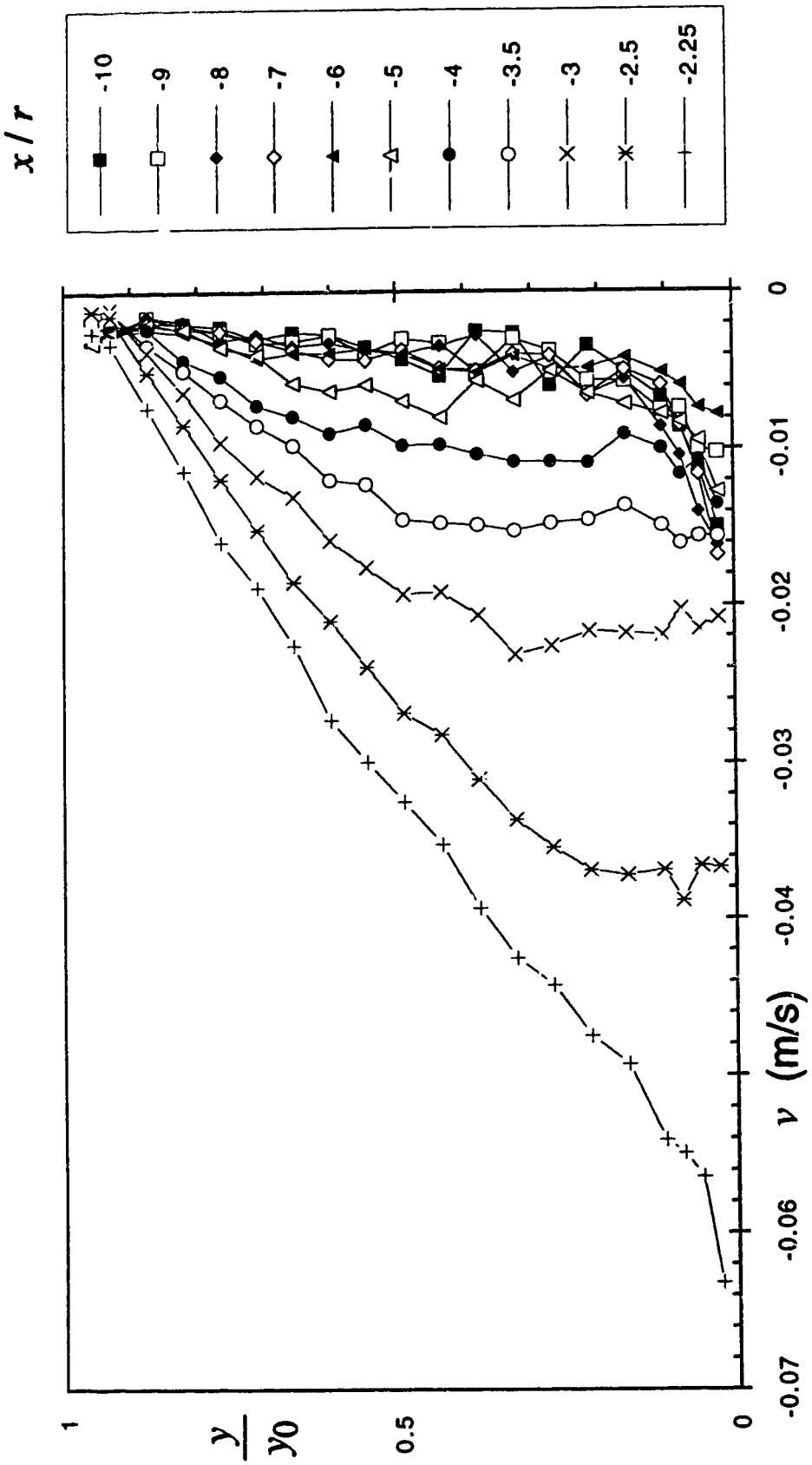

Figure 4.2.11 (a-i) Velocity Distribution on the POS (Expt. C2M)
(f) Vertical component of velocity

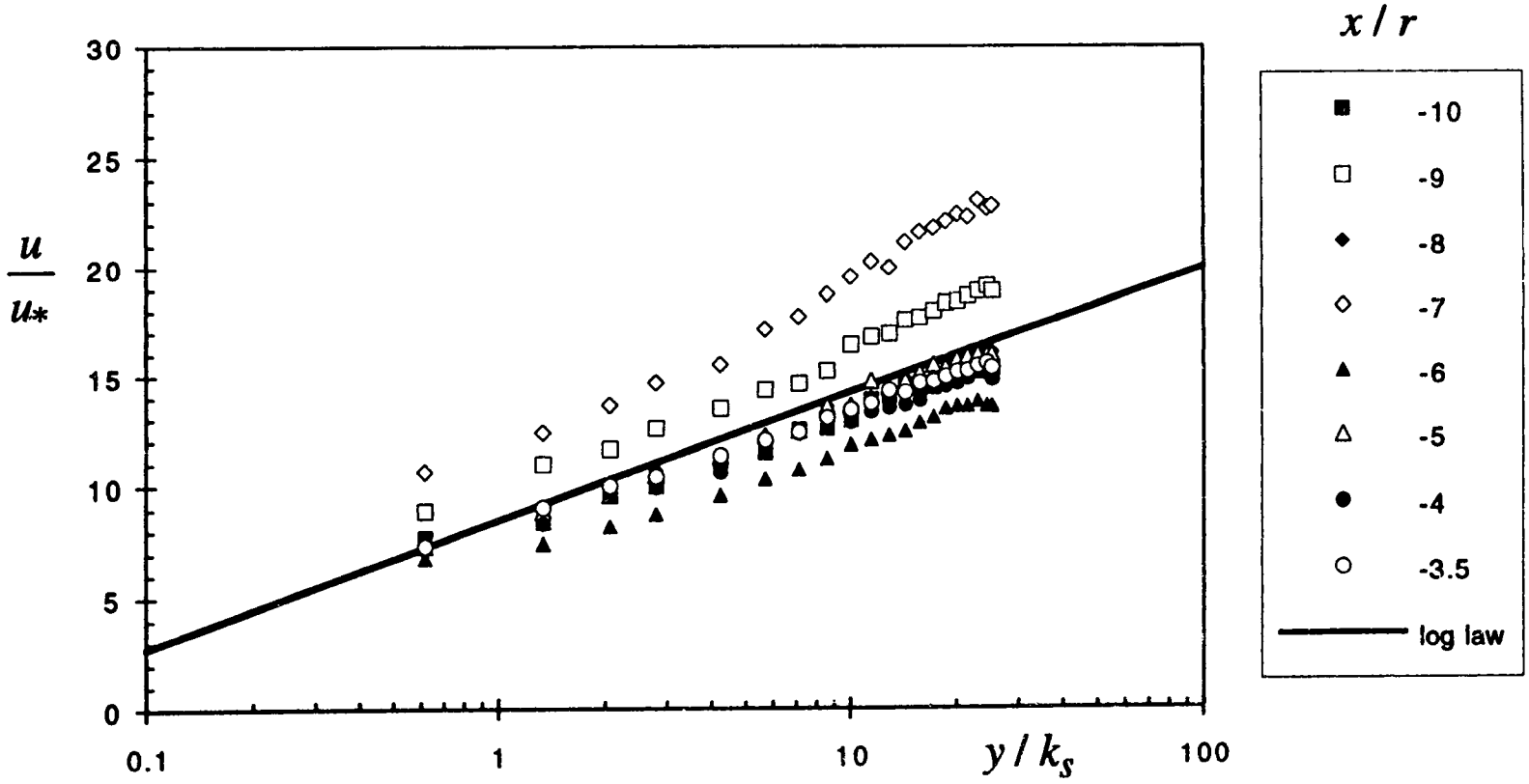

Figure 4.2.11 (a-i) Velocity Distribution on the POS (Expt. C2M)
(g) Comparison with log law

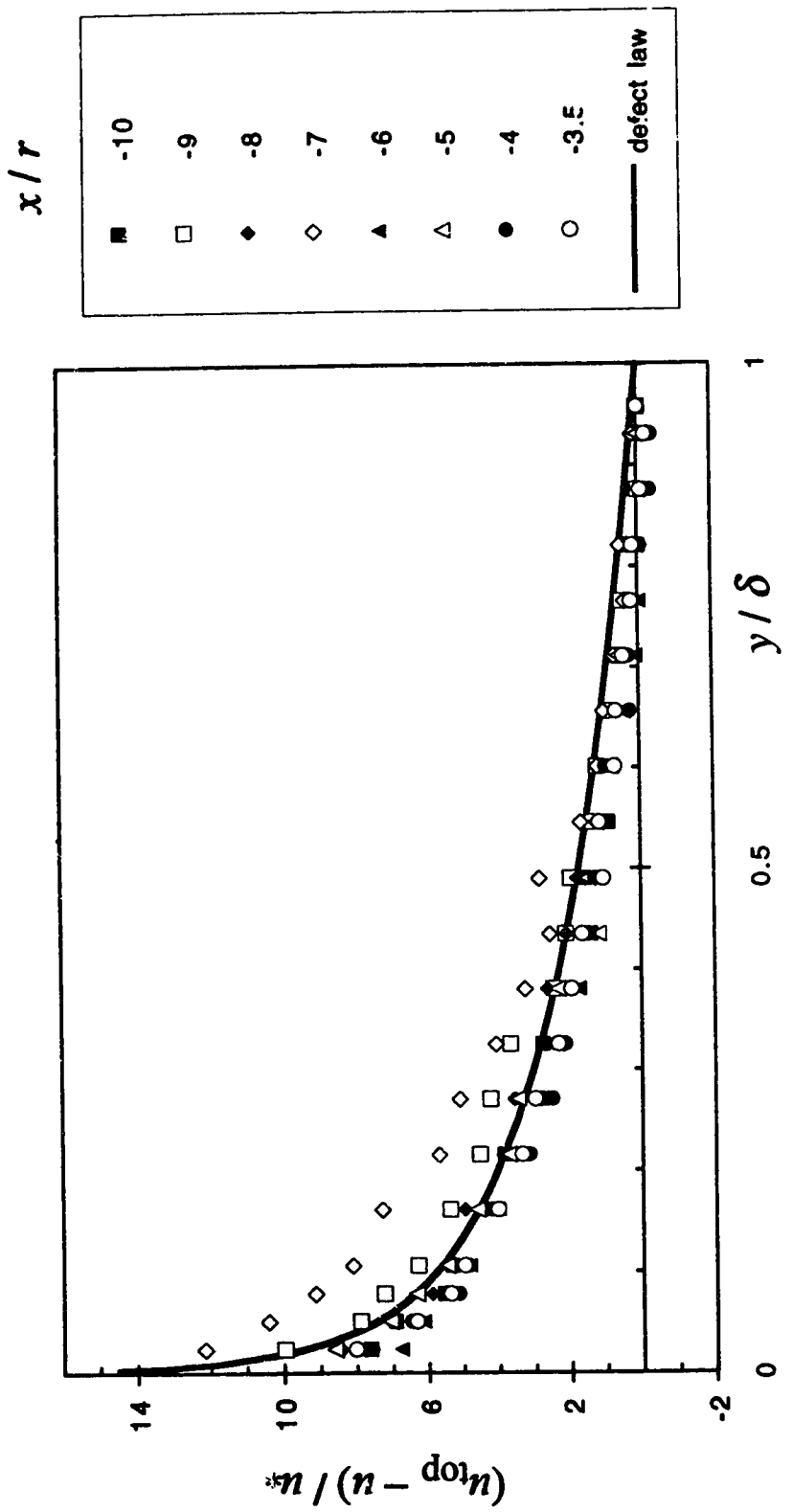

Figure 4.2.11 (a-i) Velocity Distribution on the POS (Expt. C2M)
(h) Comparison with defect law

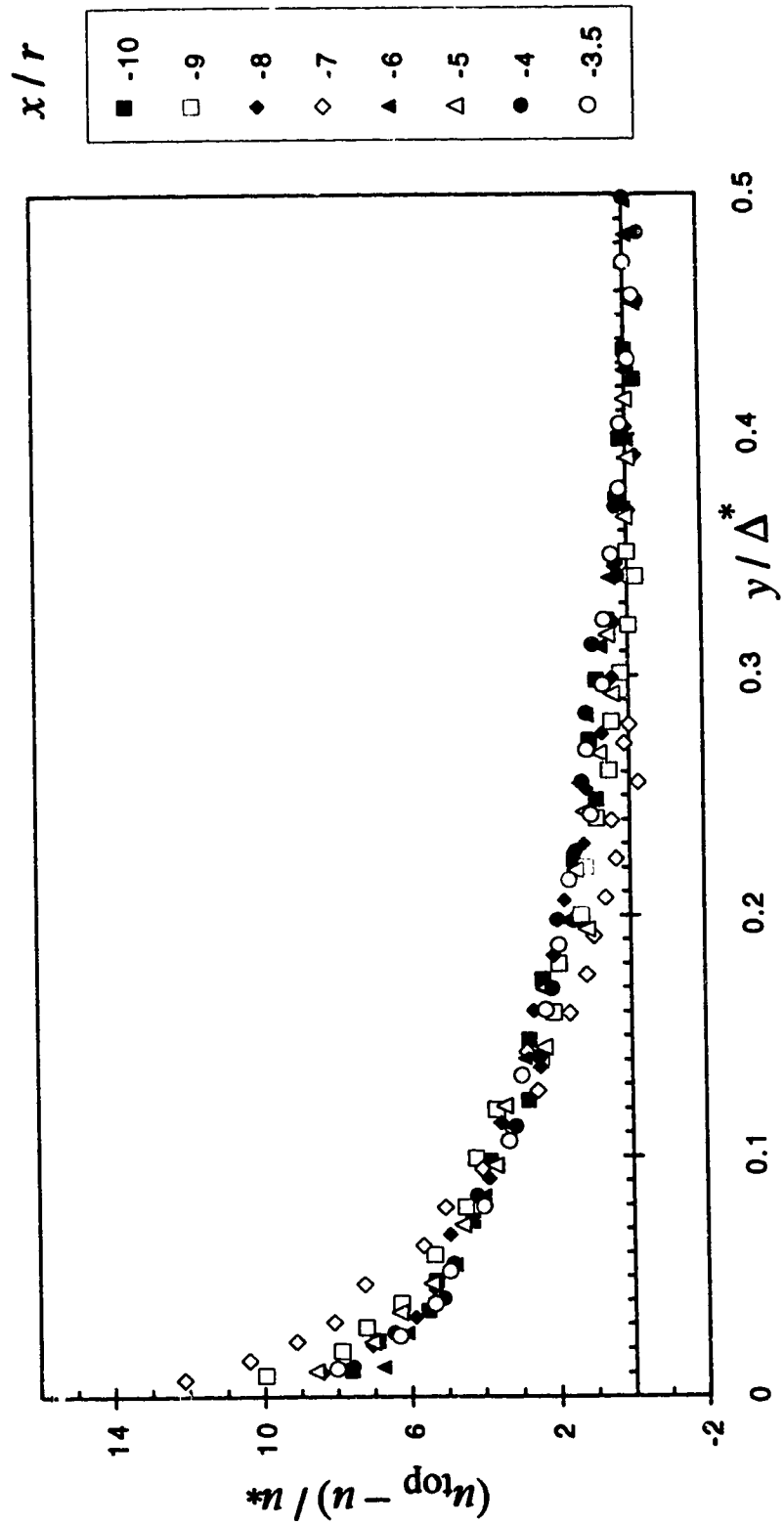

Figure 4.2.11 (a-i) Velocity Distribution on the POS (Expt. C2M)
(i) Comparison with Clauser's scheme

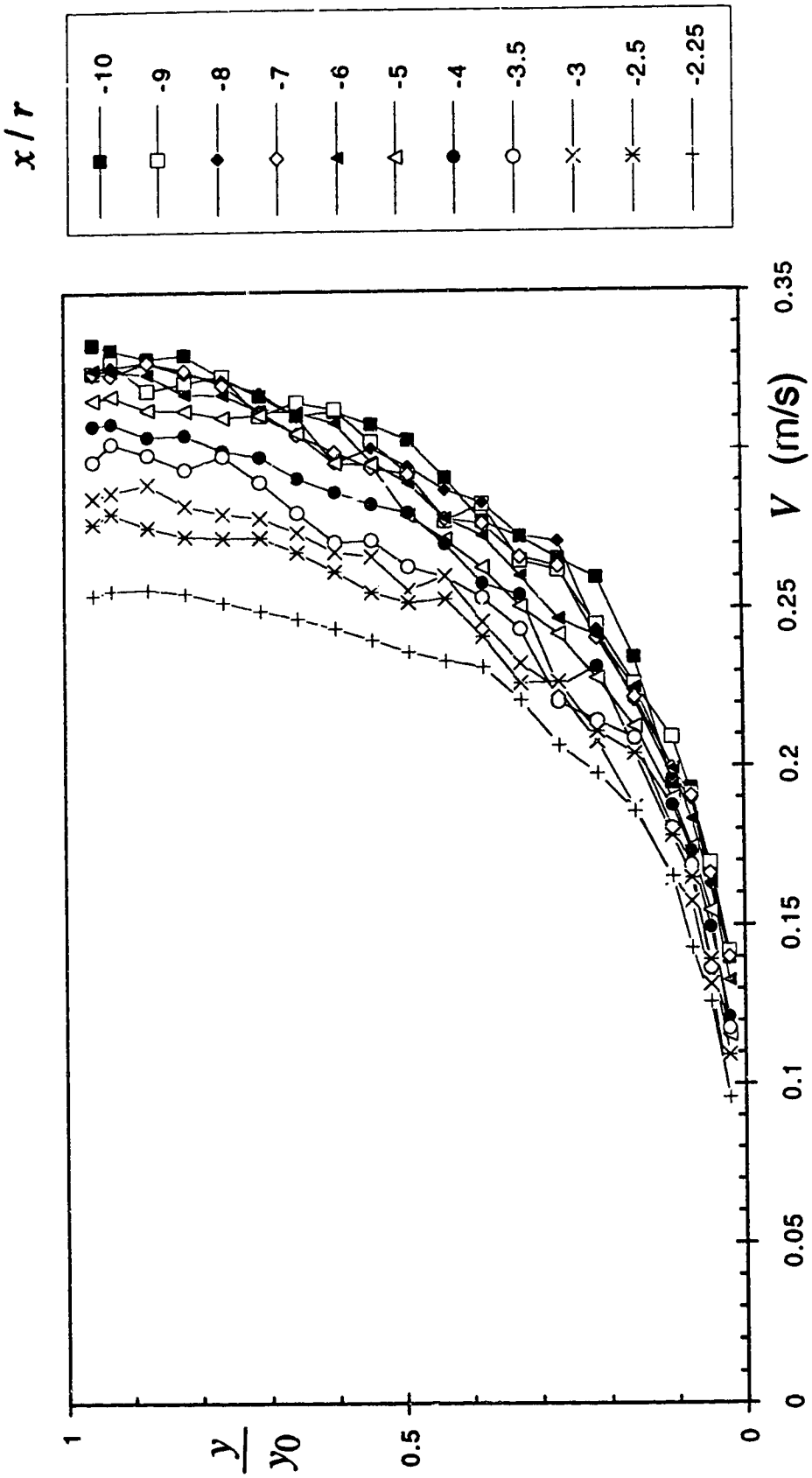

Figure 4.2.12 (a-i) Velocity Distribution on the POS (Expt. C2R)
(a) Velocity magnitude

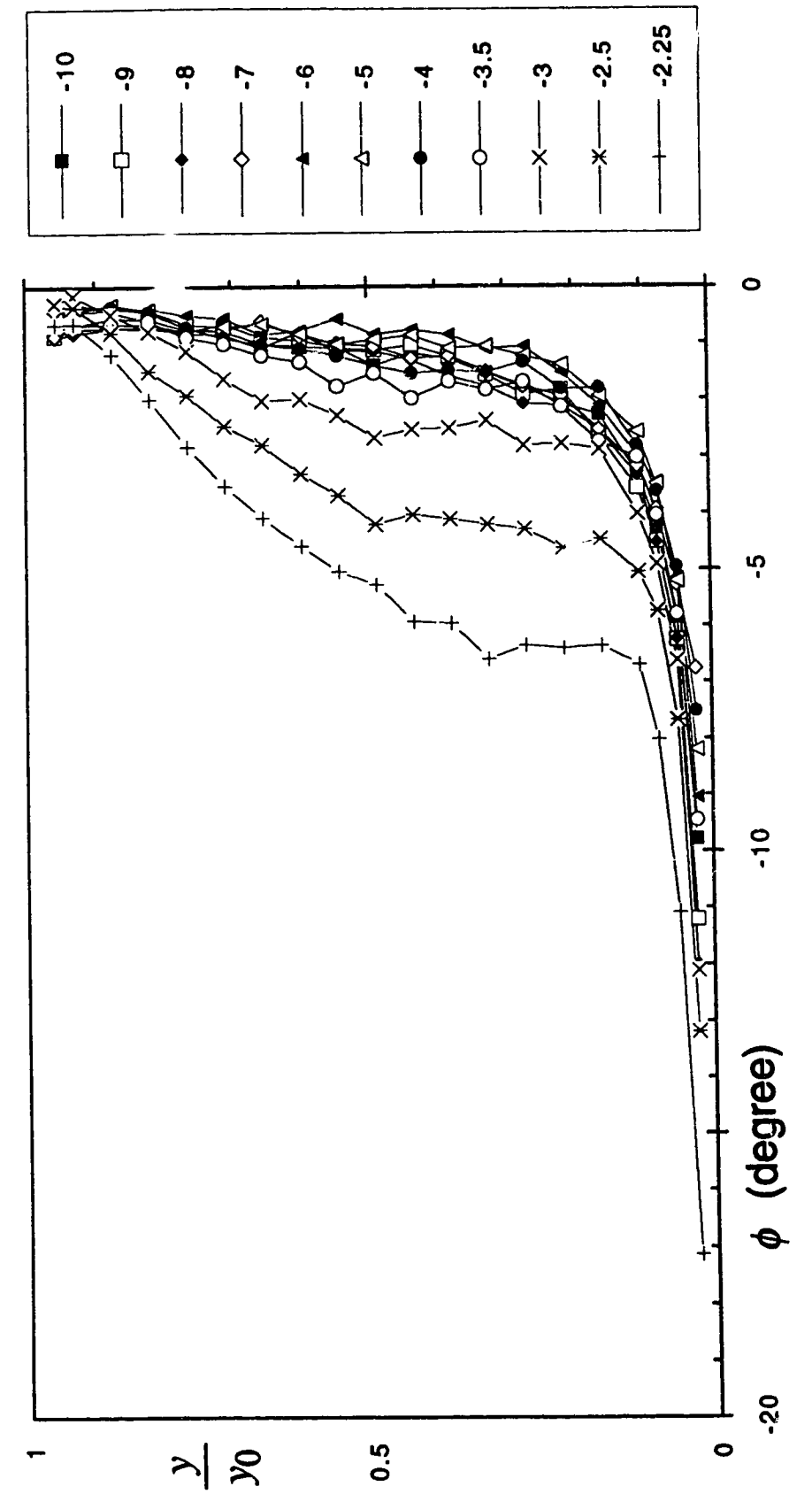

Figure 4.2.12 (a-i) Velocity Distribution on the POS (Expt. C2R)
(b) Angle of pitch

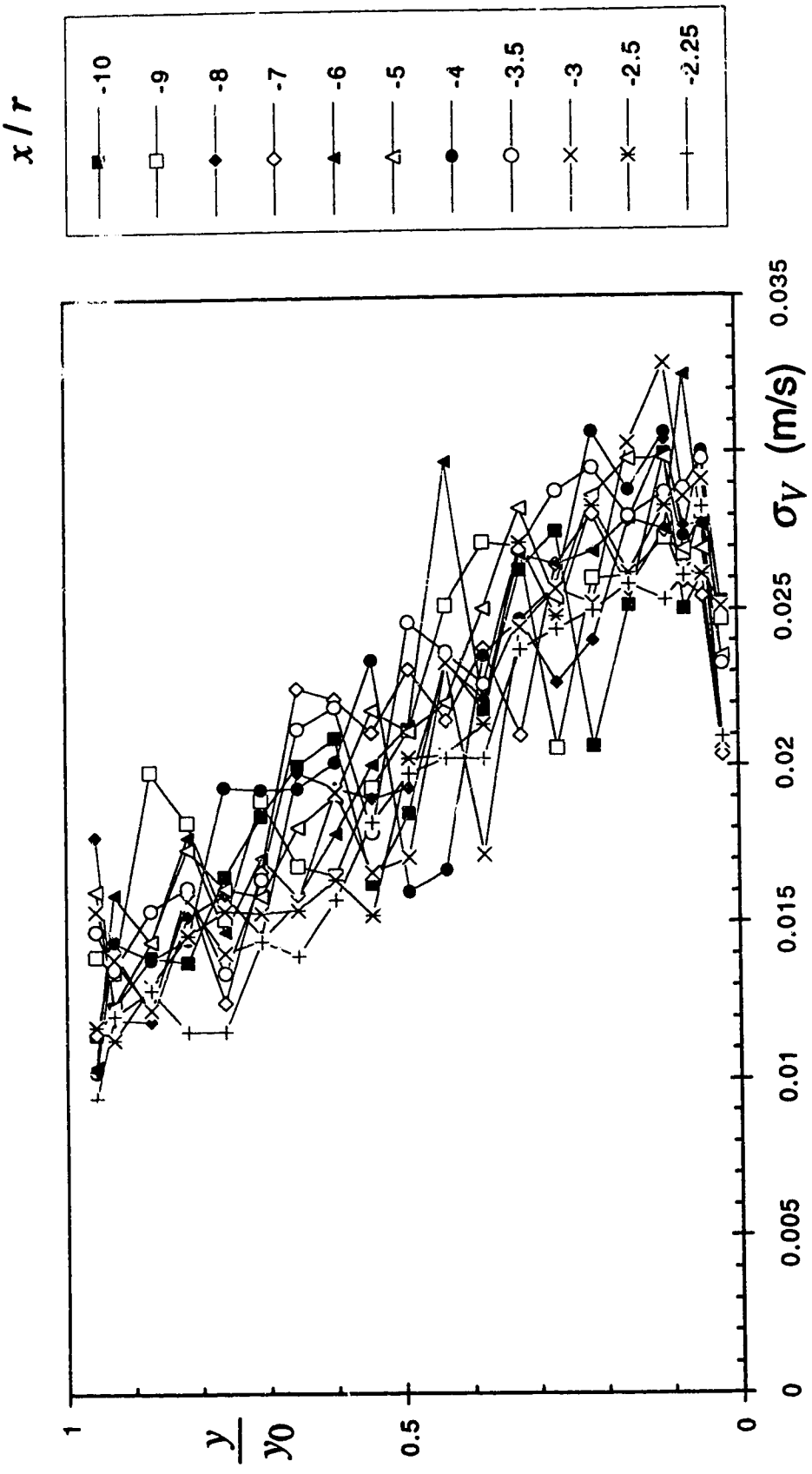

Figure 4.2.12 (a-i) Velocity Distribution on the POS (Expt. C2R)
(c) Standard deviation of the velocity magnitude

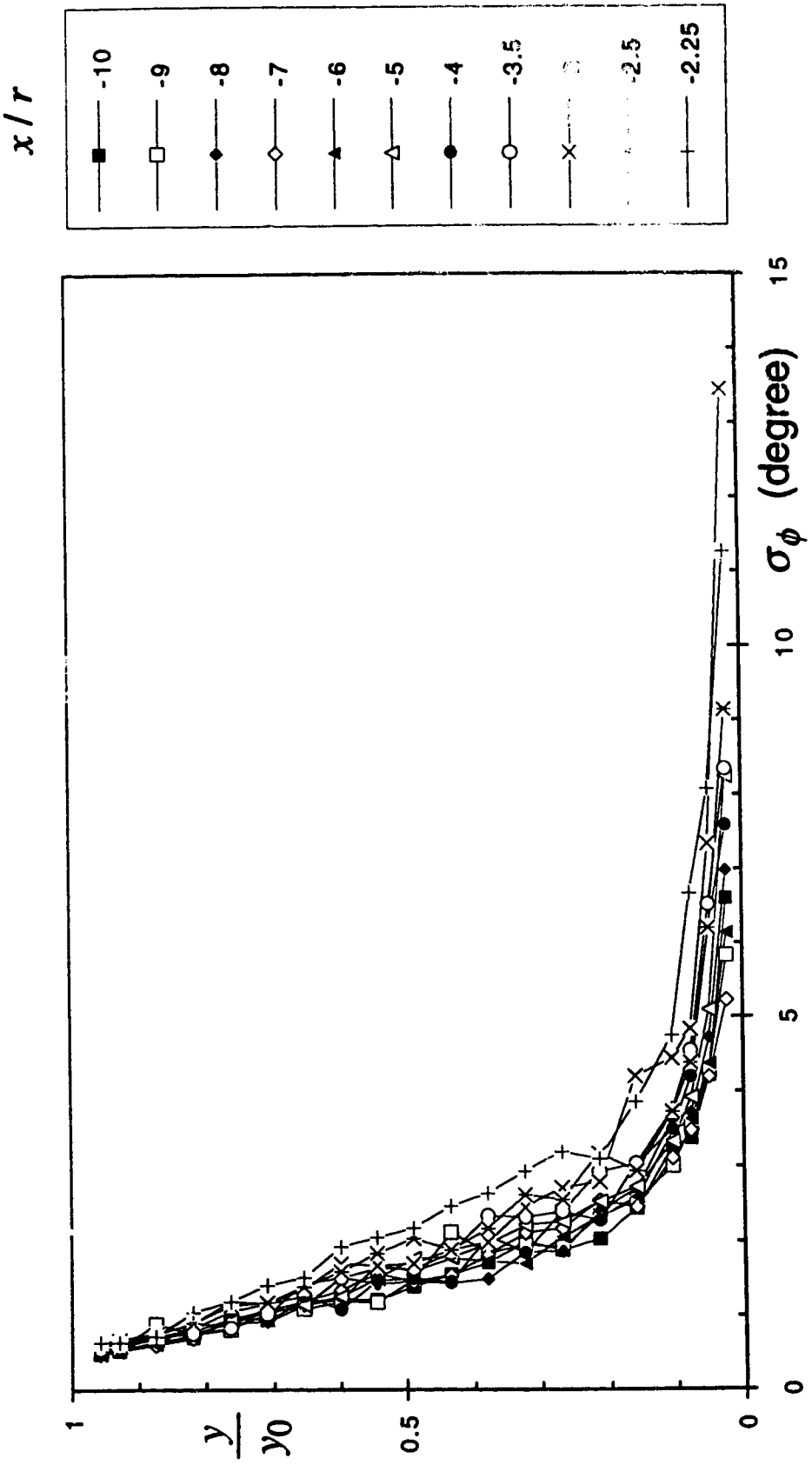

Figure 4.2.12 (a-i) Velocity Distribution on the POS (Expt. C2R)
(d) Standard deviation of the pitch angle

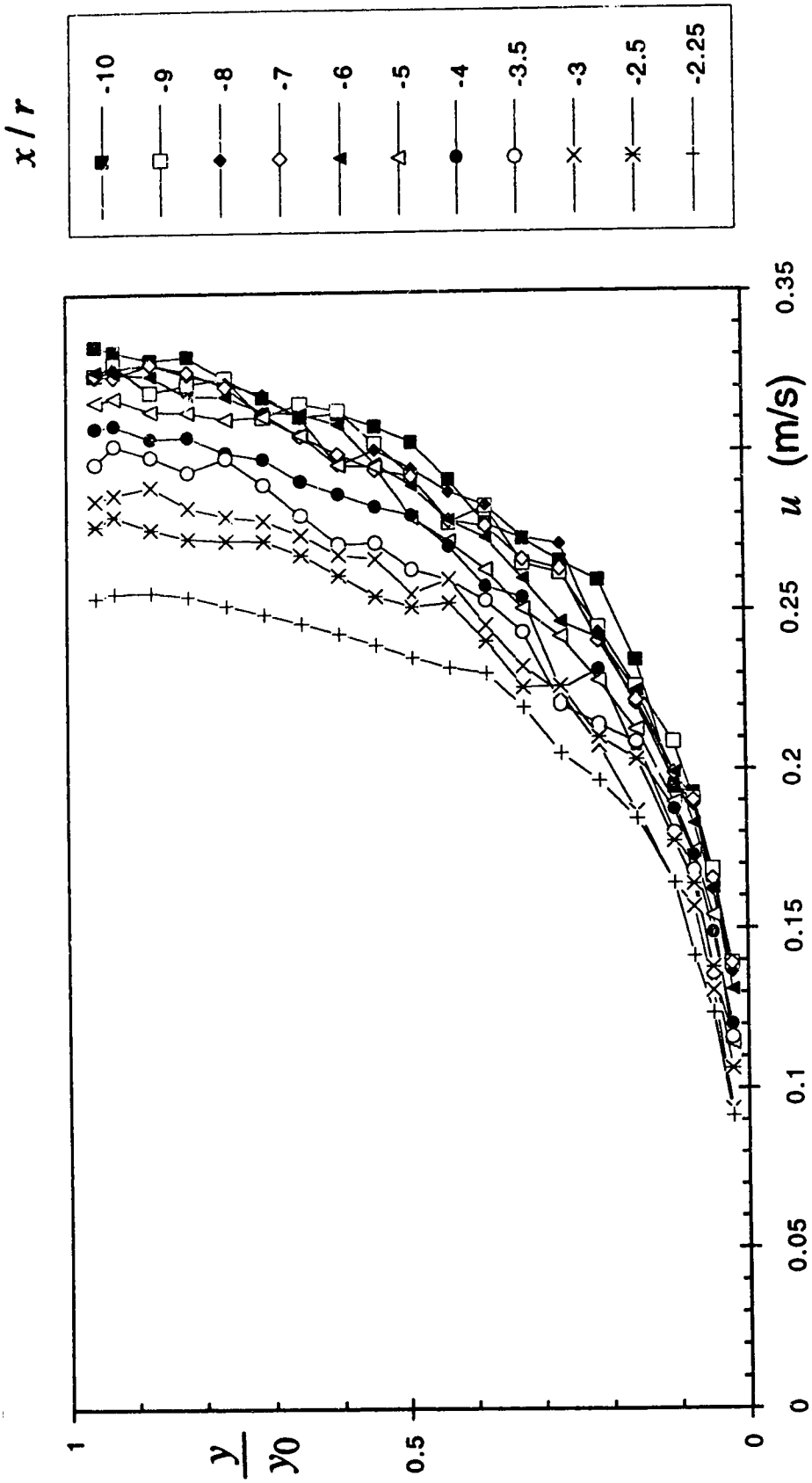

Figure 4.2.12 (a-i) Velocity Distribution on the POS (Expt. C2R)
(e) Longitudinal component of velocity

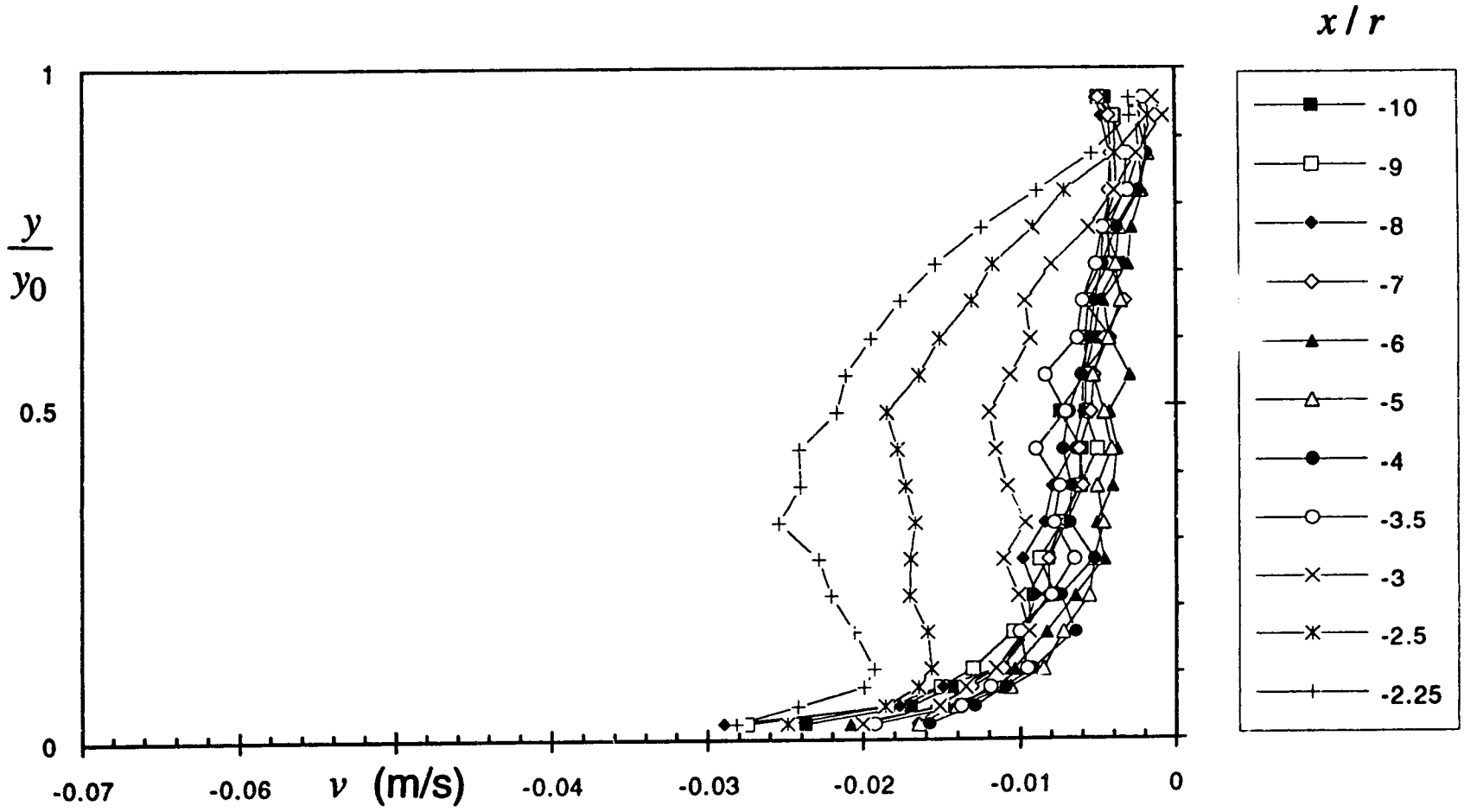

Figure 4.2.12 (a-i) Velocity Distribution on the POS (Expt. C2R)
(f) Vertical component of velocity

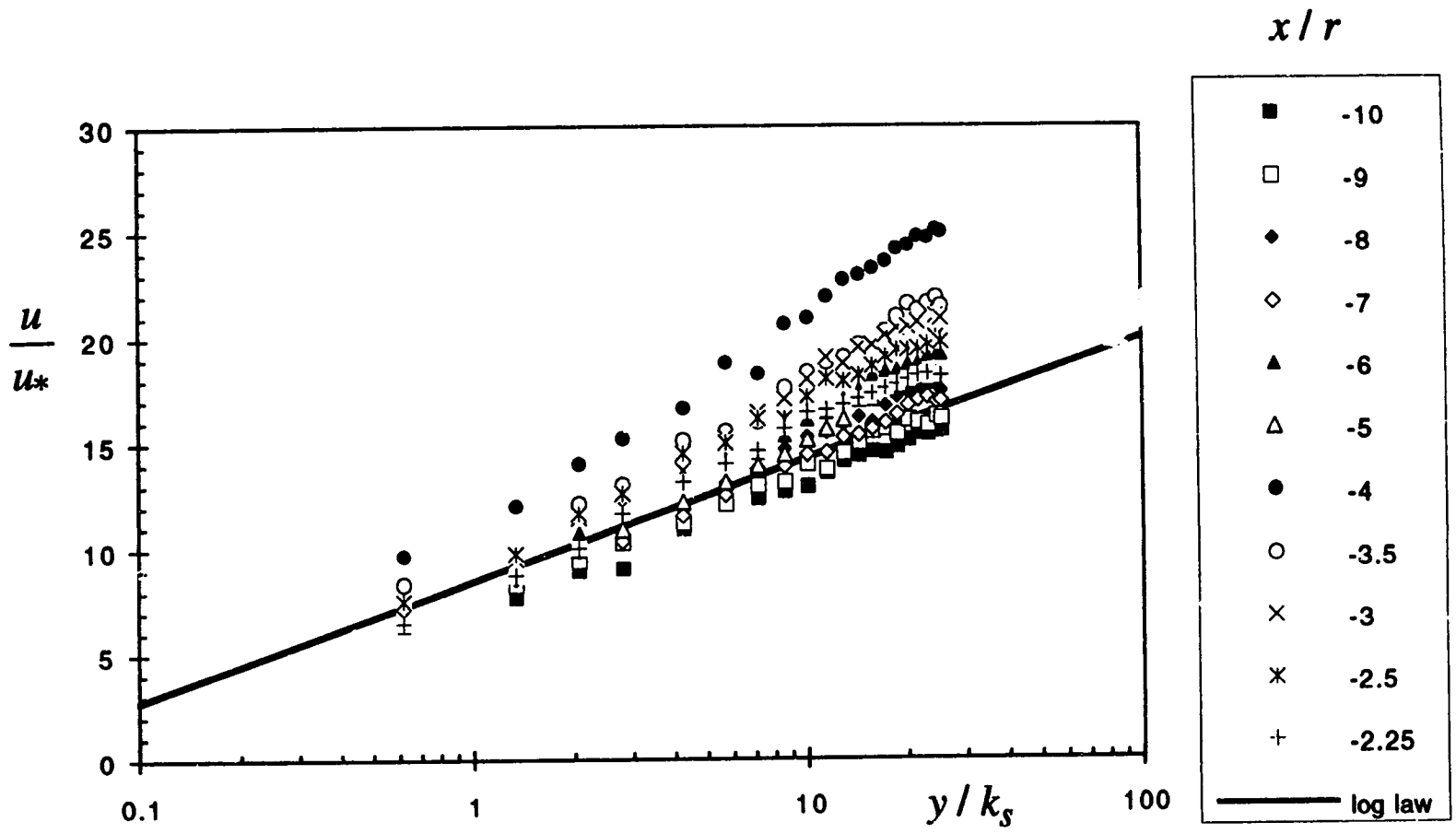

Figure 4.2.12 (a-i) Velocity Distribution on the POS (Expt. C2R)
(g) Comparison with log law

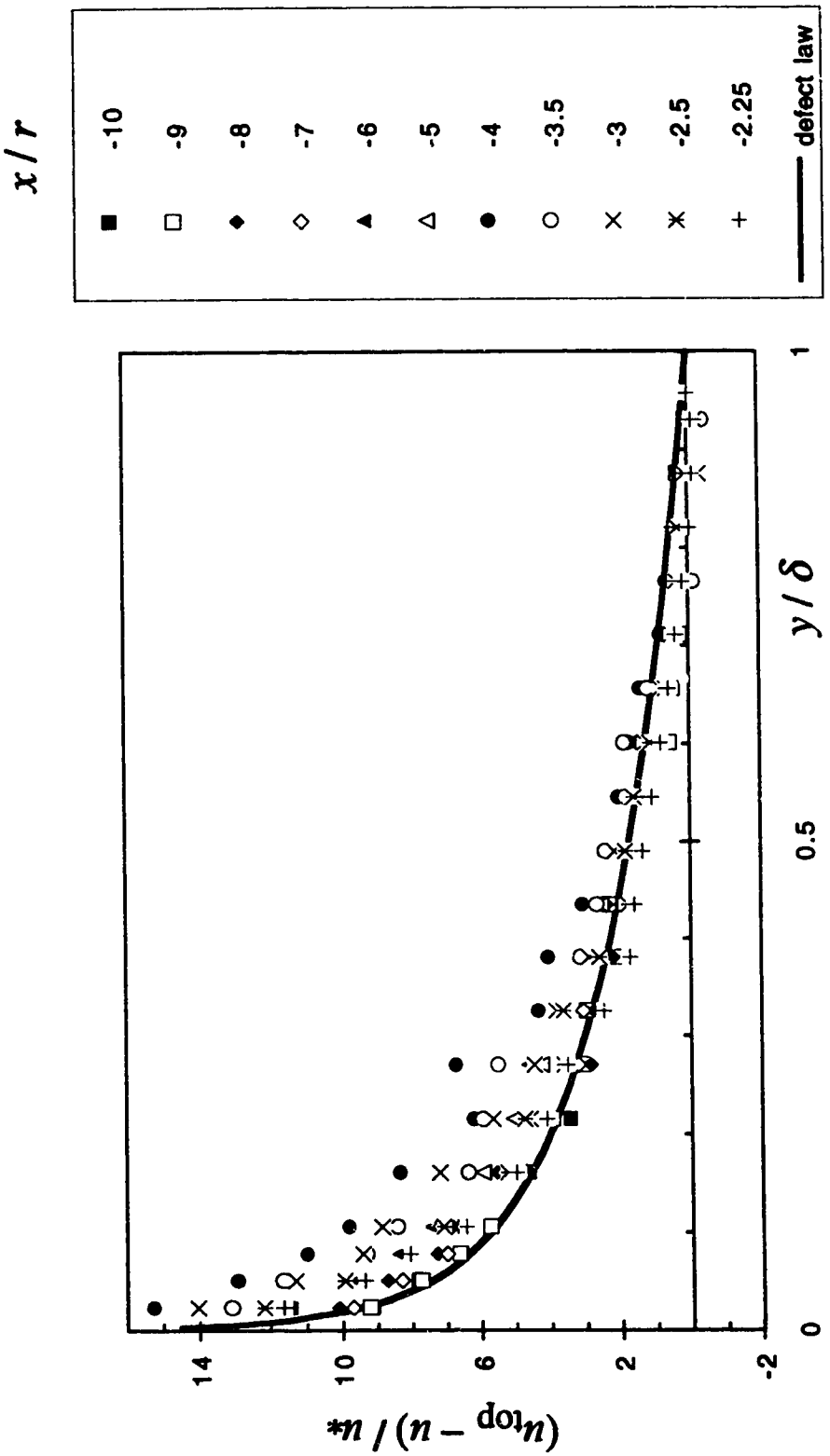

Figure 4.2.12 (a-i) Velocity Distribution on the POS (Expt. C2R)
(h) Comparison with defect law

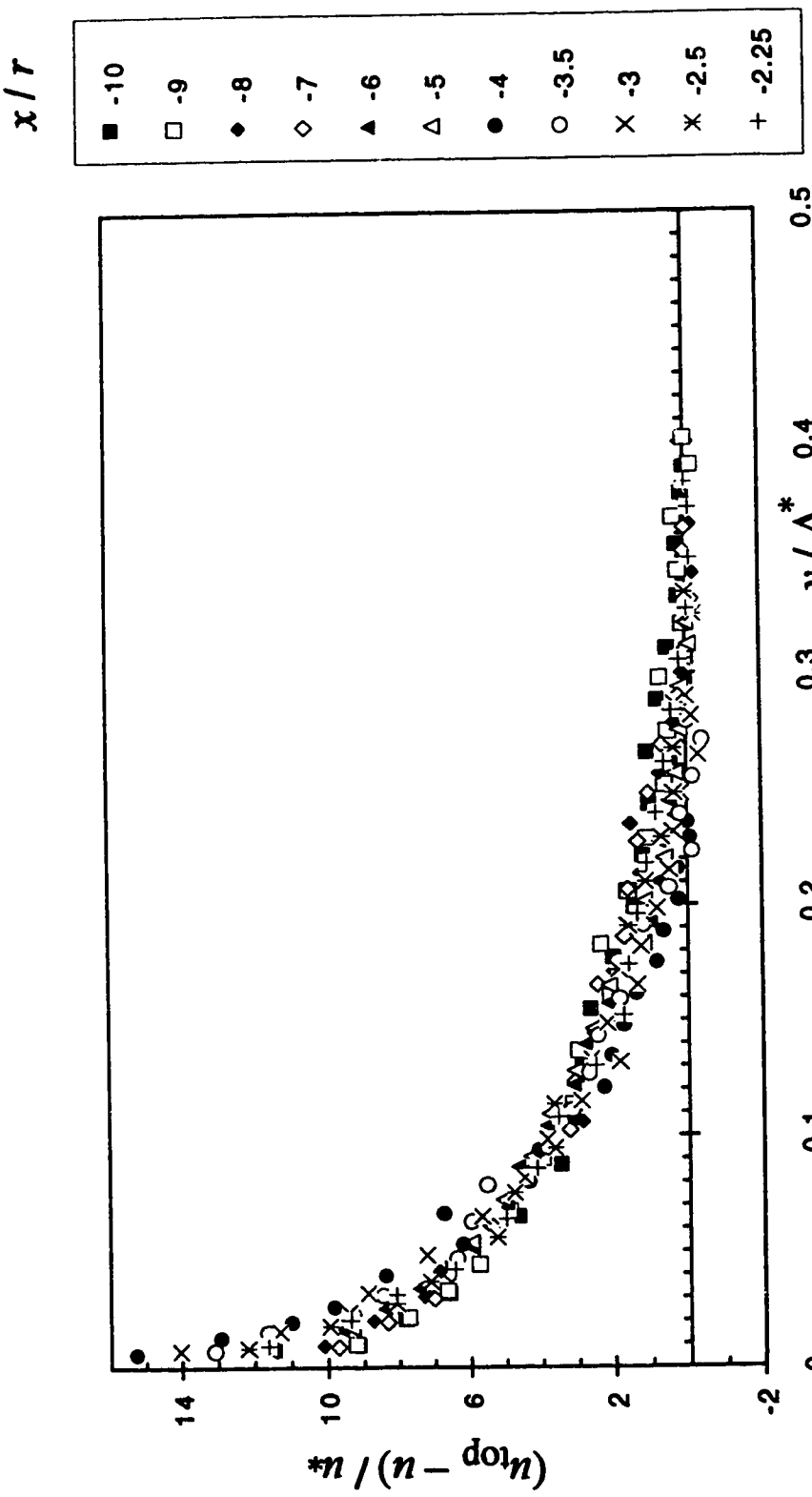

Figure 4.2.12 (a-i) Velocity Distribution on the POS (Expt. C2R)
(i) Comparison with Clauser's scheme

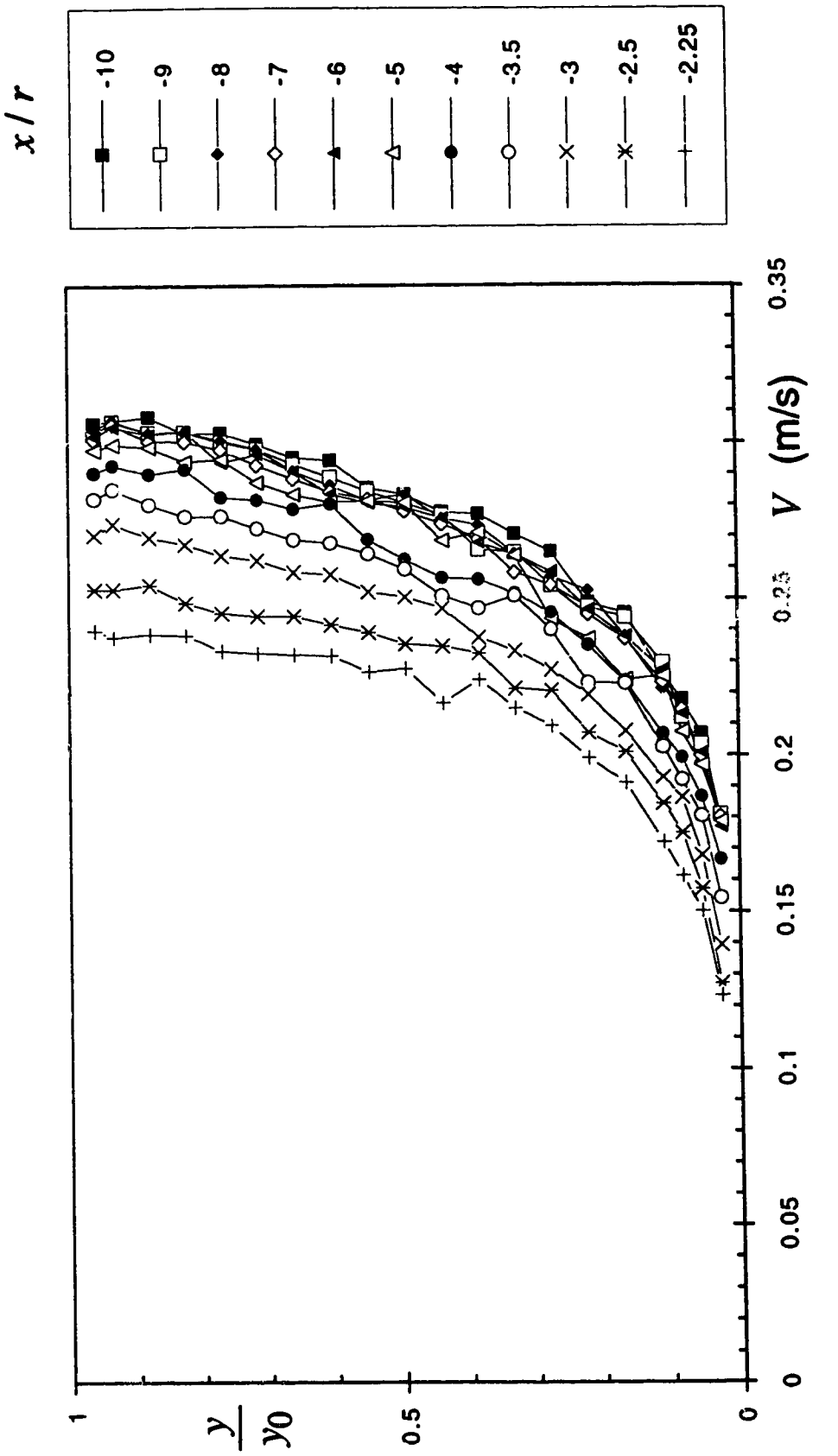

Figure 4.2.13 (a-i) Velocity Distribution on the POS (Expt. E2S)
(a) Velocity magnitude

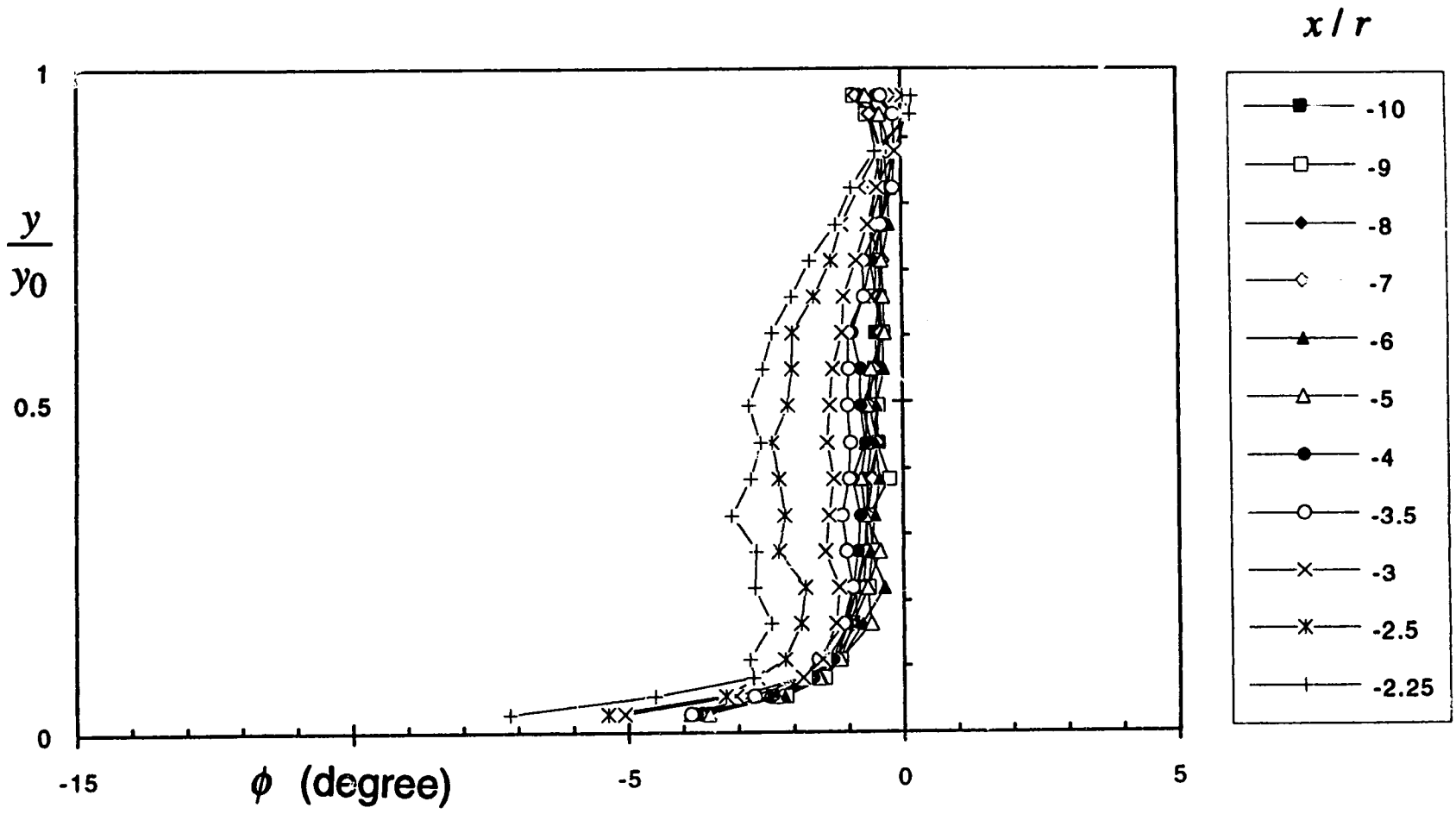

Figure 4.2.13 (a-i) Velocity Distribution on the POS (Expt. E2S)
(b) Angle of pitch

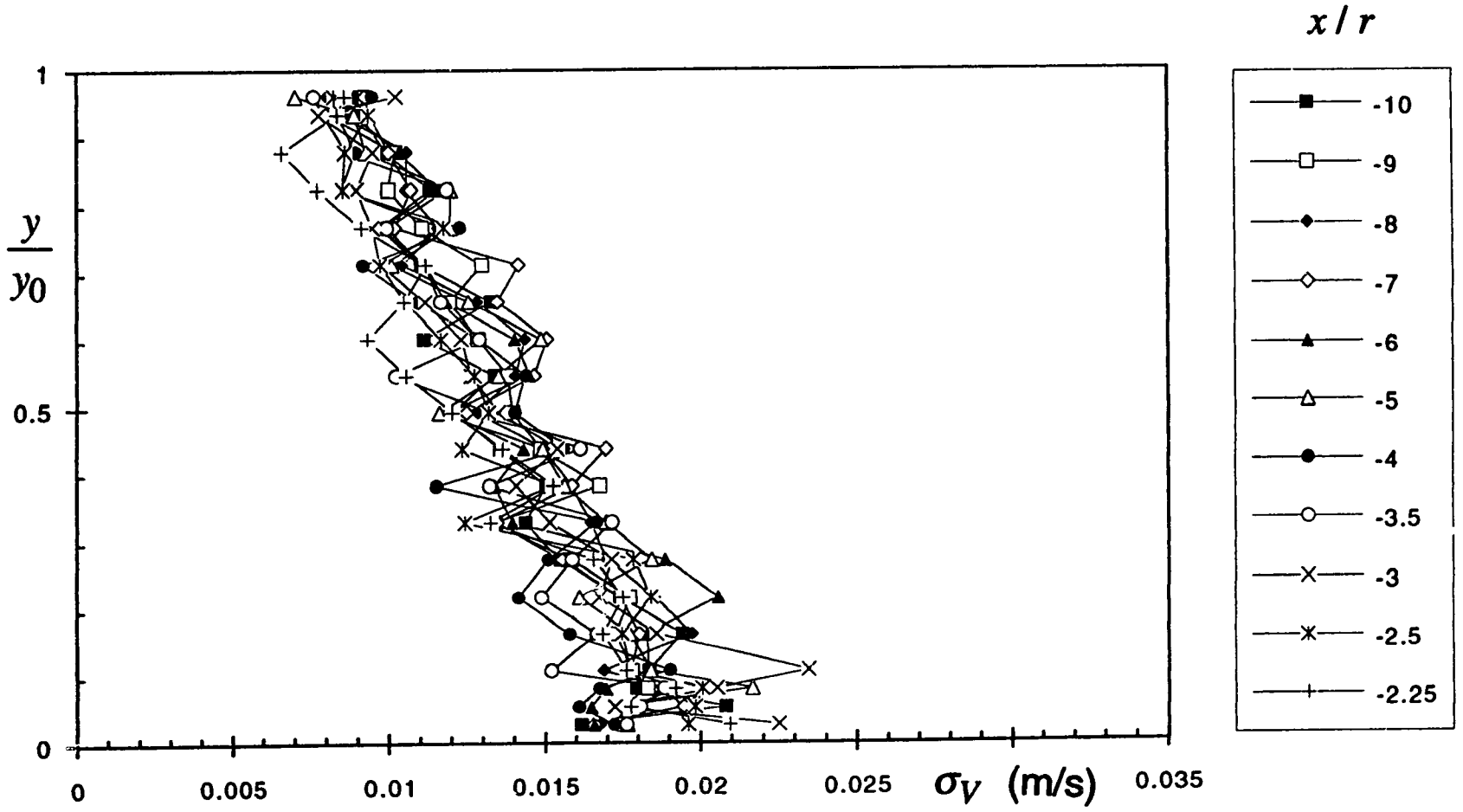

Figure 4.2.13 (a-i) Velocity Distribution on the POS (Expt. E2S)
(c) Standard deviation of the velocity magnitude

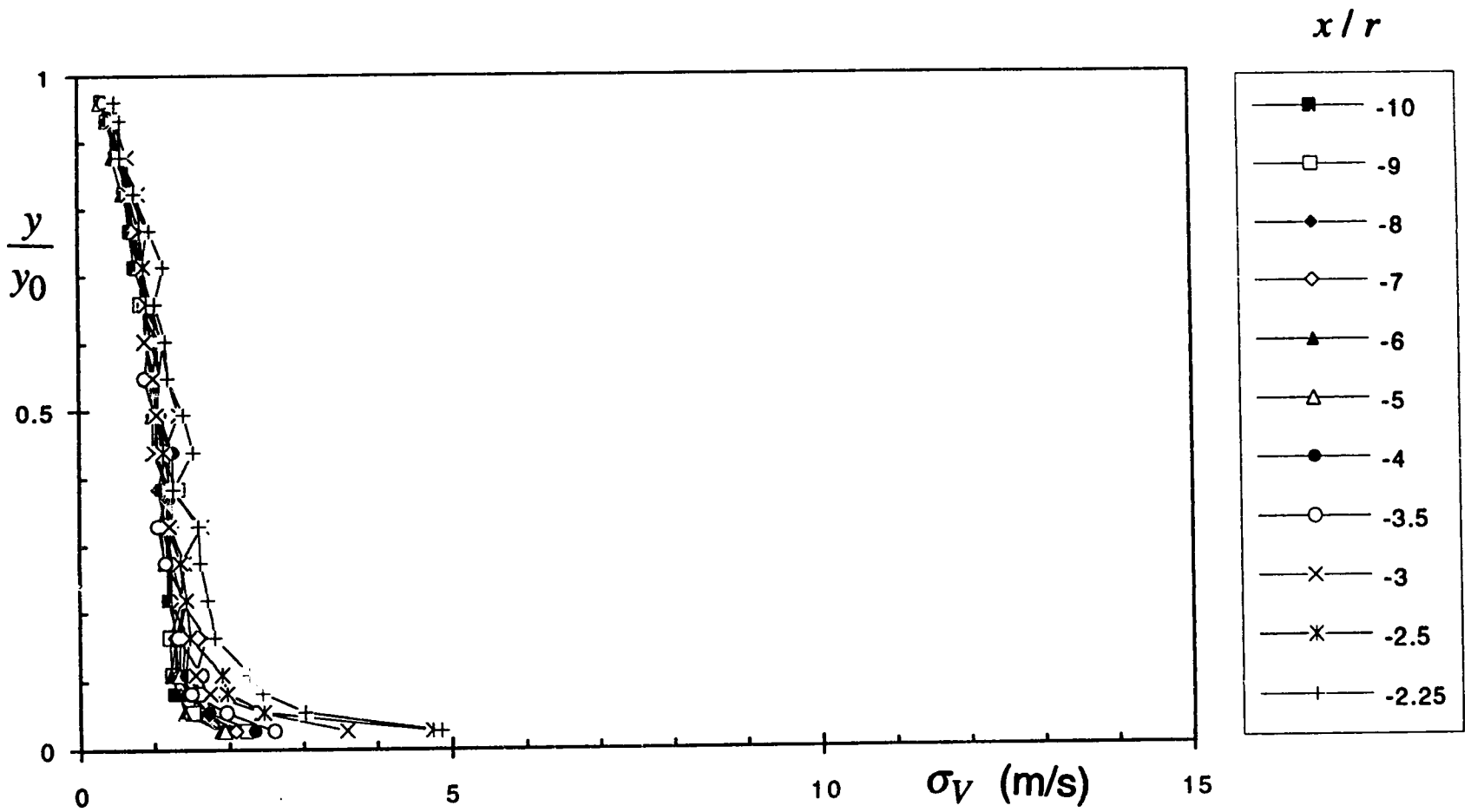

Figure 4.2.13 (a-i) Velocity Distribution on the POS (Expt. E2S)
(d) Standard deviation of the pitch angle

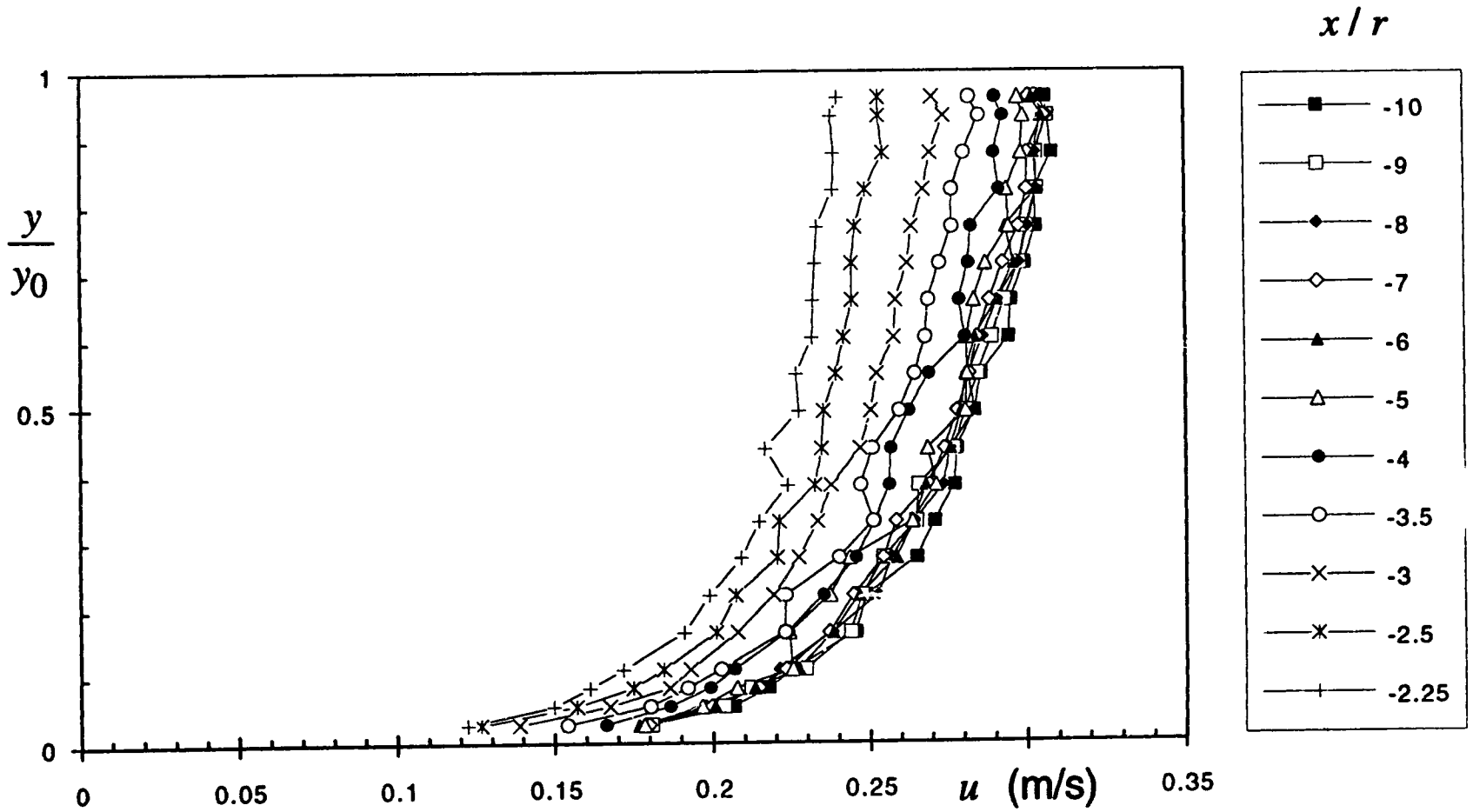

Figure 4.2.13 (a-i) Velocity Distribution on the POS (Expt. E2S)
(e) Longitudinal component of velocity

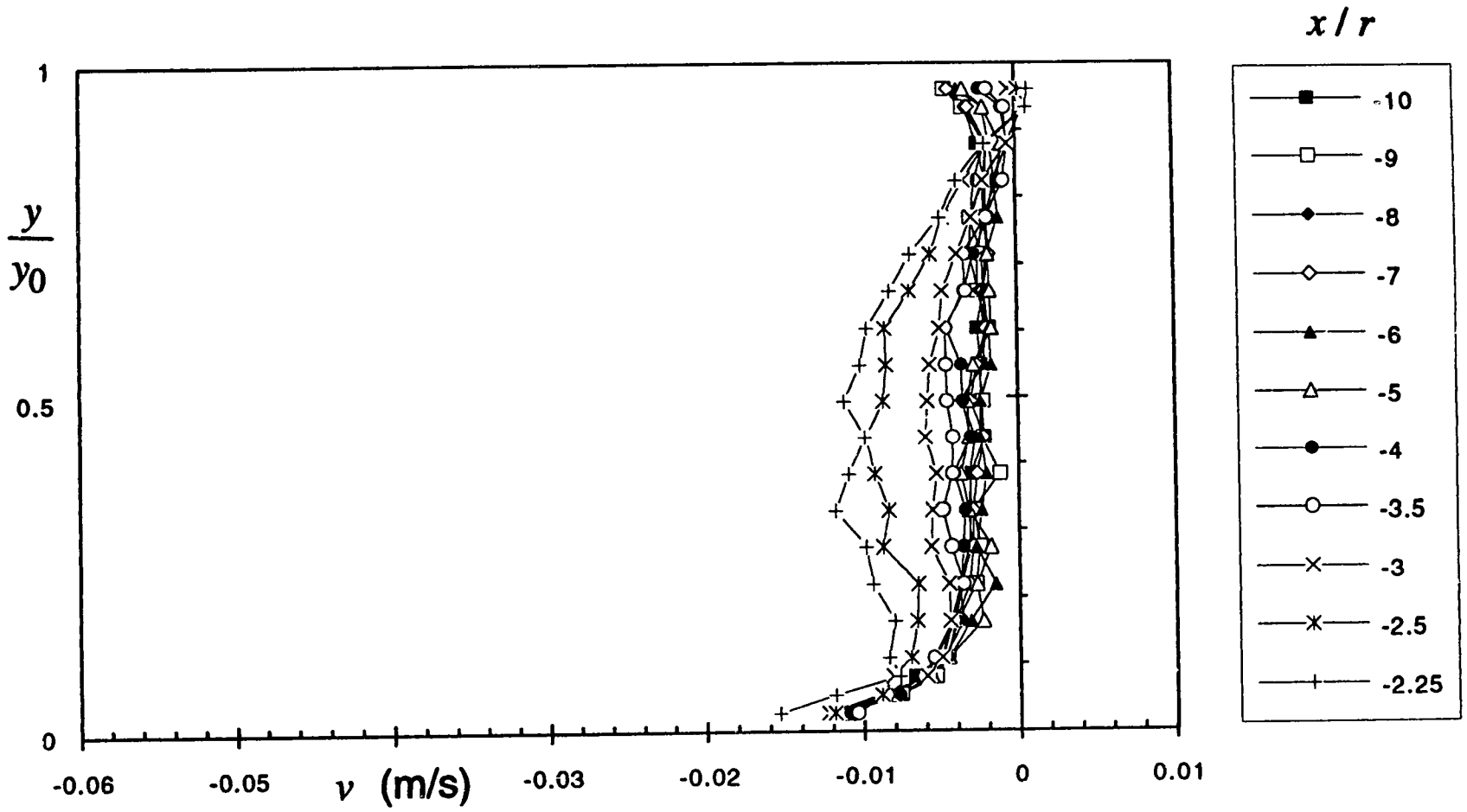

Figure 4.2.13 (a-i) Velocity Distribution on the POS (Expt. E2S)
(f) Vertical component of velocity

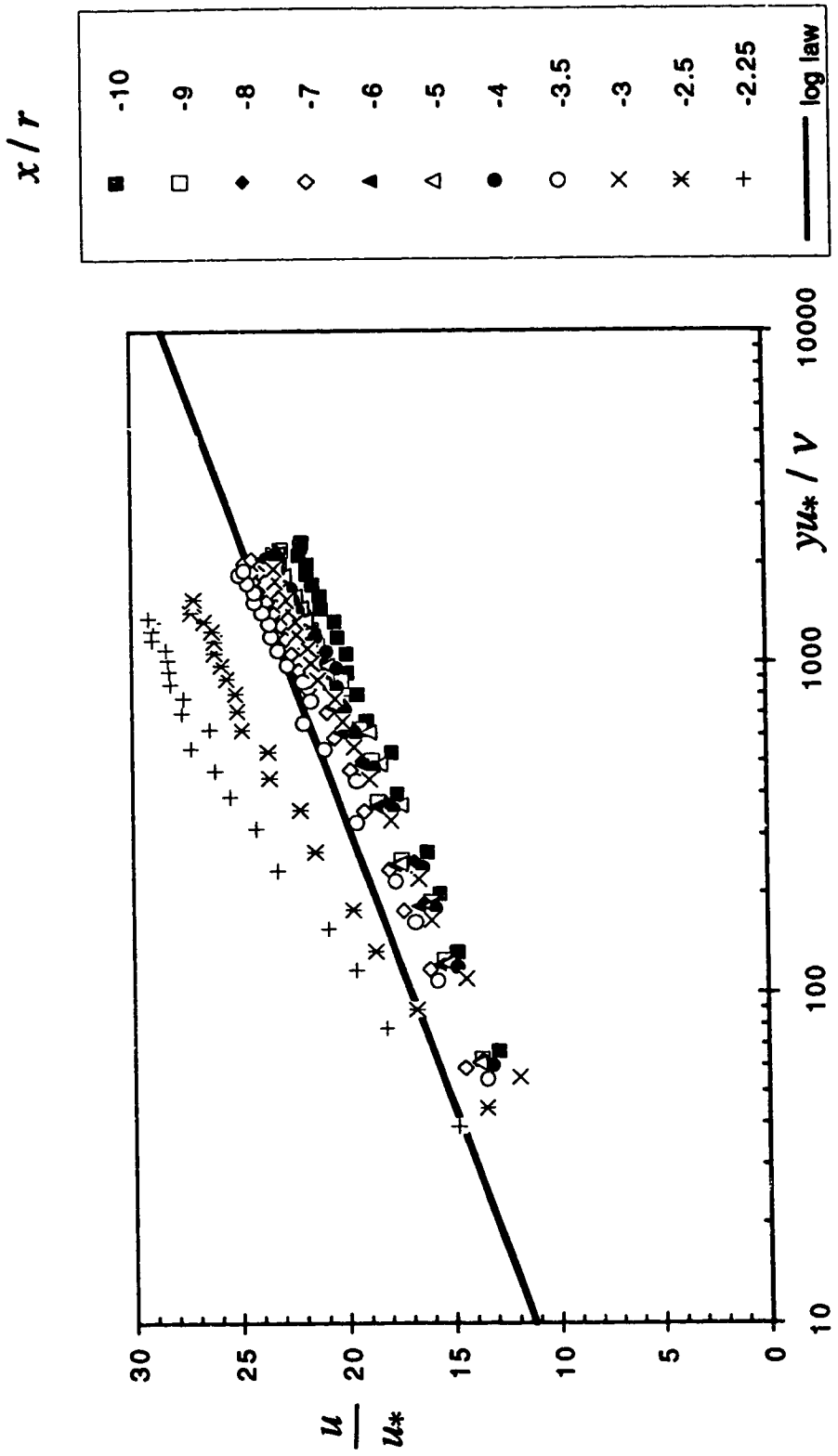

Figure 4.2.13 (a-i) Velocity Distribution on the POS (Expt. E2S)
(g) Comparison with log law

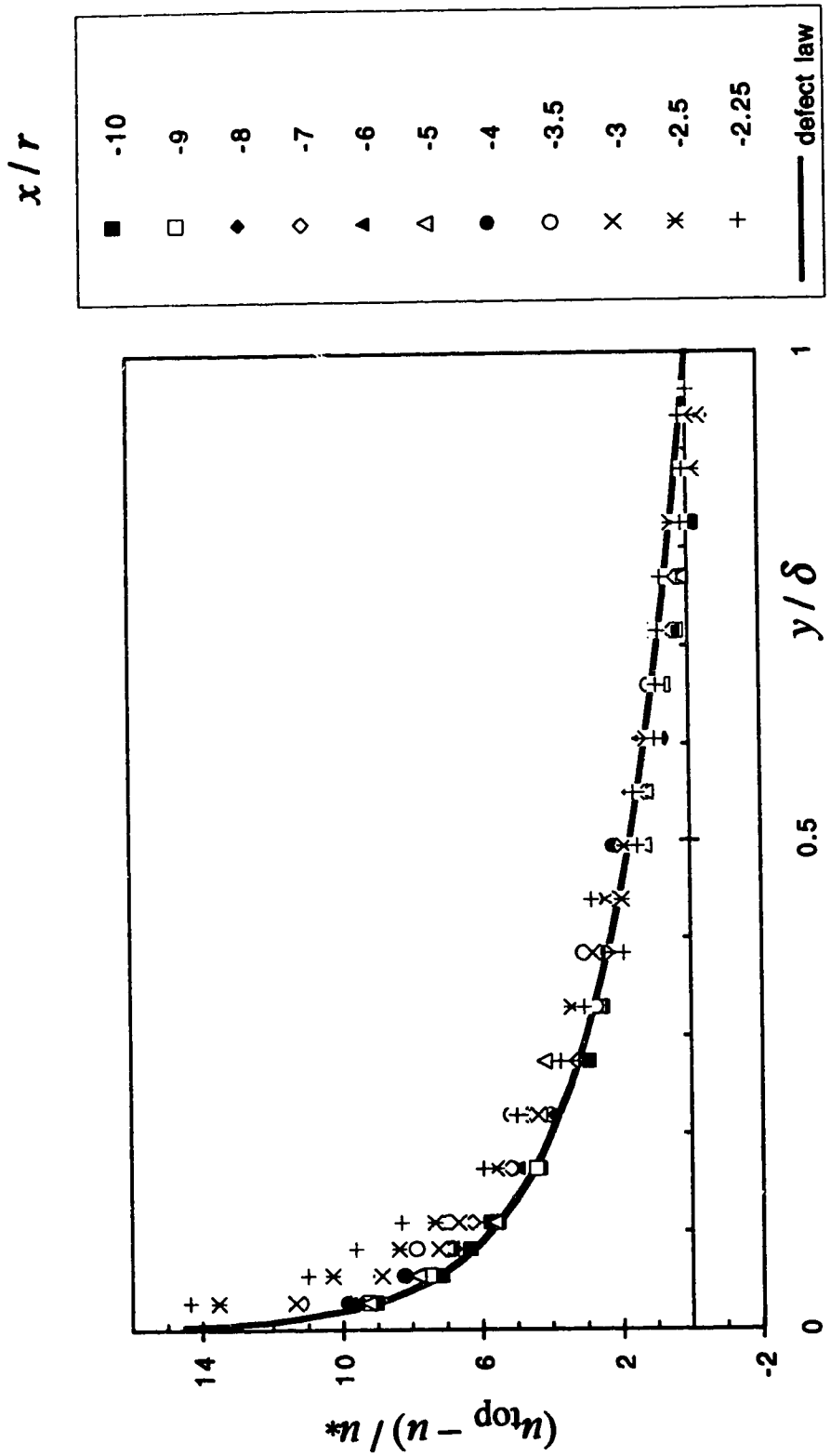

Figure 4.2.13 (a-i) Velocity Distribution on the POS (Expt. E2S)
(h) Comparison with defect law

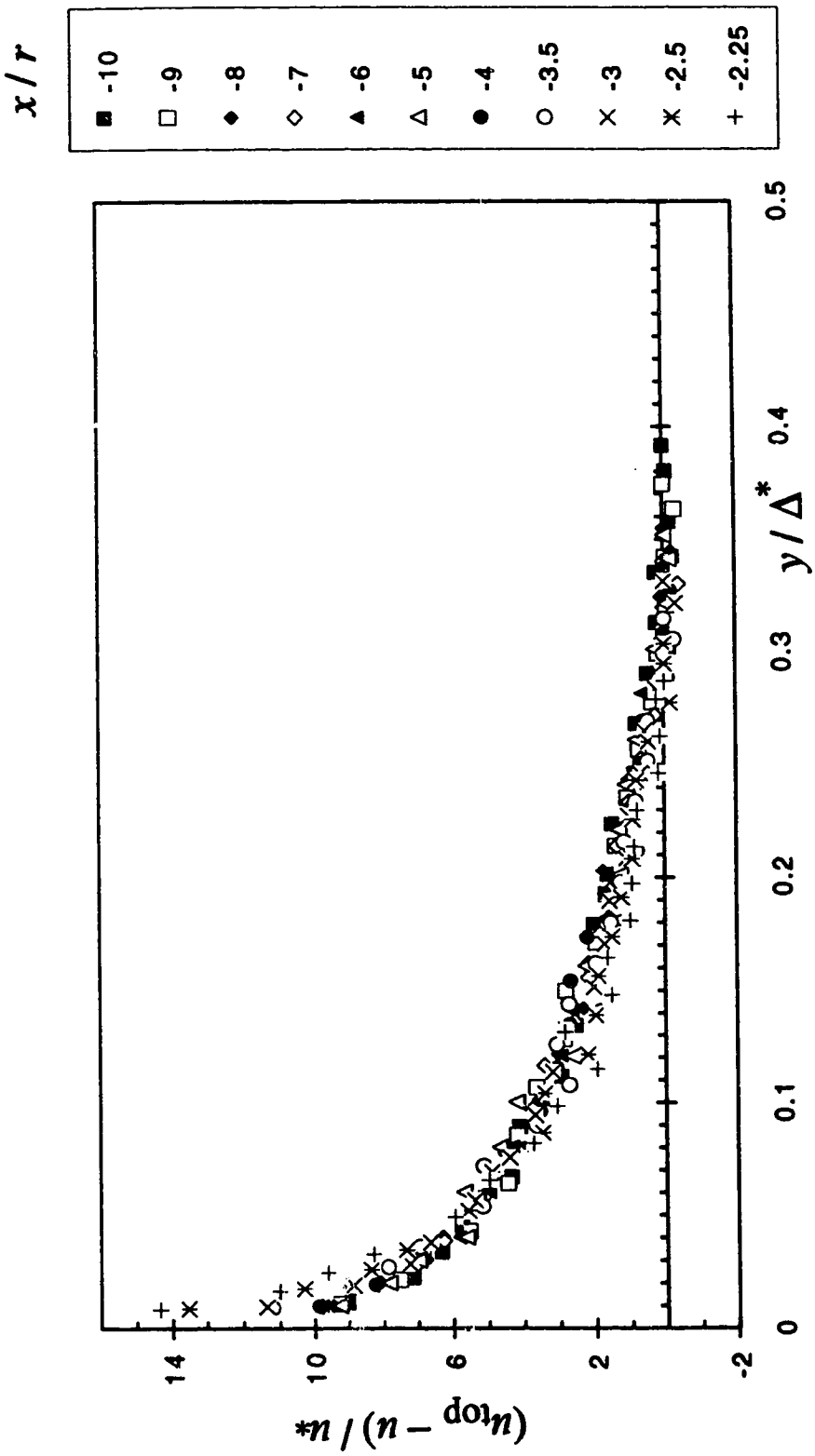

Figure 4.2.13 (a-i) Velocity Distribution on the POS (Expt. E2S)
(i) Comparison with Clauser's scheme

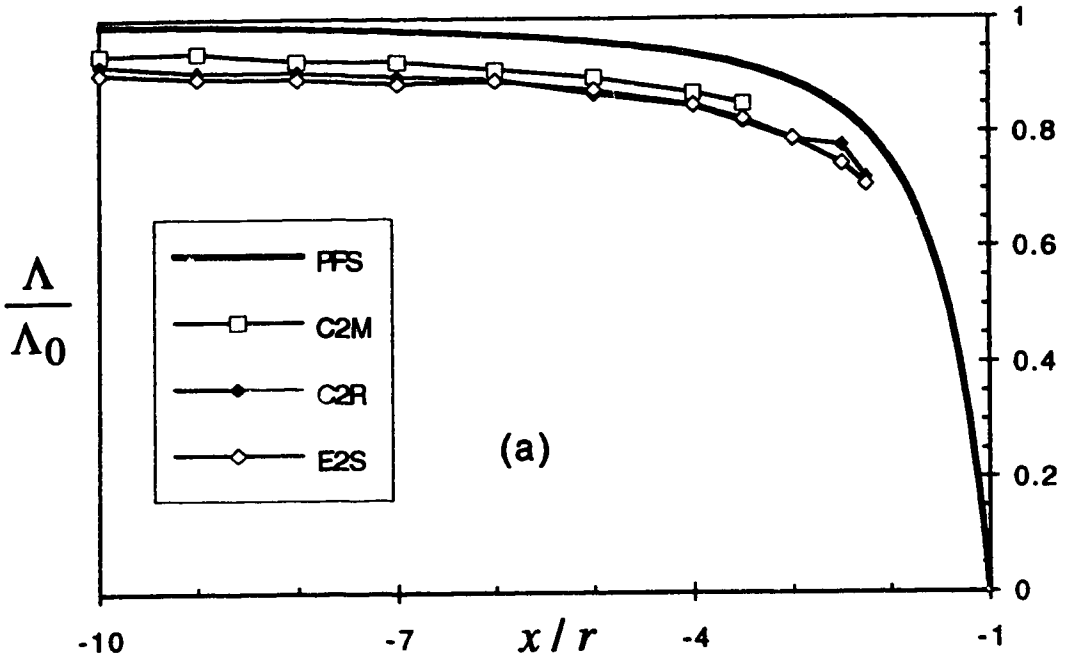

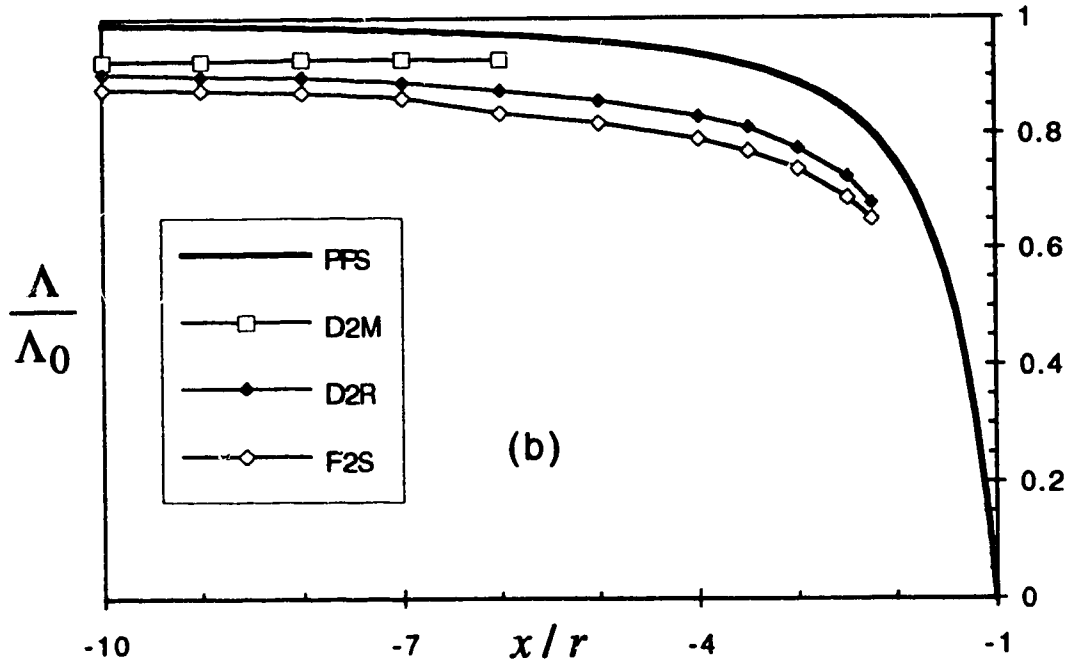

Figure 4.2.14 (a-b) Variation of mass flux on the POS
(a) Expt. C2M, C2R and E2S
(b) Expt. D2M, D2R and E2S

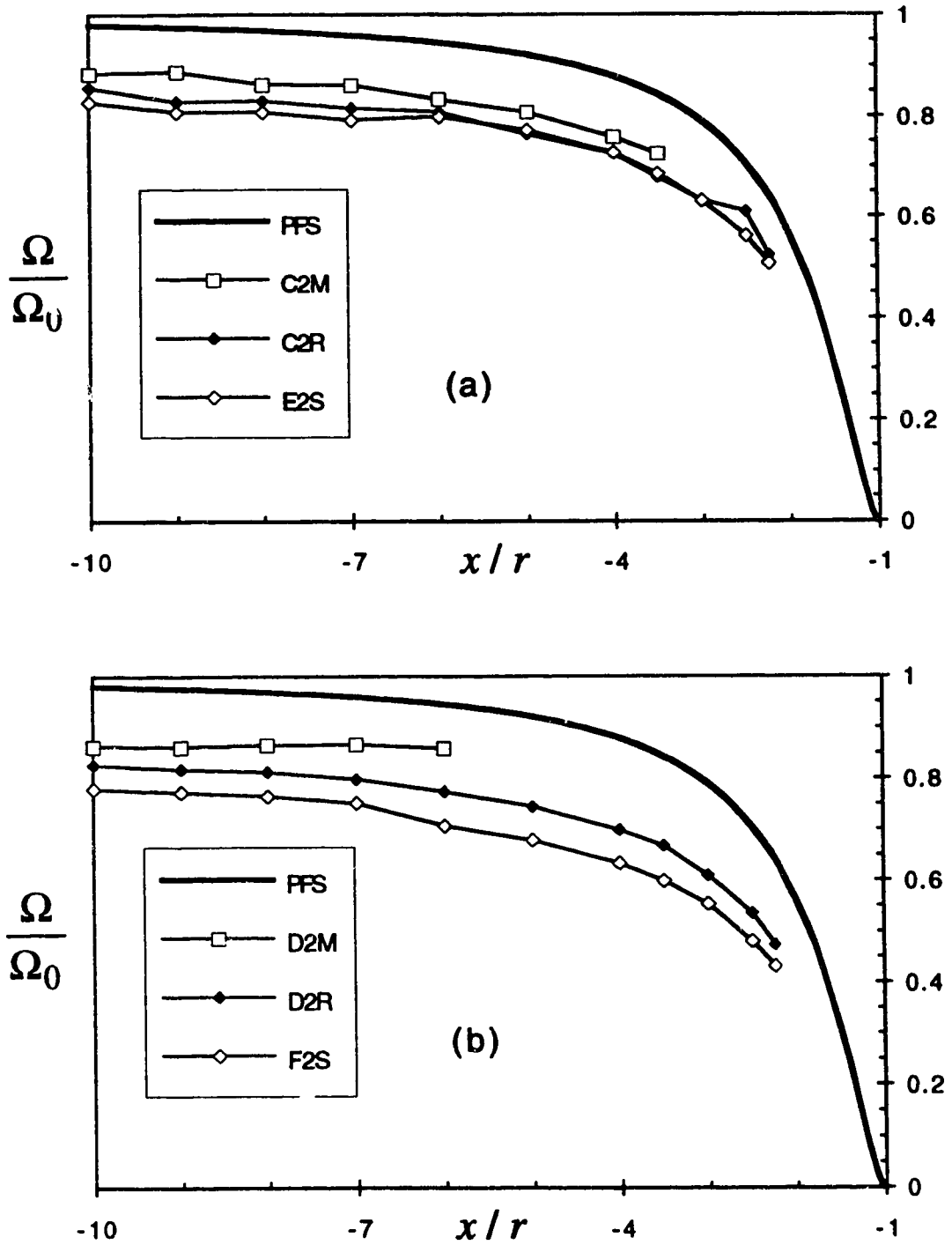

Figure 4.2.15 (a-b) Variation of momentum flux on the POS
(a) Expt. C2M, C2R and E2S
(b) Expt. D2M, D2R and E2S

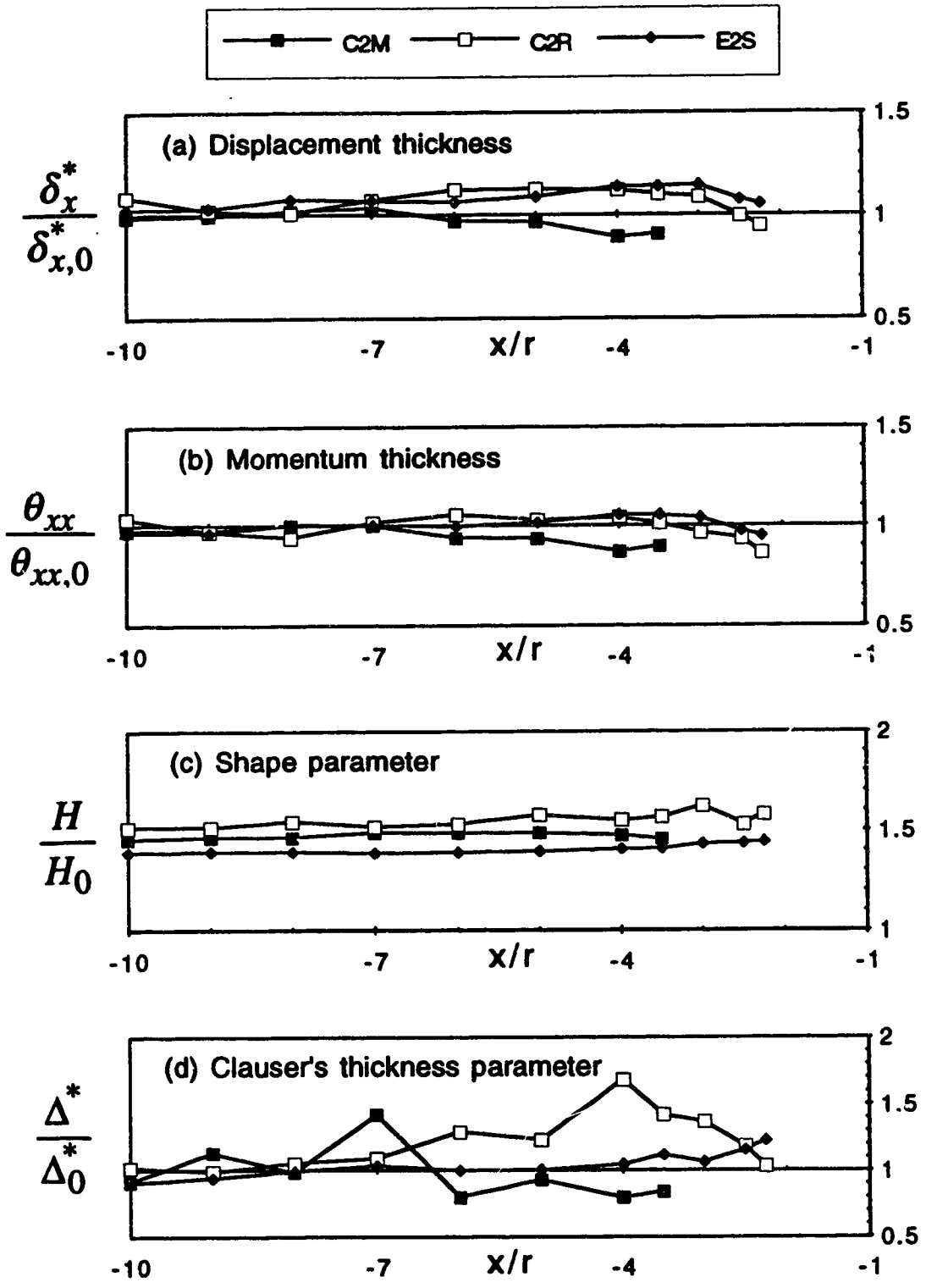

Figure 4.2.16 (a-d) Variation of boundary layer parameters on the POS (Expt. C2M, C2R and E2S)

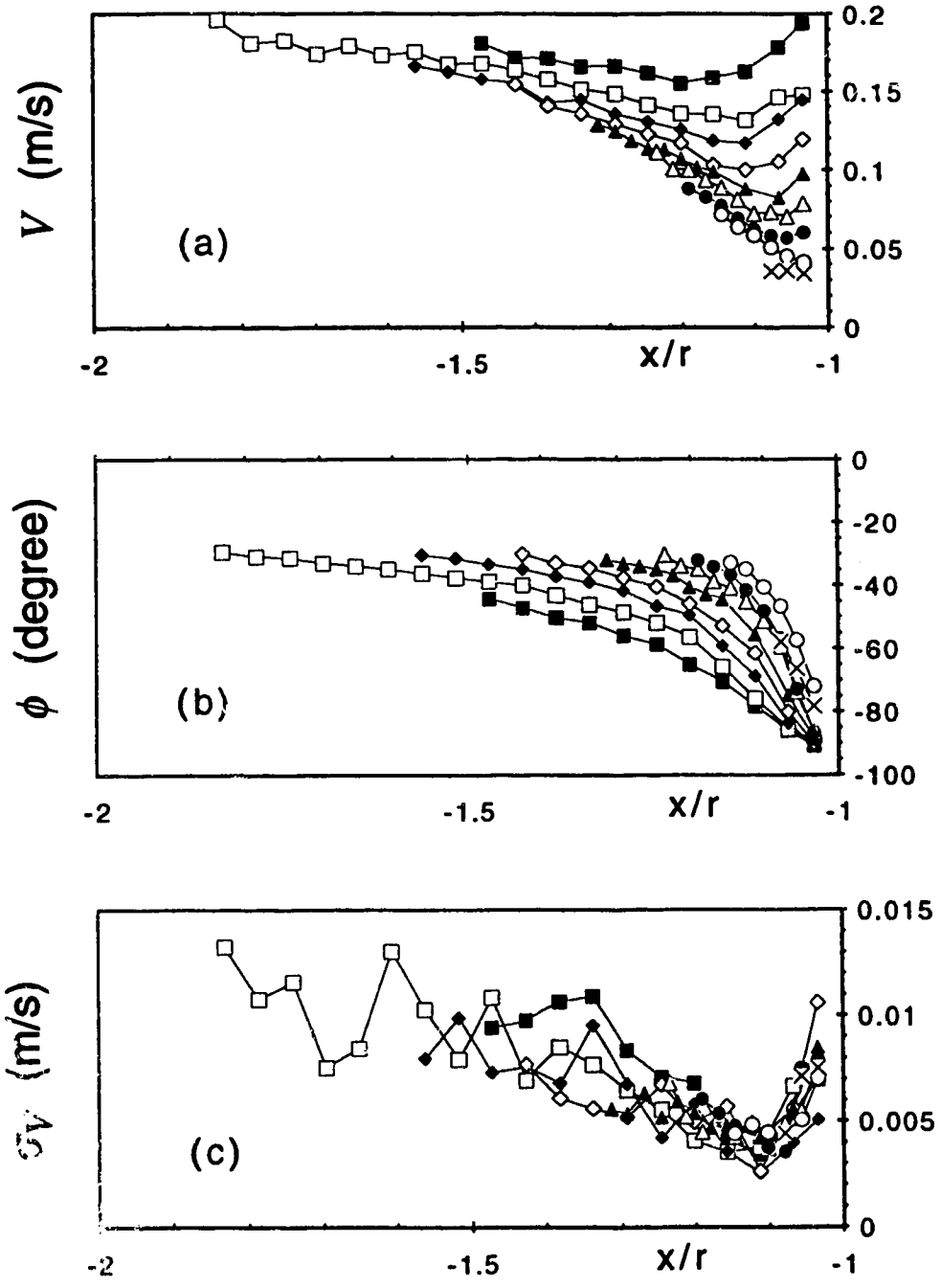

Figure 4.2.17 (a-h) Downflow in front of the pier (Expt. C2M);
(a) velocity magnitude
(b) angle of pitch
(c) fluctuation of velocity

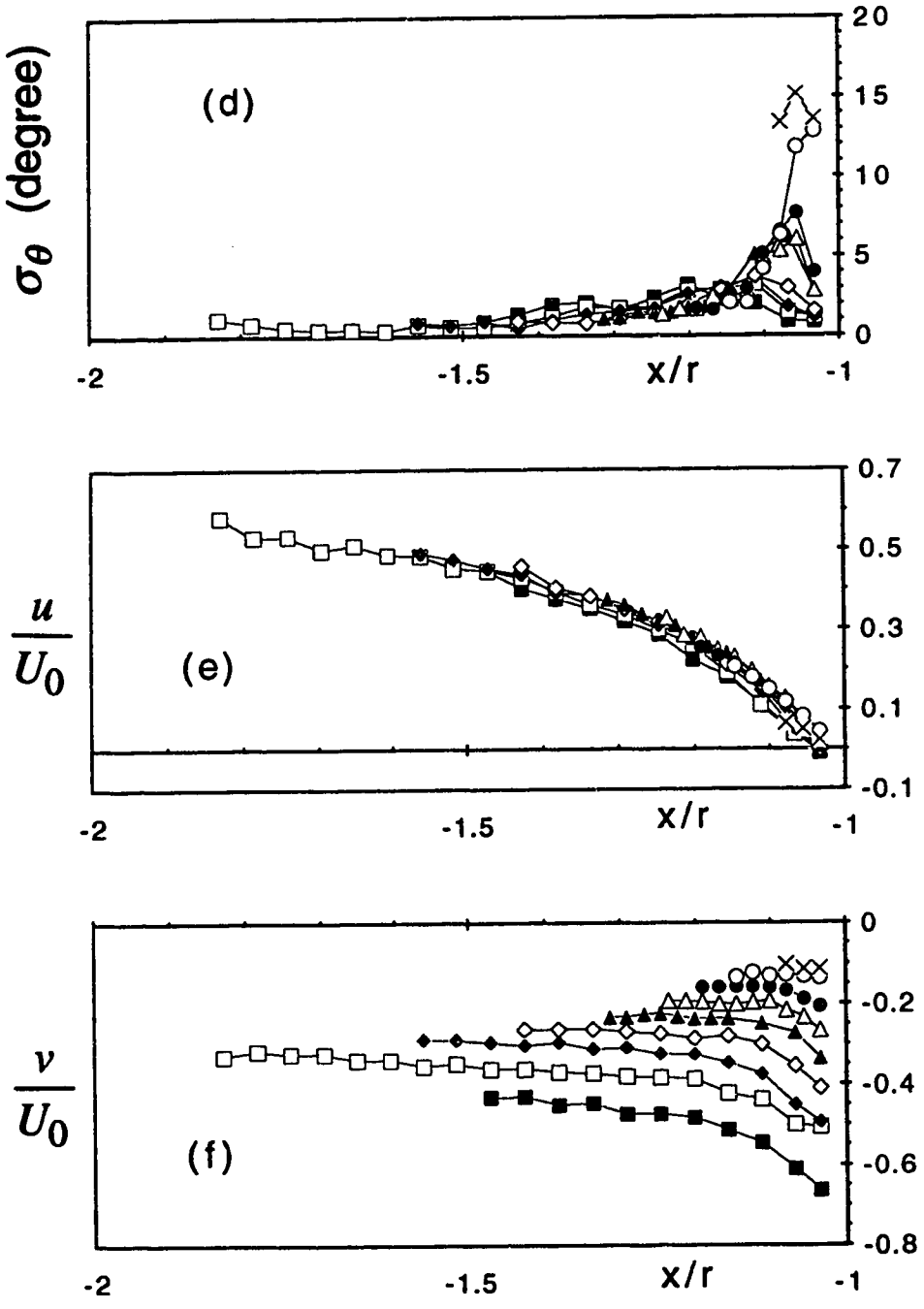

Figure 4.2.17 (a-h) Downflow in front of the pier (Expt. C2M);
(d) fluctuation of pitch angle
(e) longitudinal component of velocity
(f) vertical component of velocity

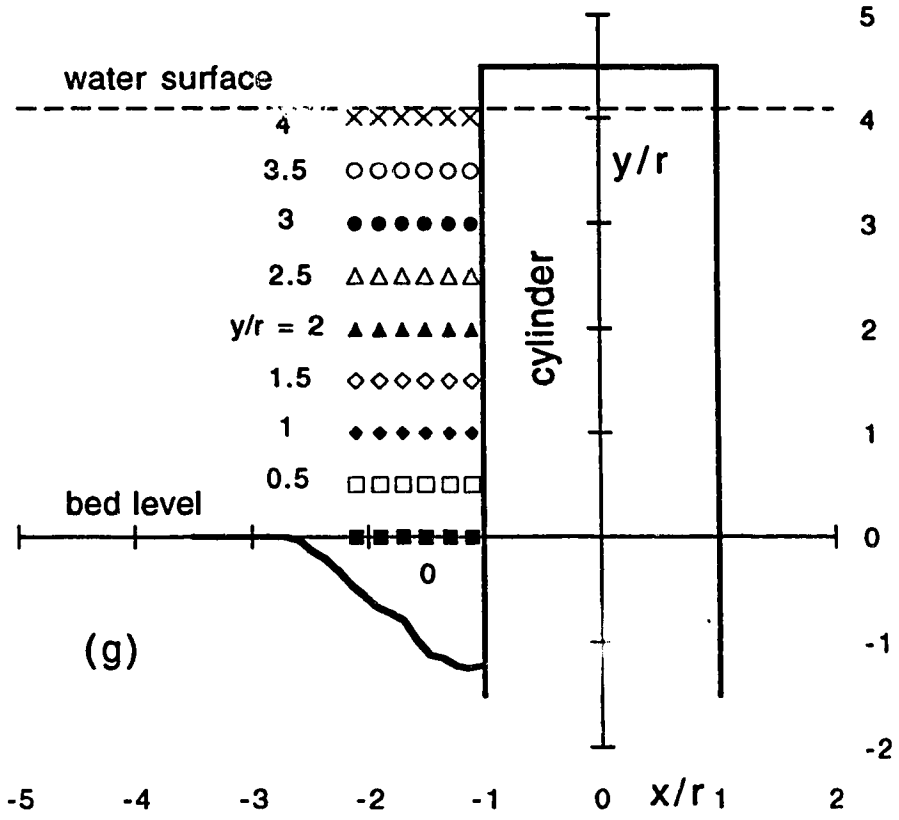

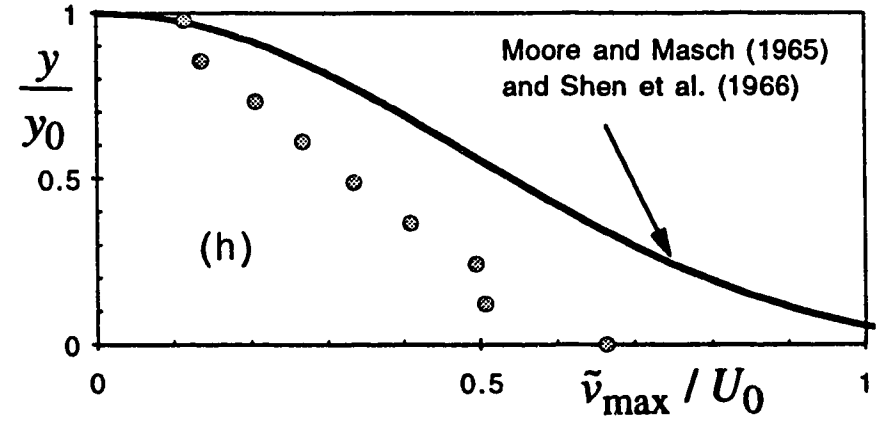

Figure 4.2.17 (a-h) Downflow in front of the pier (Expt. C2M);
(g) location of measurement lines
(h) variation of downflow with depth

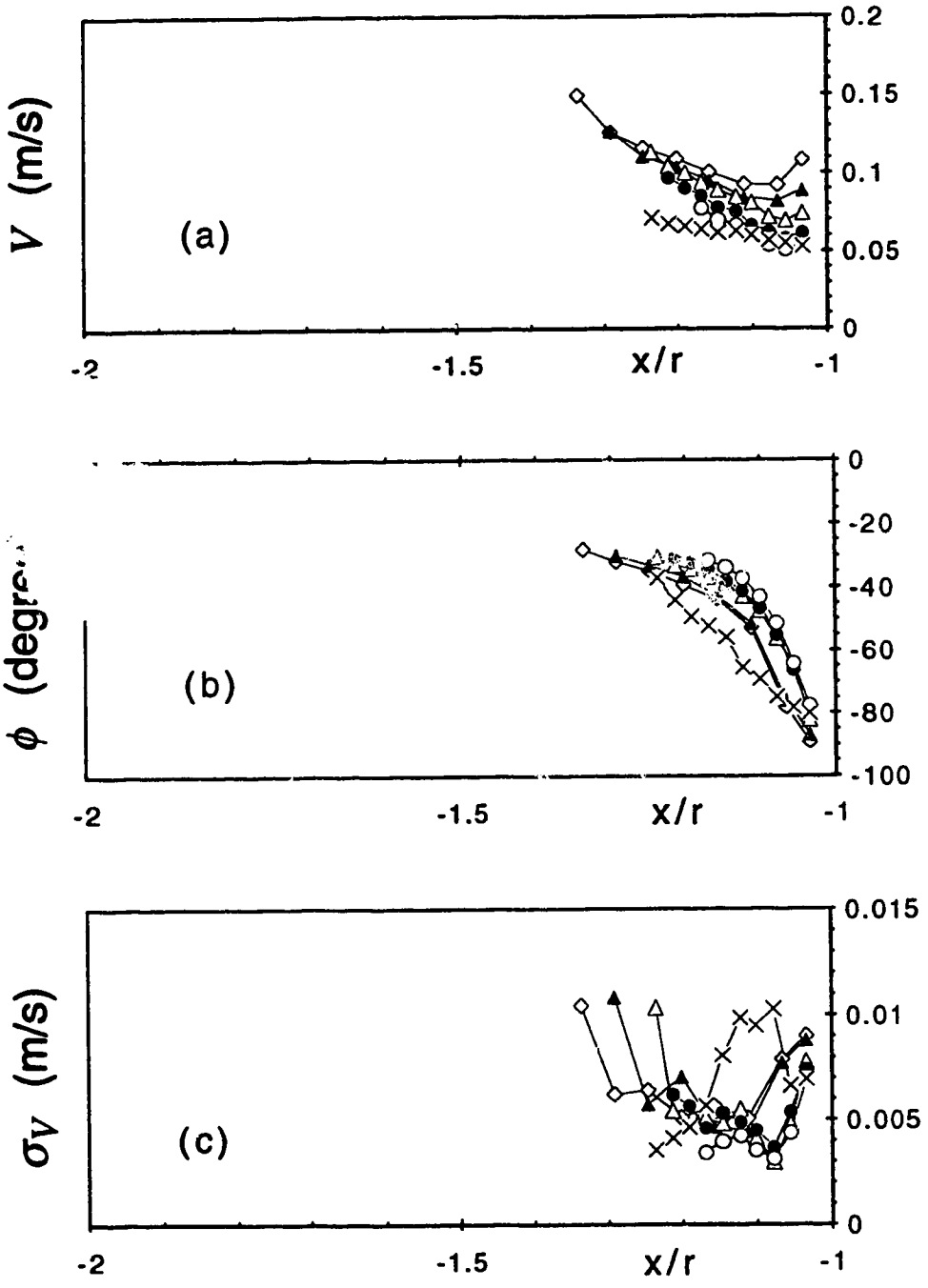

Figure 4.2.18 (a-f) Downflow in front of the pier (Expt. C2R);
(a) velocity magnitude
(b) angle of pitch
(c) fluctuation of velocity
Note: symbols same as Figure 4.2.17

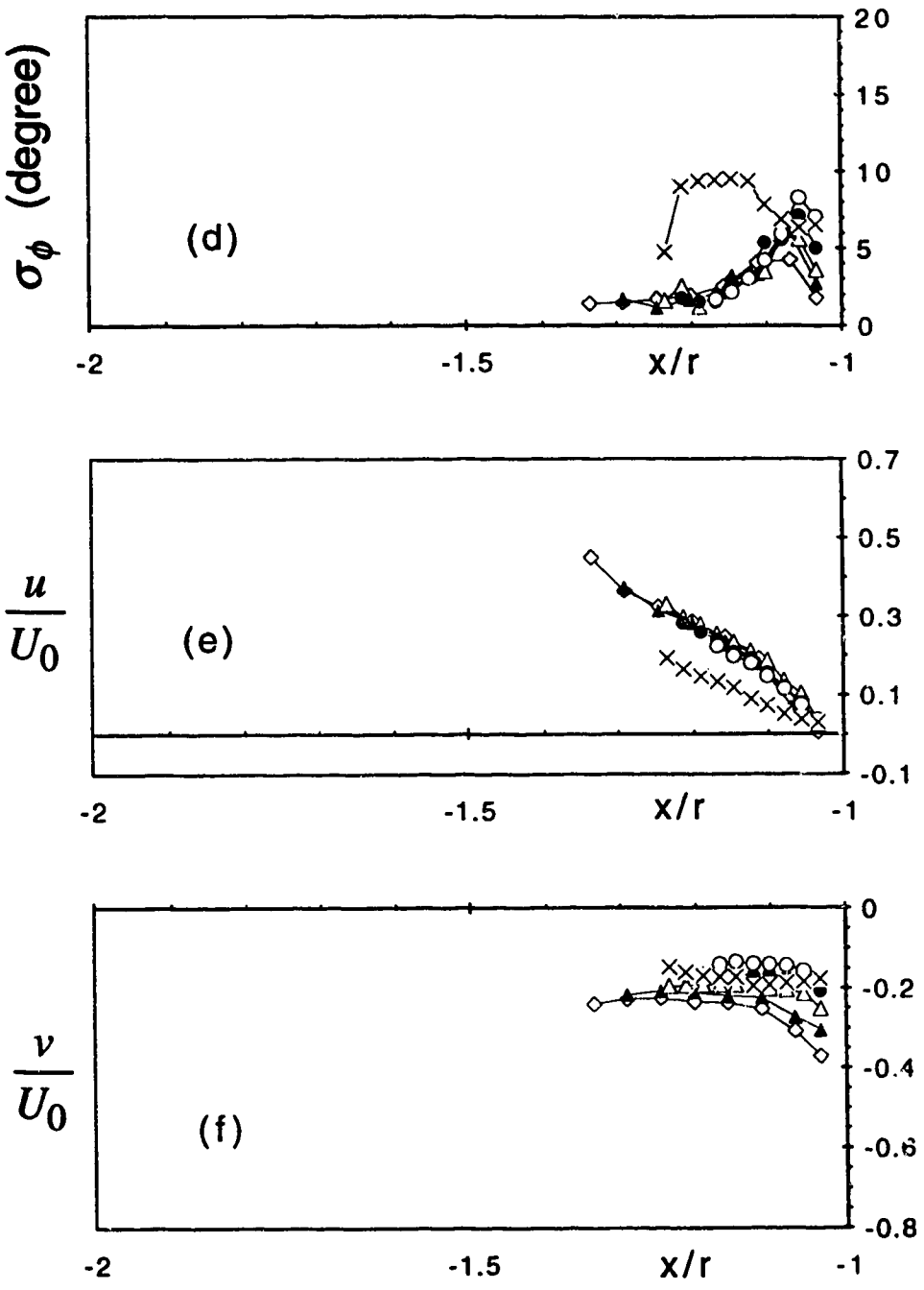

Figure 4.2.18 (a-f) Downflow in front of the pier (Expt. C2R);
(d) fluctuation of pitch angle
(e) longitudinal component of velocity
(f) vertical component of velocity
Note: symbols same as Figure 4.2.17

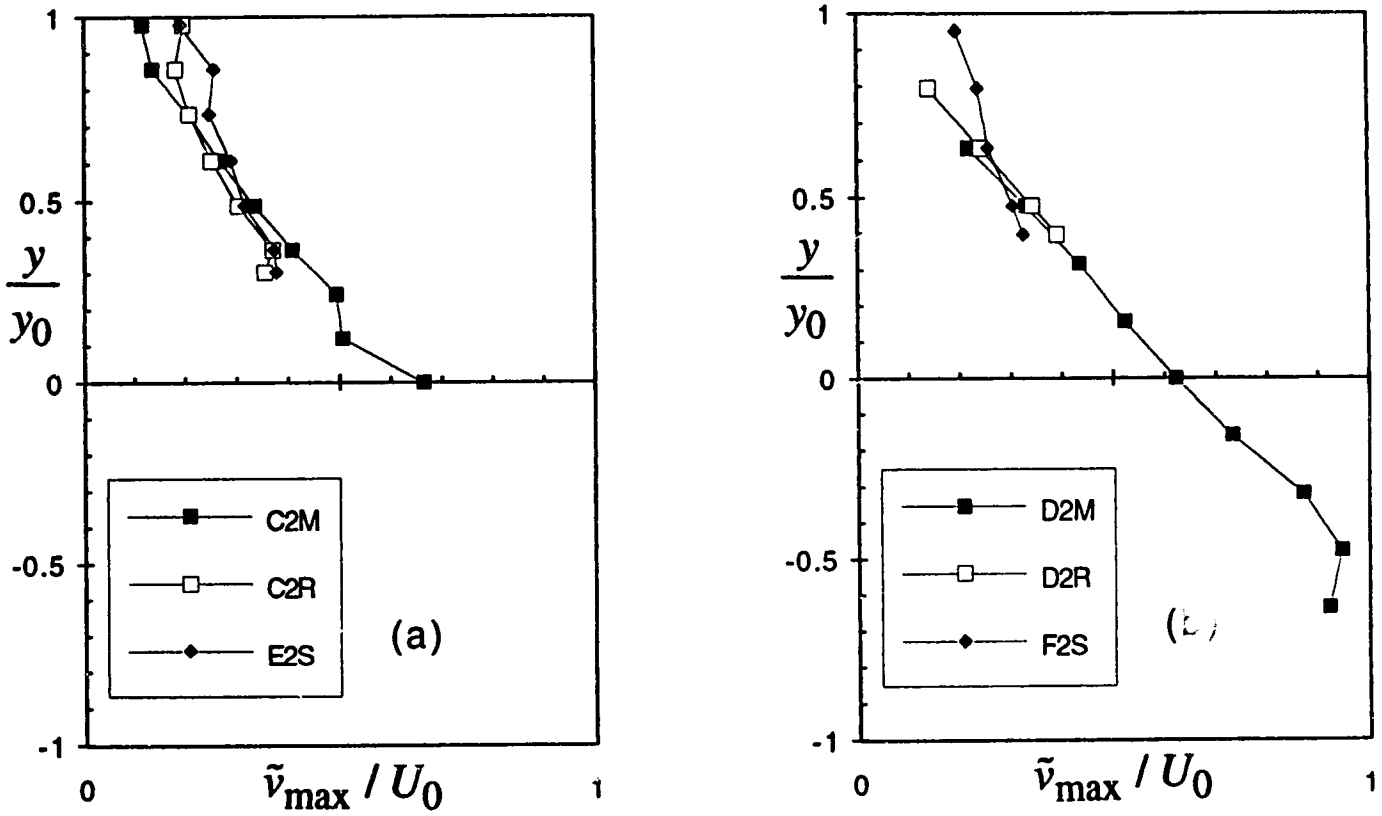

Figure 4.2.19 Variation of maximum downflow velocity with depth
(a) Expt. C2M, C2R and E2S; (b) Expt. D2M, D2R and F2S

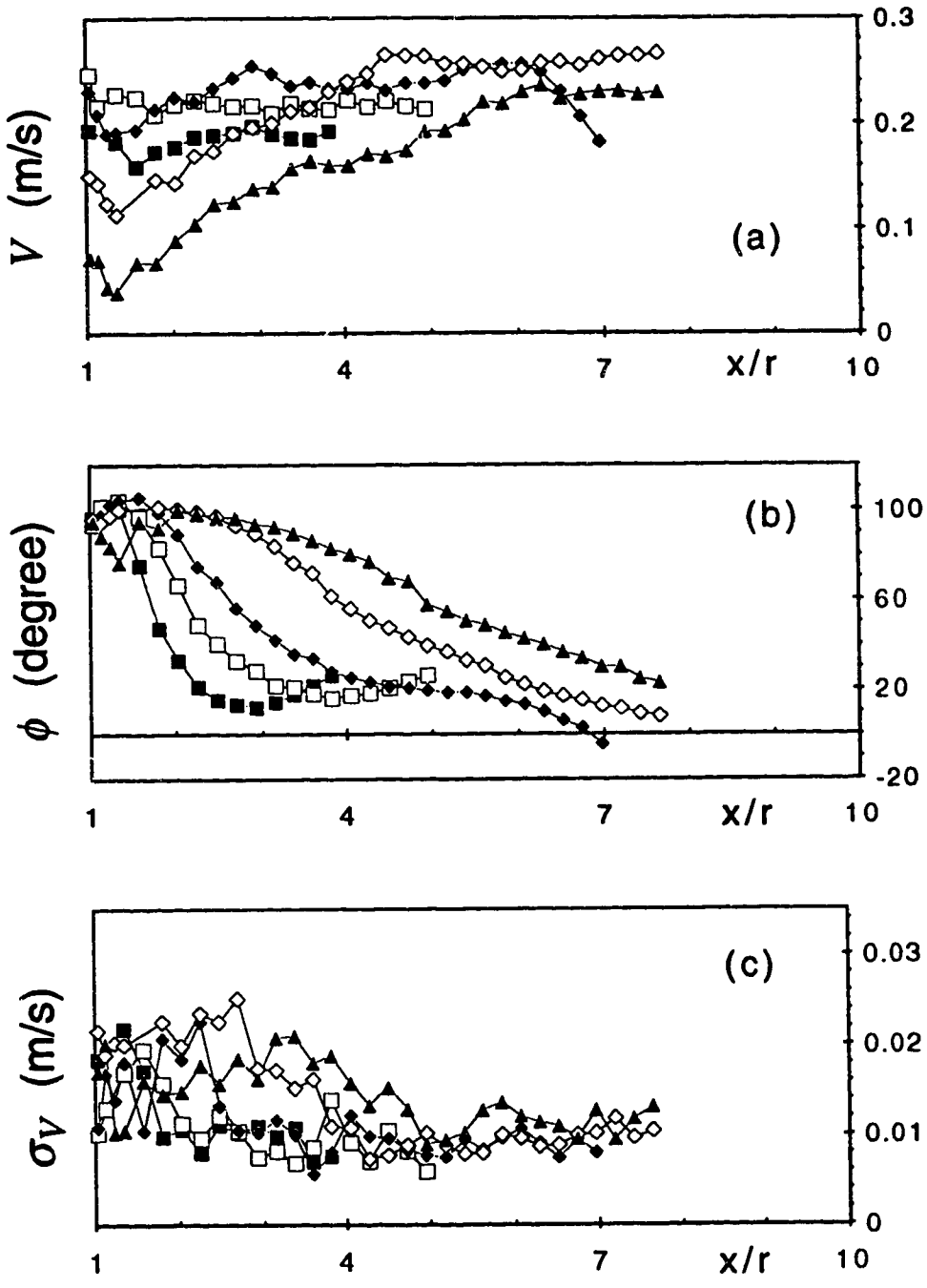

Figure 4.2.20 (a-g) Flow along horizontal lines downstream of the pier (Expt. C2M);
(a) velocity magnitude
(b) angle of pitch
(c) fluctuation of velocity

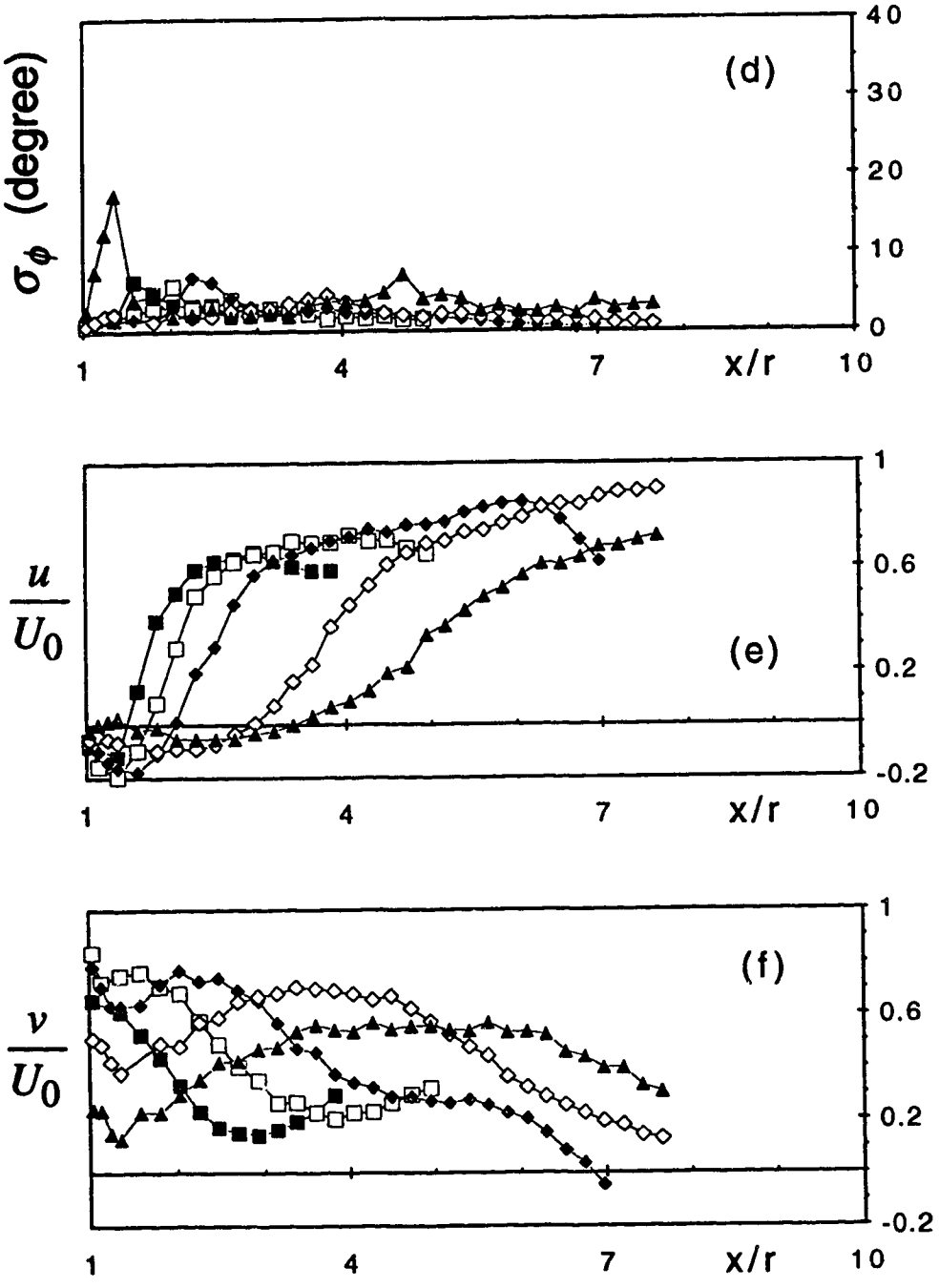

Figure 4.2.20 (a-g) Flow along horizontal lines downstream of the pier (Expt. C2M);
(d) fluctuation of pitch angle
(e) longitudinal component of velocity
(f) vertical component of velocity

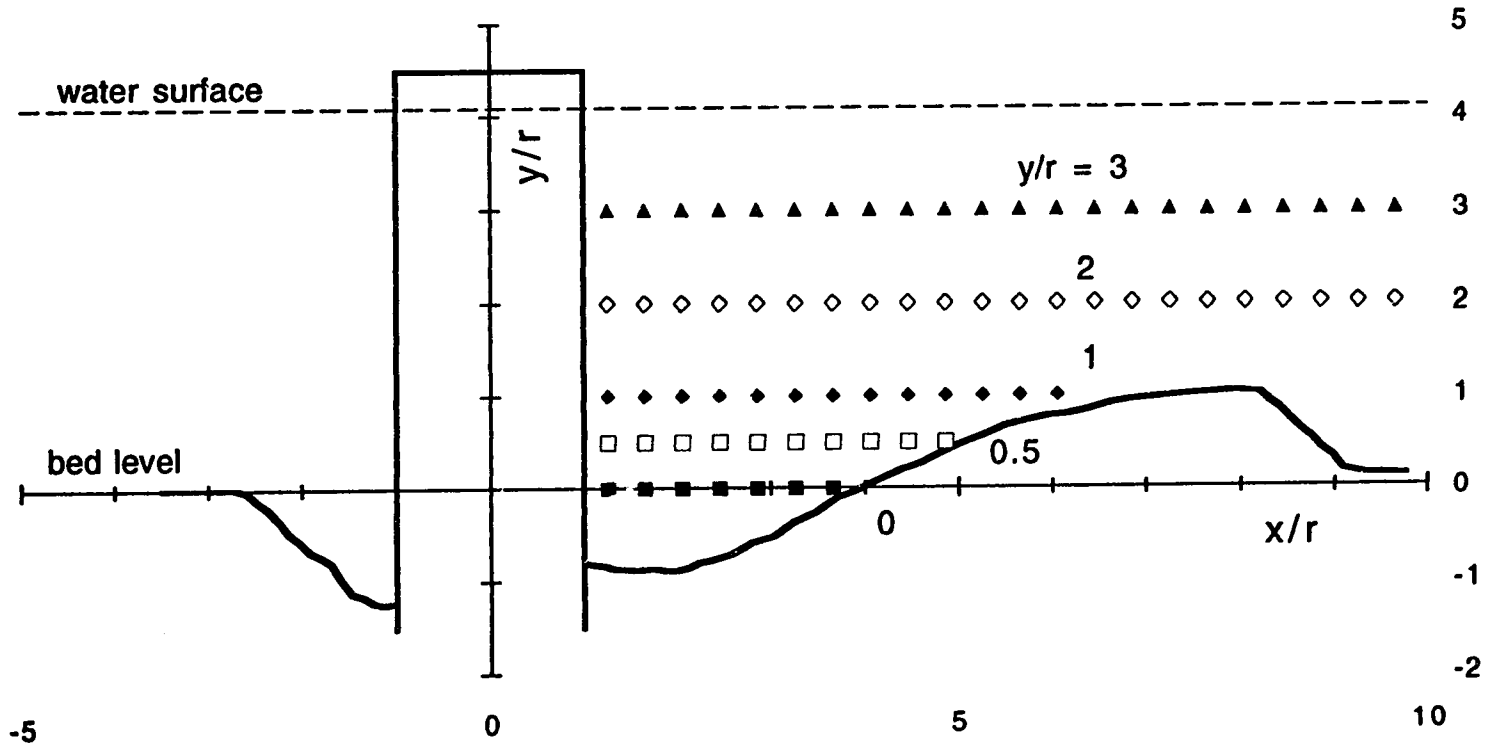

Figure 4.2.20 (a-g) Flow along horizontal lines downstream of the pier (Expt. C2M); (g) location of measuremer' lines

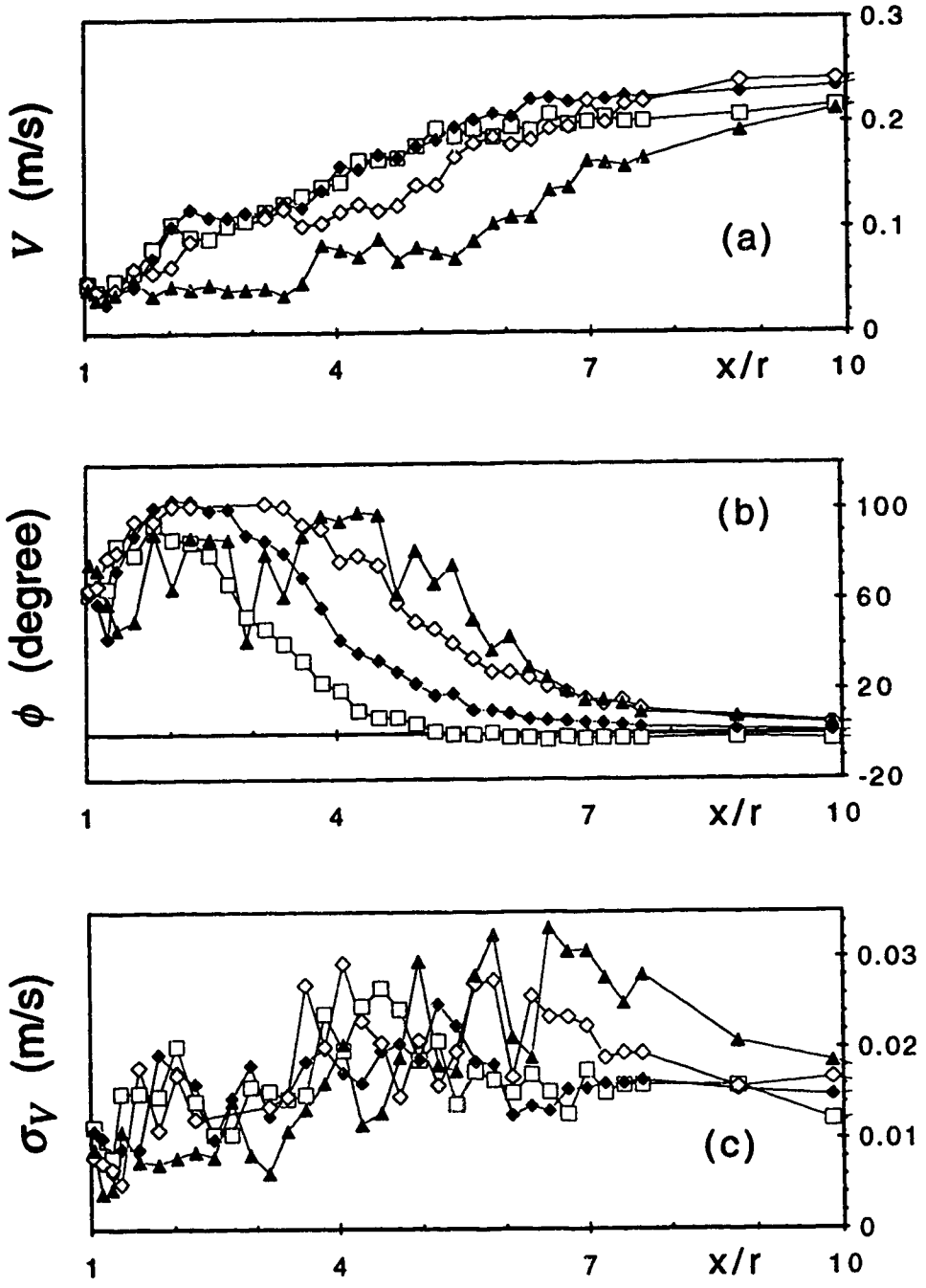

Figure 4.2.21 (a-f) Flow along horizontal lines downstream of the pier (Expt. C2R);
(a) velocity magnitude
(b) angle of pitch
(c) fluctuation of velocity
Note: symbols same as Figure 4.2.20

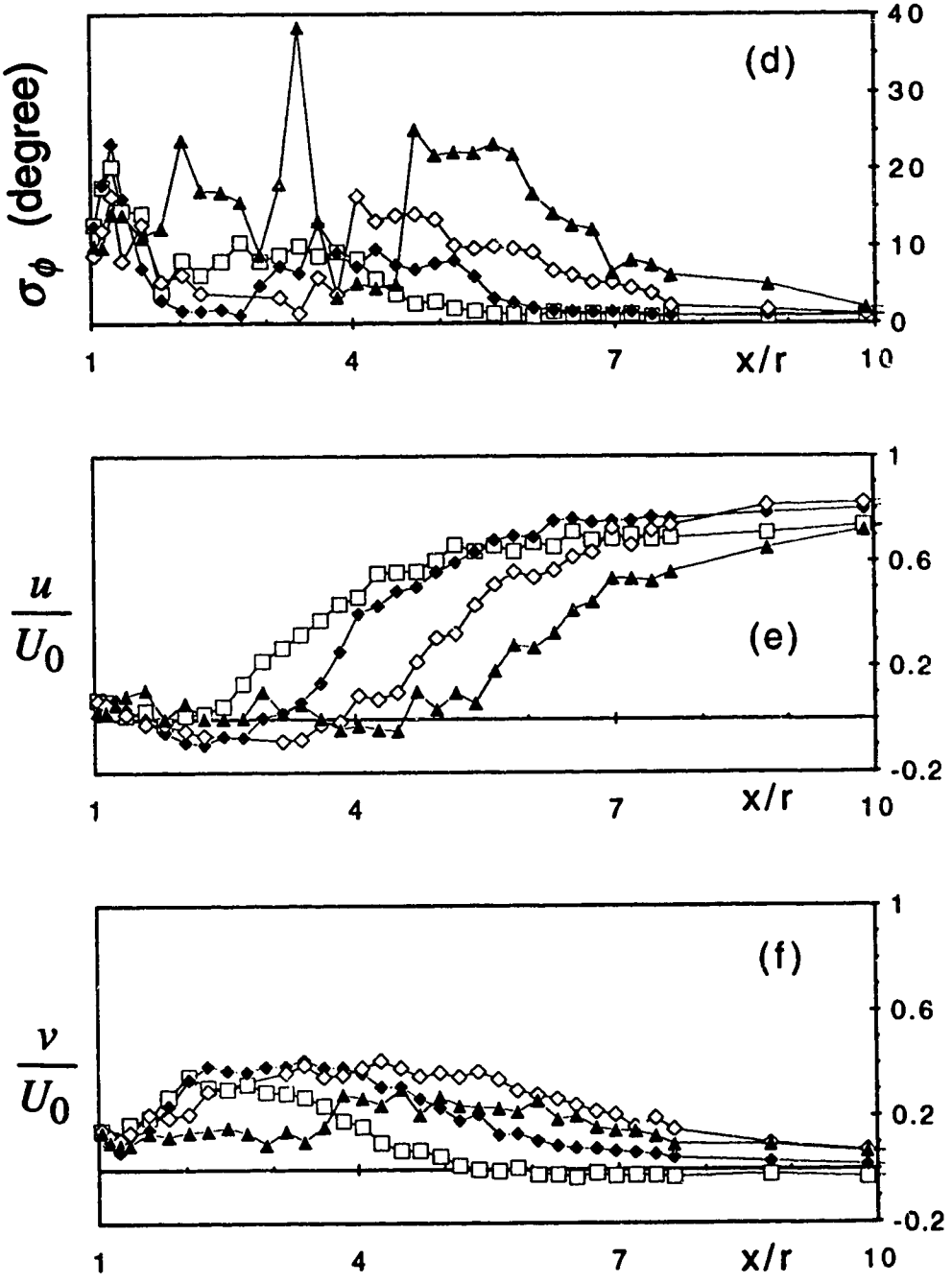

Figure 4.2.21 (a-f) Flow along horizontal lines downstream of the pier (Expt. C2R);
(d) fluctuation of pitch angle
(e) longitudinal component of velocity
(f) vertical component of velocity
Note: symbols same as Figure 4.2.20

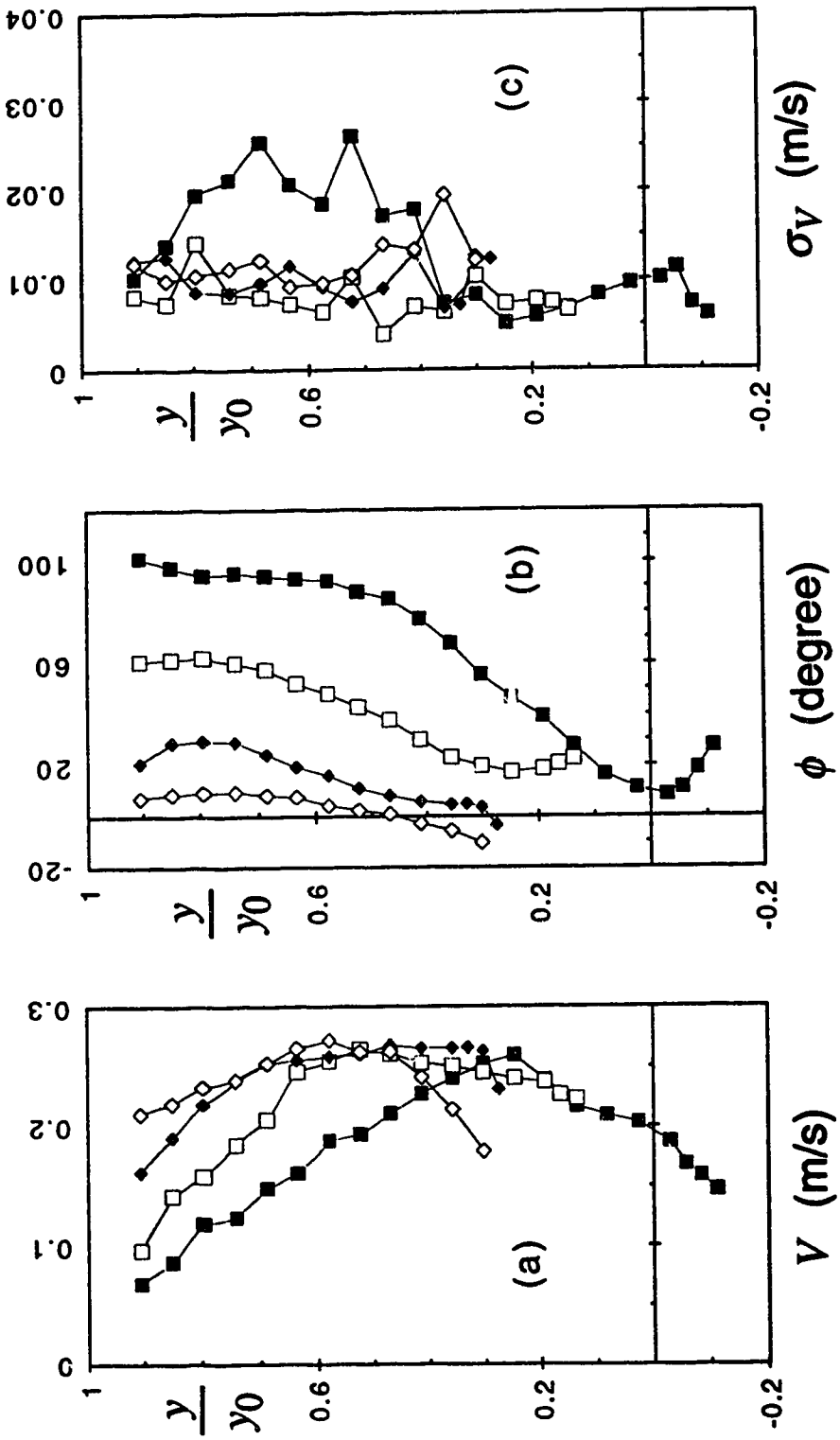

Figure 4.2.22 (a-g) Flow along vertical lines downstream of the pier (Expt. C2M);
(a) velocity magnitude; (b) angle of pitch; (c) fluctuation of velocity

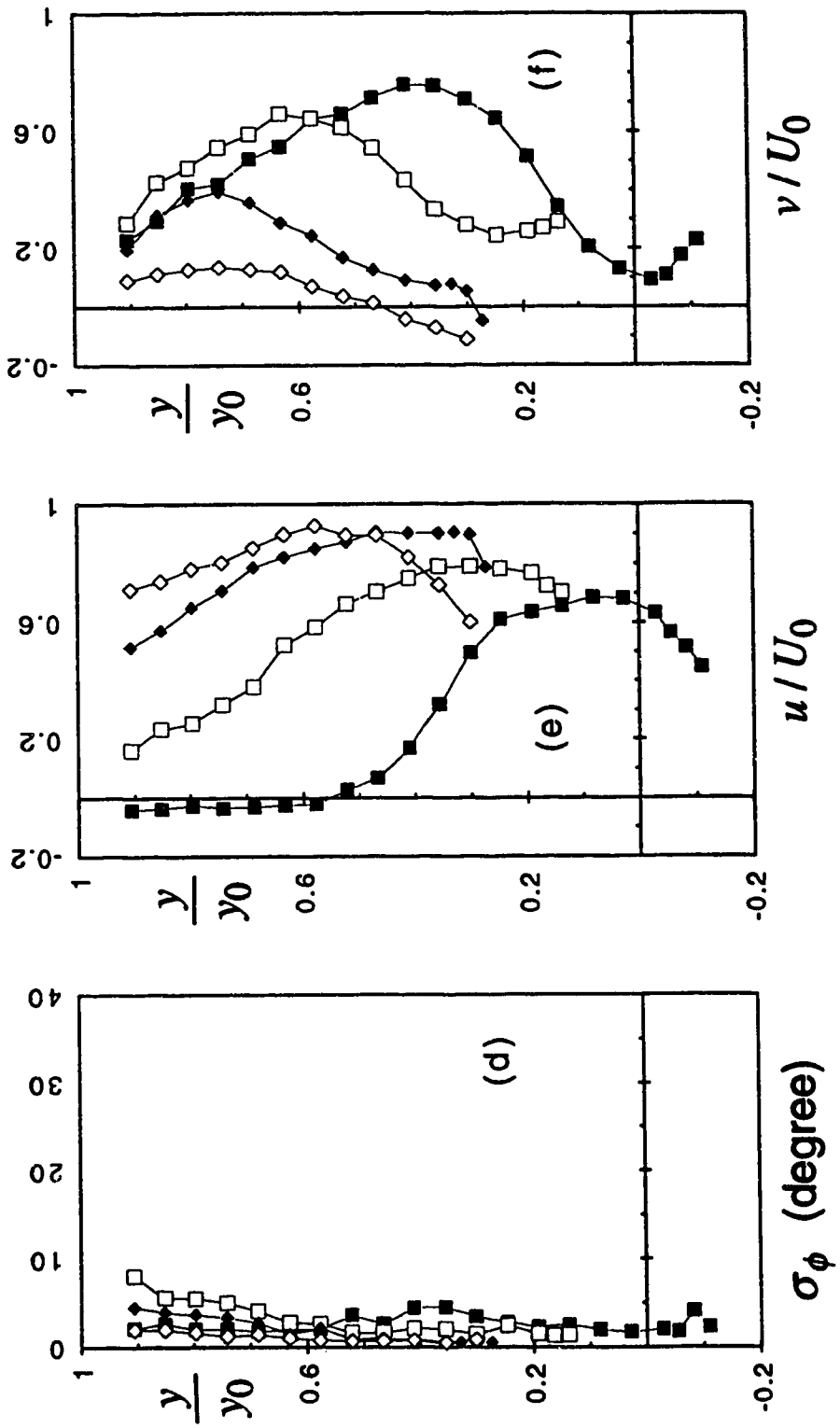

Figure 4.2.22 (a-g) Flow along vertical lines downstream of the pier (Expt. C2M);
(d) fluctuation of pitch angle; (e) vertical component of velocity;
(f) vertical component of velocity

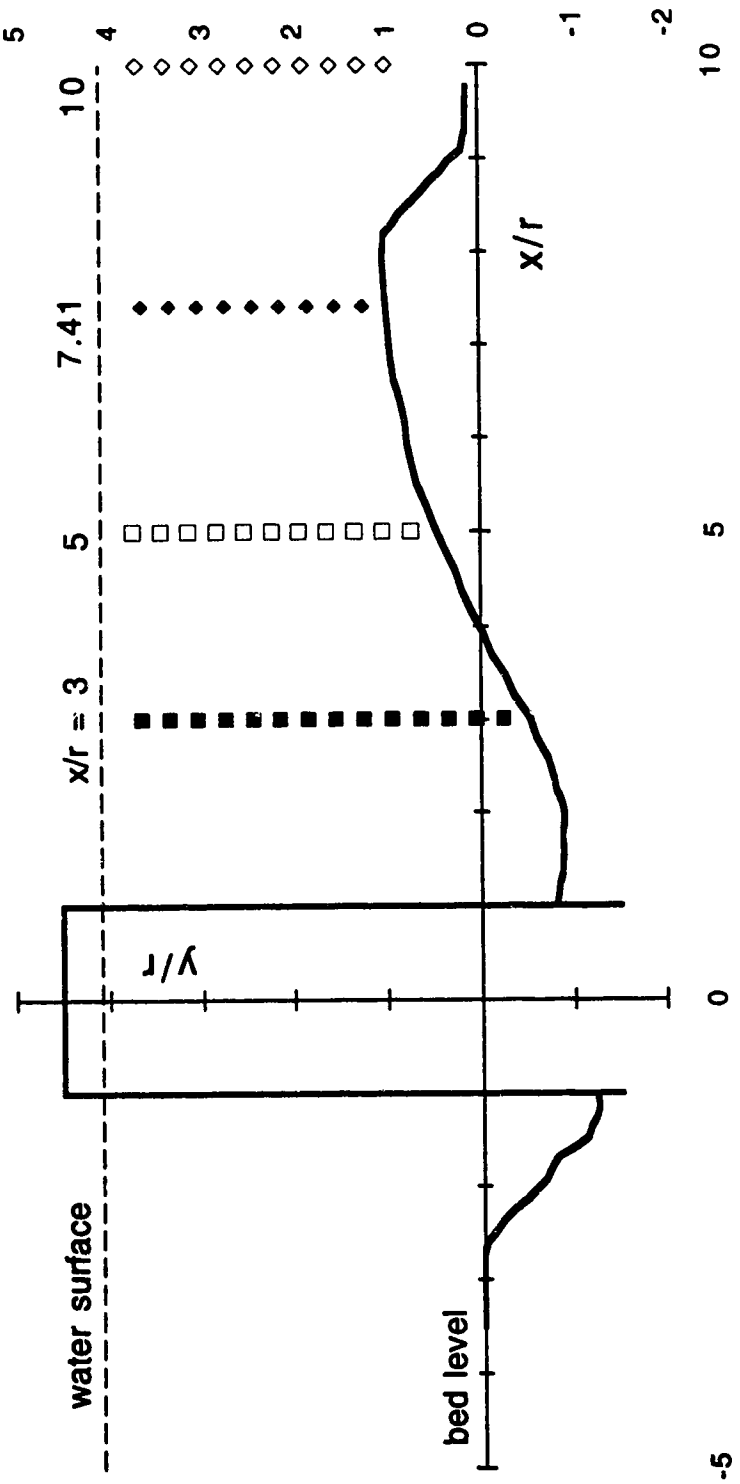

Figure 4.2.22 (a-g) Flow along vertical lines downstream of the pier (Expt. C2M); (g) location of measurement lines

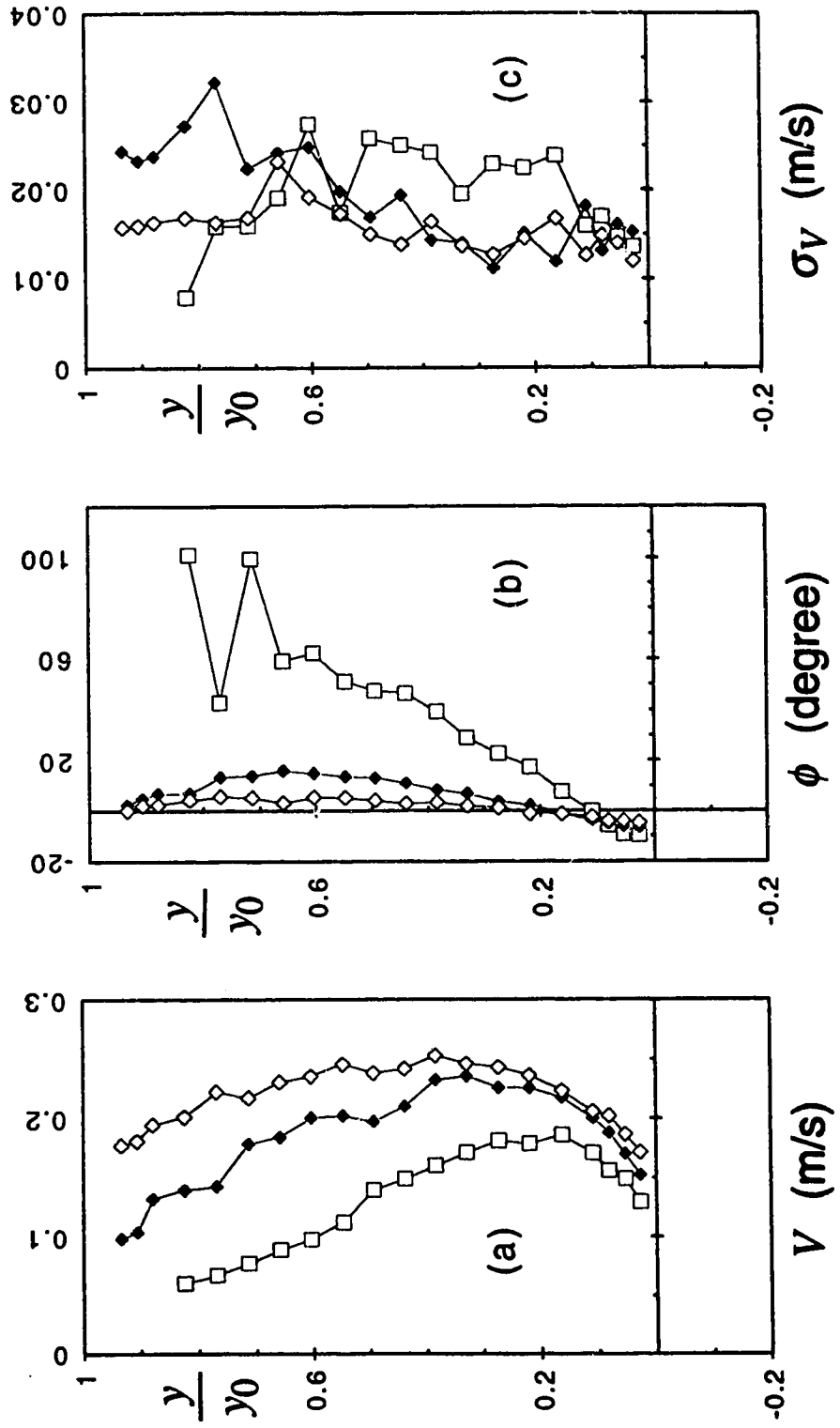

Figure 4.2.23 (a-f) Flow along vertical lines downstream of the pier (Expt. C2R);
(a) velocity magnitude; (b) angle of pitch; (c) fluctuation of velocity
Note: symbols same as Figure 4.2.22

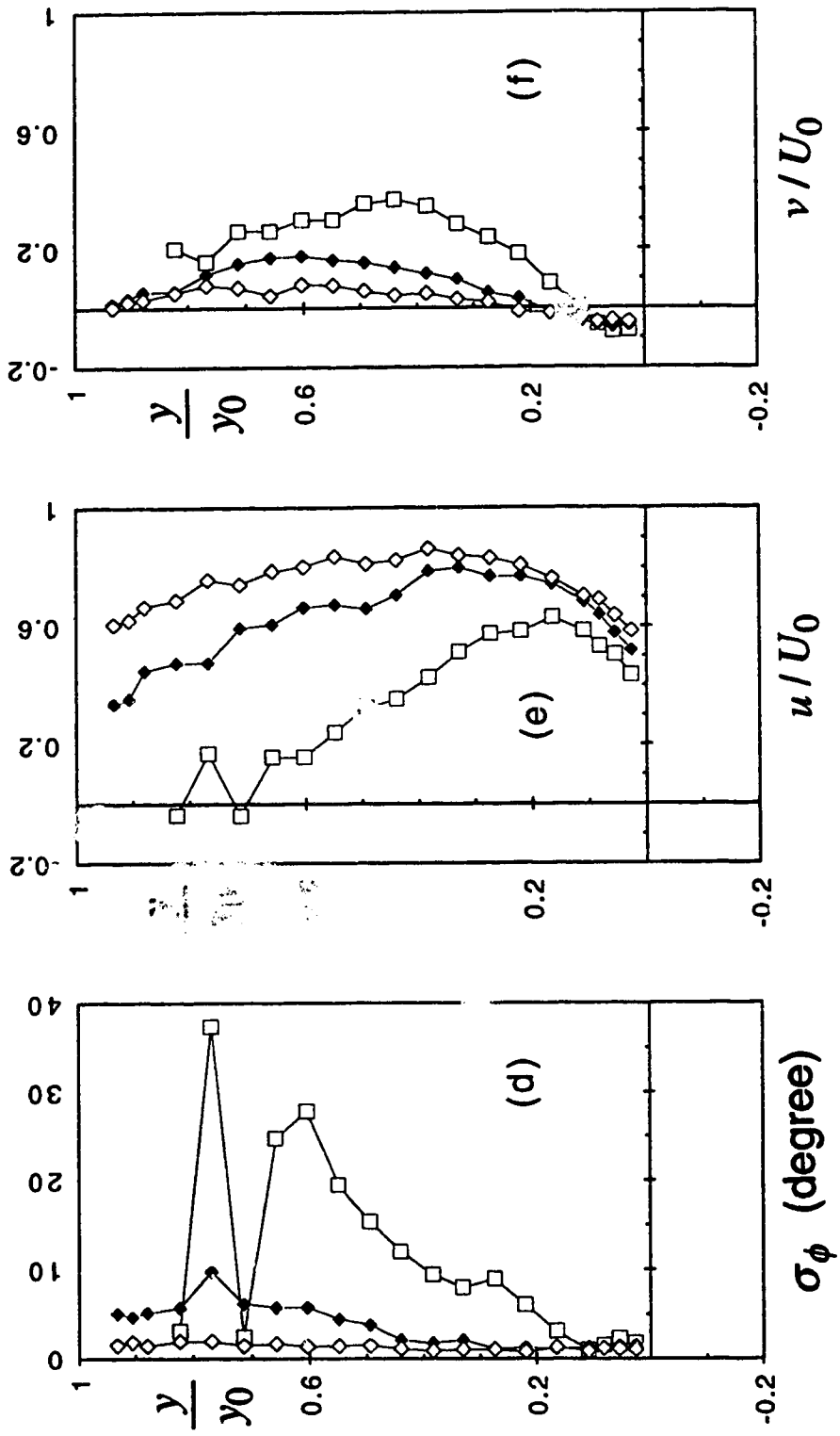

Figure 4.2.23 (a-f) Flow along vertical lines downstream of the pier (Expt. C2R);
(d) fluctuation of pitch angle; (e) vertical component of velocity;
(f) vertical component of velocity
Note: symbols same as Figure 4.2.22

Figure 4.3.1 (a-b) Pressure distribution in the upstream region
(a) Series C and E

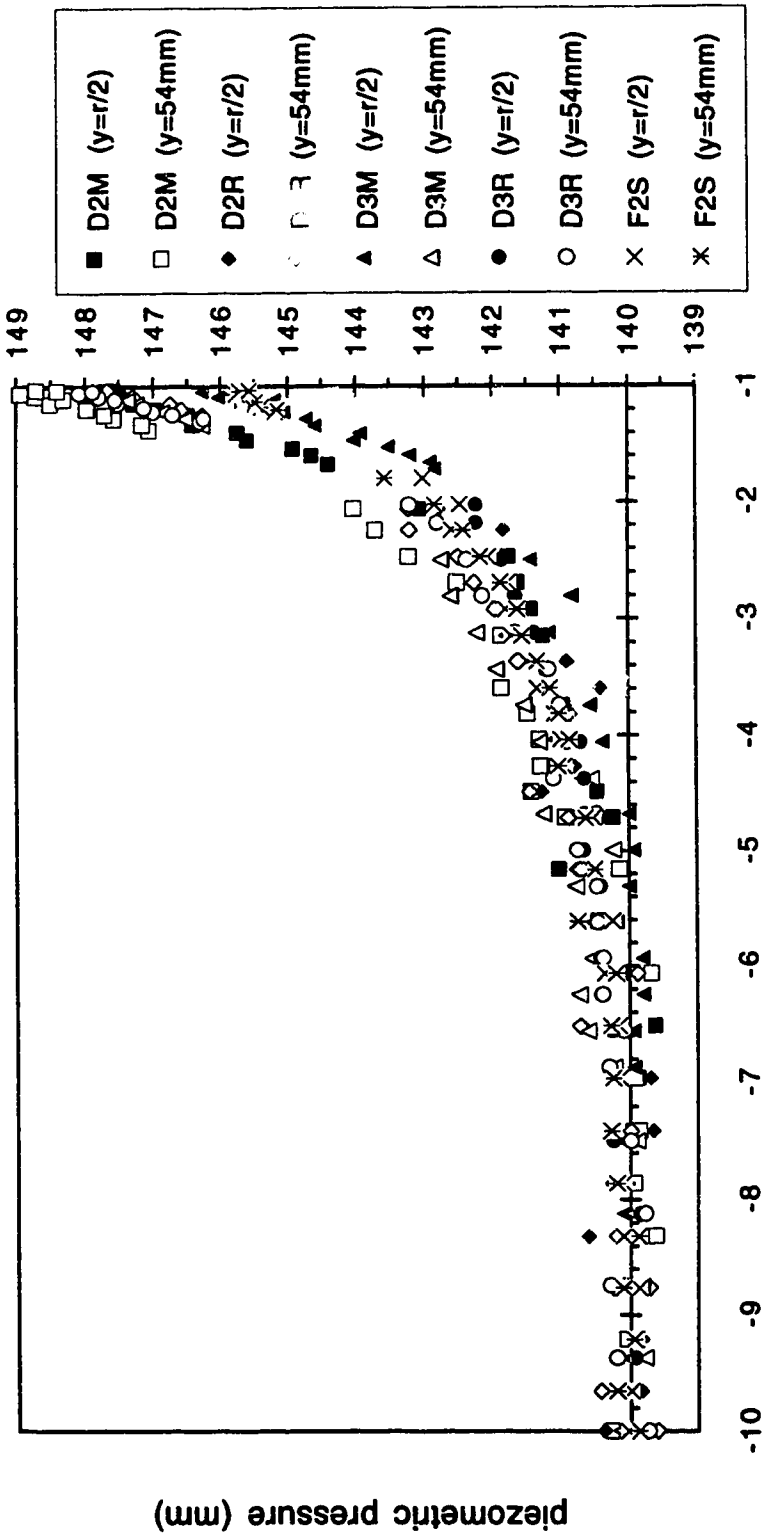

Figure 4.3.1 (a-b) Pressure distribution in the upstream region
(b) Series D and F

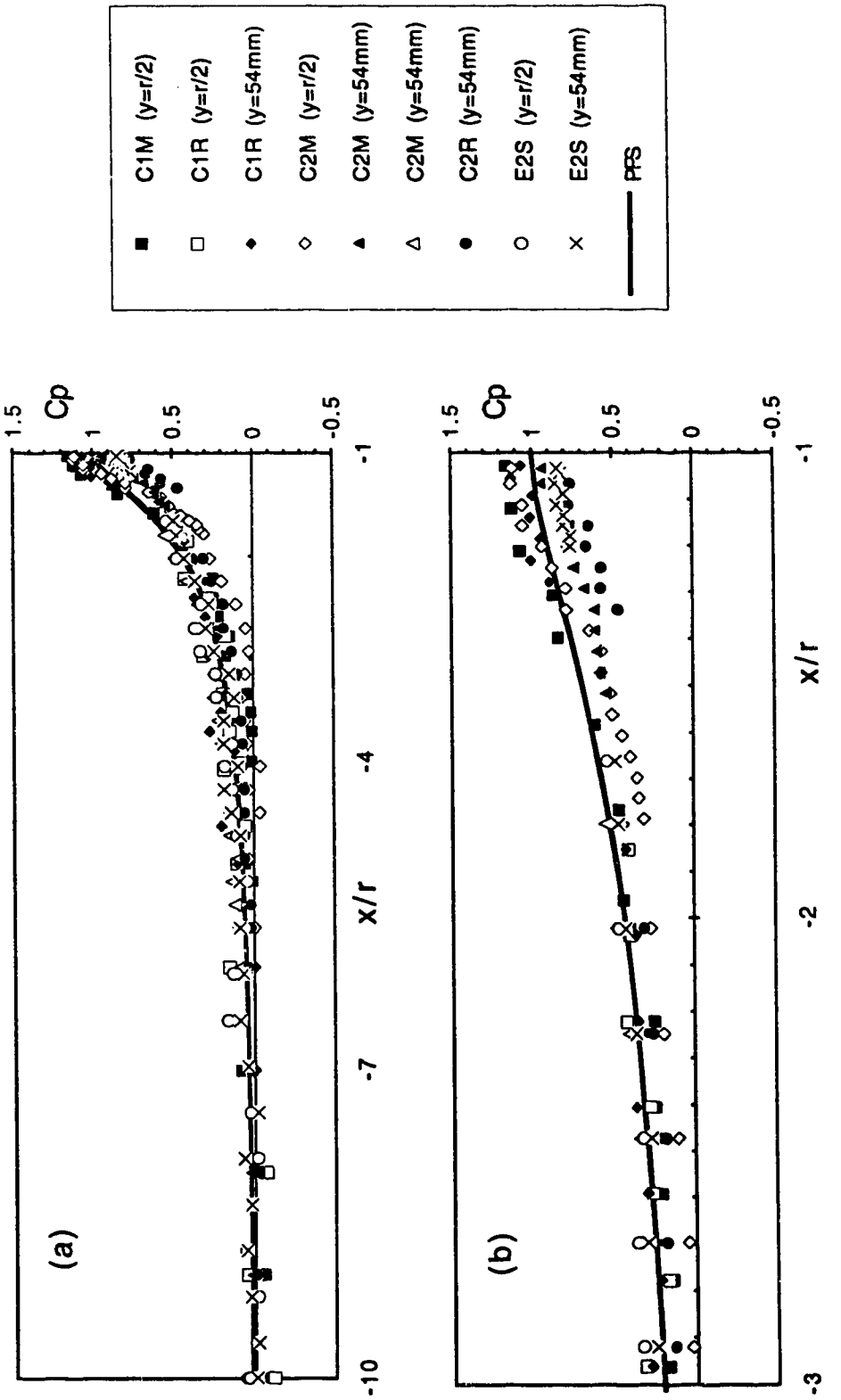

Figure 4.3.2 (a-d) Variation of pressure coefficient in the upstream region
(a) Series C and E; (b) Series C and E (details near the cylinder)

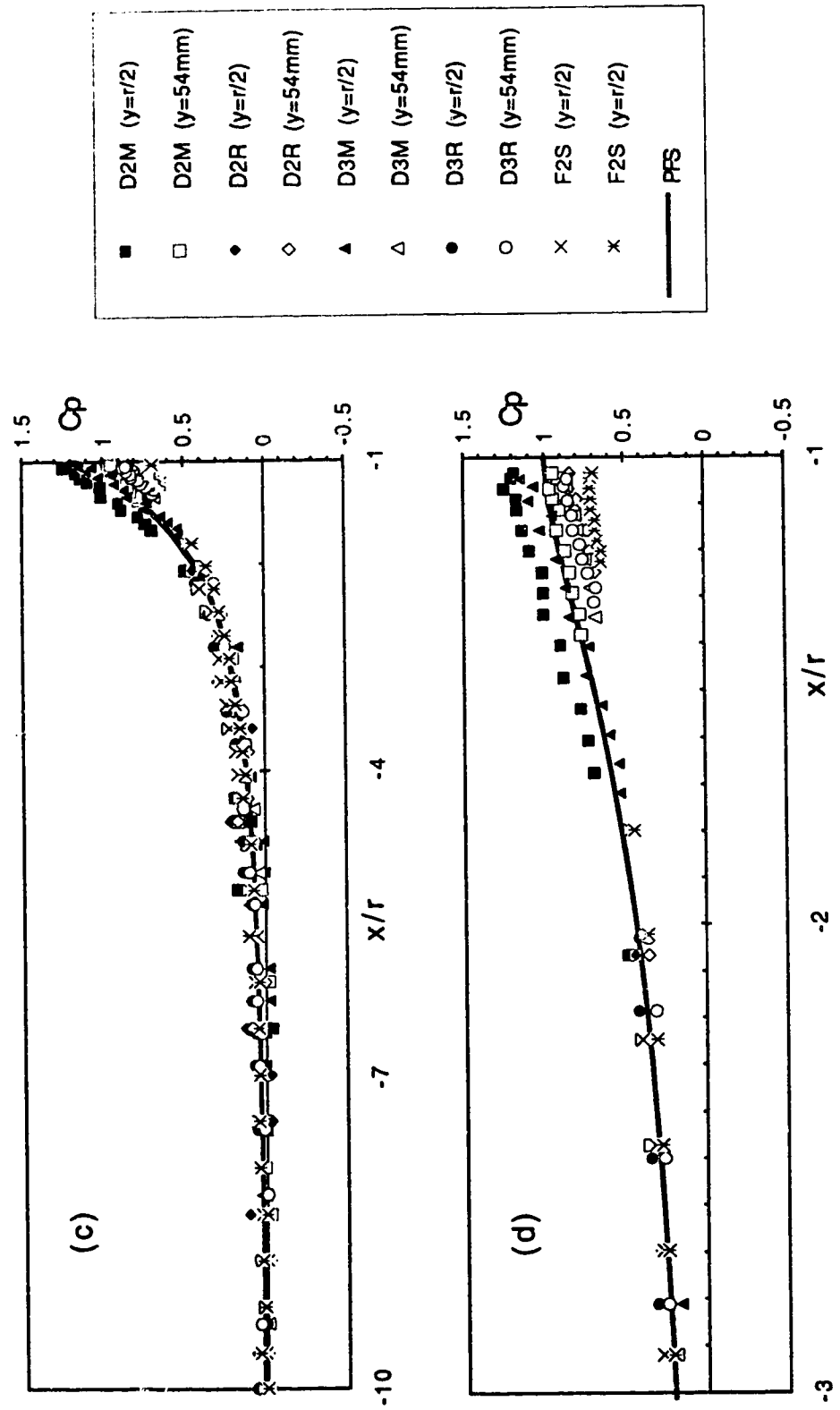

Figure 4.3.2 (a-d) Variation of pressure coefficient in the upstream region
(c) Series D and F; (d) Series D and F (details near the cylinder)

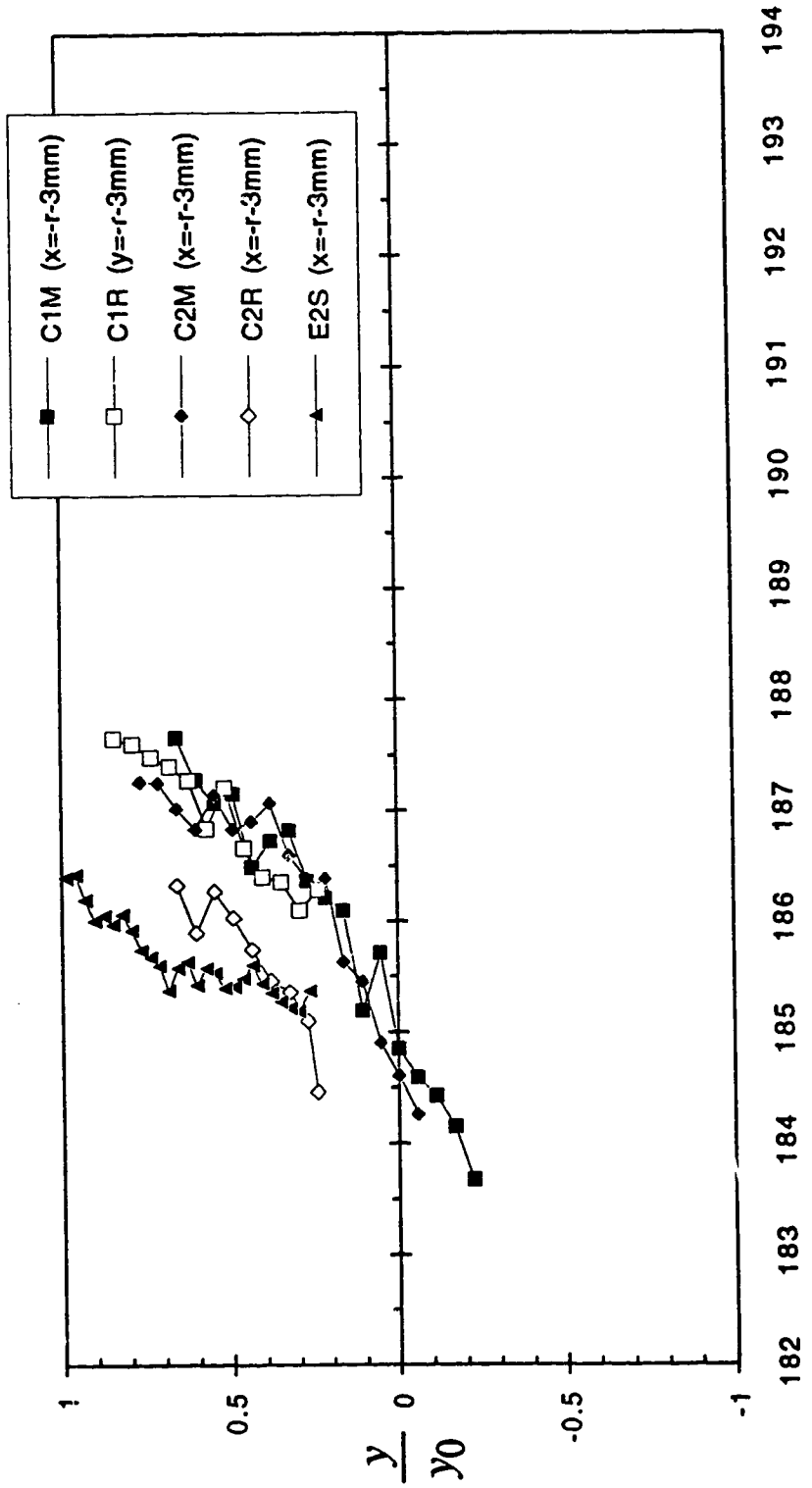

Figure 4.3.3 (a-b) Pressure distribution in front of the cylinder
(a) Series C and E

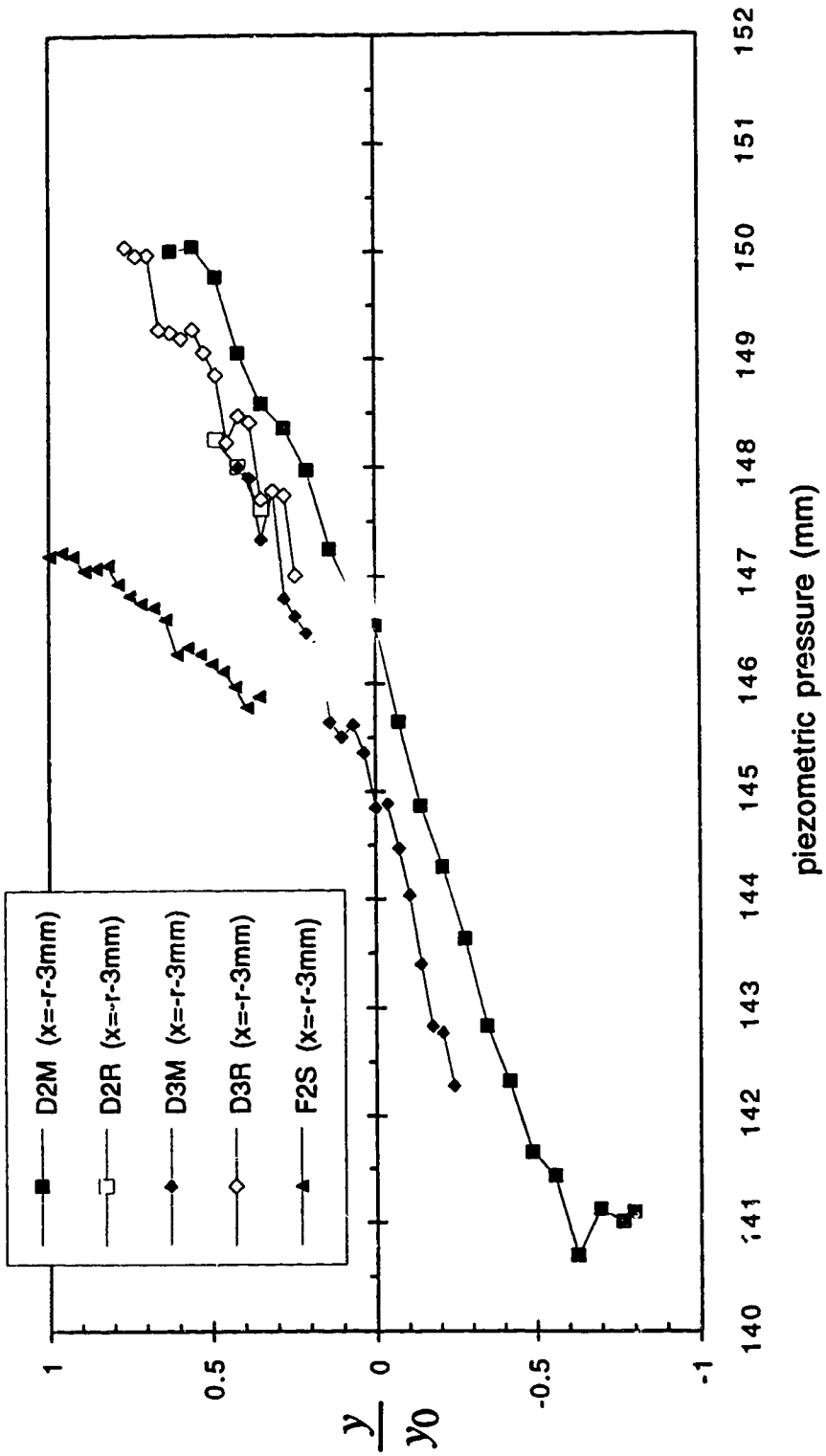

Figure 4.3.3 (a-b) Pressure distribution in front of the cylinder
(b) Series D and F

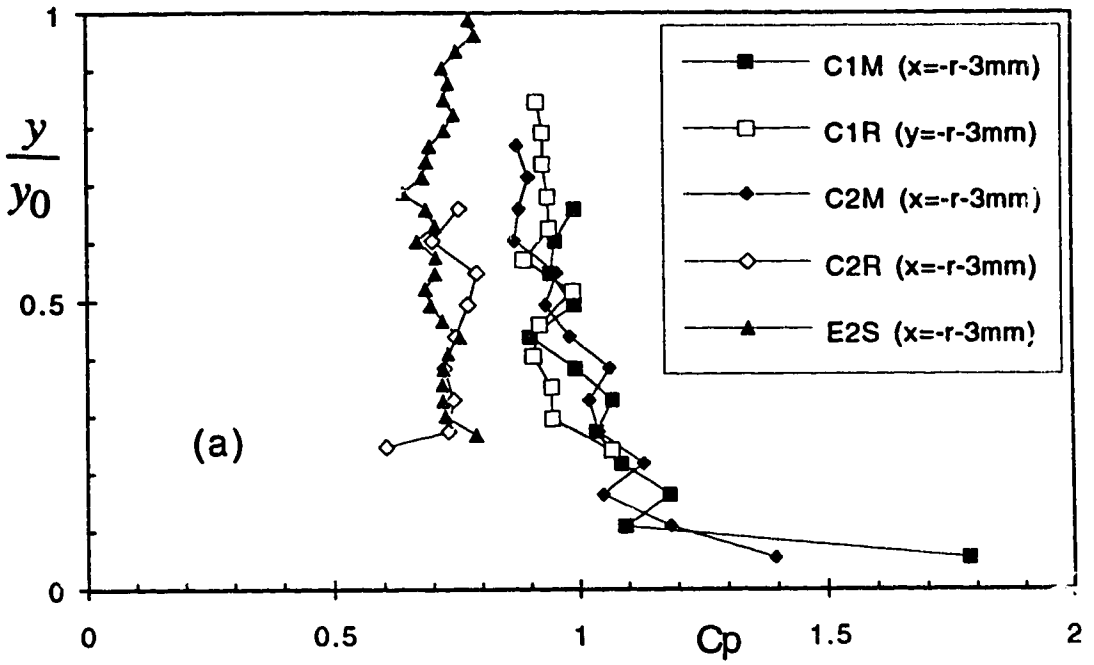

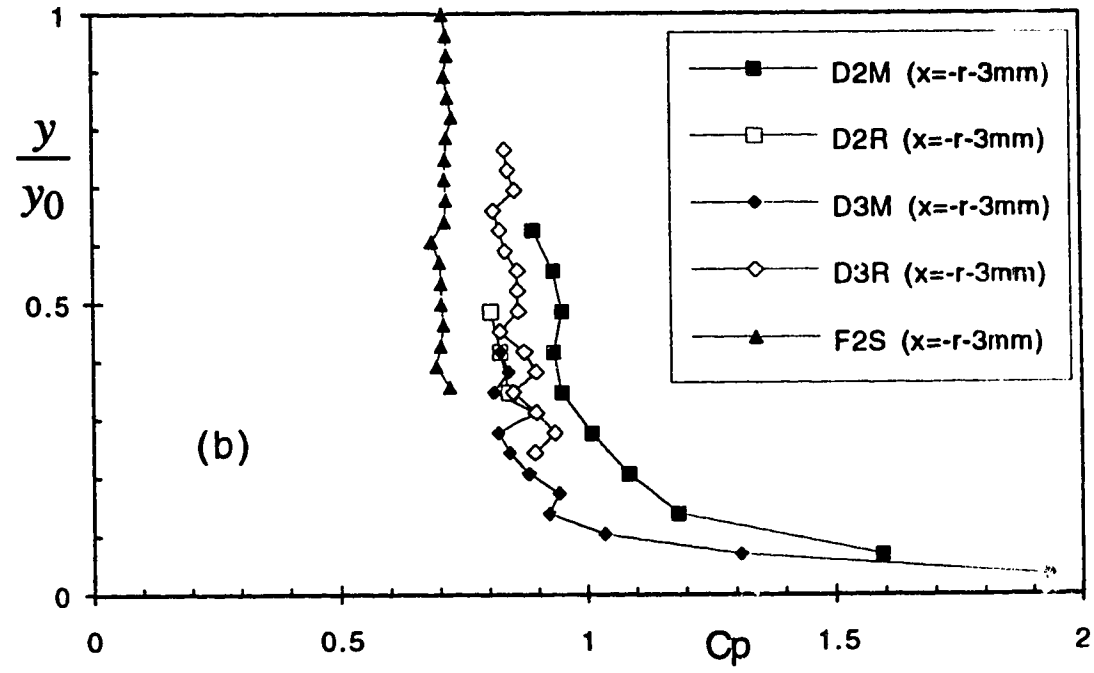

Figure 4.3.4 (a-b) Variation of pressure coefficient in front of the cylinder
(a) Series C and E; (b) Series D a

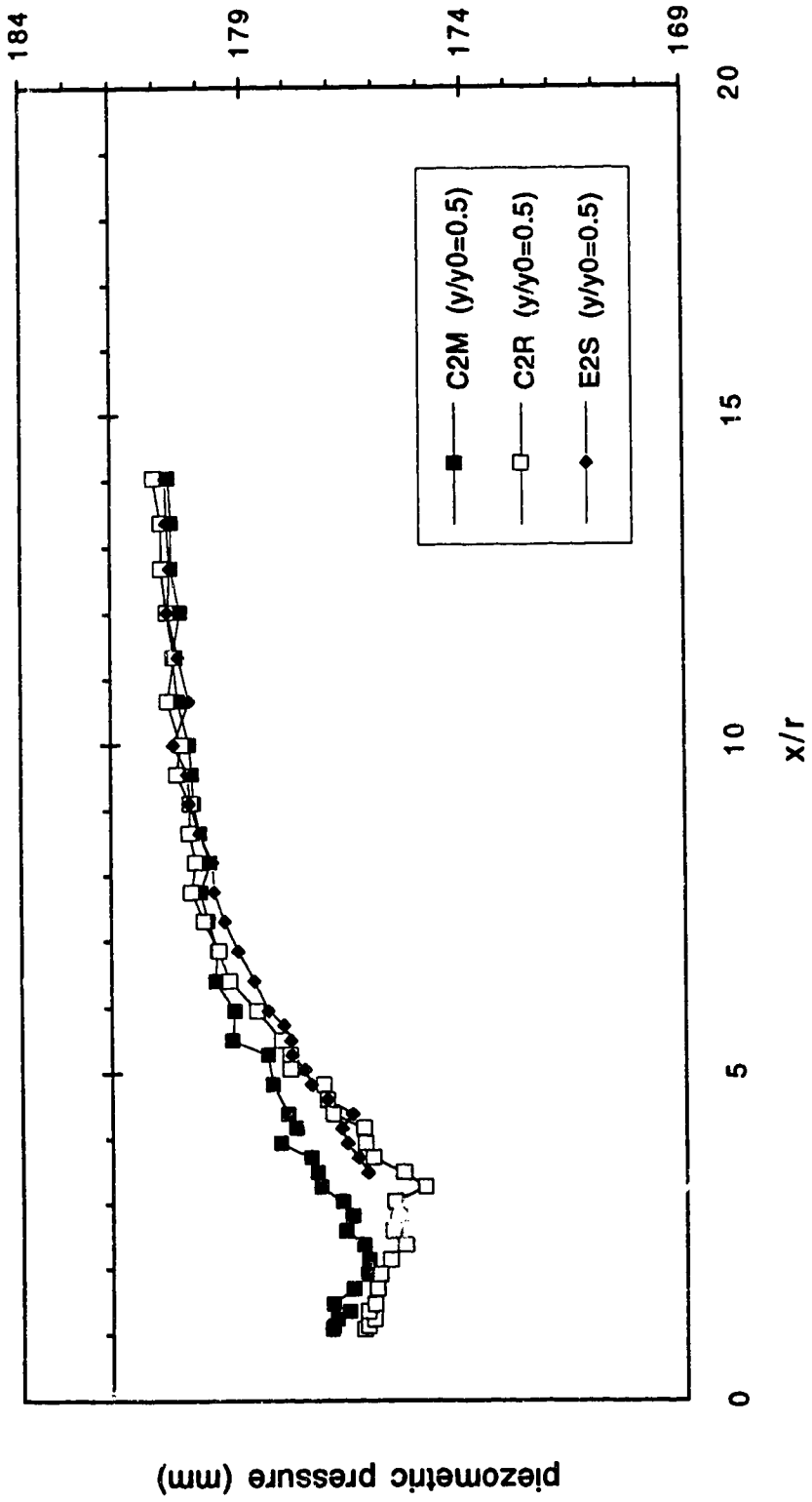

Figure 4.3.5 (a-b) Pressure distribution in the downstream region
(a) Series C and E

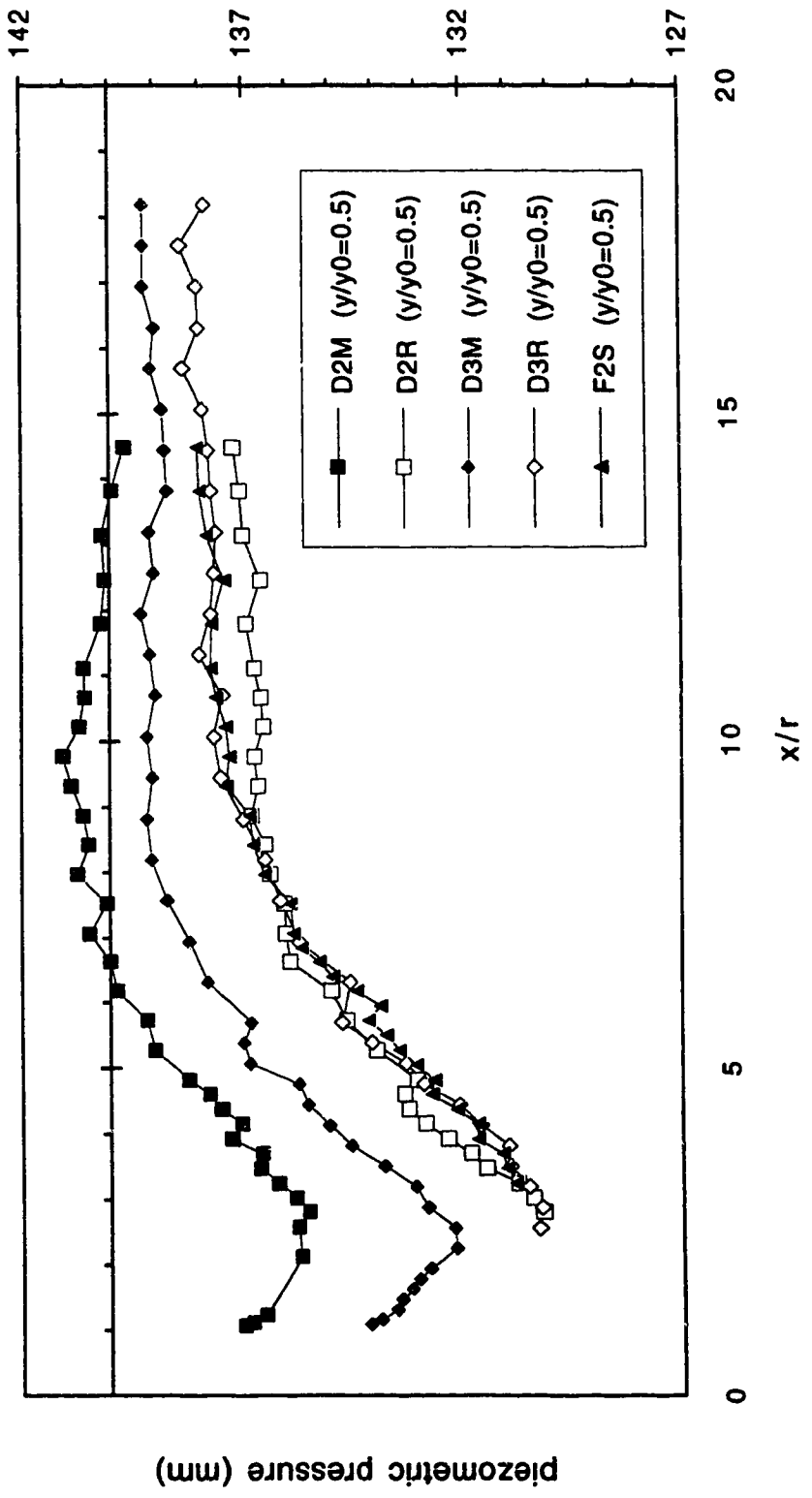

Figure 4.3.5 (a-b) Pressure distribution in the downstream region
(b) Series D and F

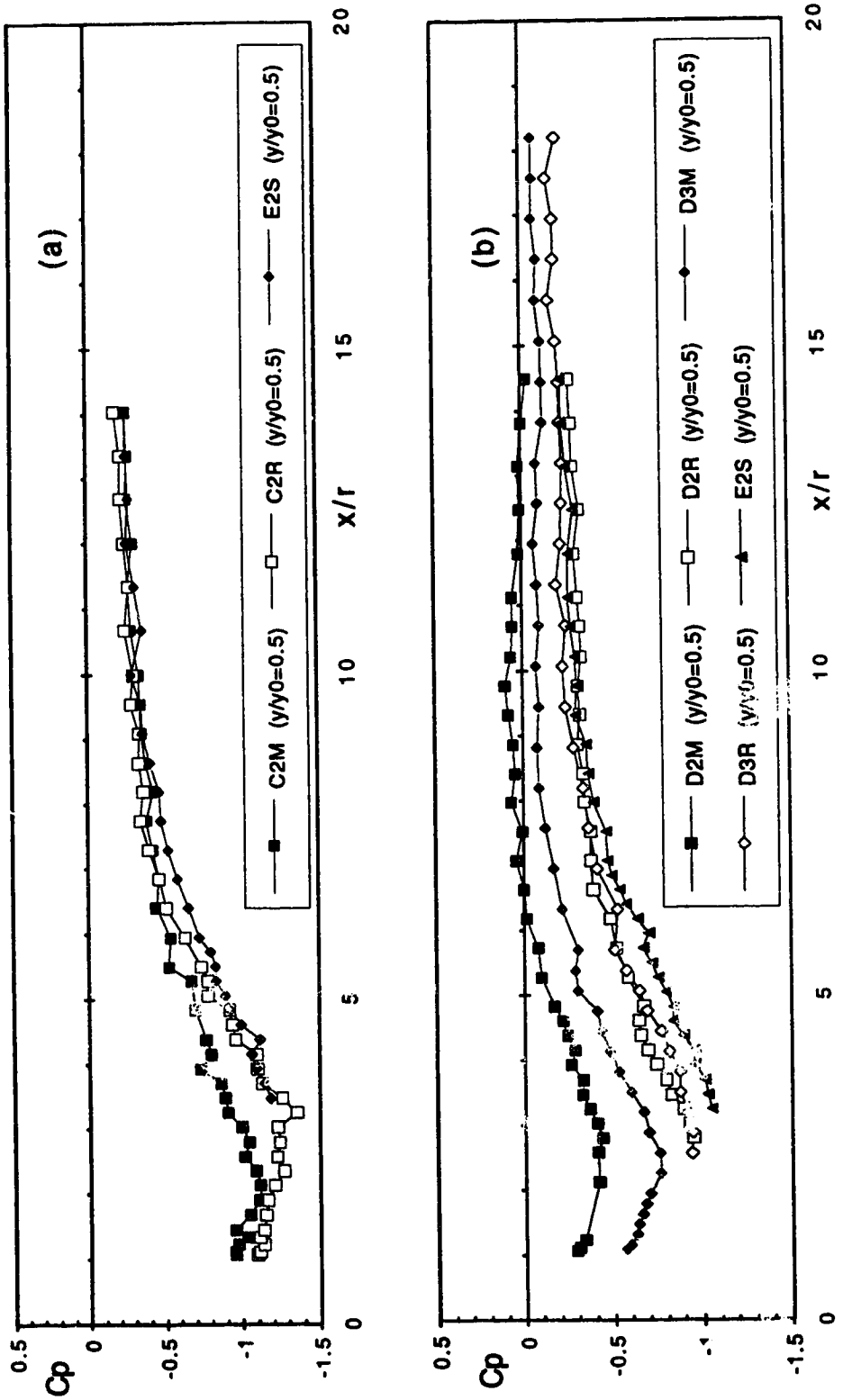

Figure 4.3.6 (a-b) Variation of pressure coefficient in the downstream region
(a) Series C and E; (b) Series D and F

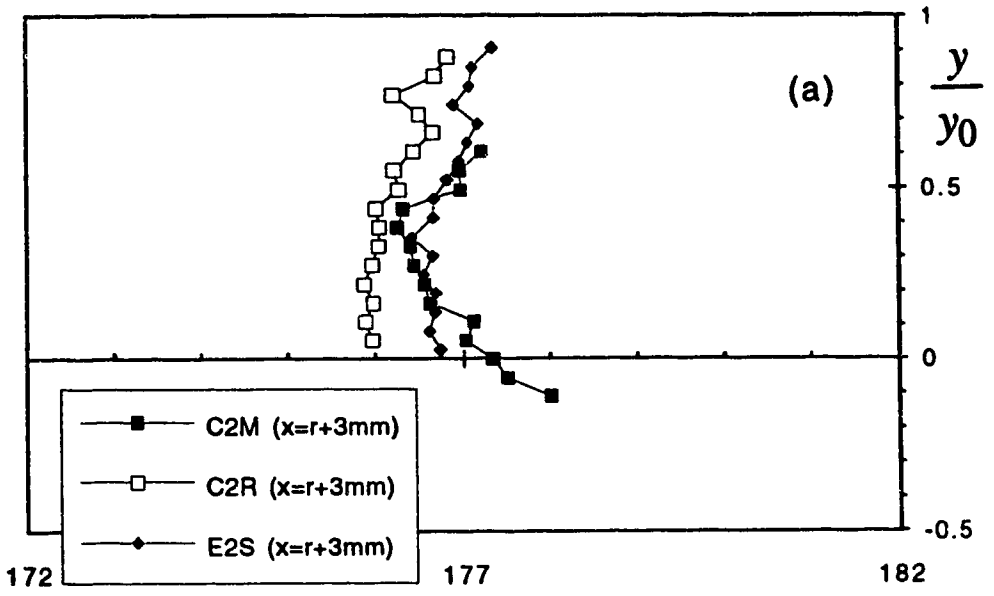

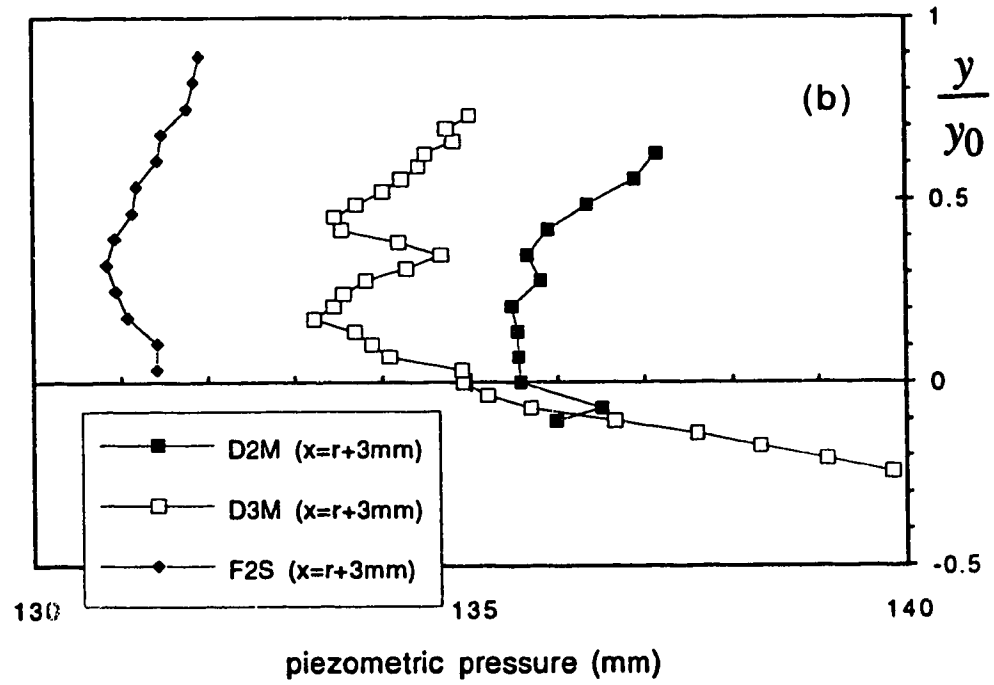

Figure 4.3.7 (a-b) Pressure distribution at the back of the cylinder
(a) Series C and E; (b) Series D and F

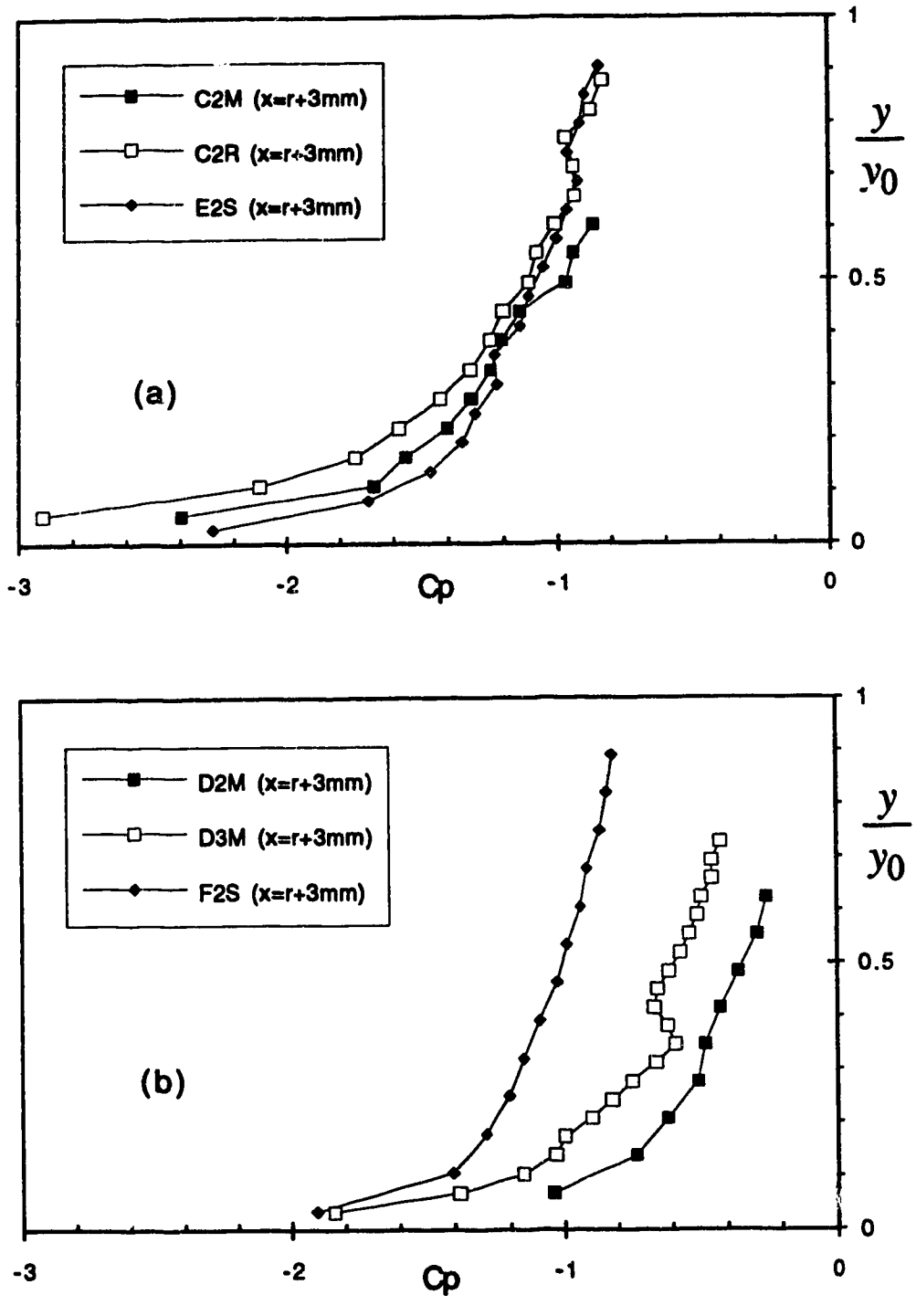

Figure 4.3.8 (a-b) Variation of pressure coefficient at the back of the cylinder
(a) Series C and E; (b) Series D and F

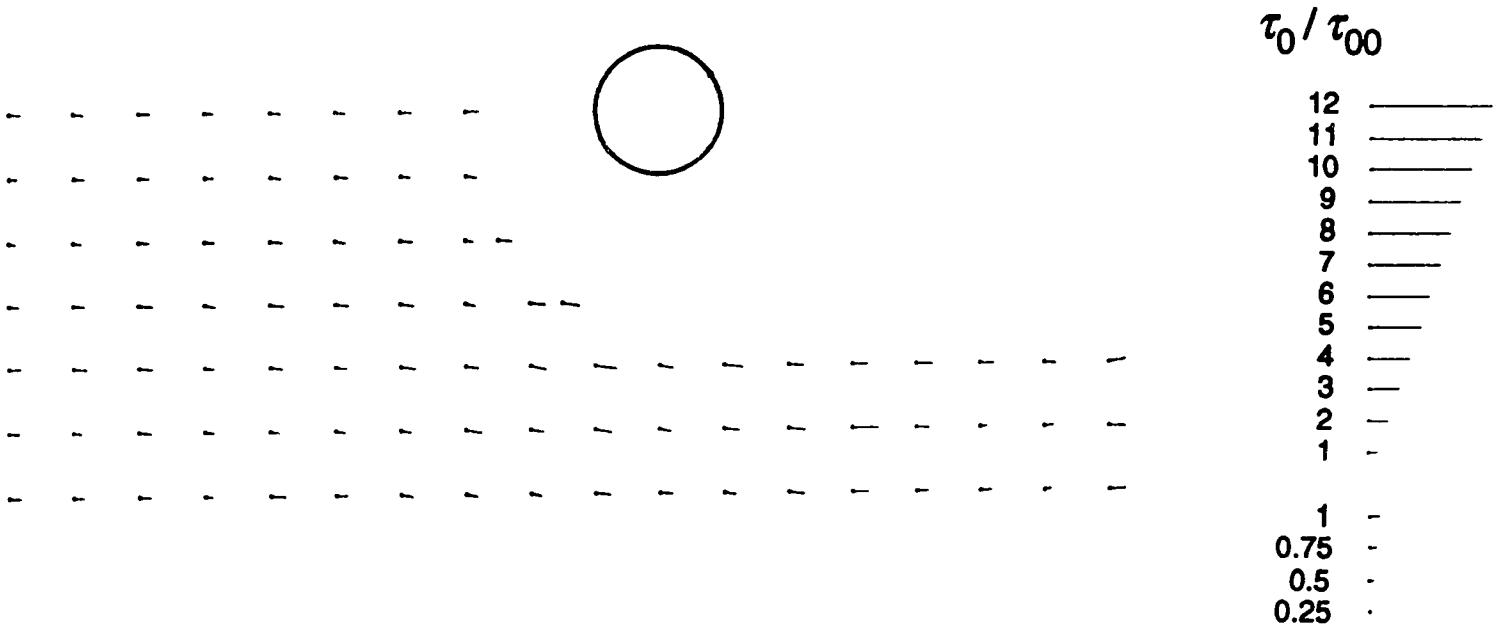

Figure 4.4.1 (a-j): Bed shear stress field (a) Expt. C1M

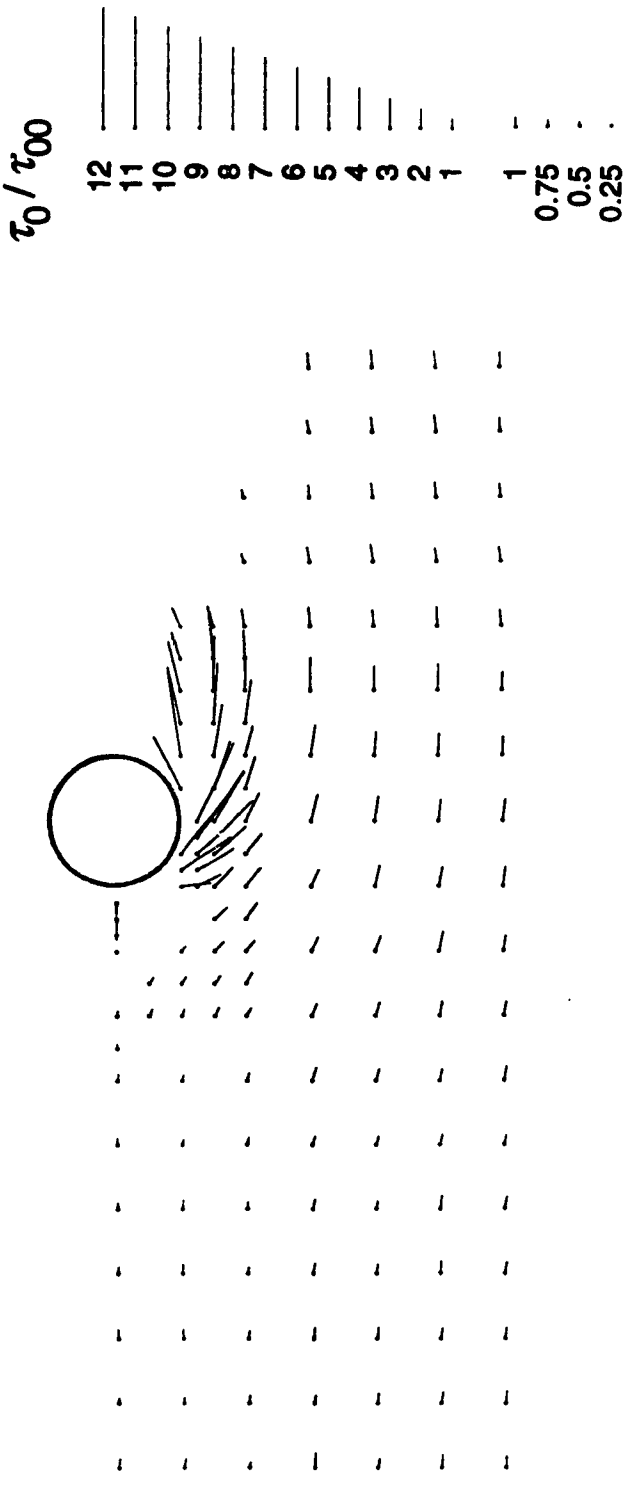

Figure 4.4.1 (a-j) Bed shear stress field (b) Expt. C1R

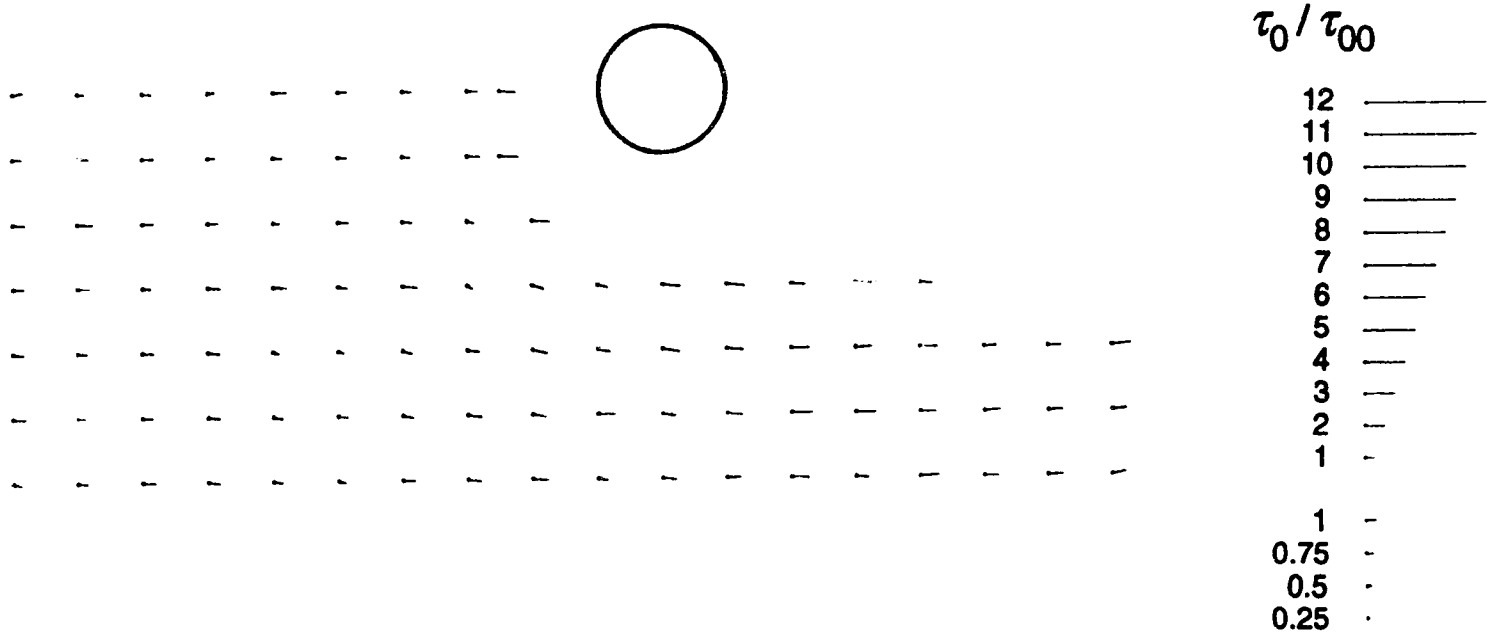

Figure 4.4.1 (a-j) Bed shear stress field (c) Expt. C2M

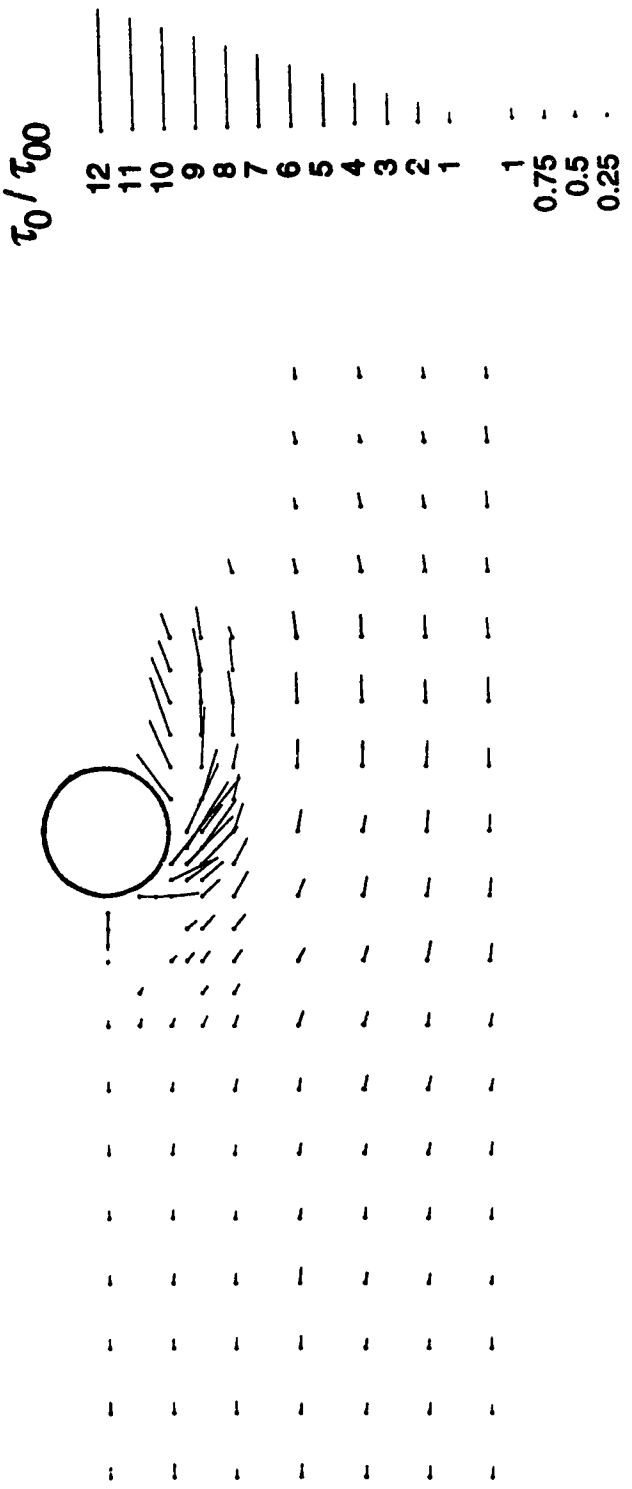

Figure 4.4.1 (a-j) Bed shear stress field (d) Expt. C2R

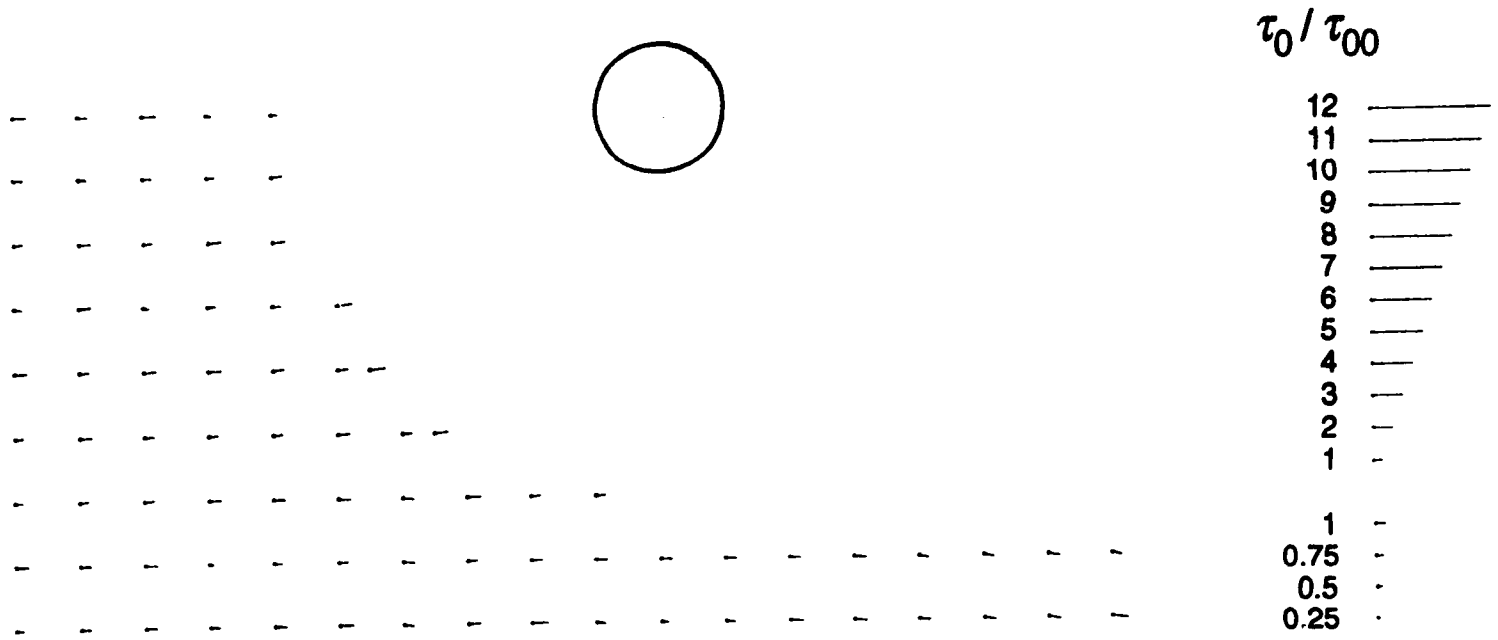

Figure 4.4.1 (a-j) Bed shear stress field (e) Expt. D2M

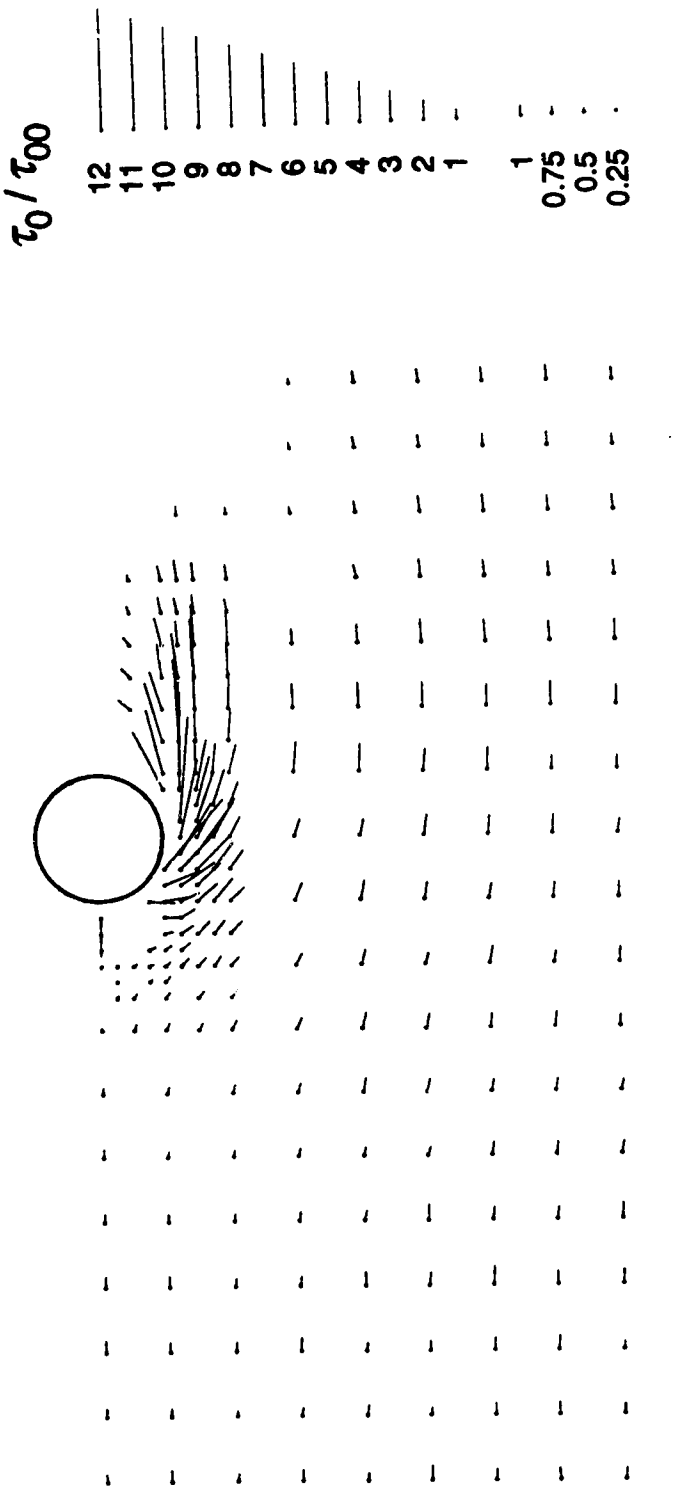

Figure 4.4.1 (a-j) Bed shear stress field (f) Expt. D2R

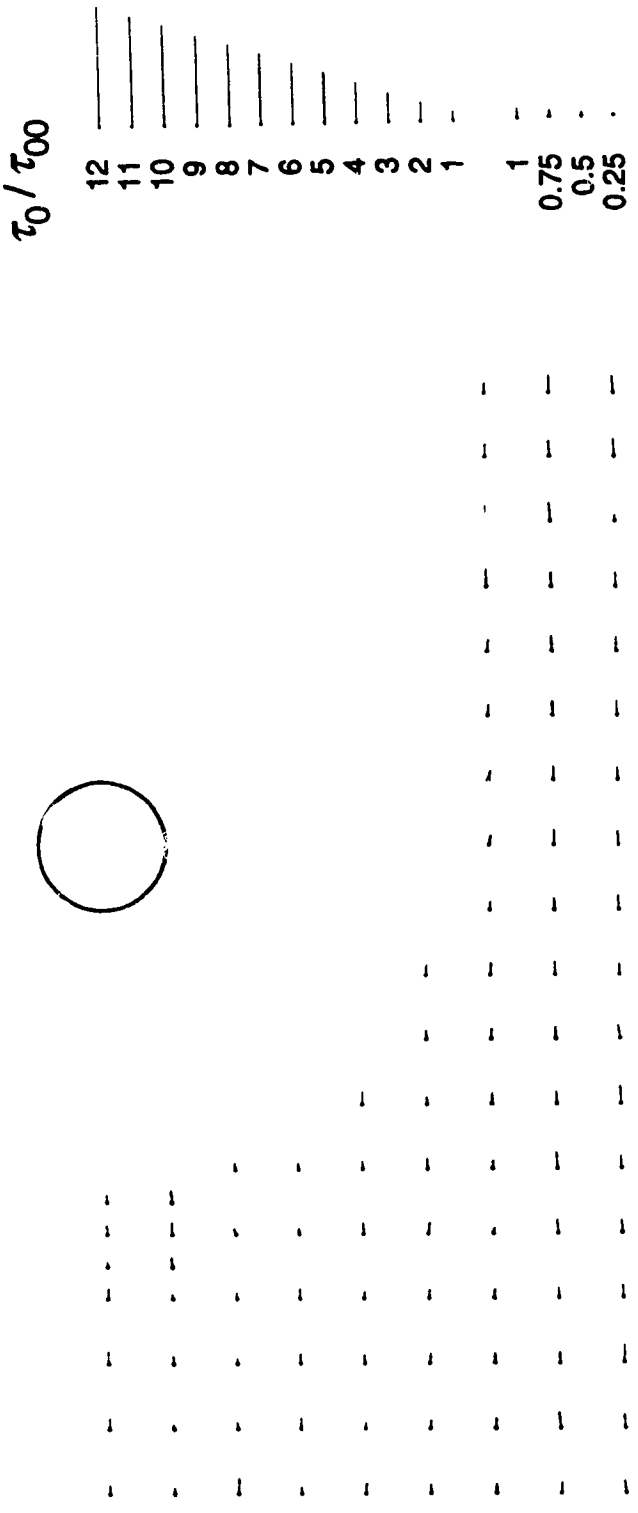

Figure 4.4.1 (a-j) Bed shear stress field (g) Expt. D3M

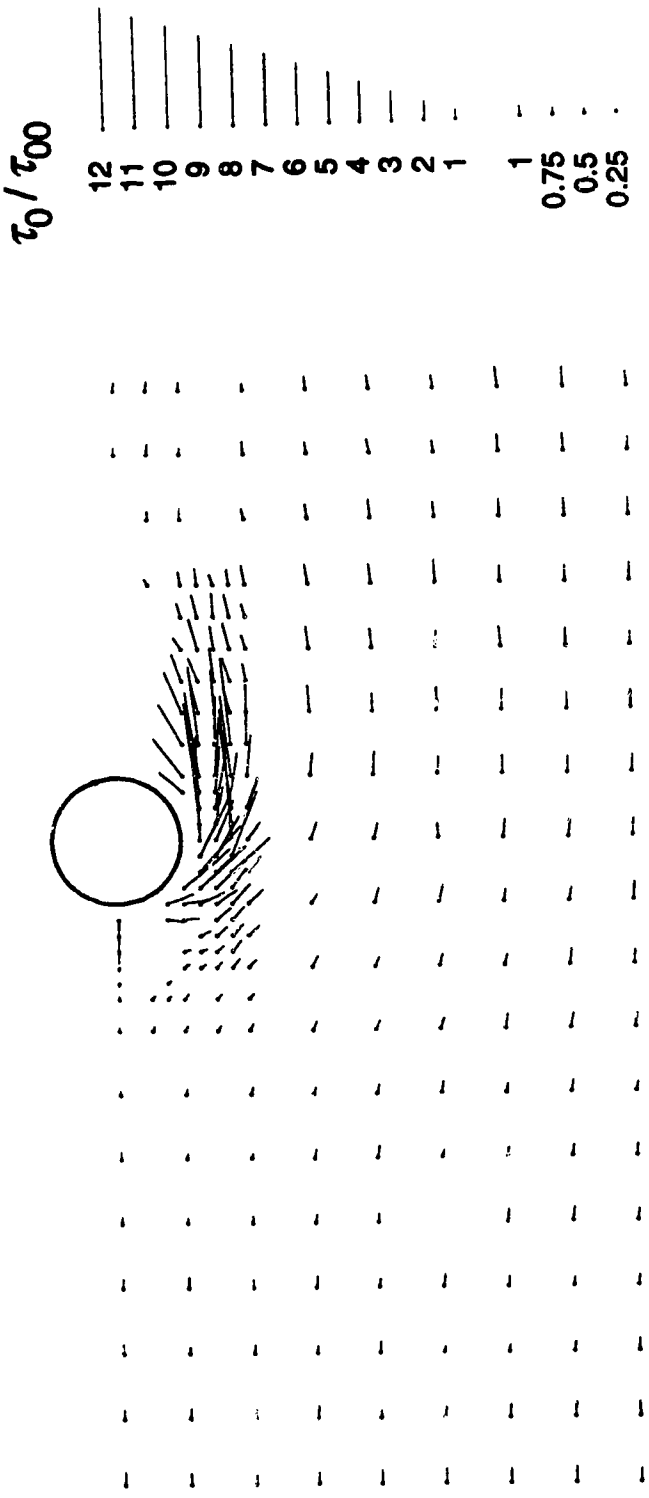

Figure 4.4.1 (a-j) Bed shear stress field (h) Expt. D3R

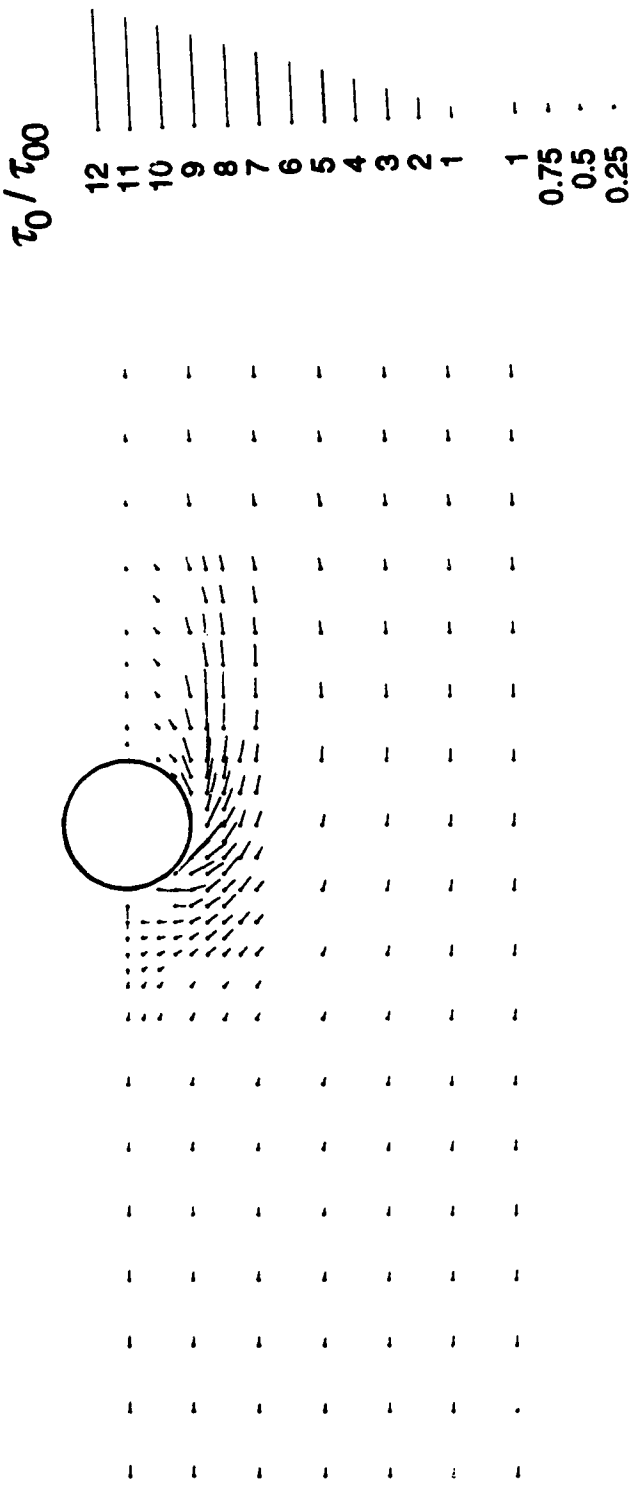

Figure 4.4.1 (a-j) Bed shear stress field (i) Expt. E2S

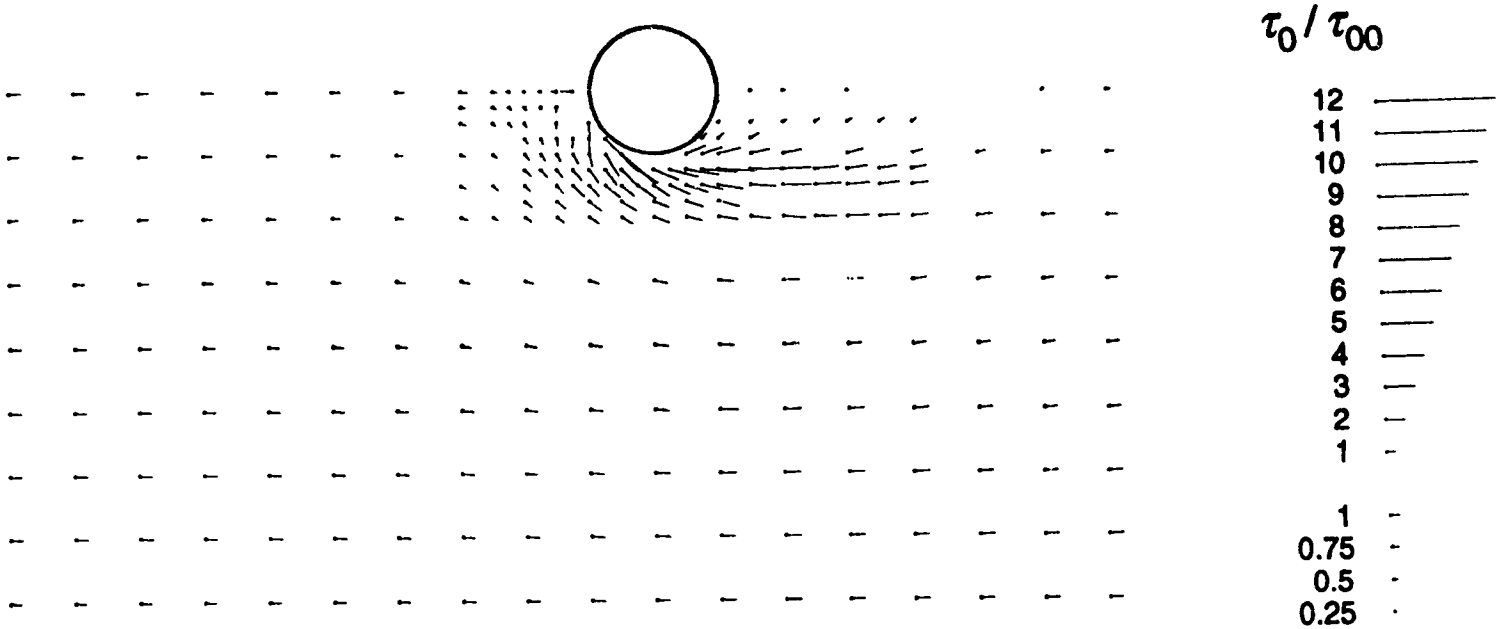

Figure 4.4.1 (a-j) Bed shear stress field (j) Expt. F2S

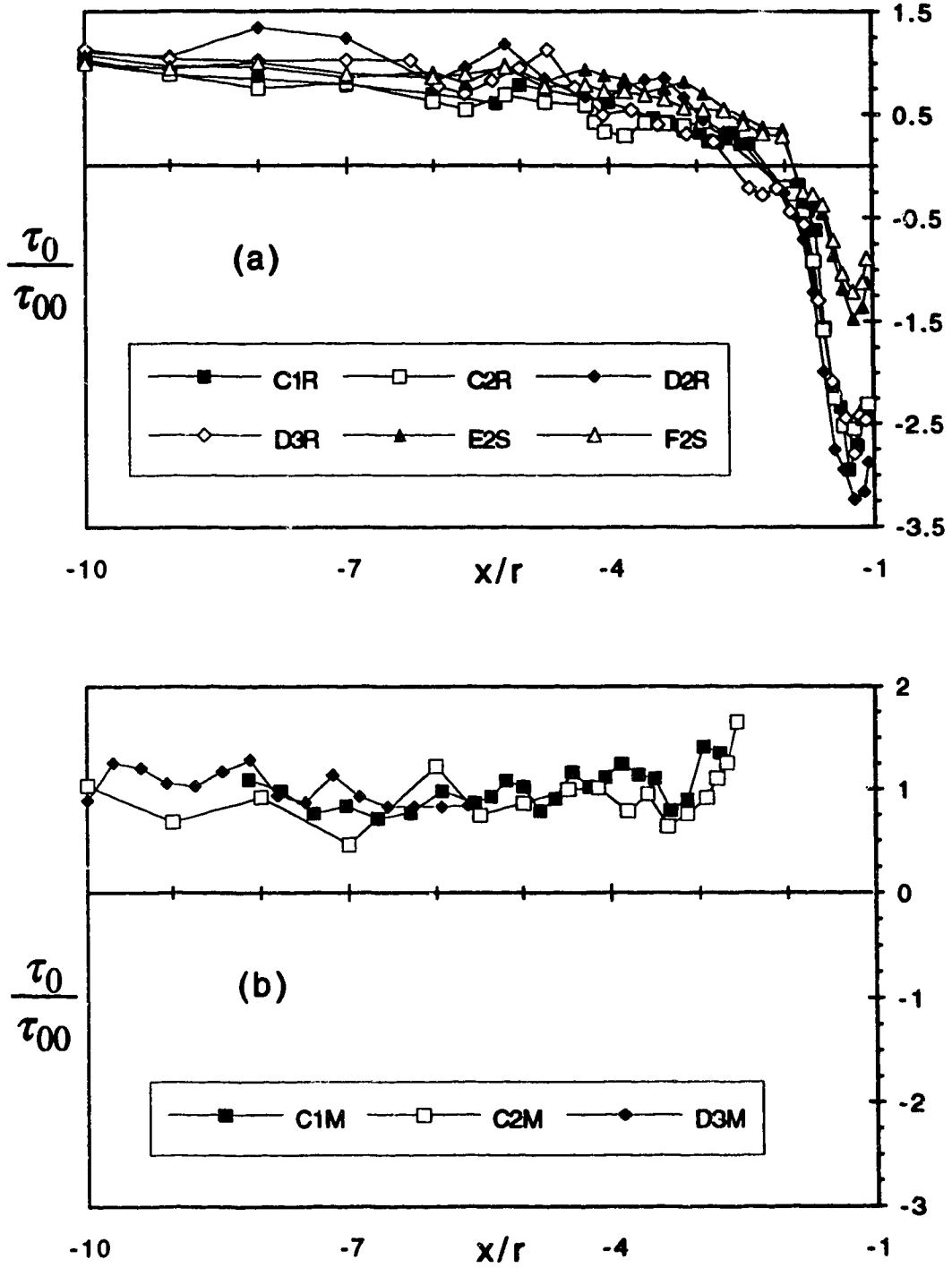

Figure 4.4.2 (a-b) Bed shear stress on the POS
(a) Rigid and smooth bed runs
(b) Mobile bed runs

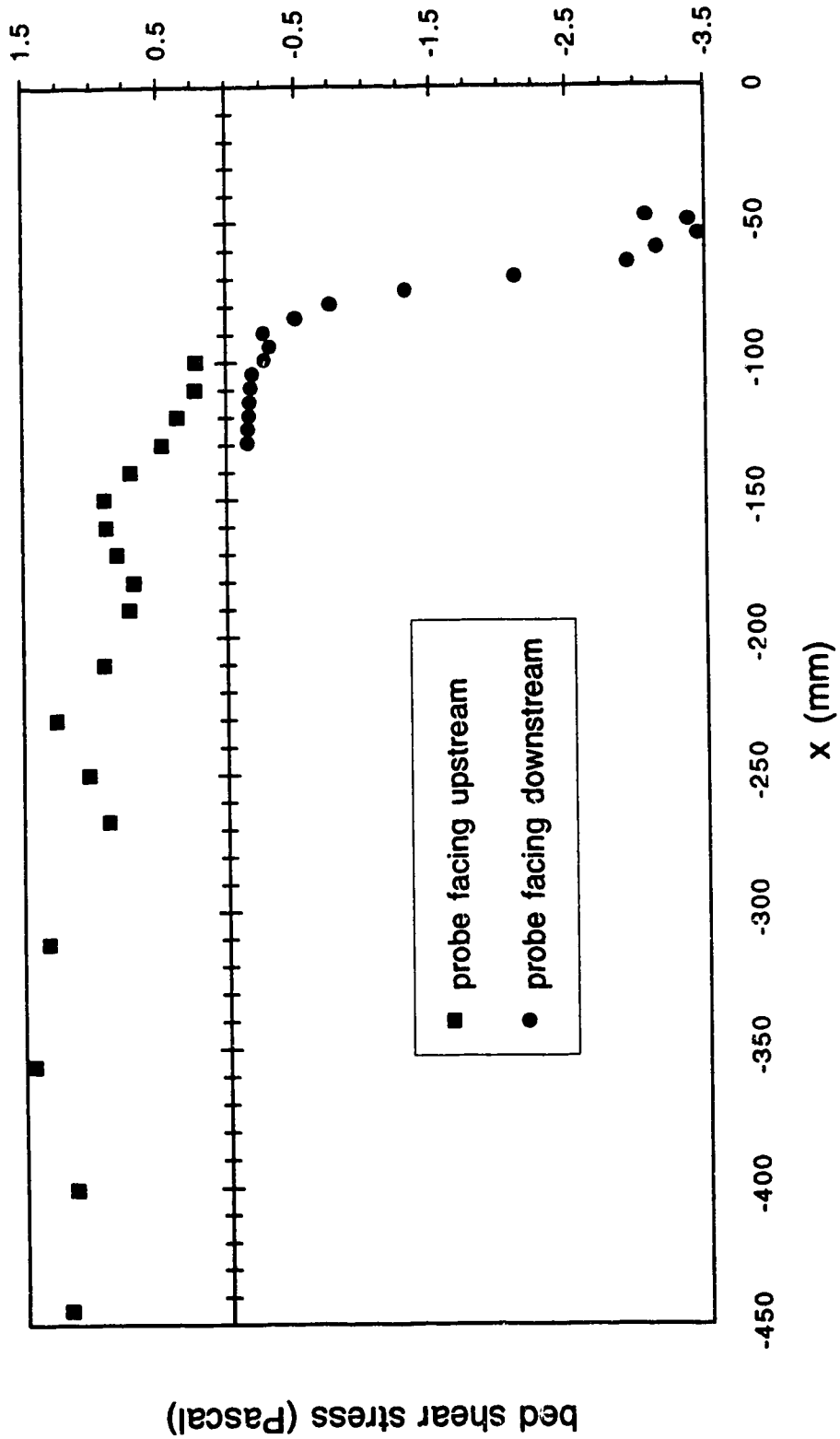

Figure 4.4.3 Typical raw bed shear data on the POS (Expt. D2R)

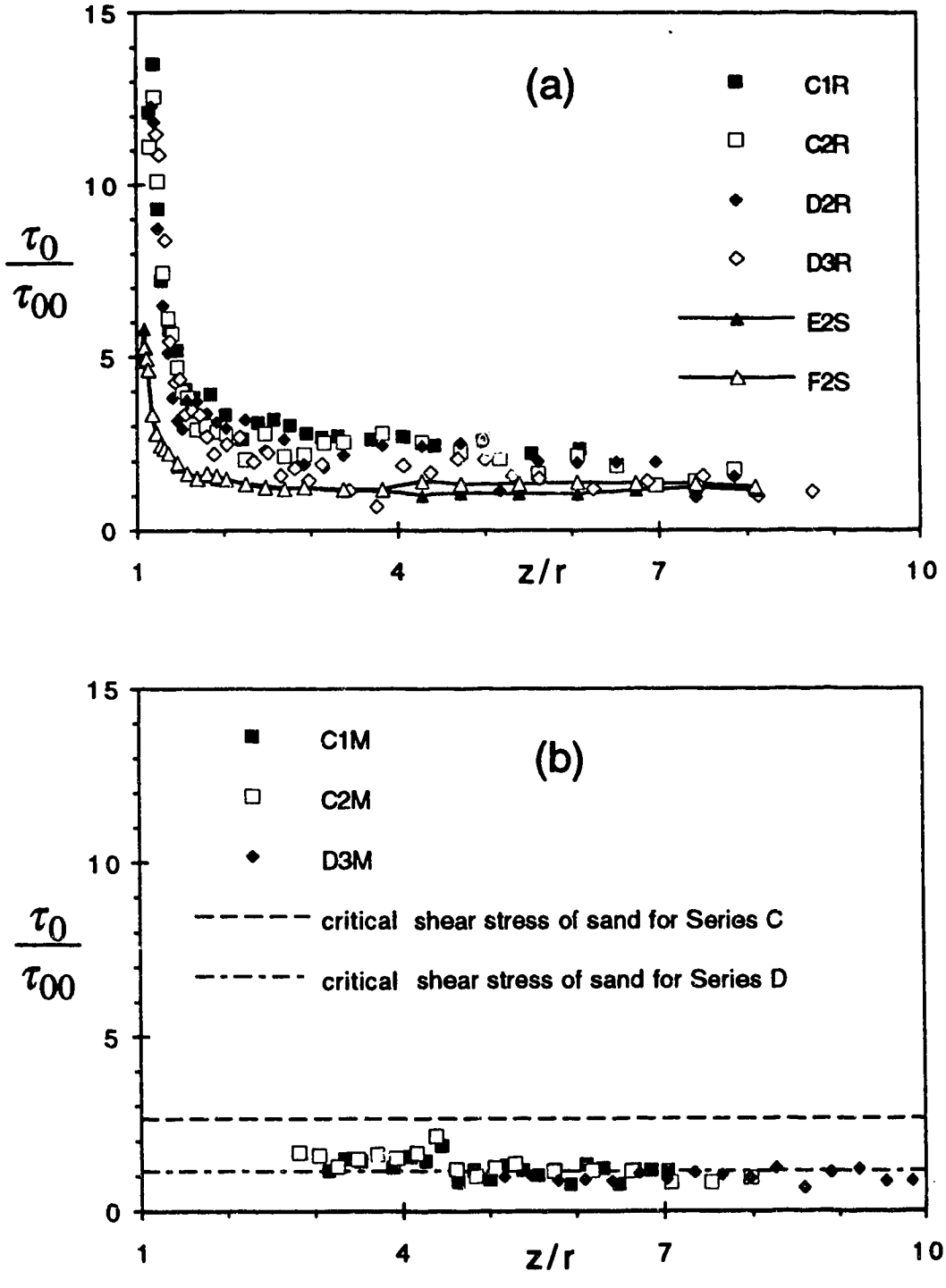

Figure 4.4.4 (a-b) Bed shear stress on the x=0 plane
(a) Rigid and smooth bed runs
(b) Mobile bed runs

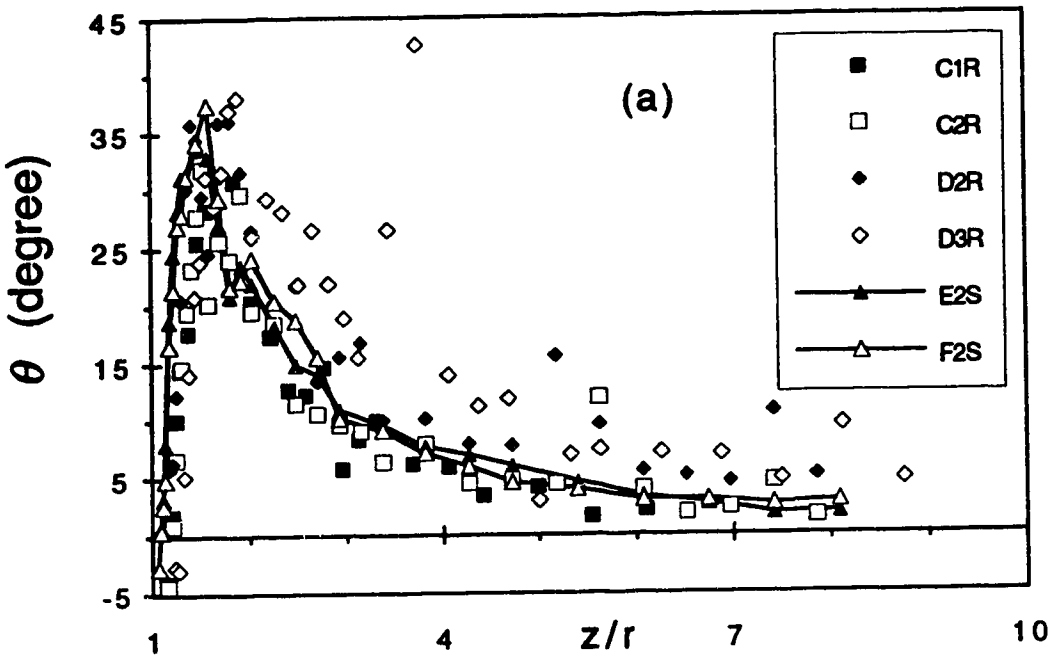

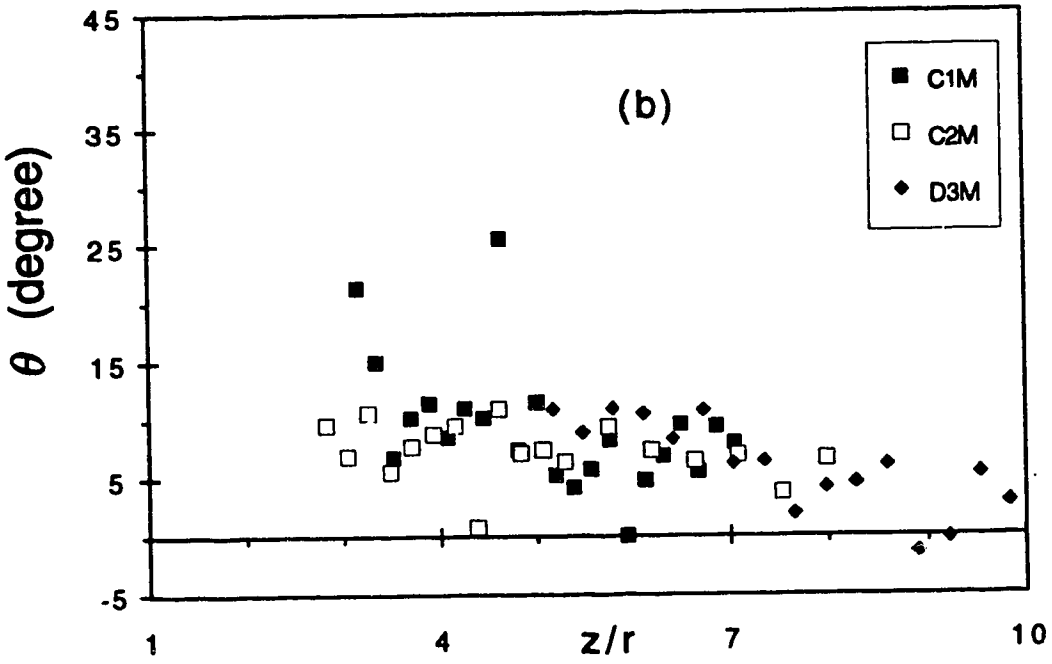

Figure 4.4.5 (a-b) Bed shear angle on the x=0 plane
(a) Rigid and smooth bed runs
(b) Mobile bed runs

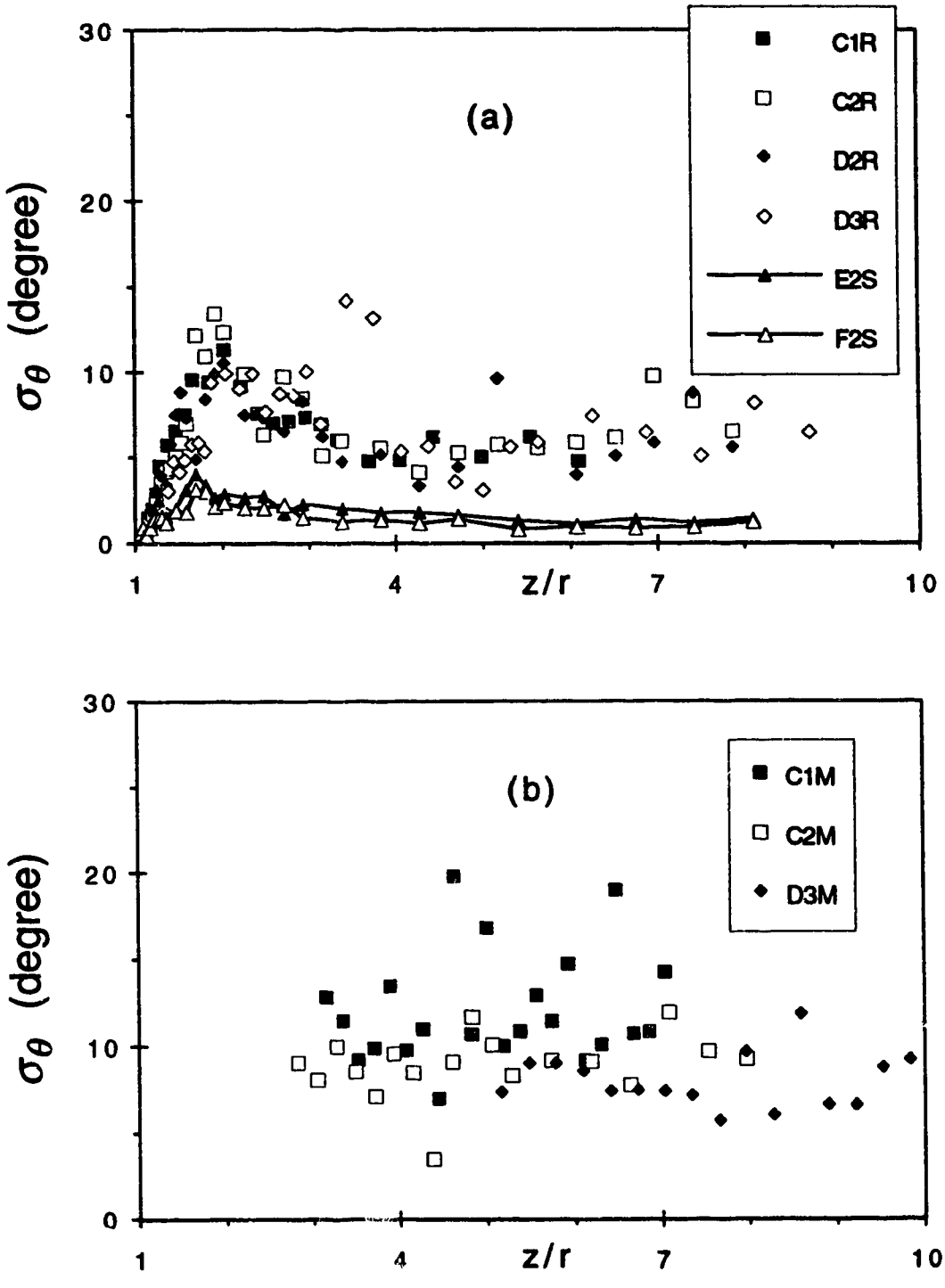

Figure 4.4.6 (a-b) Fluctuation of the bed shear angle on the x=0 plane
(a) Rigid and smooth bed runs
(b) Mobile bed runs

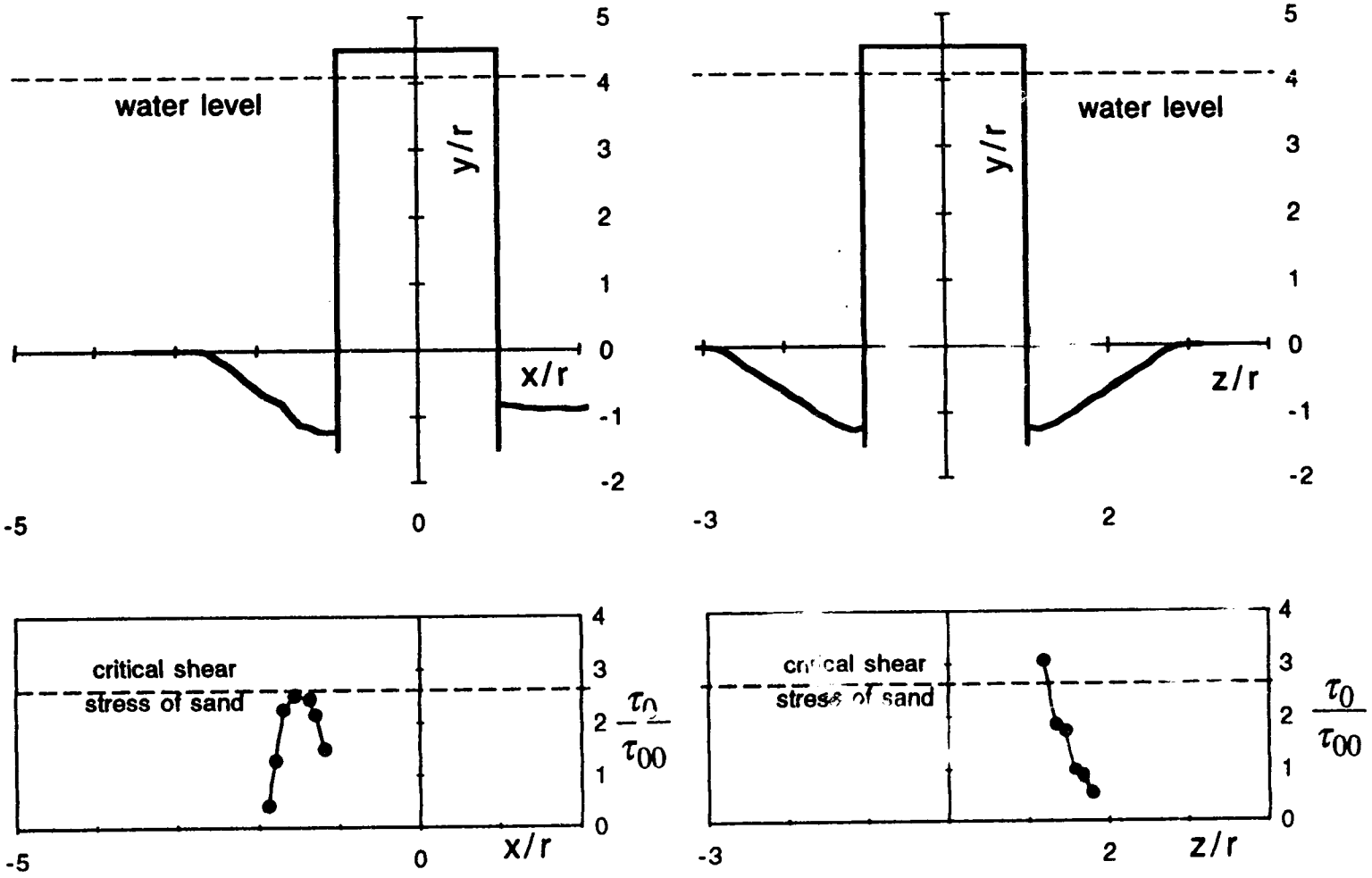

(a) front slope of scour hole

(b) side slope of scour hole

Figure 4.4.7 (a-c) Local shear stress on the deformed channel bed (Expt. C2M)

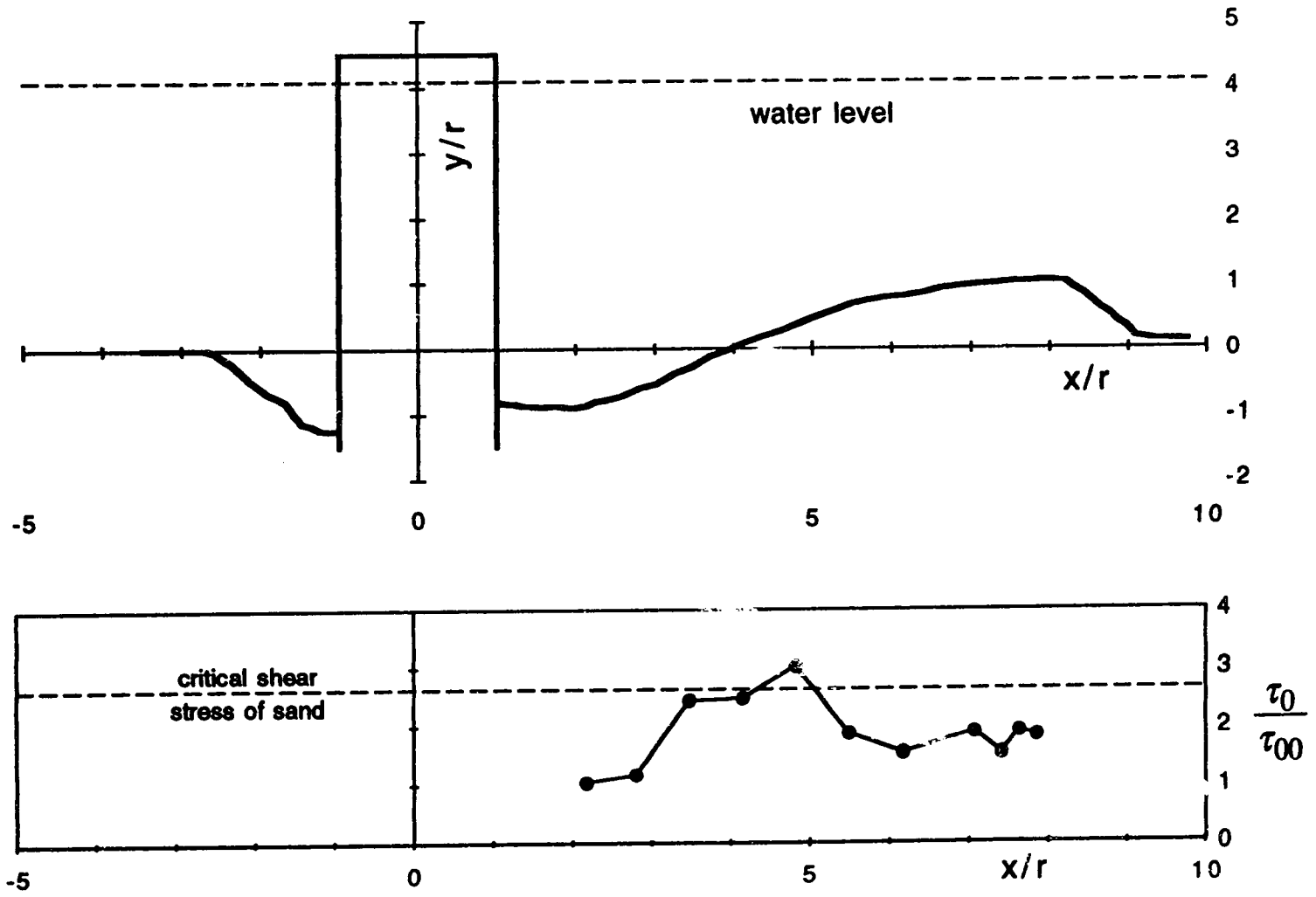

Figure 4.4.7 (a-c) Local shear stress on the deformed channel bed (Expt. C2M); (c) rear bar

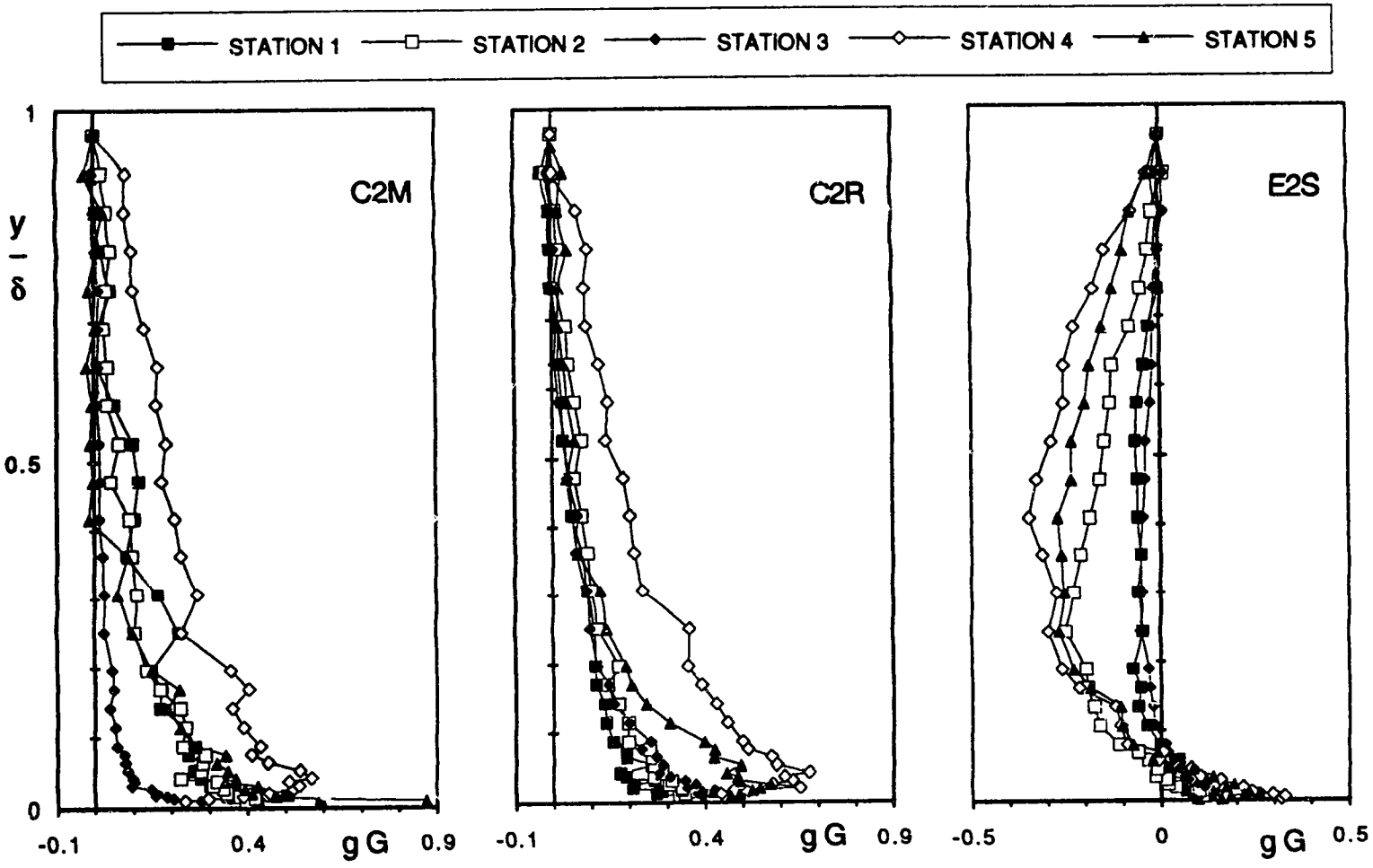

Figure 4.5.1 (a) Applicability of Prandtl's model (Expt. C2M, C2R and E2S; Stations 1 to 5)

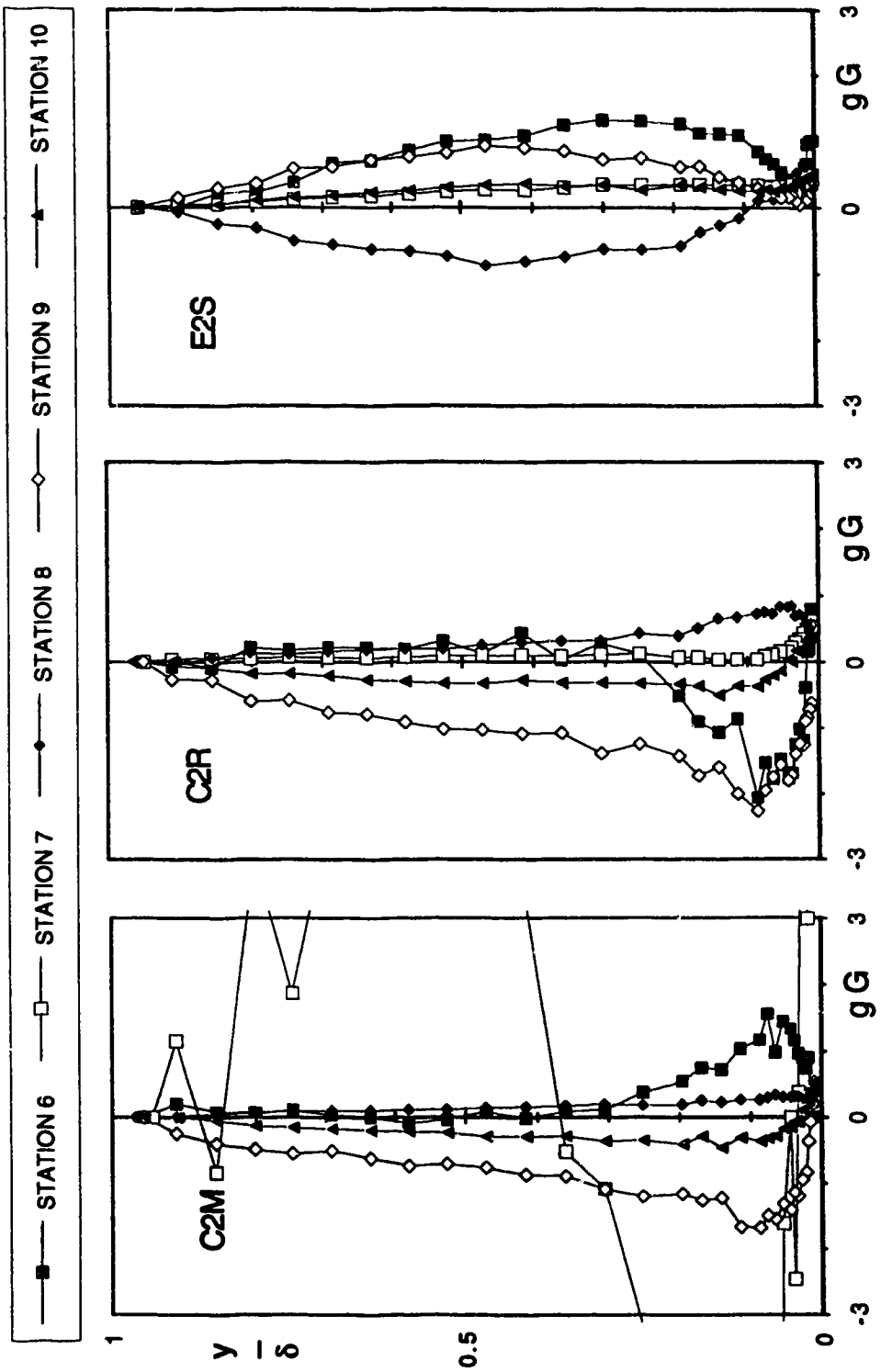

Figure 4.5.1 (b) Applicability of Prandtl's model (Expt. C2M, C2R and E2S; Stations 6 to 10)

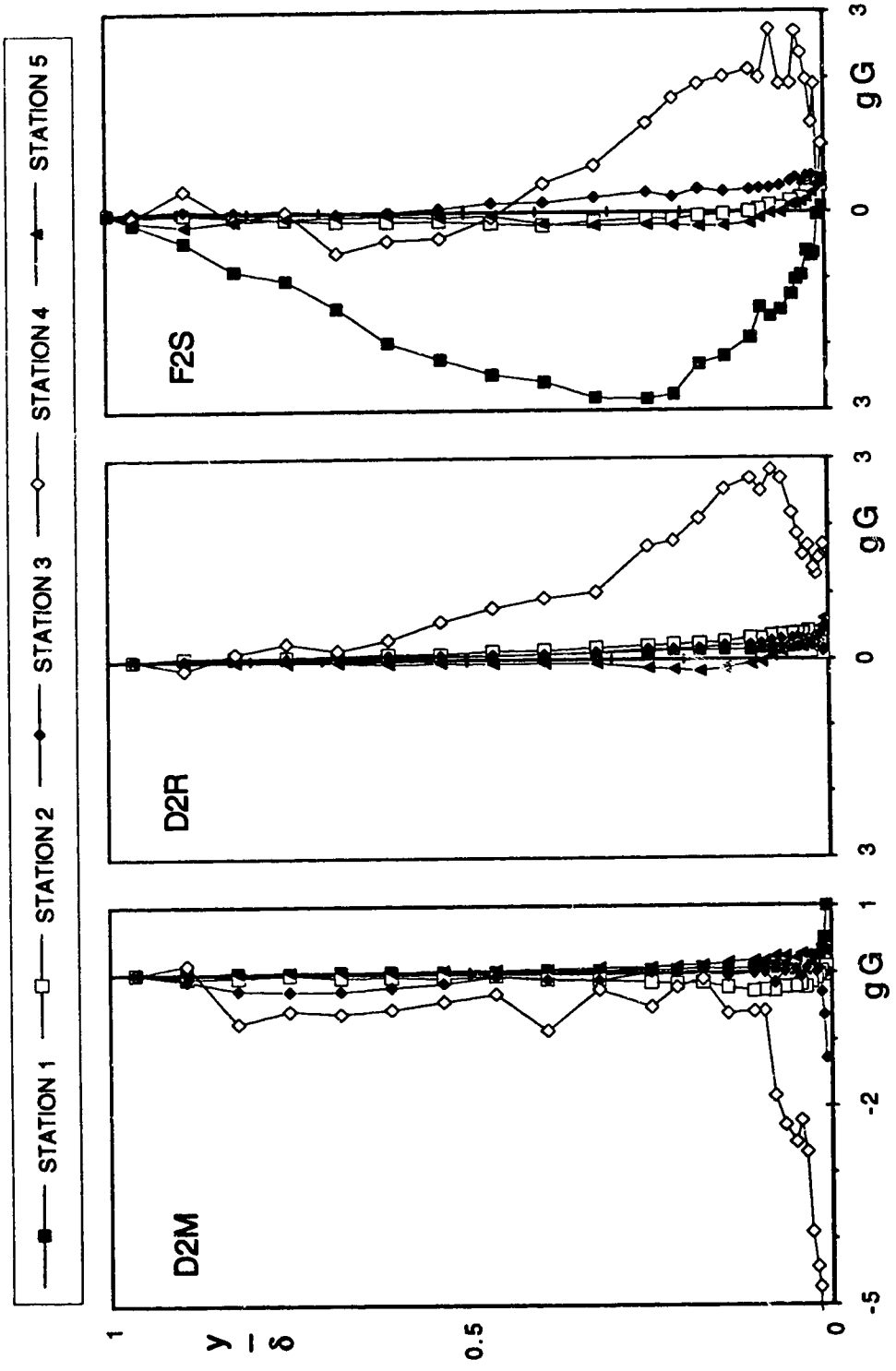

Figure 4.5.1 (c) Applicability of Prandtl's model (Expt. D2M, D2R and F2S; Stations 1 to 5)

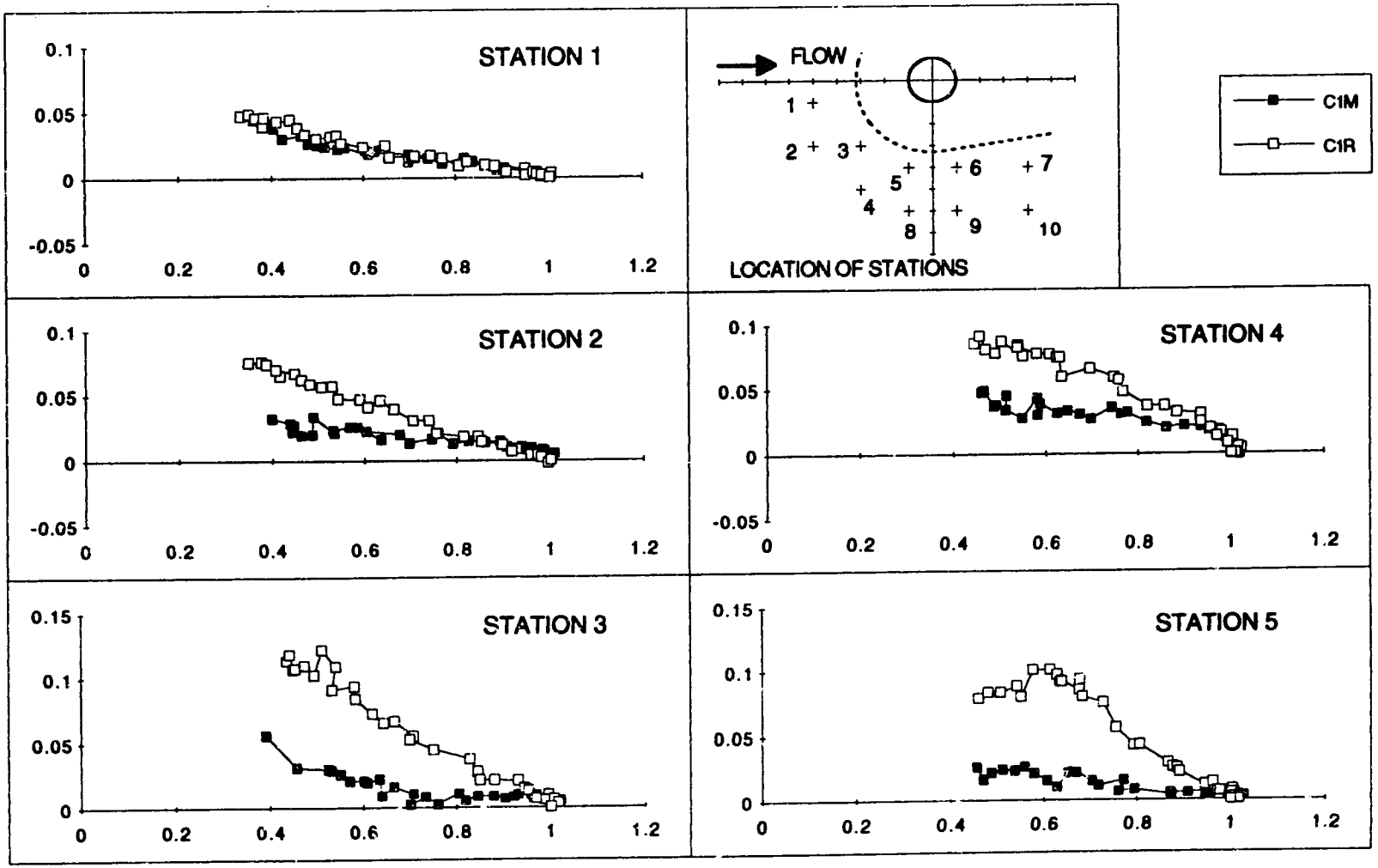

Note: normalized velocity components along and perpendicular to the free streamline direction are plotted on horizontal and vertical axes

Figure 4.5.2 (a) Polar plots of the skewed boundary layer (Expt. C1M and C1R, Stations 1 to 5)

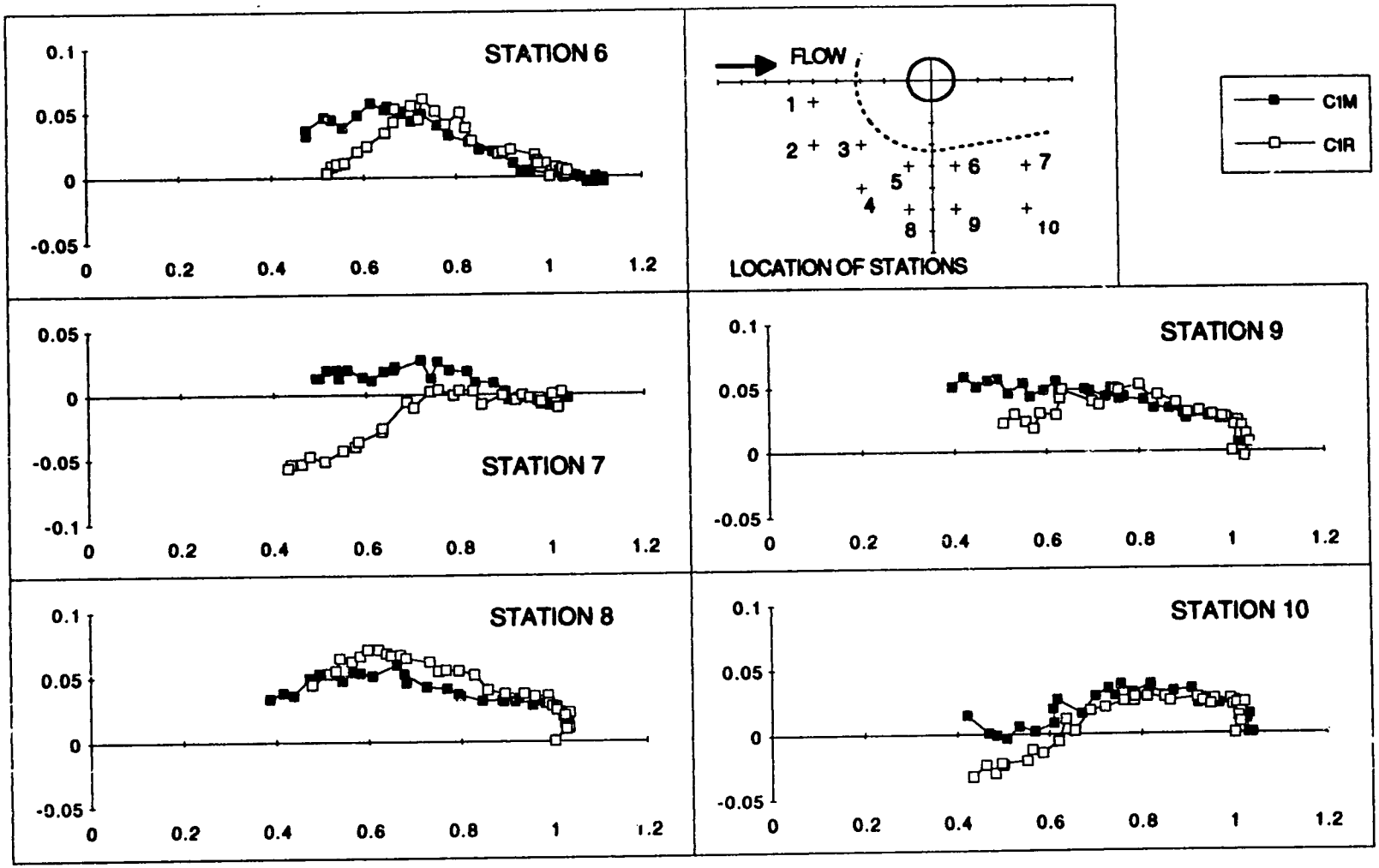

Note: normalized velocity components along and perpendicular to the free streamline direction are plotted on horizontal and vertical axes

Figure 4.5.2 (b) Polar plots of the skewed boundary layer (Expt. C1M and C1R, Stations 6 to 10)

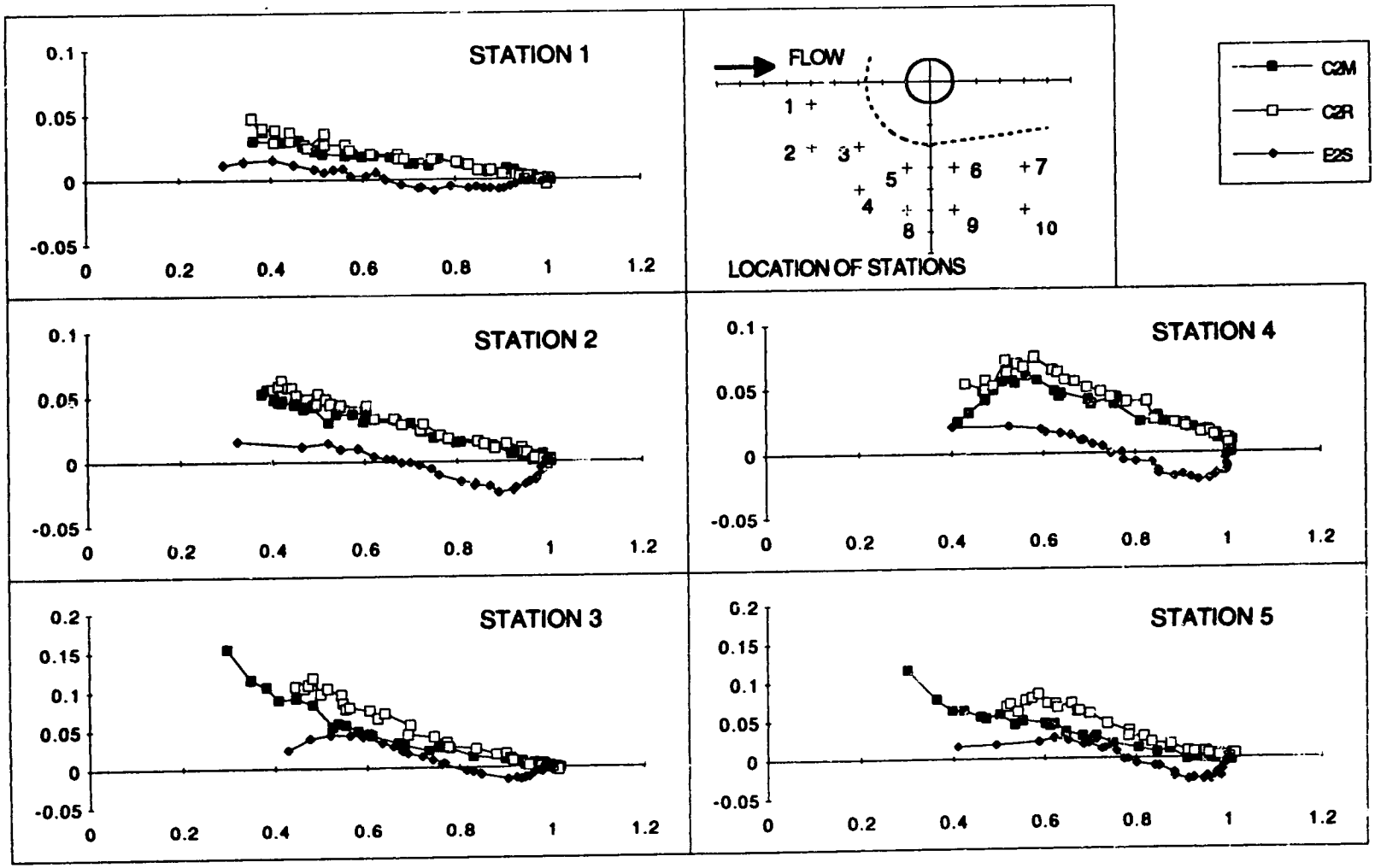

Note: normalized velocity components along and perpendicular to the free streamline direction are plotted on horizontal and vertical axes

Figure 4.5.2 (c) Polar plots of the skewed boundary layer (Expt. C2M, C2R and E2S, Stations 1 to 5)

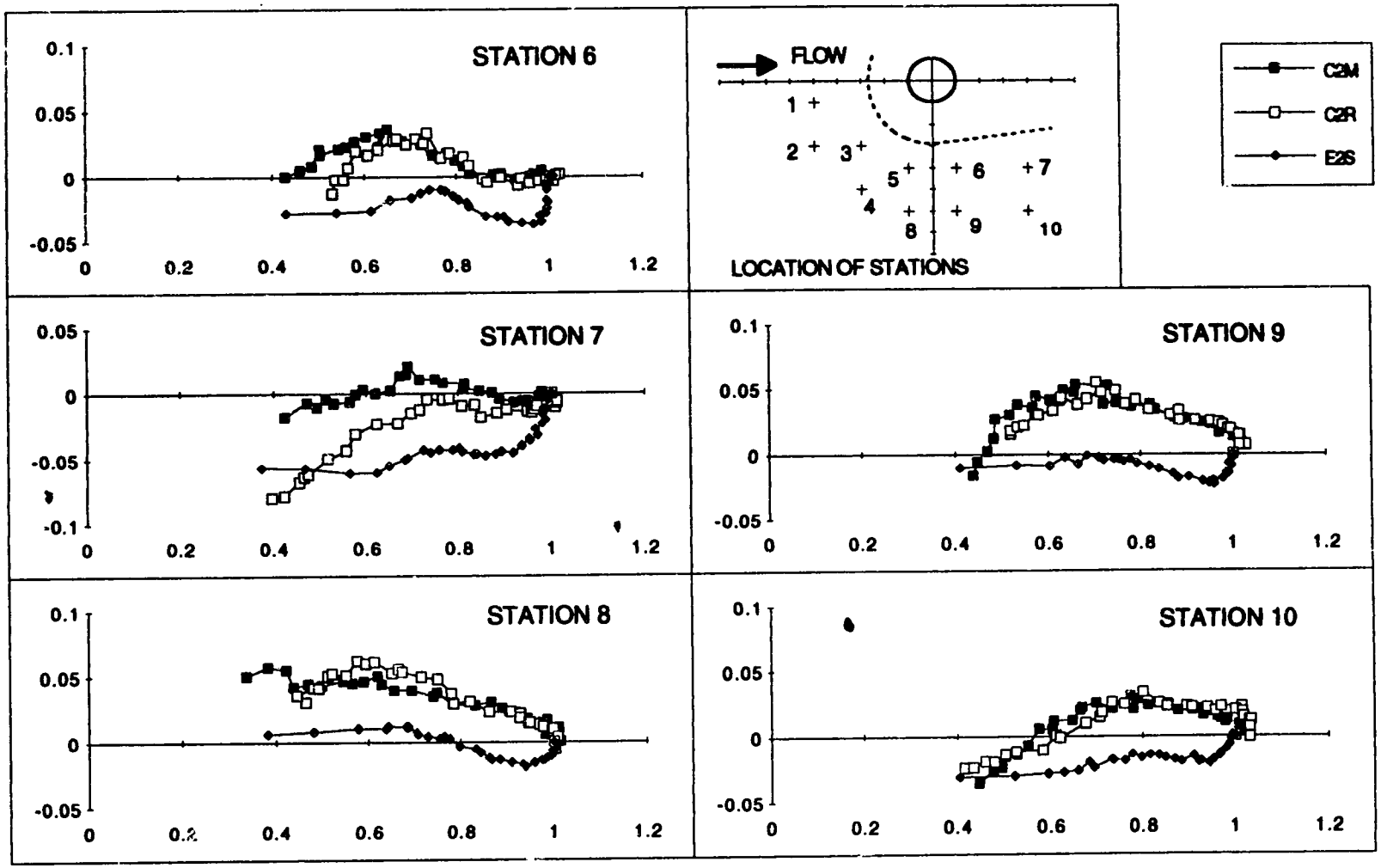

Note: normalized velocity components along and perpendicular to the free streamline direction are plotted on horizontal and vertical axes

Figure 4.5.2 (d) Polar plots of the skewed boundary layer (Expt. C2M, C2R and E2S, Stations 6 to 10)

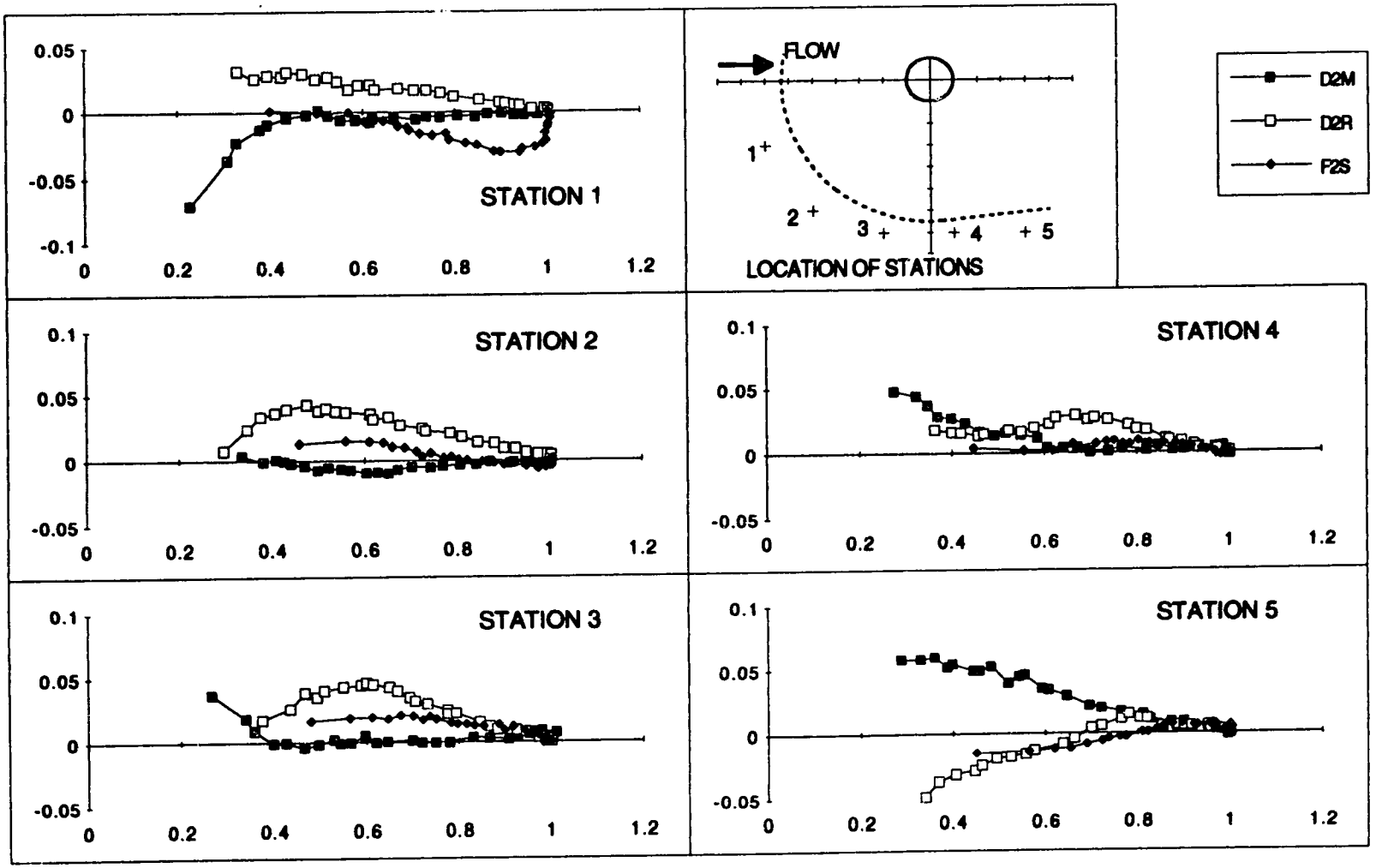

Note: normalized velocity components along and perpendicular to the free streamline direction are plotted on horizontal and vertical axes

Figure 4.5.2 (e) Polar plots of the skewed boundary layer (Expt. D2M, D2R and F2S, Stations 1 to 5)

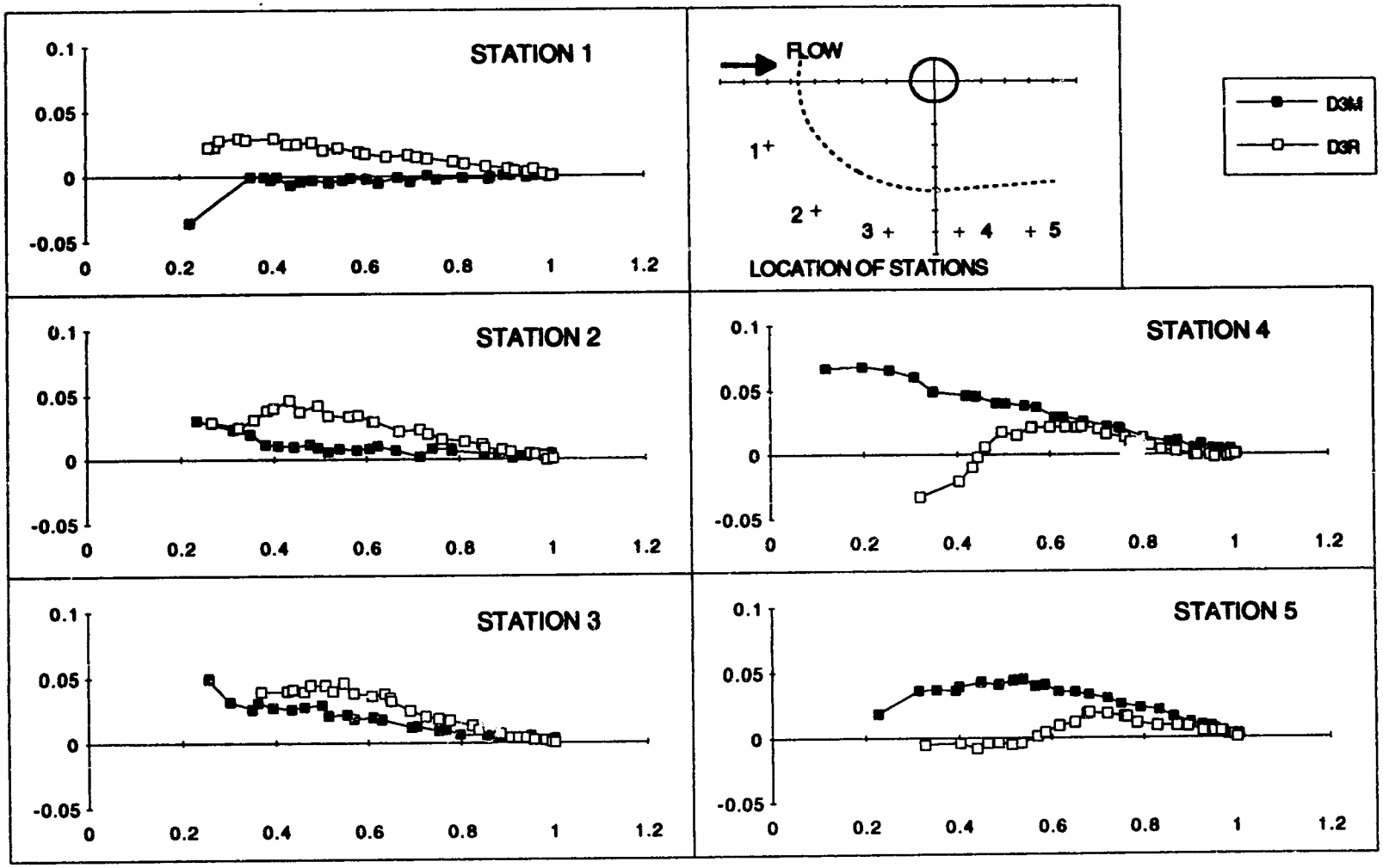

Note: normalized velocity components along and perpendicular to the free streamline direction are plotted on horizontal and vertical axes

Figure 4.5.2 (f) Polar plots of the skewed boundary layer (Expt. D3M and D3R, Stations 1 to 5)

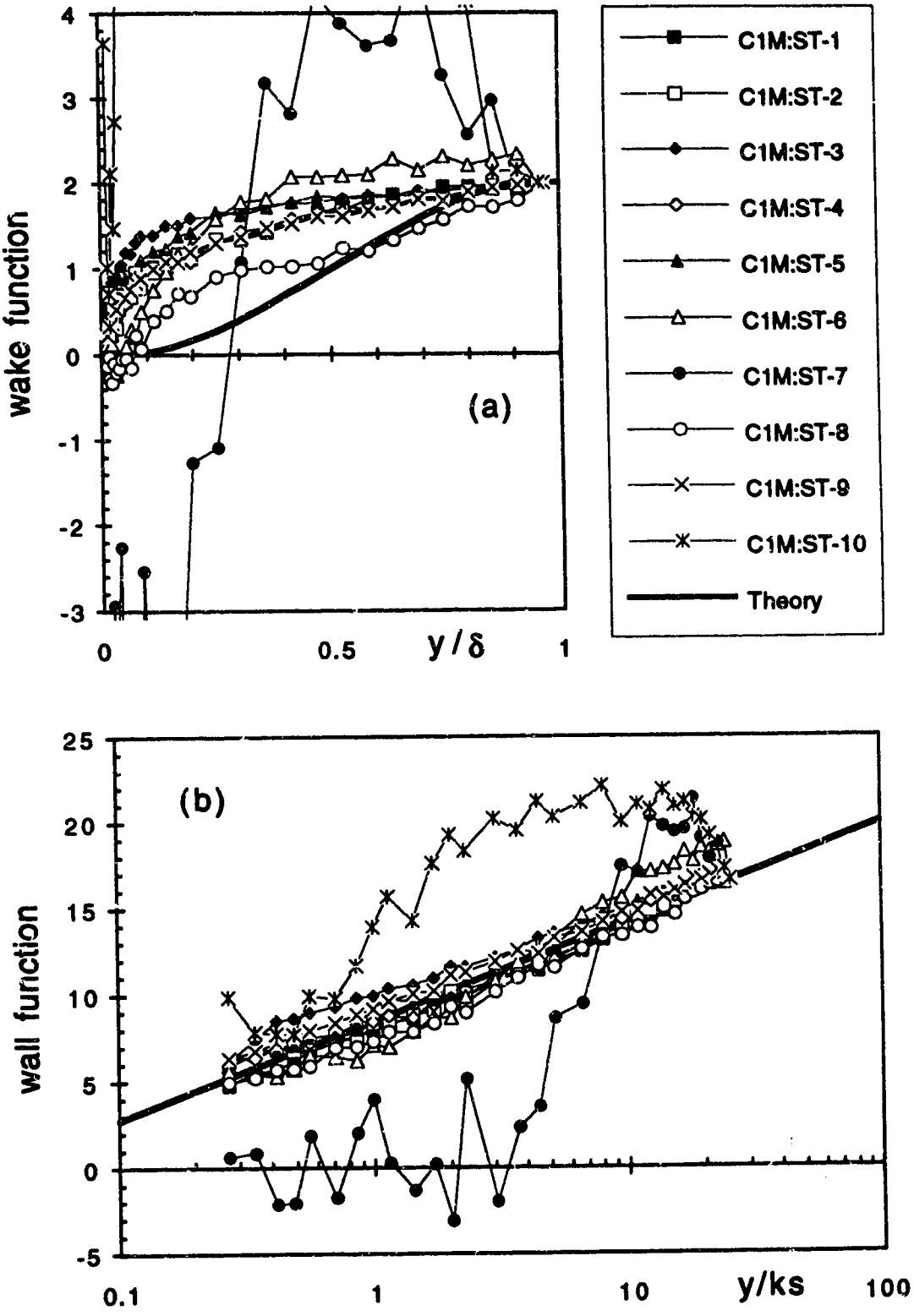

Figure 4.5.3 (a) Applicability of Coles' model (Expt. C1M)

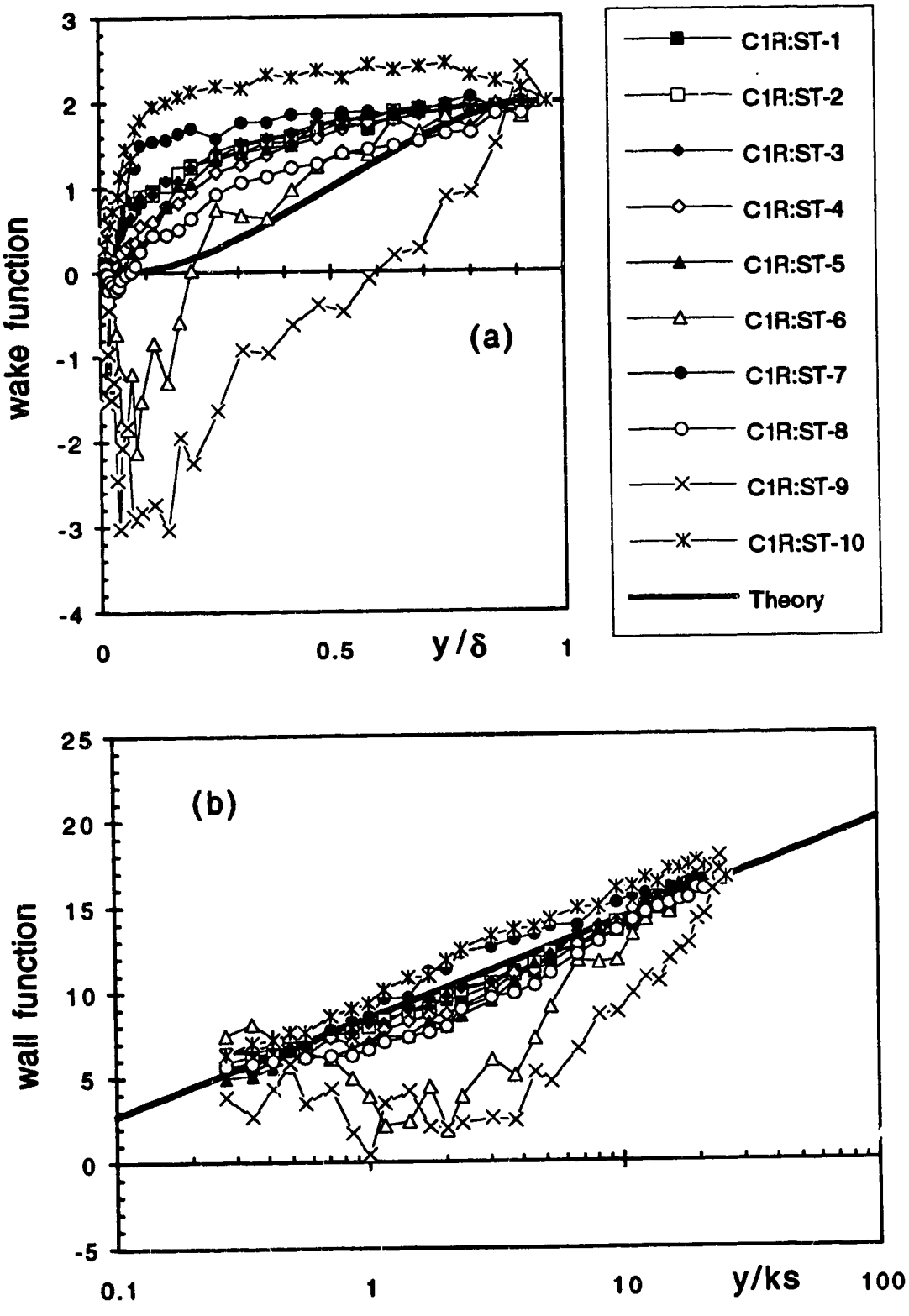

Figure 4.5.3 (b) Applicability of Coles' model (Expt. C1R)

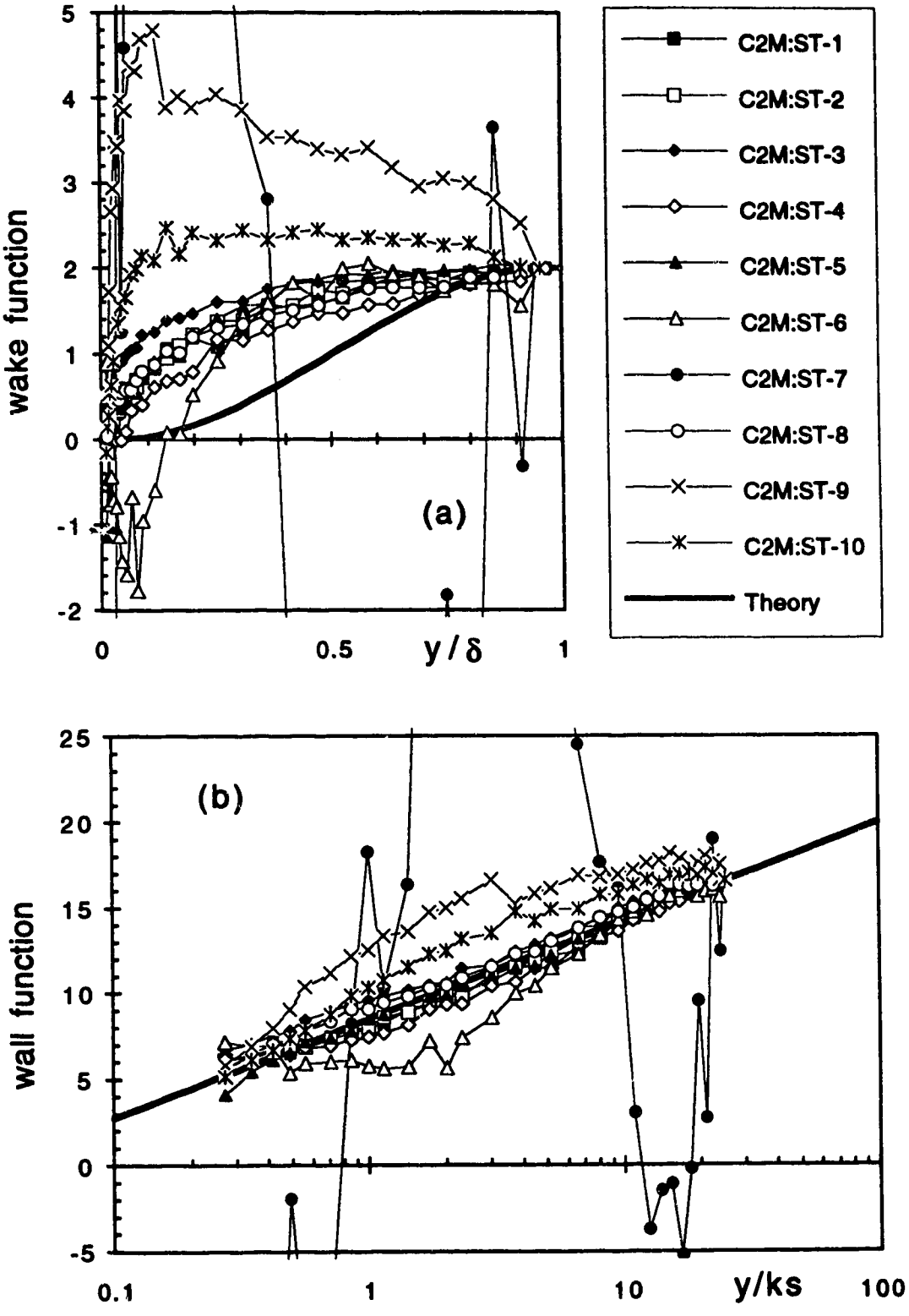

Figure 4.5.3 (c) Applicability of Coles' model (Expt. C2M)

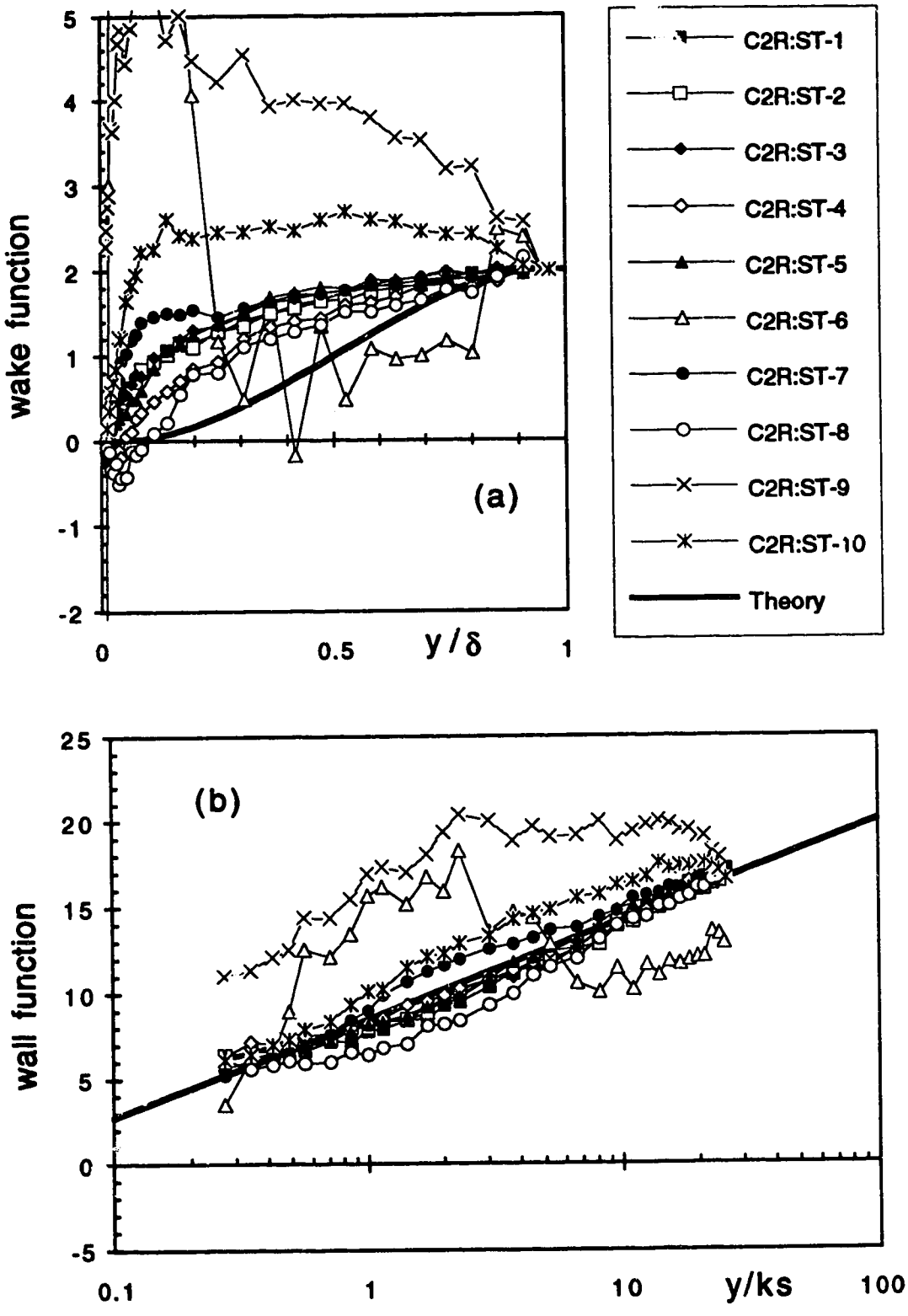

Figure 4.5.3 (d) Applicability of Coles' model (Expt. C2R)

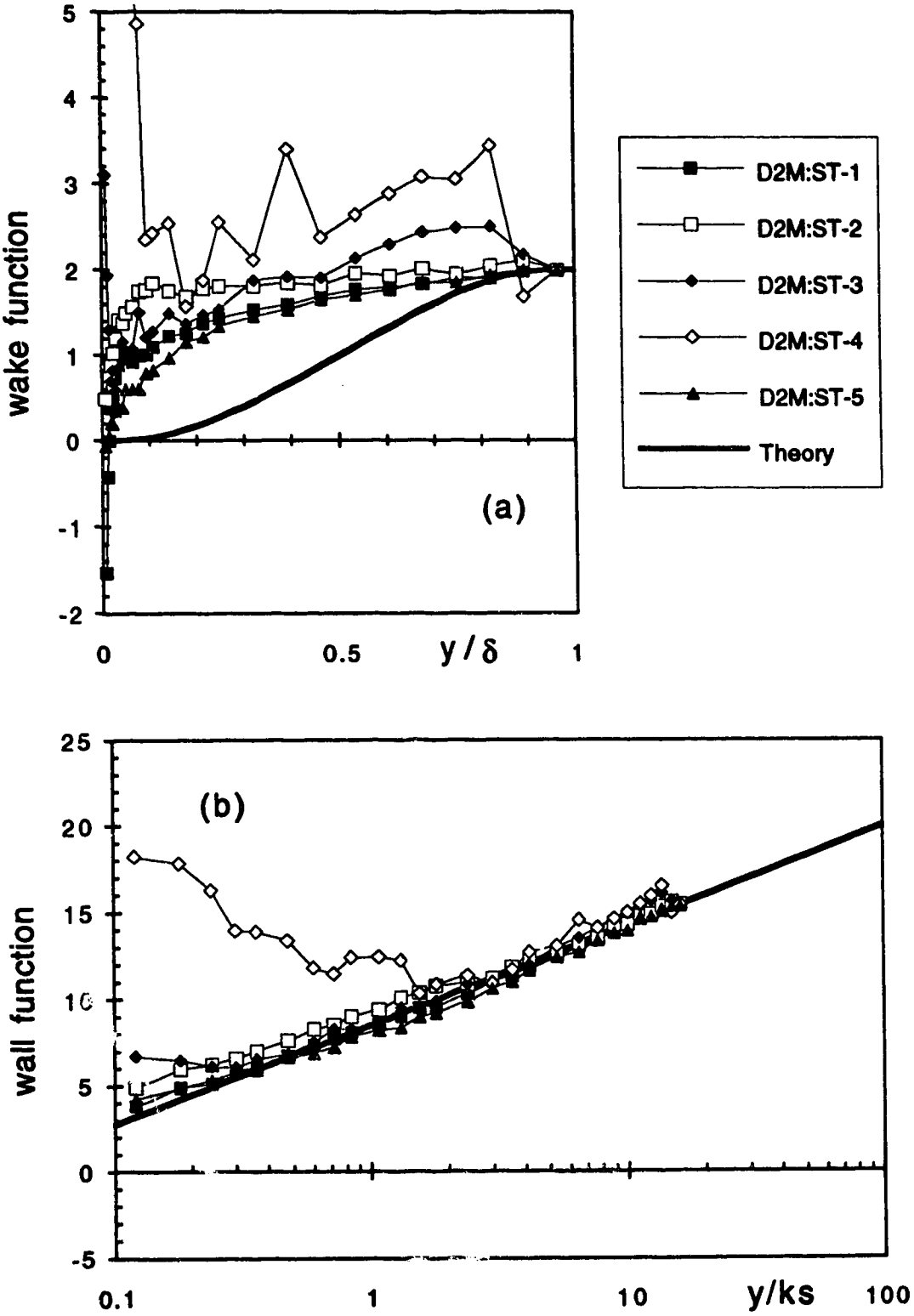

Figure 4.5.3 (e) Applicability of Coles' model (Expt. D2M)

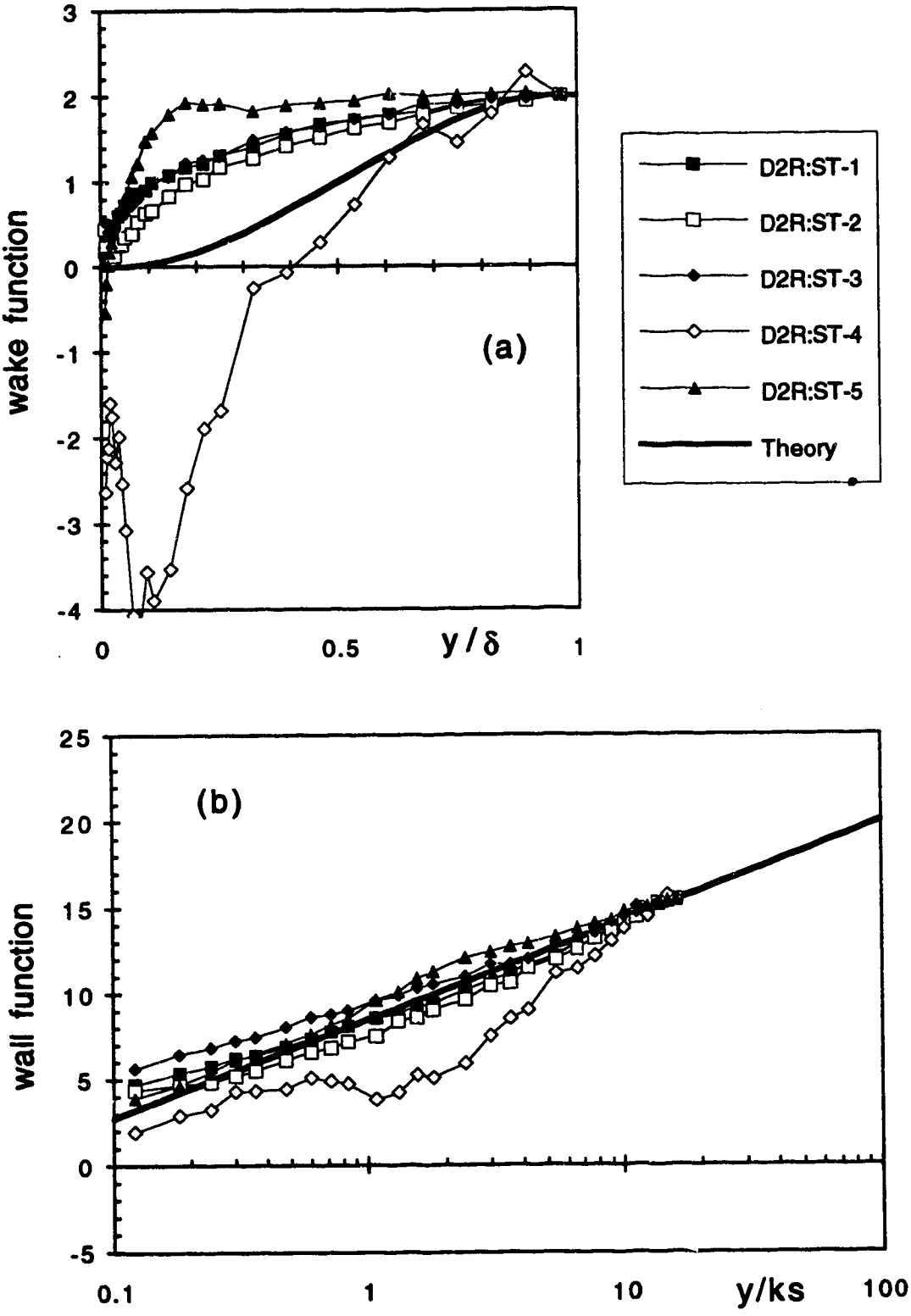

Figure 4.5.3 (f) Applicability of Coles' model (Expt. D2R)

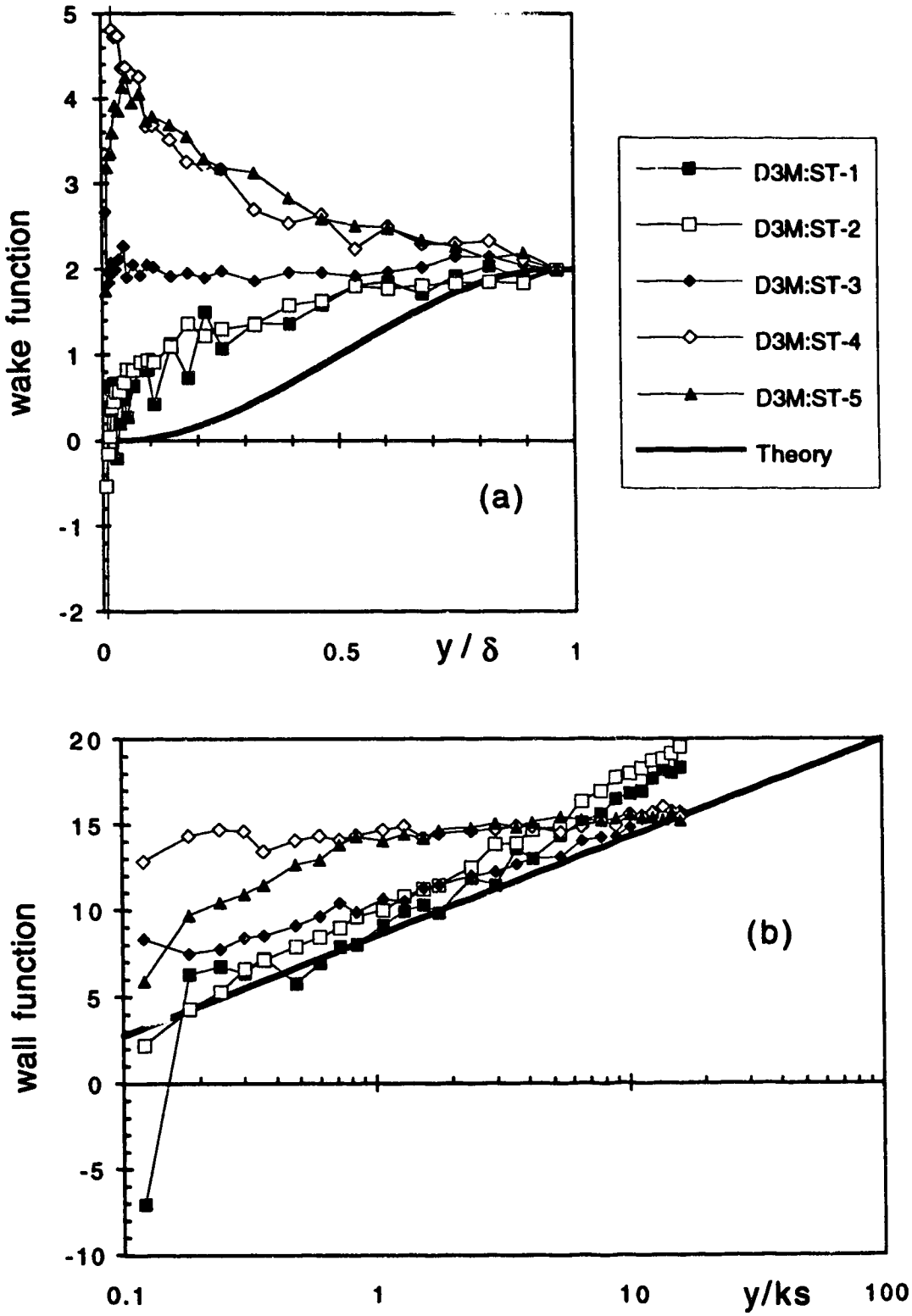

Figure 4.5.3 (g) Applicability of Coles' model (Expt. D3M)

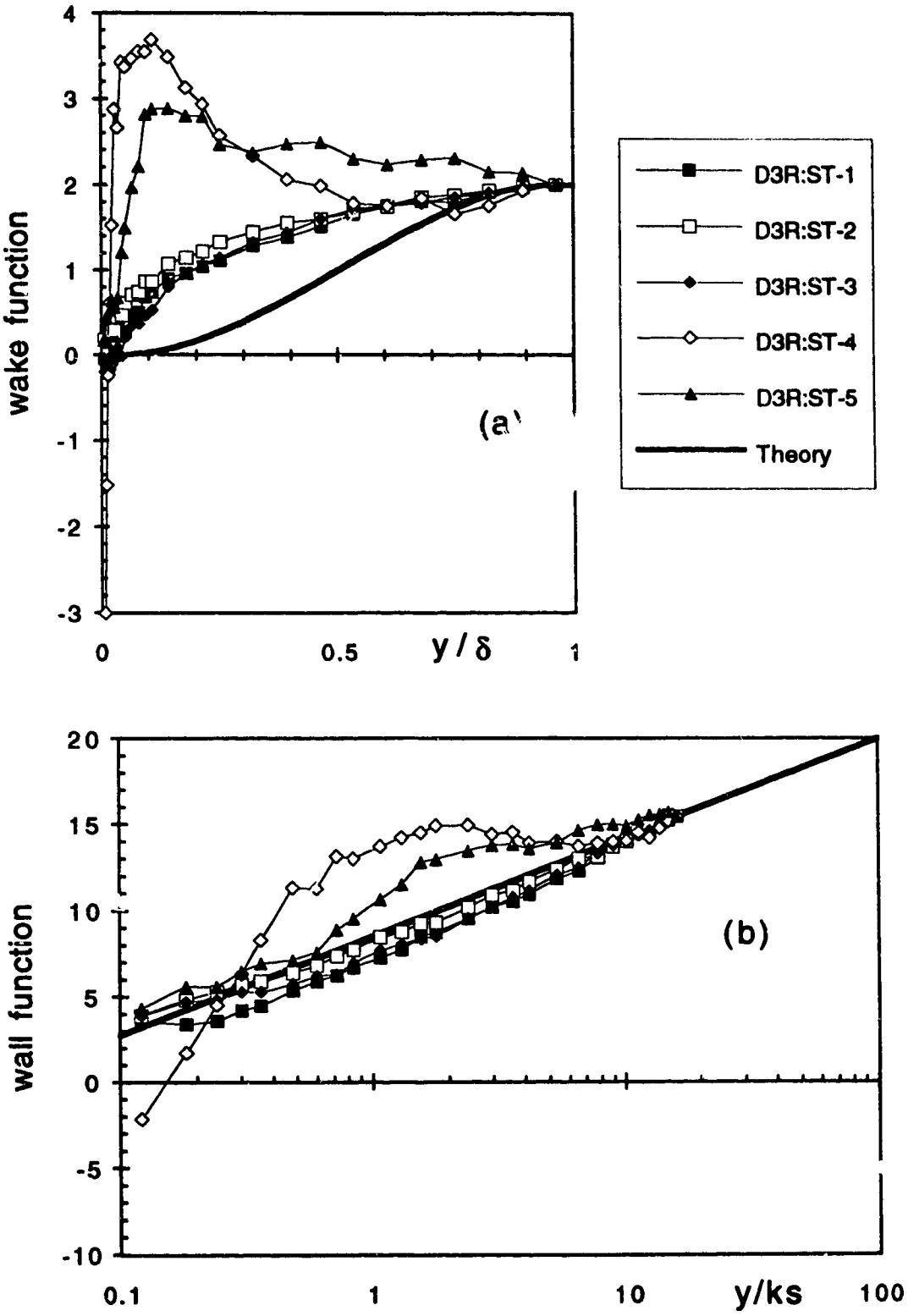

Figure 4.5.3 (h) Applicability of Coles' model (Expt. D3R)

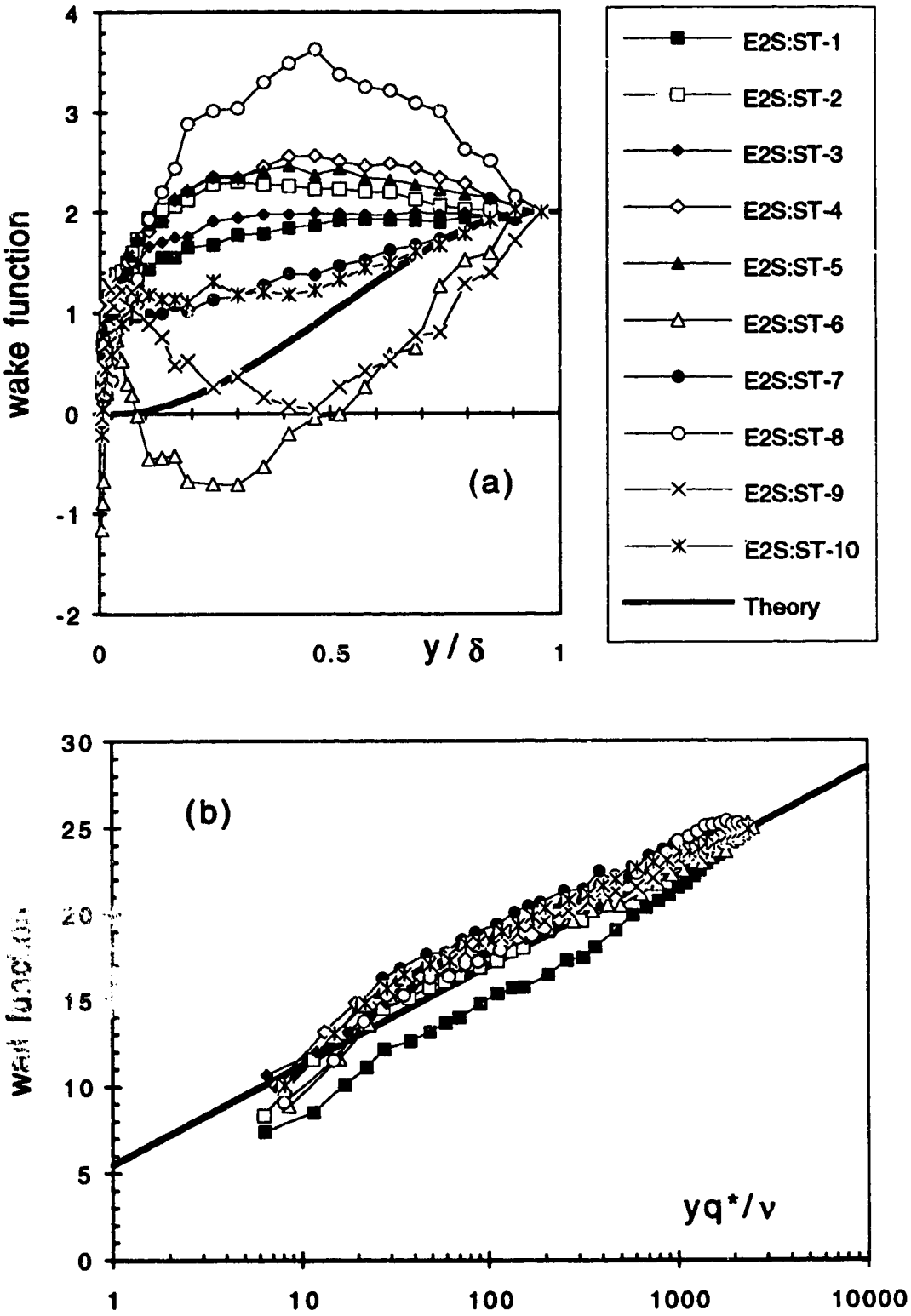

Figure 4.5.3 (i) Applicability of Coles' model (Expt. E2S)

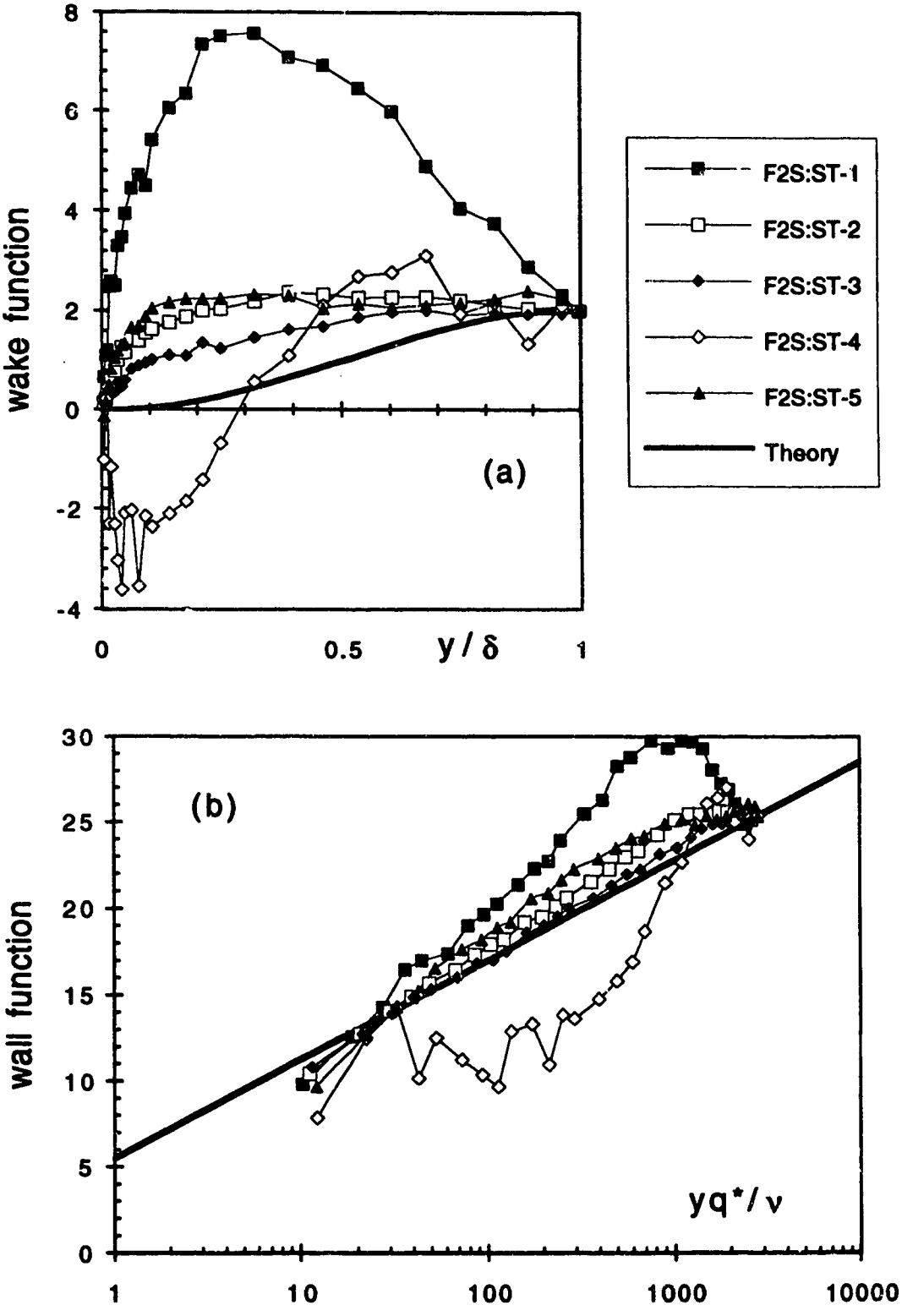

Figure 4.5.3 (j) Applicability of Coles' model (Expt. F2S)

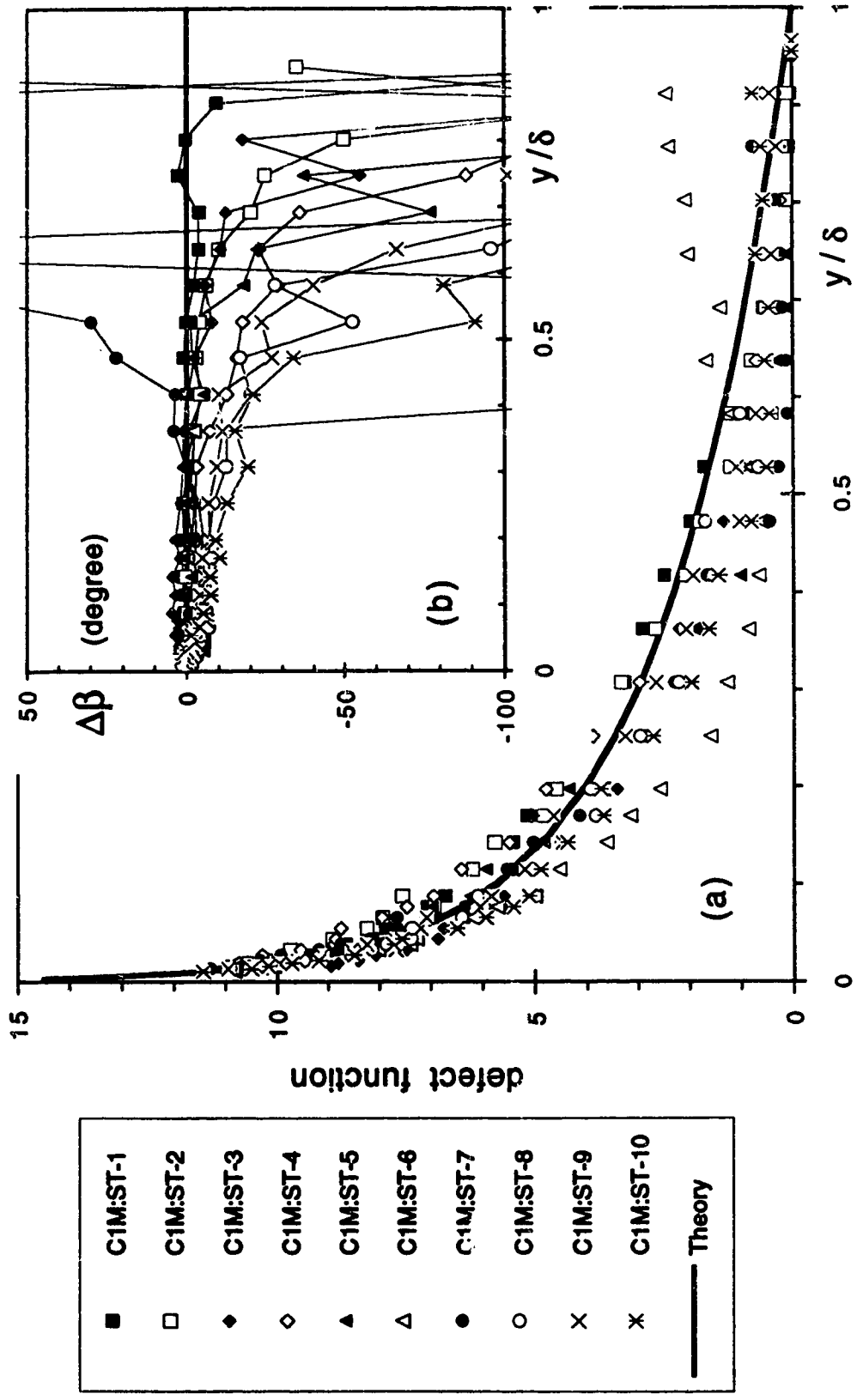

Figure 4.5.4 (a) Applicability of Perry and Joubert's model (Expt. C1M)

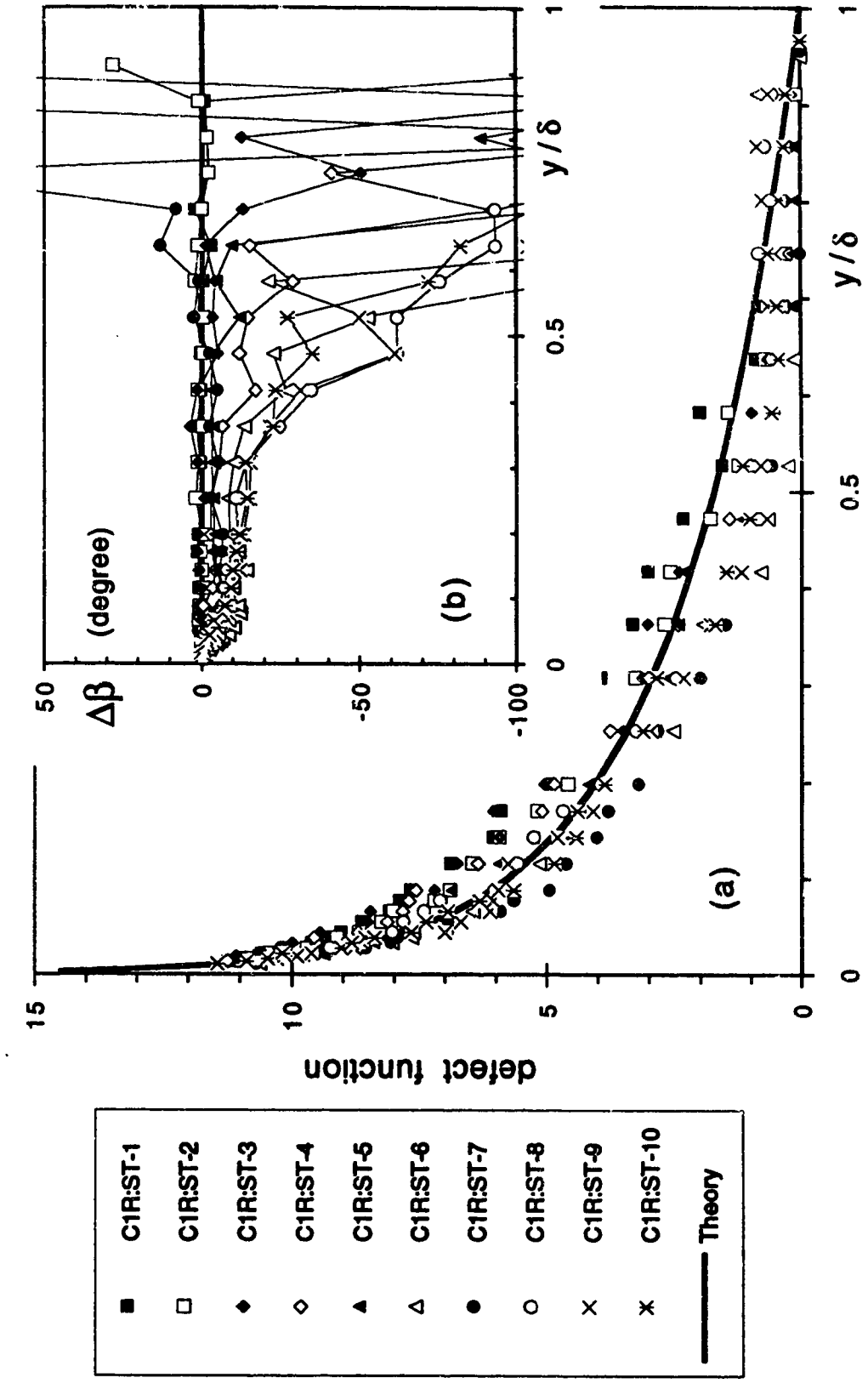

Figure 4.5.4 (b) Applicability of Perry and Joubert's model (Expt. C1R)

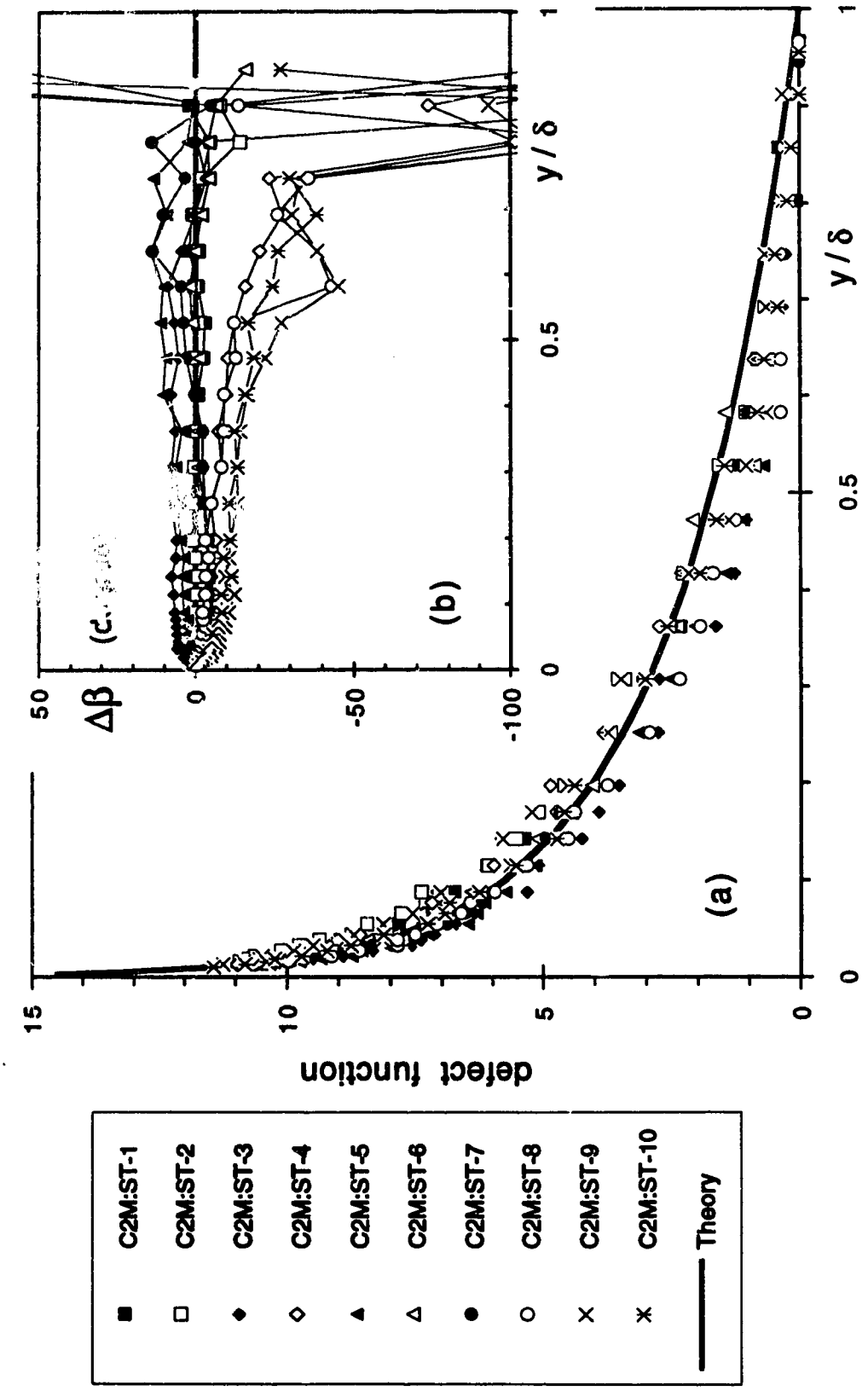

Figure 4.5.4 (c) Applicability of Perry and Joubert's model (Expt. C2M)

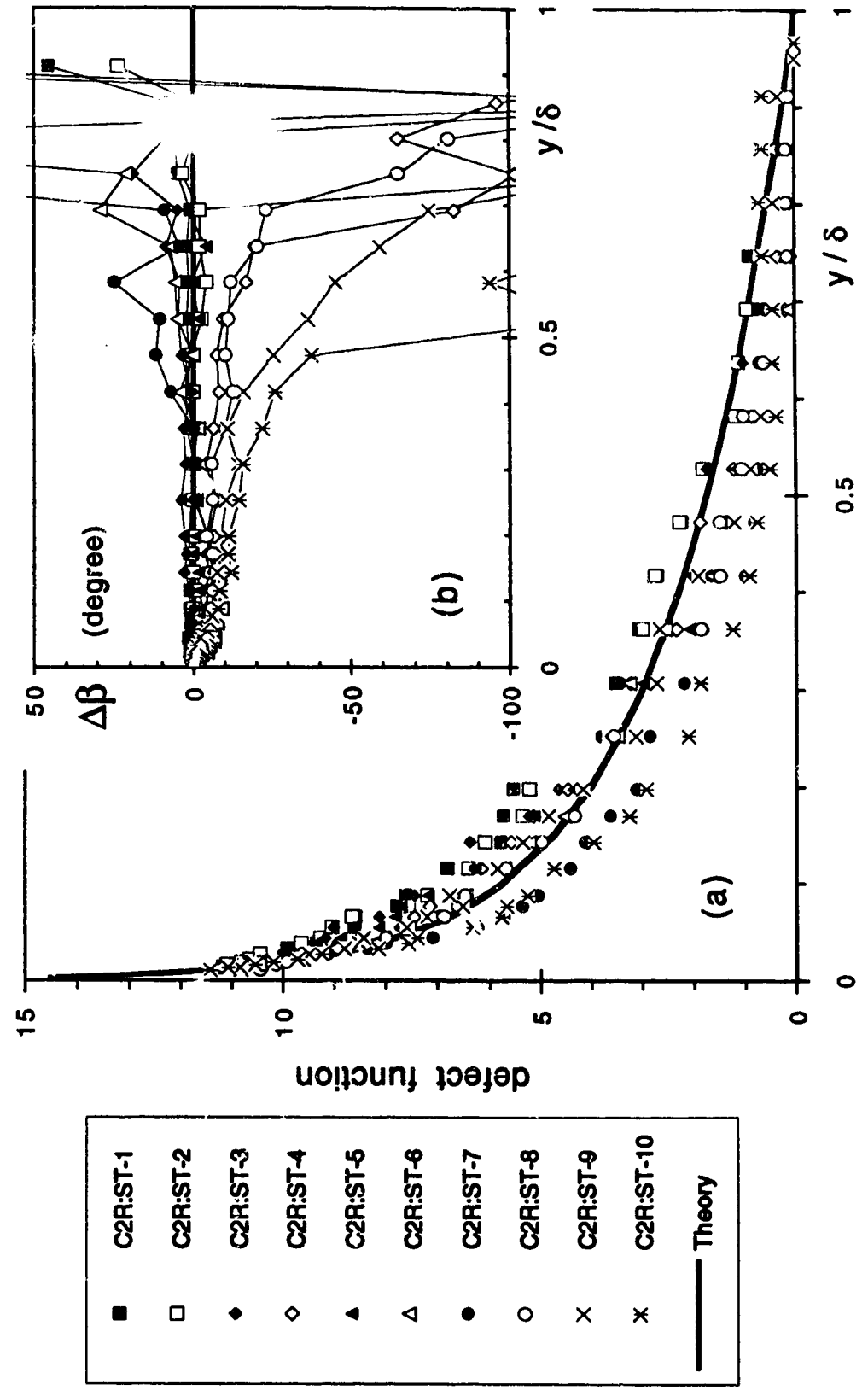

Figure 4.5.4 (d) Applicability of Perry and Joubert's model (Expt. C2R)

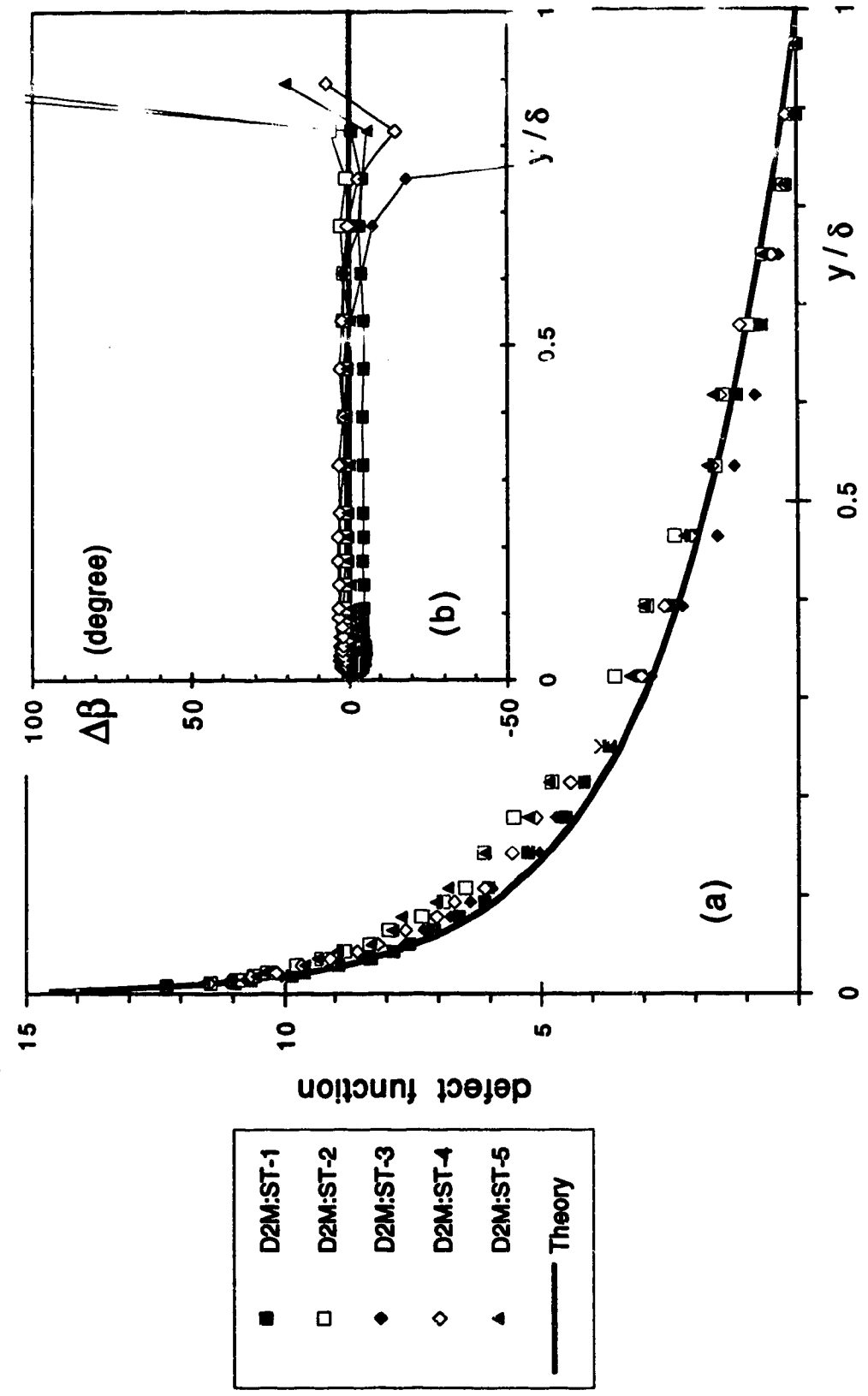

Figure 4.5.4 (e) Applicability of Perry and Joubert's model (Expt. D2M)

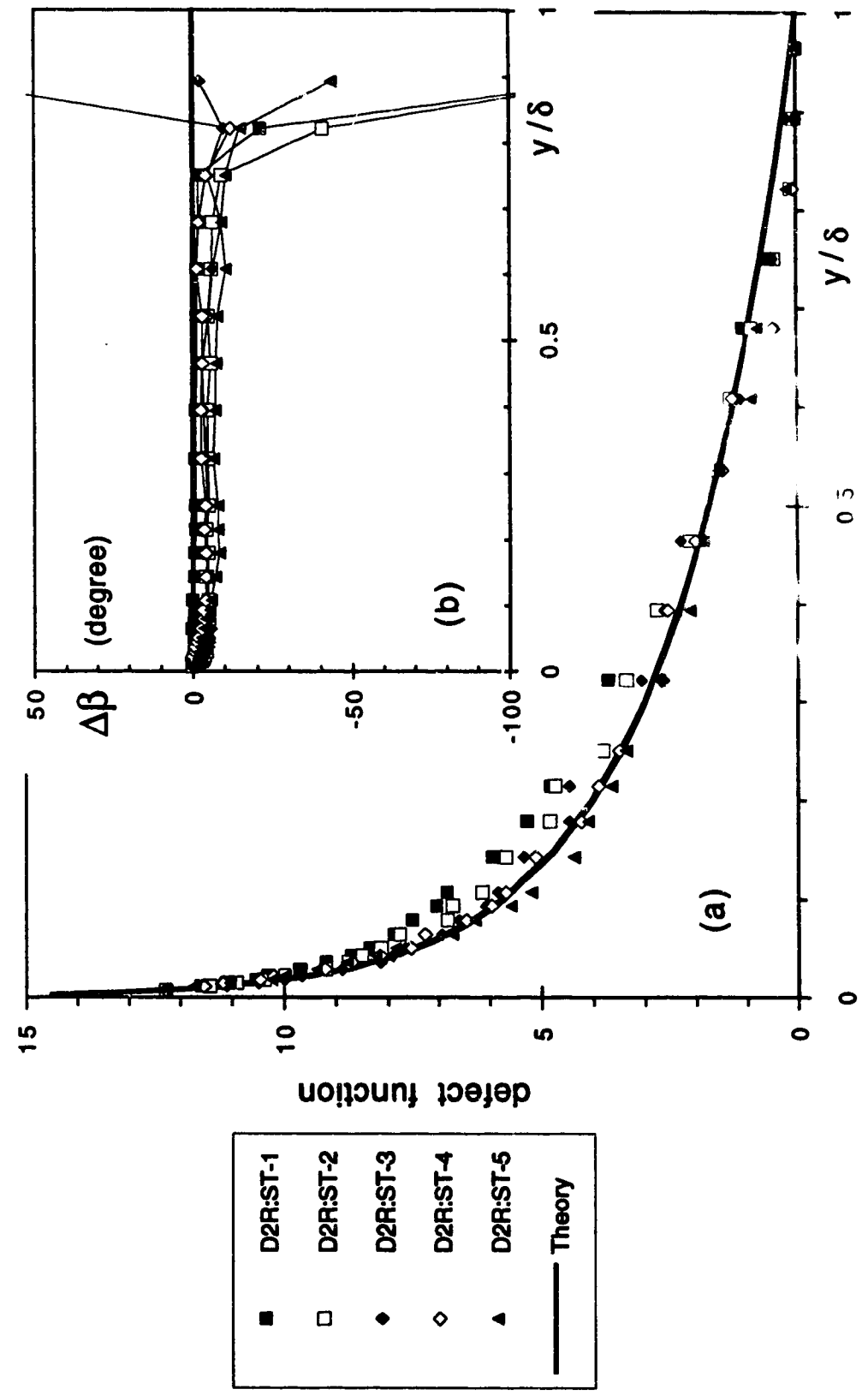

Figure 4.5.4 (f) Applicability of Perry and Joubert's model (Expt. D2R)

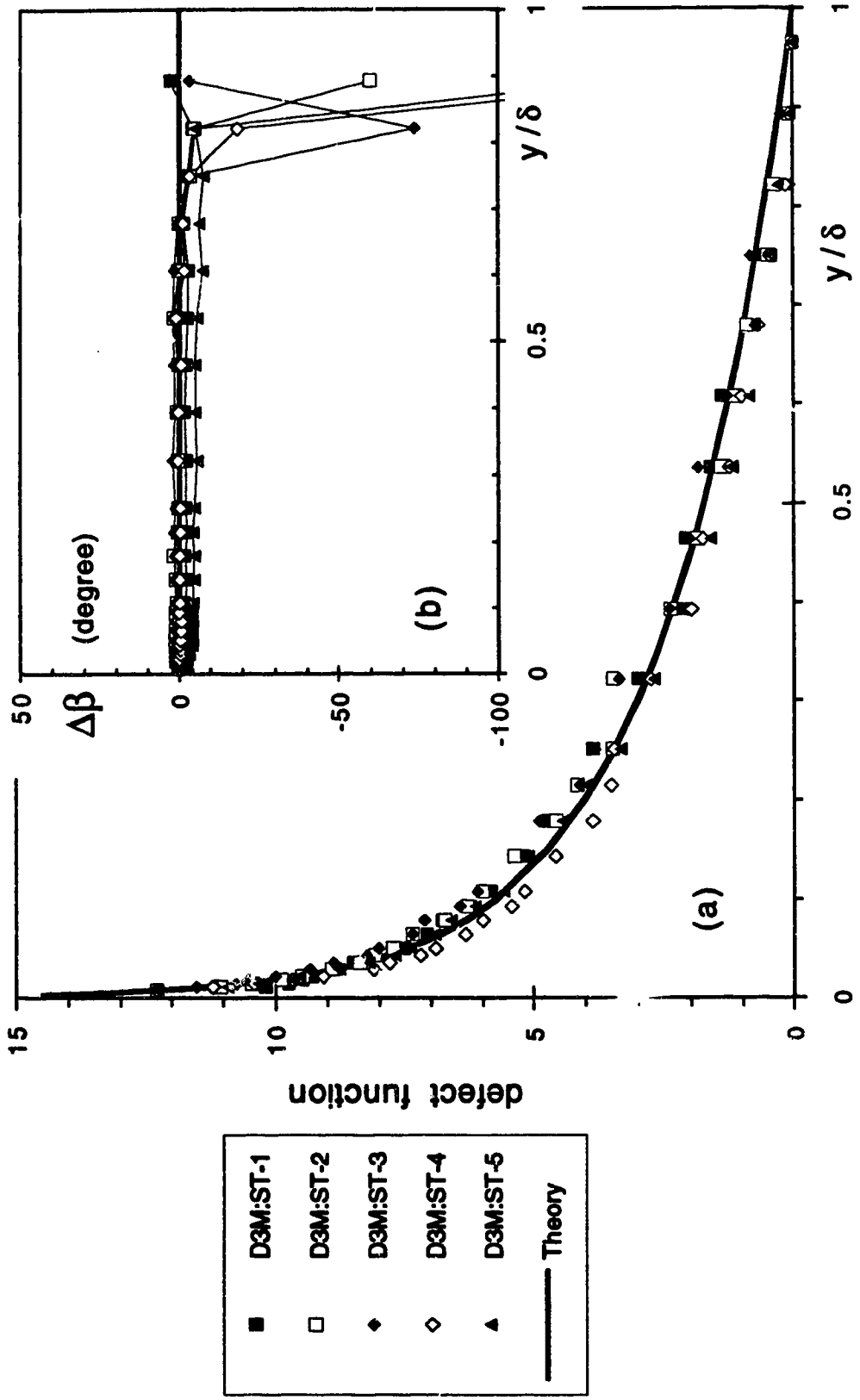

Figure 4.5.4 (g) Applicability of Perry and Joubert's model (Expt. D3M)

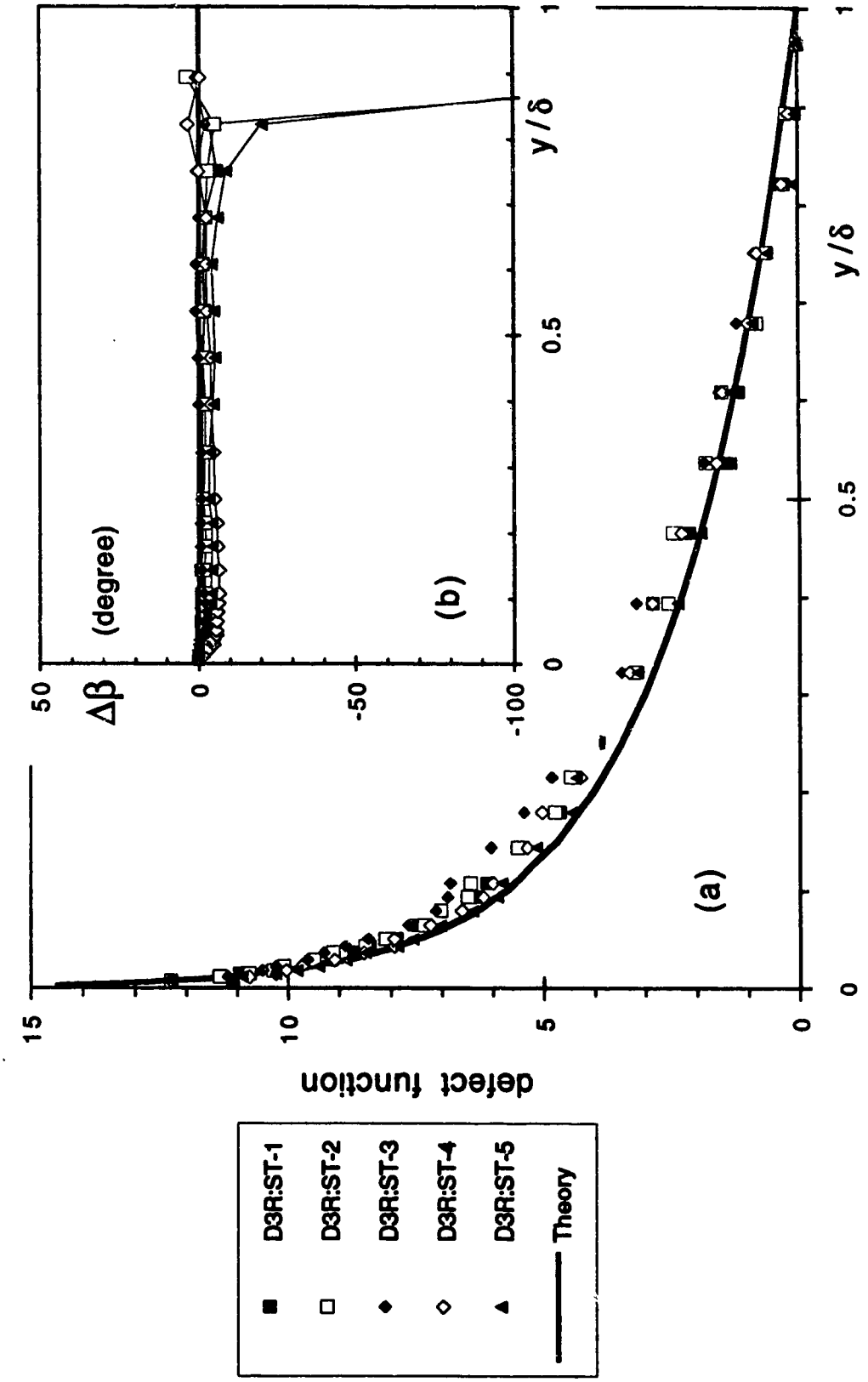

Figure 4.5.4 (h) Applicability of Perry and Joubert's model (Expt. D3R)

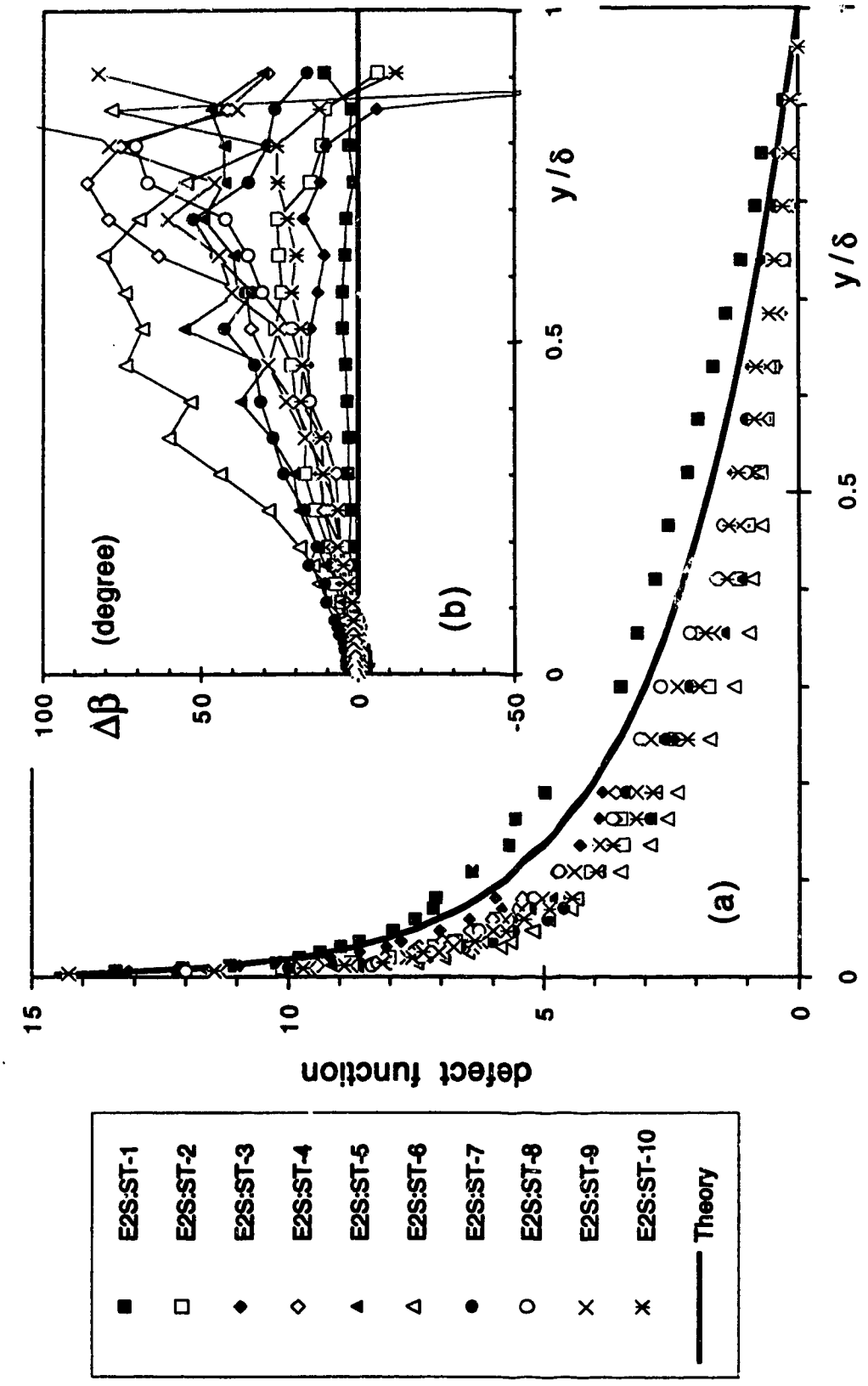

Figure 4.5.4 (i) Applicability of Perry and Joubert's model (Expt. E2S)

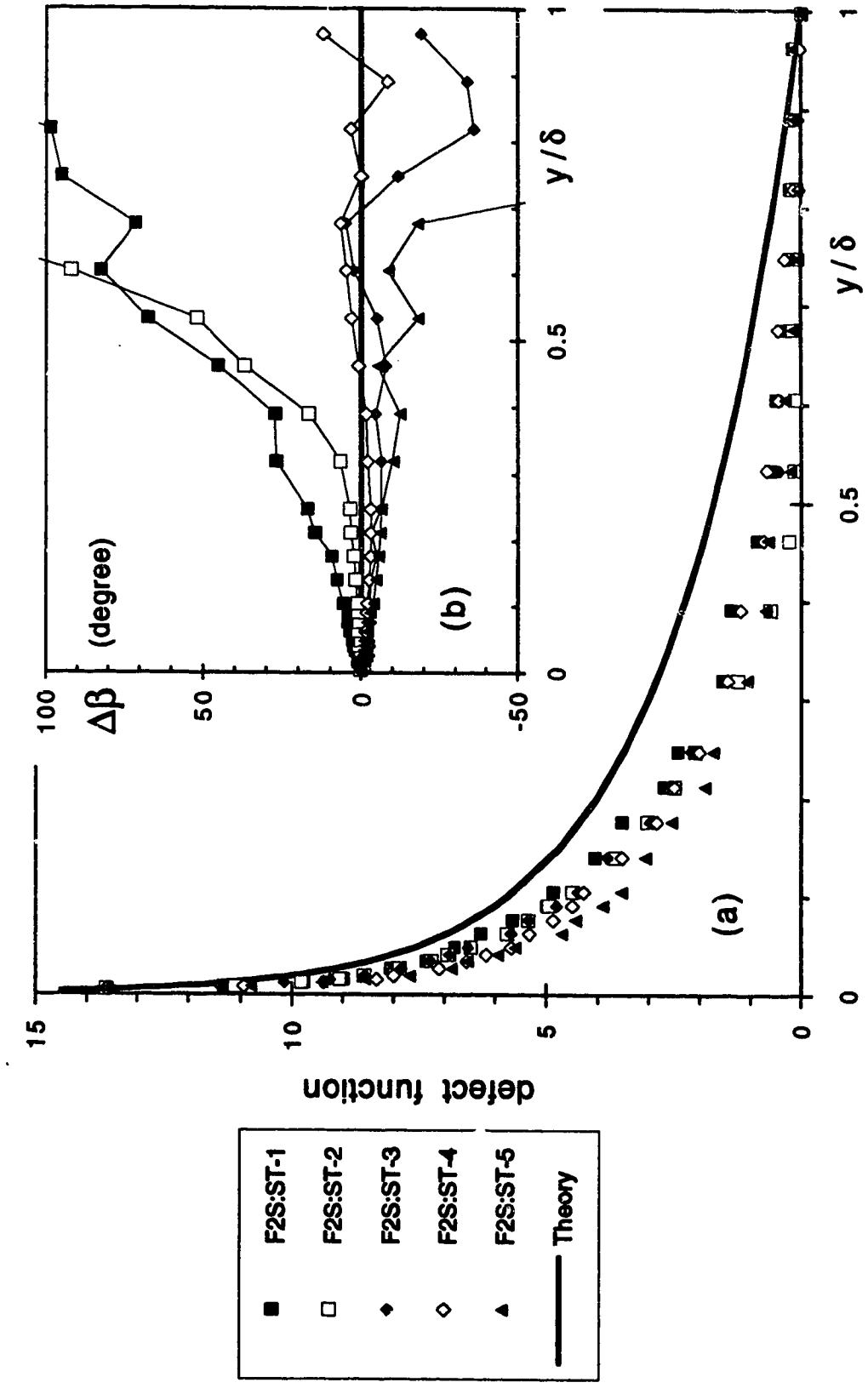

Fugure 4.5.4 (j) Applicability of Perry and Joubert's model (Expt. F2S)

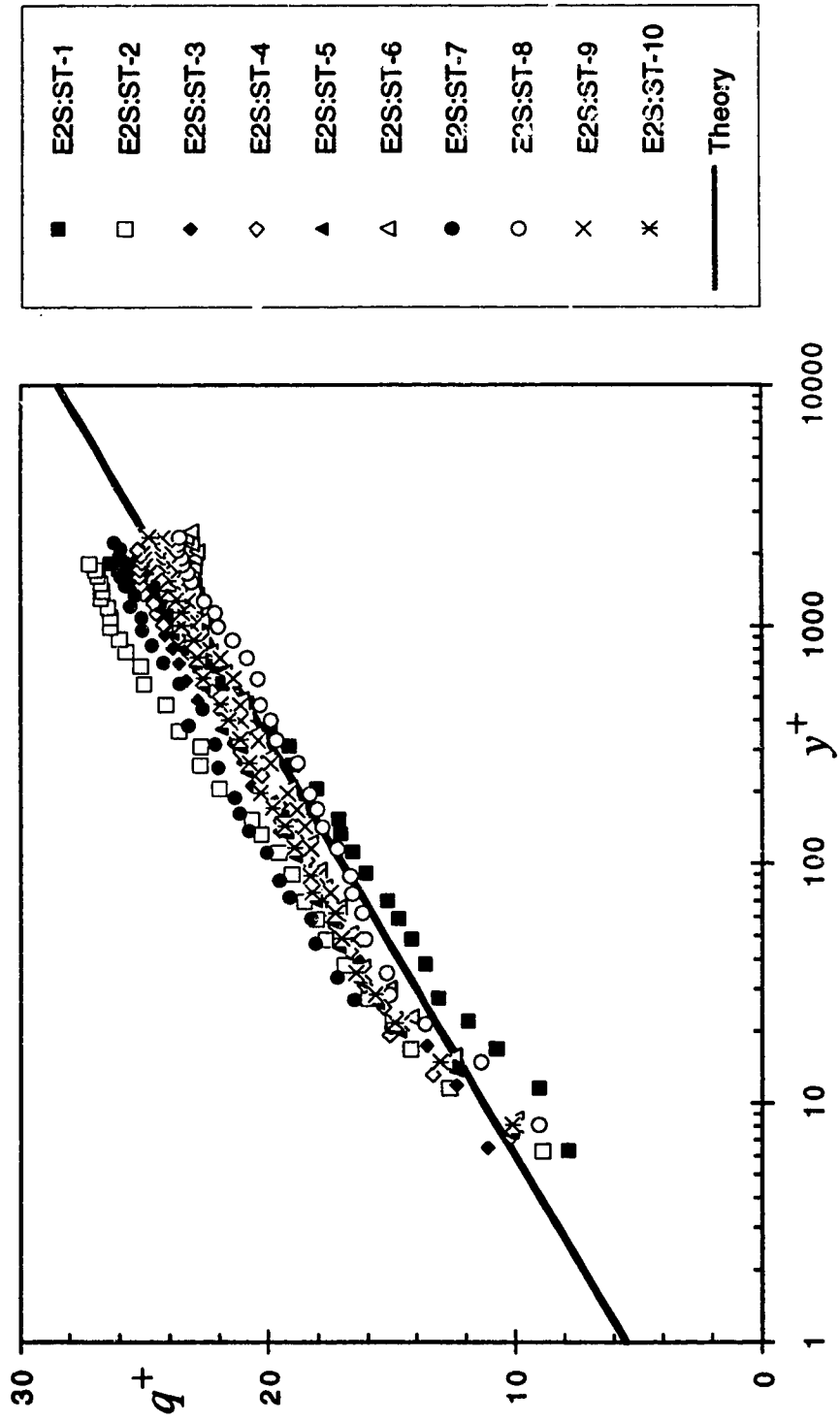

Figure 4.5.5 (a-b) Coles' near-wall similarity model
(a) Expt. E2S

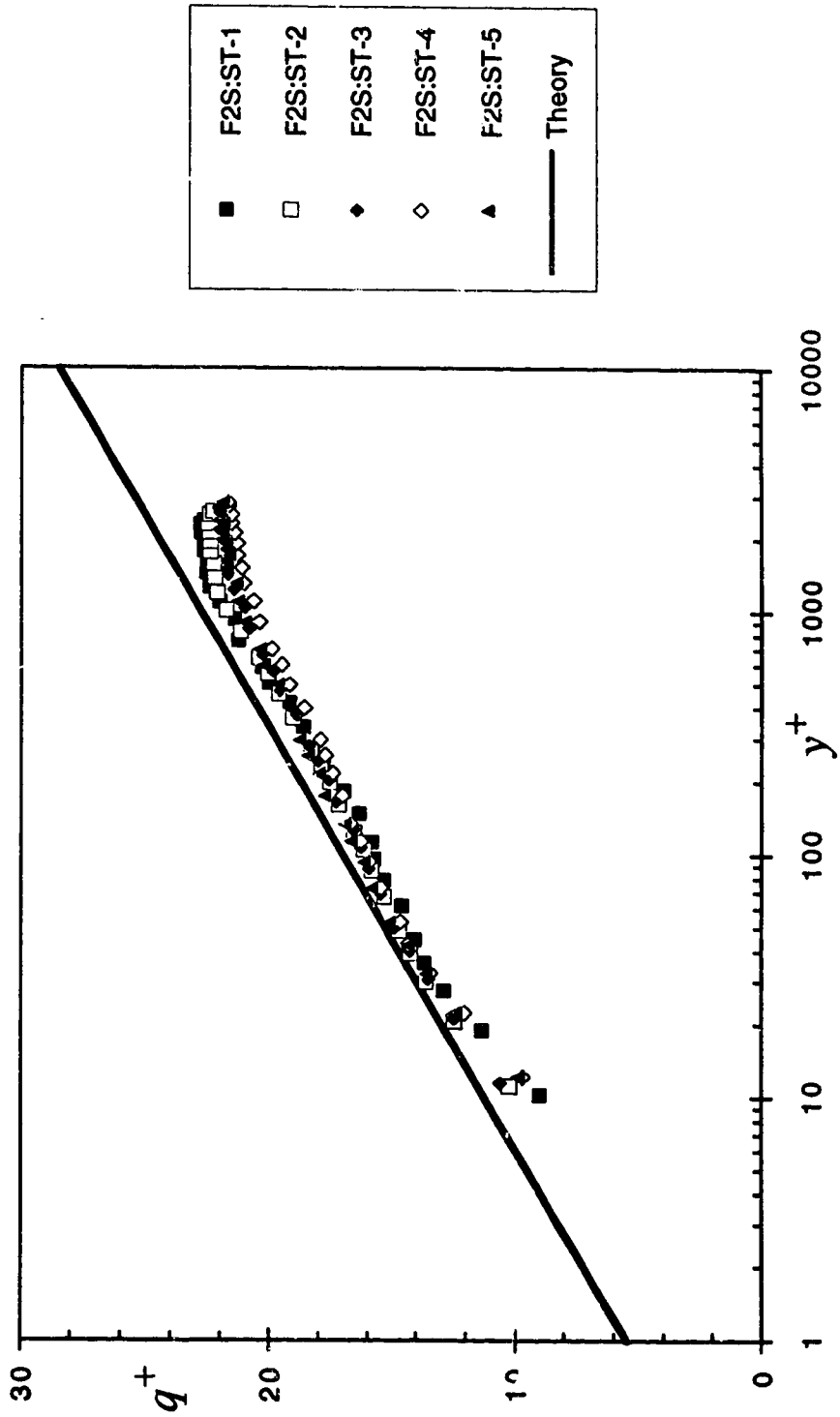

Figure 4.5.5 (a-b) Coles' near-wall similarity model
(b) Expt. F2S

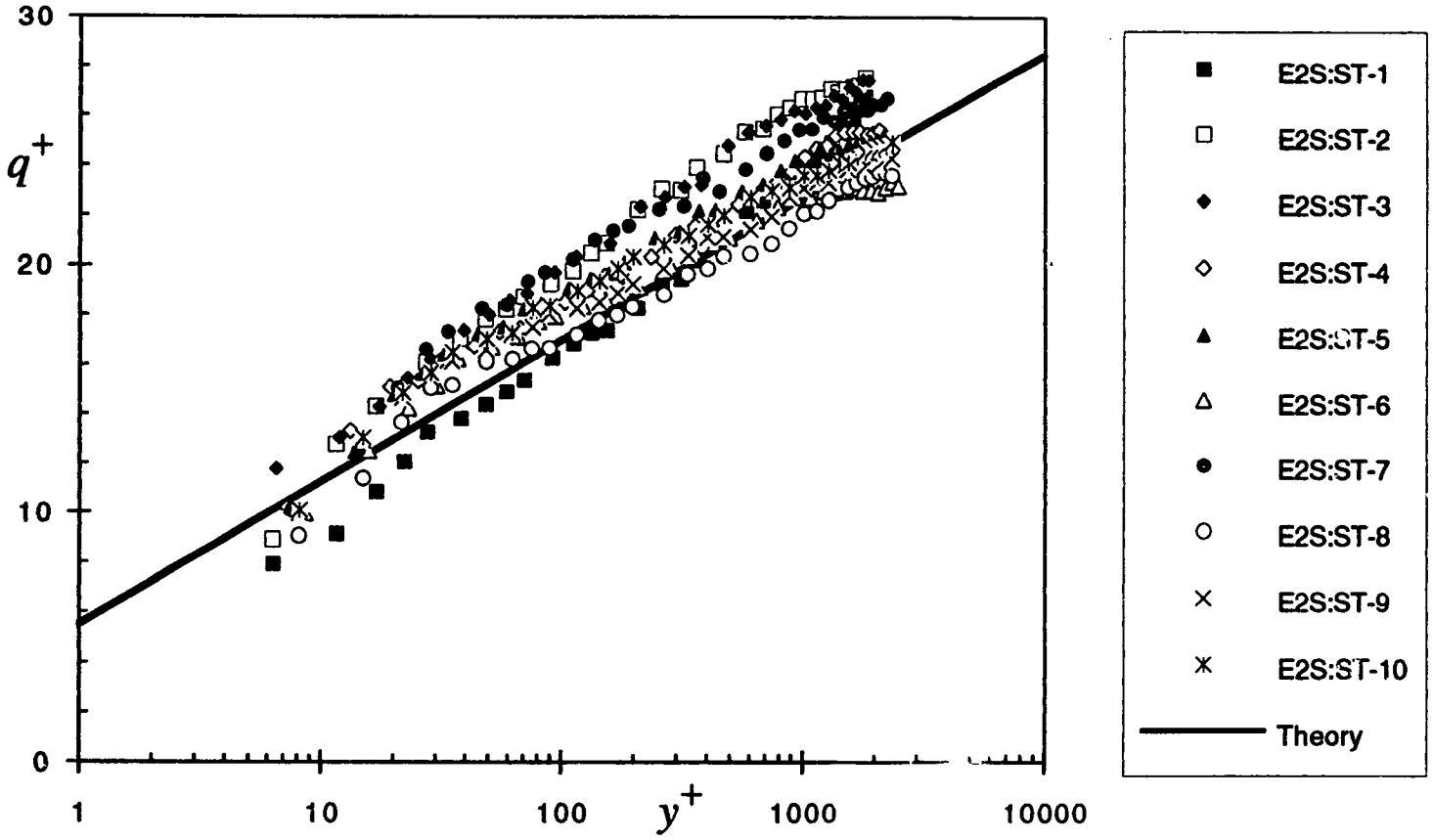

Figure 4.5.6 (a-b) Johnston's near-wall similarity model
(a) Expt. E2S

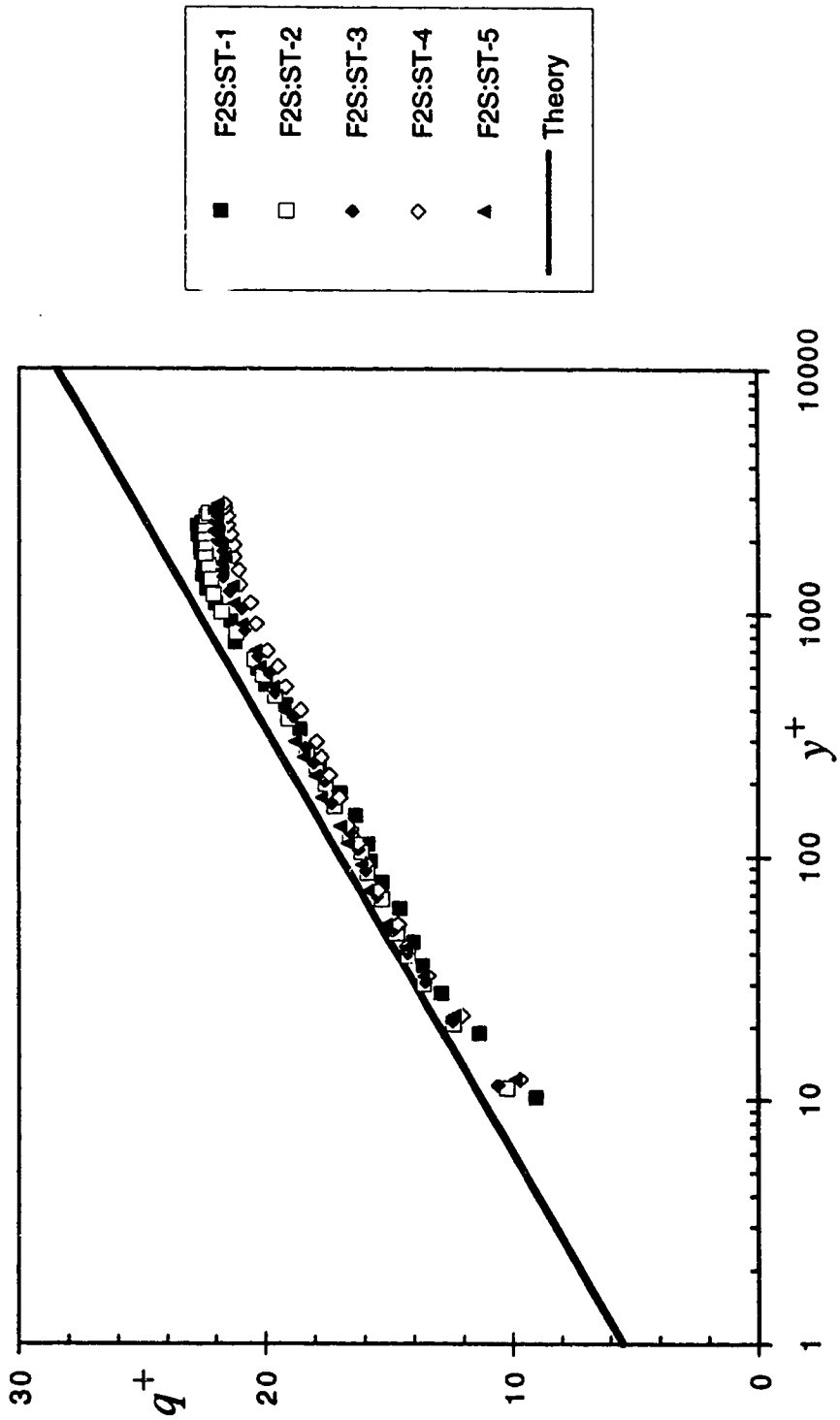

Figure 4.5.6 (a-b) Johnston's near-wall similarity model
(b) Expt. F2S

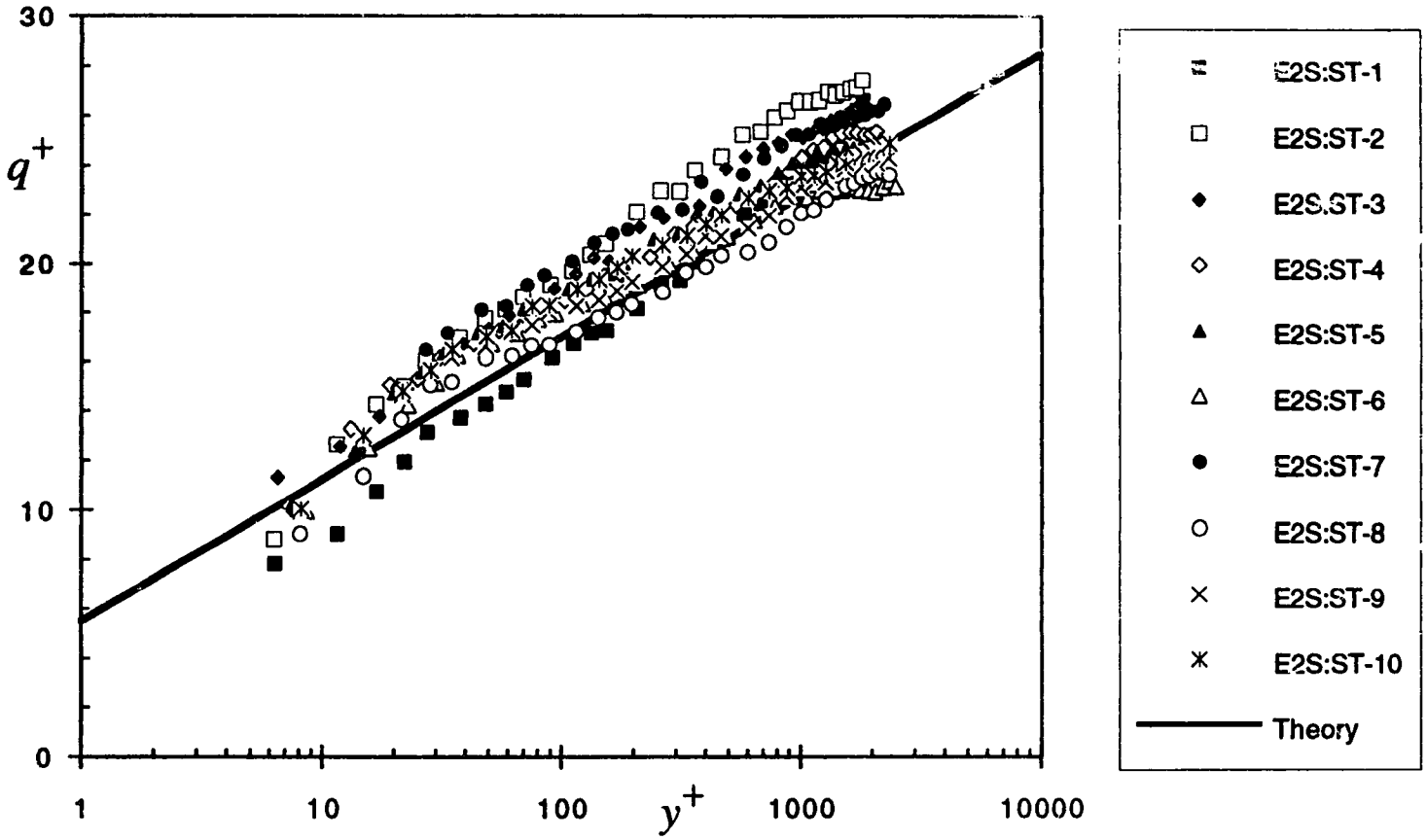

Figure 4.5.7 (a-b) Hornung and Joubert's near-wall similarity model
(a) Expt. E2S

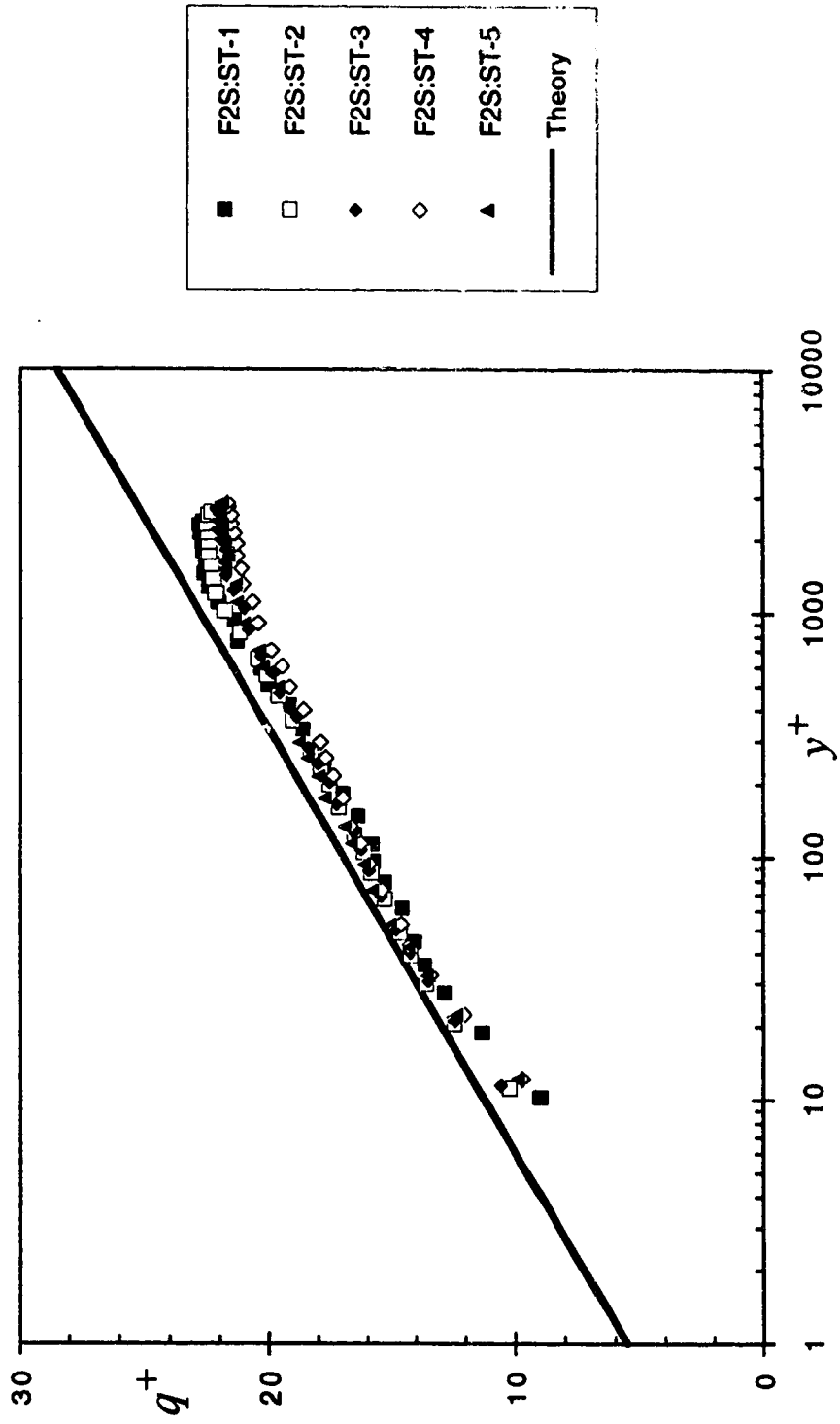

Figure 4.5.7 (a-b) Homung and Joubert's near-wall similarity model
(b) Expt. F2S

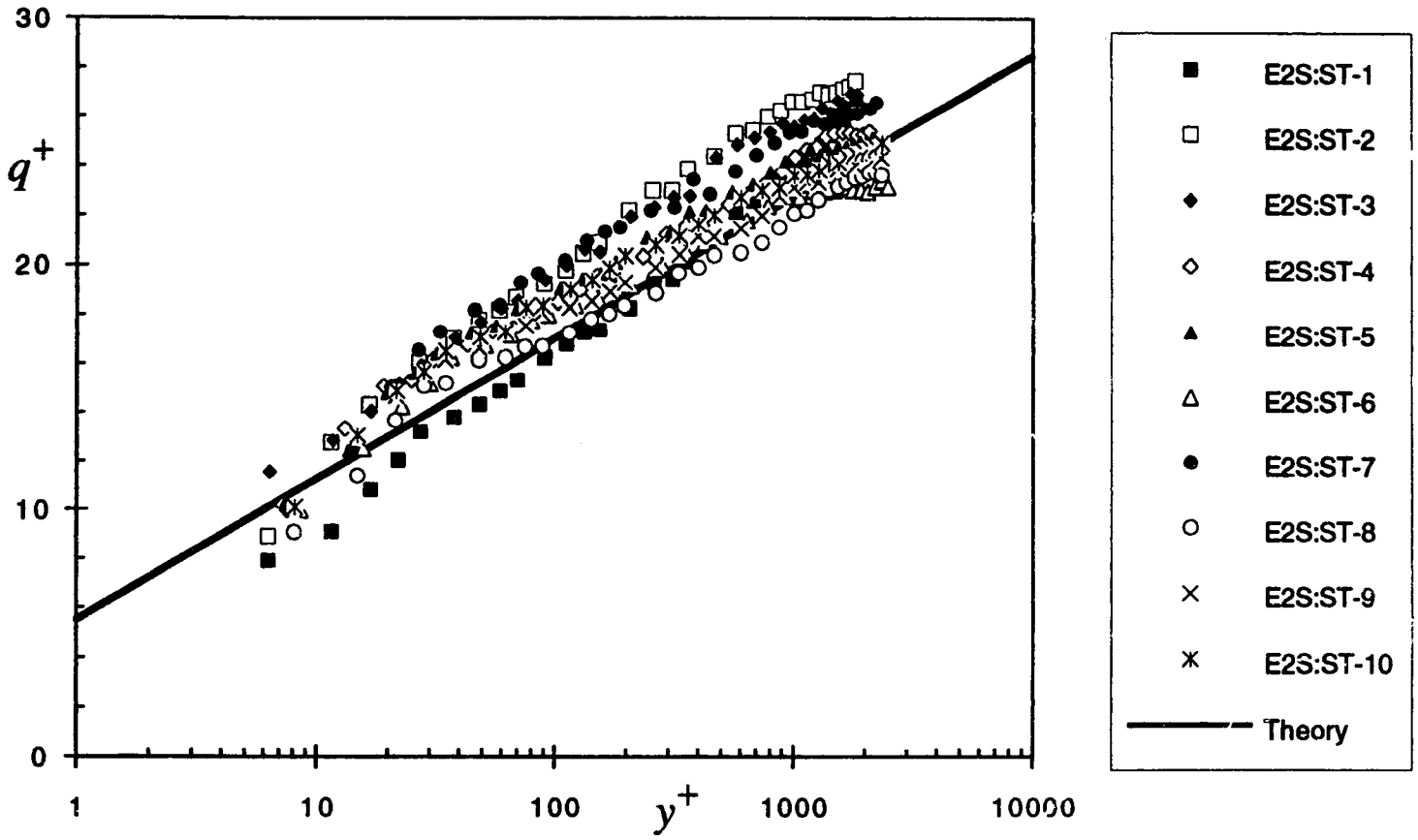

Figure 4.5.8 (a-b) Pierce and Krommenhoek's near-wall similarity model
(a) Expt. E2S

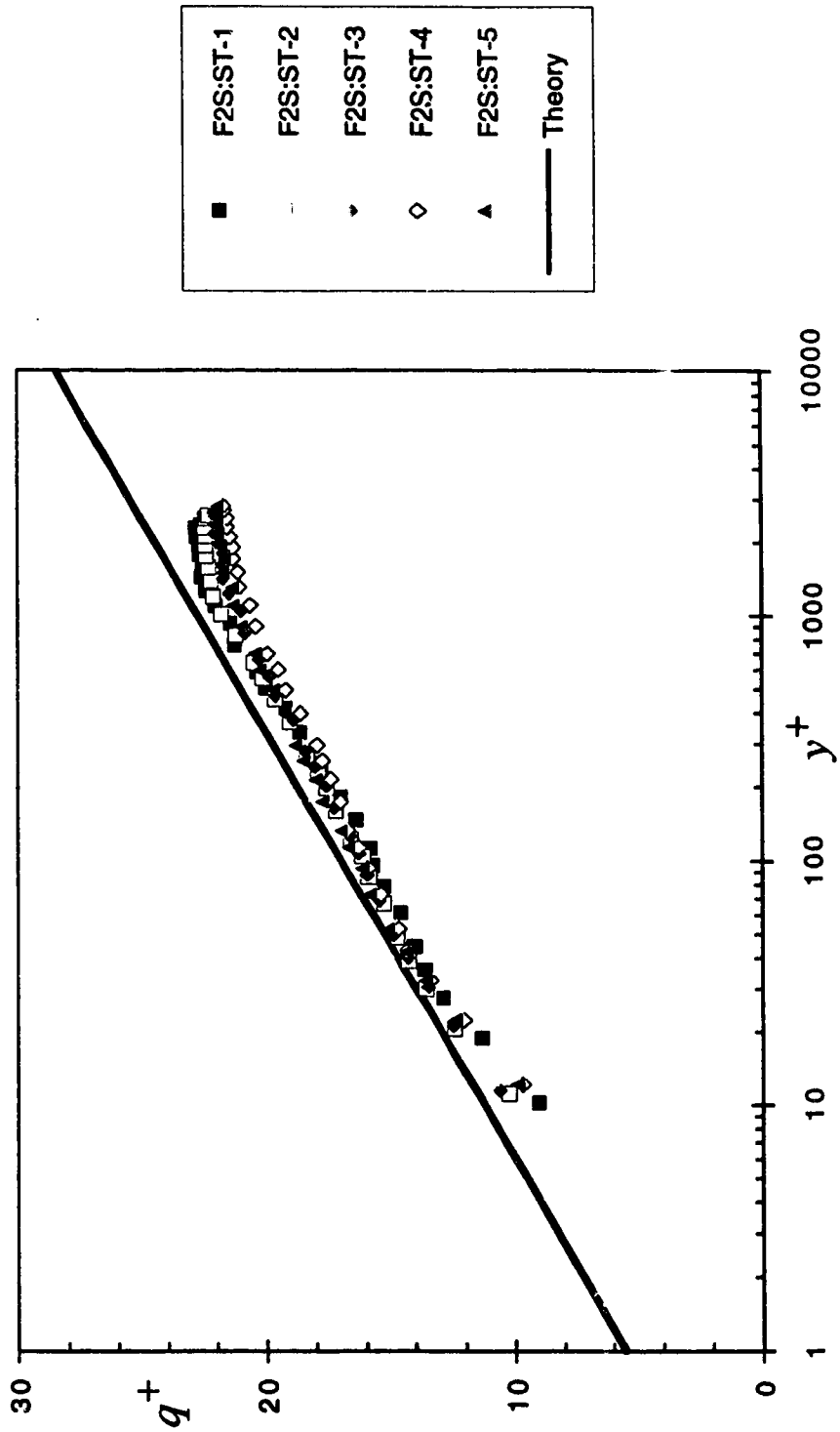

Figure 4.5.8 (a-b) Pierce and Krommenhoek's near-wall similarity model
(b) Expt. F2S

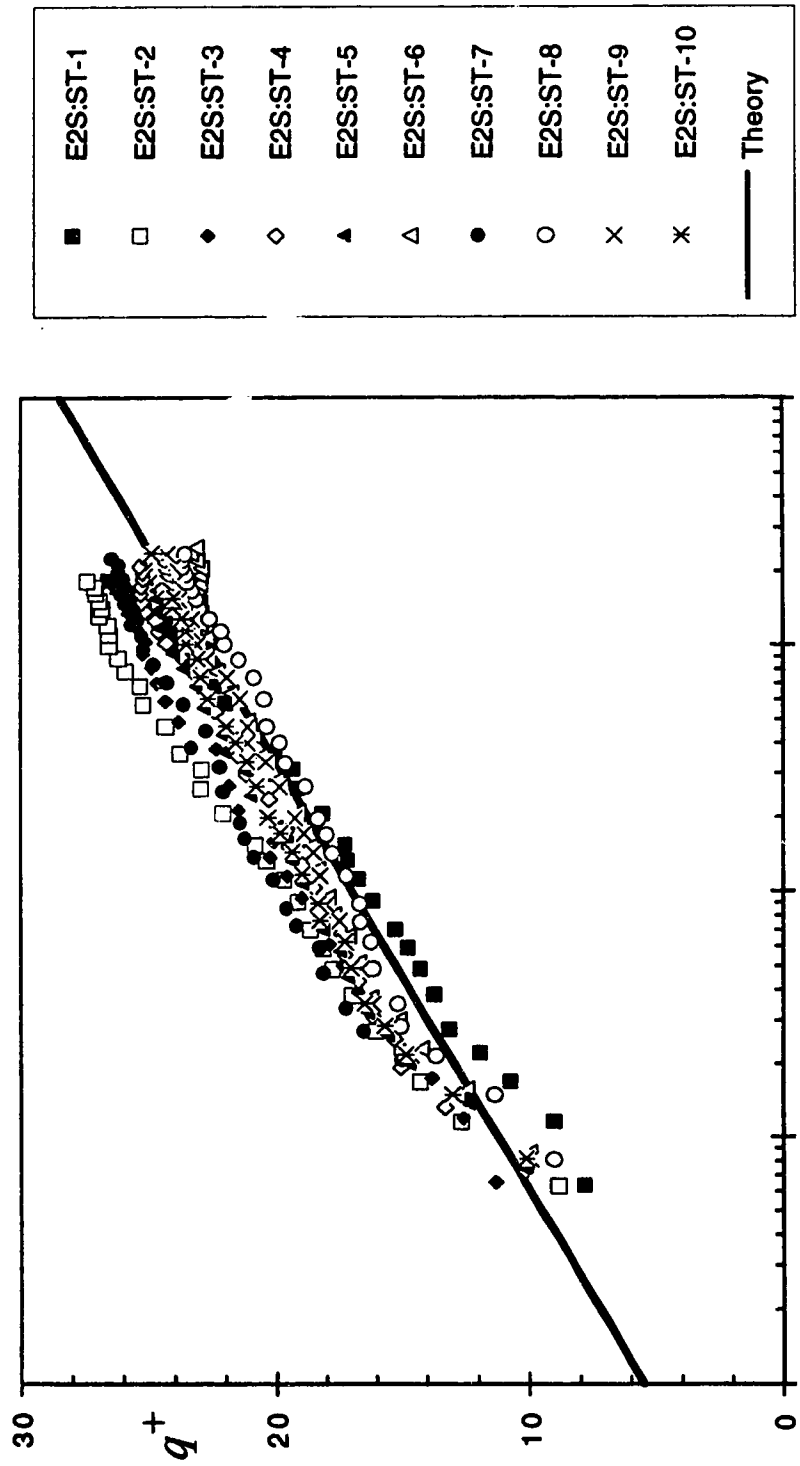

Figure 4.5.9 (a-b) Prahlad's near-wall similarity model
(a) Expt. E2S

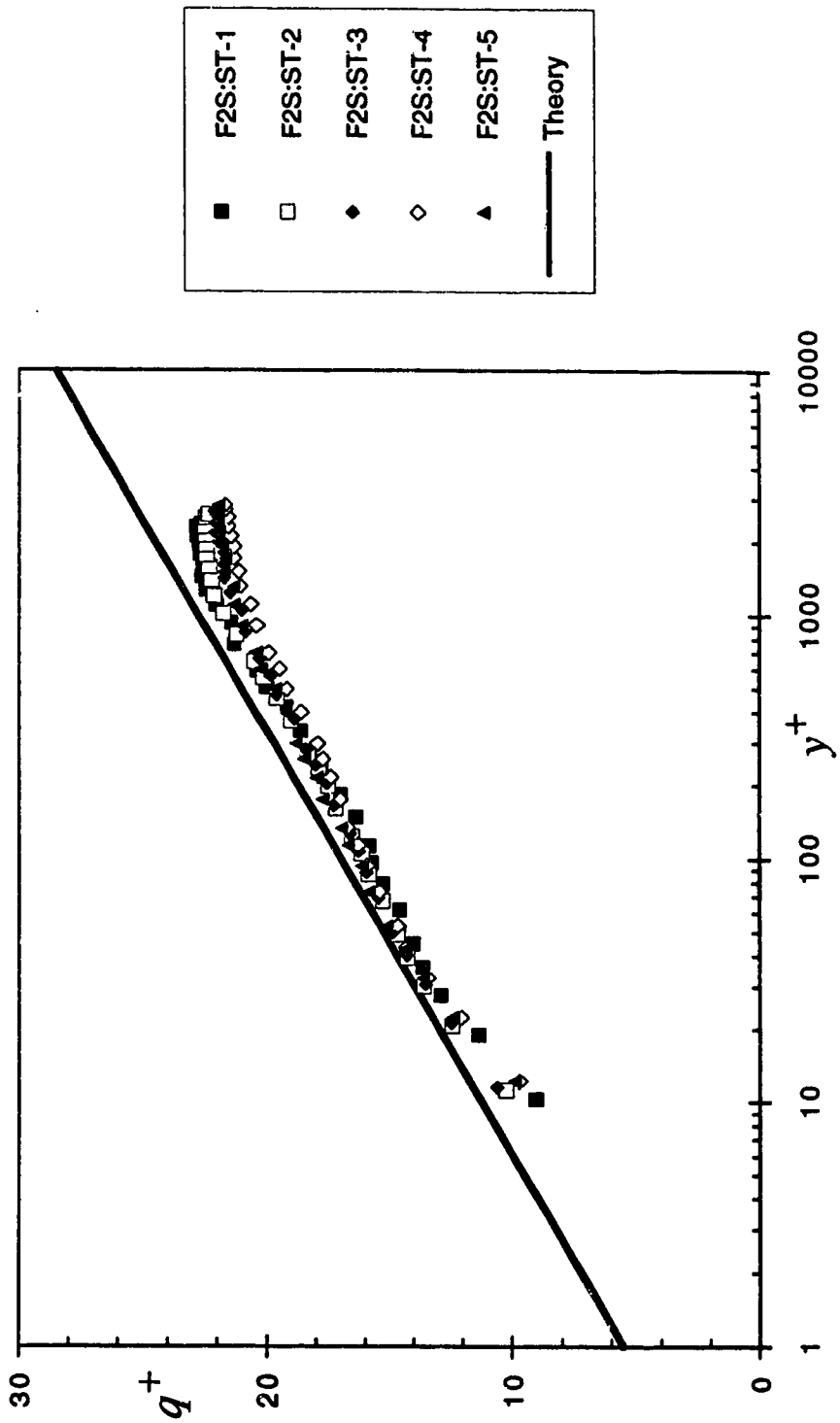

Figure 4.5.9 (a-b) Prahlad's near-wall similarity model
(b) Expt. F2S

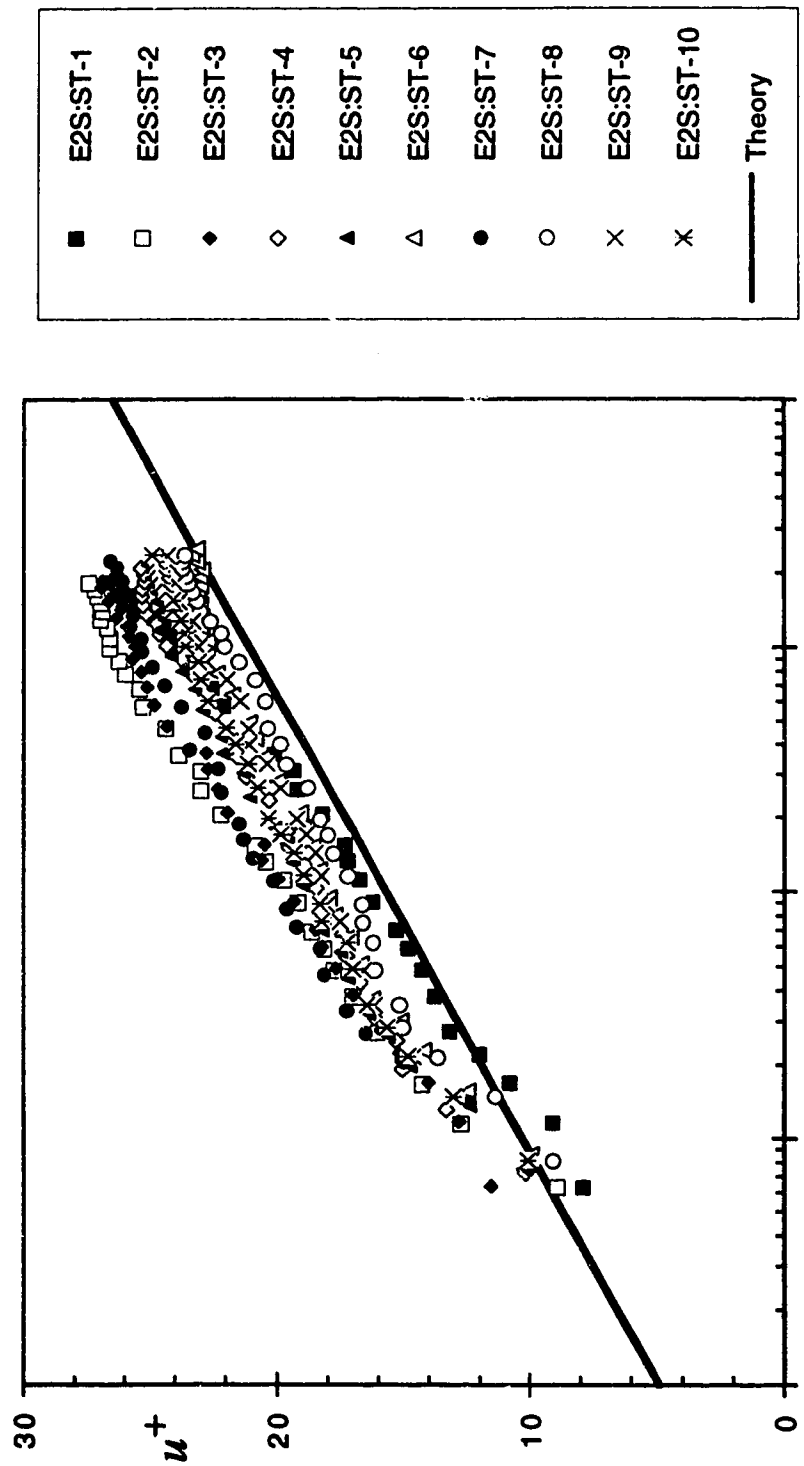

Figure 4.5.10 (a-d) Chandrashekhar and Swamy's near-wall similarity model
(a) Expt. E2S (main flow)

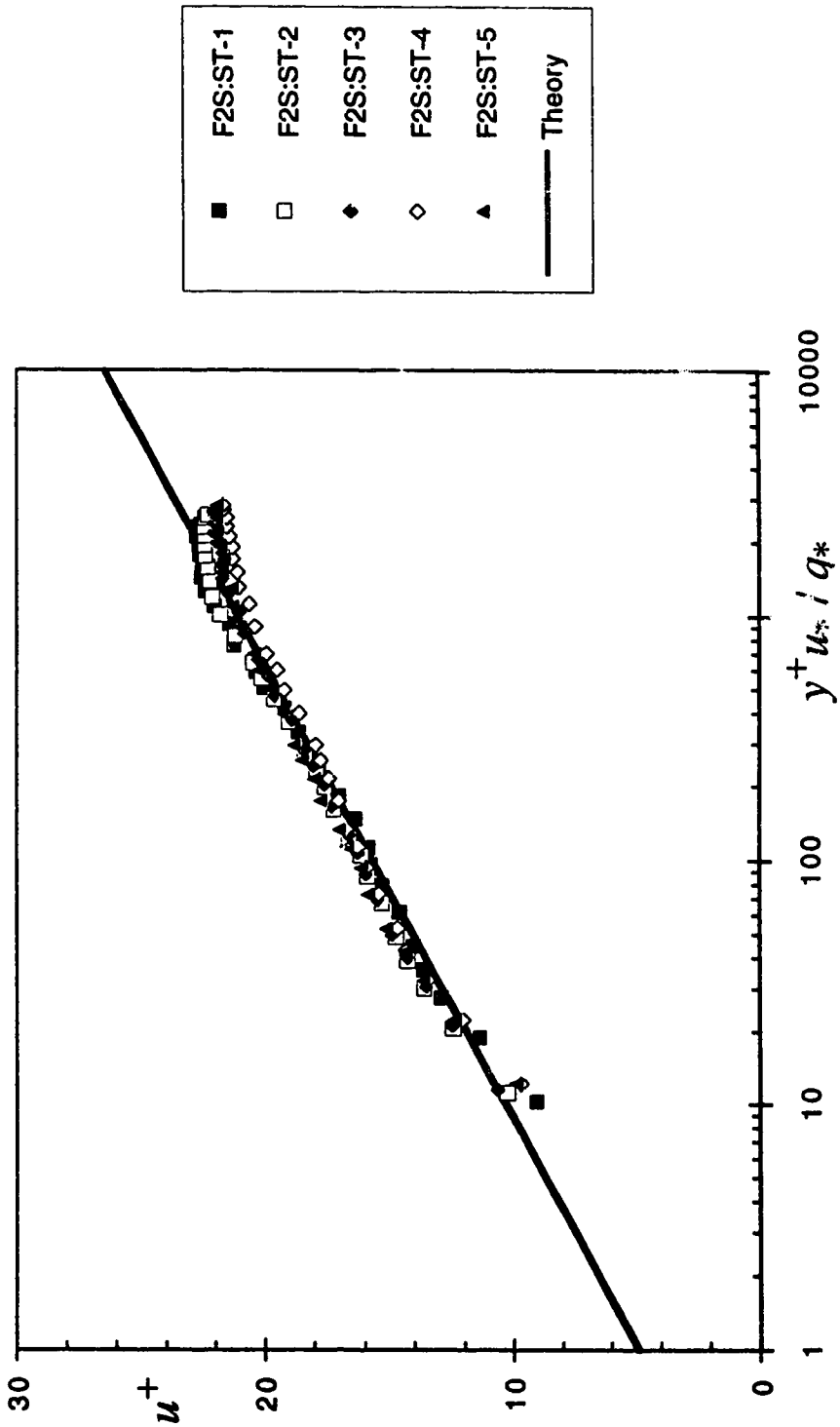

Figure 4.5.10 (a-d) Chandrashekhar and Swamy's near-wall similarity model
(b) Expt. F2S (main flow)

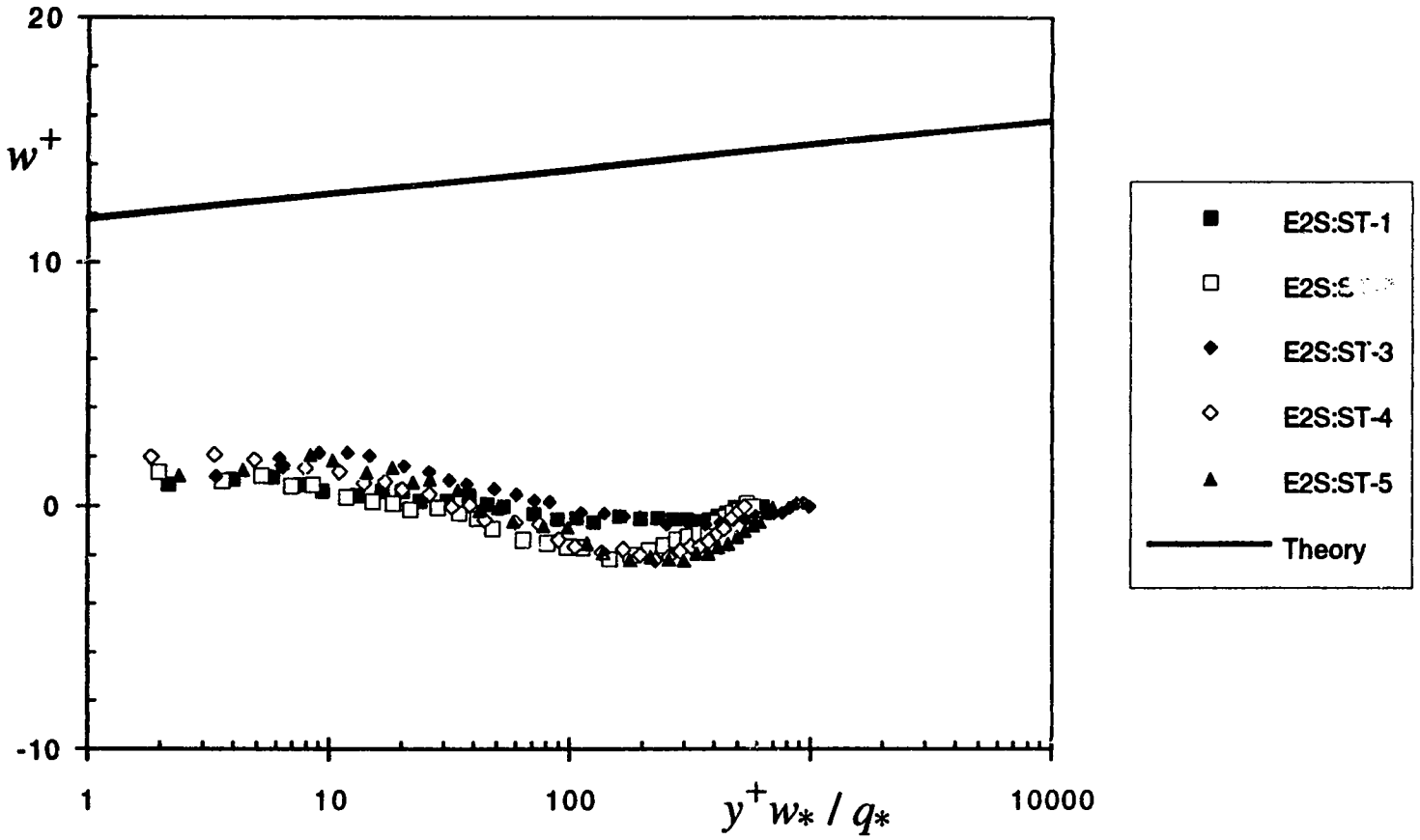

Figure 4.5.10 (a-d) Chandrashekhar and Swamy's near-wall similarity model
(c) Expt. E2S (cross flow)

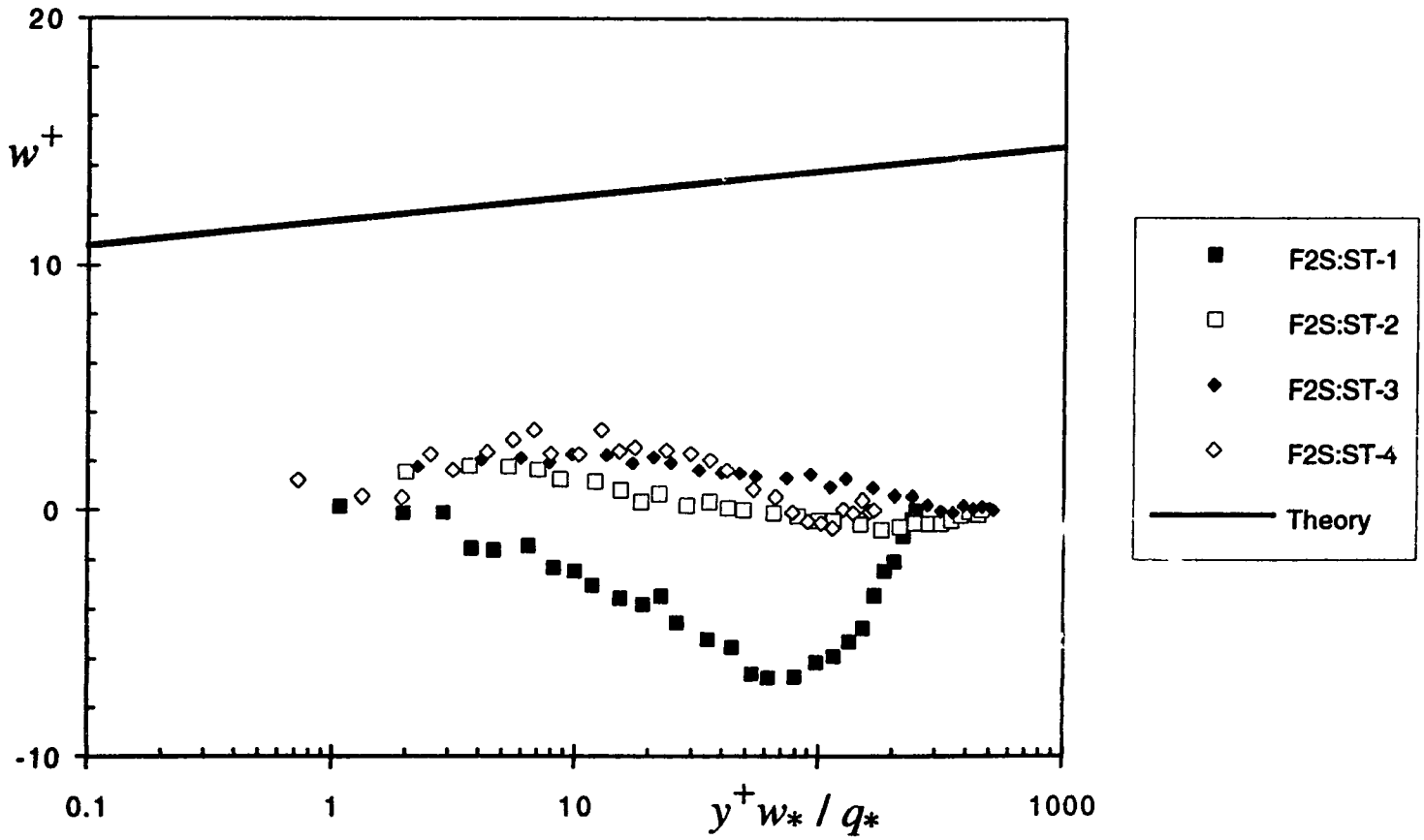

Figure 4.5.10 (a-d) Chandrashekhar and Swamy's near-wall similarity model
(d) Expt. F2S (cross flow)

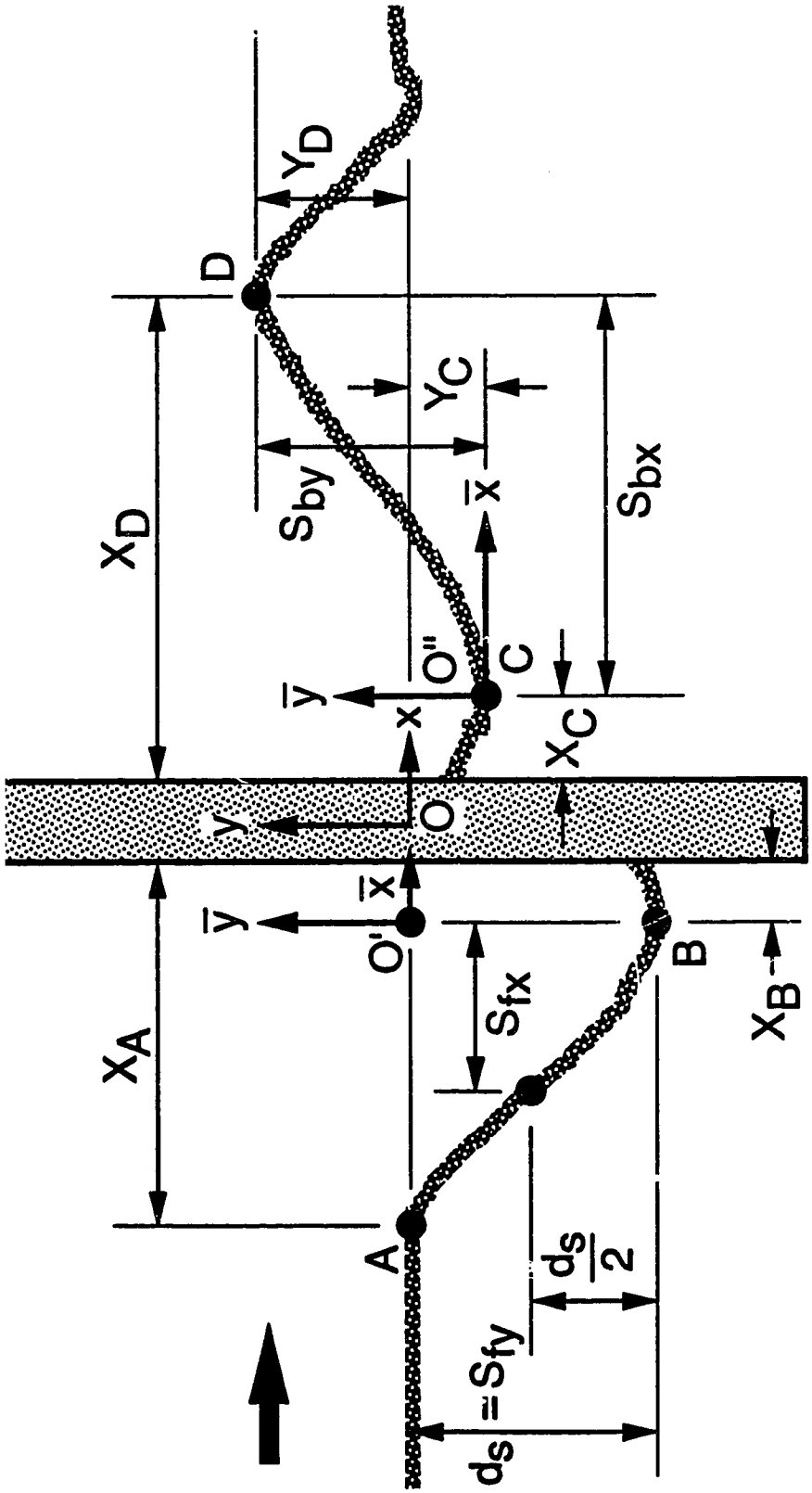

Figure 4.6.1 Length scales of the scour profile

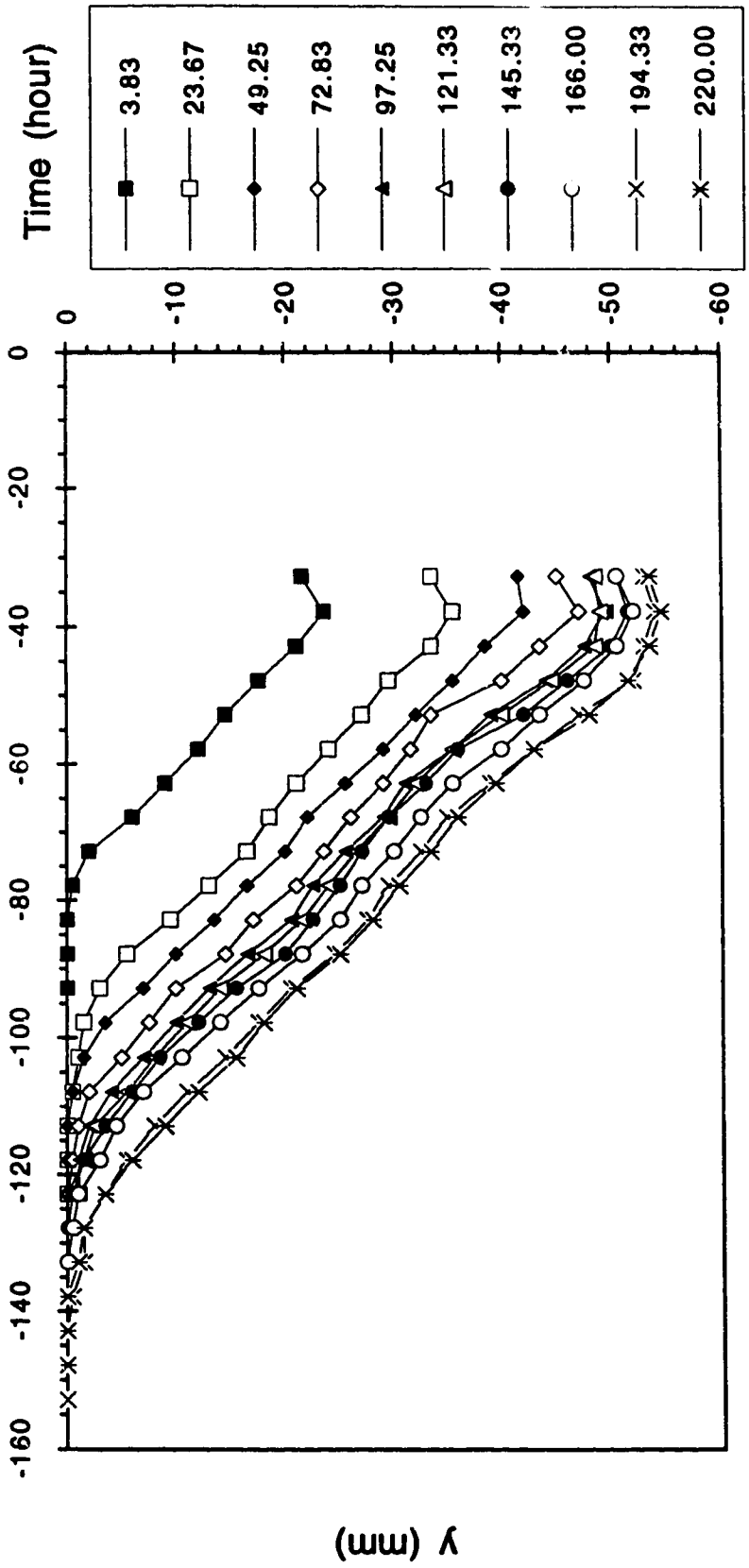

Figure 4.6.2 (a-c) Typical scour profiles (Expt. A3M)
(a) front of cylinder

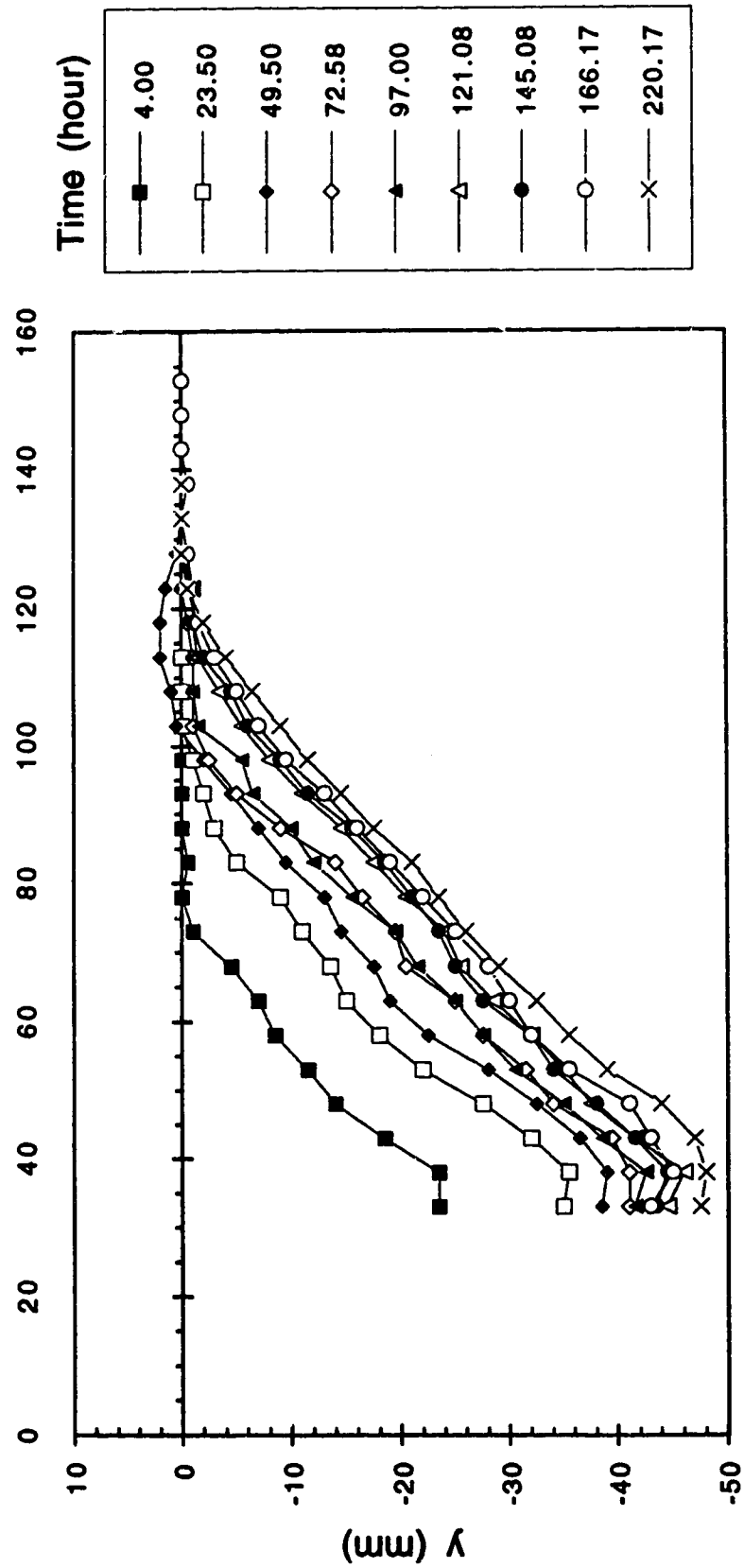

Figure 4.6.2 (a-c) Typical scour profiles (Expt. A3M)
(b) side of cylinder

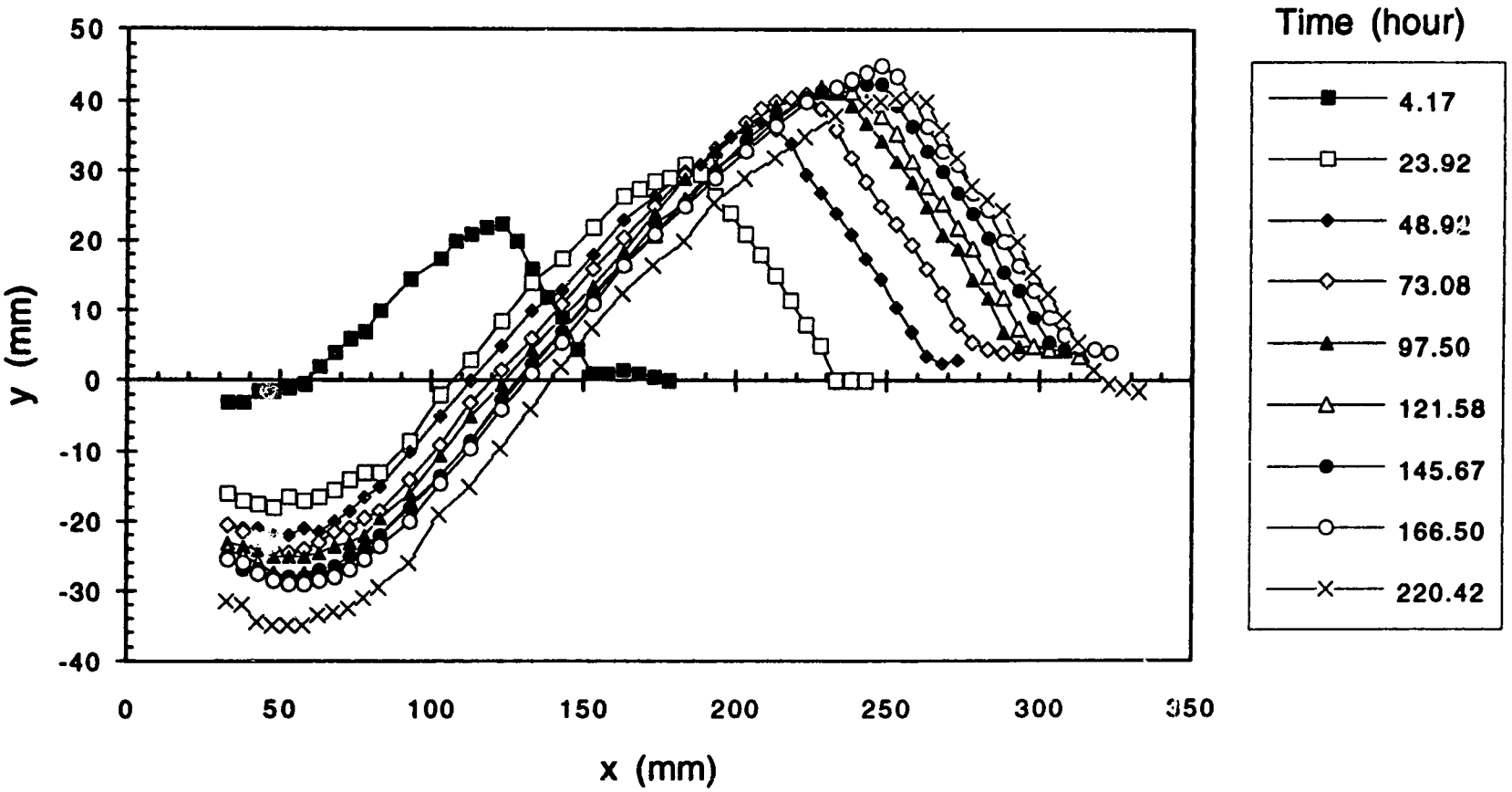

Figure 4.6.2 (a-c) Typical scour profiles (Expt. A3M)
(c) back of cylinder

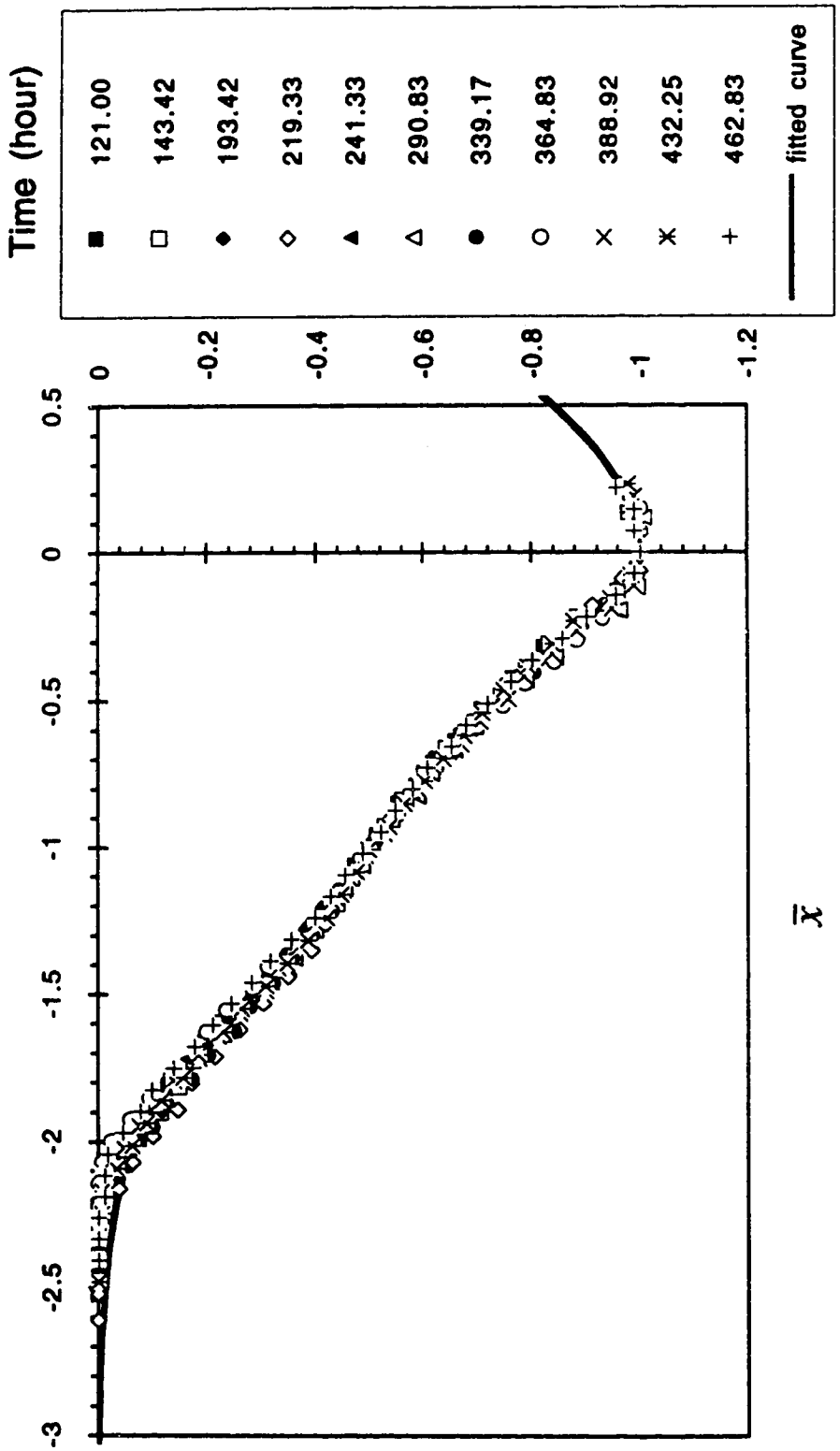

Figure 4.6.3 (a-d) Similarity of scour profile in front of cylinder
(a) Expt. A1M

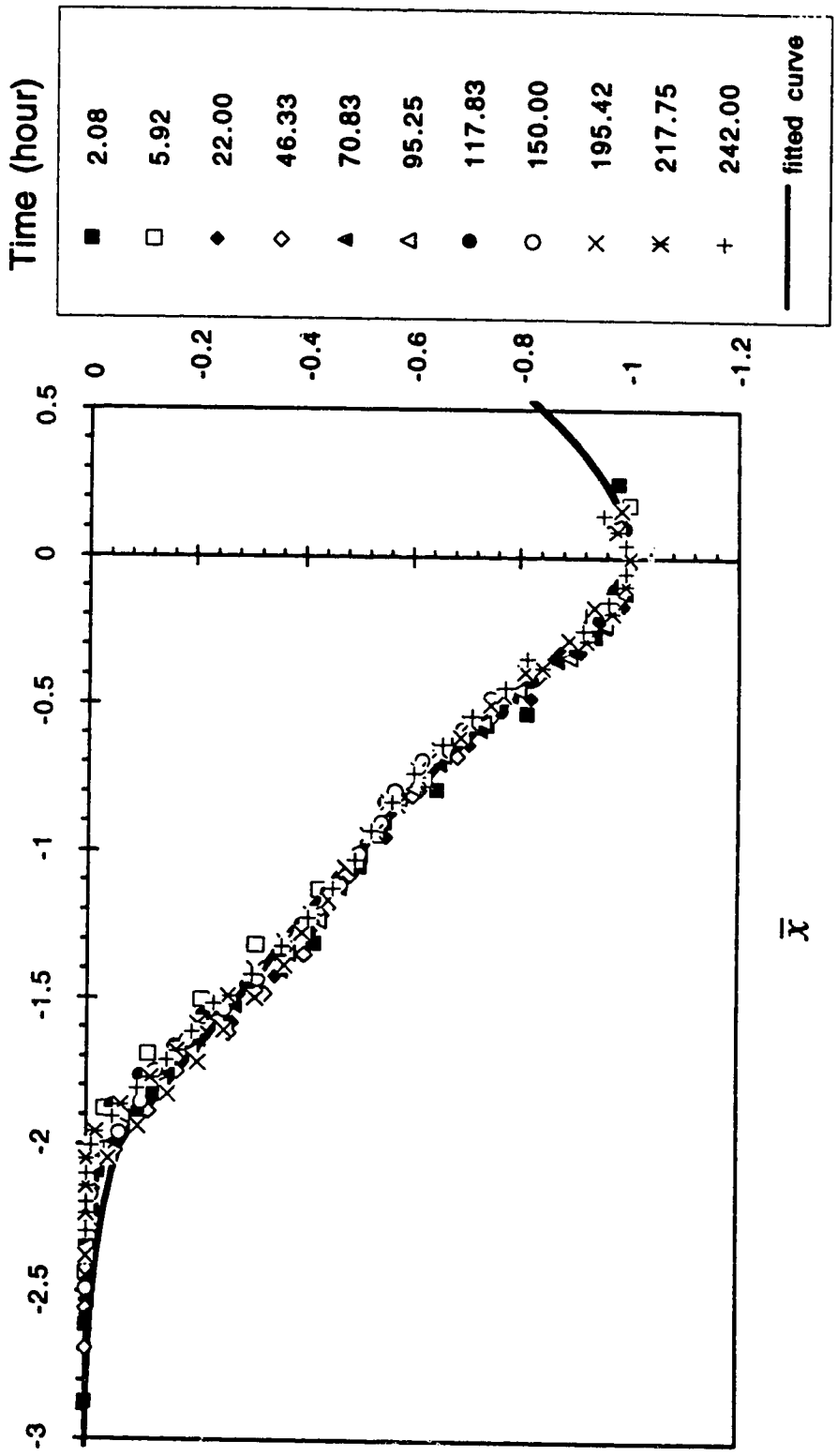

Figure 4.6.3 (a-d) Similarity of scour profile in front of cylinder (b) Expt. A2M

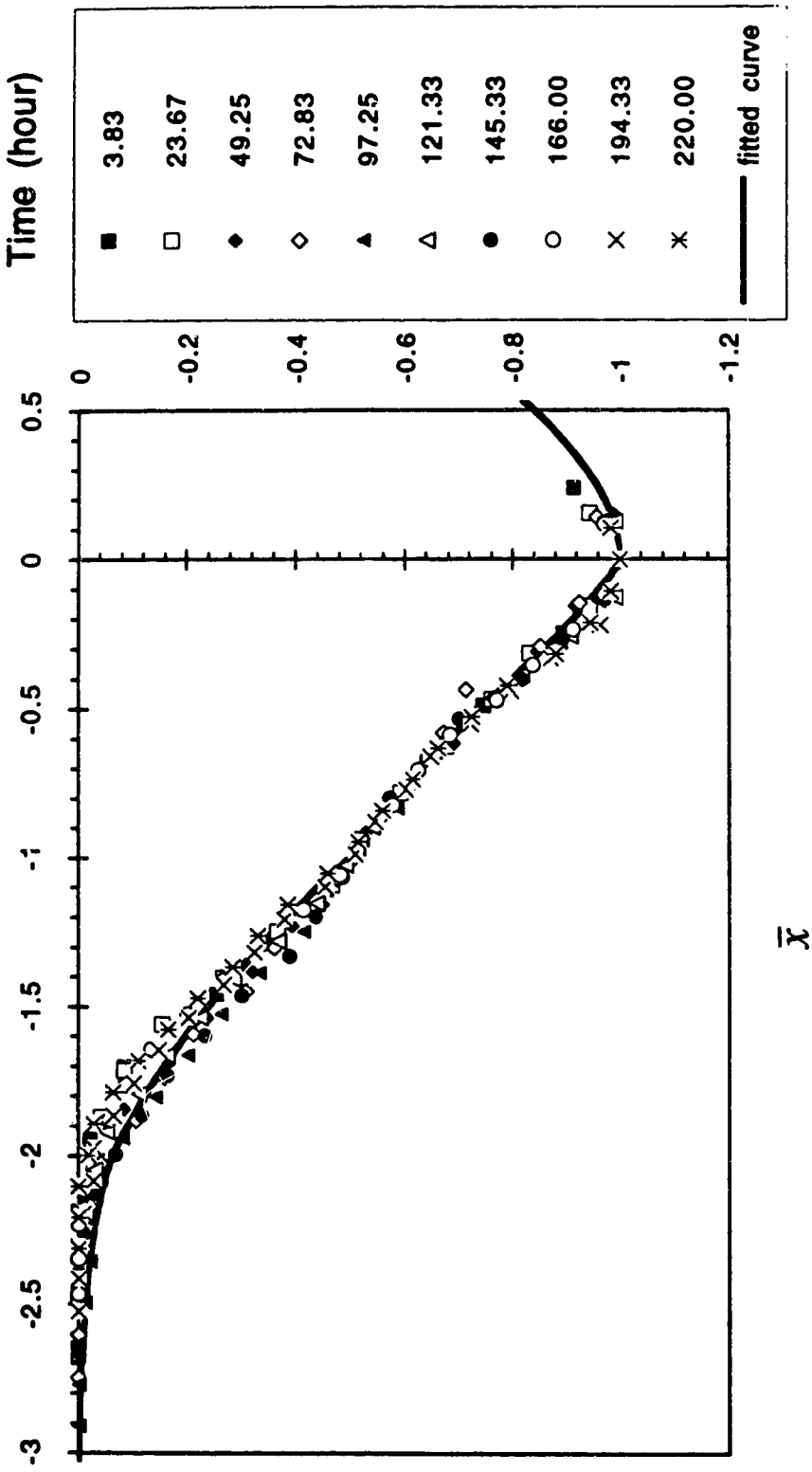

Figure 4.6.3 (a-d) Similarity of scour profile in front of cylinder
(c) Expt. A3M

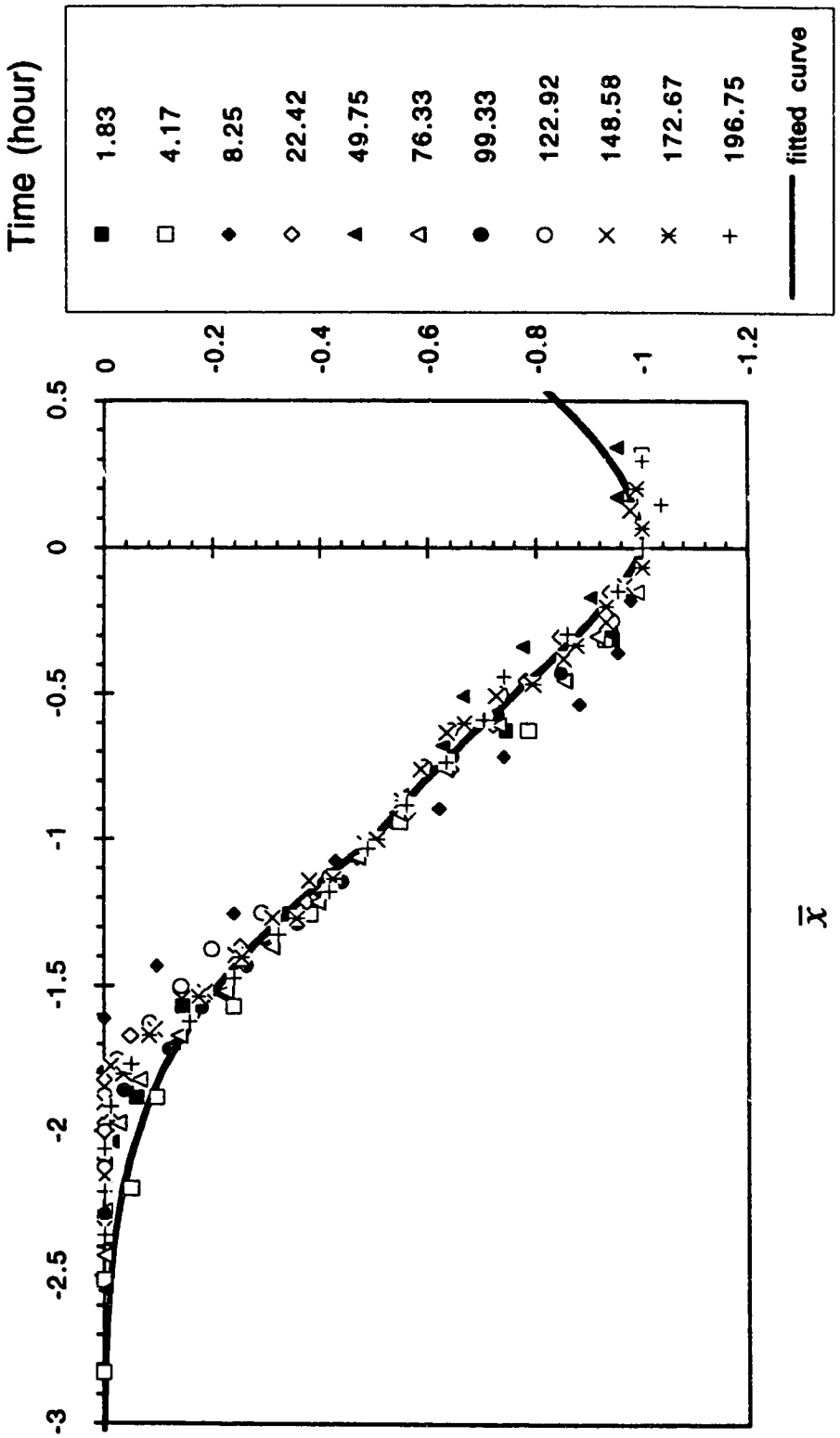

Figure 4.6.3 (a-d) Similarity of scour profile in front of cylinder
(d) Expt. A4M

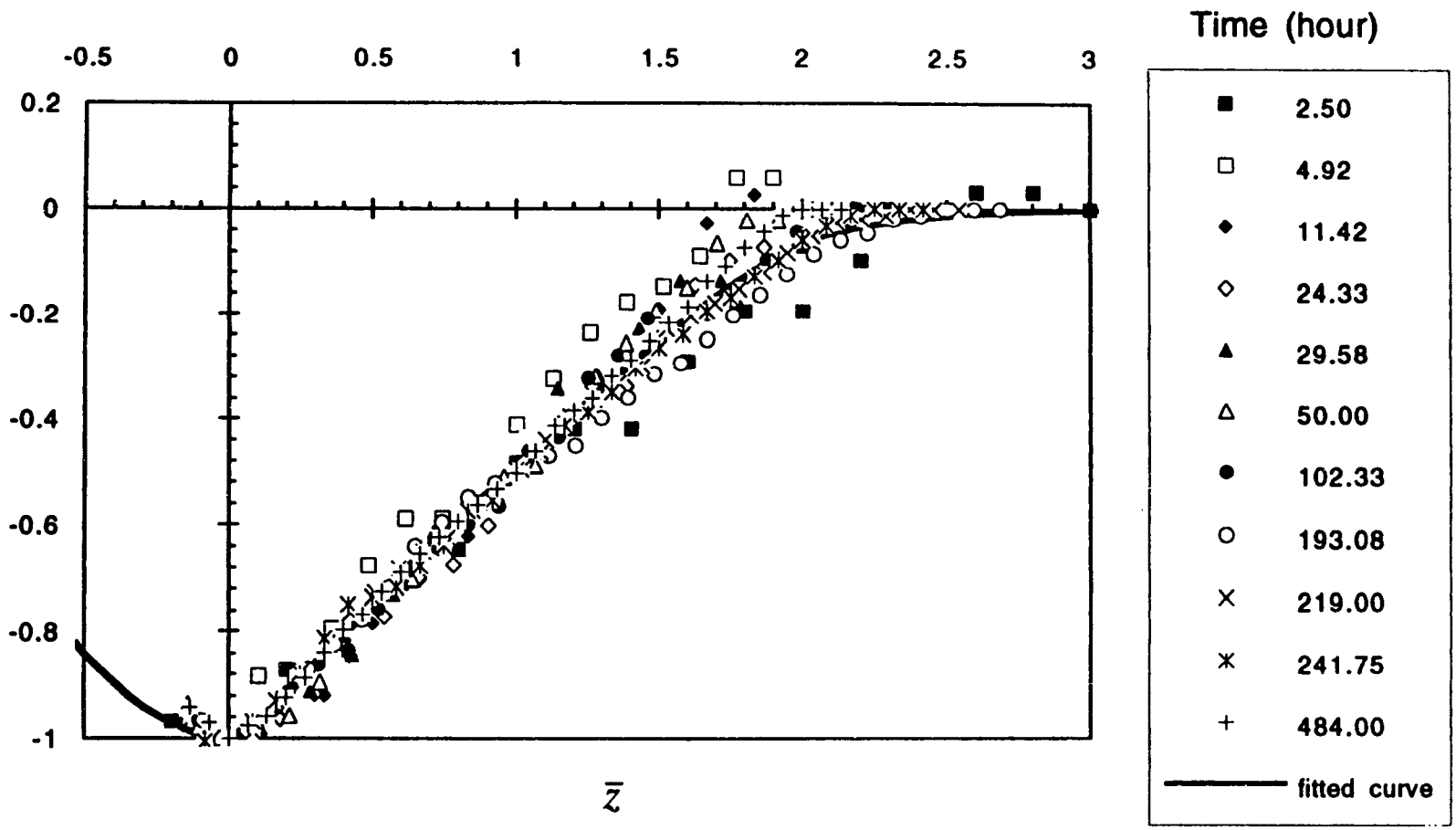

Figure 4.6.4 (a-b) Similarity of scour profile at the side of cylinder
(a) Expt. A1M

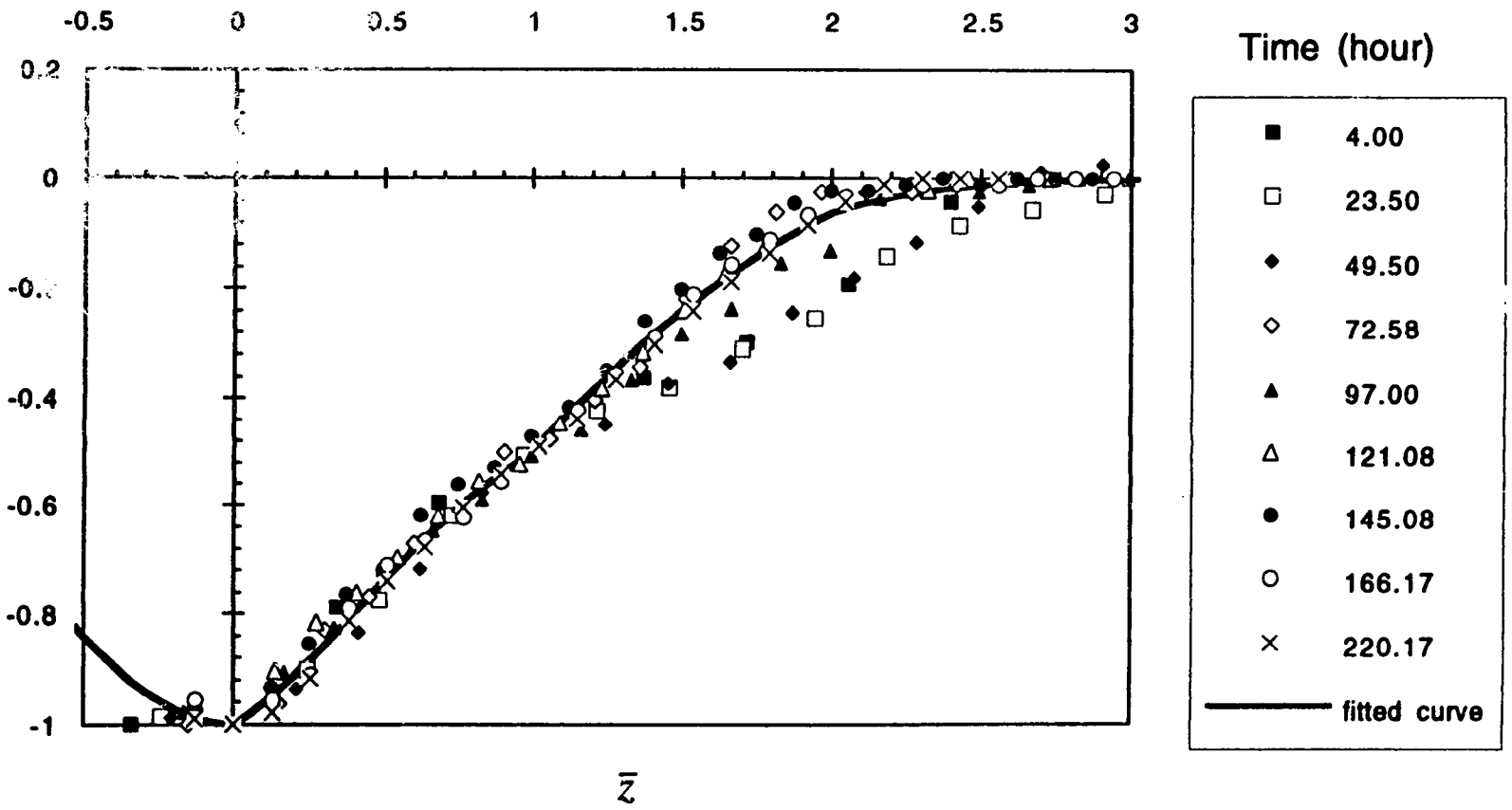

Figure 4.6.4 (a-b) Similarity of scour profile at the side of cylinder (b) Expt. A3M

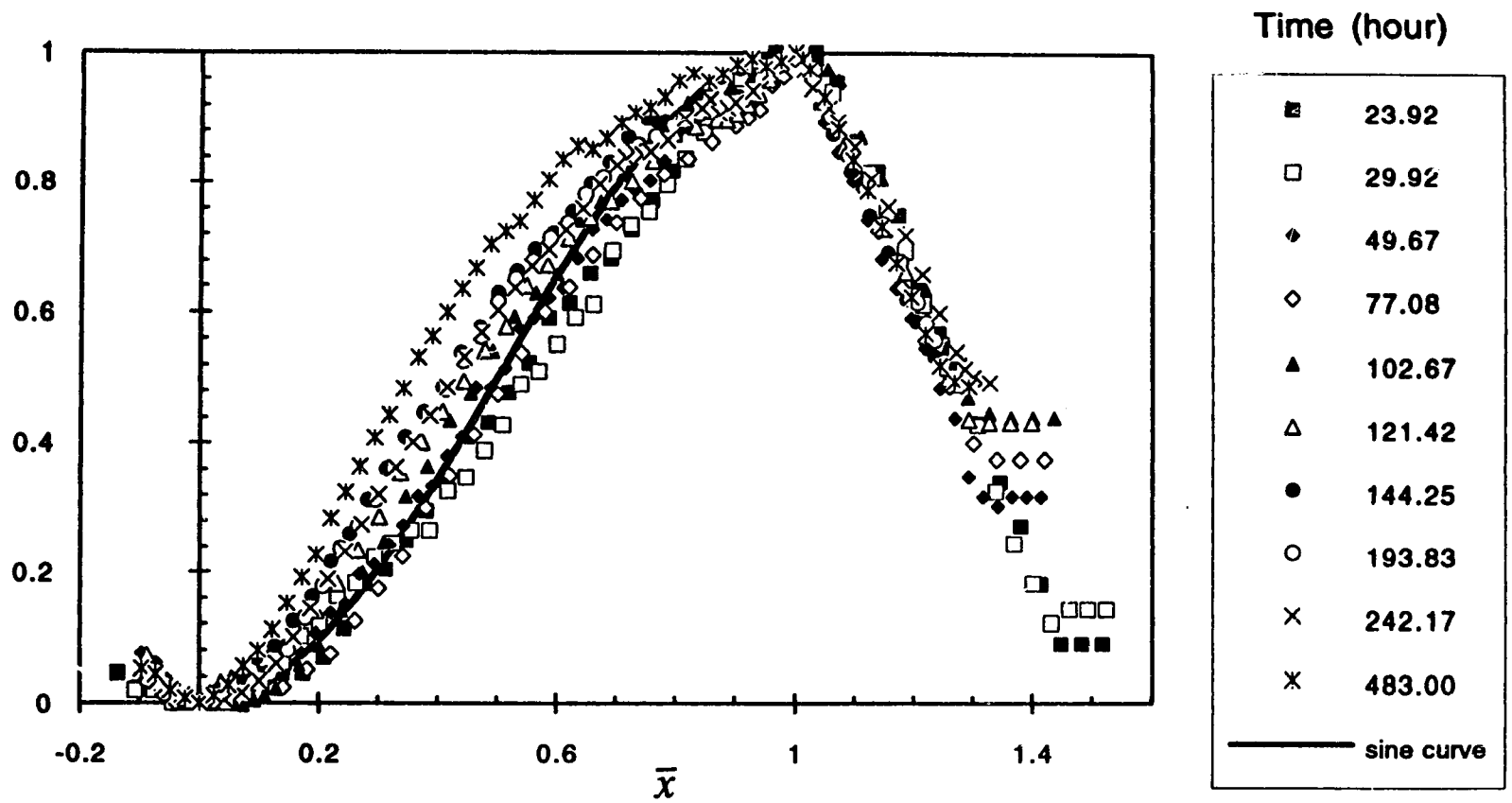

Figure 4.6.5 (a-b) Similarity of scour profile at the back of cylinder
(a) Expt. A1M

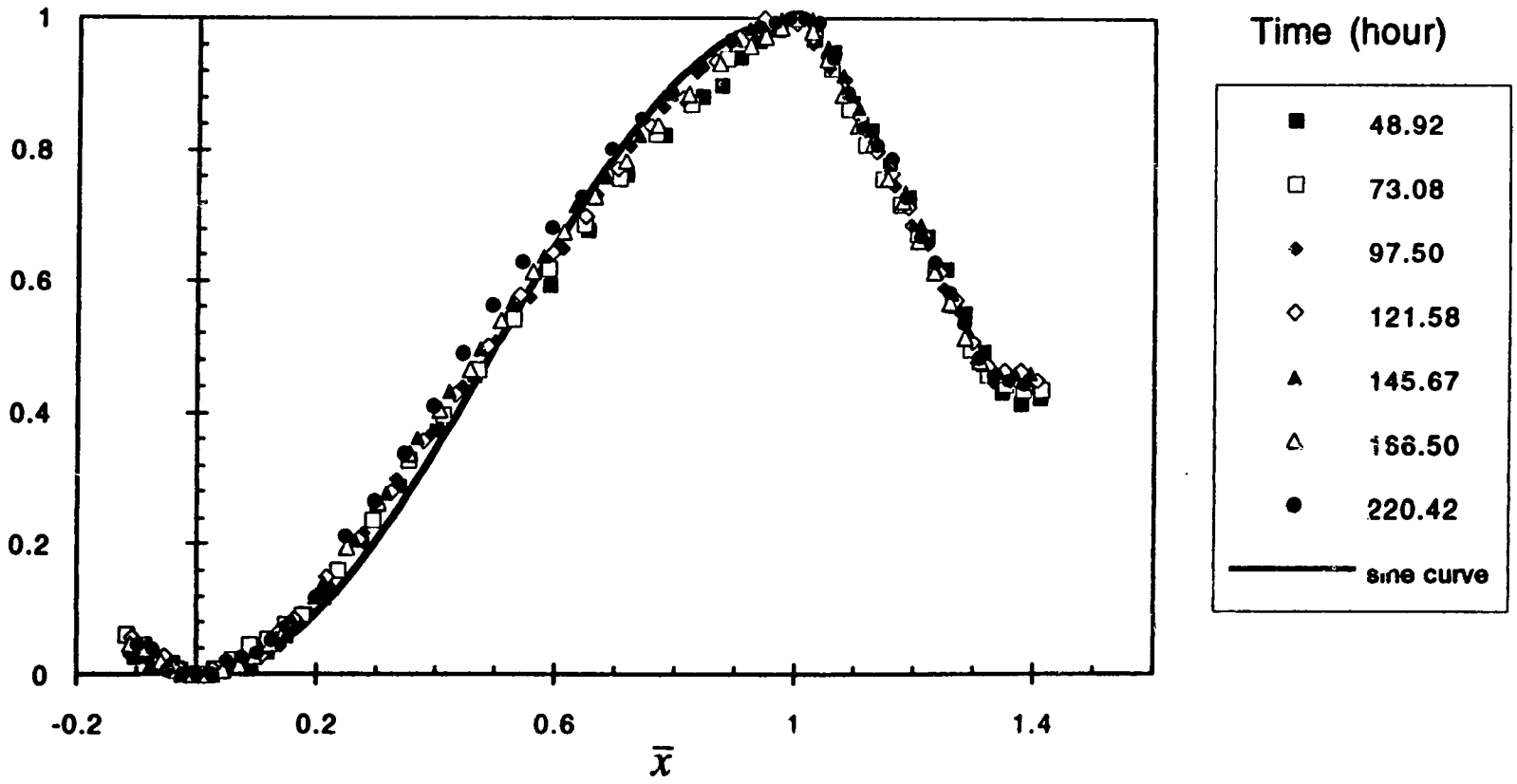

Figure 4.6.5 (a-b) Similarity of scour profile at the back of cylinder (b) Expt. A3M

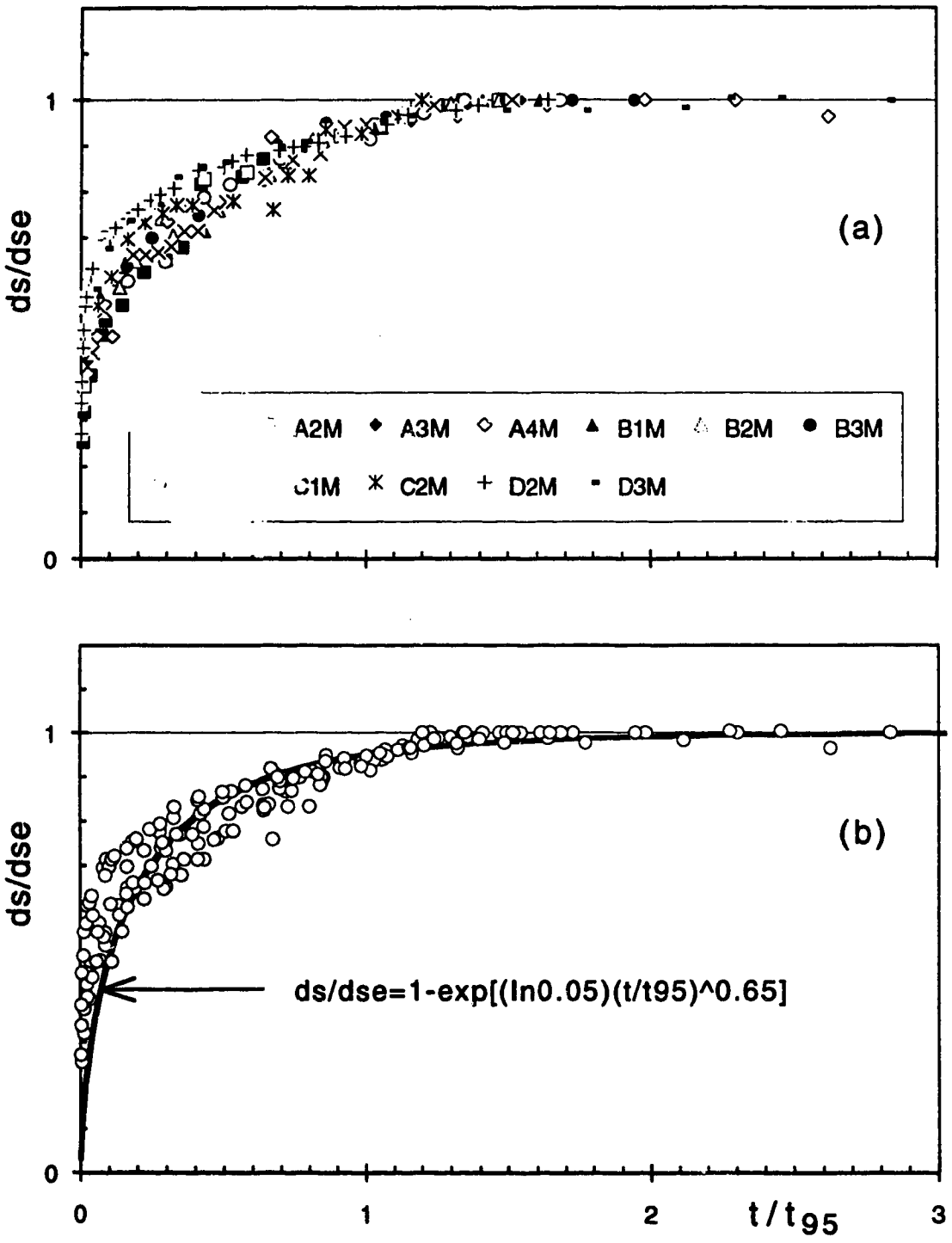

Figure 4.6.6 Similarity in the temporal growth of scour depth; (a) data from different experiments; (b) fitted line

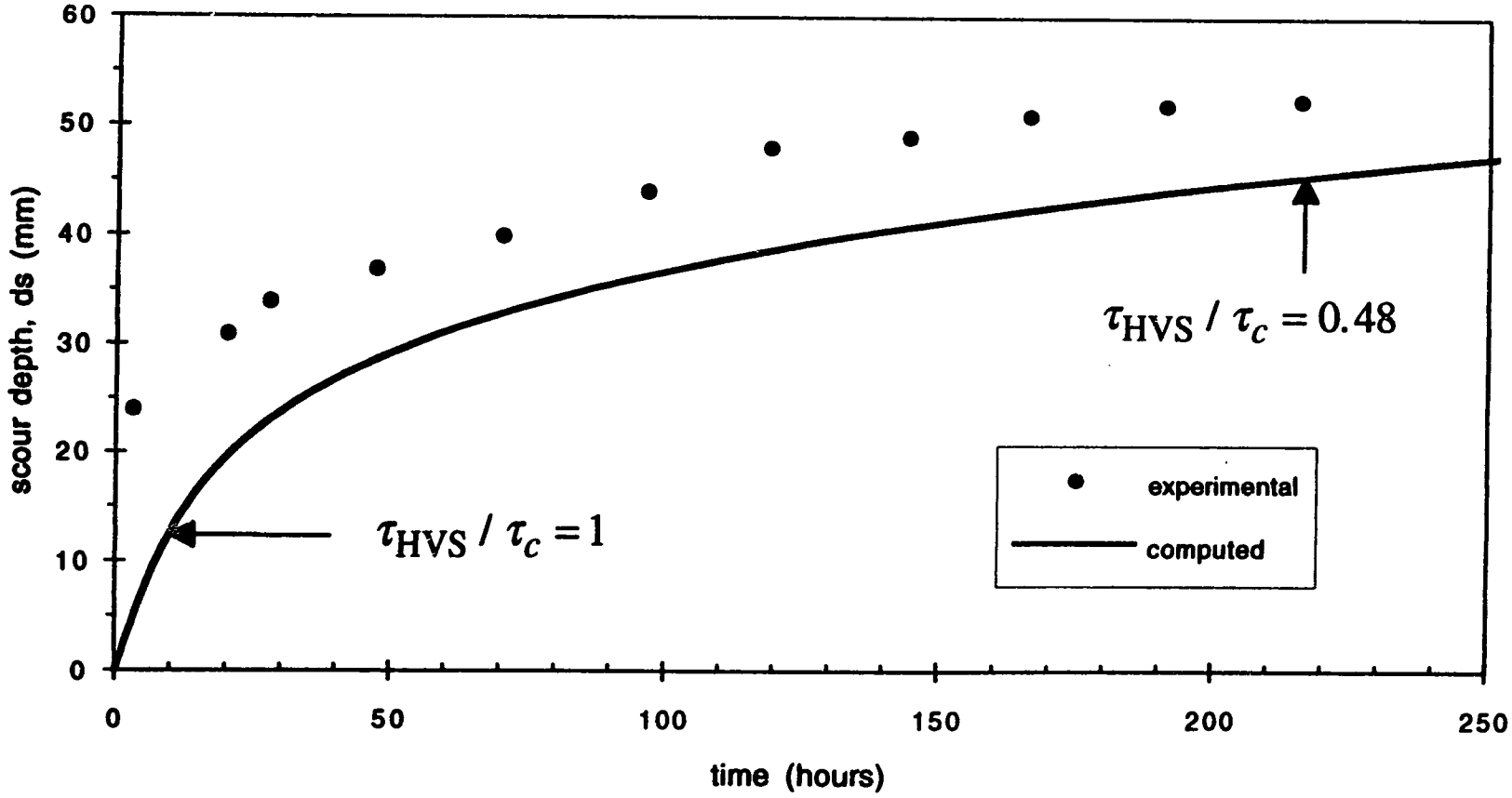

Figure 4.6.7 (a-c) Performance of Kothyari *et al.*'s model
(b) Expt. B2M

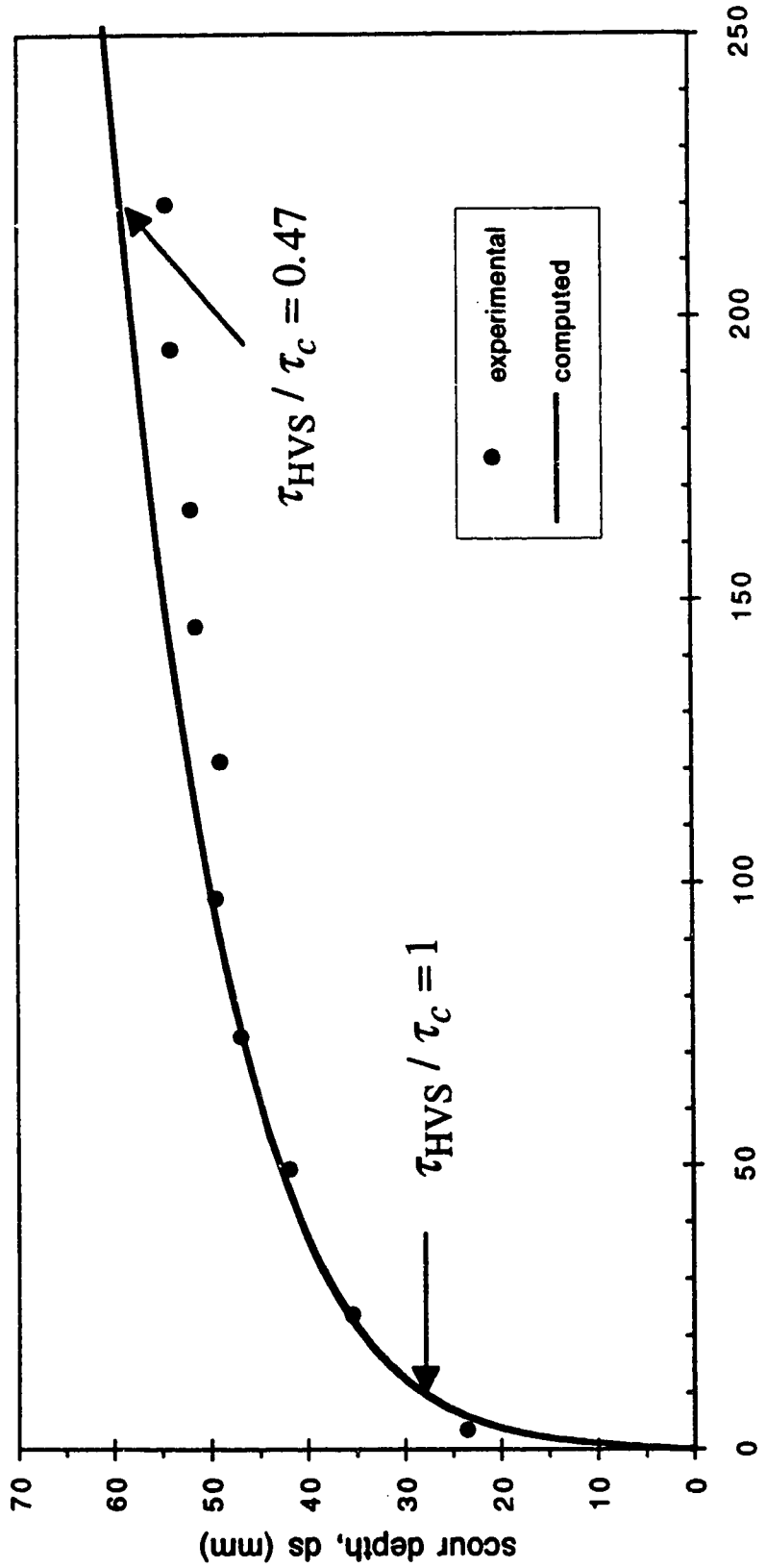

Figure 4.6.7 (a-c) Performance of Kothyari *et al.*'s model
(a) Expt. A3M

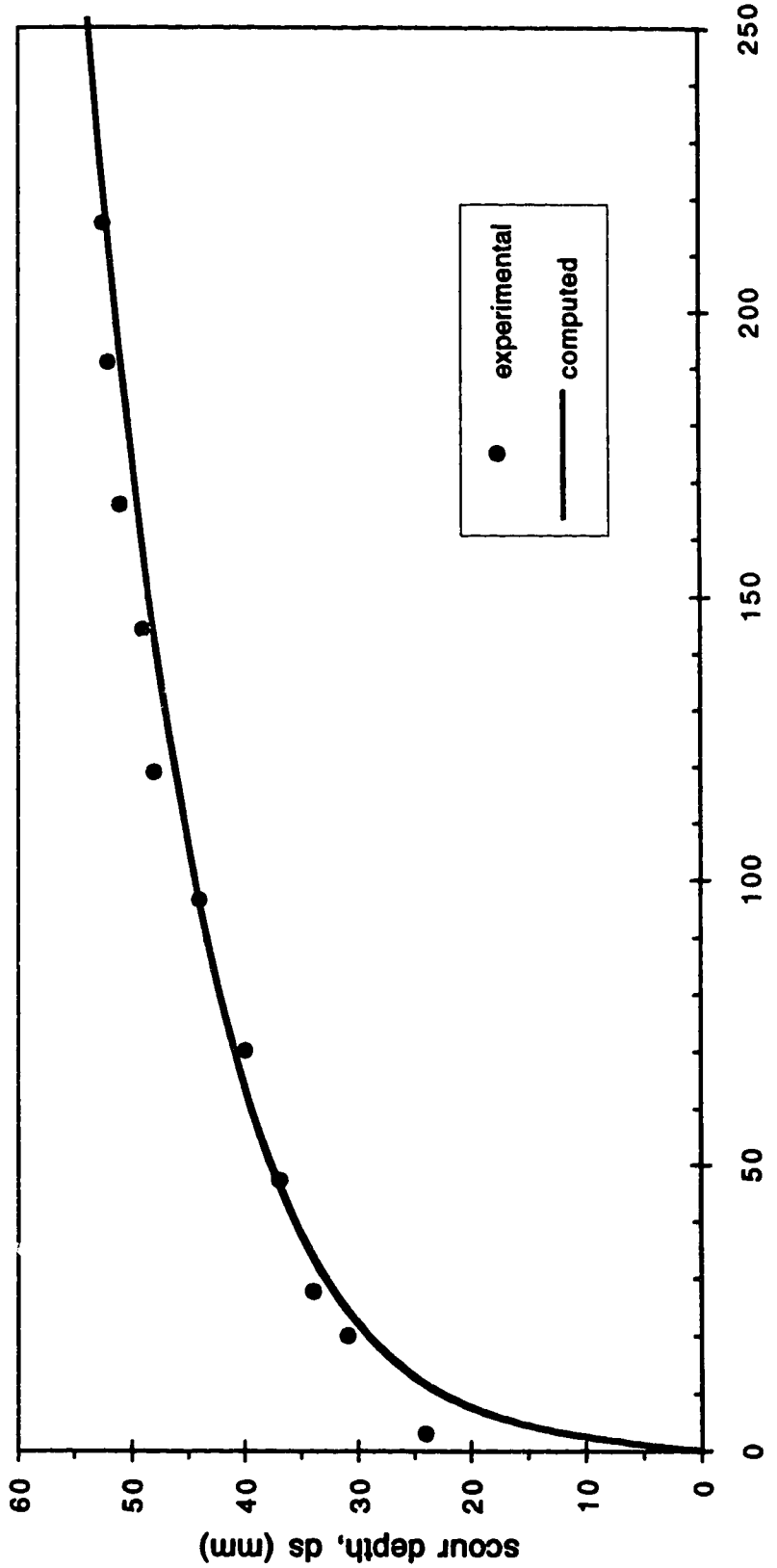

Figure 4.6.7 (a-c) Performance of Kothyari *et al.*'s model
(c) Expt. B2M with modified coefficients

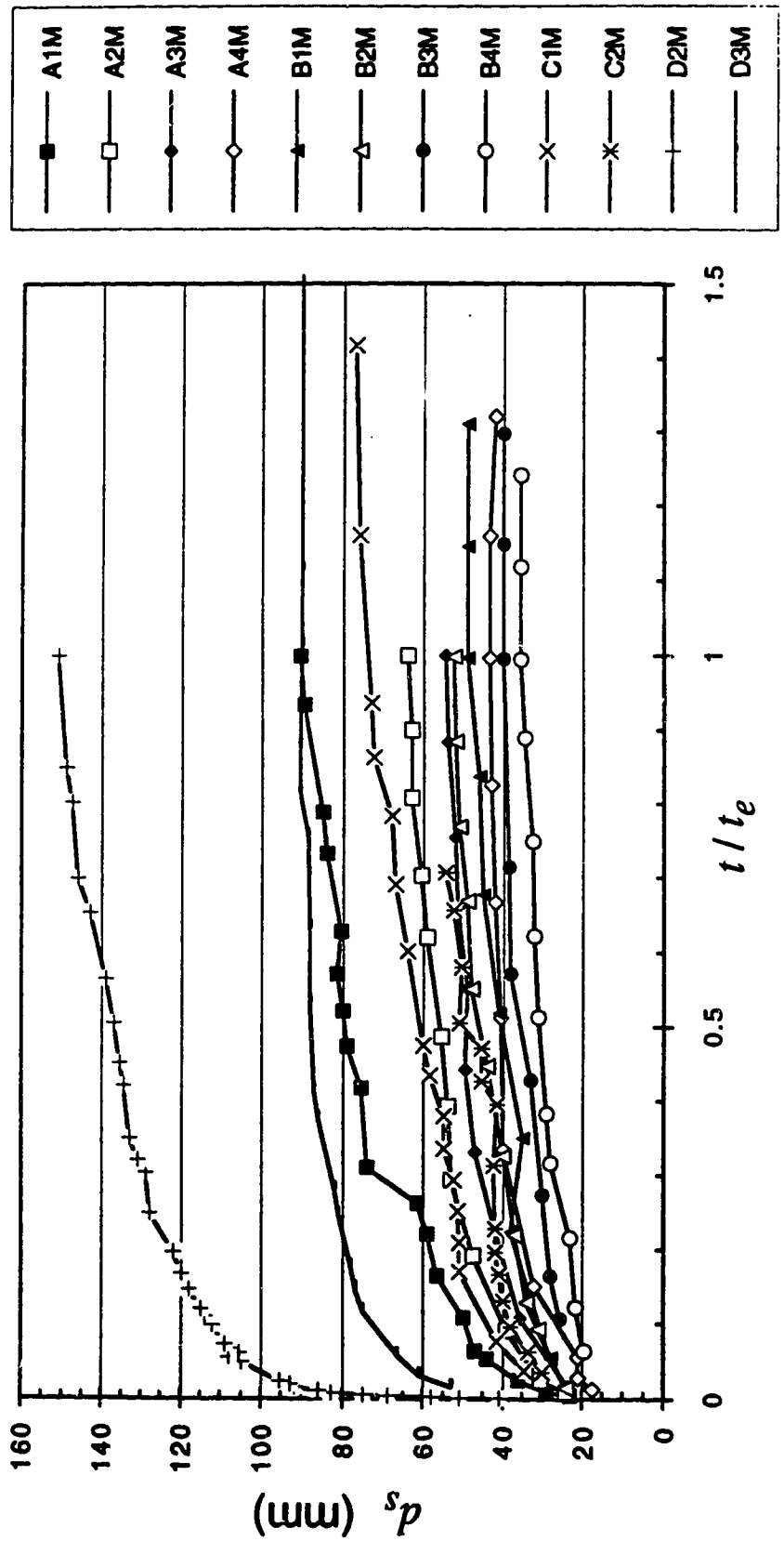

Figure 4.6.8 (a-k) Behavior of various length scales (a) scour depth, d_s

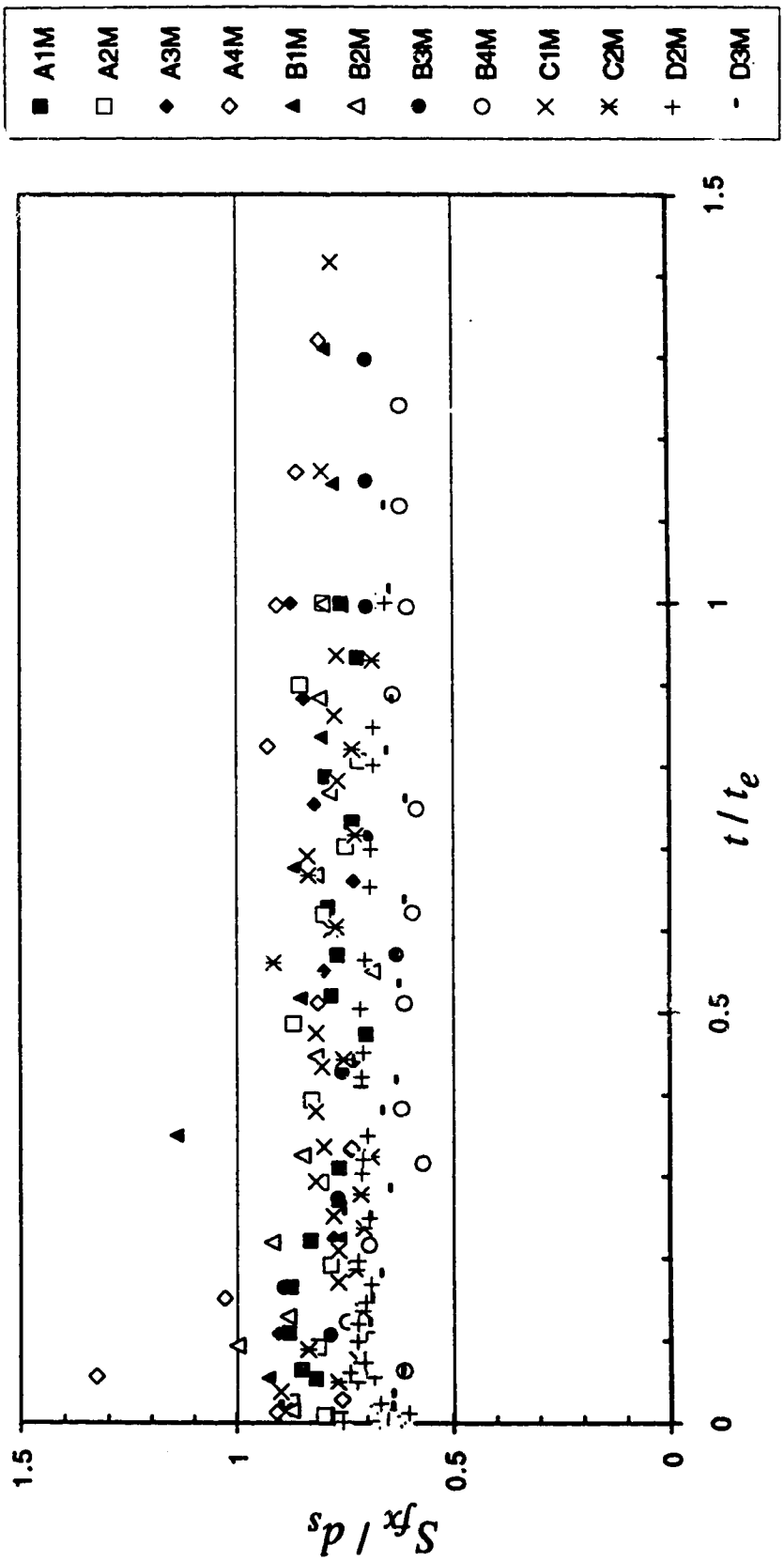

Figure 4.6.8 (a-k) Behavior of various length scales
(b) S_{fx} / d_s

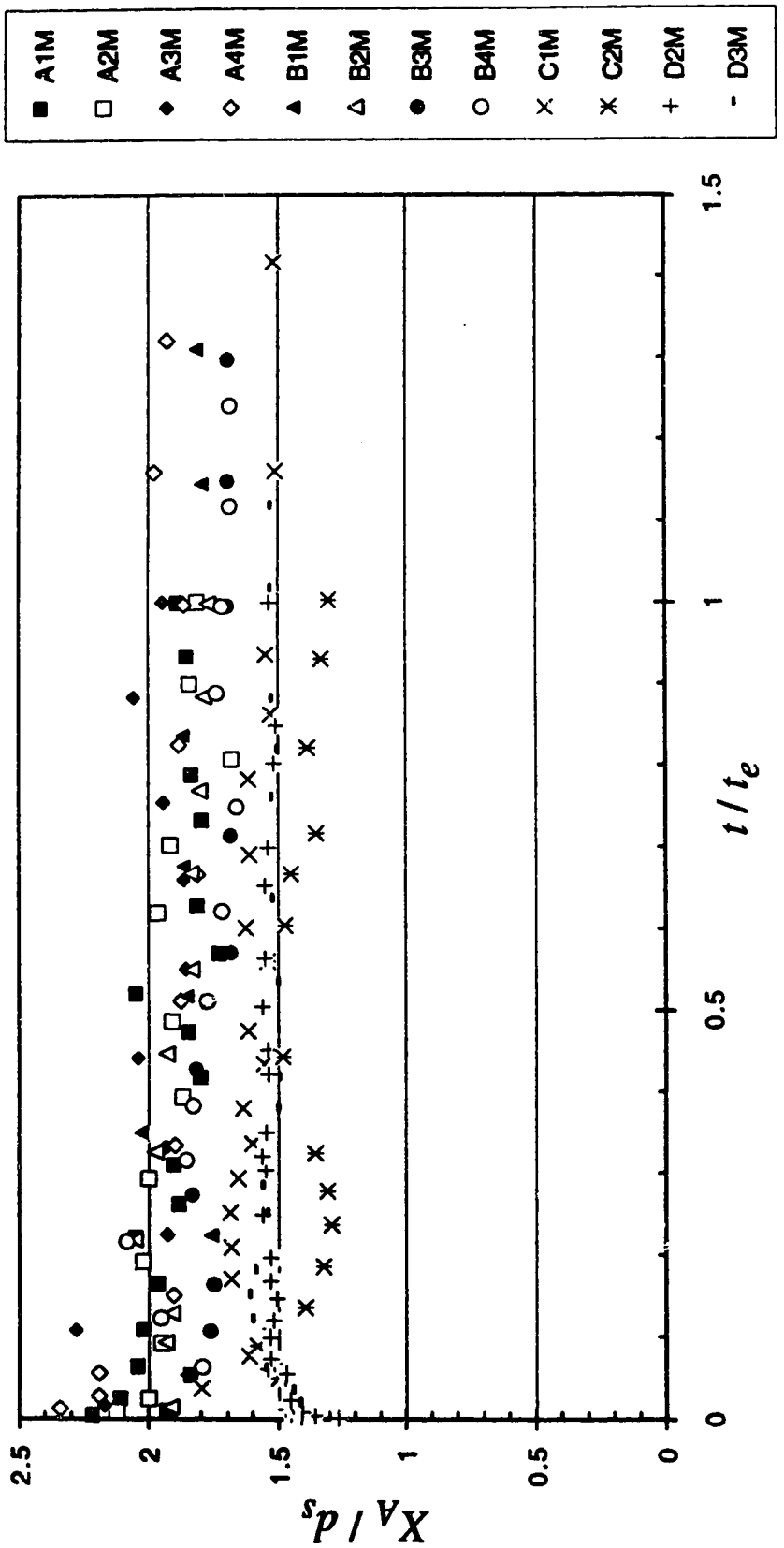

Figure 4.6.8 (a-k) Behavior of various length scales
(c) X_A / d_s

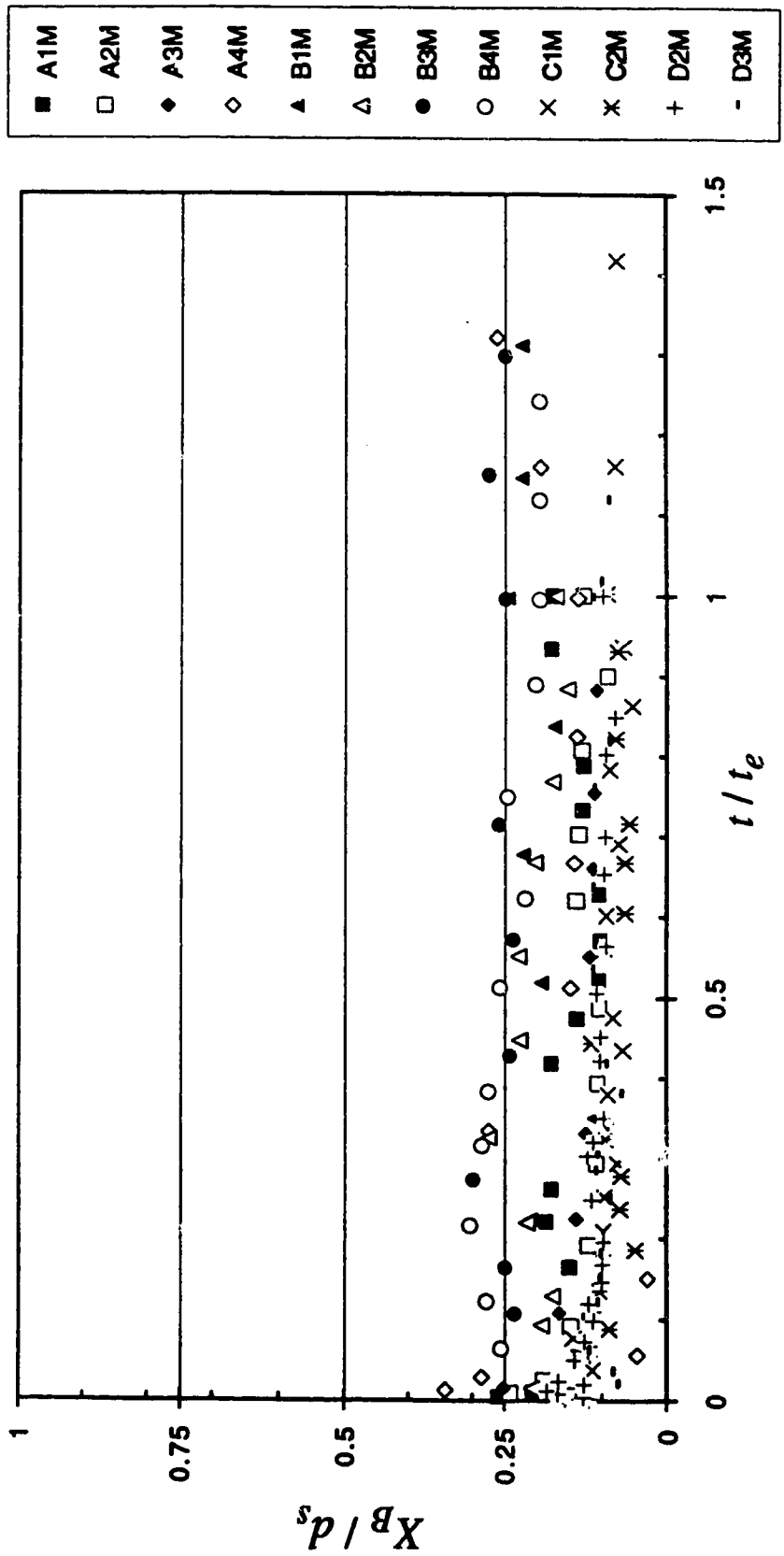

Figure 4.6.8 (a-k) Behavior of various length scales
(d) X_B / d_s

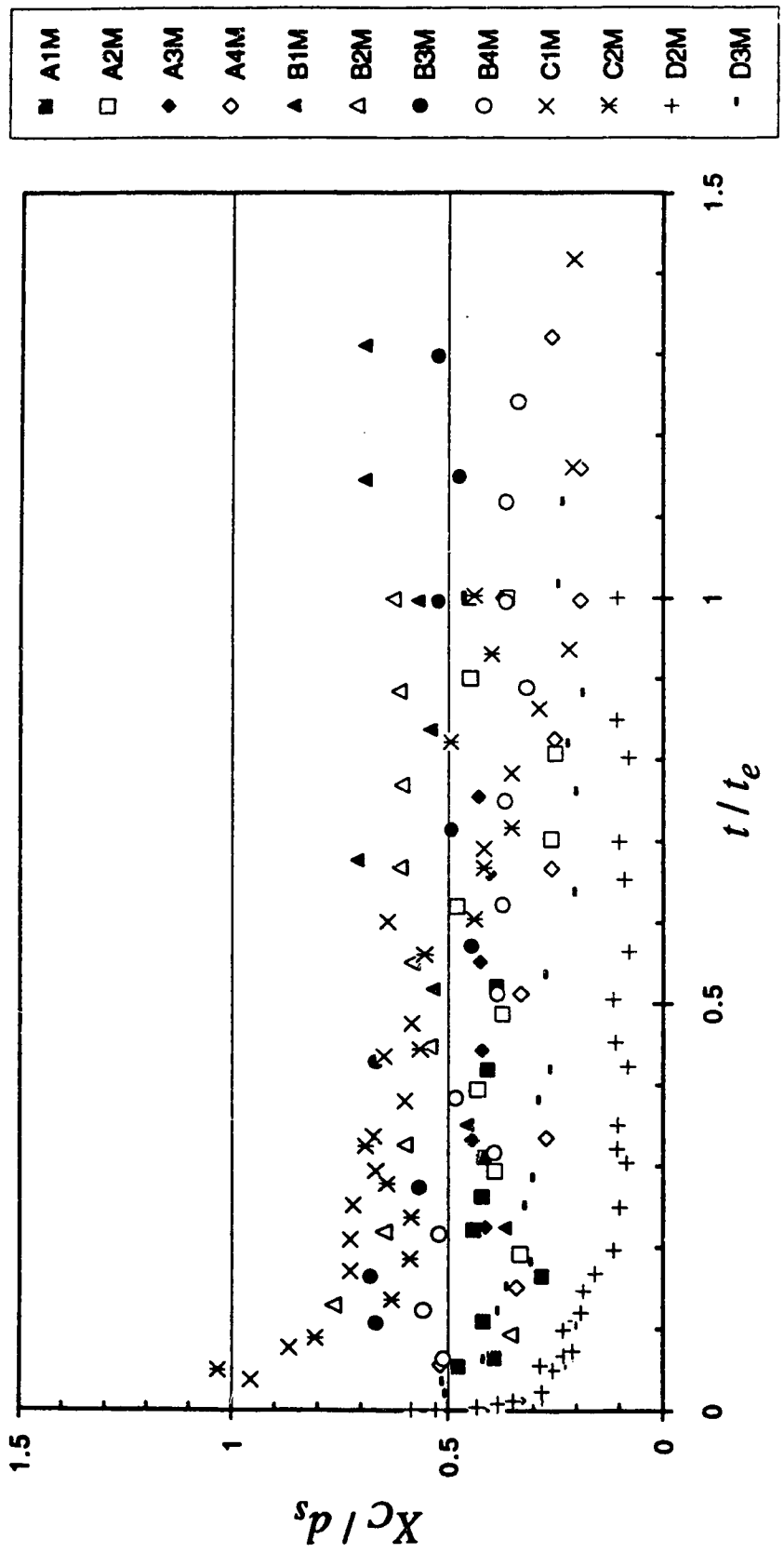

Figure 4.6.3 (a-k) Behavior of various length scales (e) X_C / d_s

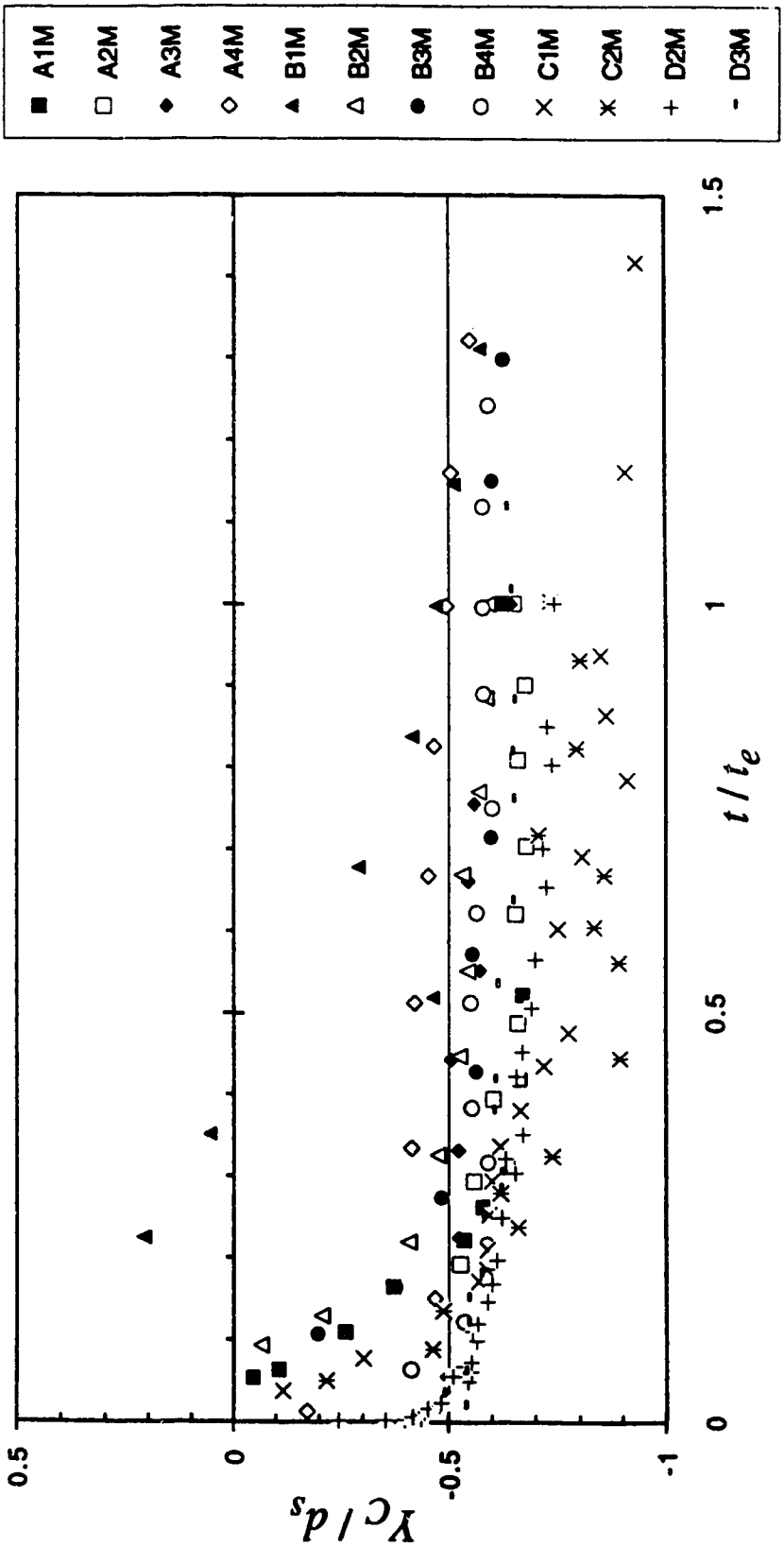

Figure 4.6.8 (a-k) Behavior of various length scales
(f) Y_C / d_s

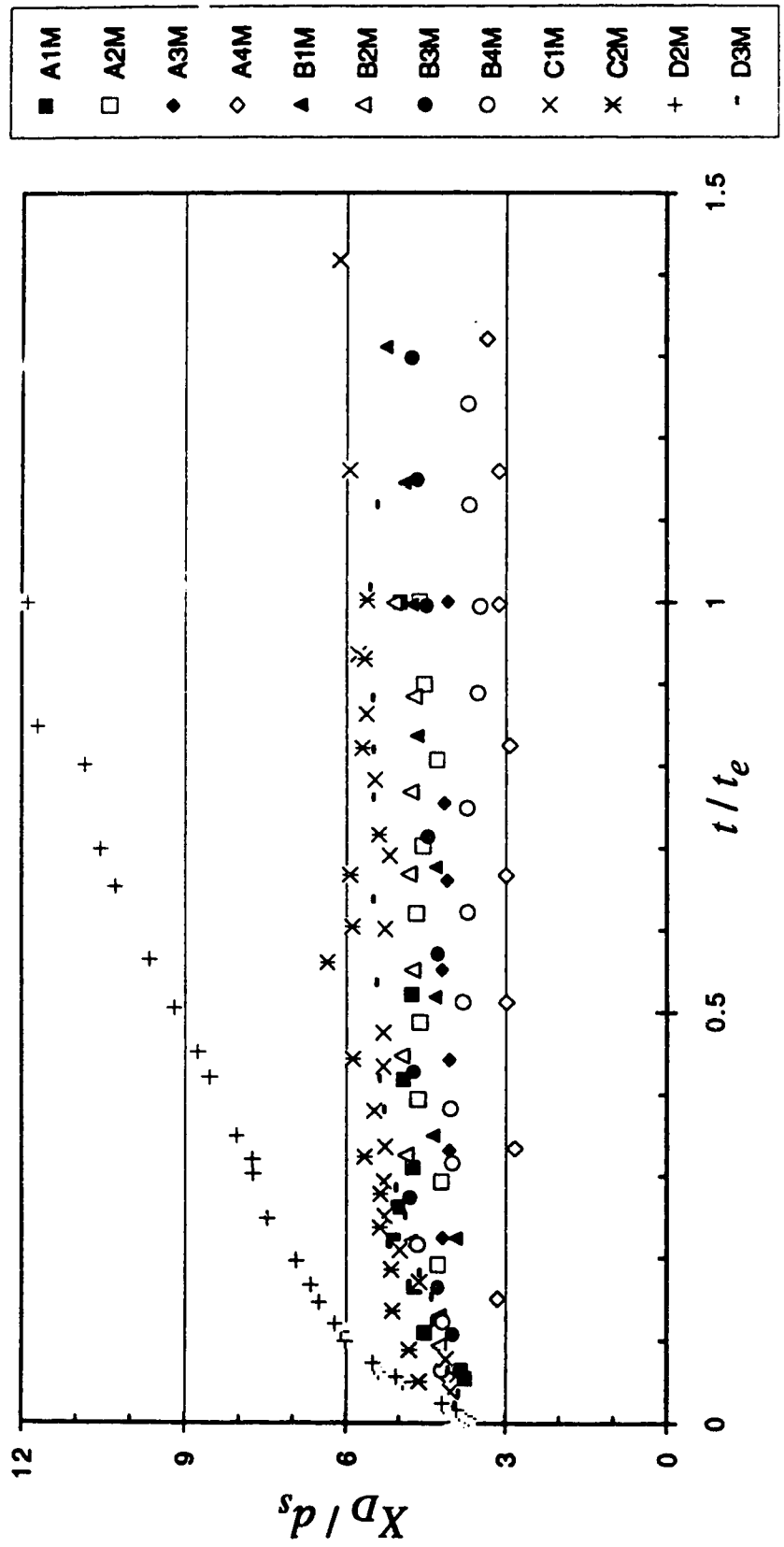

Figure 4.6.8 (a-k) Behavior of various length scales
(g) X_D / d_s

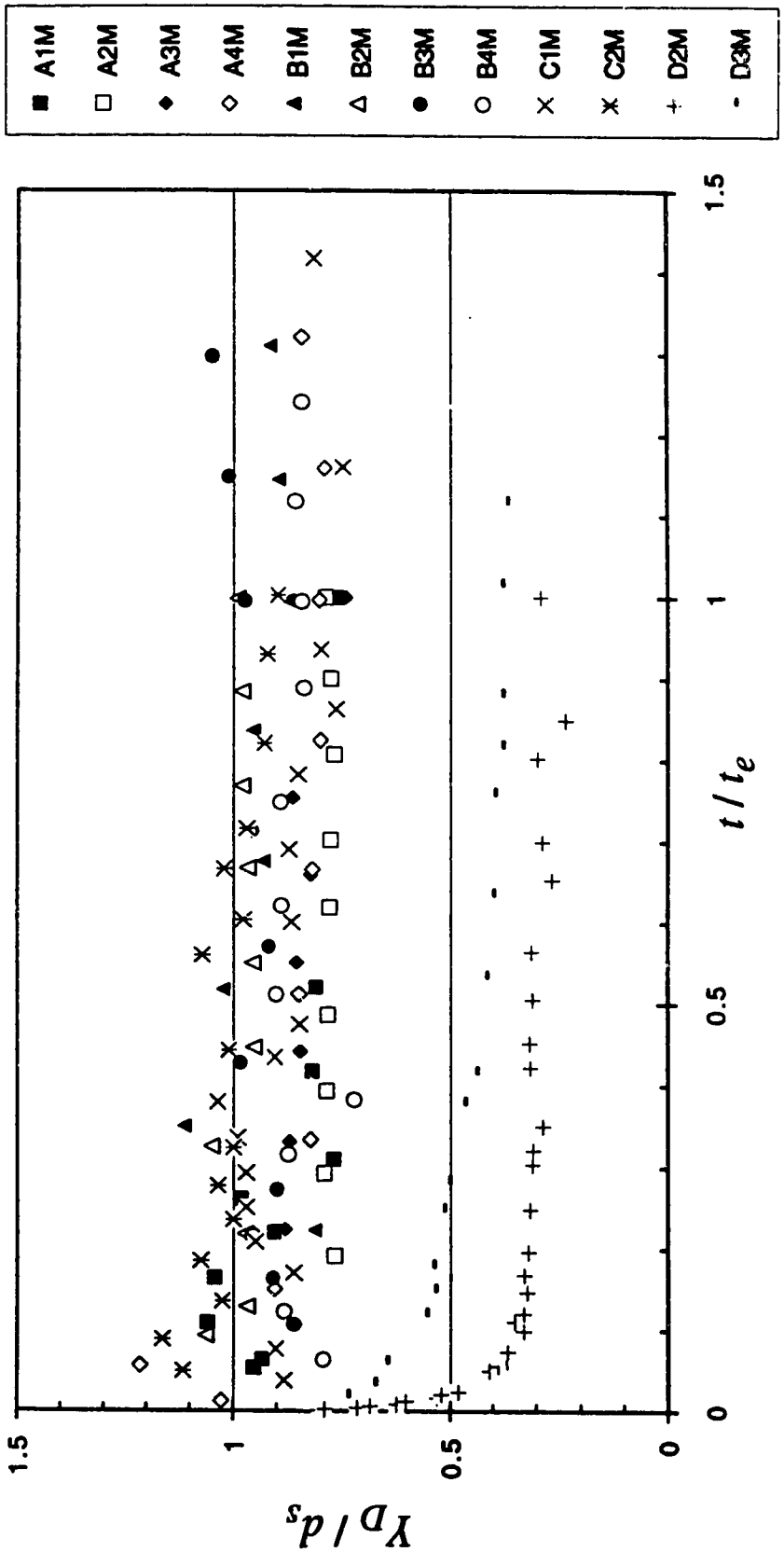

Figure 4.6.8 (a-k) Behavior of various length scales
(h) Y_D / d_s

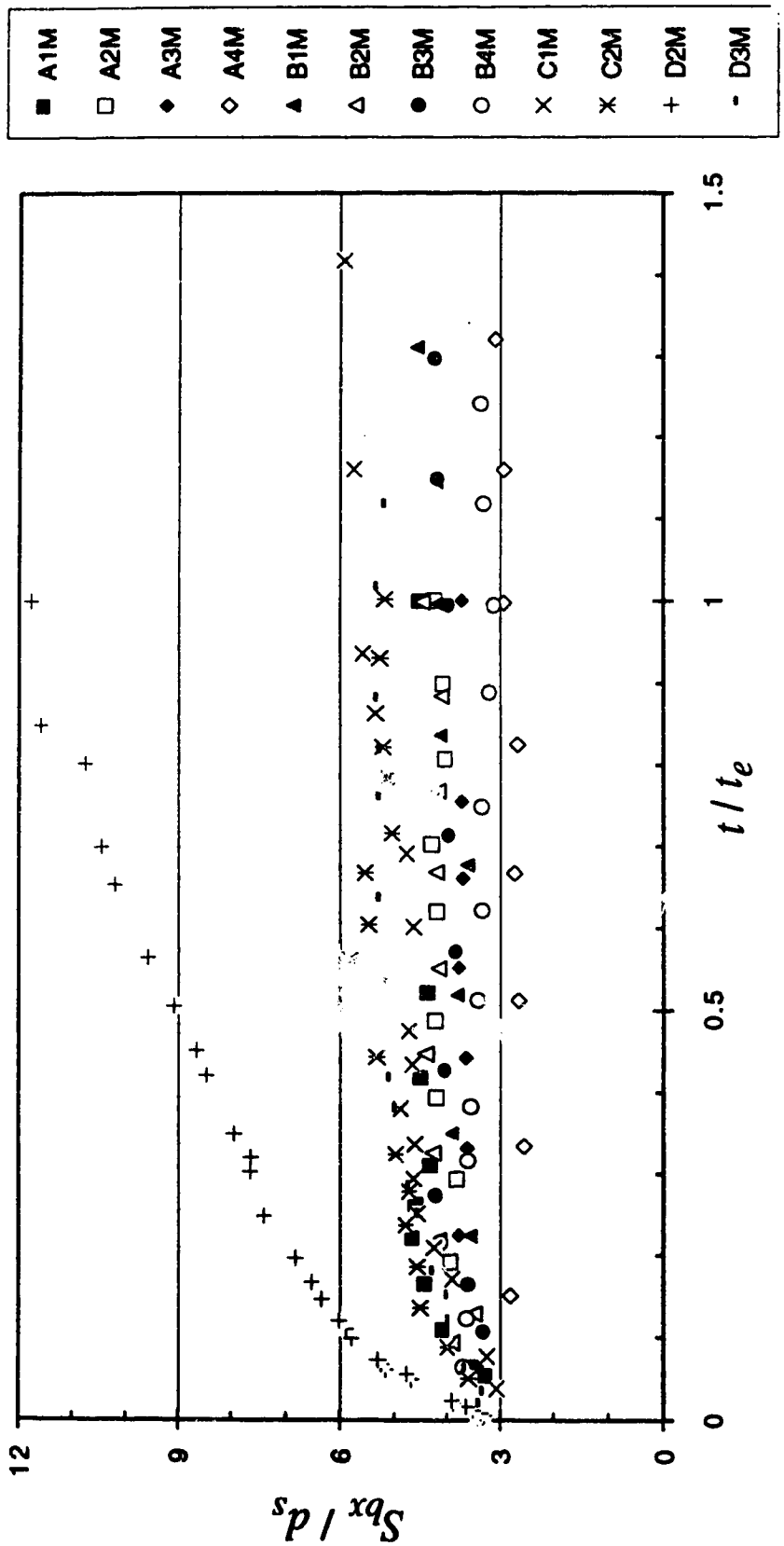

Figure 4.6.8 (a-k) Behavior of various length scales
(i) S_{bx} / d_s

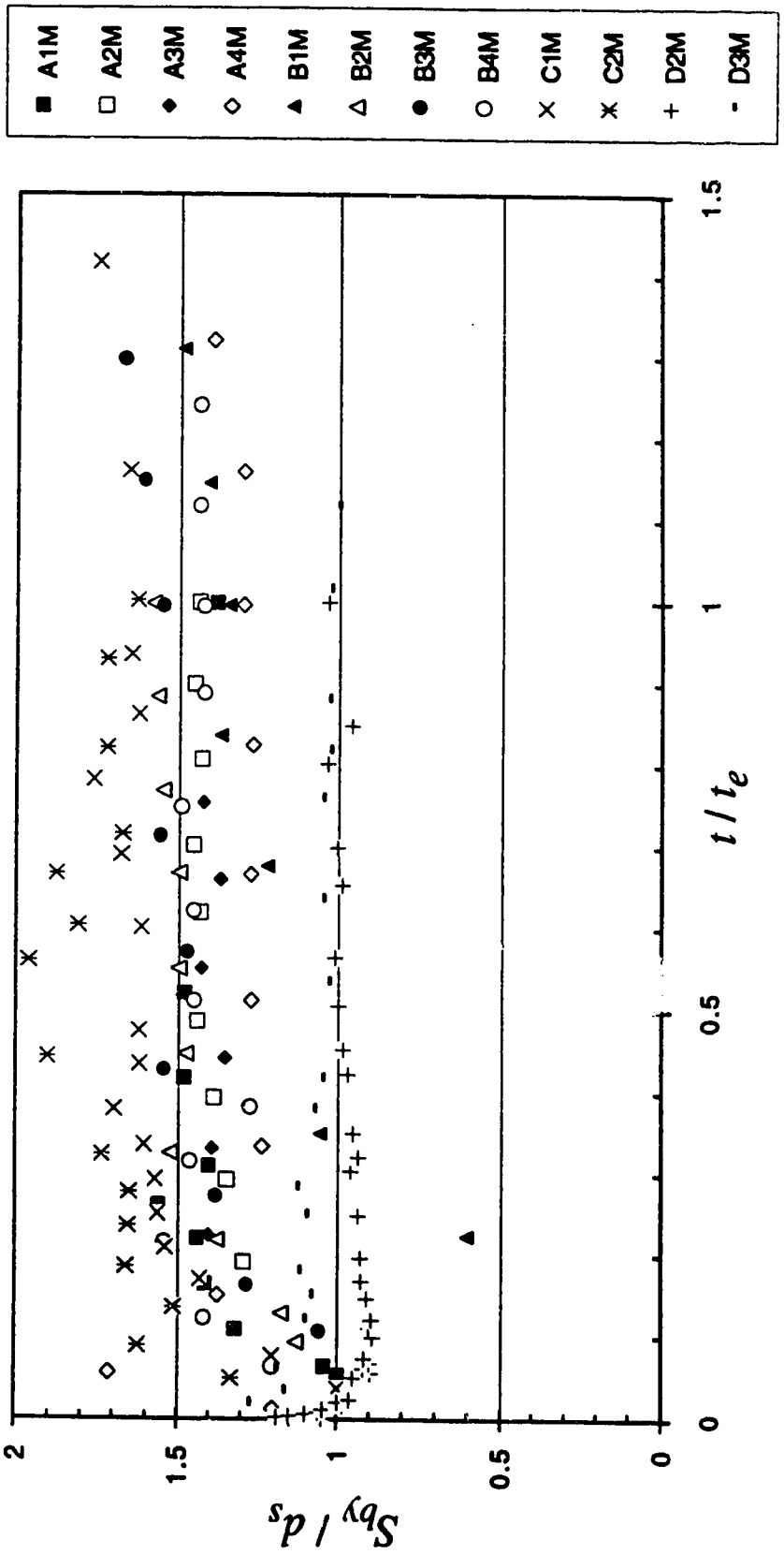

Figure 4.6.8 (a-k) Behavior of various length scales
(j) S_{by} / d_s

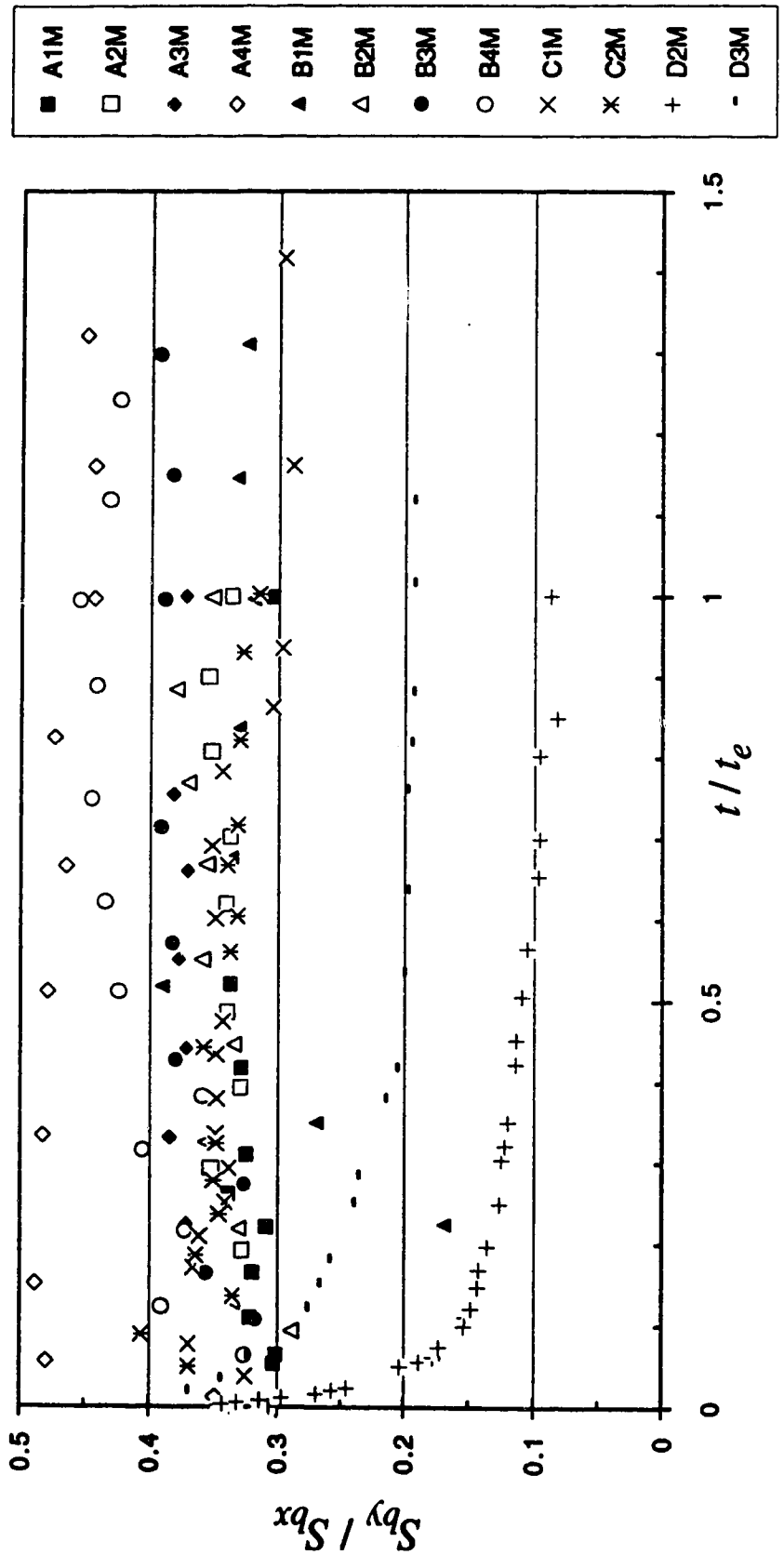

Figure 4.6.8 (a-k) Behavior of various length scales
(k) S_{by} / S_{bx}

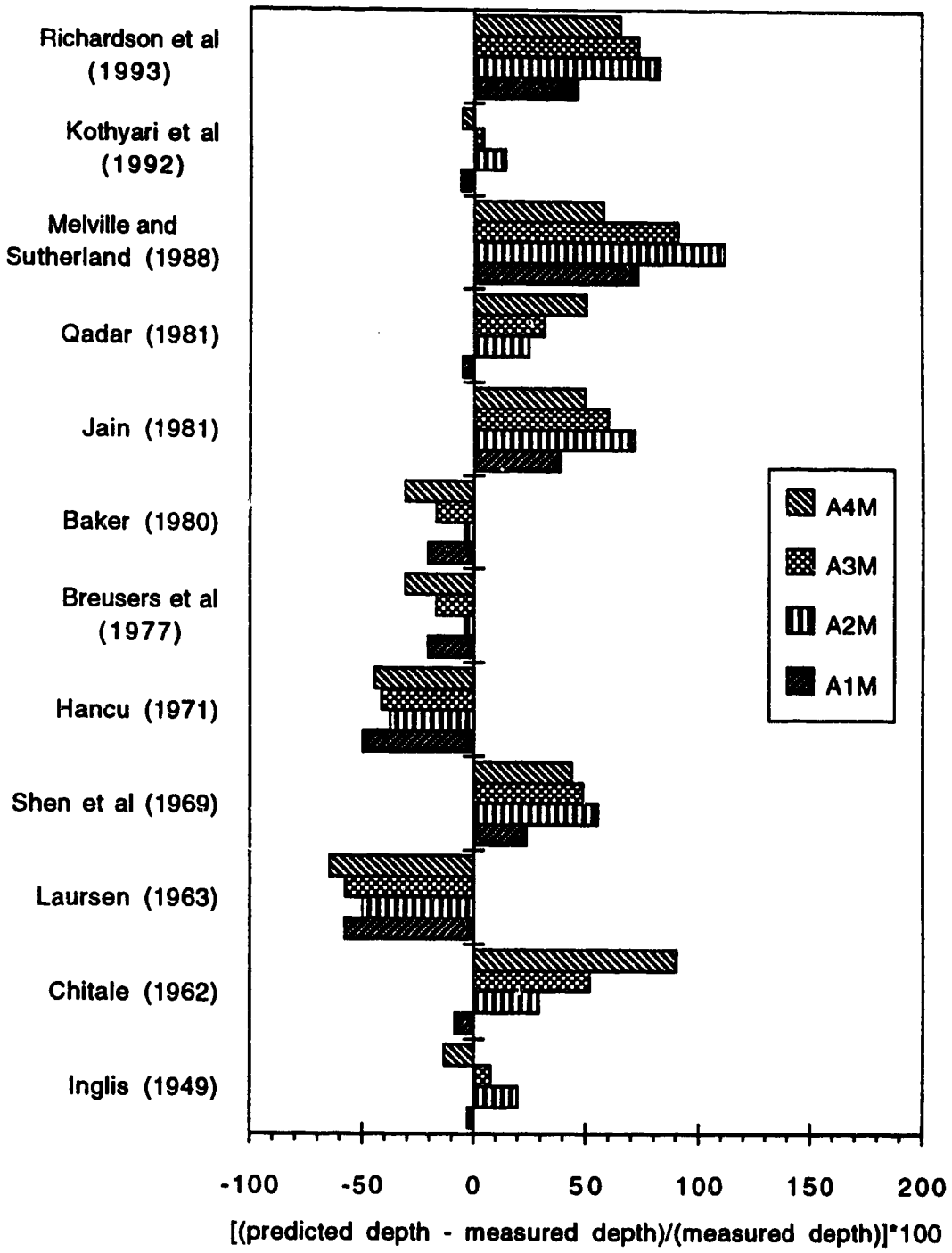

Figure 4.6.9 (a-c) Scour depth prediction; (a) Series A

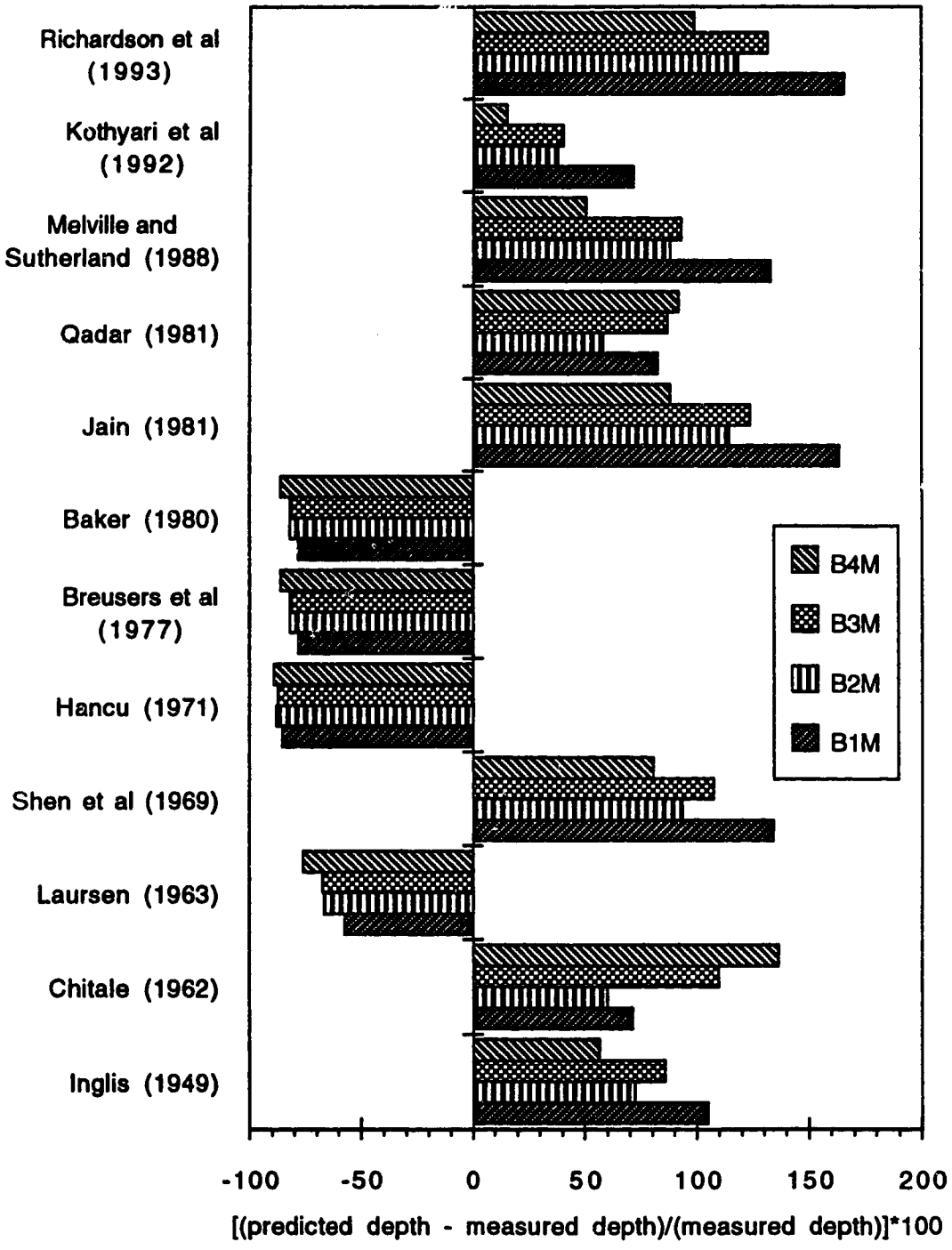

Figure 4.6.9 (a-c) Scour depth prediction; (b) Series B

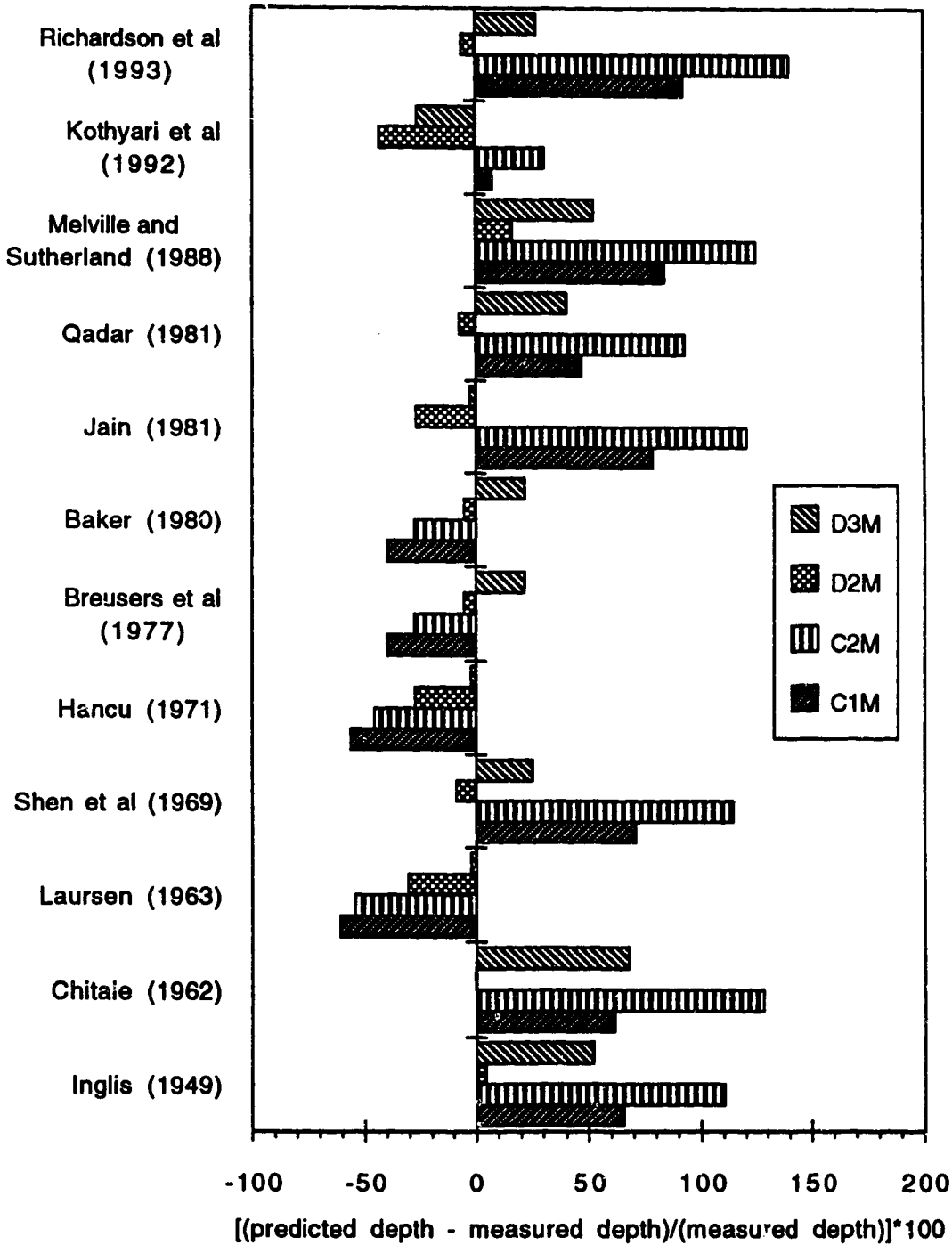

Figure 4.6.9 (a-c) Scour depth prediction; (c) Series C and D

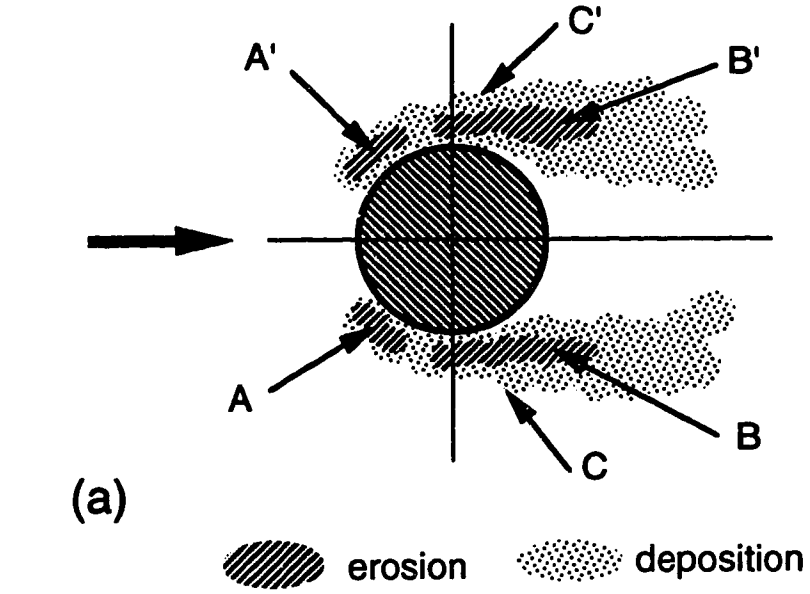

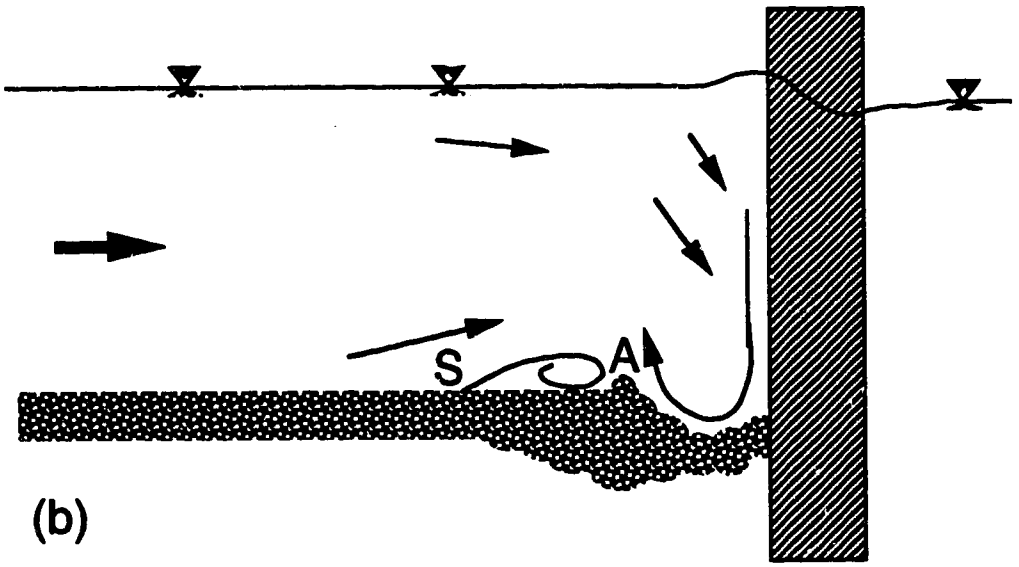

Figure 4.7.1 (a-f) Sketch of scouring process

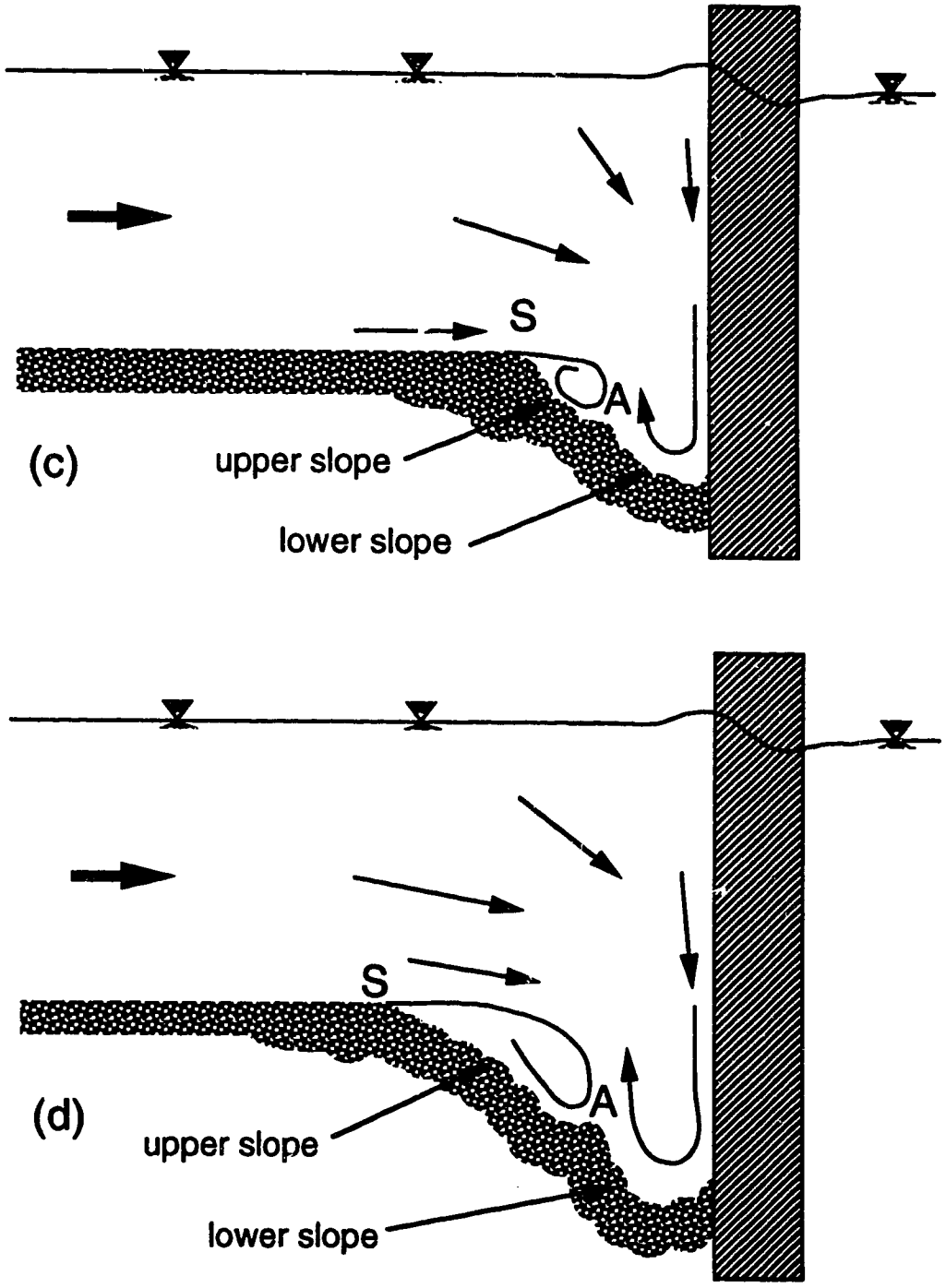

Figure 4.7.1 (a-f) Sketch of scouring process (continued)

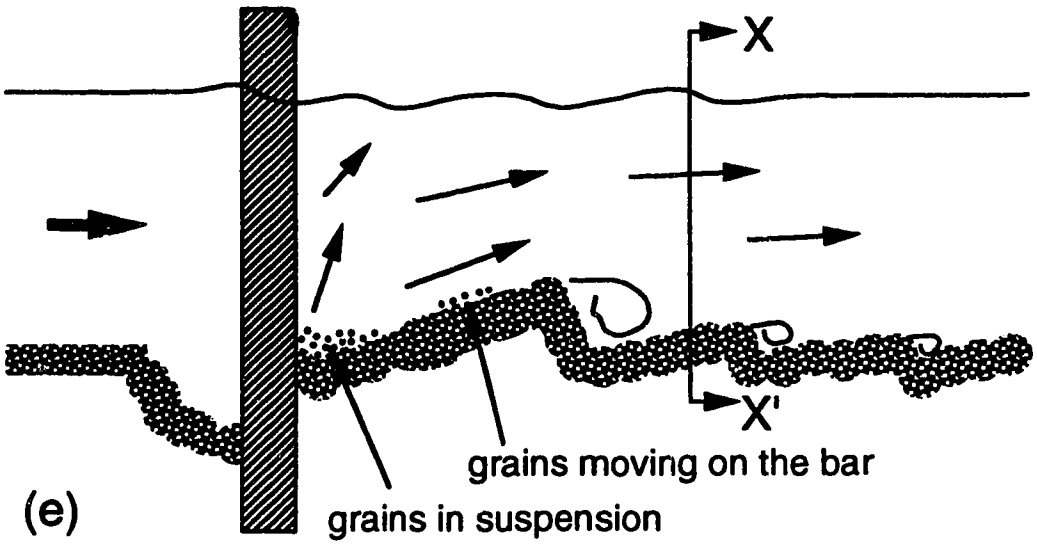

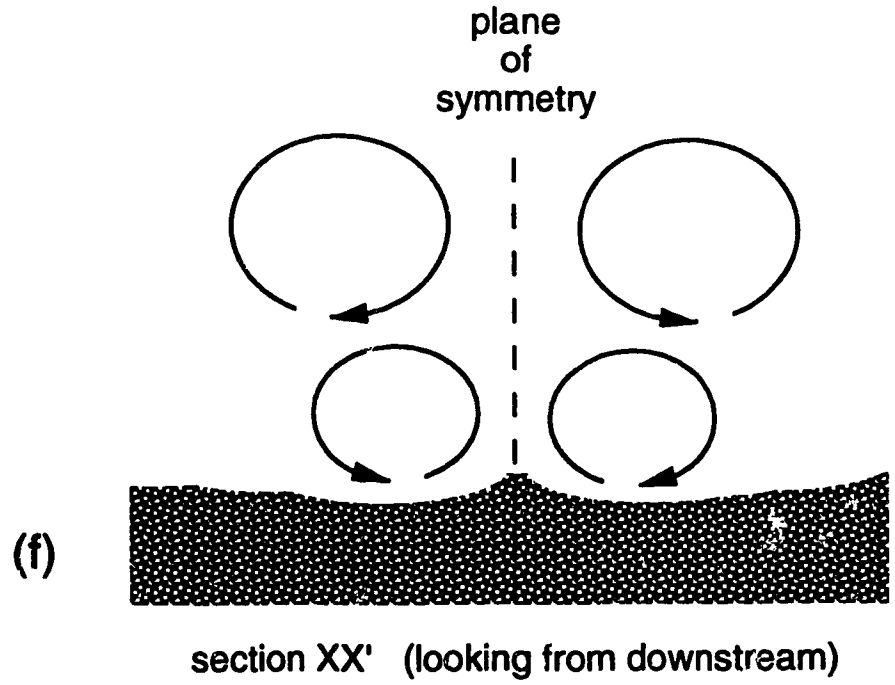

Figure 4.7.1 (a-f) Sketch of scouring process (continued)

(a) ⇑ (b) ⇓

Figure 4.7.2 (a-d) Pictures of scouring

(c) ⇑ (d) ⇓

Figure 4.7.2 (a-d) Pictures of scouring (continued)

(a) Expt. A3M, fine sand ⇑ (b) Expt. D2M, course sand ⇓

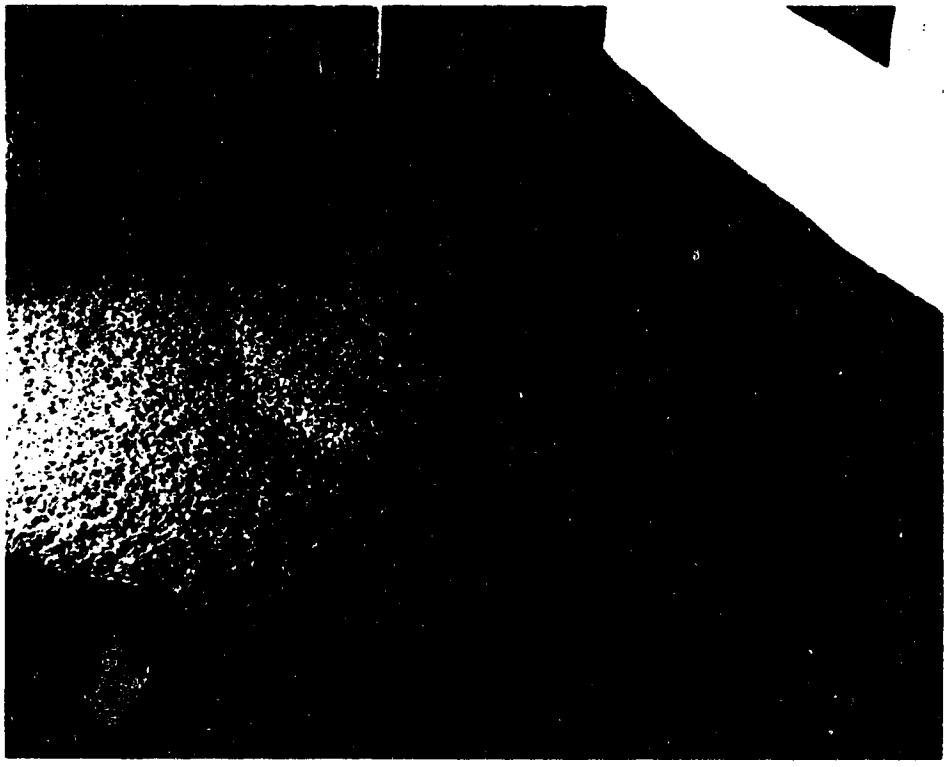

Figure 4.7.3 (a-b) Pictures of overall scour pattern

Chapter 5
Conclusion and Recommendations

5.1 Summary

In this thesis, a systematic investigation on the flow around a circular cylinder on smooth and rough beds (both with and without scour holes) and the associated local scour has been presented. A brief summary of this work follows. This is based on the more detailed discussions given in Sections 2.6, 4.8 and 4.9.

The flow around a cylinder is profoundly influenced by the scour hole. A part of the flow goes through the hole, thus relieving the accelerated flow on either side of the cylinder to some extent. It also allows more fluid to remain on and near the plane of symmetry (POS) in the upstream region, thus mitigating the skewing effect. For larger holes, the flow near the bed converges towards the POS. The variation of mass and momentum fluxes as well as other boundary layer (BL) parameters on the POS reflects these effects.

Due to experimental limitations, the horseshoe vortex system (HVS) could not be studied. From visual observations it appears, however, that the HVS plays an indirect role in erosion process through its contribution to the accelerated flow on either side of the cylinder. The effects of the downflow can be noticed only when the scour hole is well developed. Neither of them initiates the scouring on their own and once the hole is formed, the vortices become rather diffused and unable to erode sand grains. At this stage the downflow plays an active role by impinging on the bed and removing sand particles from the groove.

In the downstream region, two jet-like flows from either side of the cylinder enter into the wake through the scour hole. This induces higher velocities, less fluctuation, and less pressure drop in the wake. Some effect of the scour hole is found on the pressure distribution just behind the cylinder. The rear bar prevents the flow from converging towards the POS.

The primary effects of roughness are a stronger downflow and less skewing in the upstream region. The amplification of bed shear stress is much greater and the zone of influence of the cylinder increases. And bed shear vectors become more aligned with the longitudinal direction. The roughness effect in the wake region is not apparent.

The analysis of the flow in the light of three-dimensional turbulent boundary layer (3DTBL) theories, especially the polar plots, gave valuable insight into the effects of the roughness and the scour hole on the flow, irrespective of the applicability of various models. The model of Perry and Joubert worked well for the present experiments, especially when the stations were far away from the cylinder. Near-wall similarity models were tested only for the smooth bed runs. All the models gave nearly identical results because of the very small cross-flows. Results are better for the stations far away from the cylinder. So far no near-wall model has been proposed for rough walls. When developed, such models will be much useful for their obvious utility in the understanding of sediment transport under skewed 3DTBL flows.

The shape of the scour hole and rear bar remains similar with time and from experiment to experiment when normalized by proper scales. In the front of the cylinder, all linear scales are closely related to the scour depth, except the width of the groove which seems to depend on the sand size. In the downstream side, different scales behave differently and seem to depend on different parameters. For example, the distance of the deepest point behind the cylinder seems to depend on the shear ratio of the approach flow whereas the depth depends on the sand size. More studies are required to confirm and supplement these preliminary findings. There seems to be no simple time scale.

The performances of different scour prediction formulas are inadequate, with no improvement with time or theoretical basis noticed. This suggests that the traditional approach to scour problem may not be fruitful without further insight into the flow structure and erosion process.

Eight different modes of sand movement were identified and the contribution of each to bed deformation and sand transport has been discussed. Different modes were found to exist at different places around the cylinder at different stage of scour development.

Finally the interdependence of the flow and the erosion process was explained in the light of the experimental results. In the early stage, the flow imparted more influence on the erosion process and bed topography than was influenced by them. In the later stage, when the topography was more "aerodynamic," the flow was largely determined by the deformed bed topography.

5.2 Conclusions

- The present study is the first major attempt to map the local flow field around a circular cylinder on both smooth and rough beds, with and without scour holes. Such detailed information on the flow field and its relation to the scouring process has not been produced before.

- The skewed flow in front of and around the cylinder has been analyzed in terms of the modern concepts of three-dimensional turbulent boundary layers. Such interpretation was not done before.

- The effects of bed roughness on the flow structure have been identified.

- The effects of the scour hole on the flow structure have been identified.

- The contributions of the horseshoe vortex system, downflow, the accelerated flow on either side of the cylinder, and the shear field to the erosion process at different stages of scour development have been identified.

- The erosion was found to initiate in areas where the pressure gradient and the divergence of the bed shear vector were highest. The accelerated flow was also found in these areas.

- The horseshoe vortex system contributed to the erosion only by adding high velocity water to the accelerated flow. The contribution of downflow appeared to be insignificant at the early stage. It eroded bed material like an impinging jet only when the scour hole was well developed.

- Eight modes of sand movement and their contribution to bed deformation and sediment transport have been identified. The erosion process has been observed carefully and described in terms of these sand movement modes.

- The similarity of the scour hole geometry has been established. The development of scour depth was also found to be approximately similar in time.

- Several length scales of the scour hole have been identified and their behavior studied. Complex behaviors were found in the downstream region.

- By virtue of an extended literature review, the scour problem was placed in a broader perspective.
- The methodology developed in this study and the results produced from it will provide useful guidelines for the investigation of the flow field in the vicinity of a pier (or any other hydraulic structure for that matter) in an erodible bed.
- The data gathered may be used to construct, calibrate and verify numerical models for simulating the flow and/or erosion around circular cylinders.

5.3 Recommendations for Further Studies

- The separated region in front and around the cylinder needs to be studied more closely. Non-intrusive methods such as LDA will be most suited for this region and will provide valuable insight into the structure of the HVS and the downflow.
- The changing behavior of the HVS and the downflow with the development of scour holes may be investigated in order to understand the erosion process.
- The mutual effects of the flow and erosion in the wake region were found to be complex and need to be studied further. For example, the effects of the deformed bed topography on the cellular structure of the wake may give valuable clues to the flow and erosion in this region.
- Due to the rather broad nature of the present investigation, where a large number of different features have been explored and explained, an attempt to correlate them with different parameters did not seem feasible. A wide variation of parameters could not be achieved because each experiment took long time. However, having explored various aspects of the flow and erosion, it seems logical to systematically vary different parameters to study their effect.

References

Ahmad, M. (1962). Discussion on "Scour at Bridge Crossings" by E. M. Laursen, *ASCE Trans.*, Vol. 127, Part I, pp. 198-206.

Ahmed, F., Sabur, M. A., and Andres, D. D. (1993). "Pier scour on the South Saskatchewan River," *Proc. Hydr. Engrg. '93*, ASCE, Vol. 2, pp. 1848-1853.

Agui, J. H., and Andreopoulos, J. (1992). "Experimental Investigation of a Three-Dimensional Boundary Layer Flow in the Vicinity of an Upright Wall Mounted Cylinder," *J. Fluids Engrg.*, ASME, Vol. 114, pp. 566-576.

Arunachalam, K. (1965). "Scour Around Bridge Piers," *J. Indian Road Congress*, Vol. XXIX, Part 2, Paper No 251, 1965-66, pp. 189-207.

Baker, C. J. (1978). "Vortex Flow Around the Bases of Obstacles", *Ph.D. thesis*, Univ. of Cambridge, 123 pp. plus figures.

Baker, C. J. (1979). "The laminar horseshoe vortex," *J. Fluid Mech.*, Vol. 95, pp. 347-367.

Baker, C. J. (1980a). "The Turbulent Horseshoe Vortex," *J. Wind Engrg. & Ind. Aero.*, Vol. 6, pp. 9-23.

Baker, C. J. (1980b). "Theoretical Approach to Prediction of Local Scour Around Bridge Piers," *J. Hydr. Res.*, IAHR, Vol. 18, pp. 1-12.

Baker, C. J. (1981). "New Design Equations for Scour Around Bridge Piers," *J. Hydr. Div.*, ASCE, Vol. 107, pp. 507-511.

Baker, C. J. (1985). "The Position of Points of Maximum and Minimum Shear Stress Upstream of Cylinders Mounted Normal to Flat Plates," *J. Wind Engrg. & Ind. Aero.*, Vol. 18, pp. 263-274.

Belik, L. (1973). "The Secondary Flow about Circular Cylinders Mounted Normal to a Flat Plate," *The Aeronautical Quarterly*, Vol. XXIV, pp. 47-54.

Beltaos, S. (1974). "Turbulent Impinging Jets," *Ph.D. thesis*, Dept. of Civil Engrg., Univ. of Alberta, 335 pp.

Berg, B. van den (1975). "A three-dimensional law of the wall for turbulent shear flows," *J. Fluid Mech.*, Vol. 70, pp. 149-160.

Blench, T. (1962). Discussion on "Scour at Bridge Crossings" by E. M. Laursen, *ASCE Trans.*, Vol. 127, Part I, pp. 180-183.

Bonasoundas, M. (1973). "Strömungsvorgang und Kolkproblem am Runden Brückenpfeiler (Flow Structure and Scour Problem at Circular Bridge Piers)," *Bericht Nr. 28*, Oskar v. Miller Institut, Technischer Universität München, Germany, 108 pp. plus appendices.

Breusers, H. N. C. (1965). "Conformity and Time Scale in Two-Dimensional Local Scour," *Publication No. 40*, Delft Hydraulics Laboratory.

Breusers, H. N. C., Nicollet, G., and Shen, H. W. (1977). "Local Scour Around Cylindrical Piers," *J. Hydr. Res.*, IAHR, Vol. 15, pp. 211-252.

Brice, J. C., and Blodgett, J. C. (1978). "Countermeasures for Hydraulic Problems at Bridges, Vol. 1," *Publication No. FHWA/RD-78-162*, US Federal Highway Administration, 169 pp.

Carstens, M. R. (1966). "Similarity Laws for Localized Scour," *J. Hydr. Div.*, ASCE, Vol. 92, pp. 13-36.

Carstens, T., and Sharma, H. R. (1975). "Local Scour Around Large Obstructions," *Proc. 16th IAHR Congress*, Sao Paulo, Vol. 2, pp. 251-262.

Cebeci, T., and Smith, A. M. O. (1974). *Analysis of Turbulent Boundary Layers*, Academic Press, 404 pp.

Chabert, J., and Engeldinger, P. (1956). "Étude des affouillements autour des piles de ponts (Study of scour around bridge piers)," Laboratoire National D'Hydraulique, Série A, Chatou, France, 128 pp. (unpublished English translation by C. R. Neill, Research Council of Alberta, 1961).

Chandrashekhar, N., and Swamy, N. V. C. (1976). "Wall Shear Stress Inference for Three-Dimensional Turbulent Boundary-Layer Velocity Profiles," *J. Appl. Mech.*, ASME, Vol. 43, pp. 20-27.

Chang, P. K. (1970). *Separation of Flow*, Pergamon Press, 777 pp.

Chang, P. S., and Gessner, F. B. (1991). "Experimental Investigation of Flow About a Strut-Endwall Configuration," *AIAA J.*, Vol. 29, pp. 2105-2114.

Chee, R. K. W. (1982). "Live-Bed Scour at Bridge Piers," *Report No. 290*, School of Engrg., Univ. of Auckland, New Zealand, 79 pp.

Chiew, Y. M. (1984). "Local Scour at Bridge Piers," *Report No. 355*, School of Engrg., Univ. of Auckland, New Zealand, 200 pp.

Chiew, Y. M., and Melville, B. W. (1987). "Local Scour Around Bridge Piers," *J. Hydr. Res.*, IAHR, Vol. 25, pp. 15-26.

Chiew, Y. M., and Melville, B. W. (1989). "Local scour at bridge piers with non-uniform sediments," *Proc. Inst. Civil Engrs. (London)*, Part 2, Vol. 87, pp. 215-224.

Chitale, S. V. (1962). Discussion on "Scour at Bridge Crossings" by E. M. Laursen, *ASCE Trans.*, Vol. 127, Part I, pp. 191-196.

Clauser, F. H. (1956). "The Turbulent Boundary Layer," *Adv. Appl. Mech.*, Vol. IV, 1956, Academic Press, pp. 1-51.

Coleman, N. L. (1971). "Analyzing Laboratory Measurements of Scour at Cylindrical Piers in Sand Beds," *Proc. 14th IAHR Congress*, Paris, Vol. 3, paper C37.

Coles, D. (1956). "The law of the wake in the turbulent boundary layer," *J. Fluid Mech.*, Vol. 1, pp. 191-226.

Coutanceau, M., and Defaye, J.-R. (1991). "Circular cylinder wake configurations: A flow visualization survey," *Appl. Mech. Rev.*, Vol. 44(6), pp. 255-305.

Dargahi, B. (1982). "Local Scour at Bridge Piers - A Review of Theory & Practice," *Bulletin No. TRITA-VBI-114*, Hydraulics Laboratory, Royal Institute of Technology, Stockholm, 129 pp.

Dargahi, B. (1987). "Flow Field and Local Scouring Around a Cylinder," *Bulletin No. TRITA-VBI-137*, Hydraulics Laboratory, Royal Institute of Technology, Stockholm, 230 pp.

Dargahi, B. (1989). "The turbulent flow field around a circular cylinder," *Experiments in Fluids*, Vol. 8, pp. 1-12.

Davies, S. K., and Davis, G. de Vahl (1980). "Erosion of the Sand Bed Near Piers," *7th Australian Conf. on Hydr. and Fluid Mech.*, Brisbane, pp. 220-224.

Devenport, W. J., and Simpson, R. L. (1990). "Time-dependent and time-averaged turbulence structure near the nose of a wing-body junction," *J. Fluid Mech.*, Vol. 210, pp. 23-55.

East, L. F. (1972). "A Prediction of the Law of the Wall in Compressible Three-Dimensional Turbulent Boundary Layers," *Technical Report 72178*, Royal Aircraft Establishment, 25 pp. plus figures.

East, L. F., and Hoxey, R. P. (1969). "Low-Speed Three-Dimensional Turbulent Boundary-Layer Data," *R&M No. 3653*, Aeronautical Research Council, 82 pp.

East, J. L. Jr., and Pierce, F. J. (1972). "Explicit Numerical Solution of the Three-Dimensional Incompressible Turbulent Boundary-Layer Equations," *AIAA J.*, Vol. 10, pp. 1216-1223.

Eckerle, W. A. (1985). "Horseshoe Vortex Formation Around a Cylinder," *Ph.D. dissertation*, Univ. of Connecticut, 287 pp.

Eckerle, W. A., and Awad, J. K. (1991). "Effect of Freestream Velocity on the Three-Dimensional Separated Flow Region in Front of a Cylinder," *J. Fluids Engrg.*, ASME, Vol. 113, pp. 37-44.

Eibeck, P. A. (1990). "An Experimental Study of the Flow Downstream of a Circular and Tapered Cylinder," *J. Fluids Engrg.*, ASME, Vol. 112, pp. 393-401.

Einstein, H. A. (1950). "The Bed Load Function for Sediment Transportation in Open Channels," *Technical Bulletin 1026*, US Dept. of Agriculture, 71 pp.

Einstein, H. A., and El-Samni, E. S. A. (1949). "Hydrodynamic Forces on a Rough Wall," *Review of Modern Physics*, Vol. 21, pp. 520-524.

Elliot, K. R., and Baker, C. J. (1985). "Effect of Pier Spacing on Scour Around Bridge Piers," *J. Hydr. Div.*, ASCE, Vol. 111, pp. 1105-1109.

Ettema, R. (1976). "Influence of Bed Material Gradation on Local Scour," *Report No. 124*, School of Engrg., Univ. of Auckland, New Zealand, 147 pp.

Ettema, R. (1980). "Scour at Bridge Piers," *Report No. 216*, School of Engrg., Univ. of Auckland, New Zealand, 527 pp.

Falcón, M., and Uribe, L. (1987). "Temporal Scour Development around a Circular Pipe," in *Turbulence Measurements and Flow Modeling* edited by C. J. Chen, L.-D. Chen, and F. M. Holly, Hemisphere, pp. 805-812.

Fleming, J. L., Simpson, R. L., Cowling, J. E., and Devenport, W. J. (1993). "An experimental study of a turbulent wing-body junction and wake flow," *Experiments in Fluids*, Vol. 14, pp. 366-378.

Francis, G. P., and Pierce, F. J. (1966). "An Experimental Study of Skewed Turbulent Boundary Layers in Low Speed Flows," *J. Basic Engrg.*, ASME, Vol. 92, pp. 1-11.

Franzetti, S., Larcan, E., and Mignosa, P. (1982). "Influence of Tests Duration on the Evaluation of Ultimate Scour Around Circular Piers," *Int. Conf. on the Hydr. Modelling of Civil Engrg. Structures*, Coventry, England, pp. 381-396.

Froehlich, D. C. (1988). "Analysis of Onsite Measurements of Scour at Piers," *Hydr. Engrg.: Proc. 1988 National Conf.*, ASCE, pp. 534-539.

Gerich, D., and Eckelmann, H. (1982). "Influence of end plates and free ends on the shedding frequency of circular cylinders," *J. Fluid Mech.*, Vol. 122, pp. 109-121.

Grass, A. J. (1970). "Initial Instability of Fine Bed Sand," *J. Hydr. Div.*, ASCE, Vol. 96, pp. 619-632.

Grass, A. J. (1971). "Structural features of turbulent flow over smooth and rough boundaries," *J. Fluid Mech.*, Vol. 50, pp. 233-255.

Griffin, O. M. (1981). "Universal Similarity in the Wakes of Stationary and Vibrating Bluff Structures," *J. Fluids Engrg.*, ASME, Vol. 107, pp. 52-58.

Griffin, O. M. (1985). "Vortex Shedding From Bluff Bodies in a Shear Flow: A Review," *J. Fluids Engrg.*, ASME, Vol. 107, pp. 298-306.

Harsh, M. D. (1985). "An Experimental Investigation of a Turbulent Junction Vortex," *Ph.D. dissertation*, Dept. of Mech. Engrg., Virginia Polytechnic Inst. and State Univ., 258 pp.

Hawthorne, W. R. (1954). "The Secondary Flow About Struts and Airfoils," *J. Aero. Sci.*, Vol. 21, pp. 588-608 and 648.

Highway Research Board (1970). "Scour at Bridge Waterways," *Synthesis of Highway Practice 5*, National Cooperative Highway Research Program, Washington, 37 pp.

Hjorth, P. (1975). "Studies on the Nature of Local Scour," *Bulletin Series A No. 46*, Department of Water Resources Engineering, Univ. of Lund, Sweden.

Hjorth, P. (1976). "A Stochastic Model of Progressive Scour," *Proc. Second Int. IAHR Symp. on Stochastic Hydr.*, Lund, pp. 365-382.

Hollingshead, A. B. (1972). "Boundary Shear Distribution in Open Channel Flow," *Ph.D. thesis*, Dept. of Civil Engrg., Univ. of Alberta, 128 pp. plus appendices.

Hollingshead, A. B., and Rajaratnam, N. (1980). "A Calibration chart for the Preston tube," *J. Hydr. Res.*, IAHR, Vol. 18, pp. 313-326.

Holmes, P. S. (1974). "Analysis and prediction of scour at railway bridges in New Zealand," *New Zealand Engrg.*, Vol. 29, No. 11, pp. 313-320.

Hornung, H. G., and Joubert, P. N. (1963). "The mean velocity profile in three-dimensional turbulent boundary layers," *J. Fluid Mech.*, Vol. 15, pp. 368-384.

Hunt, J. C. R., Abell, C. J., Petarka, J. A., and Woo, H. (1978). "Kinematical studies of the flows around free or surface-mounted obstacles; applying topology to flow visualization," *J. Fluid Mech.*, Vol. 86, pp. 179-200.

Inglis, C. C. (1949). "The Behaviour and Control of Rivers and Canals," Part 1, *Research Publication No. 13*, Central Waterpower Irrigation & Navigation Research Station, Poona, India, 279 pp.

Jackson, R. G. (1976). "Sedimentological and fluid dynamic implications of the turbulent bursting phenomenon in geophysical flows," *J. Fluid Mech.*, Vol. 77, pp. 531-560.

Jain, B. P., and Modi, P. N. (1986). "Comparative Study of Various Formulae on Scour Around Bridge Piers," *J. Inst. Engrs. (India)*. Vol. 67, Part CI3, pp. 149-159.

Jain, S. C. (1981). "Maximum Clear-Water Scour Around Circular Piers," *J. Hydr. Div.*, ASCE, Vol. 107, pp. 611-626.

Jain, S. C., and Fischer, E. E. (1980). "Scour Around Bridge Piers at High Flow Velocities," *J. Hydr. Div.*, ASCE, Vol. 106, pp. 1827-1842.

Johnston, J. P. (1960a). "On the Three-Dimensional Turbulent Boundary Layer Generated by Secondary Flow," *J. Basic Engrg.*, ASME, pp. 233-248.

Johnston, J. P. (1960b). "The Turbulent Boundary Layer at a Plane of Symmetry in a Three-Dimensional Flow," *J. Basic Engrg.*, ASME, pp. 622-628.

Jones, J. S. (1984). "Comparison of Prediction Equations for Bridge Pier and Abutment Scour," *Transportation Research Record*, Vol. 950, pp. 202-209.

Joubert, P. N., Perry, A. E., and Brown, K. C. (1967). "Critical Review and Current Developments in Three-Dimensional Turbulent Boundary layers," in *Fluid Mechanics of Internal Flow* edited by G. Sovran, Elsevier, pp. 210-237.

Kline, S. J., and McClintock, F. A. (1953). "Describing Uncertainties in Single-Sample Experiments," *Mech. Engrg.*, ASME, Vol. 75, pp. 3-8.

Klinksiek, W. F., and Pierce, F. J. (1970). "Simultaneous Lateral Skewing in a Three-Dimensional Turbulent Boundary Layer," *J. Fluids Engrg.*, Vol. 92, pp. 83-90.

Klinksiek, W. F., and Pierce, F. J. (1973). "A Finite Difference Solution of the Two and Three-Dimensional Incompressible Turbulent Boundary Layer Equations," *J. Fluids Engrg.*, Vol. 95, pp. 445-458.

Kothyari, U. C., Garde, R. J., and Ranga Raju, K. G. (1992a). "Temporal Variation of Scour around Circular Bridge Piers," *J. Hydr. Engrg.*, ASCE, Vol. 118, pp. 1091-1106.

Kothyari, U. C., Garde, R. J., and Ranga Raju, K. G. (1992b). "Live-bed scour around cylindrical bridge piers," *J. Hydr. Res.*, IAHR, Vol. 30, pp. 701-715.

Kubendran, L. R., McMahon, H. M., and Hubbartt, J. E. (1986). "Turbulent Flow Around a Wing/Fuselage-Type Juncture," *AIAA J.*, Vol. 24, pp. 1447-1452.

Lagasse, P. F. *et al.* (1991). "Stream Stability at Highway Structures," *Hydraulic Engineering Circular No. 20, Publication No. FHWA-IP-90-014*, US Federal Highway Administration, 195 pp.

Laursen, E. M. (1960). "Scour at Bridge Crossings" by E. M. Laursen, *J. Hydr. Div.*, ASCE, Vol. 86, pp. 39-54. (also in *ASCE Trans.*, Vol. 127, Part I, 1962, pp. 166-209 with discussions).

Laursen, E. M. (1963). "An Analysis of Relief Bridge Scour," *J. Hydr. Div.*, ASCE, Vol. 89, pp. 93-118.

Laursen, E. M., and Toch, A. (1956). "Scour Around Bridge Piers and Abutments," *Bulletin No. 4*, Iowa Highway Research Board, 60 pp.

LeFeuvre, A. R., Altinbilek, H. D., and Carstens, M. R. (1970). "Sediment-Pickup Function," *J. Hydr. Div.*, ASCE, Vol. 96, pp. 2051-2063.

Mager, A. (1952). "Generalization of Boundary Layer Momentum Integral Equations to Three Dimensional Flows Including Those of Rotating Systems," *NACA Report 1067*, Washington.

Maskell, E. C. (1955). "Flow Separation in Three Dimensions," *Report Aero 2565*, Royal Aircraft Establishment.

Maull, D. J., and Young, R. A. (1973). "Vortex shedding from bluff bodies in a shear flow," *J. Fluid Mech.*, Vol. 60, pp. 401-409.

McAllister, J. E., Pierce, F. J., and Tennant, M. H. (1982). "Direct Force Wall Shear Measurement in Pressure-Driven Three-Dimensional Turbulent Boundary Layers," *J. Fluids Engrg.*, ASME, Vol. 104, pp. 150-155.

Melville, B. W. (1973). "Scour at Bridge Sites," *Report No. 104*, School of Engrg., Univ. of Auckland, New Zealand, 88 pp.

Melville, B. W. (1975). "Local Scour at Bridge Sites," *Report No. 117*, School of Engrg., Univ. of Auckland, New Zealand, 227 pp.

Melville, B. W. (1984). "Live-Bed Scour at Bridge Piers," *J. Hydr. Engrg.*, ASCE, Vol. 110, pp. 1234-1247.

Melville, B. W. (1992). Discussion on "Study of Time-Dependent Local Scour Around Bridge Piers," *J. Hydr. Engrg.*, ASCE, Vol. 118, pp. 1593-1597.

Melville, B. W., and Raudkivi, A. J. (1977). "Flow Characteristics in Local Scour at Bridge Piers," *J. Hydr. Res.*, IAHR, Vol. 15, pp. 373-380.

Melville, B. W., and Sutherland, A. J. (1988). "Design Method for Local Scour at Bridge Piers," *J. Hydr. Engrg.*, ASCE, Vol. 114, pp. 1210-1226.

Menna, J. D. (1984). "A Three-Dimensional Turbulent Boundary Layer Upstream and Around a Junction Vortex Flow," *Ph.D. dissertation*, Dept. of Mech. Engrg., Virginia Polytechnic Inst. and State Univ., 446 pp.

Menna, J. D., and Pierce, F. J. (1988). "The Mean Flow Structure Around and Within a Turbulent Junction or Horseshoe Vortex - Part I: The Upstream and Surrounding Three-Dimensional Boundary Layer," *J. Fluids Engrg.*, ASME, Vol. 110, pp. 406-414.

Moore, J., and Forlini, T. J. (1984). "A Horseshoe Vortex in a Duct," *J. Engrg. for Gas Turbines and Power*, ASME, Vol. 106, pp. 668-676.

Moore, W. L., and Masch, F. D. (1963). "Influence of Secondary Flow on Local Scour at Obstructions in a Channel," *Proc. Federal Inter-Agency Sedimentation Conf.*, pp. 314-320.

Mostafa, E. A, Yassan, A. A., Ettema, R., and Melville, B. W. (1993). "Local Scour at Skewed Bridge Piers," *Proc. Hydr. Engrg. '93*, ASCE, Vol. 1, pp. 1037-1042.

Nakagawa, H., and Suzuki, K. (1975). "An Application of Stochastic Model of Sediment Motion to Local Scour Around a Bridge Pier," *Proc. 16th IAHR Congress*, Sao Paulo, Vol. 2, pp. 228-235.

Nash, J. F., and Patel, V. C. (1972). *Three-Dimensional Turbulent Boundary Layers*, SBC Technical Books, Scientific and Business Consultants, Inc., Atlanta, 185 pp.

Neill, C. R. (1964a). "Local scour around bridge pies - a comparative analysis of model experiments and field data," *Unpublished Report*, Research Council of Alberta, 48 pp.

Neill, C. R. (1964b). "River-Bed Scour: A Review for Bridge Engineers," *Technical Publication No. 23*, Canadian Good Road Association, Ottawa, 37 pp.

Nikuradse, J. (1933). "Strömungsgesetze in rauhen Rohren," VDI-Forschungsheft 361, 1933. [translated as "Laws of Flow in Rough Pipes," *NACA Technical Memorandum 1292*, Washington, 1950]

Nwachukwu, B. A. (1979). "Flow and Erosion Near Groyne-Like Structures," *Ph.D. thesis*, Dept. of Civil Engrg., Univ. of Alberta, 145 pp.

Offen, G. R., and Kline, S. J. (1975). "A proposed model of the bursting process in turbulent boundary layers," *J. Fluid Mech.*, Vol. 70, pp. 209-228.

Olçmen, M. S., and Simpson, R. C. (1992). "Perspective: On the Near Wall Similarity of Three-Dimensional Turbulent Boundary Layers," *J. Fluids Engrg.*, ASME, Vol. 114, pp. 487-495.

Paintal, A. S. (1971a). "Concept of Critical Shear Stress in Loose Boundary Open Channels," *J. Hydr. Res.*, IAHR, Vol. 9, pp. 91-113.

Paintal, A. S. (1971b). "A Stochastic Model of Bed Load Transport," *J. Hydr. Res.*, IAHR, Vol. 9, pp. 527-554.

Patel, V. C. (1965). "Calibration of the Preston tube and limitations on its use in pressure gradients," *J. Fluid Mech.*, Vol. 23, pp. 185-208.

Perry, A. E., and Joubert, P. N. (1965). "A three-dimensional turbulent boundary layer," *J. Fluid Mech.*, Vol. 22, pp. 285-304.

Pierce, F. J. (1964). "The Turbulent Flow at the Plane of Symmetry of a Collateral Three-Dimensional Boundary Layer," *J. Basic Engrg.*, ASME, pp. 227-233.

Pierce, F. J. (1966). "The Law of the Wake and Plane of Symmetry Flows in Three-Dimensional Turbulent Boundary layers," *J. Basic Engrg.*, ASME, pp. 101-108.

Pierce, F. J., and East, J. L. Jr. (1972). "Near-Wall Collateral Flow in Three-Dimensional Turbulent Boundary Layers," *AIAA J.*, Vol. 10, pp. 334-336.

Pierce, F. J., and Harsh, M. D. (1988). "The Mean Flow Structure Around and Within a Turbulent Junction or Horseshoe Vortex - Part II. The Separated and Junction Vortex Flow," *J. Fluids Engrg.*, ASME, Vol. 110, pp. 415-423.

Pierce, F. J., and Krommenhoeek, D. H. (1968). "Wall Shear Stress Diagnostics in Three-Dimensional Turbulent Boundary Layers," *Interim Technical Report No. 2 ARO-D Project 6858E*, Virginia Polytechnic Inst. and State Univ.

Pierce, F. J., and McAllister, J. E. (1983). "Near-Wall Similarity in a Shear-Driven Three-Dimensional Turbulent Boundary Layer," *J. Fluids Engrg.*, ASME, Vol. 105, pp. 263-269.

Pierce, F. J., McAllister, J. E., and Tennant, M. H. (1983a). "A Review of Near-Wall Similarity Models in Three-Dimensional Turbulent Boundary Layers," *J. Fluids Engrg.*, ASME, Vol. 105, pp. 251-256.

Pierce, F. J., McAllister, J. E., and Tennant, M. H. (1983b). "Near-Wall Similarity in a Pressure-Driven Three-Dimensional Turbulent Boundary Layer," *J. Fluids Engrg.*, ASME, Vol. 105, pp. 257-262.

Pierce, F. J., and Shin, J. (1992). "The Development of a Turbulent Junction Vortex System," *J. Fluids Engrg.*, ASME, Vol. 114, pp. 559-565.

Pierce, F. J., and Tree, I. K. (1990). "The Mean Flow Structure on the Symmetry Plane of a Turbulent Junction Vortex," *J. Fluids Engrg.*, ASME, Vol. 112, pp. 16-22.

Pierce, F. J., and Zimmerman, B. B. (1973). "Wall Shear Stress Inference From Two and Three-Dimensional Turbulent Boundary Layer Velocity Profiles," *J. Fluids Engrg.*, ASME, pp. 61-67.

Posada, Lilian G., and Nordin, C. F. Jr. (1989). "Testing Design Methods for Local Scour at Bridge Piers," *Proc. Bridge Scour Symp., Report No. FHWA-RD-90-035*, Federal Highway Administration, pp. 101-111.

Prahlad, T. S. (1968). "Wall Similarity in Three-Dimensional Turbulent Boundary Layers," *AIAA J.*, Vol. 6, pp. 1772-1774.

Prahlad, T. S. (1973). "Mean Velocity Profiles in Three-Dimensional Incompressible Turbulent Boundary Layers," *AIAA J.*, Vol. 11, pp. 359-365.

Prandtl, L. (1946). "On Boundary layers in Three-Dimensional Flow," *Reports and Transactions No. 64*, British M.A.P., May 1946.

Preston, J. H. (1954). "The Determination of Turbulent Skin Friction by Means of Pitot Tubes," *J. Royal Aero. Soc.*, Vol. 54, pp. 109-121.

Qadar, A. (1981). "The vortex scour mechanism at bridge piers," *Proc. Inst. Civil Engrs. (London)*, Part 2, Vol. 71, 1981, pp. 739-757.

Rajaratnam, N. (1976). *Turbulent Jets*, Elsevier, 304 pp.

Rajaratnam, N., and Beltaos, S. (1977). "Erosion by Impinging Circular Turbulent Jets," *J. Hydr. Div.*, ASCE, Vol. 103, pp. 1191-1205.

Rajaratnam, N., and Berry, B. (1977). "Erosion by Circular Turbulent Wall Jets," *J. Hydr. Res.*, IAHR, Vol. 15, pp. 277-289.

Rajaratnam, N., and Muralidhar, D. (1967). "Yaw and Pitch Probes," *Hydraulic Instrumentation Series*, Dept. of Civil Engrg., Univ. of Alberta.

Rajaratnam, N., and Muralidhar, D. (1968). "Yaw Probe used as Preston Tube," *J. Royal Aero. Soc.*, Vol. 72, 1059-1060.

Rajaratnam, N., and Nwachukwu, B. A. (1983a). "Flow near Groyne-Like Structures," *J. Hydr. Engrg.*, ASCE, Vol. 109, No. 3, pp. 463-480.

Rajaratnam, N., and Nwachukwu, B. A. (1983b). "Erosion near Groyne-Like Structures," *J. Hydr. Res.*, IAHR, Vol. 21, pp. 277-287.

Raudkivi, A J. (1963). "Study of sediment ripple formation," *J. Hydr. Div.*, ASCE, Vol. 89, pp. 15-33.

Raudkivi, A. J. (1990). *Loose Boundary Hydraulics*, Pergamon Press, 538 pp.

Raudkivi, A. J. (1986). "Functional Trends of Scour at Bridge Piers," *J. Hydr. Engrg.*, ASCE, Vol. 112, pp. 1-13.

Raudkivi, A. J. (1991) "Scour at bridge piers," Chapter 5 in H. N. C. and A. J. Raudkivi, *Scouring: IAHR Hydraulic Structures Design Manual 2*, Balkema, Rotterdam, pp. 61-98.

Raudkivi, A. J., and Ettema, R. (1982). "Stability of Armored Layers in Rivers," *J. Hydr. Div.*, ASCE, Vol. 108, pp. 1047-1057.

Raudkivi, A. J., and Ettema, R. (1983). "Clear-Water Scour at Cylindrical Piers," *J. Hydr. Engrg.*, ASCE, Vol. 109, No. 3, pp. 338-350.

Raudkivi, A. J., and Ettema, R. (1985). "Scour at Cylindrical Bridge Piers in Armored Beds," *J. Hydr. Engrg.*, ASCE, Vol. 111, pp. 713-731.

Rhodes, J., and Trent, R. (1993). "Economics of Floods, Scour, and Bridge Failures," *Proc. Hydr. Engrg. '93*, ASCE, Vol. 2, pp. 928-933.

Richardson, E. V. *et al.* (1993). "Evaluating Scour at Bridges," *Hydraulic Engineering Circular No. 18, Publication No. FHWA-IP-90-017*, US Federal Highway Administration, pp. 129 plus appendices.

Roshko, A. (1961). "Experiments on the Flow Past a Circular Cylinder at Very High Reynolds Number," *J. Fluid Mech.*, Vol. 10, pp. 345-356.

Sarma, K. V. N. (1971). "Maximum Scour Depth at a Bridge Pier for Sediment Carrying Flows," *Fourth Australian Conf. on Hydr. and Fluid Mech.*, Melbourne, pp. 367-374.

Schlichting, H. (1968). *Boundary-Layer Theory*, McGraw-Hill, 748 pp.

Shabaka, I. M. M. A., and Bradshaw, P. (1981). "Turbulent Flow Measurements in an Idealized Wing/Body Junction," *AIAA J.*, Vol. 19, pp. 131-132.

Shanebrook, J. R., and Hatch, D. E. (1972). "A Family of Hodograph Models for the Cross Flow Velocity Component of Three-Dimensional Turbulent Boundary Layers," *J. Basic Engrg.*, ASME, pp. 321-332.

Shen, H. W., Ogawa, Y., and Karaki, S. S. (1963). "Time Variation of Bed Deformation Near Bridge Piers," *Proc. 10h IAHR Congress*, Leningrad, paper 3.14.

Shen, H. W., Schneider, V. R., and Karaki, S. S. (1966). "Mechanics of Local Scour," *Report No. CER66HWS22*, Colorado State Univ., 56 pp.

Shen, H. W., Schneider, V. R., and Karaki, S. S. (1969). "Local Scour Around Bridge Piers," *J. Hydr. Div.*, ASCE, Vol. 95, pp. 1919-1940.

Smith, D. W. (1976). "Bridge Failures," *Proc. Inst. Civil Engrs. (London).* Part 1, Vol. 60, pp. 367-383.

Spalding, D. B. (1961). "A Single Formula for the Law of the Wall," *J. Appl. Mech.*, ASME, Vol. 83, pp. 455-458.

Squire, H. B., and Winter, K. G. (1951). "The Secondary Flow in a Cascade of Aerofoils in a Non-Uniform Stream," *J. Aero. Sci.*, Vol. 18, pp. 271-277.

Sumer, B. M., and Deigaard, R. (1981). "Particle motions near the bottom in turbulent flow in an open channel. Part 2," *J. Fluid Mech.*, Vol. 109, pp. 311-337.

Tanaka, S., and Yano, M. (1967). "Local scour Around a Circular Cylinder," *Proc. 12th IAHR Congress*, Fort Collins, Vol. 3, pp. 193-201.

Taylor, E. S. (1959). "The Skewed Boundary Layer," *J. Basic Engrg.*, ASME, pp. 297-304.

Thomas, A. R. (1962). Discussion on "Scour at Bridge Crossings" by E. M. Laursen, *ASCE Trans.*, Vol. 127, Part I, pp. 196-198.

Toomre, A. (1960). "The viscous secondary flow ahead of an infinite cylinder in a uniform parallel shear flow," *J. Fluid Mech.*, Vol. 7, pp. 145-155.

Townsend, A. A. (1956). "The properties of equilibrium boundary layers," *J. Fluid Mech.*, Vol. 1, pp. 561-573.

Tree, I. K. (1986). "Laser Doppler Velocimeter Measurements in a Turbulent Junction Vortex," *Ph.D. dissertation*, Dept. of Mech. Engrg., Virginia Polytechnic Inst. and State Univ., 262 pp.

Utami, T. (1975). "The Local Flow around the Upstream Side of Bridge Piers," *Bulletin Disaster Prevention Res. Inst.*, Vol. 25, Part 4, No. 233, pp. 55-75, Kyoto Univ., Japan.

Vallentine, H. R. (1967). *Applied Hydrodynamics*, Plenum Press, New York, 296 pp.

Vanoni, V. A., (editor) (1975). "Sedimentation Engineering," *ASCE Manuals and Reports on Engineering Practice No. 54*, 745 pp.

Varzeliotis, A. N. (1960). "Model Studies on Scour Around Bridge Piers and Stone Aprons," *M.S. thesis*, Dept. of Civil Engrg., Univ. of Alberta, 159 pp.

White, F. M., Lessmann, R. C., and Christoph, G. H. (1975). "A Three-Dimensional Integral Method for Calculating Incompressible Turbulent Skin Friction," *J. Fluids Engrg.*, ASME, Vol. 97, pp. 550-557.

Yalin, M. S. (1977). *Mechanics of Sediment Transport*, Pergamon Press, 298 pp.

Yanmaz, A. M., and Altinbilek, H. D. (1991). "Study of Time-Dependent Local Scour around Bridge Piers," *J. Hydr. Engrg.*, ASCE, Vol. 117, pp. 1247-1268.

Appendix A
Equations of 3DTBL in Curvilinear Coordinates

A.1 Governing equations

Let us consider a triply-orthogonal curvilinear coordinate system (ξ,η,ζ) with metrical coefficients h_1, h_2 and h_3 which are in general functions of (ξ,η,ζ). The curvature parameters are defined as

$$K_{ij} = \frac{1}{h_i h_j}\frac{\partial h_i}{\partial h_j} \qquad (i,j = 1,2,3)\ .$$

Now it is possible to write the Navier-Stokes and continuity equations in this general coordinate system. These equations after the Reynolds decomposition and time averaging process are given in Nash and Patel (1972). These equations are very lengthy and cumbersome to work with in their general form. However, for the present purpose, *i.e.*, the flow over a flat plate with a cantilevered circular cylinder, the equations could be considerably simplified.

A surface is called "developable" if one of the principal radii is zero. For a flat plate both of them are zero. Hence, $K_{12} = K_{21} = K_{32} = K_{23} = 0$ everywhere. Moreover, h_1, h_2, K_{31} and K_{13} become independent of η. These simplifications resulting from the geometry of the surface on which the boundary layer develops and the choice of coordinate system can be complemented by the usual boundary layer approximations of Prandtl, and an order of magnitude analysis can be performed on the equations of motion. The simplified equations for a steady, incompressible fluid are

$$\begin{aligned}&\frac{u}{h_1}\frac{\partial u}{\partial \xi} + \frac{v}{h_2}\frac{\partial u}{\partial \eta} + \frac{w}{h_3}\frac{\partial u}{\partial \zeta} + (K_{13}u - K_{31}w)w \\ &+\frac{1}{h_1}\frac{\partial}{\partial \xi}\left(\frac{p}{\rho}\right) - \frac{1}{h_2}\frac{\partial}{\partial \eta}\left(\nu\frac{1}{h_2}\frac{\partial u}{\partial \eta} - \overline{u'v'}\right) = 0\end{aligned} \qquad \text{[A.1]}$$

$$\frac{\partial}{\partial \eta}\left(\frac{p}{\rho} + \overline{v'^2}\right) = 0 \qquad \text{[A.2]}$$

$$\frac{u}{h_1}\frac{\partial w}{\partial \xi}+\frac{v}{h_2}\frac{\partial w}{\partial \eta}+\frac{w}{h_3}\frac{\partial w}{\partial \zeta}+(K_{31}w-K_{13}u)u$$
$$+\frac{1}{h_3}\frac{\partial}{\partial \zeta}\left(\frac{p}{\rho}\right)-\frac{1}{h_2}\frac{\partial}{\partial \eta}\left(\nu\frac{1}{h_2}\frac{\partial w}{\partial \eta}-\overline{w'v'}\right)=0 \qquad [A.3]$$

$$\frac{1}{h_1}\frac{\partial u}{\partial \xi}+\frac{1}{h_2}\frac{\partial v}{\partial \eta}+\frac{1}{h_3}\frac{\partial w}{\partial \zeta}+K_{31}u+K_{13}w=0 \qquad [A.4]$$

This form of the equations are most suitable for computational work since h_2 can be conveniently used to manipulate the grid size. However, we can also let η be equal to the physical distance from the surface by simply putting $h_2 = 1$. Then the following equations are the obtained which is considered to be in the most useful form.

$$\frac{u}{h_1}\frac{\partial u}{\partial \xi}+v\frac{\partial u}{\partial \eta}+\frac{w}{h_3}\frac{\partial u}{\partial \zeta}+(K_{13}u-K_{31}w)w+\frac{1}{h_1}\frac{\partial}{\partial \xi}\left(\frac{p}{\rho}\right)-\frac{\partial}{\partial \eta}\left(\frac{\tau_\xi}{\rho}\right)=0 \qquad [A.5]$$

$$\frac{\partial}{\partial \eta}\left(\frac{p}{\rho}+\overline{v'^2}\right)=0 \qquad [A.6]$$

$$\frac{u}{h_1}\frac{\partial w}{\partial \xi}+v\frac{\partial w}{\partial \eta}+\frac{w}{h_3}\frac{\partial w}{\partial \zeta}+(K_{31}w-K_{13}u)u+\frac{1}{h_3}\frac{\partial}{\partial \zeta}\left(\frac{p}{\rho}\right)-\frac{\partial}{\partial \eta}\left(\frac{\tau_\zeta}{\rho}\right)=0 \qquad [A.7]$$

$$\frac{1}{h_1}\frac{\partial u}{\partial \xi}+\frac{\partial v}{\partial \eta}+\frac{1}{h_3}\frac{\partial w}{\partial \zeta}+K_{31}u+K_{13}w=0 \qquad [A.8]$$

Note that only the following two turbulent stresses remain for which two closure equations are required.

$$\frac{\tau_\xi}{\rho}=\nu\frac{\partial u}{\partial \eta}-\overline{u'v'} \qquad [A.9]$$

$$\frac{\tau_\zeta}{\rho}=\nu\frac{\partial w}{\partial \eta}-\overline{v'w'} \qquad [A.10]$$

At the outer edge of the boundary layer, the viscous and turbulent stress terms become vanishingly small and v_e becomes small compared to u_e and w_e Here Equations [A.5] to [A.8] take the following form.

$$\frac{u_e}{h_1}\frac{\partial u_e}{\partial \xi}+\frac{w_e}{h_3}\frac{\partial u_e}{\partial \zeta}+(K_{13}u_e-K_{31}w_e)w_e+\frac{1}{h_1}\frac{\partial}{\partial \xi}\left(\frac{p}{\rho}\right)=0 \qquad [A.11]$$

$$\frac{\partial}{\partial \eta}\left(\frac{p}{\rho}\right)=0 \qquad [A.12]$$

$$\frac{u_e}{h_1}\frac{\partial w_e}{\partial \xi}+\frac{w_e}{h_3}\frac{\partial w_e}{\partial \zeta}+(K_{31}w_e-K_{13}u_e)u_e+\frac{1}{h_3}\frac{\partial}{\partial \zeta}\left(\frac{p}{\rho}\right)=0 \qquad [A.13]$$

$$\frac{1}{h_1}\frac{\partial u_e}{\partial \xi}+\frac{\partial v_e}{\partial \eta}+\frac{1}{h_3}\frac{\partial w_e}{\partial \zeta}+K_{31}u_e+K_{13}w_e=0 \qquad [A.14]$$

These are essentially Euler's equations valid outside the boundary layer with the following condition of irrotationality.

$$\frac{1}{h_3}\frac{\partial u_e}{\partial \zeta}-\frac{1}{h_1}\frac{\partial w_e}{\partial \xi}+K_{13}u_e-K_{31}w_e=0 \qquad [A.15]$$

The pressure gradient terms may be evaluated from the outer potential flow and inserted in the boundary layer equations ([A.5] to [A.8]). Alternately, pressure gradient terms can be eliminated between Equations [A.11] and [A.5] and between Equations [A.13] and [A.7] to get the following.

$$\begin{aligned}&\frac{u_e}{h_1}\frac{\partial u_e}{\partial \xi}+\frac{w_e}{h_3}\frac{\partial u_e}{\partial \zeta}+(K_{13}u_e-K_{31}w_e)w_e-\frac{u}{h_1}\frac{\partial u}{\partial \xi}-\nu\frac{\partial u}{\partial \eta}\\&-\frac{w}{h_3}\frac{\partial u}{\partial \zeta}-(K_{13}u-K_{31}w)w+\frac{\partial}{\partial \eta}\left(\frac{\tau_\xi}{\rho}\right)=0\end{aligned} \qquad [A.16]$$

$$\begin{aligned}&\frac{u_e}{h_1}\frac{\partial w_e}{\partial \xi}+\frac{w_e}{h_3}\frac{\partial w_e}{\partial \zeta}+(K_{31}w_e-K_{13}u_e)u_e-\frac{u}{h_1}\frac{\partial w}{\partial \xi}-\nu\frac{\partial w}{\partial \eta}\\&-\frac{w}{h_3}\frac{\partial w}{\partial \zeta}-(K_{31}w-K_{13}u)u+\frac{\partial}{\partial \eta}\left(\frac{\tau_\zeta}{\rho}\right)=0\end{aligned} \qquad [A.17]$$

All the equations written so far are valid for any curvilinear coordinate system. Further simplification is possible when the streamline coordinate system is chosen. In this system the ξ = constant and ζ = constant surfaces are generated, respectively, by the projections of the boundary edge streamlines and the orthogonal trajectories of these projections onto the η = constant surfaces. Hence K_{13} and K_{31} become the geodesic curvatures of the projections of streamlines and their orthogonal trajectories respectively, and are given by

$$K_{13}=-\frac{1}{h_1}\frac{\partial \alpha}{\partial \xi} \qquad [A.18]$$

and

$$K_{31} = +\frac{1}{h_3}\frac{\partial \alpha}{\partial \zeta} \qquad [A.19]$$

where α is the angle between the boundary edge streamline and the plane of symmetry as shown in Figure 2.4.2(a-b). With these values of K_{13} and K_{31} and noting that in the streamline coordinate system $w_e = 0$ and $q_e = u_e$, the main flow Equations ([A.11] to [A.14]) become

$$u_e \frac{\partial u_e}{\partial \xi} + \frac{\partial}{\partial \xi}\left(\frac{p}{\rho}\right) = 0 \qquad [A.20]$$

$$\frac{\partial}{\partial \eta}\left(\frac{p}{\rho}\right) = 0 \qquad [A.21]$$

$$u_e^2 \frac{1}{h_1}\frac{\partial \alpha}{\partial \xi} + \frac{1}{h_3}\frac{\partial}{\partial \zeta}\left(\frac{p}{\rho}\right) = 0 \qquad [A.22]$$

$$\frac{1}{h_1}\frac{\partial u_e}{\partial \xi} + u_e \frac{1}{h_3}\frac{\partial \alpha}{\partial \zeta} = 0 \qquad [A.23]$$

and, the irrotationality condition becomes

$$\frac{1}{h_3}\frac{\partial u_e}{\partial \zeta} - u_e \frac{1}{h_1}\frac{\partial \alpha}{\partial \xi} = 0 \qquad [A.24]$$

The boundary layer equations can also be written in a slightly simplified way as follows.

$$\frac{u}{h_1}\frac{\partial u}{\partial \xi} + v\frac{\partial u}{\partial \eta} + \frac{w}{h_3}\frac{\partial u}{\partial \zeta} - uw\frac{1}{h_1}\frac{\partial a}{\partial \xi} - w^2\frac{1}{h_3}\frac{\partial \alpha}{\partial \zeta} + \frac{1}{h_1}\frac{\partial}{\partial \xi}\left(\frac{p}{\rho}\right) - \frac{\partial}{\partial \eta}\left(\frac{\tau_\xi}{\rho}\right) = 0 \qquad [A.25]$$

$$\frac{\partial}{\partial \eta}\left(\frac{p}{\rho} + \overline{v'^2}\right) = 0 \qquad [A.26]$$

$$\frac{u}{h_1}\frac{\partial w}{\partial \xi} + v\frac{\partial w}{\partial \eta} + \frac{w}{h_3}\frac{\partial w}{\partial \zeta} + uw\frac{1}{h_3}\frac{\partial \alpha}{\partial \zeta} + u^2\frac{1}{h_1}\frac{\partial \alpha}{\partial \xi} + \frac{1}{h_3}\frac{\partial}{\partial \zeta}\left(\frac{p}{\rho}\right) - \frac{\partial}{\partial \eta}\left(\frac{\tau_\zeta}{\rho}\right) = 0 \qquad [A.27]$$

$$\frac{1}{h_1}\frac{\partial u}{\partial \xi} + \frac{\partial v}{\partial \eta} + \frac{1}{h_3}\frac{\partial w}{\partial \zeta} + u\frac{1}{h_3}\frac{\partial \alpha}{\partial \zeta} - w\frac{1}{h_1}\frac{\partial \alpha}{\partial \xi} = 0 \qquad [A.28]$$

A.2 Integral Relations

The continuity equation [A.8] multiplied by $(u_e - u)$ is added to the ξ-momentum equation [A.16], and the whole expression is then integrated with respect to η from $\eta = 0$ to $\eta = \delta$ to get the momentum integral equation in ξ-direction.

$$\frac{1}{h_1}\frac{\partial}{\partial \xi}\left(\theta_{\xi\xi}\right)+\frac{1}{h_3}\frac{\partial}{\partial \zeta}\left(\theta_{\xi\zeta}\right)+\frac{\theta_{\xi\xi}}{q_e^2}\frac{1}{h_1}\frac{\partial}{\partial \xi}\left(q_e^2\right)+\frac{\theta_{\xi\zeta}}{q_e^2}\frac{1}{h_3}\frac{\partial}{\partial \zeta}\left(q_e^2\right)$$
$$+\frac{\delta_\xi^*}{q_e}\frac{1}{h_1}\frac{\partial}{\partial \xi}(u_e)+\frac{\delta_\zeta^*}{q_e}\frac{1}{h_3}\frac{\partial}{\partial \zeta}(u_e)+K_{31}\left(\theta_{\xi\xi}-\theta_{\zeta\zeta}-\frac{w_e}{q_e}\delta_\zeta^*\right) \qquad \text{[A.29]}$$
$$+K_{13}\left(\theta_{\xi\zeta}+\theta_{\zeta\xi}+\frac{w_e}{q_e}\delta_\xi^*\right)-\frac{\tau_{0\xi}}{\rho q_e^2}=0$$

Similarly multiplying the continuity equation by $(w_e - w)$ and using Equation [A.17] we get the momentum integral equation in the ζ-direction.

$$\frac{1}{h_3}\frac{\partial}{\partial \zeta}\left(\theta_{\zeta\zeta}\right)+\frac{1}{h_1}\frac{\partial}{\partial \xi}\left(\theta_{\zeta\xi}\right)+\frac{\theta_{\zeta\zeta}}{q_e^2}\frac{1}{h_3}\frac{\partial}{\partial \zeta}\left(q_e^2\right)+\frac{\theta_{\zeta\xi}}{q_e^2}\frac{1}{h_1}\frac{\partial}{\partial \xi}\left(q_e^2\right)$$
$$+\frac{\delta_\zeta^*}{q_e}\frac{1}{h_3}\frac{\partial}{\partial \zeta}(w_e)+\frac{\delta_\xi^*}{q_e}\frac{1}{h_1}\frac{\partial}{\partial \xi}(w_e)+K_{13}\left(\theta_{\zeta\zeta}-\theta_{\xi\xi}-\frac{u_e}{q_e}\delta_\xi^*\right) \qquad \text{[A.30]}$$
$$+K_{31}\left(\theta_{\zeta\xi}+\theta_{\xi\zeta}+\frac{u_e}{q_e}\delta_\zeta^*\right)-\frac{\tau_{0\zeta}}{\rho q_e^2}=0$$

The energy integral equation is obtained by integrating the summation of the continuity equation [A.8] multiplied by $(u_e^2 + w_e^2 - u^2 - w^2)$, Equation [A.16] multiplied by $2u$ and Equation [A.17] multiplied by $2w$. The final equation is shown below.

$$\frac{1}{h_1}\frac{\partial}{\partial \xi}\left(\varepsilon_\xi\right)+\frac{1}{h_3}\frac{\partial}{\partial \zeta}\left(\varepsilon_\zeta\right)+\left(K_{31}+\frac{3}{q_e}\frac{1}{h_1}\frac{\partial q_e}{\partial \xi}\right)\varepsilon_\xi+\left(K_{13}+\frac{3}{q_e}\frac{1}{h_3}\frac{\partial q_e}{\partial \zeta}\right)\varepsilon_\zeta$$
$$+\frac{1}{\rho q_e^3}\int_0^\delta\left\{u\frac{\partial}{\partial \eta}\left(\frac{\tau_\xi}{\rho}\right)+w\frac{\partial}{\partial \eta}\left(\frac{\tau_\zeta}{\rho}\right)\right\}d\eta=0 \qquad \text{[A.31]}$$

In the above integral equations the following displacement, momentum and energy thicknesses were used.

$$\delta_\xi^*=\frac{1}{q_e}\int_0^\delta(u_e-u)d\eta \qquad \text{[A.32]}$$

$$\delta_\zeta^*=\frac{1}{q_e}\int_0^\delta(w_e-w)d\eta \qquad \text{[A.33]}$$

$$\theta_{\xi\xi} = \frac{1}{q_e^2}\int_0^{\delta}(u_e - u)u\,d\eta \qquad [A.34]$$

$$\theta_{\xi\zeta} = \frac{1}{q_e^2}\int_0^{\delta}(u_e - u)w\,d\eta \qquad [A.35]$$

$$\theta_{\zeta\xi} = \frac{1}{q_e^2}\int_0^{\delta}(w_e - w)u\,d\eta \qquad [A.36]$$

$$\theta_{\zeta\zeta} = \frac{1}{q_e^2}\int_0^{\delta}(w_e - w)w\,d\eta \qquad [A.37]$$

$$\varepsilon_{\xi} = \frac{1}{q_e^3}\int_0^{\delta}\frac{1}{2}\left(q_e^2 - q^2\right)u\,d\eta \qquad [A.38]$$

$$\varepsilon_{\zeta} = \frac{1}{q_e^3}\int_0^{\delta}\frac{1}{2}\left(q_e^2 - q^2\right)w\,d\eta \qquad [A.39]$$

The above integral equations and the definitions of different thicknesses are valid for any orthogonal coordinate system. The use of streamline coordinate system slightly simplifies them because then $w_e = 0$ and $q_e = u_e$ and K_{13} and K_{31} can be expressed in terms of α (Equations [A.18] and [A.19]). More importantly the following relation emerges.

$$\theta_{\xi\zeta} = \theta_{\zeta\xi} - \delta_{\zeta}^{*} \qquad [A.40]$$

A.3 Plane of Symmetry

On the plane of symmetry, w, w_e, $\partial w/\partial\xi$, $\partial w/\partial\eta$, $\partial u/\partial\zeta$, $\partial p/\partial\zeta$, $\overline{v'w'}$, K_{13}, δ_{ζ}^{*}, $\theta_{\xi\zeta}$, $\theta_{\zeta\xi}$, $\theta_{\zeta\zeta}$ and ε_{ζ} become equal to zero. However, it should be noted that, K_{31} and $\partial w/\partial\zeta$ do not necessarily vanish on symmetry plane. Furthermore h_1 may be assigned a value of unity and from the mainflow continuity equation [4.23] the deflection angle α can be related to the potential flow as

$$\frac{1}{h_3}\frac{\partial\alpha}{\partial\zeta} = -\frac{1}{u_e}\frac{\partial u_e}{\partial\xi} \qquad [A.41]$$

The ξ-momentum, the continuity and the momentum integral equations take the following form in the plane of symmetry.

$$u\frac{\partial u}{\partial \xi}+v\frac{\partial u}{\partial \eta}+\frac{\partial}{\partial \xi}\left(\frac{p}{\rho}\right)-\frac{\partial}{\partial \eta}\left(\frac{\tau_\xi}{\rho}\right)=0 \qquad \text{[A.42]}$$

$$\frac{\partial u}{\partial \xi}+\frac{\partial v}{\partial \eta}+\frac{1}{h_3}\frac{\partial w}{\partial \zeta}+u\frac{1}{h_3}\frac{\partial \alpha}{\partial \zeta}=0 \qquad \text{[A.43]}$$

$$\frac{\partial}{\partial \xi}\left(\theta_{\xi\xi}\right)+\left(2\theta_{\xi\xi}+\delta_\xi^*\right)\frac{1}{u_e}\frac{\partial}{\partial \xi}(u_e)+\frac{1}{h_3}\frac{\partial}{\partial \zeta}\left(\theta_{\xi\zeta}\right)+\theta_{\xi\xi}\frac{1}{h_3}\frac{\partial \alpha}{\partial \zeta}=\frac{\tau_{0\xi}}{\rho u_e^2} \qquad \text{[A.44]}$$

The above equations on the plane of symmetry, when written in Cartesian coordinate systems, are sometimes easy to work with. From Figure 2.4.2(b) the following relations are evident.

$$u=\frac{u_x}{\cos\alpha}+w\tan\alpha \qquad \text{[A.45]}$$

and

$$w=\frac{u_z}{\cos\alpha}-u\tan\alpha \qquad \text{[A.46]}$$

These may be approximated by

$$u\approx u_x+\alpha w \quad \text{and} \quad w\approx u_z-\alpha u$$

as the plane of symmetry is approached or as α tends to zero. In this limiting case it can be shown that

$$\frac{1}{h_3}\frac{\partial}{\partial \zeta}\left(\theta_{\xi\zeta}\right)=\frac{\partial}{\partial z}(\theta_{xz})-\theta_{xx}\frac{\partial \alpha}{\partial z} \qquad \text{[A.47]}$$

and

$$\frac{\partial}{\partial z}(\theta_{xz})=\theta_{xx}\frac{\partial \alpha}{\partial z} \qquad \text{[A.48]}$$

With these relations the ξ-momentum equation [A.42] becomes the x-momentum in the Cartesian coordinate.

$$u_x\frac{\partial u_x}{\partial x}+u_y\frac{\partial u_x}{\partial y}+\frac{\partial}{\partial x}\left(\frac{p}{\rho}\right)-\frac{\partial}{\partial y}\left(\frac{\tau_x}{\rho}\right)=0 \qquad \text{[A.49]}$$

And the momentum integral equation [A.44] in the ξ-direction becomes the same in x-direction in the Cartesian coordinate system.

$$\frac{\partial}{\partial x}(\theta_{xx})+\left(2\theta_{xx}+\delta_x^*\right)\frac{1}{u_e}\frac{\partial}{\partial x}(u_e)-\theta_{xx}\frac{1}{u_e}\frac{\partial}{\partial x}(u_e)=\frac{\tau_{0x}}{\rho u_{xe}^2} \qquad [A.50]$$

The equations in the z-direction vanishes identically. Of course, $\tau_0 = \tau_{0x}$ and $u_e = u_{xe}$ since $\tau_{0z} = 0$ and $u_{ze} = 0$ on this plane. The continuity equation takes back the familiar Cartesian form.

$$\frac{\partial u_x}{\partial x}+\frac{\partial u_y}{\partial y}+\frac{\partial u_z}{\partial z}=0 \qquad [A.51]$$

The following thicknesses were used in the above equations.

$$\delta_x^*=\frac{1}{q_e}\int_0^\delta(u_{xe}-u_x)dy \qquad [A.52]$$

$$\theta_{xx}=\frac{1}{q_e^2}\int_0^\delta(u_{xe}-u_x)u_x\,dy \qquad [A.53]$$

$$\theta_{xz}=\frac{1}{q_e^2}\int_0^\delta(u_{xe}-u_x)u_z\,dy \qquad [A.54]$$

Appendix B
Potential Flow Approximation

B.1 Introduction

There are elegant mathematical solutions for the potential flow around a circular cylinder. These solutions are based on the assumptions of incompressible "ideal fluid" with zero viscosity and irrotational flow. The flow is assumed to be two-dimensional and of infinite extent. Although the actual flow around a bridge pier is three-dimensional and the water is viscous, the potential flow solution can be used as a convenient benchmark to which to compare the experimental results.

B.2 Potential Flow Equations

In reference to Figure B.1, let an uniform approach flow with an ambient velocity U_∞ pass around a circular cylinder of radius r. The stream function ψ may be defined in such a way that the velocity components are given by:

$$u = \frac{\partial \psi}{\partial z} \qquad \text{[B.1a]}$$

and

$$w = -\frac{\partial \psi}{\partial x} \qquad \text{[B.1b]}$$

Then it follows from the potential theory (Vallentine 1967) that

$$\psi = U_\infty y\left(1 - \frac{r^2}{x^2 + z^2}\right) \qquad \text{[B.2]}$$

This expression for ψ can be differentiated with respect to z and x to get the longitudinal and transverse components of the velocity vector $\mathbf{V}$ at any point (x, z) as a function of x and z or X (= x/r) and Z (= z/r). Thus we get

$$\frac{u}{U_\infty} = \frac{1}{U_\infty}\frac{\partial \psi}{\partial z} = 1 - \frac{r^2\left(x^2 - z^2\right)}{\left(x^2 + z^2\right)^2} = 1 - \frac{\left(X^2 - Z^2\right)}{\left(X^2 + Z^2\right)^2} \qquad \text{[B.3a]}$$

and

$$\frac{w}{U_\infty} = -\frac{1}{U_\infty}\frac{\partial \psi}{\partial x} = -\frac{2r^2 xz}{\left(x^2+z^2\right)^2} = -\frac{2XZ}{\left(X^2+Z^2\right)^2} \qquad \text{[B.3b]}$$

The magnitude of the velocity vector **V** and the angle θ it makes with x-axis (see Figure B.1) are given by

$$\frac{V^2}{U_\infty^2} = \frac{u^2}{U_\infty^2} + \frac{w^2}{U_\infty^2} = 1 + r^2\frac{r^2 - 2\left(x^2 - z^2\right)}{\left(x^2+z^2\right)^2} = 1 + \frac{1 - 2\left(X^2 - Z^2\right)}{\left(X^2+Z^2\right)^2} \qquad \text{[B.4]}$$

and

$$\tan\theta = \frac{w}{u} = \frac{2r^2 xz}{r^2\left(x^2 - z^2\right) - \left(x^2+z^2\right)^2} = \frac{2XZ}{\left(X^2 - Z^2\right) - \left(X^2+Z^2\right)^2} \qquad \text{[B.5]}$$

Now if p_∞ is the ambient pressure at $x = \infty$, then Bernoulli's equation can be written as

$$p + \frac{1}{2}\rho V^2 = p_\infty + \frac{1}{2}\rho U_\infty^2 \qquad \text{[B.6]}$$

from which the pressure coefficient defined as

$$C_p = \frac{p - p_\infty}{\frac{1}{2}\rho U_\infty^2} \qquad \text{[B.7]}$$

is given by the following expression.

$$C_p = r^2\frac{2\left(x^2 - z^2\right) - r^2}{\left(x^2+z^2\right)^2} = \frac{2\left(X^2 - Z^2\right) - 1}{\left(X^2+Z^2\right)^2} \qquad \text{[B.8]}$$

Now, substituting the value of V from Equation [B.4] into Equation [B.6] and noting that both U_∞ and p_∞ are constants, Equation [B.6] can be differentiated with respect to x and z to get the pressure gradients in those directions. Thus we get

$$\frac{r}{\frac{1}{2}\rho U_\infty^2}\frac{\partial p}{\partial x} = \frac{4r^3 x\left(r^2 - x^2 + 3z^2\right)}{\left(x^2+z^2\right)^3} = \frac{4X\left(1 - X^2 + 3Z^2\right)}{\left(X^2+Z^2\right)^3} \qquad \text{[B.9a]}$$

and

$$\frac{r}{\frac{1}{2}\rho U_\infty^2}\frac{\partial p}{\partial z} = \frac{4r^3 z\left(r^2 - 3x^2 + z^2\right)}{\left(x^2+z^2\right)^3} = \frac{4Z\left(1 - 3X^2 + Z^2\right)}{\left(X^2+Z^2\right)^3} \qquad \text{[B.9b]}$$

The expression of total pressure gradient is

$$\nabla p = \frac{\partial p}{\partial x}\mathbf{i} + \frac{\partial p}{\partial z}\mathbf{k} \qquad \text{[B.10]}$$

where $\mathbf{i}$ and $\mathbf{k}$ are the unit vectors in x and z directions respectively. With the values of $\partial p / \partial x$ and $\partial p / \partial z$ from Equation [B.9], the magnitude of ∇p can be easily computed as follows.

$$|\nabla p|^2 = \left(\frac{\partial p}{\partial x}\right)^2 + \left(\frac{\partial p}{\partial z}\right)^2 \qquad \text{[B.12]}$$

If it makes an angle θ_p with the x-axis, then this angle is given by

$$\tan\theta_p = \frac{z\left(r^2 - 3x^2 + z^2\right)}{x\left(r^2 - x^2 + 3z^2\right)} = \frac{Z\left(1 - 3X^2 + Z^2\right)}{X\left(1 - X^2 + 3Z^2\right)} \qquad \text{[B.12]}$$

B.3 Numerical Computation

In the present study, the actual flow was approximated by an infinite number of sheets of infinitely small thickness at different heights from the bed flowing around the cylinder (Figure B.2). It was also assumed that these sheets glides one over another freely without any mass or momentum transfer. The flow of a sheet at a certain level y was further approximated by the potential flow with $U_\infty\langle y\rangle$ given by the measured longitudinal velocity $u\langle y\rangle$ at $(x=0,\ z=0)$ without the cylinder in place. p_∞ was assumed to be equal to the piezometric pressure at $(x=0,\ z=0)$ under the same condition. The effect of side walls can be accounted for by the image technique. But this was not done in the present study because it called for much additional complications without adding significant insight.

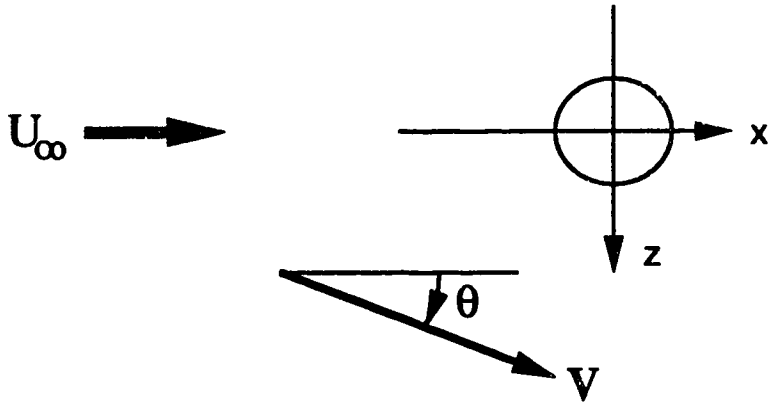

Figure B.1 Two-dimensional potential flow around a circular cylinder

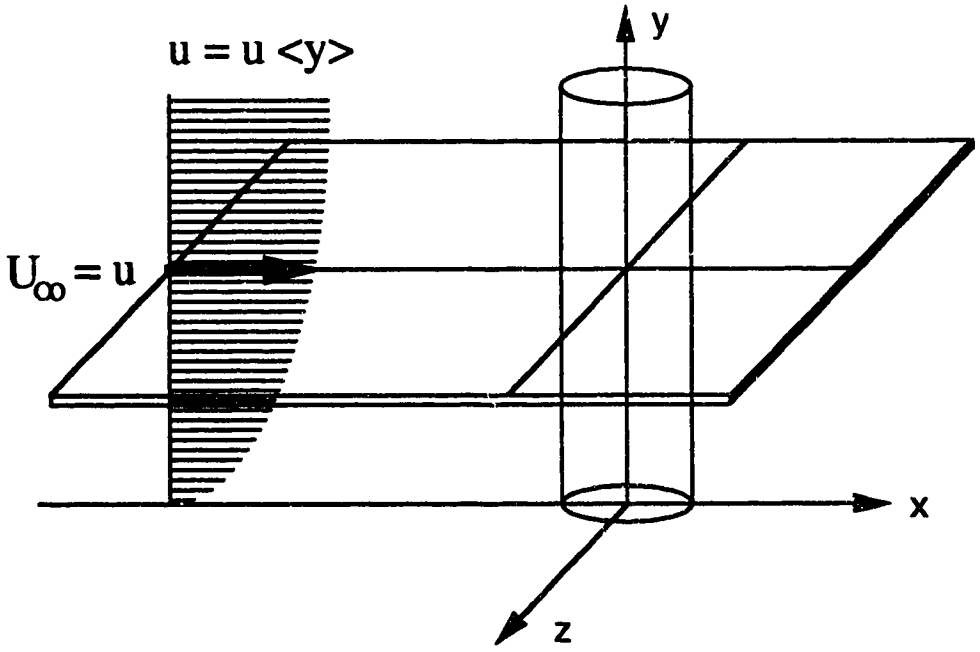

Figure B.2 Potential flow approximation of the flow